

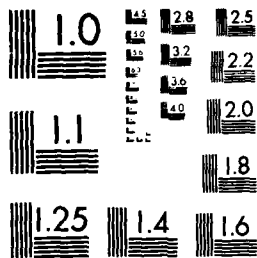
AD-A199 357

UNCLASSIFIED

AERODYNAMIC AND RELATED HYDRODYNAMIC STUDIES USING  
WATER FACILITIES (U) ADVISORY GROUP FOR AEROSPACE  
RESEARCH AND DEVELOPMENT NEUILLY-SUR-SEINE (FRANCE)  
JUN 87 AGARD-CP-413

1/3

ML



MICROCOPY RESOLUTION

AD-A199 357

②

AGARD-CP-413

AGARD-CP-413

# AGARD

ADVISORY GROUP FOR AEROSPACE RESEARCH & DEVELOPMENT

7 RUE ANCELLE 92200 NEUILLY SUR SEINE FRANCE

AGARD CONFERENCE PROCEEDINGS No.413

## Aerodynamic and Related Hydrodynamic Studies Using Water Facilities

\*Original contains color  
photos. All DTIC reproductions  
will be in black and  
white.

DTIC  
ELECTE  
S APR 14 1988 D  
H

NORTH ATLANTIC TREATY ORGANIZATION



DISTRIBUTION AND AVAILABILITY  
ON BACK COVER

DISTRIBUTION STATEMENT A

Approved for public release  
Distribution Unlimited

88 4 11 291

AGARD-CP-413

2

NORTH ATLANTIC TREATY ORGANIZATION  
ADVISORY GROUP FOR AEROSPACE RESEARCH AND DEVELOPMENT  
(ORGANISATION DU TRAITE DE L'ATLANTIQUE NORD)

AGARD Conference Proceedings No.413  
AERODYNAMIC AND RELATED HYDRODYNAMIC STUDIES  
USING WATER FACILITIES

DTIC  
ELECTE  
S APR 14 1988 D  
H

**DISTRIBUTION STATEMENT A**

Approved for public release;  
Distribution Unlimited

Papers presented and discussions held at the Symposium of the Fluid Dynamics Panel in Monterey,  
California, United States, 20-23 October 1986.



## THE MISSION OF AGARD

The mission of AGARD is to bring together the leading personalities of the NATO nations in the fields of science and technology relating to aerospace for the following purposes:

- Exchanging of scientific and technical information;
- Continuously stimulating advances in the aerospace sciences relevant to strengthening the common defence posture;
- Improving the co-operation among member nations in aerospace research and development;
- Providing scientific and technical advice and assistance to the Military Committee in the field of aerospace research and development (with particular regard to its military application);
- Rendering scientific and technical assistance, as requested, to other NATO bodies and to member nations in connection with research and development problems in the aerospace field;
- Providing assistance to member nations for the purpose of increasing their scientific and technical potential;
- Recommending effective ways for the member nations to use their research and development capabilities for the common benefit of the NATO community.

The highest authority within AGARD is the National Delegates Board consisting of officially appointed senior representatives from each member nation. The mission of AGARD is carried out through the Panels which are composed of experts appointed by the National Delegates, the Consultant and Exchange Programme and the Aerospace Applications Studies Programme. The results of AGARD work are reported to the member nations and the NATO Authorities through the AGARD series of publications of which this is one.

Participation in AGARD activities is by invitation only and is normally limited to citizens of the NATO nations.

The content of this publication has been reproduced  
directly from material supplied by AGARD or the authors.

Published June 1987

Copyright © AGARD 1987  
All Rights Reserved

ISBN 92-835-0419-4



*Printed by Specialised Printing Services Limited  
40 Chigwell Lane, Loughton, Essex IG10 3TZ*

## PREFACE

In recent years there has been an increasing use of water facilities for aerodynamic research and preliminary design. These include water tunnels, towing channels and stationary tanks and some special devices. The main thrust has been in the application of flow visualization techniques for recognizing and helping in the solution of difficult flow problems in both external and internal aerodynamics. Examples include flow fields of fighter airplanes; inlet flows; recirculating flow patterns in VTOL; ramjet simulation; etc. The difficult problems in such flows are usually connected with large regions of three dimensional flow in which vortices or separated regimes are prominent features.

Water is generally more effective than air for flow visualization because of its much lower diffusivity. There are a number of modern developments which will make water facilities even more effective and productive in the future both for flow visualization and for various quantitative measurements. These include laser-Doppler velocimetry, which is easier to use in water than in air; laser induced fluorescence; and computer aided particle tracking. These techniques are very well suited to the lower speeds and higher densities of water.

The Symposium recorded in these Proceedings was organized with the purpose of discussing experiences, results and future direction in the application of water facilities in aeronautical research and development. An exchange of experiences with the hydrodynamics community was also desired.

These objectives were largely achieved. The Symposium started with an overview of the uses of water facilities, in the paper by Erickson, Peake, Del Frate, Skow and Malcolm; continued with papers on various facilities, techniques, applications and results; and ended with an illuminating historical survey, by M.Tulin, of research on fluid resistance in ship hydrodynamics and its connections to aerodynamics.

\*\*\*

Depuis quelques années, on utilise de plus en plus fréquemment des installations hydrauliques pour la recherche en aérodynamique et les calculs préliminaires. Parmi ces installations, on compte les tunnels hydrodynamiques, les bassins d'essai des carènes et les réservoirs à eau stationnaire, ainsi que quelques dispositifs spéciaux. On constate en particulier l'application accrue des techniques de visualisation de l'écoulement qui permettent d'identifier et de faciliter la solution des problèmes difficiles d'écoulement, à la fois en aérodynamique externe et en aérodynamique interne, tels que les champs d'écoulement autour des avions de combat, l'écoulement d'entrée, les diagrammes de l'écoulement de recirculation lors des décollages et atterrissages verticaux, la simulation de statoréacteur, etc. Les problèmes posés par ces écoulements concernent généralement les vastes zones d'écoulement tri-dimensionnel caractérisées essentiellement par des tourbillons et des décollements d'écoulement.

L'eau est en général plus appropriée que l'air pour la visualisation de l'écoulement à cause du moindre coefficient de diffusion. Il existe un grand nombre de techniques modernes qui permettront à l'avenir de rendre encore plus rentables et plus productives les installations hydrauliques à la fois pour la visualisation, et pour différentes mesures quantitatives. Au nombre de ces méthodes figurent la vélocimétrie laser-Doppler qui est plus facile à appliquer dans l'eau que dans l'air, la fluorescence induite par laser, et le suivi de particules assisté par ordinateur. Ces techniques sont bien appropriées aux faibles vitesses et à la forte densité de l'eau.

Le Congrès qui a fait l'objet de ces comptes rendus a été organisé dans le but d'étudier les expériences et d'examiner des résultats et les orientations futures des applications des installations hydrauliques dans la recherche et le développement aéronautiques. Un échange de vues avec les hydrodynamiciens était aussi souhaité.

Ces objectifs ont été largement atteints. Le symposium a commencé par une vue d'ensemble des installations hydrauliques qui ont fait l'objet du rapport établi par Erickson, Peake, Del Frate, Skow et Malcolm; ensuite des rapports ont été présentés sur différentes installations techniques, applications et résultats; enfin M.Tulin a brossé un lumineux tableau historique des travaux de recherche effectués sur la résistance du fluide dans l'hydrodynamique des navires et ses relations avec l'aérodynamique.

\*Original contains color  
plates: All DTIC reproductions  
will be in black and  
white"



DTIC TAB		<input checked="" type="checkbox"/>
Unannounced		<input type="checkbox"/>
Justification		<input type="checkbox"/>
By _____		
Distribution/		
Availability Codes		
Dist	Avail. and/or	
	Special	
A-1		

#### AGARD FLUID DYNAMICS PANEL

Chairman: Dipl. Ing. P.W.Sacher  
Messerschmitt-Bölkow-Blohm GmbH  
LK 122  
Postfach 80 11 60  
D-8000 München 80  
Federal Republic of Germany

Deputy Chairman: Mr D.H.Peckham  
Superintendent AE1 Division  
Royal Aircraft Establishment  
R141 Building  
Farnborough Hants GU14 6TD  
UK

#### PROGRAMME COMMITTEE

Professor A.Roshko (Co-Chairman)  
Dept. of Aeronautics (MD 105-50)  
California Institute of Technology  
Pasadena  
California 91125, USA

Professor J.J.Ginoux  
Director  
Von Kármán Institute for Fluid Dynamics  
Chaussée de Waterloo 72  
B-1640 Rhode-Saint-Genèse, Belgium

Dr K.J.Orlik-Ruckemann  
National Aeronautics Establishment  
National Research Council, Montreal Rd  
Ottawa, Ontario K1A 0R6, Canada

M.G.Durand  
DRET/SDR/G61  
75996 Paris Arnières, France

Professor H.Hornung, Ph.D.  
DFVLR  
Institut für Experimentelle Strömungsmechanik  
Bunsenstrasse 10  
D-3406 Göttingen, Federal Republic of Germany

Dr Ing. G.Bucciantini  
Aeritalia-Società Aerospaziale Italiana  
Gruppo Velivoli Combattimento  
Corso Marche 41  
10146 Torino, Italy

Professor Dr It. J.A.Steketee  
Department of Aerospace Engineering  
Delft University of Technology  
Kluyverweg 1  
2629 HS Delft, The Netherlands

Professor L.N.Persen  
Institut of Mechanikk  
The University of Trondheim  
N-7034 Trondheim-NTH, Norway

Ir. J.W.Slooff (Co-Chairman)  
National Aerospace Laboratory, NLR  
Anthony Fokkerweg 2  
1059 CM Amsterdam, The Netherlands

Professor A.F. de O.Falcao  
Pavilhao de Maquinas  
Instituto Superior Tecnico  
1096 Lisboa Codes, Portugal

Major M.Akca  
Ministry of Defence (MSC)  
Department of R and D (ARGE)  
Ankara, Turkey

Mr P.R.Bignell  
BAe PLC, Sowerby Research Centre  
Naval Weapons Division  
FPC 067, P.O. Box 5  
Filton  
Bristol BS12 7QW, UK

Professor E.Reshotko  
Dept. of Mechanical & Aerospace Eng.  
Case Western Reserve University  
Cleveland  
Ohio 44106, USA

Dr F.H.Schmitz  
Chief, Fluid Mechanics Division  
Aeromechanics Laboratory  
US Army Research & Technology Lab. AVSCOM  
NASA Ames Research Center  
Moffett Field, CA 94035-1, USA

#### FLUID DYNAMICS PANEL EXECUTIVE

M.C.Fischer  
AGARD/NATO (Mail from Europe)  
7 rue Ancelle  
92200 Neuilly-sur-Seine  
France

AGARD/NATO (mail from US and Canada)  
APO New York 09777

# CONTENTS

	Page
PREFACE	iii
FLUID DYNAMICS PANEL	iv
 <u>SESSION 1 – FACILITIES AND APPLICATIONS – PART 1</u> Session Chairman: K.J.Orlik-Ruckemann	
WATER FACILITIES IN RETROSPECT AND PROSPECT – AN ILLUMINATING TOOL FOR VEHICLE DESIGN by G.E.Erickson, D.J.Peake, J.Del Frate, A.M.Skow and G.N.Malcolm	1
VORTEX BREAKDOWN AND CONTROL EXPERIMENTS IN THE AMES-DRYDEN WATER TUNNEL by F.K.Owen and D.J.Peake	2
QUALIFICATION D'UN TUNNEL HYDRODYNAMIQUE POUR DES PESEES DE MAQUETTES AERONAUTIQUES par B.Chezleprêtre et Y.Brocard	3
AN EXPERIMENTAL STUDY TO DETERMINE THE FLOW AND THE SUBSONIC STATIC AND DYNAMIC STABILITY CHARACTERISTICS OF AIRCRAFT OPERATING AT HIGH ANGLES-OF-ATTACK by A.Goodman and C.E.Brown	4
FLOW VISUALIZATION STUDY OF VORTEX MANIPULATION ON FIGHTER CONFIGURATIONS AT HIGH ANGLES OF ATTACK by G.N.Malcolm and A.M.Skow	5
 <u>SESSION 1 – FACILITIES AND APPLICATIONS – PART 2</u> Session Chairman: P.R.Bignell	
OSCILLATING FLOW OVER BLUFF BODIES IN A U-SHAPED WATER TUNNEL by T.Sarpkaya	6
THE USE OF THE NRC/NAE WATER FACILITIES IN CANADIAN AERONAUTICAL RESEARCH AND DEVELOPMENT by R.H.Wickens and N.E.Jeffreys	7
PRESENTATION D'UN BASSIN HYDRODYNAMIQUE – ETUDE D'UN MISSILE AUX GRANDES INCIDENCES par J.Perinelle et A.Lupieri	8
SHORT DURATION FLOW ESTABLISHMENT ON A PROFILE IN A WATER-LUDWIG-TUNNEL by W.Kerres and H.Grönig	9
EXPERIMENTAL INVESTIGATION OF HOVER FLOWFIELDS IN WATER AT THE McDONNELL DOUGLAS RESEARCH LABORATORIES by K.R.Saripalli, J.C.Kroutil and J.R.van Horn	10
AN INVESTIGATION ON DUCTED PROPELLERS IN AXISYMMETRIC SHEAR FLOW by J.A.C.Falcão de Campos	11
MEASUREMENTS OF AERODYNAMIC FORCES ON UNSTEADILY MOVING BLUFF PARACHUTE CANOPIES by D.J.Cockrell, R.J.Harwood and C.Q.Shen	12
WATER FLOW VISUALISATION OF A RAMROCKET COMBUSTION CHAMBER by P.J.Boszko and G.S.Owen	13

**SESSION II – TECHNIQUES AND APPLICATIONS – PART 1**

Session Chairman: E.Reshotko

POSSIBILITES D'ESSAI OFFERTES PAR LES TUNNELS HYDRODYNAMIQUES A VISUALISATION DE L'ONERA DANS LES DOMAINES AERONAUTIQUE ET NAVAL par H.Werlé	14
THE USE OF A WATER TOWING TANK FOR AERODYNAMIC TESTING AND METHODS FOR QUANTITATIVE EVALUATION OF PHOTOGRAPHS by H.Bippes	15
FLOW MEASUREMENTS IN A WATER TUNNEL USING A HOLOCINEMATOGRAPHIC VELOCIMETER by L.M.Weinstein and G.B.Beeler	16
ETUDE EXPERIMENTALE DE NAPPES TOURBILLONNAIRES EN ECOULEMENT PLAN par C.Berger, M.Bourgeois, G.Lavergne, C.Lempereur et J-M.Mathe	17

**SESSION II – TECHNIQUES AND APPLICATIONS – PART 2**

Session Chairman: H.Hornung

THREE-DIMENSIONAL FLOW VISUALIZATION USING LASER-SHEET SCANNING by D.M.Nosenchuck and M.K.Lynch	18
APPLICATION OF HIGH SPEED HOLOGRAPHY TO AERODYNAMIC AND HYDRODYNAMIC THREE-DIMENSIONAL VELOCIMETRY by M.Stanislas, O.Rodriguez, M.Dadi and F.Beluche	19
MATCHED INDEX LASER ANEMOMETRY SYSTEMS FOR FLOW STUDIES IN COMPLEX GEOMETRIES by A.Dybbs, R.V.Edwards and E.Reshotko	20
MESURES EN TUNNEL HYDRODYNAMIQUE PAR METHODE ELECTROCHIMIQUE par C.Tournier et P.Florent	21
FLOW VELOCITY MEASUREMENTS BY IMAGE PROCESSING OF OPTICALLY MODULATED TRACES by M.Gharib, B.Dyne, O.Thomas and C.Yap	22
A NON-INVASIVE EXPERIMENTAL TECHNIQUE FOR THE MEASUREMENT OF UNSTEADY VELOCITY AND VORTICITY FIELDS by L.Lourenco, A.Krothapalli, J.M.Buchlin and M.L.Riethmuller	23

**SESSION III – RESEARCH RESULTS**

Session Chairman: G.Bucciantini

USE OF WATER TOWING TANKS FOR AERODYNAMICS AND HYDRODYNAMICS by M.Gad-el-Hak	24
A NEW LAMINAR WATER TUNNEL TO STUDY THE TRANSITION PROCESS IN A BLASIUS LAYER AND IN A SEPARATION BUBBLE AND A NEW TOOL FOR INDUSTRIAL AERODYNAMICS AND HYDRODYNAMIC RESEARCH by M.Strunz and J.F.Speth	25
A COMPARATIVE STUDY OF VORTEX FLOWS IN WIND AND WATER TUNNELS by A.G.Davies	26
INVESTIGATION ON THE MOVEMENT OF VORTEX BURST POSITION WITH DYNAMICALLY CHANGING ANGLE OF ATTACK FOR A SCHEMATIC DELTA WING IN A WATER TUNNEL WITH CORRELATION TO SIMILAR STUDIES IN WIND TUNNEL by K.W.Wolffelt	27
SOME VISUALIZATION STUDIES ON TURBULENT BOUNDARY LAYERS USING MULTIWIRED HYDROGEN BUBBLE GENERATION by R.Blokland and K.Krishna Prasad	28

	Page
STRUCTURE OF UNSTEADY FLOWS AT LEADING- AND TRAILING-EDGES: FLOW VISUALIZATION AND ITS INTERPRETATION by D.Rockwell, R.Atta, L.Kramer, R.Lawson, D.Lusseyran, C.Magness, D.Sohn and T.Staubli	29
MEASUREMENTS OF THE TIME DEPENDENT VELOCITY FIELD SURROUNDING A MODEL PROPELLER IN UNIFORM WATER FLOW by J.Blaurock and G.Lammers	30
 <u>SESSION IV – MARINE RELATED TOPICS</u> Session Chairman: J.A.Steketee	
AERONAUTICS AND NAVAL HYDRODYNAMICS – CONNECTIONS by M.P.Tulin	31
Paper 32 withdrawn	
EXPERIMENTS TO INVESTIGATE THE VORTICES SHED FROM A SUBMARINE-LIKE BODY OF REVOLUTION by A.R.J.M.Lloyd and I.M.C.Campbell	33
A REVIEW OF THE NATO SPECIAL GROUP OF EXPERTS ON NAVAL HYDROMECHANICS AND RELATED PROBLEMS by J.Charlesworth and L.J.Leggat	34
ROUND TABLE DISCUSSION	RTD

# WATER FACILITIES IN RETROSPECT AND PROSPECT-- AN ILLUMINATING TOOL FOR VEHICLE DESIGN

Gary E. Erickson, David J. Peake, and John Del Frate  
NASA Ames Research Center  
Moffett Field, California 94035  
USA

and

Andrew M. Skow and Gerald N. Malcolm  
Eidetics International  
Torrance, California 90505  
USA

## SUMMARY

Water facilities play a fundamental role in the design of air, ground, and marine vehicles by providing a qualitative, and sometimes quantitative, description of complex flow phenomena. Water tunnels, channels, and tow tanks used as flow-diagnostic tools have experienced a renaissance in recent years in response to the increased complexity of designs suitable for advanced technology vehicles. These vehicles are frequently characterized by large regions of steady and unsteady three-dimensional flow separation and ensuing vortical flows. The visualization and interpretation of the complicated fluid motions about isolated vehicle components and complete configurations in a time- and cost-effective manner in hydrodynamic test facilities is a key element in the development of flow control concepts and, hence, improved vehicle designs.

This paper presents a historical perspective of the role of water facilities in the vehicle design process. The application of water facilities to specific aerodynamic and hydrodynamic flow problems is discussed, and the strengths and limitations of these important experimental tools are emphasized.

## 1. INTRODUCTION

The successful development of vehicles suitable for aerodynamic and hydrodynamic applications requires an understanding of the configuration flow field at design and off-design conditions. Water facilities (tunnels, channels, and tow tanks) have historically provided valuable information on the fundamental fluid mechanics of two-dimensional (2-D) and three-dimensional (3-D) aerodynamic and hydrodynamic shapes operating at low speeds. The application of hydrodynamic facilities to basic aerodynamic research problems that was pioneered by Ludwig Prandtl in the early days of flight continues to the present day. The advent of high-performance flight vehicles that incorporate flow separation by design has promoted a surge of interest in water facilities as a diagnostic tool. The utilization of water tunnels, channels, and tow tanks to visualize the 3-D separated and vortical flow fields about advanced, highly swept, military aircraft and slender missile configurations operating at extreme attitudes (angles of attack and sideslip) has been demonstrated by many researchers. The increased level of confidence attained by correlating study results with aerodynamic facility and flight results has led to a substantial increase in the applications of relatively simple water facilities to the complex aerodynamic and hydrodynamic shapes of interest for present- and future-generation vehicles. Concurrently, flow visualization and nonintrusive measurement techniques have been developed, modified, and implemented to provide qualitative and quantitative information on the steady and unsteady flow fields about isolated vehicle components and complete configurations. In general, the use of hydrodynamic facilities has risen in direct proportion to the advancement of air, ground, and marine vehicle technologies. As a consequence, water facilities are now an important element in the design process, yielding insight into the complicated vortical fluid mechanisms and structures that are characteristic of flows about advanced-technology vehicles.

The visualization of a flow phenomenon represents a major advancement toward understanding and, subsequently, controlling the fluid mechanism. Flow visualization is easily performed in water and, as a consequence, aerodynamic as well as hydrodynamic problems have long been studied in water facilities. The flow properties of water are similar to those in air, provided the flow simulations are restricted to the incompressible regime. The selection of water as a flow-visualization medium is largely based on the 800-fold increase in the density relative to air and, consequently, the excellent light-reflecting characteristics of tracers injected into the flow field. Suitable illumination of the tracer particles (aluminum powder, dye, or hydrogen bubbles, for example) provides direct visualization of steady and unsteady flows. At the same scale and speed, the Reynolds number is 15 times greater in water than in air. However, cost, complexity, and facility space are factors that constrain the test section size; hence, the model scale is generally relatively small. In addition, the fluid velocities are typically less than 10 ft/sec in order to preserve the clarity of the flow structure, to avoid excessive model loads, and to preclude cavitation when it is an undesired phenomenon. The combination of small model scale and low fluid velocities results in Reynolds numbers that are orders of magnitude less than those achievable on larger-scale models in wind tunnels or on full-scale air, ground, and marine vehicles operating in their respective environments. As a consequence of this Reynolds number mismatch, the fluid motion under

consideration must be the kind that is insensitive to changes in the Reynolds number. At the least, the fundamental structure of the flow must be similar, regardless of the Reynolds number. It is fortunate that many of the complex flow phenomena, particularly 3-D motions with vortices or predominantly separated regimes, associated with advanced-technology vehicles, lend themselves to qualitative (and sometimes quantitative) evaluation in these facilities. The interpretation and application of the results obtained in water tunnels, channels, and towing tanks at low Reynolds numbers are topics of considerable debate in the technical community. This meeting is both timely and useful as it provides a forum for the discussion of the strengths and limitations of hydrodynamic test facilities applied to flow problems in aeronautical and maritime fluid dynamics.

Section 2 of this paper will present a historical review of water facilities. Because of the large number of water facilities that have been in operation over the years and that remain in operation today, the discussion will center on representative facilities. The applications of water facilities to vehicle design, encompassing the interests of the various sessions of this meeting, are discussed in Section 3. Of necessity, only the flavor of the myriad basic and applied aerodynamic and related hydrodynamic studies will be provided to demonstrate the utility and current potential of water facilities.

## 2. HISTORICAL PERSPECTIVE

### 2.1 From Antiquity to the Renaissance

The visualization of complex flow phenomena in a water medium spans millennia. Observations and speculations on vortical flows in nature go back to prehistoric times (Ref. 1). Stone Age artifacts depicted the spiral motions that were frequently observed in a water medium. Over 2,000 years ago, the writings of Aristotle (384-322 B.C.) described the observations of whirlpools at sea and the resultant loss of ships caught in this powerful fluid motion (Ref. 1). Von Karman (Ref. 2) wrote of an early painting in Bologna, Italy, of St. Christopher walking through a flowing stream that showed alternating vortices, or Karman "vortex streets," behind the saint's foot. In the centuries to follow, the nonscientific observations of flows in water persisted.

The earliest documentation of flow mechanisms in water for scientific purposes appears to be in the writings and elaborate drawings of Leonardo da Vinci (1452-1519) (Ref. 3). As pointed out by Lugt (Ref. 1), Leonardo's artistic descriptions of nature single out a particular phenomenon, such as a vortex, from a global flow field and are, therefore, in common with scientific experiment. Examples of his fluid flow sketches are shown in Fig. 1 taken from Ref. 1. Leonardo frequently discussed the similarity of fluid motions in water and air. According to the account of Truesdell (Ref. 4), such a conclusion could come only from direct observation of the fluid motions in both media. In fact, Leonardo was the first to discuss water and air as fluids, and he designed the first water tunnel flow-visualization facility as shown in Fig. 2 (from Ref. 5). Leonardo also recognized the limitations of simulations of airflow in a water medium due to the effects of compressibility.

### 2.2 From 1600 to 1800

A century after Leonardo's passing, Sir Isaac Newton (1642-1727) claimed that his so-called "sine-square law of air resistance" applied as well to water, where the forces were proportional to the respective densities (Ref. 2). Newton's statement was noteworthy in that it promoted the application of experimental results in water to motion in air and vice versa. Newton's influence was present in the experiment of Edme Mariotte (1670-1684), who measured the force acting on a flat plate submerged in a stream of water. Jean Charles de Borda (1733-1799) performed experiments in a water facility using bodies of various shapes, which were put in motion by means of a rotating, or whirling, arm. Jean Le Rond d'Alembert (1717-1783), Antoine Condorcet (1743-1794), and Charles Bossut (1730-1814) towed ship models in still water (see Ref. 2). These investigations represented perhaps the first application of the towing-tank technique that is so prevalent today. In 1780, J. C. Wilke used a water facility to study atmospheric vortices (Ref. 1).

### 2.3 From 1800 to 1900

Sporadic experiments using water as the working fluid continued into the 19th century. In 1839, Hagen (Ref. 6) conducted studies of water flowing through cylindrical tubes, where he observed the transition from laminar to turbulent flow. Hagen subsequently conducted more detailed testing of flow stability in tubes and documented his results in 1854 (Ref. 7). In 1883, Osborne Reynolds conducted his classic experiments (Ref. 8) in which he demonstrated that flow transition occurred when a parameter, now called the Reynolds number, exceeded a certain value. His flow-visualization results were documented by sketches rather than photographs. Interestingly, Reynolds' experiments were repeated nearly 100 years later in his original apparatus at the University of Manchester and representative results are documented by Van Dyke (Ref. 9). In 1897, Hele Shaw performed experiments (Ref. 10) in a thin tank to study 2-D highly-viscous flows. The experiments of researchers spanning four centuries, starting with the work of Leonardo, contributed to the development of new flow-visualization facilities and techniques which led to major advances in fluid mechanics.



## 2.4 From 1900 to 1935

The utilization of water facilities as tools to study a wide range of fundamental aerodynamic and hydrodynamic problems was pioneered by Ludwig Prandtl in Germany beginning in the early 1900s. Prandtl conducted experiments on 2-D shapes in a water channel where the flow was visualized on the free surface using aluminum powder. His flow-visualization method was first documented in 1904 in Ref. 11. A compilation of Prandtl's 2-D flow-visualization results obtained at the Kaiser Wilhelm Institute (KWI) for Flow Research in Göttingen, Germany was provided by Prandtl and Tietjens (Ref. 12) in 1934. His studies included (1) the propagation of turbulence in boundary layers, (2) vortex shedding downstream of a plate, (3) vortex development behind a nonrotating cylinder and the development of Karman vortices, (4) laminar and turbulent boundary layers, (5) flow development around a rotating cylinder, (6) starting vortex generated by an airfoil, (7) flow in a diffuser with and without suction at the walls, and (8) cavitation phenomena. Examples of Prandtl's results are shown in Fig. 3 (from Ref. 12). The advancement of fluid mechanics through the use of a water facility and the intuitiveness of the experimenter is exemplified by item (3) above. Karl Hiemenz, a student of Prandtl, built a water channel in 1911 to observe the flow separation behind a cylinder. The oscillatory vortex shedding that he observed was unexpected and the phenomenon was at first attributed to model and tunnel wall asymmetries. The flow situation was always repeatable, however, despite careful checks of the model and test facility. This attracted the attention of von Karman (Ref. 2) who speculated that there may be a natural and intrinsic reason for the phenomenon. He calculated the stability of such a system of vortices, which led to the understanding of the now-famous Karman "vortex street."

The efforts of Prandtl and his colleagues confirmed that, under certain conditions, the flow patterns in the vicinity of a body are similar in air, water, or other liquid or gaseous fluids. On this basis, Prandtl demonstrated that the fluid dynamic characteristics of a body exposed to a flow in one medium could be predicted from experiments in a different medium. Prandtl's work overlapped the development of flight vehicles for military and commercial applications, and airplane wings were, accordingly, investigated in hydrodynamic facilities. It is noted that hydrodynamic can refer to incompressible flow characteristics in any fluid, including air at low Mach numbers. Since the practical design of aircraft did not seriously account for compressibility during the first 20-30 years of its history because of the low flight speeds, water facilities were applied to flight-vehicle design, albeit on a limited basis.

From approximately 1910 to 1935 the majority of water-facility investigations of aerodynamic flow problems were of a 2-D nature and emphasized the boundary-layer behavior and flow-separation characteristics of airfoil shapes suitable for the relatively unswept wings of this period. The KWI in Göttingen, Germany, maintained its role as a leader in the study of laminar and turbulent boundary layers and the drag of aerodynamic shapes (Ref. 12). More frequently, however, water channel facilities were employed for hydrodynamic flow problems relating to cavitation phenomena and the resistance of surface ships and submersibles. Hoerner (Ref. 13) provides an extensive list of references of water tunnel, channel, and towing-tank investigations of marine vehicles conducted during this period.

## 2.5 From 1935 to 1950

The contributions of water facilities to vehicle design increased during the period 1935-1950, largely because of the global political climate that would lead to World War II and the ensuing demands for military air and sea superiority. The water facilities in Göttingen were used by the German aircraft industry to improve the design of propeller and jet aircraft during World War II. Reichardt (Ref. 14) described the results of hydrodynamic tests to develop efficient low-speed aerodynamic shapes using a cavitation method. The basis of this study was that gaseous flows at sonic speed had a certain resemblance to fluid motions at cavitation. The test models were streamlined in the water tunnel to delay cavitation onset. The resultant shapes provided a rough approximation of the desired geometries in air that would exhibit delayed onset of locally sonic flow on the surface. The nacelles, nacelle-wing fairing, and wing-body transition on the Me 262 were modified in this manner. The Germans also utilized a water facility to aid in the development of marine vehicles. An advanced submarine type "XXI" was developed, in part, from towing-tank investigations (Ref. 13). The test results led to a hull having a continuous shape, a streamlined conning tower, and guns integrated into the tower.

The Allies also used water facilities during World War II for the improved design of marine and flight vehicles. Notable water tunnel, channel, and towing-tank facilities were located at the National Physical Laboratory (NPL) and Admiralty Research Laboratory (ARL) in England and at the California Institute of Technology (CalTech), National Advisory Committee for Aeronautics (NACA), and David Taylor Model Basin (DTMB) in the United States. The majority of water facility applications to vehicle design during this period pertained to marine craft. Typical studies in these facilities addressed the cavitation phenomena associated with ship propellers and hydrofoils (ship rudders and submarine planes, for example) and the drag/resistance of hydrofoils, displacement hulls, submersibles, torpedoes, surface-piercing struts, seaplane floats/skis, and planing craft (Ref. 13). Hydrodynamic problems that were addressed and solved in water facilities included that of submarine periscope vibration, associated with periodic vortex shedding; this problem was alleviated by means of guidevanes. The reduction of missile drag at water entry was achieved by improved nose shapes developed from water-facility testing (Ref. 13). A parametric study of the flow separation characteristics of projectiles having various forebody and afterbody shapes and fin arrangements was performed in 1944 by Knapp (Ref. 15) in the CalTech High Speed Water Tunnel. The detailed flow-field observations from this study were intended to aid the projectile and bomb designers during the latter stages of the war. Aircraft wings were still relatively

unswept and of high aspect ratio. As a consequence, airfoils were generally tested, and the results were corrected for 3-D effects.

A common problem was manifested in the experimental investigations of marine and flight vehicles during this period, namely, how to transfer the model results to full-scale operation. The limited dimensions and flow speeds of water tunnel, channel, and towing-tank installations generally resulted in Reynolds numbers in model testing that were typically two to three orders of magnitude less than those of the full-scale operation. For example, the drag of displacement hulls consisted of two predominant components, skin friction and wave resistance, that were governed by different similarity laws. Unless full-scale dimensions were used, it was not possible to simulate correctly the full-scale conditions in towing tanks. It became common practice, then, to satisfy the dynamic similarity (Froude number), producing the proper wave pattern, and to correct the skin-friction component on the basis of the Reynolds number. The Reynolds number could be increased by heating the water. However, the disparity between model- and full-scale conditions was still large. The scaling of cavitation phenomena observed in water-facility testing of ship propellers and hydrofoils was a persistent challenge, particularly under conditions of incipient and fully developed cavitation.

The introduction of jet-powered aircraft toward the end of World War II and the ensuing emphasis on high-speed flight posed particular problems for water-facility simulations owing to the significant Reynolds number gap and the effects of compressibility (Mach number). Operation of water facilities at higher speeds resulted in undesired cavitation phenomena that restricted the speed up to which a flow pattern in water could be expected to represent that around the same shape in air. Cavitation could occur within the fluid at some distance from the model surface, in the cores of vortices from aircraft propeller blade tips or in the separated flow past blunt or bluff bodies, for example, which precluded the correlation of the water-facility data to the conditions in air. Closed-section facilities could be pressurized to delay cavitation onset; however, this was done at increased facility complexity and cost. As a result of these considerations, constraints were necessarily imposed on the use of water facilities as a design tool, particularly with regard to flight vehicles.

## 2.5 From 1950 to 1960

The work of German researchers during World War II and of R. T. Jones in the United States during the same period led to wing sweep as a means of delaying transonic flow effects (see Ref. 2). The fluid mechanics associated with these wings was not well-understood owing to the 3-D nature of the flow. At off-design conditions, the swept separation lines and ensuing vortices were important features of the 3-D flow field. The early 1950s also marked the advent of first-generation supersonic transport (SST) aircraft featuring thin, slender wings. By design, the configurations utilized leading-edge vortex-induced lift for improved takeoff and landing performance. This was a significant departure from the time-honored attached-flow wing designs.

The complexity of the wing vortical flow field and the associated aerodynamic nonlinearities were demonstrated in the late 1940s and early 1950s by researchers in England, France, the United States, Canada, and Sweden (Refs. 16-20, for example). These experimental investigations underscored the need for a flow-visualization tool in order to understand and control the powerful fluid motions. The early studies suggested that once flow separation occurred everywhere along the leading edge of a swept wing, the fundamental character of the vortex was insensitive to the Reynolds number (Ref. 21). The vortex flow structure also remained much the same over a wide range of the Mach number (Ref. 22), provided the wing leading edge was swept within the Mach cone and shock waves did not interact with the vortices. A new era of water-facility applications to aircraft design therefore emerged and was characterized by extensive testing of slender wings suitable for commercial and military aircraft configurations with a requirement for supersonic operation.

The principal advocates of water-facility applications to air-vehicle design in the 1950s included the NPL in England, the Office National d'Etudes et de Recherches Aéronautiques (ONERA) in France, the National Aeronautical Establishment (NAE) in Canada, the NACA and Caltech in the United States, and Kungl Tekniska Högskolan (KTH) in Sweden. The pump-driven horizontal water tunnels at the NPL and NAE, the vertical water tunnel at ONERA operating by gravity discharge, the towing tank at the NACA, the free-surface water channel and pressurized high-speed water tunnel at Caltech, and the water tank at the KTH represented several different facility designs that were used for a common purpose, namely, to develop a flow-visualization data base on aircraft and aircraft-related configurations. The clarity of the flow visualization from experiments conducted in these installations established water facilities as a useful diagnostic tool to study the flow about 3-D aerodynamic shapes operating within an expanded flight envelope. For example, the water tunnels at the NPL and ONERA contributed to the understanding of the controlled flow separations and vortical motions on the SST Concorde developed jointly by the English and the French. The water tank at the KTH was utilized in Sweden's pioneering studies of canard-wing aircraft. The water tunnel at the NAE deserves special note owing to its colorful history. The facility was built at the Aerodynamische Versuchsanstalt in 1939 in Göttingen, Germany, and, subsequently, was shipped to Canada after World War II (Ref. 23). One of the early investigations conducted at the NAE was related to the design of cockpit canopy shapes for the CF-100 and CF-103 aircraft by generating a cavitation bubble whose shape conformed to the constant-pressure contour (Ref. 24). This experimental approach was similar to Reichardt's (Ref. 14), whose work in Germany was discussed earlier. An undocumented study was performed of the lateral instability caused by asymmetric breakdown of wing leading-edge vortices. This subject remains of great interest to modern-day fighter aircraft configurations. The NAE facility was

also utilized to study the effects of the exhaust from jet-powered aircraft on the flow about tail surfaces.

Water facilities maintained their role in the marine-vehicle design process in the post-World War II years. Major contributions to the design of surface ships, submarines, and marine propulsion systems were made by researchers in many countries. Primary contributors to marine vehicle technology included the NACA, DTMB, Iowa Institute of Hydraulic Research, St. Anthony Falls Hydraulic Laboratory (University of Minnesota), and CalTech in the United States; the Ship Model Basin in the Netherlands; the Supramar company in Switzerland; and the State Shipbuilding in Sweden. Reference 25 lists many of the research installations involved in maritime testing during this period. An upsurge in the use of hydrofoil craft began in the late 1950s. As noted by Acosta (Ref. 26), the successful achievements of hydrofoil craft and the possibility of high speeds at sea were due to the greatly increased understanding of the flow past hydrofoils. In a manner similar to the field of aeronautics, water facilities played a key role in the advancement of hydrofoil technology.

## 2.7 From 1960 to 1970

Numerous slender-wing aircraft configurations emerged during the 1960s that were characterized by leading-edge vortex formation at off-design conditions. These aircraft included the F-111, YF-12, and XB-70 in the United States; the Mirage III and IV in France; the HP-115 experimental aircraft in England; the Concorde in a joint English/French effort; and the Viggen in Sweden. In addition, the design of highly maneuverable transonic fighter aircraft began during this period in the United States, and this work would culminate in the F-16 and F-18 fighters in the 1970s. From the outset, these designs employed wing-body strakes or leading-edge extensions (LEXes) to generate concentrated vortices for enhanced lift at takeoff and landing and at subsonic/transonic maneuvering conditions.

The water tunnels at the NPL in England, ONERA in France, and NAE in Canada continued to be utilized successfully in the study of slender-wing vortices. A copy of the NPL tunnel was built at the University of Southampton, England, and static and dynamic testing of slender-wing vortex flows was performed (Ref. 27). Excellent correlations were obtained by Werlé (Ref. 28) at ONERA of the vortex behavior on delta wings and specific aircraft configurations such as the Concorde and the Douglas F-5D (Ref. 29) in water tunnels, wind tunnels, and flight. These results established confidence that, for the special case of leading-edge vortices on thin, highly swept surfaces, water facilities could be used as a diagnostic tool despite the Reynolds number gap. ONERA assembled a laboratory consisting of two vertical water tunnels and a water tank that was dedicated to the study of aerodynamic and hydrodynamic flow phenomena. The French were at the forefront of flow-visualization technology and they applied water facilities to a wide range of aerodynamic flow situations. These included laminar and turbulent boundary layers, boundary-layer separation on 2-D and 3-D shapes, vortex-dominated flows on slender bodies and wings, jet mixing and interaction phenomena, blowing for boundary-layer control, vortex enhancement by spanwise blowing, ground effects on the flow about the Concorde using a moving ground board, models with internal flows (engine intakes, for example), and a helicopter rotor in translation and hover (Ref. 30). The ONERA laboratory became the standard of excellence in flow visualization and was the forebearer of numerous other water facilities throughout the world.

The NAE water tunnel was a consistent source of useful flow-field information on complex flow phenomena in the 1960s. The 3-D separated flow-characteristics about numerous aerodynamic shapes were investigated. The circulation-control concept for enhanced, high-lift aerodynamics was studied on round airfoils, flaps, etc. Other experiments featured lifting propellers at high angles of inclination, ducted fans, and fan-in-wing arrangements. The wing-submerged lifting-fan investigations were indicative of the increased sophistication of water-facility experiments of aircraft models and of the information gained from these studies. In this case, the fan-airfoil interactions and wing-fan efflux interactions were observed in order to assess the flow effects leading to changes in the configuration forces and moments.

The heavy commercial and military transport aircraft that appeared during this period generated powerful trailing vortex systems that posed a flight safety hazard to trailing aircraft. Water towing-tank facilities were well suited to study the vortex patterns and methods of wake alleviation, and the National Aeronautics and Space Administration (NASA), the Douglas Aircraft Company, and the Lockheed-Georgia Company in the United States employed such facilities for this purpose. The NAE conducted water tunnel experiments of the vortex flows shed from upswept rear fuselages similar to those of rear-loading aircraft. The vortices were found to promote adverse effects on the pitch stability and cruise drag and to produce undesirable loadings on rear cargo doors (Ref. 31).

## 2.8 From 1970 to 1980

Vehicle designers in the 1970s were once again confronted with a large experimental data gap caused by the emerging requirement for advanced tactical missile and fighter aircraft configurations to operate in a controlled manner at extreme attitudes. The vortex-dominated flows shed from the slender bodies and wings of highly maneuverable flight vehicles were not well understood. The flow-visualization and flow-measurement techniques in wind tunnels and in flight were inadequate for the detailed definition of the highly 3-D flow fields that were often characterized by multiple vortex development, vortex interactions, and vortex breakdown. As a consequence, the 1970s marked a significant upsurge in the use of water facilities in the vehicle design process.

To improve the understanding of the structure of vortex core breakdown, experiments were conducted by Sarpkaya in the United States using a water facility (Ref. 32). Water to which swirl was imparted by upstream vanes flowed through a slightly divergent tube and the forms of vortex bursting were observed. The experimental results also supported the development of computational methods to predict vortex core instabilities.

Water tunnels, channels, and towing tanks were in operation in many countries, and studies in support of vehicle design were performed in the United States, Canada, France, England, Belgium, Germany, Switzerland, the Netherlands, Sweden, Russia, Australia, Japan, and China. The confidence in water facilities as a flow-diagnostic tool was reflected by the diversity of research subjects encompassing air, ground, and marine vehicles.

A leader in the application of water tunnels to the simulation of fighter aircraft flow fields at high angles of attack was Northrop Corporation in the United States. Influenced in large part by the work of Werlé (ONERA) in France, M. S. Cahn and G. R. Hall led the effort at Northrop in the mid-1970s to develop a water facility that would augment the aircraft design process (Ref. 33). An early application of a small pilot tunnel modeled after the ONERA gravity-discharge facility was the visualization of the LEX vortex flows on a small-scale model of the Northrop YF-17 lightweight fighter configuration. The vivid definition of the YF-17 vortical flows stimulated sufficient support to construct a larger water tunnel that is still in operation today. This facility was used extensively in all of the military aircraft programs at Northrop to understand and control the forebody and wing vortex flows, vortex interactions and breakdown, and vortex-empennage interactions. Models of virtually every fighter aircraft in the United States inventory and of numerous foreign military aircraft configurations were tested in the Northrop installation. The role of this tunnel rapidly expanded to include the study of 2-D nozzle exhaust effects on afterbody flow separation, nozzle exhaust plumes and jet mixing processes, forebody and wing vortex control by active and passive means, hot-gas reingestion phenomena on V/STOL aircraft in ground proximity, vortex flow management for improved performance of top-mounted inlets, thrust reverser plume trajectories and the effects on wing and tail flow fields, the structure of swirling jets, self-induced lateral oscillations (wing rock) of slender planforms, deflected wing leading- and trailing-edge flap effects on vortex stability, oscillating wing control surfaces for flow control, vortex shedding on an aircraft model in a flat spin, and canard-wing, forward-swept wing, and oblique wing flow fields (Ref. 34).

ONERA in France and the NAE in Canada continued to excel in their high-quality and diverse applications of water facilities to vehicle design. The confidence gained from years of experience in hydrodynamic testing led to the use of the ONERA and NAE facilities to study ground vehicle configurations such as high-speed trains, trucks, automobiles, and snowmobiles. The water facilities were used to identify regions of 3-D flow separation and to develop aerodynamic "fixes" to improve the vehicle performance. Marine vehicle investigations were also undertaken in these tunnels to study the separated flow fields about the superstructure of surface ships and highly maneuverable submarines. The trend toward high-performance air, ground, and marine vehicles facilitated the acceptance of water facilities as a design tool, owing to the complicated fluid motions that were often vortex-dominated.

The French and Canadians were leaders in the investigation of unsteady vortical motions. The ONERA installation was utilized to study the vortex formation on the upper surface of an oscillating profile, which simulated the cyclic variation in pitch of a helicopter rotor blade (Ref. 30). In addition, the vortex-shedding characteristics of a spinning fighter model were investigated. The NAE performed forced oscillation testing of a modern aircraft configuration to identify the effects of the body vortices on the static and dynamic cross derivatives (Ref. 35).

Interest in the unsteady aerodynamics of helicopter rotor blades led to numerous investigations of the dynamic stall behavior of oscillating airfoils (Ref. 36) at the U.S. Army Research and Technology Laboratories (AVRADCOM) at NASA Ames Research Center. A unique feature of the water tunnel experiments was the measurement of the force and moment time histories in combination with vivid off-body flow visualization.

The Flow Research Company towing tank and the Tracor Hydronautics Ship Model Basin in the United States emerged as important water facilities for aerodynamic flow simulations. The Flow Research facility was used in the general research of unsteady aerodynamics; separated flows; and laminar, transitional, and turbulent boundary layers. The Tracor model basin was used extensively by NASA for measurements of the trailing vortex systems generated by models of wide-body commercial transport aircraft such as the Boeing 747.

The continued interest in V/STOL aircraft prompted the development of water facilities at Rockwell International (Ref. 37) and the McDonnell-Douglas Corporation (Ref. 38). These were dedicated to the visualization of ground-effect phenomena associated with multijet arrangements.

The U.S. Air Force Wright Aeronautical Laboratories (AFWAL) constructed a small water tunnel operating by gravity discharge. This facility proved useful in visualizing the vortex flows about advanced fighter models, including several forward-swept-wing configurations.

Water facilities also experienced a renaissance in the European government, industry, and university communities. The towing tank at Deutsche Forschungs- und Versuchsanstalt für Luft- und Raumfahrt (DFVLR) in Göttingen, Germany, was applied to the study of wing leading-edge vortices (Ref. 39). A water tunnel

built at Messerschmitt-Bölkow-Blohm (MBB) in Munich, Germany, became a useful aid in recognizing and solving flow problems during the aircraft development phase (Refs. 40 and 41). The University of Stuttgart, with a history of water facility experience dating back to 1950, continued its fundamental fluid mechanics research. The behavior of slender missile vortices at extreme attitudes was investigated in a water tunnel at the British Aerospace Military Aircraft Division (Ref. 42). A study of the Reynolds number sensitivity of delta wing vortex breakdown was performed in a water tunnel by Svenska Aeroplan Aktiebolaget (SAAB) in Sweden (Ref. 43). Leading-edge vortex flow studies were also conducted in a water facility at the von Karman Institute (VKI) in Belgium (Ref. 44). The Netherlands Ship Model Basin maintained a leadership role in hydrodynamic testing of displacement hulls and marine propulsion systems.

The Aeronautical Research Laboratories (ARL) of the Australian Department of Defence conducted systematic experiments of vortex flows in the mid-1970s using water towing tank and water tunnel installations. The trailing-vortex system generated by a rectangular planform wing was investigated in the towing tank and the experimental trends pertaining to the vortex structure and dissipation were in qualitative agreement with available wind tunnel and flight test results (Ref. 45). The structure and breakdown of the leading-edge vortices shed from slender delta and cranked wing planforms were observed in the water tunnel (Ref. 46).

## 2.9 From 1980 to the Present

Water facilities have gained general acceptance throughout the world as valuable diagnostic tools to aid in the vehicle design process. The unique ability of these installations to visualize 3-D vortical motions about complicated aerodynamic and hydrodynamic shapes has been utilized in vehicle development programs in several countries. Vortical flows have become a "way of life" on all classes of vehicles as shown in the sketches in Fig. 4 (from Ref. 1). The emphasis on low-observable flight vehicles has led to aerodynamic shapes that are dominated by vortex flows. Clearly, the identification and control of these 3-D separated regimes is an important element in air, ground, and marine vehicle performance optimization.

The sophistication of water facilities and flow visualization and measurement techniques has increased in concert with the advancement in vehicle technology. In addition to the qualitative information gained from water-flow experiments, efforts are now under way to extract more quantitative data than previously possible. As indicated by Gad-el-Hak (Ref. 47), the advent of advanced computers capable of handling high-resolution images has made it possible to combine flow-visualization and digital-image processing techniques to obtain quantitative information. Lasers have become a key element in many water facility installations. Quantitative flow-field information has been obtained in recent water-flow experiments of vortical motions using 2-D laser velocimetry (Ref. 48). Laser optics have also been used to generate an intense sheet of light to enhance the visualization of the flow structure in arbitrary planes (Ref. 49). A laser-induced fluorescence visualization technique can provide more detailed information on the structure of complex flows (Ref. 50). The interest in unsteady aerodynamics has led to more sophisticated model support apparatus and instrumented models.

The water facility "standard bearers" of the 1970s continue to make major contributions in this decade to the understanding and control of the flow about advanced vehicles. In recent years, emphasis at Northrop has been placed on the establishment of a flow visualization data base on present- and future-generation fighter aircraft configurations that are characterized by highly coupled forebody and wing vortex systems at extreme attitudes (see Ref. 51). ONERA in France and the NAE in Canada continue a long-standing tradition of excellence in water facility applications to air, ground, and marine vehicle design (Refs. 52 and 53, respectively).

Several water-facility installations in the United States have assumed leadership positions in aeronautical and related hydrodynamic research in recent years. The water tunnel at NASA Ames-Dryden Flight Research Facility, modeled after the Northrop tunnel, has become a "workhorse" for NASA since its inception in the early 1980s. Considerable work has been done in cooperation with industry, universities, and other U.S. government agencies to increase the experimental data base on advanced military aircraft configurations. The Flow Research Company towing tank has most recently been used in support of the Air Force supermaneuverability program to study the unsteady aerodynamics of slender wings and bodies undergoing pitching oscillations (Refs. 54 and 55). The Tracor model basin was used to simulate the pitch-up maneuvers of a slender generic fighter model (Ref. 56).

Several other organizations have recently acquired water tunnels. NASA's Langley Research Center constructed a facility with a vertical test section similar to the NASA Ames-Dryden tunnel and is initiating a number of projects to support their aeronautics research programs. The success of the pilot water tunnel at AFWAL at Wright-Patterson Air Force Base has led to the installation of a larger ONERA-type water tunnel with a vertical 24- by 24-in. test section. This tunnel is undergoing operational checkout tests and is expected to be in use as a research facility in November 1986. Eidetics International has completed a new water tunnel/channel with a 15- by 20-in. horizontal test section incorporating a unique downstream viewing window to permit flow visualization in the cross-flow plane as well as the usual planform and side views. A larger version of the same tunnel with 24- by 36-in. test section is also under construction and is intended primarily to provide a capability for performing both static and dynamic experiments at higher angles of attack (to 90°) to support technology advancements related to fighter aircraft. A water tunnel designed by the Visual Aerodynamics Division of Eidetics International with a 24- by 24-in. test section was recently installed at the General Dynamics Corporation in Fort Worth to support their in-house research programs in advanced fighter technology.

The installations cited above have equally significant counterparts in Europe. In addition to ONERA, the Bertin and Company water tunnel in France was utilized recently to test a canard-wing arrangement for which flow-visualization, pressures, velocities, and forces were obtained (Ref. 57). Numerous installations are in operation in England and are used for diverse aerodynamic and hydrodynamic flow problems. The No. 2 Ship Tank and Rotating Arm in the Maneuvering Tank at the Admiralty Research Establishment, which has been in operation for decades, demonstrated the powerful vortex flows shed from the hull of a modern, highly maneuverable submarine model (Ref. 58). A systematic comparison of vortex positions obtained on slender missile configurations in water tunnel and wind tunnel facilities was recently made at the British Aerospace Military Aircraft Division (Ref. 59). Qualitative and quantitative testing of parachute canopies of various shape and porosity was conducted in the Southampton (England) Towing Channel to evaluate pitch stability characteristics (Ref. 60). IMI Summerfield in England studied the internal flow characteristics of a ramrocket combustion chamber (Ref. 61), and the flow-visualization results led to an improved fuel supply design. Unsteady flow phenomena were investigated in the towing tank of DFVLR in Germany, where aircraft models underwent prescribed accelerations and decelerations (Ref. 62). The University of Stuttgart constructed two new water facilities, and recent results of research work conducted in these installations are provided in Ref. 63. Models of complete military and commercial aircraft configurations and isolated airframe components have been tested in the MBB water tunnel (Ref. 41).

Water facilities are an important element in vehicle design in Asian countries. A high-speed water tunnel (up to 10 ft/sec) designed by the Visual Aerodynamics Division of Eidetics International was installed in a research laboratory at the Aero Industry Development Center in Taiwan in 1984 to support the aircraft development programs in that country. This tunnel has a 24- by 24-in. horizontal test section. The Peking Institute in the People's Republic of China has employed a water tunnel to visualize the vortex flows about strake-wing planforms (Ref. 64). Japanese researchers have made extensive use of water facilities to understand the fluid flows about the various aerodynamic and hydrodynamic shapes. Examples of their work are provided in Ref. 9. Mitsubishi Heavy Industries employed a towing tank to study surface ship designs. A study (Ref. 65) at Mitsubishi led to the solution of a vibration problem by improved hull design obtained through systematic water facility testing.

The burgeoning applications of water facilities to the design of vehicles are apparent from the preceding historical review. The following section will discuss specific investigations in water facilities to demonstrate their role in the vehicle design process. These representative investigations will demonstrate the strengths and limitations of water facilities in aeronautical and related hydrodynamic research.

### 3. SPECIFIC APPLICATIONS OF WATER FACILITIES TO AERONAUTICAL AND RELATED HYDRODYNAMIC PROBLEMS

Experiments performed in the NAE, CalTech, Northrop, and NASA Ames-Dryden water facilities are described in this section to provide a flavor of the myriad applications of these installations to air, ground, and marine vehicle design. NAE and CalTech have long-standing traditions in the application of water tunnels to aeronautical and related hydrodynamic problems. The Northrop and NASA Ames-Dryden facilities represent a "new generation" of water tunnels that have made significant contributions to vehicle design. Collectively, these installations represent over 100 years of water-facility experience. Emphasis will be placed on experiments pertinent to current and future commercial and military vehicles.

#### 3.1 National Aeronautics Establishment, Ottawa, Canada

The NAE water tunnel (Fig. 5) is a continuous-flow, closed-circuit design having a 10- by 13-in. horizontal test section. Flow velocities in the working section can vary from 0.2 to 10 ft/sec. The diverse experiments conducted in this facility encompass steady and unsteady, and attached and separated flows about air, ground, and marine vehicles. A detailed description of this installation is provided by Dobrodzicki (Ref. 23).

Figure 6 illustrates the flow about a wing with a submerged lifting fan in proximity to the ground. The fluid tracers reveal the fan efflux, recirculation region, and fountain effect. The fan-wing and jet-wing flow interactions were useful in interpreting the anomalies in the lift, drag, and pitching moment characteristics obtained in wind tunnel tests. The simulation of this flow situation is of current interest to advanced fighter aircraft configurations with a requirement for short takeoff and vertical landing (STOVL) capability. For such configurations, water flow visualization could provide insight regarding the jet-induced effects on the configuration aerodynamics and potential hot-gas reingestion problems.

Figure 7 shows the interaction of the simulated exhaust from a wing-mounted engine with a wing and slotted trailing-edge flap arrangement. This is representative of the externally blown-flap (EBF) concept that was applied to the McDonnell-Douglas YC-15 military transport configuration. The supercirculation effect induced by the high-velocity jet is clearly illustrated in the flow-visualization photograph. It is noted that the boundary-layer separation characteristics of the unpowered wing and flap combination are not accurately represented in the water tunnel owing to the subcritical Reynolds number and the subsequent laminar separation. However, the ability of the jet exhaust to reattach the flow to the wing and flap surface is qualitatively represented. At higher jet momentum, the jet-induced effects on the potential flow field are simulated in a quantitative sense.

The boundary-layer flow-separation characteristics of a military transport model are shown in Fig. 8. Results of such tests must be carefully interpreted because of the low Reynolds number conditions typical of water tunnel operation. Used judiciously, however, flow visualization can indicate regions on the aircraft surface that may be susceptible to flow separation.

A related study concerns the flow separation from the upswept rear fuselage typical of a rear-loading transport aircraft. The vortex pair shed from the aft fuselage section is shown in Fig. 9. The strength and location of the vortices will vary with the Reynolds number because of the lack of a fixed line of boundary-layer separation. Despite this, the water flow simulation was used to identify the source of degraded performance and stability problems as well as unsteady loads on cargo doors. This flow situation resembles the vortex formation on displacement hulls and submersible vehicles.

The aerodynamic cross-coupling effects associated with an oscillating generic fighter model were studied in water tunnel flow-visualization experiments. A representative result is shown in Fig. 10. The water flow simulation revealed a lateral oscillation of the forebody vortices caused by an oscillation in pitch and, as a result, the vortices were observed to shift from one side to the other of a top-mounted vertical fin. The relatively simple experiment provided a plausible flow mechanism that would lead to secondary lateral aerodynamic forces in response to a primary pitching maneuver. This study indicated that the unsteady, separated flow field about a slender configuration could be studied in a qualitative sense in a water facility despite the sensitivity of the forebody vortical motions to the Reynolds number.

The modulation of the flow-separation characteristics to improve ground vehicle performance was effectively demonstrated in the water tunnel. Figure 11 reveals a large improvement in the flow about a tractor-trailer due to the installation of a cab deflector. This modification led to reduced drag and increased stability and is now a standard "fix" on most ground transport vehicles of this class. The results from this investigation indicate that small-scale model testing in a water facility operating at low Reynolds number can yield substantial design improvements on vehicles that are Reynolds-number-sensitive and nonvortex-dominated.

### 3.2 California Institute of Technology, Pasadena, California

The Hydrodynamics Laboratory at CalTech consists of the Free Surface Water Tunnel (FSWT) and the High Speed Water Tunnel (HSWT). The FSWT depicted in Fig. 12 is a closed-circuit circulation system lying in a vertical plane. The horizontal test section is 20 in. wide by 30 in. deep and flow speeds up to 25 ft/sec can be obtained. The top, or free, surface is an air-water interface. This arrangement allows investigations to be performed on bodies acting on or at a prescribed distance below the water surface, such as a ventilated hydrofoil. The HSWT is also a closed-circuit design lying in a vertical plane and features interchangeable 2-D and axisymmetric working sections. The 2-D section, used principally to obtain sectional characteristics of hydrofoils, is 6 in. by 30 in. by 50 in. long, whereas the axisymmetric section is 14 in. in diameter and 46 in. long. Flow speeds up to 100 ft/sec and pressures from 100 psig to the vapor pressure of water are achievable.

In addition to flow visualization, the capabilities exist to measure steady and unsteady forces and moments and to obtain quantitative flow-field information using a laser doppler velocimeter (LDV). A detailed account of the CalTech facilities is provided by Ward (Ref. 66).

Applications of the CalTech water facilities to vehicle design have typically pertained to marine craft. The inception and scaling of cavitation on hydrodynamic shapes have been studied extensively. Studies performed in the HSWT demonstrated the importance of the boundary layer in cavitation inception. This was accomplished using a Schlieren system to visualize the origin and migration of cavitation bubbles within the boundary layer on a bluff body and their subsequent entrainment into the mainstream. A representative result from a study of cavitation phenomena is shown in Fig. 13, which depicts the cavitating flow over a 2-D wedge at high angle of attack.

Recent emphasis has been placed on the development of inlets suitable for water-jet propulsion systems. Sophisticated inlet models have been tested in the HSWT and FSWT that featured translating and rotating lips, variable-geometry walls, and auxiliary or secondary inlets. The influence of upstream air content, the thickness of the approaching boundary layer, and numerous boundary-layer control devices on the inception of cavitation and inlet recovery efficiency have been determined in these investigations.

Hydrofoil development projects have addressed the effects of flaps in cavity flow, the study of hydrofoil sections having good performance in fully wetted and cavity flow, and the performance of ventilated foils near a free surface. The latter experiment provided verification of a theory by Furuya (Ref. 67) to predict the forces on supercavitating or ventilated hydrofoils of finite aspect ratio, arbitrary shape, and variable submergence.

Aeronautical research projects pertaining to the trailing vortex systems generated by lifting surfaces were undertaken in the FSWT. The axial and tangential velocity profiles in the wake region were measured using an LDV system and the data were used to confirm a theory for the structure and decay rate of a trailing vortex.

The experiments performed in the CalTech installations exemplify the capabilities of water facilities to yield qualitative and quantitative surface and off-body flow-field information to aid in theory development and marine and flight vehicle design.

### 3.3 Northrop Corporation, Aircraft Division, Hawthorne, California

The Northrop Corporation water tunnel is a continuous-flow, closed-circuit facility having 16- by 24-in. vertical test section (Fig. 14). This installation has been used as a diagnostic tool to aid in the aircraft design process since its inception in 1977. It was preceded by a small pilot water tunnel having a 6- by 6-in. vertical test section that could operate in gravity discharge and continuous-flow modes.

The Northrop installations marked the advent of water facilities that were dedicated to the study of the vortex flows developed on advanced tactical/fighter aircraft operating at extreme attitudes. These installations satisfied the need for a visualization tool to improve the understanding and control of the complex vortical flows that have become characteristic of highly maneuverable military aircraft beginning with the General Dynamics YF-16 and the Northrop YF-17 lightweight fighters in the 1970s.

At a very early stage of its operation, the pilot tunnel demonstrated the utility of a water facility operating at very low speed (0.25 ft/sec) and low Reynolds number (10,000/ft) to vividly depict the vortical motion about a small-scale model of a complete fighter configuration. Figure 15 shows the vortex arising from flow separation along the sharp edge of a wing LEX on a 1/72-scale YF-17 at an angle of attack of 20°. Wortmann has commented in a recent paper (Ref. 68) that this, and similar water facility results, bear little resemblance to the real flow and are principally of public relations value. This is hardly the case, however, because this single flow-visualization photograph demonstrates several important flow-field features that have been observed in wind tunnels and in flight (Ref. 34). In addition, the interpretation of the nonlinear forces and moments and vortex-induced surface pressures is facilitated by the detailed 3-D flow visualization. For example, the development of a concentrated vortical flow above the wing surface and the favorable LEX vortex-induced effects on the wing flow-separation characteristics correlate well with the nonlinear lift increase at moderate and high angles of attack. The breakdown of the vortex core over the wing surface limits the maximum vortex-induced lift increment and can promote pitch instability. The proximity of the unburst vortical flows to suitably placed twin vertical tails enhances the stabilizer effectiveness. Under certain conditions, however, the occurrence of vortex bursting near the tail surfaces can induce a severe buffet environment leading to structural failure. The flow through the boundary-layer bleed slots at the juncture of the LEX and fuselage was observed to have an adverse effect on the LEX vortex core stability at high angles of attack, thereby reducing the maximum lift in comparison to the configuration with slots closed. Clearly, the availability of off-body flow-field trends through simple water-facility experiments is of great value in the aircraft design process.

To establish confidence in the water flow simulations, flow-visualization studies were performed in the pilot and larger-scale water tunnels of the leading-edge vortex behavior on thin, sharp-edged delta wings encompassing a wide range of the leading-edge sweep angle. The vortex positions determined from the water tunnel testing were in reasonable agreement with results obtained at higher Reynolds numbers in wind tunnels (Ref. 34). This was due to the insensitivity of the primary flow separation at the sharp leading edge to changes in the Reynolds number. The fact that theoretical methods which ignore viscous effects can reasonably predict vortex flow aerodynamics is one indication of the Reynolds number insensitivity of such phenomenon. The agreement between the vortex positions determined in the water tunnel and the wind tunnel is limited, however, because of the viscous effects near the wing surface. The upper-surface boundary-layer flow separates near the leading edge, generating a secondary vortex having a sense of rotation which is opposite to that of the primary vortex. The secondary separation line and the strength and location of the secondary vortex vary with the Reynolds number. The location of the primary vortex core will be affected by the state of the boundary layer and will be somewhat inboard and higher off the wing surface when subcritical (laminar) separation occurs.

The vortex breakdown characteristics compared favorably with similar observations made in wind tunnels and in flight, as shown in Fig. 16. This correlation indicated that under certain restrictive conditions the relative importance of inertia and viscous and pressure terms was simulated in the water tunnel. Experience suggests that the adverse pressure gradient in the external potential flow field is the dominant parameter affecting the vortex breakdown at high angles of attack. The apparent success of the inviscid Euler methods to "capture" the vortex breakdown phenomenon on this class of aerodynamic shape is based on similar reasoning (Ref. 69). Provided flow separation occurs simultaneously everywhere along a sharp leading edge, a water flow simulation is expected to provide an acceptable representation of the size and structure of the wake shed from a thin wing at a high angle of attack and, consequently, the pressure field through which a vortex core must traverse. The water tunnel photograph of Fig. 17 illustrates this flow situation on a small-scale model of an advanced fighter featuring a sharp, highly swept LEX. At a similar angle of attack, pilots of this aircraft have detected a sudden increase in the external noise intensity which is associated with the forward advance of the vortex breakdown position on either side of the canopy. Another water tunnel-to-flight correlation of a qualitative nature is shown in Fig. 18, which depicts LEX vortex breakdown on a current fighter aircraft at high angle of attack. The water tunnel model (an inexpensive, plastic model) exhibits vortex bursting over the wing panel at a location approximating the burst position on the full-scale aircraft. It is upon this premise--the dominance of the adverse pressure gradient in the external potential flow field--that water-facility vortex-breakdown results can be applied to higher-Reynolds-number phenomena in air at high angles of attack.

The water tunnel became an important element in the major aircraft programs at Northrop as a result of these preliminary investigations. The ensuing flow-visualization experiments spanning the next several years demonstrated the strengths and limitations of water-facility simulations of fighter aircraft flow



fields. Emphasis was placed on studies at high angles of attack where the phenomenological aspects of the vortex-dominated flow field were insensitive to the Reynolds number.

The F-5E, F-5F, and F-20A fighter configurations were the subject of extensive flow-visualization experiments. The water tunnel was used primarily to obtain off-body flow-field information on airframe modifications for which wind tunnel and flight test data were available. For example, the LEX planform and area modifications shown in Fig. 19 increased the maximum lift and improved the static lateral-directional stability characteristics at high angles of attack. The water tunnel testing revealed enhanced stability of the LEX vortical flow at angles of attack near maximum lift, a delay to higher angle of attack of the pronounced vortex breakdown asymmetry in sideslip, and increased dynamic pressure in the vicinity of the centerline vertical tail arising from the delayed breakdown of the windward LEX vortex.

It was determined from the flow-visualization testing of these models that faired-over engine inlets could yield misleading results regarding the vortex behavior at high angles of attack. For example, the LEX vortex breakdown characteristics indicated that influx into the side-mounted inlets at moderate to high angles of attack induced a local upwash near the LEX apex so that the effective  $\alpha$  in this region was approximately 2° higher in comparison to the blocked-inlet case. As a consequence, all ensuing fighter models were tested with flowing inlets.

The ability to visualize the vortex-engine inlet interactions subsequently led to detailed studies of fighter configurations with top-mounted inlets. The water tunnel flow visualization, in combination with wind tunnel test results, showed that careful integration of the inlet on the fuselage to take advantage of the LEX vortex-induced sweeping action could effectively control the inlet pressure recovery and dynamic distortion at high angles of attack (Ref. 70).

The F-5 configuration was also used as a test bed to evaluate propulsive lift-enhancement concepts. A representative study featured the application of spanwise blowing to the wing upper surface to reenergize the LEX vortex at high  $\alpha$ . At sufficiently high blowing rates, a discrete vortex from the wing leading edge was also apparent, as shown in Fig. 20. In general, it was found that the blowing momentum required in water tunnel simulations to effect a particular change in the flow field was somewhat higher than that in wind tunnel testing performed at higher Reynolds numbers. This was due to the increased blowing rates that were necessary to energize the laminar boundary layer on the wing upper surface.

Water tunnel studies confirmed that the asymmetric shedding of the vortices from the slender forebody of the F-5F at zero sideslip was responsible for the large aerodynamic asymmetries at high angles of attack that were encountered in wind tunnel and flight testing. A representative result from these studies is shown in Fig. 21. Although the primary separation along the forebody sides was sensitive to the Reynolds number, the forebody vortex asymmetry was promoted by an inviscid hydrodynamic instability associated with a crowding together of the vortices near the nose (Ref. 71). As a result, the flow mechanism was amenable to study in the water tunnel. Because of the laminar separation, however, the vortices were more widely spaced along the forebody in comparison to the case of turbulent separation. Therefore, the angle of attack for onset of the vortex asymmetry was typically a few degrees higher than the onset of aerodynamic asymmetries determined from wind tunnel and flight tests.

The ability of the F-5 "shark nose" depicted in Fig. 22 to alleviate the vortex asymmetry was demonstrated in water tunnel flow-visualization tests. The broader planform and flattened cross section near the nose increased the lateral spacing of the vortices and, therefore, reduced the susceptibility to flow-field asymmetries. Wind tunnel and flight testing of the F-5F/shark nose combination revealed a significant decrease in the aerodynamic asymmetries along with improved departure/spin resistance. Similarly, the nose shape on the reconnaissance version of the F-5F with its forward-looking oblique window (RECCE nose) was shown in water flow studies to reduce the asymmetric vortex shedding at high  $\alpha$ .

The latter studies demonstrated the sensitivity of the vortex flows to the geometry of the forebody apex region and the ability of a water facility to visualize the flow-field changes. This led to the study of numerous other active and passive methods of asymmetric sideload alleviation in the water tunnel. These included nose strakes, helical separation trips, and normal and tangential blowing on the forebody. The flow-visualization experiments provided a rapid assessment of the ability of the flow-control devices to reduce/eliminate/reverse the body vortex asymmetry. The devices that were identified as promising flow modulators in the water tunnel proved effective in controlling the  $\alpha$ -zero asymmetries in wind tunnel testing of subscale F-5 models.

The water tunnel was a useful tool in analyzing the directional stability trends obtained in wind tunnels and in flight since at high angles of attack the forebody can strongly affect the static directional stability. An example includes the F-5F forebody, which develops an unusual vortex orientation in sideslip as shown in Fig. 23. On the basis of water tunnel/wind tunnel/flight correlations, the forebody vortices and their unique orientation were identified as the primary source of static directional stability at high angles of attack. As a consequence, the effect of forebody modifications on the yaw stability could generally be surmised from water tunnel testing by observing any changes to the forebody vortex structure and location.

The water tunnel testing of the F-5 and related fighter models revealed several limitations to the water facility simulations. At low angles of attack, generally less than 10°, the vortex core in a water tunnel is influenced by the wake region produced by laminar separation from the rear portion of the wing. As shown in Figs. 24 and 25, this alters the vortex path and also produces premature dissipation of

the vortex because of entrainment of turbulent fluid from the separated wake. In contrast, observations of the vortex behavior in wind tunnels and in flight at similar angles of attack indicated that the vortex does not burst over the wing (see Fig. 25). Rather, the discrete vortex core exhibits a trajectory that conforms closely to the curvature of the wing, particularly when leading- and trailing-edge flaps are deflected, and can interact with downstream airframe components. For similar reasons, the laminar boundary-layer separation at the subcritical conditions in the water tunnel masks the quantitative effects of deflected leading- and trailing-edge devices on the vortex stability. The simulation of the vortex behavior on wings with thickness, camber, twist, and/or leading-edge bluntness is also inadequate at low- $\alpha$  conditions. Investigations of these configurations, therefore, are limited to high angles of attack where flow separation occurs everywhere along the wing leading edge. Under such conditions, the fundamental character of the vortex-dominated flow is similar to that observed at higher Reynolds number. This was the justification for water tunnel studies of the Space Shuttle Orbiter by Lorincz (Ref. 72).

The scale of the vortical motions relative to the boundary-layer thickness will determine the degree to which the water-facility results can be extrapolated to higher Reynolds number. The vortices generated from wing leading-edge snags and lower and upper surface fences, for example, generally proved difficult to simulate in the water tunnel because of the strong interaction between the separated wing boundary layer and the vortical motions. An attempt to represent the interaction of the vortex generated from the nacelle strake, or engine "ear," of a commercial transport model with the wing upper surface proved futile. In flight, however, the strake vortex observed under conditions of natural condensation traversed the wing upper surface and closely followed the curvature of the wing without breakdown.

A major contribution of the water tunnel pertained to the visualization of multiple vortex flows, vortex interactions, and breakdown on fighter aircraft featuring relatively large LEXes in proximity to the forebody. Such configurations were shown to develop strong flow interactions throughout the extended angle-of-attack range owing to the persistence of the vortical motions and their proximity to one another. An example of the strong coupling of forebody and LEX vortices on a small-scale model of the F-18 is shown in Fig. 26. The flow field is characterized by symmetric forebody vortex shedding at zero sideslip and the entrainment of this vortex pair by the dominant LEX vortical flows. This multiple vortex interaction was very sensitive to small changes in the sideslip angle. Furthermore, modulation of the forebody vortex orientation in sideslip was found, under certain conditions, to influence the wing stall behavior and, hence, the lateral stability characteristics (Ref. 73). For example, the forebody vortices were resistant to asymmetric orientation in sideslip when radome strakes were installed at  $40^\circ$  above the maximum half-breadth. At small sideslip angles, the body vortex system was actually biased toward the windward side of the aircraft. This flow situation was unsteady, however, as the leeward body vortex would periodically pass underneath the windward vortical flow. The strake effects on the forebody-LEX vortex interactions resulted in powerful vortex-induced downwash and sidewash on the windward wing panel, thereby delaying complete wing stall to angles of attack greater than  $40^\circ$ . This effect was also observed in wind tunnel smoke-flow visualization. The increased roll stability arising from the strake installation was confirmed in subscale wind tunnel and full-scale flight testing. In addition, the wind tunnel model installed on a free-to-roll rig and the full-scale vehicle in flight revealed modest strake-induced lateral oscillations, or wing rock, which was consistent with the unsteady forebody-LEX vortex interactions observed in the water tunnel and wind tunnel flow-visualizations. The investigations demonstrated how changes to the forebody flow could be amplified downstream to affect the wing aerodynamics and how the understanding of complicated flow interactions could be improved through water tunnel experiments.

The simulation of multiple vortex interactions was extended to canard-wing fighter configurations. At the higher angles of attack, the water tunnel provided useful flow-field results regarding the effects of the canard downwash on the wing flow field. For example, the delay of leading-edge flow separation on the wing, the progressive development of the wing vortex with increased angle of attack, and the enhancement of the latter at high  $\alpha$  in the presence of the canard downwash field were demonstrated in water flow experiments. The flow-visualization photograph of Fig. 27 shows a discrete wing vortex on a small-scale model of the Swedish Viggen aircraft at  $\alpha = 30^\circ$ , which is well beyond the angle of attack for stall of the isolated wing.

The lateral sensitivity at high angles of attack associated with asymmetric vortex breakdown in sideslip is an inherent characteristic of any fighter aircraft employing large amounts of vortex lift. Flow-visualization investigations were conducted to improve the flow situation depicted in Fig. 28 by suitable modifications to the LEX planform and addition of LEX fences and slots to modulate the vortex core breakdown behavior in sideslip. Excellent correlations were obtained between the flow-field observations and low-speed wind tunnel data trends.

The occurrence of wing rock is common to slender-wing aircraft at high angles of attack. Water tunnel studies of a slender hypersonic research configuration unconstrained in roll revealed a self-induced, bounded lateral oscillation similar to that observed in the wind tunnel. The visualization of the oscillatory leading-edge vortex core and breakdown phenomena provided insight into possible triggering and sustaining mechanisms of this single-degree-of-freedom oscillation.

Water tunnel tests were performed on a 2-D ejector nozzle to study the effects of swirl on the exhaust plume characteristics. The flow-visualization experiments indicated that swirl dramatically reduced the primary nozzle potential core and, hence, the mixing shroud length as shown in Fig. 29. The results, which confirmed a theory developed by Chu (Ref. 74), were useful for such applications as jet noise reduction.

Another application of the water tunnel to a nonvortex-dominated flow field pertained to thrust reversers on an advanced fighter configuration in and out of ground proximity. A representative result from these experiments is shown in Fig. 30. The reverser plume shape and trajectory were observed for ranges of the nozzle geometry, orientation, and jet velocity ratio. Emphasis was placed on the jet blockage and entrainment effects on the vertical and horizontal stabilizer flow fields. It was difficult to identify the pertinent flow mechanisms, however, and the correlations with tail loads information obtained in wind tunnel tests were necessarily limited.

#### 3.4 NASA Ames Research Center, Dryden Flight Research Facility, Edwards, California

The NASA Ames-Dryden Flow Visualization System (FVS) (Fig. 31) is a single-return facility with a 16-by 24-in. vertical test section. This installation, modeled after the Northrop water tunnel, has been in operation since 1983. The NASA facility has been used almost exclusively for the visualization and measurement of the separated flow fields about advanced military aircraft configurations. In addition to NASA in-house research, numerous cooperative ventures have been undertaken with industry, universities, and other government agencies. The NASA facility has expanded on the Northrop tunnel capabilities by developing laser-enhanced visualization (LEV) and 2-D laser velocimeter (LV) techniques for the water flow studies. In addition, successful attempts have been made to obtain quantitative information using instrumented models.

Many of the flow-visualization studies have been made in support of the NASA High-Alpha Technology Program. Flow-field information has been obtained on small-scale models of the F/A-18, as shown in Fig. 32, to identify effective passive and active vortex flow-control concepts for future wind tunnel and flight testing.

A related study sponsored by the Navy featured quantitative measurements of the F/A-18 twin vertical tail buffet characteristics in the presence of LEX vortex breakdown. The water tunnel investigation, in combination with existing wind tunnel and flight test data, provided an improved understanding of vortex-empennage interactions at high angles of attack that can lead to severe tail buffeting. The surface hot-film anemometer results showed high turbulence activity on the fins at conditions coincident with vortex bursting observed from flow visualization. The vortex frequencies, vortex bursting, and dominant frequencies from the water tunnel tests correlated well with wind tunnel tests at higher Reynolds number (Ref. 75).

A generic study (Ref. 48) was made of a concept to improve the vertical-tail buffet environment. This test featured the generation of a "free vortex" with an imposed downstream pressure gradient to promote core bursting. Blowing along the core was then initiated to delay the onset of bursting. LV measurements showed that the active flow control significantly reduced the turbulence intensity. It can be inferred from these preliminary results that core blowing applied to the F/A-18 configuration would have a favorable effect on the vortex-empennage interactions at high angles of attack.

A qualitative study was made of an F/A-18 model undergoing pitch oscillations and ramp-type motions to evaluate potential dynamic lift benefits at angles of attack beyond the static maximum lift. The flow visualization revealed a lag in the flow-field response to the aircraft motion and a delay of the LEX vortex bursting in comparison to the static case. The latter phenomenon was very transient, however, as the flow field rapidly assumed its steady-state condition upon termination of the maneuver. In contrast to the results obtained at NAE on a slender generic fighter model, there was no significant lateral oscillation of the vortex flows due to the pitching maneuver. This was attributed to the dominance of the LEX vortices which emanated from fixed lines of separation and therefore were resistant to large lateral excursions.

The Space Shuttle Orbiter configuration was tested to evaluate the vortex-shedding patterns on the thick cranked wing at high angles of attack. A representative result is shown in Fig. 33. This model was used to develop a LEV capability (Ref. 49) and the resultant technique was then applied to several other configurations, including a powered AV-8A Harrier model in ground proximity and a drag-reduction concept featuring a trailing disk behind the base of a cylinder. A typical flow visualization in a streamwise plane from the latter study is shown in Fig. 34.

Other aircraft configurations that have been studied in the NASA installation include the McDonnell-Douglas F-15 and F-4, the Grumman/DARPA X-29, the General Dynamics F-16XL, and the NASA/General Dynamics F-106 with vortex flaps. The vortex flow behavior on the NASA/LTV/Rockwell F-8 oblique wing test aircraft configuration was visualized as shown in Fig. 35. Of particular interest was the asymmetric vortex formation and breakdown on this skewed wing arrangement and the interaction of the vortical flows with the vertical tail. The understanding and control of these phenomena are essential in order to obtain acceptable levels of static lateral-directional stability at moderate and high angles of attack.

In addition to experiments on specific aircraft configurations, basic aerodynamic research programs have also been supported by water tunnel experiments in the NASA Ames-Dryden facility. One example is a recent study (Ref. 76) performed by Eidetics International for the Air Force to investigate methods of vortex control to enhance aerodynamic control on fighter aircraft at high attitudes. The aim of this flow-visualization study was to explore methods of altering the natural state of the forebody and LEX vortices by interjecting into the flow field either small surfaces or blowing jets.

## 4. SUMMARY

A review has been made of the role of water facilities in vehicle design. The use of water as a flow-visualization medium began very early. The scientific application of water flow visualization began in the 15th century with the observations and sketches of Leonardo da Vinci, who also designed the first water tunnel. Leonardo hypothesized that flows in water and air were similar, which was of great importance to the advancement of fluid mechanics.

In the centuries to follow, sporadic experiments on simple shapes were performed in water, primarily for marine craft applications. The pioneering research of Ludwig Prandtl and his colleagues and the dawning of the era of flight in the early 20th century marked an upsurge in the use of water facilities for vehicle design. In the ensuing decades up through World War II, water tunnels, channels, and towing tanks yielded useful qualitative, and sometimes quantitative, information on various aerodynamic and hydrodynamic shapes suitable for flight and marine vehicles.

The trend toward increased vehicle size and speed posed a scaling problem for water facility simulations. The matching of the Froude number in marine craft testing was generally at the expense of a large Reynolds number gap. The scaling of cavitation phenomena was a continual challenge. Water flow simulations were necessarily restricted to the incompressible flow regime and could not represent the phenomena encountered on high-speed aircraft that emerged during World War II. A significant Reynolds number mismatch was also present in the testing of flight vehicles in water facilities. These problems continue to the present day.

The utilization of controlled flow separations and vortex flows by design to improve vehicle performance emerged in the 1950s. This increased the utility of water facilities as a vehicle design tool largely because the fundamental structure of these flows was insensitive to the Reynolds number. The rapid advancement of vehicle technology since that time has resulted in expanded operating envelopes and corresponding increase in the flow-field complexity. Water facility applications and capabilities have kept pace with these technology developments and these installations have assumed a prominent role in the design of air, ground, and marine vehicles. Water tunnel, channel, and towing-tank facilities are in operation in several countries around the world, providing detailed flow-field information that will assist in solving myriad present and future aeronautical and related hydrodynamic problems.

## REFERENCES

1. Lugt, H. J., Vortex Flows in Nature and Technology, New York, John Wiley & Sons, 1983.
2. von Karman, T., Aerodynamics, New York, McGraw-Hill Book Company, 1954.
3. Flachsbarth, O., Handbuch der Experimentalphysik, Pt. 2 (of four volumes), Germany, 1932.
4. Truesdell, C., Essays in the History of Mechanics, New York, Springer-Verlag, 1968.
5. Aermacchi World, Mondo Aermacchi Periodico Trimestrale, Italy, Nov. 1982, Anno I-N.3.
6. Hagen, G. H. L., "On the Motion of Water in Narrow Cylindrical Tubes" (In German), Poggendorfs Annalen, Vol. 46, 1839, p. 423.
7. Hagen, G. H. L., "On the Influence of Temperature on the Movement of Water Through Pipes" (In German), Abhandl. Akad. Wiss., Berlin, 1854, p. 17.
8. Reynolds, O., "An Experimental Investigation of the Circumstances Which Determine Whether the Motion of Water Will Be Direct or Sinuous, and of the Law of Resistance in Parallel Channels," Phil. Trans. Roy. Soc., Vol. 2, 1883, p. 51.
9. Van Dyke, M., An Album of Fluid Motion, Stanford, Calif., The Parabolic Press, 1982.
10. Hele Shaw, H. J. S., Trans. Inst. Nav. Arch., Vol. 39, 1897, pp. 145-56.
11. Prandtl, L., "On Fluid Motions With Very Small Friction" (In German), Proc. 3rd Intern. Math. Cong., Heidelberg, 1904.
12. Prandtl, L. and Tietjens, O. G., Applied Hydro- and Aeromechanics, New York, Dover Publications, 1934.
13. Hoerner, S. F., Fluid Dynamic Drag, published by the author, Bricktown, N.J., 1965.
14. Riechardt, H., "On the Determination of Favorable Shapes of Bodies for High Speed by Cavitation Tests," Gottingen, Germany, M. A. P. Volkenrode, MAP-VG88-49T, 1946.
15. Knapp, R. T., "Flow Diagrams of Projectile Components," CalTech Report, O. S. R. & D., National Defense Research Committee, Div. Six-Section 6.1, 1944.

16. Roy, M., "Caracteres de l'ecoulement autour d'une fleche accentuee," C. R. Acad. Sci. Paris, Vol. 234, 1952, pp. 2501-2504.
17. Legendre, R., "Ecoulement au voisinage de la pointe avant d'une aile a forte fleche aux incidences moyennes," Rech. Aeronaut., No. 30-31-32, 1952-1953.
18. Orlik-Rückemann, K., "Experimental Determination of Pressure Distributions and Transition Lines of Plane Delta Wings at Low Speeds and Zero Yaw," Stockholm, KTH-Aero TN 3, 1948.
19. Peckham, D. H., "Low-Speed Wind Tunnel Tests on a Series of Uncambered Slender Pointed Wings with Sharp Edges," A.R.C. R&M 3186, December 1958.
20. Bird, J. D., "Visualization of Flow Fields by Use of a Tuft Grid Technique," J. Aeron. Sci., Vol. 19, 1952, p. 481.
21. Lambourne, N. C. and Pusey, P. S., "Some Visual Observations of the Effects of Sweep on the Low-Speed Flow over a Sharp-Edged Plate at Incidence," NPL R&M 3106, Teddington, England, Jan. 1958.
22. Örnberg, T., "A Note on the Flow Around Delta Wings," KTH-Aero TN 38, Stockholm, 1954.
23. Dobrodzicki, G. A., "Flow Visualization Water Tunnel - Its Construction and Capabilities," National Aeronautical Establishment Aeronautical Report LR-610, NRC No. 20235, Ottawa, Apr. 1982.
24. Wickens, R. H., Private Communication, 1986.
25. Cavitation in Hydrodynamics, Proc. Symp. National Physical Laboratory, Teddington, England, September 14-17, 1955.
26. Acosta, A. J., "Hydrofoils and Hydrofoil Craft," Ann. Rev. Fluid Mech., Vol. 5, 1973, pp. 161-184.
27. Lowson, M. V., "Some Experiments with Vortex Breakdown," J. Roy. Aeron. Soc., Vol. 68, May 1964, pp. 343-346.
28. Poisson-Quinton, P. and Werlé, H., "Water Tunnel Visualization of Vortex Flow," Astronaut. Aeronaut., Vol. 5, 1967, pp. 64-66.
29. Rolls, S. L., Koenig, D. G., and Drinkwater, F. J., III, "Flight Investigation of the Aerodynamic Properties of an Ogee Wing," NASA TN D-3071, Dec. 1965.
30. Werlé, H., "Hydrodynamic Flow Visualization," Ann. Rev. Fluid Mech., Vol. 5, 1973, pp. 361-382.
31. Peake, D. J., Rainbird, W. J., and Atraghji, E. G., "Some Problems of Three-Dimensional Flow Separation about Aircraft Components," AIAA Paper 69-622, June 1969.
32. Sarpkaya, T., "On Stationary and Traveling Vortex Breakdowns," J. Fluid Mech., Vol. 45, Pt. 3, 1971, pp. 545-559.
33. Van Every, K., "Letters," Aviation Wk Space Technol., Vol. 124, No. 23, June 9, 1986, p. 164.
34. Erickson, G. E., "Vortex Flow Correlation," AFWAL-TR-80-3143, Jan. 1981 (also ICAS Paper 82-6.6.1, Aug. 1982).
35. Orlik-Rückemann, K. J., "Effects of High Angles of Attack on Dynamic Stability Parameters," AGARD-CP-247, Jan. 1979.
36. McAlister, K. W. and Carr, L. W., "Water Tunnel Experiments on an Oscillating Airfoil at  $Re=21,000$ ," NASA TM-78446, March 1978.
37. Renselaeer, D. J., "Description and Test Results of a Water Basin to Determine Ground Effect in Hover Using Small Models," AIAA Paper 75-145, Jan. 1975.
38. Saripalli, K. R., "Visualization of Multi-Jet Impingement Flow," AIAA Paper 81-1364, July 1981.
39. Wedemeyer, E. H., "Stable and Unstable Vortex Separation," AGARD-CP-247, Jan. 1979.
40. Stieb, R., "Description of the MBB-Water Tunnel," MBB Report MBB/FE123/R/1526, Munich, 1981.
41. Gross, U., Stieb, R., and Zacharias, A., "Aerodynamic Flow Phenomena Observation in the MBB Water Tunnel," presented at the AGARD Fluid Dynamics Panel Symposium on Aerodynamic and Related Hydrodynamic Studies Using Water Facilities, 20-23 Oct. 1986, Monterey, Calif.

42. Deane, J. R., "Wind and Water Tunnel Investigations of the Interaction of Body Vortices and the Wing Panels of a Missile Configuration," AGARD-CP-247, Jan. 1979.
43. Behrbohm, H., "New Observations and Some Elementary Results on Free-Stream Incompressible Flow Past Delta Wings With Sharp Leading Edges," SAAB Report L-0-1 R61, Stockholm, Sept. 1970.
44. Demurie, F., Muylaert, J. M., and Wendt, J. F., "Investigation on the Interaction Between Body Vortices and the Strake Wing Panels of a Missile Configuration," VKI IN 63, Brussels, 1980.
45. Thompson, D. H., "An Experimental Study of Axial Flow in Wing Tip Vortices," ARL/A-Note-355, Melbourne, May 1975.
46. Thompson, D. H., "A Water Tunnel Study of Vortex Breakdown Over Wings with Highly Swept Leading Edges," ARL/A-Note-356, Melbourne, May 1975.
47. Gad-el-Hak, M., "Use of Water Towing Tanks for Aerodynamics and Hydrodynamics," presented at the AGARD Fluid Dynamics Panel Symposium on Aerodynamic and Related Hydrodynamic Studies Using Water Facilities, 20-23 Oct. 1986, Monterey, Calif.
48. Owen, F. K. and Peake, D. J., "Vortex Breakdown and Control Experiments in the Ames-Dryden Water Tunnel," presented at the AGARD Fluid Dynamics Panel Symposium on Aerodynamic and Related Hydrodynamic Studies Using Water Facilities, 20-23 Oct. 1986, Monterey, Calif.
49. Beckner, C. and Curry, R. E., "Water Tunnel Flow Visualization Using a Laser," AIAA Paper 85-5016, Oct. 1985.
50. Escudier, M. P. and Keller, J. J., "Vortex Breakdown: A Two-Stage Transition," AGARD-CP-342, July 1983.
51. Erickson, E. G., "Water Tunnel Flow Visualization and Wind Tunnel Data Analysis of the F/A-18," NASA CR-165859, May 1982.
52. Werlé, H., "Possibilités D'Essai Offertes Par Les Tunnels Hydrodynamiques a Visualisation de l'ONERA Dans Les Domaines Aeronautique et Naval," presented at the AGARD Fluid Dynamics Panel Symposium on Aerodynamic and Related Hydrodynamic Studies Using Water Facilities, 20-23 Oct. 1986, Monterey, Calif.
53. Wickens, R. H., "The Use of the NAE Water Tunnel in Canadian Aeronautical Research and Development," presented at the AGARD Fluid Dynamics Panel Symposium on Aerodynamic and Related Hydrodynamic Studies Using Water Facilities, 20-23 Oct. 1986, Monterey, Calif.
54. Gad-el-Hak, M. and Ho, C.-M., "The Pitching Delta Wing," AIAA J., Vol. 23, No. 11, Nov. 1985, pp. 1660-1665.
55. Gad-el-Hak, M. and Ho, C.-M., "Three Dimensional Effects on a Pitching Lifting Surface," AIAA Paper 85-0041, Jan. 1985.
56. Goodman, A. and Brown, C., "An Experimental Study to Determine the Vortex-Flow and the Subsonic and Dynamic Stability Characteristics of Aircraft Operating at High Angles-of-Attack," presented at the AGARD Fluid Dynamics Panel Symposium on Aerodynamic and Related Hydrodynamic Studies Using Water Facilities, 20-23 Oct. 1986, Monterey, Calif.
57. Chezelepretre, B. and Brocard, Y., "Qualification d'un Tunnel Hydrodynamique Pour Des Pesées de Maquettes Aeronautiques," presented at the AGARD Fluid Dynamics Panel Symposium on Aerodynamic and Related Hydrodynamic Studies Using Water Facilities, 20-23 Oct. 1986, Monterey, Calif.
58. Lloyd, A. R. J. M. and Campbell, I. F., "Experiments to Investigate the Vortices Shed From a Submarine-Like Body of Revolution," presented at the AGARD Fluid Dynamics Panel Symposium on Aerodynamic and Related Hydrodynamic Studies Using Water Facilities, 20-23 Oct. 1986, Monterey, Calif.
59. Davies, A. G., "A Comparative Study of Vortex Flows in Wind and Water Tunnels," presented at the AGARD Fluid Dynamics Panel Symposium on Aerodynamic and Related Hydrodynamic Studies Using Water Facilities, 20-23 Oct. 1986, Monterey, Calif.
60. Cockrell, D. J., Polpitiye, S. J., Yavuz, T., and Shen, C., "Measurements of Aerodynamic Forces on Unsteadily-Moving Bluff Parachute Canopies," presented at the AGARD Fluid Dynamics Panel Symposium on Aerodynamic and Related Hydrodynamic Studies Using Water Facilities, 20-23 Oct. 1986, Monterey, Calif.
61. Boszko, P. J. and Owen, G. S., "Water Flow Visualization of a Ramrocket Combustion Chamber," presented at the AGARD Fluid Dynamics Panel Symposium on Aerodynamic and Related Hydrodynamic Studies Using Water Facilities, 20-23 Oct. 1986, Monterey, Calif.

62. Bippes, H., "The Use of a Water Towing Tank for Aerodynamic Testing and a Method for Quantitative Evaluation of Stereo Photographs," presented at the AGARD Fluid Dynamics Panel Symposium on Aerodynamic and Related Hydrodynamic Studies Using Water Facilities, 20-23 Oct. 1986, Monterey, Calif.
63. Strunz, M., "A New Laminar Water Tunnel to Study the Transition Process in a Blasius Layer and a Separation Bubble," presented at the AGARD Fluid Dynamics Panel Symposium on Aerodynamic and Related Hydrodynamic Studies Using Water Facilities, 20-23 Oct. 1986, Monterey, Calif.
64. Wenhan, S., Mouji, L., Bocheng, Zhou, Chenghao, Q., and Shanwen, X., "An Experimental Investigation of Leading-Edge Spanwise Blowing," Intern. Council of Aeron. Sci., ICAS-82-6.6.2, Aug. 1982.
65. Fujita, T., "Flow Visualization of Ship Model in Towing Tank," Flow Visualization II, Proc. 2nd Intern. Symp. on Flow Visualization, September 9-12, 1980, Bochum, W. Germany (Ed. by W. Merzkirch).
66. Ward, T. M., "The Hydrodynamics Laboratory at the California Institute of Technology - 1976," Trans. ASME, J. Fluid Eng., Dec. 1976, pp. 740-748.
67. Furuya, O., "Three-Dimensional Theory on Supercavitating Hydrofoils Near a Free Surface," J. Fluid Mech., Vol. 71, Pt. 2, 1987, pp. 339-359.
68. Wortmann, A., "On Reynolds Number Effects in Vortex Flow Over Aircraft Wings," AIAA Paper 84-0037, Jan. 1984.
69. Hitzel, S. M., "Vortex Breakdown of Leading-Edge Vortices Above Swept Wings," Dornier Report, Aktenvermerk BF30-2576/84, Friedrichshafen, Jan. 1980.
70. Williams, T. L. and Hunt, B. L., "Top Mounted Inlet System Feasibility for Transonic-Supersonic Fighter Applications," AIAA Paper 80-1809, Aug. 1980.
71. Keener, E. R. and Chapman, G. T., "Similarity in Vortex Asymmetries Over Slender Bodies and Wings," AIAA J., Vol. 15, No. 9, Sept. 1977, pp. 1370-1372.
72. Lorincz, D. J., "Space Shuttle Orbiter Flow Visualization Study," NASA CR-163092, Feb. 1980.
73. Erickson, G. E. and Gilbert, W. P., "Experimental Investigation of Forebody and Wing Leading-Edge Vortex Interactions at High Angles of Attack," AGARD-CP-342, July 1983.
74. Chu, C.-W., Der, J., Jr., Ortiz, V. M., and Widynski, T. C., "Effect of Swirl on the Potential Core in Two-Dimensional Ejector Nozzles," J. Aircraft, Vol. 20, No. 2, Feb. 1983, pp. 191-192.
75. Lan, C. E., Lee, I. G., and Wentz, W. H., "Investigation of Empennage Buffeting," Technical Report CRINC-FRL-714-1, Flight Research Laboratory, Univ. Kansas Center for Research, Inc., July 1986.
76. Malcolm, G. N. and Skow, A. M., "Enhanced Controllability Through Vortex Manipulation on Fighter Aircraft at High Angles of Attack," AIAA Paper 86-2277-CP, Aug. 1986.

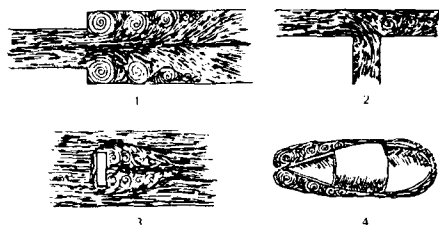


Figure 1. Fluid flow sketches by Leonardo da Vinci (from Ref. 1).

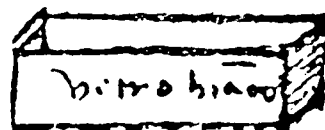
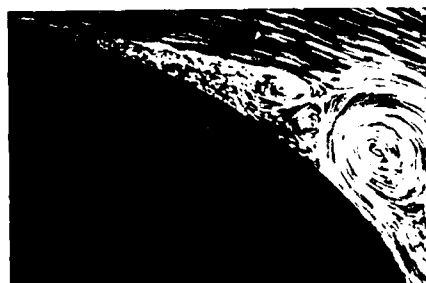


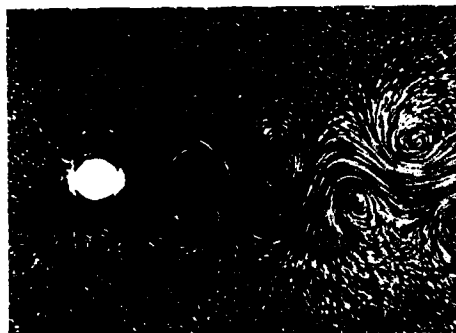
Figure 2. The box with the inscription "white glass," read from right to left as was Leonardo's habit, represents the first historic example of a water tunnel (from Ref. 5).



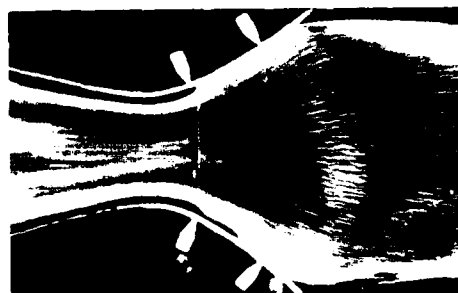
(a) Flow past a knife edge.



(b) Flow along aft portion of blunt body.



(c) Kármán vortex street downstream of cylinder.



(d) Flow in a sharply diverging channel with wall suction.

Figure 3. Representative water flow-visualization results of Prandtl (Prandtl, L. and Tietjens, O. G., Applied Hydro- and Aeromechanics, Dover Publications, 1934).



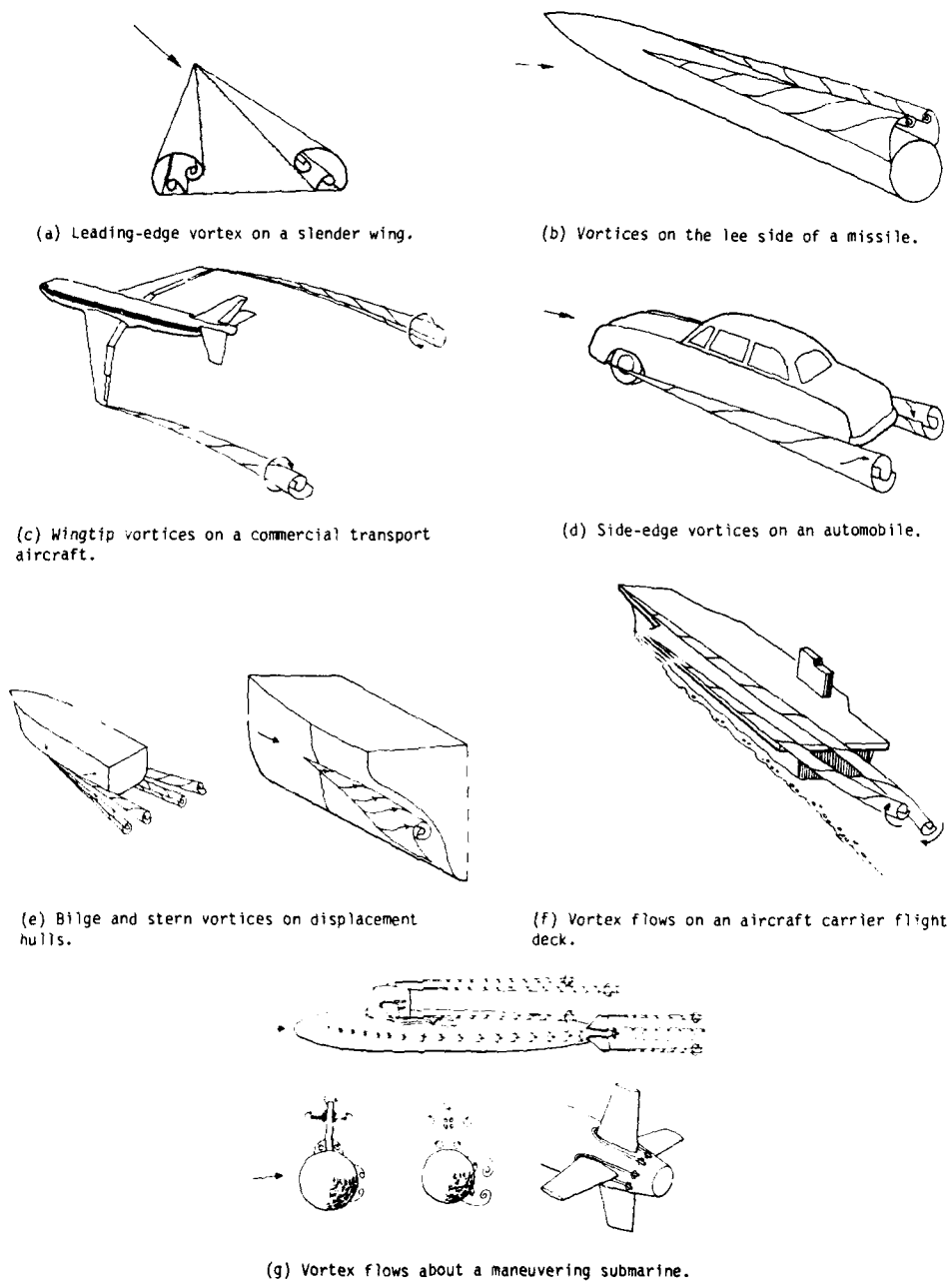


Figure 4. Sketches of vortex flows shed from air, ground, and marine vehicles (Lugt, H. J., Vortex Flows in Nature and Technology, John Wiley & Sons, 1983).

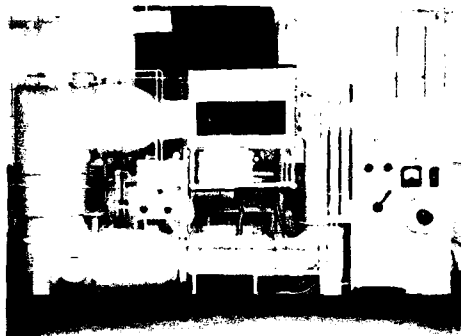


Figure 5. NAE water tunnel.



Figure 6. Wing-submerged lifting fan (NAE water tunnel).



Figure 7. EBF arrangement (NAE water tunnel).



Figure 8. Surface flow on a C-5 transport model (NAE water tunnel).



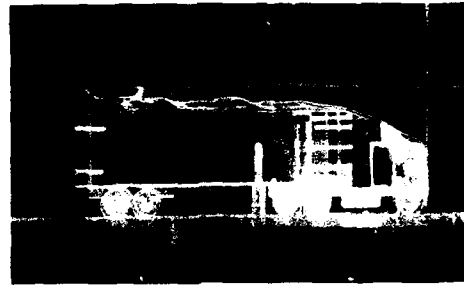
Figure 9. Vortex wake of lifting fuselage, side view (NAE water tunnel).



Figure 10. Modern aircraft with long forebody--angle of attack 45°--vortices asymmetrical (NAE water tunnel).



(a) Original version.



(b) With deflector on cab.

Figure 11. Truck trailer (NAE water tunnel).

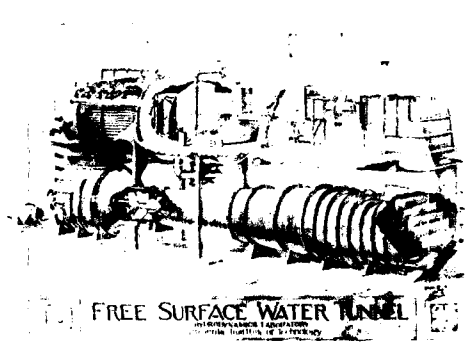


Figure 12. Sketch of the CalTech FSWT.



Figure 13. Cavitating flow about 2-D wedge at high angle of attack (CalTech FSWT).



Figure 14. Northrop Corporation water tunnel.

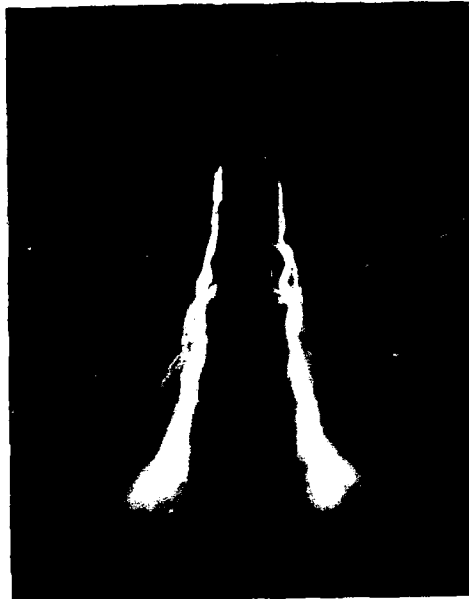


Figure 15. Vortex flows about YF-17 model at  $\alpha = 20^\circ$  (Northrop water tunnel).

REYNOLDS NO.  
(BASED ON CENTER-  
LINE CHORD)

○	WATER TUNNEL	$4.1 \times 10^4$
■	WATER TUNNEL	$9.8 \times 10^3$
+	WATER TUNNEL	$1.0 \times 10^4$
□	WIND TUNNEL	$1.5 \times 10^6$
△	WIND TUNNEL	$1.3 \times 10^6$
●	WIND TUNNEL	$9.0 \times 10^5$
×	WIND TUNNEL	$1.4 \text{ \& } 1.7 \times 10^6$
⋈	WIND TUNNEL	$2.0 \times 10^6$
○	FLIGHT	$40.0 \times 10^6$
◆	WATER TUNNEL	$1.0 \text{ \& } 8.0 \times 10^4$
◊	WIND TUNNEL	$2.0 \times 10^6$
▲	WIND TUNNEL	$1.0 \times 10^6$
⬤	WATER TUNNEL	$3.0 \times 10^4$
⬥	WATER TUNNEL	$3.0 \times 10^4$

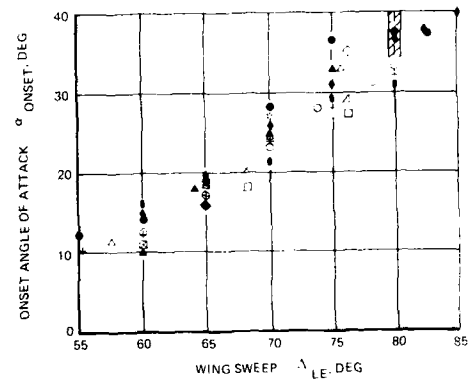


Figure 16. Effects of wing sweep and Reynolds number on delta wing vortex breakdown at the trailing edge (from Ref. 34).

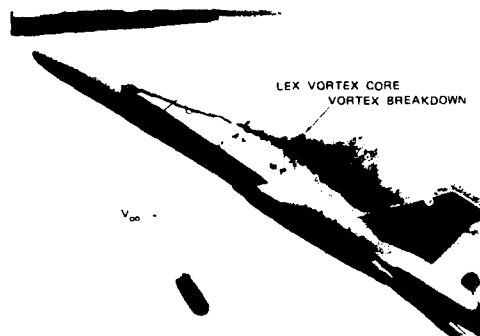
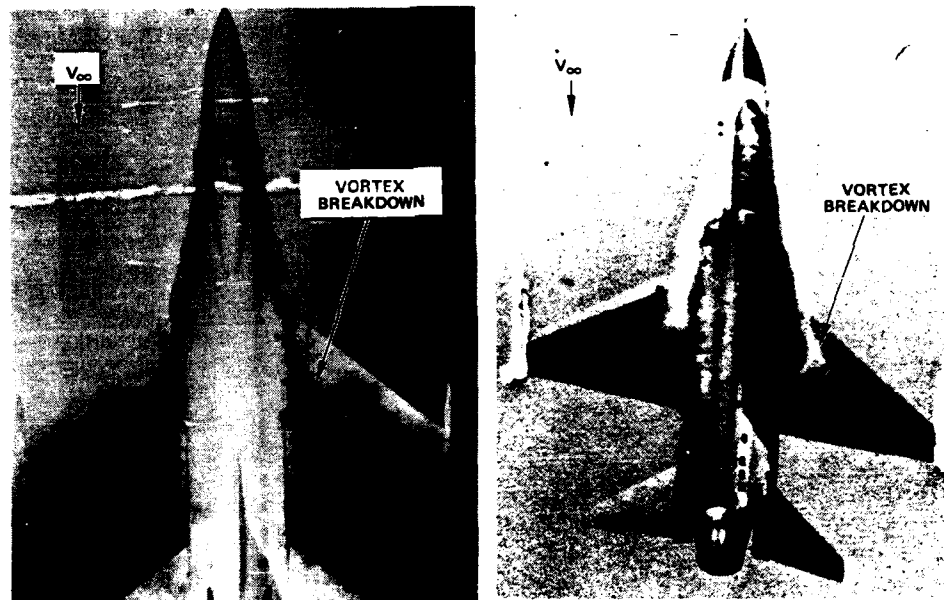


Figure 17. Vortex breakdown on a small-scale model of an advanced fighter configuration (Northrop water tunnel).



(a) Northrop water tunnel--dye injection.

(b) Flight--natural condensation.

Figure 18. Correlation of vortex breakdown on a current fighter aircraft at high angle of attack.

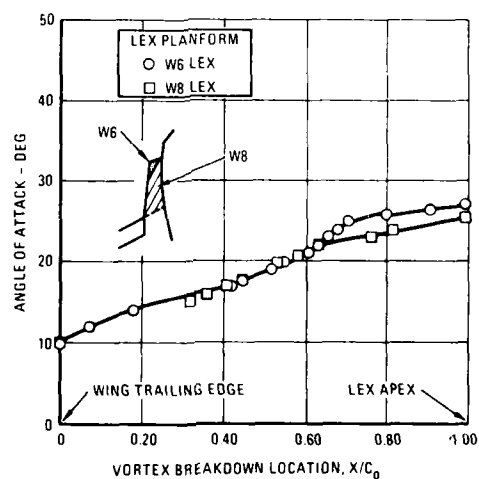
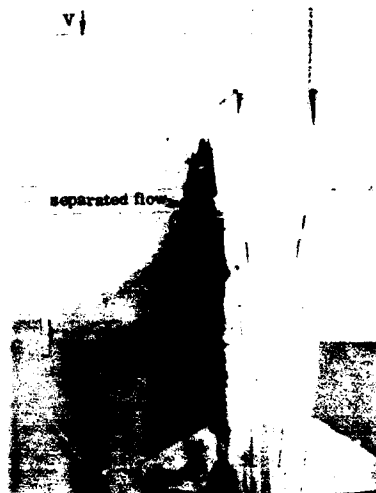
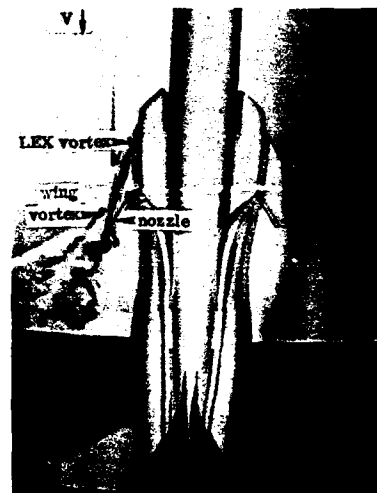


Figure 19. Effect of LEX planform modification on the progression of vortex bursting with the angle of attack (from Ref. 34).



(a) Blowing off.



(b) Blowing on.

Figure 20. Effect of wing upper surface spanwise blowing on the leading-edge vortex behavior at  $\alpha = 24^\circ$  (Northrop water tunnel).

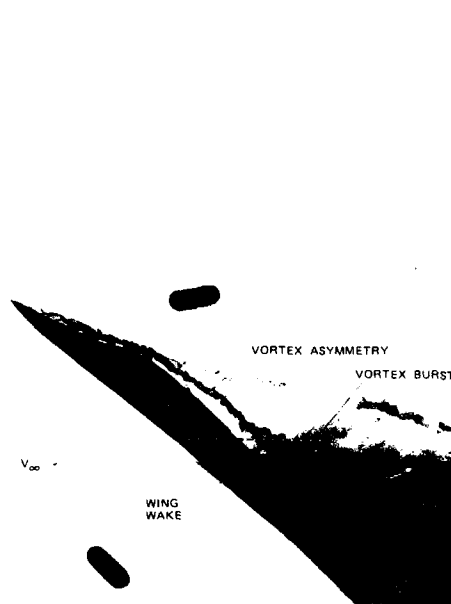


Figure 21. Asymmetric forebody vortex shedding at zero sideslip (Northrop water tunnel).

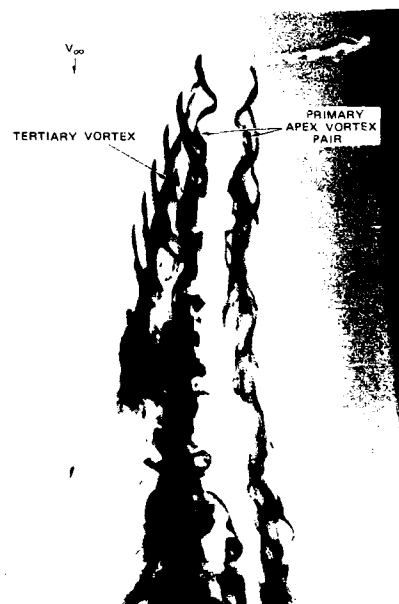


Figure 22. Close-up of vortex flows developed on forebody with shark nose (Northrop water tunnel).

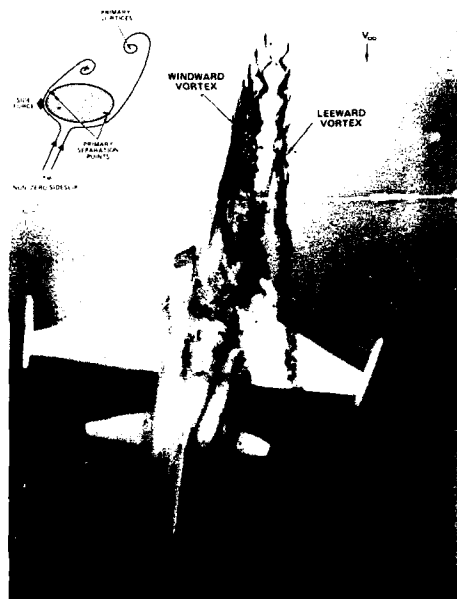


Figure 23. Forebody vortex orientation in sideslip (Northrop water tunnel).

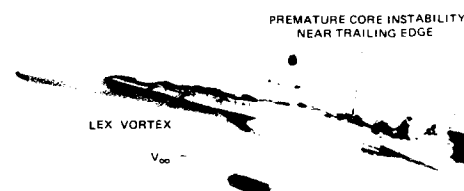


Figure 24. Vortex flow at low angle of attack (Northrop water tunnel).

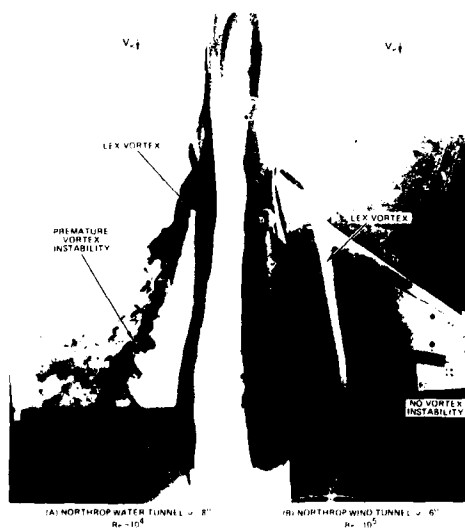


Figure 25. Comparison of vortex flow behavior in water and wind tunnel facilities (Northrop).

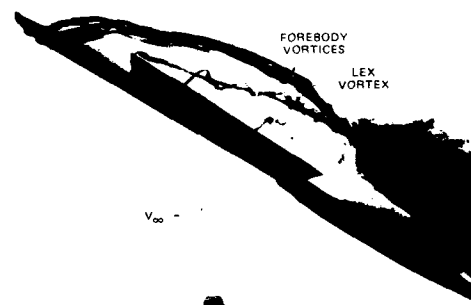


Figure 26. Forebody-wing vortex flow interactions on an advanced fighter model (Northrop water tunnel).

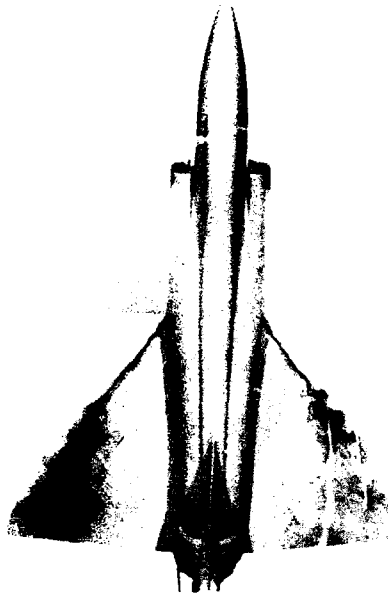


Figure 27. Vortex flows on a canard-wing fighter model (Northrop water tunnel).

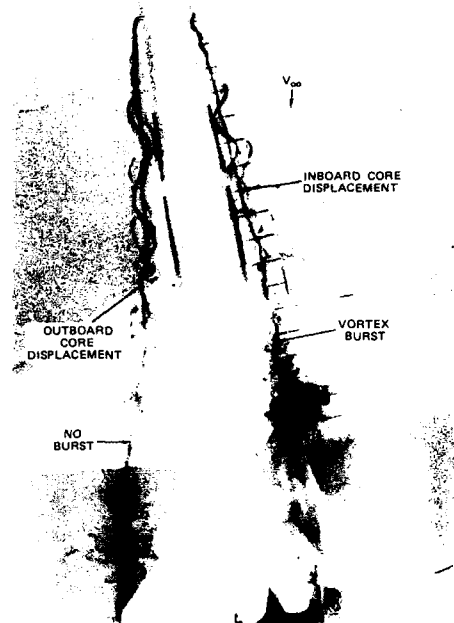


Figure 28. Asymmetric vortex breakdown in sideslip (Northrop water tunnel).

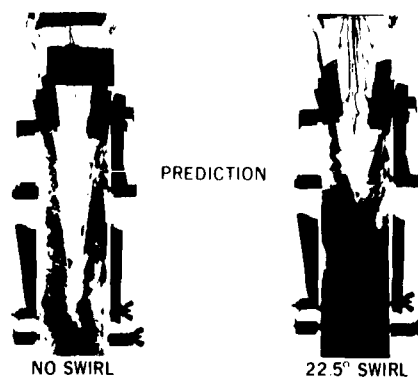


Figure 29. Effect of swirl on 2-D ejector nozzle flow (Northrop water tunnel).

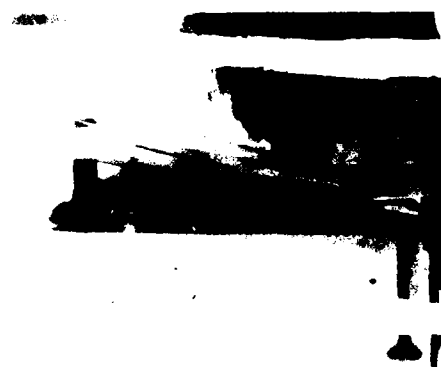


Figure 30. Thrust-reverser effect in ground proximity (Northrop water tunnel).





Figure 31. NASA Ames-Dryden FVS.



Figure 32. Vortex flows about a small-scale model of the F/A-18 (NASA Ames-Dryden water tunnel).



Figure 33. Vortex flows about a small-scale model of the Space Shuttle Orbiter (NASA Ames-Dryden water tunnel).



Figure 34. Laser-enhanced visualization of the flow about a cylinder with trailing disk (NASA Ames-Dryden water tunnel).



(a) Low angle of attack.



(b) High angle of attack.

Figure 35. Flow visualization of a small-scale model of the F-8 oblique wing aircraft configuration (NASA Ames-Dryden water tunnel).

## VORTEX BREAKDOWN AND CONTROL EXPERIMENTS IN THE AMES-DRYDEN WATER TUNNEL

F. K. Owen  
Complere, Inc.  
P. O. Box 1697  
Palo Alto, California 94302  
USA  
and

D. J. Peake  
NASA Ames Research Center  
Moffett Field, California 94035  
USA

## SUMMARY

Flow-field measurements have been made to determine the effects of core blowing on vortex breakdown and control. The results of these proof-of-concept experiments clearly demonstrate the usefulness of water tunnels as test platforms for advanced flow-field simulation and measurement.

## 1. INTRODUCTION

At present, there are significant efforts being made to effect design changes which will improve aircraft agility, maneuverability, and performance. But although significant progress has been made in computational aerodynamics, reliable design changes still cannot be made without recourse to experiment. Attempts to extend tactical flight envelopes require extensive, preflight, ground-based model testing. Unfortunately, conventional wind tunnel testing is expensive and time consuming and most facilities were built before present-day optical methods for quantitative flow field measurements were envisaged. Consequently, there are few nonintrusive, detailed measurements of lee-side vortex flow fields, which are often required to support design evaluation and optimization.

However, in the past, qualitative water tunnel simulations have guided many practical designs and, since most of these facilities have been built with excellent optical access, they are ideally suited for use in advanced flow-field diagnostics. Since the performance of most lifting and maneuvering bodies is governed by extensive viscous wakes and vortical lee-side flows, nonintrusive optical measurement techniques are required. Consequently, water tunnels offer the opportunity to obtain inexpensive, detailed, flow-field measurements to support "cut and try" designs and basic research. Water tunnels are excellent media for conventional and scanning laser velocimetry research (Ref. 1) and laser fluorescence anemometer studies of mixing processes (Ref. 2).

This paper describes an experiment in which detailed qualitative and quantitative flow-field observations of vortex breakdown were obtained and describes some of the results of attempts to control its occurrence. Specifically, the experiment was designed to determine the mechanisms and feasibility of controlling vortex breakdown by introducing relatively low rates of jet blowing along the vortex core.

## 2. BACKGROUND

When a slender delta wing is at an angle of attack to an oncoming stream, the upper- and lower-surface boundary layers flow outward and separate from the leading edges to form two free shear layers that roll up into a pair of vortices above the wing. Increasing angle of attack strengthens the vortices until the induced wing pressure field and associated adverse streamwise pressure gradients cause vortex breakdown. The flow is further complicated as the leading-edge vortices mix with the wake from the trailing edge downstream of the wing. The phenomenon of vortex breakdown (or vortex bursting) can have a significant influence on control-surface performance and unsteady loading. The inherent unsteadiness of the breakdown process compounds the problem as it continually moves the breakdown region back and forth along the vortex axis. This creates serious time-dependent flow problems and asymmetrically disposed breakdown positions above the wing that are aggravated with sideslip.

Wide variations of breakdown patterns have been observed. With increasing swirl, the patterns change from spiral to near axisymmetric (Ref. 3). Spiral breakdown most commonly occurs over delta wings. In this breakdown process, the filament of fluid along the axis does not spread out symmetrically from a fixed stagnation point but, instead, takes on a spiral form around an unsteady "stagnation point" which varies in both space and time. Axisymmetric breakdown over delta wings, although rare, can also occur (Ref. 4). In this case, the vortex has a roughly axisymmetric breakdown pattern with a characteristic bubble, which can have single or multiple tails (Ref. 5).

Unfortunately, the parameters and conditions that result in vortex breakdown are poorly understood because reliable quantitative experimental data are difficult to obtain. With limited experimental information to guide flow-field modeling, numerical studies of vortex breakdown and control have met with only limited success (Ref. 6). There have been two principal reasons for this. First, flow-field unsteadiness associated with breakdown produces directional intermittency. This leads to large uncertainties in mean and unsteady flow measurements obtained with conventional pitot and hot-wire probes. Second, and perhaps

more important, is the fact that vortex breakdown is known to be extremely sensitive to any form of introduced disturbance. Probes, because of their blockage, may drastically alter the breakdown position. For these reasons, almost complete reliance has been placed on flow-visualization techniques to determine flow-field characteristics. But, with the advent of the laser velocimeter, there are now opportunities to determine accurate, quantitative, flow-field velocity measurements of the vortex bursting process.

### 3. EXPERIMENTAL DETAILS

The experiment discussed here was conducted in the NASA Ames-Dryden Water Tunnel. A general layout of this closed-return facility which has a 41- by 61-cm vertical test section is shown in Fig. 1. The four walls are made of plexiglass, which provides excellent optical access for both flow visualization and laser velocimetry. The tunnel is driven by a 50-hp ac motor and the volume flow rate is controlled by a butterfly valve to produce test section flow velocities of up to 35 cm/sec. The flow quality is controlled by three honeycombs in the tunnel circuit, one of which is located at the test section entry after an effective contraction ratio of 5:1 (Fig. 1).

The test configuration which consisted of a 45° half delta planform model upstream of a 16-mesh screen is shown in Fig. 2. The tests were conducted at a free-stream velocity of 11 cm/sec and a model angle of attack of 15°. The purpose of the screen was to produce an adverse pressure gradient sufficient to cause vortex breakdown in the test section ahead of the screen. To control vortex bursting, a small blowing tube was installed at the apex of the half-delta wing through which jets, at velocities higher than the free stream, could be pumped along the core of the tip vortex. The blowing system provided for a maximum jet-momentum coefficient, based on wing planform area, of 0.14 at the maximum jet blowing pressure.

In the past, air or hydrogen bubbles have been used as tracers to visualize flow patterns in water tunnels. For steady flows, streak lines can be identified with streamline patterns. However, in more complex flows of practical interest, the use of bubbles for flow visualization has distinct drawbacks. First of all, their introduction acts as a fluid lubricant which alters the apparent fluid viscosity and therefore its turbulent structure. Second, light refraction at the gas/water interfaces will destroy laser beam coherence and make it impossible to obtain laser velocimeter measurements in the regions where the tracer is present. In the current experiment, the vortex flow field was visualized by injecting fluorescent dyes of different colors through the vortex control tube and from a port near the apex of the model. Horizontal and vertical laser light sheets were generated using an argon-ion laser and a series of cylindrical lenses which produced a variable, thin sheet of laser light that could be focused at different planes in the flow field. The horizontal fluorescent sheets showed flow features in the cross-flow plane, whereas the vertical sheets showed the streamwise flow development. Axial and radial flow visualization scans were recorded on video tape.

Three component laser velocimeter measurements were made with the system shown in Fig. 3. This fringe mode, forward scatter system, which utilized the 4880- and 5145-Å lines of an argon-ion laser, was specifically designed to measure all three components of the vortex velocities by measuring the flow with two different traverse configurations. The computer-controlled traverse system was configured such that successive orthogonal scans measured the axial and tangential (swirl) components and the axial and radial velocities, respectively. Bragg-cell frequency-shifting, which is required for probing directionally intermittent flow fields, was incorporated in both spectral lines. Two traversing systems are shown. The one on the opposite side of the test section from the laser holds the collecting lens and photodetectors for forward-scatter light collection. The traversing system on the laser side of the test section supports the transmitting lenses. Mirrors fixed to this traversing system permit three-dimensional scanning of the velocimeter's sensing volume; the other optics remain stationary. Both traversing systems are driven with computer-controlled stepper motors.

Naturally occurring particles in the tunnel flow were used for light scattering. No additional seeding was required. Single-particle signal processing was used to determine local time-dependent velocities. From these determinations, the local time-averaged velocities and velocity fluctuation levels were calculated. Fluctuating velocity cross-correlations were also obtained by requiring co-incidence on each pair of instantaneous velocity occurrences. On-line data acquisition and display were achieved by means of desk-top computer analysis. Details are given in Ref. 7. Prudent selection of data-acquisition electronics and optical components enabled us to achieve velocity sensitivities down to 1 mm/sec, which were adequate for the present investigation.

### 4. TEST RESULTS

#### 4.1 Laser Vapor Screen

In the absence of jet blowing, vortex breakdown was clearly visible ahead of the mesh screen. Large-scale, unsteady motions associated with directional intermittency throughout the vortex core were apparent. These motions were associated with time-dependent axial changes in vortex breakdown position. Closer visual inspection showed that the breakdown was of a spiral type, which is the form most commonly observed in the flow over delta wings at high angle of attack. At breakdown, the dye filament marking the spiral axis decelerated to form an abrupt kink. But the filaments did not spread out initially. Instead, they took the form of a spiral that persisted for several turns before breaking up into large-scale

turbulent-like flow. These time-dependent spiraling occurrences appeared to move randomly in the cross-flow plane and along the vortex axis.

The effects of jet blowing can be divided into stabilizing and destabilizing regimes that are dependent on the jet excess velocity relative to the free stream. At low blowing rates, the time-dependent spiraling movement along the axis is suppressed, although breakdown still occurs and cross-flow visualization shows that there is still significant large-scale turbulent-like mixing and movement of the vortex core prior to breakdown. As the jet intensity is increased, the flow in both the longitudinal and cross-flow planes is continually stabilized until at an optimum jet momentum coefficient of 0.05, for these experiments, bursting is completely suppressed and vortex trajectory meandering is stabilized. Further increases in jet velocity tend to increase lateral growth and motion. There is, then, a general increase in flow-field large-scale unsteadiness although vortex bursting continues to be suppressed. Examples of cross-flow, laser-light-sheet-fluorescence flow visualization are shown in Fig. 4.

#### 4.2 Flow-Field Measurements

Based on the visual observations, three axial stations were chosen for extensive mean and unsteady flow documentation. These stations covered the initial and developing jet interaction, and the spiraling and breakdown regions. Tunnel centerline velocity measurements were also made with the model removed to determine the flow-field adverse pressure gradient caused by the screen. These results, shown in Fig. 5, provide a necessary boundary condition for any future flow-field computations.

The mean axial and tangential velocity profiles measured three and four chords from the model apex are shown in Figs. 6 and 7. The "no blowing" axial velocity profiles show that there is a progressive decrease in vortex core momentum as breakdown approaches. Comparisons of the no-blowing axial profiles at  $x/c = 3.0$  and  $4.0$  show not only a general deceleration of the mean flow as the time-dependent breakdown region is approached, but also a much wider spanwise deficit at the  $x/c = 4.0$  station because of accentuated meandering of the vortex spiral. Clearly, axial blowing along the core can overcome and reverse this momentum deficit for a substantial distance downstream. This effect is shown in more detail over the entire jet-blowing pressure range in Fig. 8.

The swirl profiles show that initially each vortex has an outer free vortex form with an inner viscous core. The swirl number of 0.3, based on the ratio of the measured maximum local tangential and free-stream velocities is indicative of "moderate" vortex strength. The principal feature of each set of tangential velocity profiles is the progressive downstream decrease in the maximum induced velocity and mean gradient across the core. A comparison of these tangential and axial velocity profiles shows that the momentum addition due to blowing enhances the core of the swirling flow in such a way that deceleration of both axial and tangential velocity components is alleviated near the axis. As a result, vortex strength is increased and breakdown is delayed. Radial velocity profiles, Fig. 9, show that there are also significant increases due to core meandering associated with vortex breakdown. It is also an indication of increased time-dependent flow angularity in the cross-flow plane.

Detailed analysis of the test results shows that there is an optimum blowing rate for vortex stabilization and control. Consider first the comparison of the tangential velocity profiles shown in Fig. 10. Clearly, the highest jet-blowing pressure degrades the vortex, reducing both the maximum induced tangential velocity and the mean gradient across the viscous core. Comparisons of this type have been used to determine the increases in maximum tangential velocity and vorticity induced by jet blowing. Figure 11 shows the effect of jet blowing on the measured maximum induced tangential velocity normalized by the value observed without blowing. The effect is clearly significant, especially at the  $x/c = 4.0$  station. An indication of the vorticity induced by jet blowing is given in Fig. 12, where it can be seen that vorticity levels of up to three times the baseline value can be achieved at the optimum jet-velocity ratio. At higher blowing pressures, significant reductions occur, and even detrimental results are apparent at the highest blowing rates. Calculated vorticity decay rates shown in Fig. 13 confirm the favorable effects of moderate axial blowing, which can double the extent of axial vortex preservation. Figure 14 shows that, with optimum blowing, the axial vorticity transport can be increased by almost an order of magnitude.

Some insight into the unsteady features of vortex breakdown can be determined from the fluctuating flow measurements. The axial velocity disturbance levels, measured along the core, Fig. 15, show that, although some flow reversal is still present at the lower velocities, jet blowing produces a dramatic improvement in vortex stability followed by some slight degradation at high jet velocities. Dramatic disturbance-level reductions across the entire vortex core can be achieved with optimum jet blowing (Fig. 16). Since local unsteadiness levels above 30% indicate points in the flow at which instantaneous flow reversal occurs, we can see that, without jet blowing, there is a significant region of directionally intermittent flow. This region is completely removed with blowing. There is a significant stabilization of the flow field as vortex breakdown no longer occurs and local ratios of the dynamic loadings are reduced by factors of up to 20. Tangential centerline turbulent-like mixing-length scales have also been calculated using the local disturbance levels and mean flow gradients. These results, Fig. 17, show that, without blowing, the mixing-length scales, which are related to vortex movement in the cross-flow plane, are about equal to the extent of the local time-averaged viscous core. Optimum blowing reduces these scales by almost a factor of three, although the detrimental effects of excess jet blowing are more clearly evident. Centerline axial mixing-length scales based on measured axial velocity fluctuation levels and mean axial velocity gradient are significantly larger. They indicate that, without jet blowing, the extent of the breakdown region is comparable to that of the model chord length.

Turbulence modeling of these flows will also require an understanding of the mixing mechanisms between a free jet issuing into a surrounding swirling flow field. Figure 18 compares the free-jet velocity profile with that measured within the vortex. It is apparent, from the differences in spreading rate, that there are significant changes in the entrainment and mixing mechanisms in the two cases. Apparently there is some centrifugal-force stabilization of the large-scale mixing and entrainment mechanisms. The effect of swirl is to restrict the jet entrainment and confine its influence along the core. This confinement improves jet effectiveness in providing an effective sink which preserves vortex coherence, lifetime, and stability. Additional insight into the turbulent-like nature of the vortex flow fields, with and without jet blowing, can be deduced from Figs. 19 and 20, which show the correlation between the large-scale axial and tangential fluctuations. Comparisons of the results at the  $x/c = 3.0$  and  $4.0$  stations clearly show the spanwise increase in vortex meandering as breakdown occurs in the zero jet-flow velocity case. This wandering generates an extensive region of high levels of apparent shear stress that can be significantly confined and stabilized with blowing.

##### 5. CONCLUDING REMARKS

The results of this simple experiment show that vortex breakdown can be controlled, and eliminated, by relatively small amounts of jet blowing along the vortex axis. For this particular experiment, an optimum value of jet-momentum coefficient for vortex control has been identified. This optimum value of 0.05 corresponds to a jet excess momentum equal to the vortex-core-momentum deficit without blowing. In retrospect, it is not too surprising that the most efficient jet-blowing pressure minimized the axial mean-velocity gradients across the vortex. In simplistic terms, this means that the jet gave the wing vortex an initial "push," which moved it with the local mean velocity; therefore, in the Lagrangian frame it was "unaware" of convection. Consequently, minimal energy was extracted from the vortex by mean-axial-velocity gradients.

Of course, optimum blowing conditions may well be different in other, more practical situations. However, this optimization criterion may still hold and the experimental approach investigated here could well prove effective if it is applied to leading-edge-extension (LEX) vortex control of twin-tail fighter aircraft. Successful application could lead to significant reductions in time-dependent dynamic loading and flow angularity associated with vortex breakdown. Vortex control could greatly alleviate structural fatigue and improve control-surface effectiveness and response.

Finally, this work clearly demonstrates how water tunnels can be used in conjunction with advanced optical techniques to provide nonintrusive, detailed, flow-field measurements of complex fluid flows with a minimum of expense.

##### REFERENCES

1. Owen, F. K., "A Scanning Laser Velocimeter for Turbulence Research," NASA CR-172493, 1984.
2. Owen, F. K., "Measurements of Instantaneous Velocity and Concentration in Turbulent Mixing Flows," AGARD CPP-193, 1976.
3. Sarpkaya, T., "Vortex Breakdown in Swirling Conical Flows," AIAA J., Vol. 9, No. 9, 1971, p. 1792.
4. Lambourne, M. C. and Bryer, D. W., "The Bursting of Leading Edge Vortices--Some Observations and Discussion of the Phenomenon," Brit. A.R.C.R. & M., No. 3282, 1962.
5. Faler, J. H. and Leibovich, S., "Disrupted States of Vortex Flow and Vortex Breakdown. Phys. Fluids, Vol. 20, No. 9, 1977, p. 1385.
6. Karashima, K. and Kitama, S., "The Effect of a Small Blowing on Vortex-Breakdown of a Swirling Flow," Computational Techniques & Applications: CTAC-83, 1984, p. 553.
7. Owen, F. K., Orngard, G. M. and McDevitt, T. K., "A New 3D LDV System for the NASA Ames 6 x 6 ft. Wind Tunnel," IEEE, 85-CH-2210-3, 1985, p. 257.

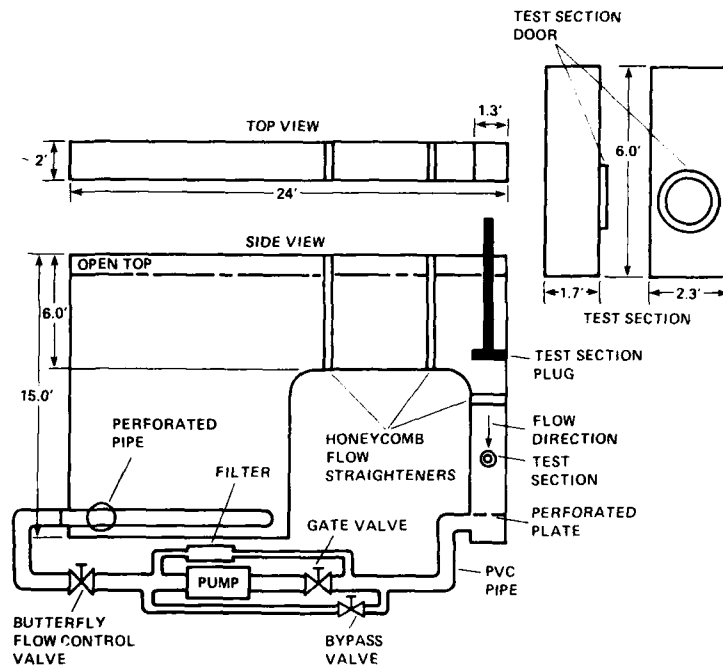


Figure 1. Layout of NASA Ames-Dryden water tunnel.

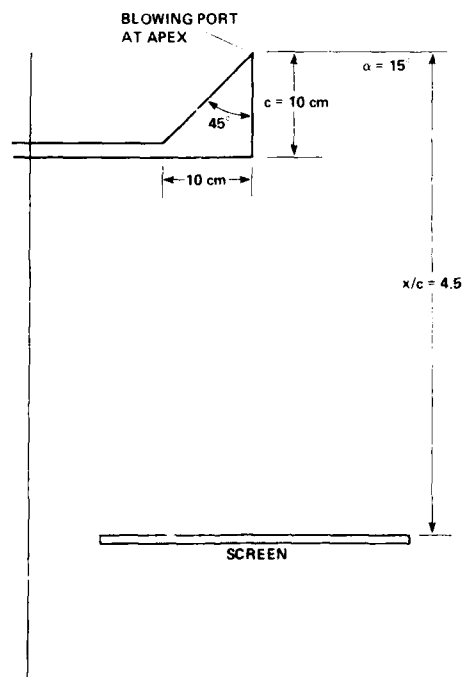


Figure 2. Water tunnel test apparatus.

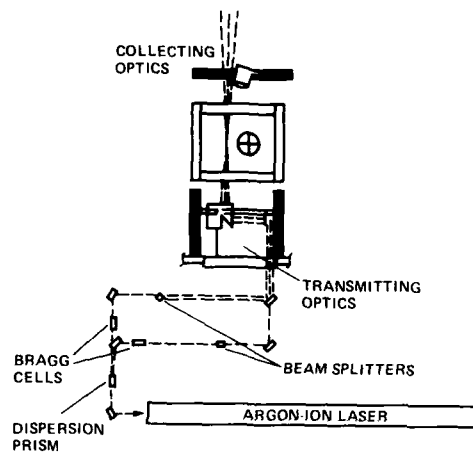
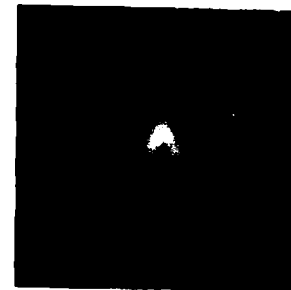
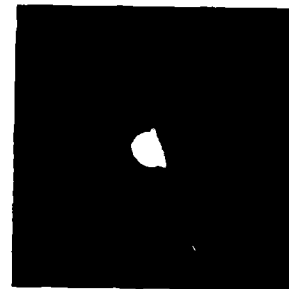


Figure 3. Laser velocimeter.

 $C_\mu = 0$  $C_\mu = 0.05$  $C_\mu = 0.10$ Figure 4. Laser fluorescence light sheets illuminating the cross-flow plane,  $x/c = 4.0$ .



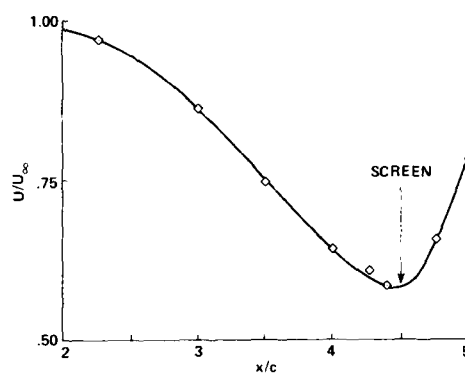


Figure 5. Axial velocity profile along the centerline of the test section with the screen installed.

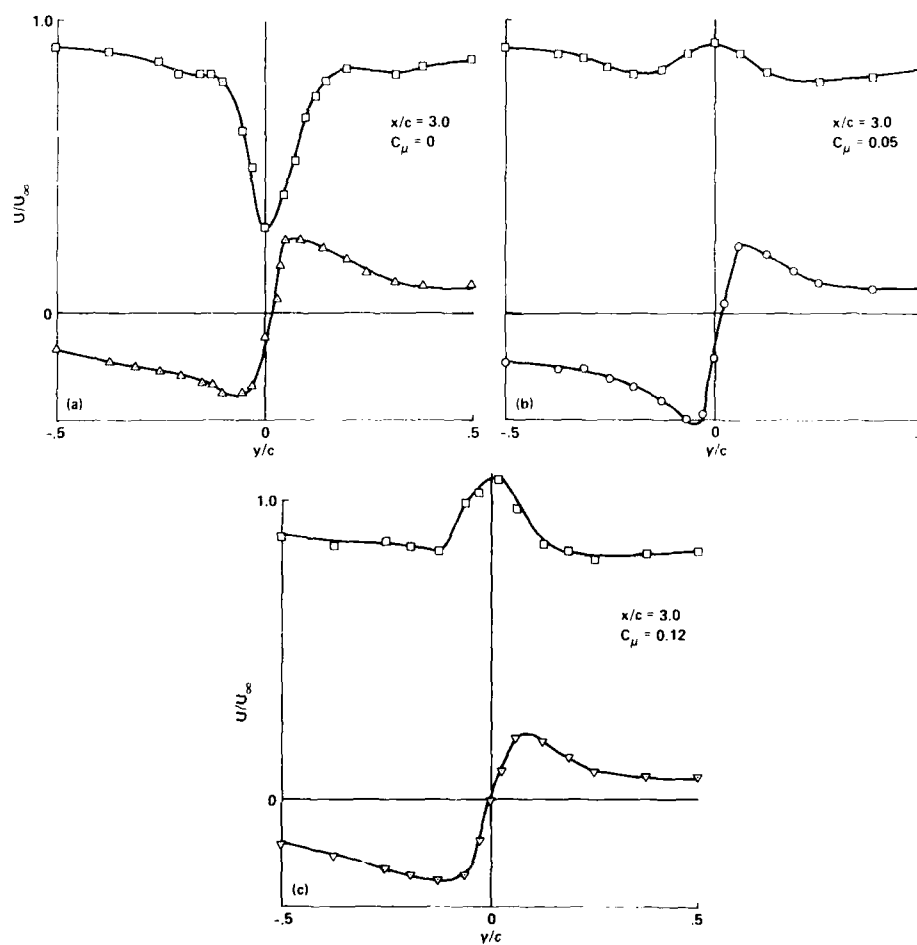


Figure 6. Time-averaged axial and tangential velocity profiles,  $x/c = 3.0$ .

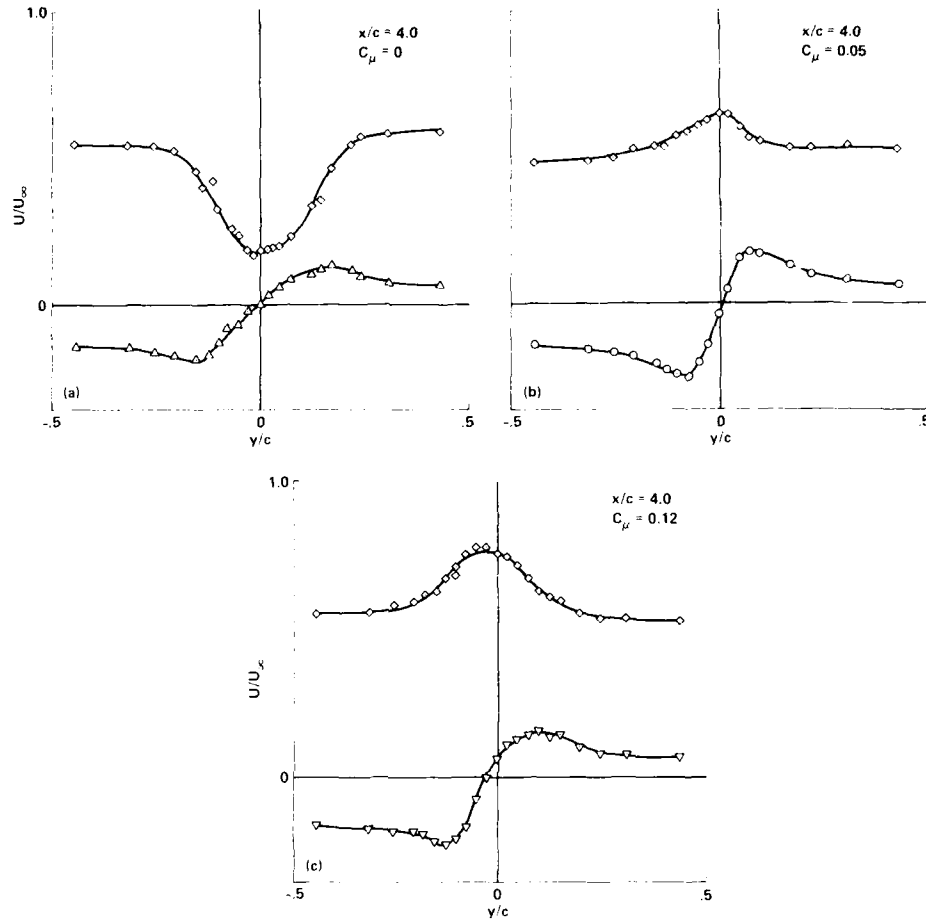
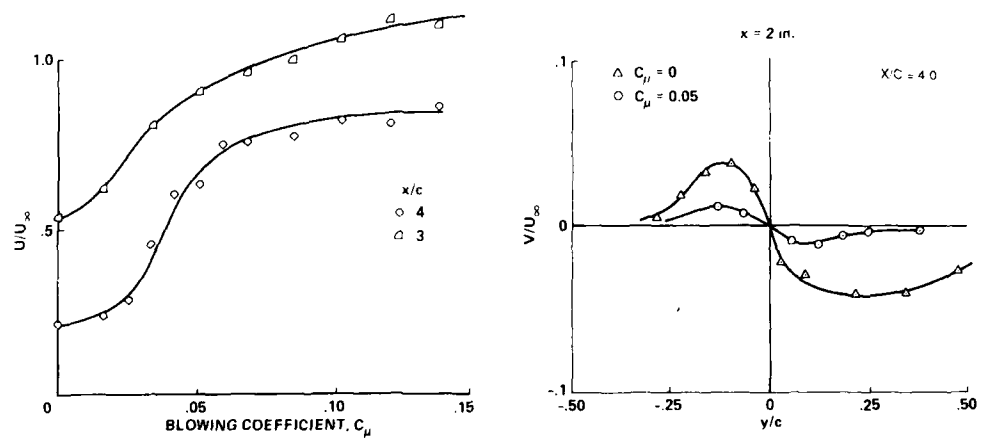
Figure 7. Time-averaged axial and tangential velocity profiles,  $x/c = 4.0$ .

Figure 8. Influence of jet blowing on vortex-core axial velocity profiles.

Figure 9. Influence of jet blowing on radial velocity profiles.

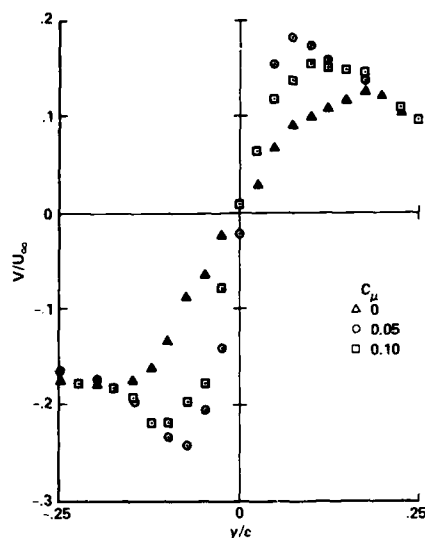


Figure 10. Comparison of tangential velocity profiles,  $x/c = 4.0$ .

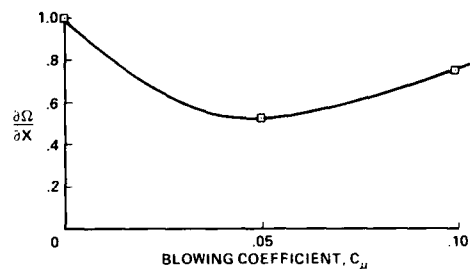


Figure 13. Streamwise vorticity decay rates.

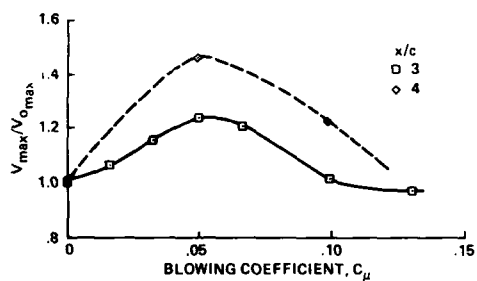


Figure 11. Tangential velocity induced by blowing.

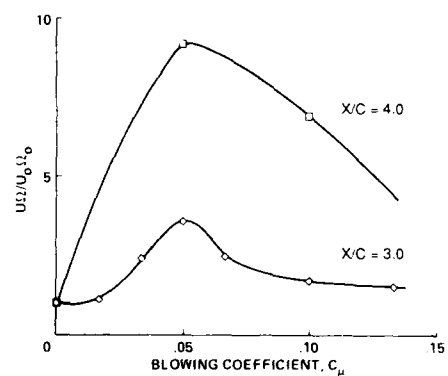


Figure 14. Streamwise vorticity convection rates.

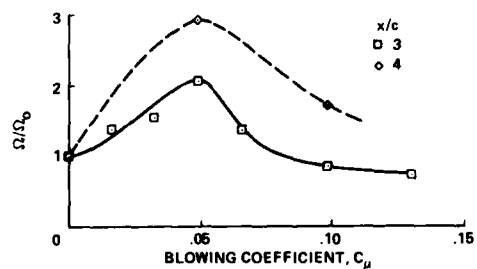


Figure 12. Streamwise vorticity induced by blowing.

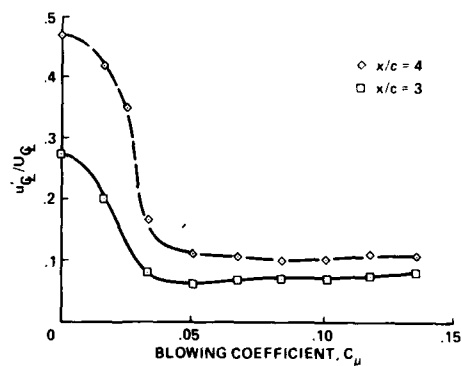


Figure 15. Influence of jet blowing on axial velocity fluctuation levels.

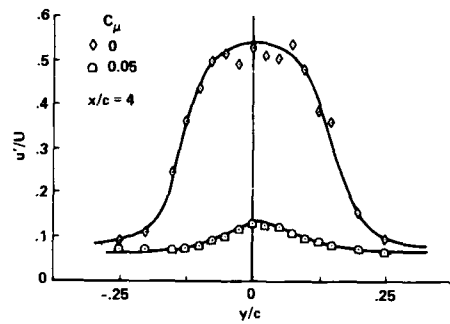


Figure 16. Influence of jet blowing on local axial fluctuation levels.

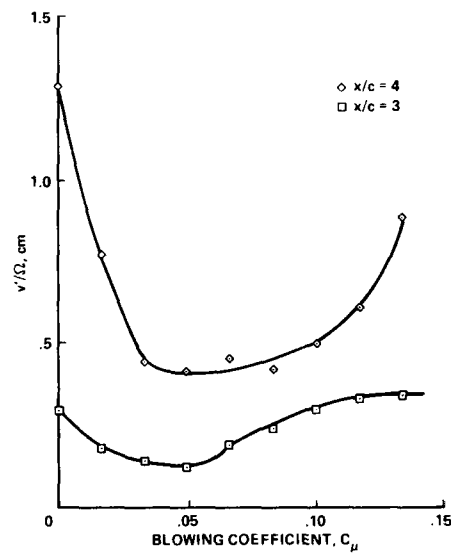


Figure 17. Influence of jet blowing on tangential velocity fluctuating length scales.

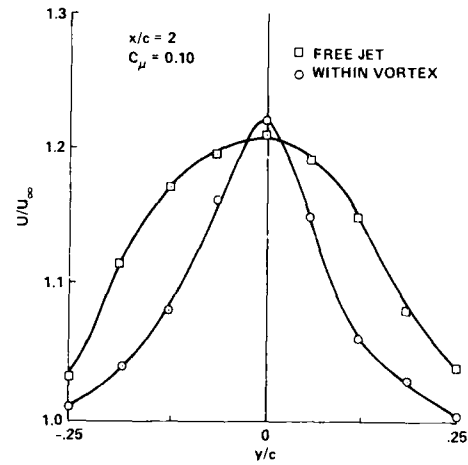


Figure 18. Free- and confined-jet flow profiles.

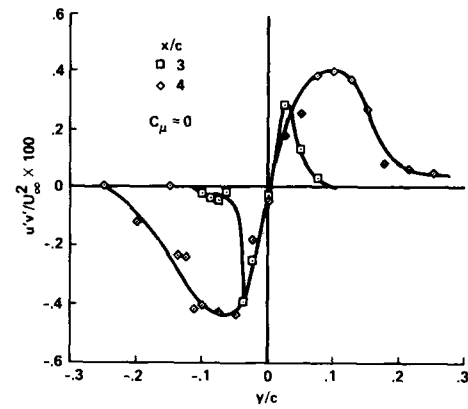


Figure 19. Axial variation of fluctuating velocity cross correlations.

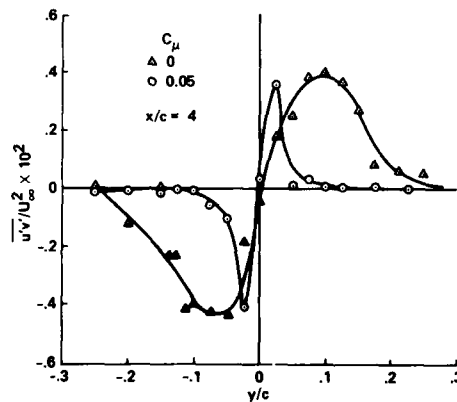


Figure 20. Influence of blowing on the fluctuating velocity cross correlations.

# **QUALIFICATION D'UN TUNNEL HYDRODYNAMIQUE POUR DES PESÉES DE MAQUETTES AÉRONAUTIQUES**

**B. CHEZLEPRETRE, Y. BROCARD  
BERTIN & Cie - 78373 PLAISIR - FRANCE**

## **RESUME**

BERTIN & Cie dispose d'un tunnel hydrodynamique à grand nombre de Reynolds dans lequel sont effectuées des pesées, des visualisations et des mesures par vélocimétrie laser.

L'objet de la communication est de présenter d'abord le moyen d'essais, puis les résultats d'essais récents de qualification du tunnel pour des pesées à caractère aéronautique.

La qualification a consisté à comparer les résultats issus du tunnel à ceux obtenus par l'ONERA en soufflerie sur la même maquette (il s'agit d'une aile-canard : nombre de Reynolds : tunnel 560 000, soufflerie : 900 000).

Le recouplement, tout-à-fait satisfaisant, met en évidence l'intérêt de ce type de tunnel pour l'étude de nouveaux concepts en Aéronautique grâce à l'association de pesées qualifiées et de visualisations tridimensionnelles de l'écoulement, la vélocimétrie laser pouvant de plus, compléter l'analyse par des mesures locales de vitesse.

## **SHORT ABSTRACT**

BERTIN and Co is running a water-tunnel where visualisation, velocity and force measurement are performed.

Recently, force measurements were done on a wing-canard model which was also tested in a wind tunnel at ONERA.

The paper focuses on the presentation of the facility (including its laser anemometer and the computerized data acquisition system) and on the satisfactory comparison of the balance measurements obtained in the water tunnel and in the wind tunnel.

## **NOTATIONS :**

C<sub>x</sub> : coefficient de traînée

C<sub>z</sub> : coefficient de portance

C<sub>m</sub> : coefficient de moment de tangage (par rapport à l'axe ONERA, figure 5)

S : surface de référence : surface de la demi-aile sans tenir compte de la présence ou de l'absence du canard  
(S = 0.01981 m<sup>2</sup>)

$\alpha$  : angle d'incidence de la maquette.

## **1. - INTRODUCTION**

La Société BERTIN dispose depuis 1976 d'un tunnel hydrodynamique à grand nombre de Reynolds dans lequel ont été traités (références 1 et 2) de nombreux problèmes d'Aérodynamique ou d'Hydrodynamique.

Peu à peu, il est apparu indispensable d'affiner les investigations effectuées dans ce tunnel, ce qui a conduit à :

- améliorer la qualité de l'écoulement dans la veine d'essais (par diverses modifications de l'installation),
- développer les moyens de mesure.

C'est dans cet esprit que le tunnel a été équipé progressivement d'un ordinateur pour l'acquisition et le traitement des mesures, puis d'un vélocimètre laser.

Récemment (1986), une campagne d'essais de qualification du tunnel pour des pesées de maquettes aéronautiques a été effectuée sous contrat de la Direction des Recherches Etudes et Techniques (DRET).

La qualification a consisté à comparer sur la même maquette les résultats mesurés au tunnel hydrodynamique à ceux obtenus par l'ONERA (référence 3), dans la soufflerie transsonique S3 Chalais utilisée à basse vitesse (M = 0,3).

L'objet de cette communication est de présenter la confrontation des résultats provenant des deux moyens d'essais après une description du tunnel et de son équipement ainsi que de la maquette et de son montage en soufflerie et en tunnel hydrodynamique.

## **2. - LE TUNNEL ET SON EQUIPEMENT**

### **2.1. - Caractéristiques principales**

Le tunnel situé à PLAISIR (figure 1) fonctionne par gravité à charge constante (environ 12 m) : deux pompes de recirculation assurent un fonctionnement en continu par aspiration dans une réserve d'eau de 80 m<sup>3</sup> et par refoulement dans une cuve à niveau constant.

Des veines de diverses dimensions peuvent être installées ; la plus utilisée est une veine horizontale de 400 x 400 mm<sup>2</sup> dans laquelle la vitesse peut être réglée entre 0 et 4,5 m/s :

dimensions veine :	400 x 400 mm <sup>2</sup>
vitesse veine :	0 à 4,5 m/s

## 2.2. - Nombre de Reynolds

Dans la plupart des cas traités au tunnel, il y a intérêt à fonctionner au voisinage de la vitesse maximale pour bénéficier d'un nombre de Reynolds élevé et ainsi obtenir des résultats représentatifs du fonctionnement réel.

En supposant une maquette dont la longueur caractéristique est égale à 0,42 m, le nombre de Reynolds atteint  $10^6$

$$R = 10^6$$

Cette valeur relativement élevée classe le tunnel BERTIN parmi les plus performants en nombre de Reynolds.

## 2.3. - Qualité de l'écoulement

L'installation a été conçue avec le même souci de qualité qu'une soufflerie, le circuit comporte divers dispositifs régularisateurs et une contraction au niveau de la veine (rapport égal à 7 dans le cas de la veine 400 x 400).

De plus, le choix d'une alimentation par cuve à niveau constant assure à l'écoulement dans la veine des conditions génératrices stables et bien découplées du bruit hydrodynamique des pompes, les excitations mécaniques générées par ces dernières étant par ailleurs filtrées par des raccords souples.

Grâce à ces précautions, le tunnel permet l'exécution d'études d'Hydroacoustique, d'Hydrodynamique ... et d'Aérodynamique.

La qualité de l'écoulement est satisfaisante :

- vitesse dans la veine quasi-uniforme,
- niveau de turbulence (en dehors des couches limites) de l'ordre du pourcent à 4 m/s.

## 2.4. - Equipement de la veine de 400 x 400 mm<sup>2</sup>

La veine comporte, grâce à une structure reportée à l'extérieur, de grands hublots en plexiglass assurant une visibilité intégrale sur les 4 faces et sur 1200 mm de longueur ; cela est particulièrement intéressant pour :

- les visualisations d'écoulement,
- l'investigation par vélocimétrie laser en tout point de la veine et en particulier dans les couches limites y compris dans les angles de la veine.

Pour le montage de maquettes à la paroi (figure 2), le hublot inférieur est remplacé par une plaque métallique comportant un piege à couche limite, un puits de balance et des traversées étanches pour l'introduction des ondes.

## 2.5. - Equipement du tunnel

L'équipement du tunnel comprend :

- des moyens de mesure,
- des moyens d'acquisition et de traitement de mesure,
- des moyens de visualisation.

### 2.5.1. - Moyens de mesure (reliés à l'ordinateur)

- les pressions dynamiques et les pressions locales sont mesurées par des sondes adaptées, reliées à des capteurs à membrane,
- les efforts sont déterminés par des balances à jauges extensométriques, l'étanchéité à l'eau étant obtenue par enrobage,
- les vitesses (valeurs moyennes et fluctuations) sont mesurées depuis 1984 par vélocimétrie laser (figure 3) ; en décembre 1985, l'installation hélium-néon à 1 composante a été remplacée par un équipement Argon à deux composantes ; un exemple d'application est donné fig. 4 : sondage horizontal à travers le tourbillon en aval de l'aile rectangulaire pour  $\alpha = 16^\circ$ ,
- l'incidence des maquettes est déterminée par un codeur optique (précision 1/12 de degré).

### 2.5.2. - Moyens d'acquisition et de traitement de mesures

Le tunnel hydrodynamique est équipé d'un ordinateur Digital Equipment PDP 11/23 avec écran et imprimante graphiques.

Grâce à ce matériel et à des logiciels adaptés, chaque point de fonctionnement peut être caractérisé par la moyenne et l'écart type d'un large échantillonnage acquis à cadence élevée (par exemple 1000 points par voie en 1 seconde). A la fin de l'essai, un listing regroupant les résultats numériques et les conditions de l'essai, est établi et l'évolution des paramètres peut être tracée aussitôt.

### 2.5.3. - Moyens de visualisation

Compte tenu des vitesses relativement élevées pratiquées généralement dans le tunnel ( $\approx 4$  m/s), les visualisations sont principalement effectuées par injection d'air.

Les modes d'injection utilisés assurent par cisaillement la création de fines bulles qui dans ces conditions sont fort peu perturbées par l'effet l'Archimède comme le montre l'exemple donné figures 29 et 30 (absence d'ascendance des bulles).

Pour les essais à faible vitesse, des injections colorées sont utilisées, mais le fonctionnement s'effectue alors en circuit ouvert pour éviter la pollution de l'installation.

## 3. - MAQUETTE, MONTAGE EN VEINE ET EFFETS DE PAROIS

### 3.1. - La maquette ONERA

La maquette représente une demi-aile non cambrée, à forte flèche ( $55^\circ$ ) avec bord d'attaque à profil symétrique et bord de fuite tronqué ; elle comporte les variantes suivantes (figures 5 et 6) :

- présence ou non d'un canard en amont,
- forme en plan "rectangulaire" ou en delta, en conservant l'identité de la surface ( $0,01981 \text{ m}^2$ ), de l'allongement ( $\approx 2$ ) et de la corde aérodynamique moyenne ( $C = 0,1395 \text{ m}$ ).

Cette maquette appartient à l'ONERA qui l'a aimablement prêtée à la société BERTIN, afin de supprimer toute incertitude sur l'identité des formes testées en soufflerie puis au tunnel hydrodynamique.

### 3.2. - Montage en soufflerie ONERA et au tunnel BERTIN

#### 3.2.1. - Comparaison des veines

La soufflerie S3 Ch de l'ONERA est une soufflerie transsonique dont la veine qui a une section approximative de  $800 \times 800 \text{ mm}^2$  comporte 2 parois perforées et des coins arrondis (figure 7).

Pour la comparaison, on a retenu des essais réalisés à  $M = 0,3$ , ce qui correspond à des effets de compressibilité négligeables et à un nombre de Reynolds de l'aile de 900 000.

Le tunnel BERTIN possède une veine carrée de section nettement plus faible :  $400 \times 400 \text{ mm}^2$  (figure 8) et une vitesse de  $4 \text{ m/s}$  (nombre de Reynolds de l'aile 560 000).

#### 3.2.2. - Montage de la maquette à la paroi

La demi-aile est montée à la paroi de la veine.

Dans la soufflerie S3 Ch, la veine comporte au niveau de la maquette une légère contraction obtenue par un décalage de 50 mm de la paroi supportant la maquette (figure 7) ; il existe un dispositif d'aspiration (par paroi poreuse), mais ce dernier n'a pas été mis en fonctionnement pour les essais considérés et l'épaisseur de la couche limite au niveau de la maquette n'a pas été mesurée à  $M = 0,3$  (elle est égale à 15 mm en l'absence de remplissage à  $M = 0,8$ ).

Dans le cas du tunnel, la maquette est positionnée (figures 2 et 8) en aval d'un piège à couche limite qui assure au niveau de la maquette un profil de vitesse uniforme et une couche limite faible (3 mm, mesure effectuée par vélocimétrie laser).

#### 3.2.2. - Pesée et rotation de la maquette (figure 5)

Le montage de la maquette s'effectue par l'intermédiaire d'une balance ; il permet la rotation d'ensemble de l'aile et du canard, avec possibilité que le canard soit pesé ou non avec l'aile.

L'axe de rotation de la maquette coïncide avec celui de la mesure du moment de tangage :

- pour le montage ONERA, cet axe correspond au bord de fuite de l'implanture de l'aile rectangulaire
- pour le montage BERTIN, cet axe est situé 50 mm en amont du précédent.

### 3.3. - Correction des effets de parois

Dans le cas des essais à la soufflerie S3 Ch, les dimensions de la veine sont suffisamment grandes pour que l'on puisse négliger l'effet des parois sur les pesées.

Par contre, dans le cas des essais au tunnel hydrodynamique, dont les dimensions sont nettement plus faibles (§ 3.2.1.), il a semblé préférable de tenir compte de ces effets.

Les corrections de blocage, d'incidence et de moment de tangage ont été déterminées par la méthode de Monsieur VAUCHERET (ONERA), référence 4, qui est basée sur un calcul par singularités en écoulement stationnaire, isentropique et irrotationnel.

#### 4. - COMPARAISON DES PESEES

La comparaison des pesées effectuées successivement en soufflerie puis au tunnel hydrodynamique à porte ouverte pour quatre configurations :

- aile "rectangulaire" sans canard,
- aile "rectangulaire" avec canard non pesé,
- aile "rectangulaire" avec canard pesé,
- aile delta sans canard.

##### 4.1. - Comparaison tunnel-soufflerie

Les comparaisons tunnel-soufflerie étant qualitativement similaires pour les 4 configurations testées, on ne présente ici à titre d'exemple que celle relative à l'aile "rectangulaire" sans canard.

Les résultats du tunnel hydrodynamique figurent avec et sans correction des effets de parois, mais on peut constater que les corrections apportées restent relativement faibles, malgré les dimensions réduites de la veine d'essais.

##### 4.1.1. - Courbes $C_x = f(\alpha)$ (figure 9)

- On constate dans l'ensemble une bonne concordance pour la plage centrale d'incidence (écart inférieur à 5 % pour  $10^\circ < \alpha < 30^\circ$ ), les courbes ONERA étant situées entre les courbes BERTIN corrigées et non corrigées des effets de parois,
- à faible incidence, les valeurs obtenues au tunnel sont sensiblement plus élevées que celles mesurées en soufflerie ; cela peut être dû :
  - à la différence des nombres de Reynolds (soufflerie 960 000, tunnel 560 000)
  - à des différences d'épaisseur de la couche limite ou de montage (jeu entre parties pesées et non pesées ...)
  - au faible niveau des valeurs mesurées rendant les mesures difficiles
- à très forte incidence ( $\alpha > 30^\circ$ ), on observe une divergence progressive des traînes due vraisemblablement au fonctionnement en régime décroché, non pris en compte dans la modélisation des effets de parois.

##### 4.1.2. - Courbes $C_z = f(\alpha)$ (figure 10)

- bonne concordance entre les valeurs de  $C_z$  (écart inférieur dans l'ensemble à 5 % entre les valeurs BERTIN corrigées et les valeurs ONERA) jusqu'à une incidence relativement importante ( $\alpha \sim 30^\circ$ ) ; au-delà on observe une divergence progressive,
- à basse incidence, les courbes relatives au tunnel sont bien linéaires (jusqu'à environ  $7^\circ$ ), alors que celles provenant de la soufflerie présentent une cassure pour  $\alpha \sim 1^\circ$ , peut-être imputable à un manque de sensibilité de la balance dans cette plage à  $M = 0,3$  ; au-delà de  $7^\circ$ , l'apparition du tourbillon apporte un supplément de portance bien visible sur les courbes.

##### 4.1.3. - Courbes $C_m = f(\alpha)$ (figure 11)

Les moments de tangage sont considérés dans les axes ONERA (figure 5), ce qui implique pour les valeurs mesurées au tunnel dans les axes BERTIN un transfert de moment et introduit un élément supplémentaire d'incertitude.

Néanmoins, les courbes de  $C_m$  présentent des évolutions voisines, les écarts restant relativement modérés jusqu'à  $\alpha = 20^\circ$  et étant plus marqués au-delà.

Le foyer aérodynamique reste au voisinage de l'axe de mesure ( $C_m \sim 0$ ), sauf en présence du canard pesé qui introduit un effet cabreur marquant (figure 17).

##### 4.1.4. - Courbes de finesse $C_z/C_x = f(\alpha)$ (figure 12)

L'examen des courbes de finesse conduit aux remarques suivantes :

- la finesse maximum (pour  $\alpha = 6$  à  $7^\circ$ ) est nettement plus élevée pour les résultats de soufflerie, ce qui est principalement dû à des traînes plus faibles (§ 4.1.1.),
- à faible incidence, les courbes provenant du tunnel sont linéaires alors que celles relatives à la soufflerie présentent une cassure (pour  $\alpha \sim 1^\circ$ ), imputables à l'évolution similaire de la portance (§ 4.1.2.)
- au-delà de  $\alpha = 20^\circ$ , les courbes deviennent pratiquement identiques.

##### 4.2. - Comparaison des configurations entre elles

La comparaison des configurations entre elles permet de juger en relatif de l'influence d'une modification de maquette évaluée soit en soufflerie, soit au tunnel hydrodynamique.

Deux influences sont considérées :

- influence du canard pour l'aile "rectangulaire"
- influence de la forme en plan de l'aile (en l'absence de canard).



Dans les deux cas, l'analogie des résultats obtenus avec les deux moyens d'essais est remarquable, quel que soit le paramètre.

#### 4.2.1. - Influence du canard (figures 13 à 20)

La présence du canard non pesé apporte une diminution de l'incidence effective de l'aile qui se traduit par :

- une réduction jusqu'à  $\alpha \sim 28^\circ$  des coefficients  $C_x$ ,  $C_z$  et  $C_m$  associée à une petite dégradation de la finesse,
- un recul de l'incidence de décrochage qui passe de  $26$  à  $31^\circ$  accompagné d'un léger gain de portance maximale
- un accroissement au-delà de  $\alpha > 30^\circ$  des coefficients  $C_x$ ,  $C_z$  et  $C_m$  sans modification de la finesse.

Cette réduction de l'incidence effective due à la présence du canard apparaît également sur les visualisations effectuées par bulles d'air (figures 29 et 30 pour  $\alpha < 20^\circ$ ) ; elle se manifeste par un certain retard dans le développement de l'éclatement du tourbillon. Par ailleurs, la pesée du canard entraîne un accroissement sensible des coefficients  $C_x$ ,  $C_z$  et  $C_m$ , dû principalement à la conservation comme surface de référence de celle de l'aile seule.

#### 4.2.2. - Influence de la forme en plan de l'aile (figures 21 à 28)

Les deux formes en plan essayées en l'absence du canard donnent des résultats assez voisins ; on remarque cependant :

- pour l'aile rectangulaire, une portance tourbillonnaire plus forte pour  $13 < \alpha < 28^\circ$
- pour l'aile delta :
  - . un décrochage plus tardif,
  - . un certain effet cabreur,
  - . une perte de finesse jusqu'à  $\alpha > 25^\circ$ .

### 5. - CONCLUSIONS

La campagne d'essais effectuée a permis de qualifier le tunnel hydrodynamique pour des pesées à caractère aéronautique.

En effet, malgré les dimensions réduites de la veine d'essais, les résultats obtenus au tunnel hydrodynamique pour plusieurs configurations d'une maquette prêtée par l'ONERA, sont très voisins de ceux obtenus par l'ONERA en soufflerie avec cette même maquette :

- le recouplement est très bon en relatif, en effet les écarts d'évolution entre des configurations géométriquement différentes sont tout-à-fait similaires,
- le recouplement est correct dans l'absolu, les écarts restant dans l'ensemble inférieurs à 5 %, sauf à très grande incidence en régime décroché.

En conséquence, ce type de tunnel paraît tout-à-fait adapté à diverses études aéronautiques et tout spécialement à l'évaluation d'idées nouvelles grâce à la possibilité d'associer de façon simple :

- des pesées à grand nombre de Reynolds permettant de sélectionner rapidement en relatif les configurations les plus performantes et donnant cependant dans l'absolu, un bon ordre de grandeur des performances,
- des visualisations faciles à mettre en oeuvre et non limitées dans le temps, autorisant une observation directe aisée des phénomènes tourbillonnaires tridimensionnels et une corrélation avec les résultats des pesées,
- des mesures par vélocimétrie laser, pour analyser quantitativement si nécessaire le fonctionnement local.

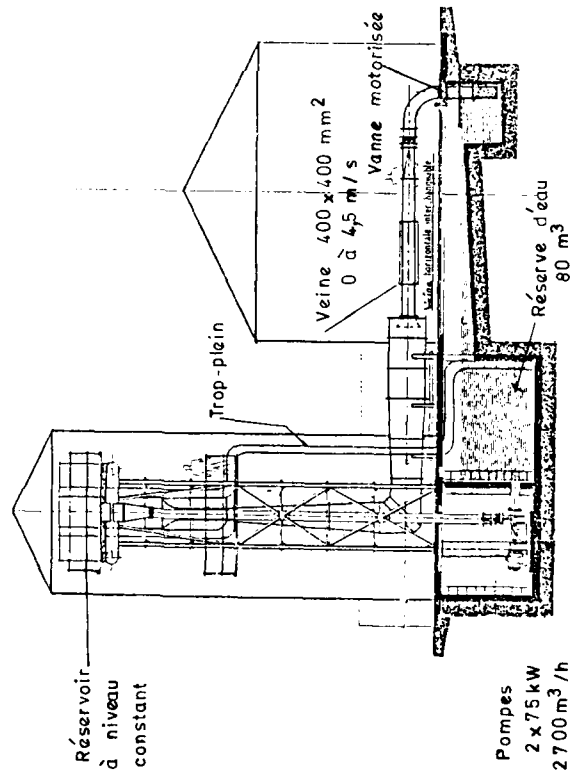
### REFERENCES

1. A Water Tunnel for Aerodynamical Studies - 5<sup>e</sup> Colloque d'Aérodynamique Industrielle - Juin 82 Auch - Sté BERTIN (B. de LAGARDE)
2. Mesures au tunnel hydrodynamique à grand Reynolds - 20<sup>e</sup> Colloque d'Aérodynamique Appliquée AAAF - Nov. 83 Toulouse - Sté BERTIN (B. CHEZLEPRETRE).
3. Interaction tourbillonnaire canard-voilure proche. Influence de la forme en plan et du profil. Pesées 5 composantes et visualisations ( $M = 0,3$  et  $0,8$  et  $0 < \alpha < 40^\circ$ ). PV ONERA 28/3072 (C. PEROUZE)
4. Corrections de parois en soufflerie transsonique. Porosité équivalente - Publication ONERA 1977-3 (X. VAUCHERET).

# TUNNEL HYDRODYNAMIQUE BERTIN

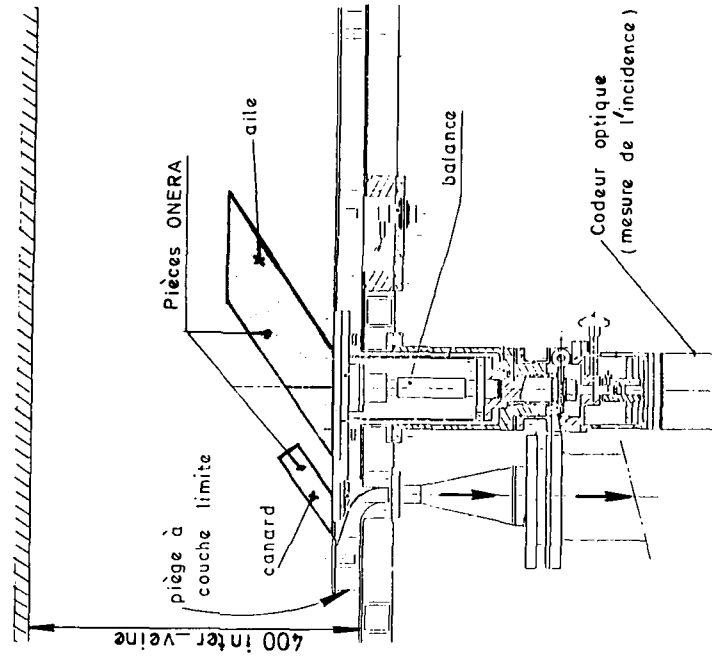
Disposition générale

fig. 1



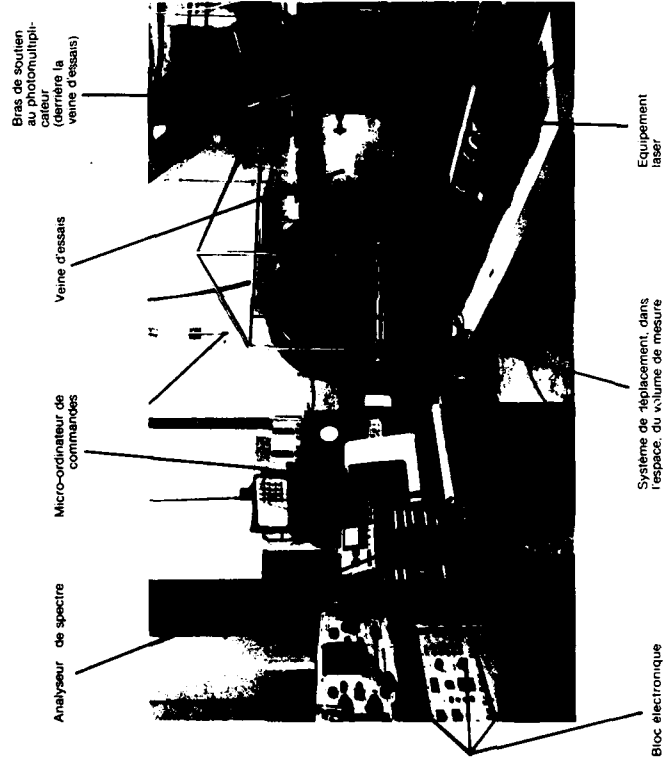
Détail du montage

fig. 2



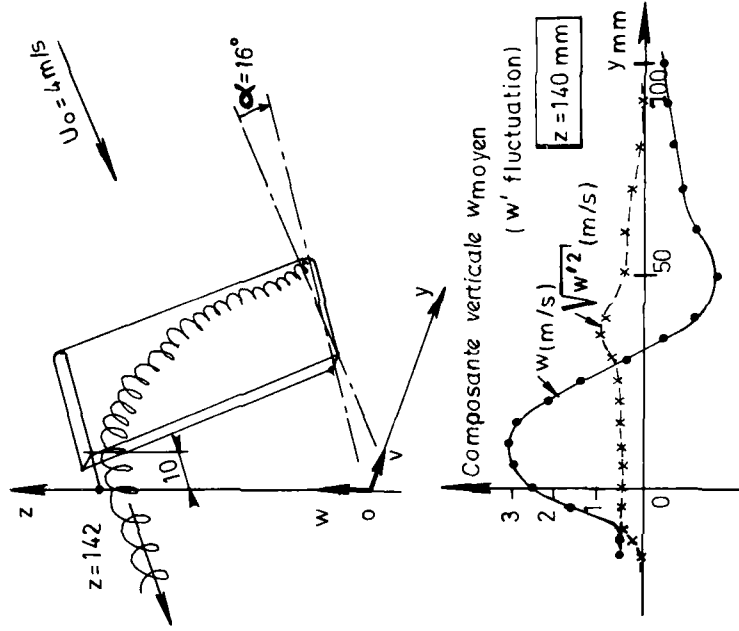
# VELOCIMETRIE LASER

Vue de l'installation (fig.3)



Utilisation du vélocimètre laser sur tunnel hydrodynamique

Exemple d'application (fig.4)  
Sondage horizontal à travers le tourbillon en aval de l'aile rectangulaire seule -  $\alpha = 16^\circ$  -



# DEFINITION DE LA MAQUETTE

fig. 5

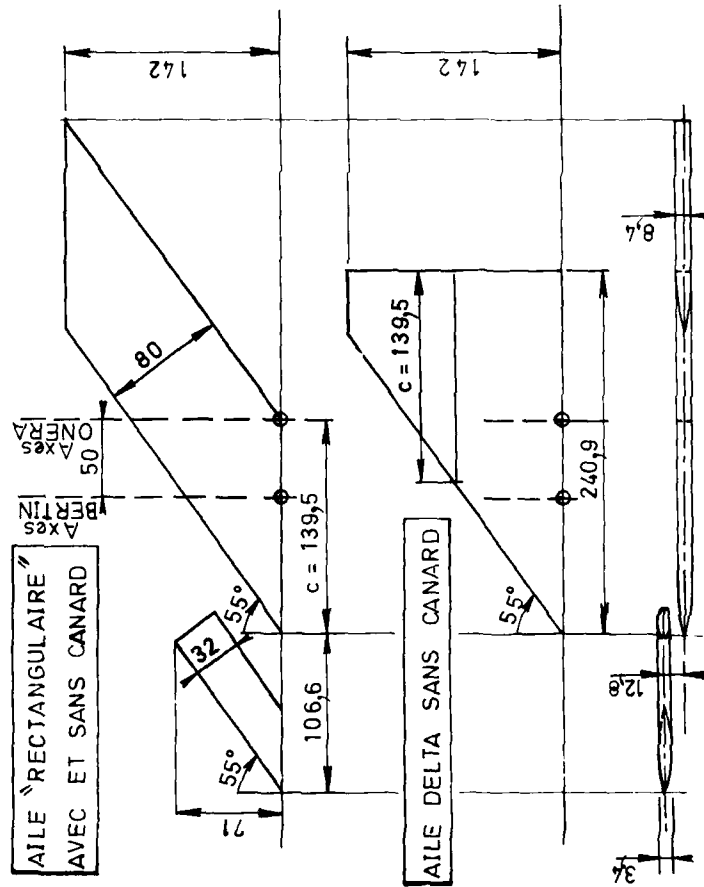
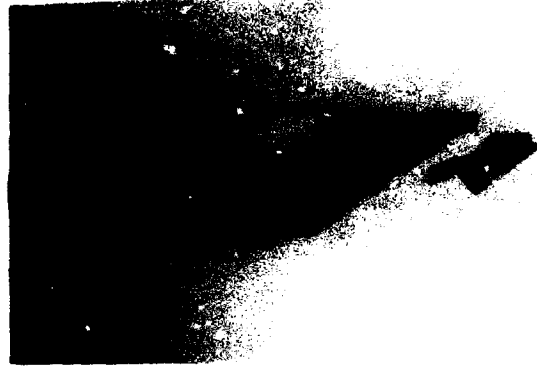


fig. 6



# MONTAGE DE LA MAQUETTE EN VEINE

SOUFFLERIE ONERA S3 Ch

TUNNEL BERTIN

fig. 7

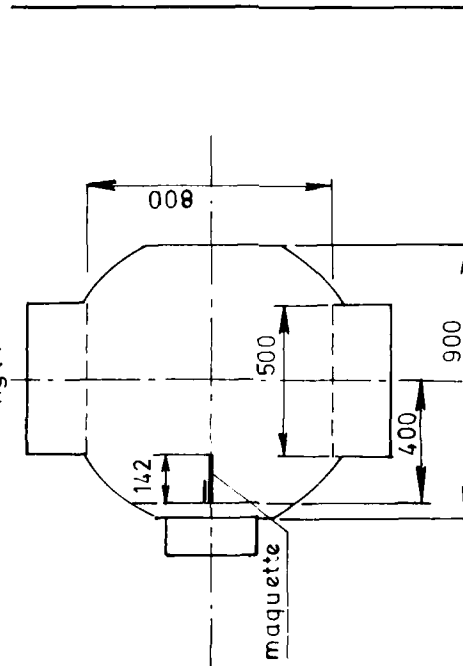
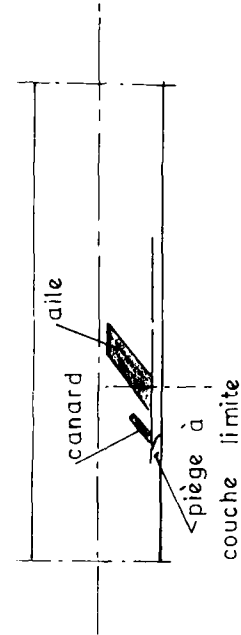
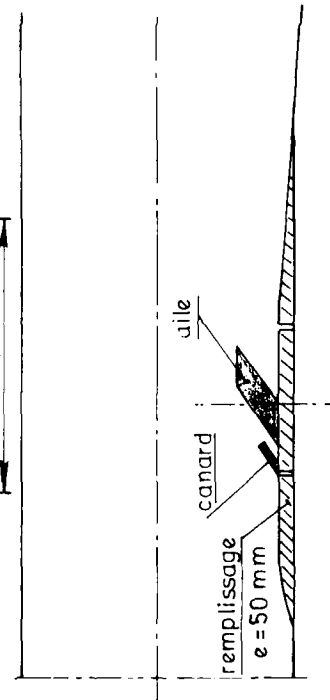
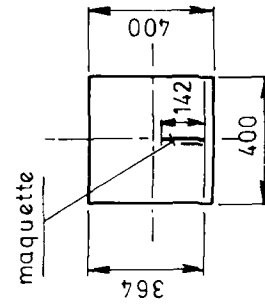


fig. 8



## COMPARAISON SOUFFLERIE - TUNNEL

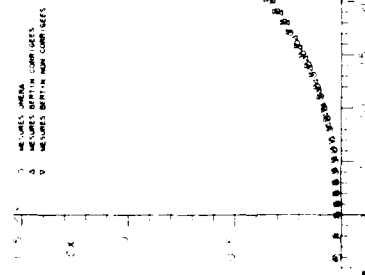
AILE "RECTANGULAIRE"  
SANS CANARD

fig. 9

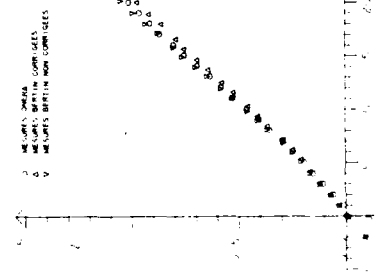


fig. 10

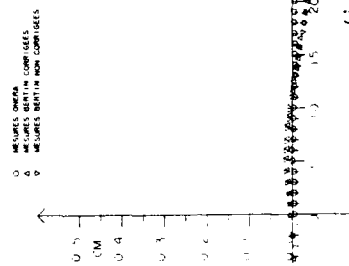


fig. 11

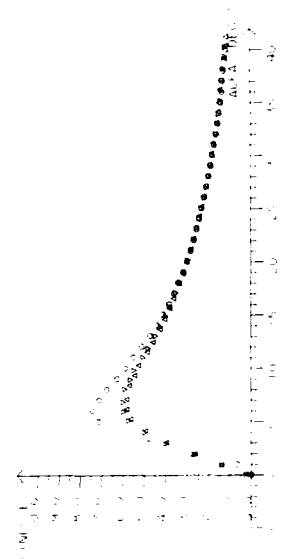
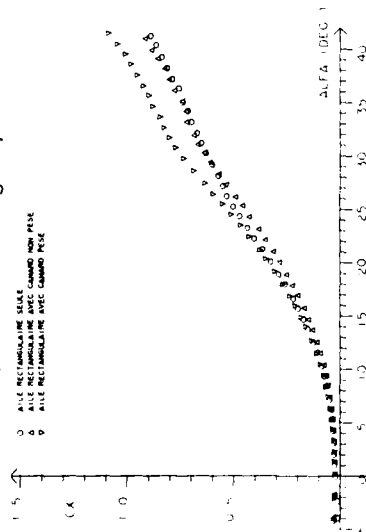


fig. 12

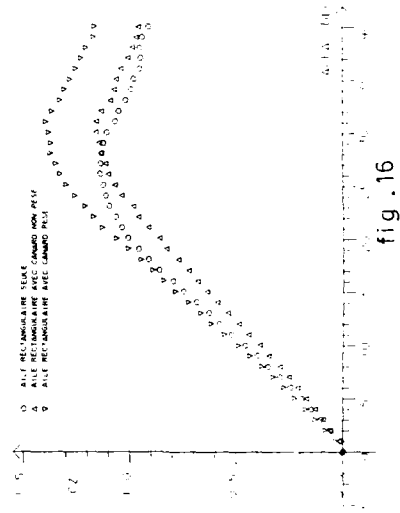
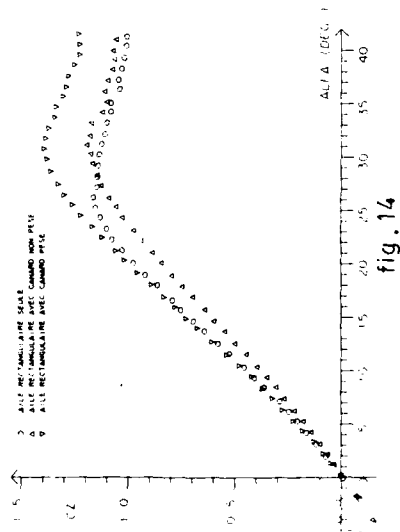
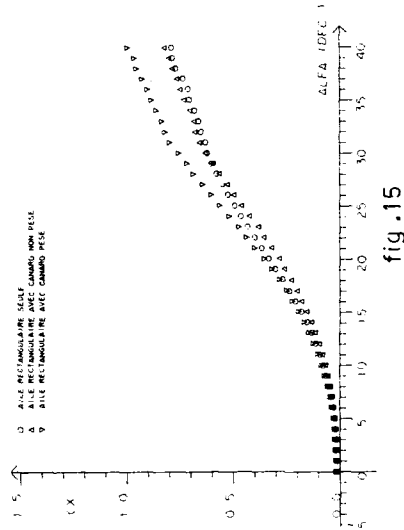
# INFLUENCE DU CANARD

## TUNNEL BERTIN

(Valeurs corrigées)



## SOUFFLERIE ONERA S3 Ch



## INFLUENCE DU CANARD

## TUNNEL BERTIN

(Valeurs corrigées)

- AILE RECTANGULAIRE SEULE  
 △ AILE RECTANGULAIRE AVEC CANARD NON PESE  
 ▽ AILE RECTANGULAIRE AVEC CANARD PESE

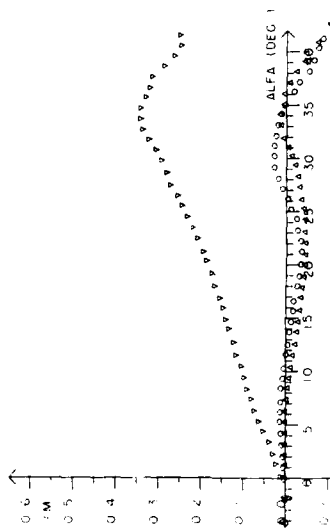


fig. 17

## SOUFFLERIE ONERA S3 Ch

- AILE RECTANGULAIRE SEULE  
 △ AILE RECTANGULAIRE AVEC CANARD NON PESE  
 ▽ AILE RECTANGULAIRE AVEC CANARD PESE

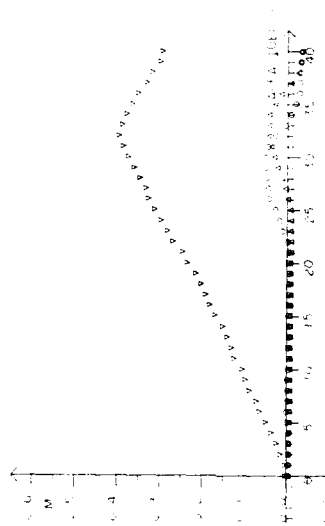


fig. 19

- AILE RECTANGULAIRE SEULE  
 △ AILE RECTANGULAIRE AVEC CANARD NON PESE  
 ▽ AILE RECTANGULAIRE AVEC CANARD PESE

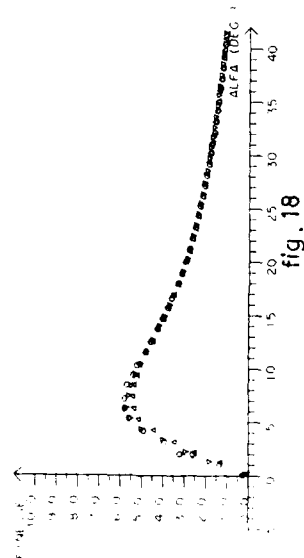


fig. 18

- AILE RECTANGULAIRE SEULE  
 △ AILE RECTANGULAIRE AVEC CANARD NON PESE  
 ▽ AILE RECTANGULAIRE AVEC CANARD PESE

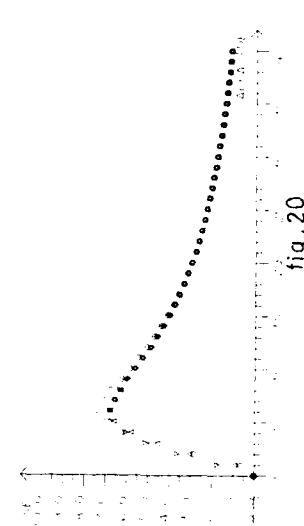


fig. 20



# INFLUENCE DE LA FORME EN PLAN

**TUNNEL BERTIN**  
(Valeurs corrigées)

**SOUFFLERIE ONERA S3Ch**

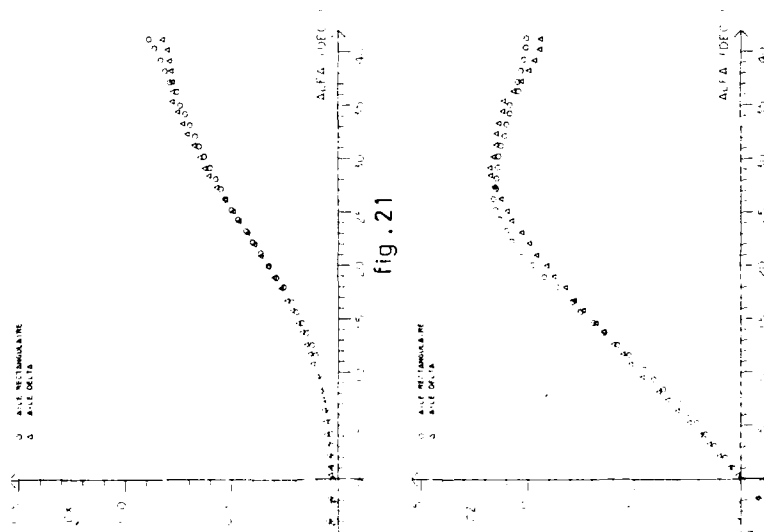


fig. 21

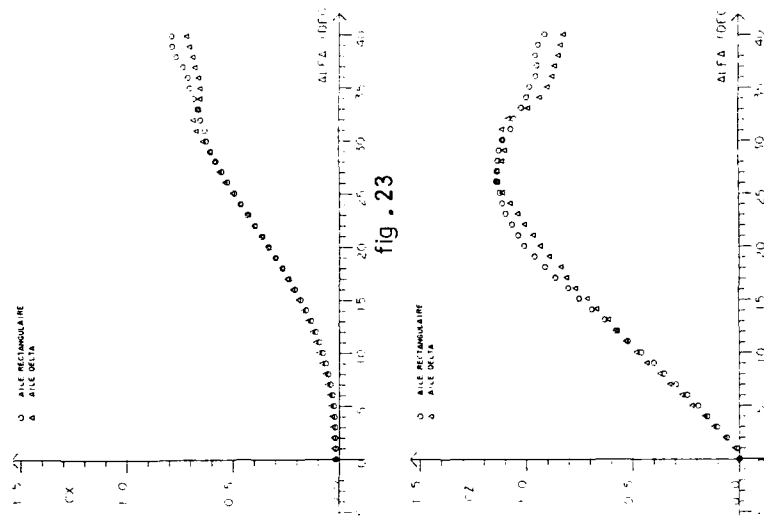


fig. 23

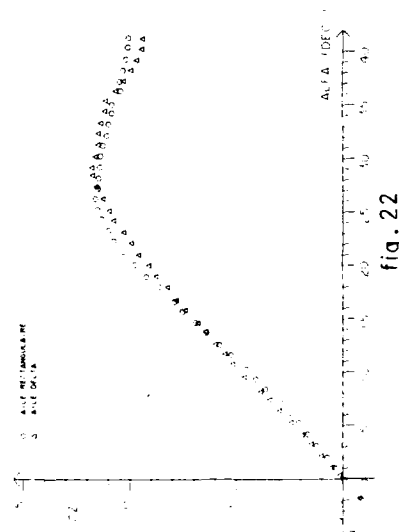


fig. 22

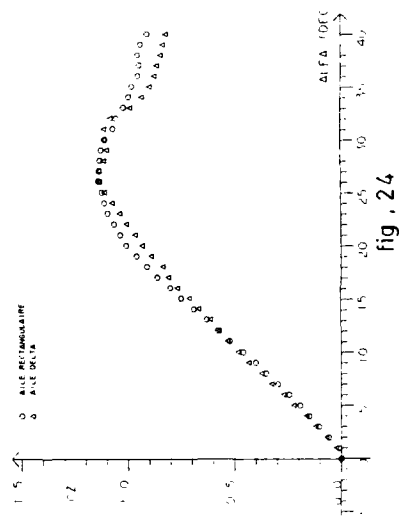


fig. 24

# INFLUENCE DE LA FORME EN PLAN

TUNNEL BERTIN  
(Valeurs corrigées)

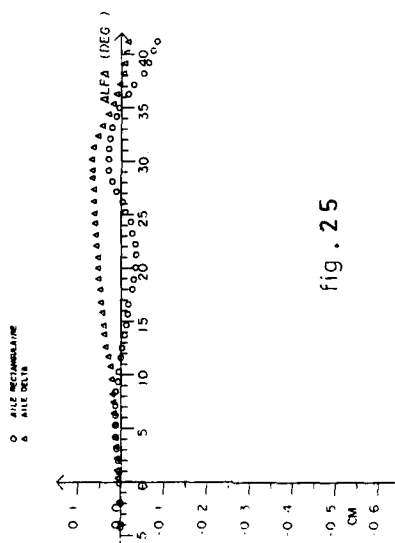


fig. 25

SOUFFLERIE ONERA S3 Ch

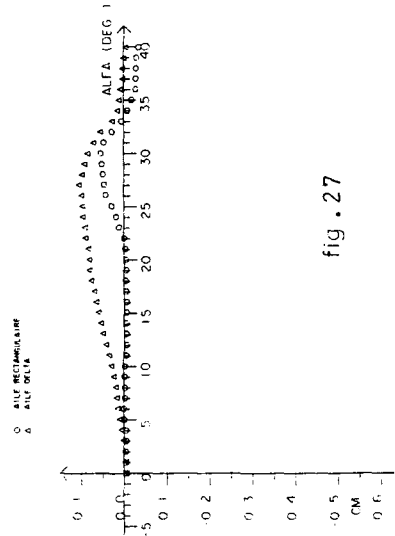


fig. 27

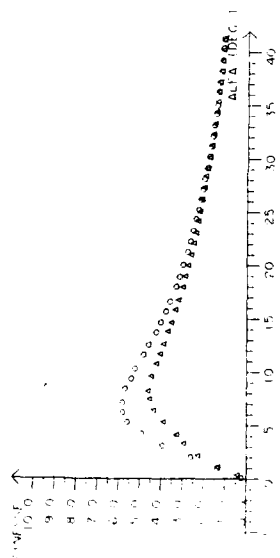


fig. 26

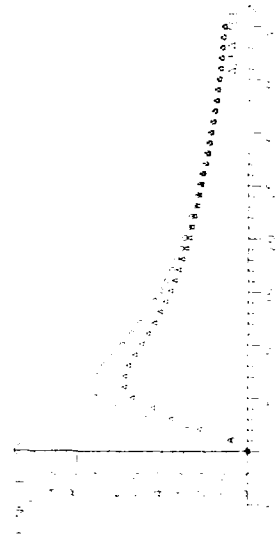


fig. 28

# VISUALISATIONS PAR BULLES D'AIR

Aile "rectangulaire"  $U_0 = 4 \text{ m/s}$  ,  $\alpha = 20^\circ$



Sans canard  
fig. 29



Avec canard  
fig. 30

AN EXPERIMENTAL STUDY TO DETERMINE THE FLOW  
AND THE SUBSONIC STATIC AND DYNAMIC STABILITY  
CHARACTERISTICS OF AIRCRAFT OPERATING AT  
HIGH ANGLES-OF-ATTACK

by

Alex Goodman and Clinton E. Brown  
Tracor Hydronautics, Inc.  
7210 Pindeil School Road  
Laurel, Maryland 20707  
U.S.A.

## 1.0 SUMMARY

A comprehensive series of experiments were conducted in the Tracor Hydronautics Ship Model basin (HSMB<sup>®</sup>) to determine the subsonic static and dynamic stability characteristics of a 3.5-foot span, 60-degree delta-high-wing fuselage model operating at high angles-of-attack up to 68-degrees. In addition, typical results of flow visualization studies for a range of Reynolds numbers from  $0.2 \times 10^6$  to  $1.6 \times 10^6$ , are presented. Also, the motions, force and moment coefficients resulting from a simulated pitchup maneuver are presented.

The paper describes the HSMB, Large Amplitude Horizontal Planar Motion Mechanism System (LAHPMM), 60-degree delta-wing-fuselage model, model-support systems, and the data acquisition and processing system used in the investigation. The advantages of performing tests in the HSMB using the LAHPMM technique over existing wind tunnel techniques, such as curved flow and combined oscillation, for determination of the dynamic stability derivatives are presented and discussed.

The results of the present investigation are compared with static and dynamic stability results, obtained in the mid 1950's from the NACA Langley Stability Tunnel, for a similar delta-wing-fuselage model operating over a range of reduced frequencies and angles-of-attack up to 36 degrees. In general, the comparisons show that the results are in good agreement. In addition, for angles-of-attack up to 32 degrees, the algebraic summation of the component longitudinal and lateral dynamic derivatives give results which are in very good agreement with derivatives obtained from combined oscillations.

## 2.0 SYMBOLS

The data are presented in the form of standard NACA coefficients of forces and moments which are referred to either the body system of axes or stability system of axes with the origin at the projection on the plane of symmetry of the quarter-chord point of the wing mean aerodynamic chord. The positive direction of forces, moments, angular displacements and velocities for both systems of axes are shown in Figure 1. The coefficients and symbols are defined as follows:

$C_L$	lift coefficient, $\frac{Lift}{q_\infty S}$
$C_D$	drag coefficient, $\frac{Drag}{q_\infty S}$
$C_N$	normal force coefficient, $\frac{F_N}{q_\infty S}$
$C_A$	axial force coefficient, $\frac{F_A}{q_\infty S}$
$C_Y$	lateral force coefficient, $\frac{F_Y}{q_\infty S}$
$C_l$	rolling-moment coefficient, $M_X/q_\infty S b$
$C_n$	yawing-moment coefficient, $M_Z/q_\infty S b$
$C_m$	pitching-moment coefficient, $M_Y/q_\infty S \bar{c}$
$M_X$	rolling moment, ft-lb
$M_Z$	yawing moment, ft-lb
$M_Y$	pitching moment, ft-lb
$q_\infty$	$\frac{1}{2} \rho U^2$
$\rho$	mass density of water, slugs/cu ft
$U$	free-stream velocity, ft/sec

S	wing area, sq ft
b	wing span, ft
c	wing chord, ft
$\bar{c}$	wing mean aerodynamic chord, $\frac{2}{S} \int_0^{b/2} c^2 dy$ , ft
d	maximum fuselage diameter
y	displacement along Y-axis, ft
$\dot{y}$ , v	velocity along Y-axis, ft/sec
$\ddot{y}$ , $\dot{v}$	acceleration along Y-axis, ft/sec <sup>2</sup>
$\beta$	angle of sideslip, radians unless otherwise specified ( $\sin^{-1} \frac{v}{U}$ )
$\dot{\beta}$	radians/sec
z	displacement along Z-axis, ft
$\dot{z}$ , w	velocity along Z-axis, ft/sec
$\ddot{z}$ , $\dot{w}$	acceleration along Z-axis, ft/sec <sup>2</sup>
$\alpha$	angle of attack, deg ( $\tan^{-1} \frac{w}{U}$ )
$\dot{\alpha}$	radians/sec
u, v, w	component velocities along X, Y, Z axis, respectively
$\omega = 2\pi f$	circular frequency, radians/sec
f	frequency, Hertz
t	time, sec.
$\frac{\omega b}{2U}$	reduced frequency for lateral parameter
$\frac{\omega \bar{c}}{2U}$	reduced frequency for longitudinal parameter
$\frac{\dot{\beta} b}{2U}$	sideslipping acceleration parameter
$\frac{\dot{\alpha} \bar{c}}{2U}$	heaving acceleration parameter
$\psi$	angle of yaw, radians
r, $\dot{\psi}$	yawing angular velocity, radians/sec
$\dot{r}$ , $\ddot{\psi}$	yawing angular acceleration, radians/sec <sup>2</sup>
$\theta$	angle of pitch, degrees or radians
q, $\dot{\theta}$	pitching angular velocity, radians/sec
$\dot{q}$ , $\ddot{\theta}$	pitching angular acceleration, radians/sec <sup>2</sup>
$\frac{rb}{2U}$	yawing angular velocity parameter
$\frac{\dot{r}b^2}{4U^2}$	yawing angular acceleration parameter
$\frac{qc}{2U}$	pitching angular velocity parameter
$\frac{\dot{q}c^2}{4U^2}$	pitching angular acceleration parameter
$m_m$	model mass, slugs
$I_{ym}$	model moment of inertia about Y-axis, slug-ft <sup>2</sup>
$I_{zm}$	model moment of inertia about Z-axis, slug-ft <sup>2</sup>

## Coefficients and Derivatives

Results presented herein are given in terms of the coefficients and derivatives defined in the tabulations that follow:

## Normal force

$$C_N = \frac{F_N}{q_\infty S}$$

$$C_{N_\alpha} = \frac{\partial C_N}{\partial \alpha}$$

$$C_{N_q} = \frac{\partial C_N}{\partial \frac{qC}{2U}}$$

$$C_{N_{\dot{\alpha}}} = \frac{\partial C_N}{\partial \frac{\dot{\alpha}C}{2U}}$$

$$C_{N_{\dot{q}}} = \frac{\partial C_N}{\partial \frac{\dot{q}C^2}{4U^2}}$$

## Axial force

$$C_A = \frac{F_A}{q_\infty S}$$

$$C_{A_\alpha} = \frac{\partial C_A}{\partial \alpha}$$

$$C_{A_q} = \frac{\partial C_A}{\partial \frac{qC}{2U}}$$

$$C_{A_{\dot{q}}} = \frac{\partial C_A}{\partial \frac{\dot{q}C}{2U}}$$

$$C_{A_{\dot{q}}} = \frac{\partial C_A}{\partial \frac{\dot{q}C^2}{4U^2}}$$

## Pitching moment

$$C_m = \frac{M_y}{q_\infty S c}$$

$$C_{m_\alpha} = \frac{\partial C_m}{\partial \alpha}$$

$$C_{m_q} = \frac{\partial C_m}{\partial \frac{qC}{2U}}$$

$$C_{m_{\dot{\alpha}}} = \frac{\partial C_m}{\partial \frac{\dot{\alpha}C}{2U}}$$

$$C_{m_{\dot{q}}} = \frac{\partial C_m}{\partial \frac{\dot{q}C^2}{4U^2}}$$

## Rolling moment

$$C_l = \frac{M_x}{q_\infty S b}$$

$$C_{l_p} = \frac{\partial C_l}{\partial \frac{pb}{2U}}$$

$$C_{l_r} = \frac{\partial C_l}{\partial \frac{rb}{2U}}$$

$$C_{l_\beta} = \frac{\partial C_l}{\partial \beta}$$

$$C_{l_{\dot{\beta}}} = \frac{\partial C_l}{\partial \frac{\dot{\beta}b}{2U}}$$

$$C_{l_{\dot{p}}} = \frac{\partial C_l}{\partial \frac{\dot{p}b^2}{4U^2}}$$

$$C_{l_{\dot{r}}} = \frac{\partial C_l}{\partial \frac{\dot{r}b^2}{4U^2}}$$

## Yawing moment

$$C_n = \frac{M_z}{q_\infty S b}$$

$$C_{n_p} = \frac{\partial C_n}{\partial \frac{pb}{2U}}$$

$$C_{n_r} = \frac{\partial C_n}{\partial \frac{rb}{2U}}$$

$$C_{n_\beta} = \frac{\partial C_n}{\partial \beta}$$

$$C_{n_{\dot{\beta}}} = \frac{\partial C_n}{\partial \frac{\dot{\beta}b}{2U}}$$

$$C_{n_{\dot{p}}} = \frac{\partial C_n}{\partial \frac{\dot{p}b^2}{4U^2}}$$

$$C_{n_{\dot{r}}} = \frac{\partial C_n}{\partial \frac{\dot{r}b^2}{4U^2}}$$

## Side force

$$C_Y = \frac{F_Y}{q_\infty S}$$

$$C_{Y_p} = \frac{\partial C_Y}{\partial \frac{pb}{2U}}$$

$$C_{Y_r} = \frac{\partial C_Y}{\partial \frac{rb}{2U}}$$

$$C_{Y_\beta} = \frac{\partial C_Y}{\partial \beta}$$

$$C_{Y_{\dot{\beta}}} = \frac{\partial C_Y}{\partial \frac{\dot{\beta}b}{2U}}$$

$$C_{Y_{\dot{p}}} = \frac{\partial C_Y}{\partial \frac{\dot{p}b^2}{4U^2}}$$

$$C_{Y_{\dot{r}}} = \frac{\partial C_Y}{\partial \frac{\dot{r}b^2}{4U^2}}$$

Dot over symbol indicates derivative with respect to time.

Subscripts:

- m maximum value
- ω denotes oscillatory derivative
- s with respect to stability axis

## 3.0 INTRODUCTION

The United States Air Force requested Tracor Hydronautics, Inc. to carry out a comprehensive program of model experiments to determine the subsonic longitudinal and lateral static and dynamic stability characteristics of a 60-degree, delta-high-wing fuselage configuration operating at high angles-of-attack beyond steady state stall. The primary objective of this investigation was to demonstrate that the Tracor Hydronautics Ship Model Basin (HSMB<sup>®</sup>) in conjunction with the Large Amplitude Horizontal Planar Motion Mechanism (LAHPMM) could provide all the individual subsonic longitudinal and lateral static and dynamic stability derivatives at high Reynolds numbers and angles of attack up to 68-degrees.

Tracor Hydronautics, for a considerable number of years, has been involved in the performance of both theoretical and experimental studies related to the prediction of the dynamic stability and control characteristics of submarines, torpedoes, surface ships, hydrofoils, and other marine vehicles. (References 2 to 9.) In general, the experimental work has been performed in the Hydronautics Ship Model Basin. Specialized test equipment such as the Sub-PMM and LAHPMM Systems described in References 10 and 11 have been used for many of these programs. The PMM Systems and techniques, in combination with the HSMB, are directly applicable to the evaluation of the individual subsonic stability derivatives of aircraft based on the experience obtained over the past twenty-four years. In addition, towing tanks have been used for many years to evaluate the performance of hydrofoils, strut fairings, and other lifting surface configurations.<sup>12,13,14</sup> The applicability of towing tanks for aerodynamic studies and the associated scaling laws is discussed in some detail in Reference 15. The use of towing tanks for aerodynamic studies is best demonstrated by the Wake-Vortex Program performed for NASA, FAA, and U.S. Air Force.<sup>16,17,18</sup> The results obtained from these studies provided the only laboratory far-field data which correlated with flight-test results.<sup>19,20</sup>

The present paper provides a brief review of the technical problem; describes the facilities and LAHPMM equipment used for the study; describes the wing-fuselage model; describes the model support systems and six component balance; describes the data acquisition system and data reduction and analysis procedure; and outlines the overall model test program; presents the nondimensional coefficients and derivatives obtained from static longitudinal tests, pure heaving, pure pitching, combined pitching tests; static lateral tests, pure swaying, pure yawing and combined yawing tests; makes comparisons with static and dynamic data obtained from NACA tests conducted in mid 1950's for similar wing-fuselage configuration. In addition, typical results of the flow visualization and the simulated pitchup tests are presented and discussed.

#### 4.0 BACKGROUND AND TECHNICAL CONSIDERATIONS

The development of methods and techniques for the experimental determination of the static and dynamic stability derivatives of aircraft has been pursued for many years by aerodynamic laboratories throughout the world. A review and description of many of the experimental techniques used by various laboratories, from 1913 to 1978, is presented in Reference 21. Two of the most productive test techniques described in Reference 21 are identified as (a) model fixed in test section, and (b) method of rigidly forced oscillation. The "model fixed in the test section technique" is typified by the "curved flow" and "rolling flow" test techniques employed by the Langley Stability Tunnel described in References 22 and 23. As discussed in Reference 23, the curved flow technique is not an exact simulation of curved flow because of the static-pressure gradient which exists normal to the streamlines in curved flow. This gradient produces a buoyancy which does not exist in curved flight. In addition, there is a tendency for the boundary layer air of the model to flow toward the center of rotation rather than outward as in normal curved flight. The data have to be corrected for these effects. Also, due to the velocity-gradient screens (see Reference 23), the turbulence level in the tunnel is quite high and could have adverse effects on model drag and maximum lift characteristics. The results obtained using these techniques provide only the linear and angular velocity dependent coefficients at subsonic speeds. (See References 23 to 33.) As described in Reference 21, various "rigidly forced oscillation" techniques have been applied in the determination of the subsonic and high-subsonic rotary stability derivatives. (See References 34 to 40.) However, many of these techniques did not permit the explicit determination of both the rotary and acceleration derivatives. Some of these investigations have indicated that large values of the coefficient,  $C_{n_r} - C_{n_{\dot{\delta}}}$ , can be produced at moderate and high angles of attack by swept and delta wing configurations. Also, the data presented in References 34 to 40 have provided some information on the effects of the reduced frequency parameter  $\frac{\omega b}{2U}$  and oscillation amplitude on the combined derivatives for swept and delta wings operating at moderate and high angles of attack.

During the mid 1950's, certain dynamic stability problems associated with high-speed aircraft having a high relative density indicated that the acceleration derivatives (which have been neglected generally when making dynamic stability calculations) may be important. A pure yawing technique was developed to directly measure the damping in yaw derivatives for the lateral stability case.<sup>41</sup> Reference 41 presents a comparison of results obtained from curved flow tests and pure-yawing oscillation tests. The results indicated that for certain configurations, the derivative  $C_{n_{\dot{\delta}}}$  and  $C_{l_{\dot{\delta}}}$  can be quite large at high angles of attack. Direct measurements of the swaying acceleration derivatives have essentially substantiated these results. (See References 42 and 43.) Unfortunately the system described in Reference 41 could only satisfy the pure yawing condition at a single amplitude and frequency of oscillation ( $\frac{\omega b}{2U} = 0.23$ ) due to the mechanics of the equipment. In addition, the model experienced a velocity and acceleration in surge during the "pure yawing mode" which could affect the results. As a result of the limitations of the equipment and associated instrumentation, the system could not be used to study directly the variation of the damping and acceleration derivatives with amplitude of oscillation and the reduced frequency parameter. Subsequent improvements in the equipment, described in References 43 and 44, permitted a broader variation in both reduced frequency and amplitude. However, the capability to perform this type of experiment was eliminated when the Langley Stability Tunnel was disassembled in 1958 and moved to V.P.I.

In the early 1950's the problems associated with the dynamic behavior of submarines and other submerged bodies became increasingly more and more important with each new increase in submerged speed. To meet this challenge, the Planar Motion Mechanism System was conceived in 1954 and placed into operation in 1956.<sup>45,46</sup> The basic PMM Systems described in References 46 and 47 incorporated in one device a means for experimentally determining all of the hydrodynamic coefficients required in the equations of motion of a body moving through a fluid in six degrees of freedom. These coefficients are usually classified into three general categories: static, rotary, and acceleration. The static coefficients are due to the components of linear velocities of the body relative to the fluid; the rotary coefficients are due to components of angular velocity; and the acceleration coefficients are due to either linear or angular acceleration components. The PMM Systems explicitly determine numerical values in each of the three foregoing categories by imparting "pure" motions to the model as described in detail in References 46 and 47. The PMM Systems can also be programmed to produce the typical combined motions that are used in present wind-tunnel studies. In addition, the means for measuring and resolving the force and moment coefficients in each category are an essential part of the system. A description of the currently used PMM data acquisition system is presented in References 10 and 11. Briefly, the static coefficients are obtained directly from measurements of the steady force in the static mode; the rotary or damping coefficients are obtained explicitly from measurement of the quadrature components of the oscillatory force in the pure yawing or pitching modes; and the acceleration coefficients are obtained explicitly from measurements of the in-phase components of the oscillatory force in pure heaving, swaying, yawing, and pitching modes. The same techniques are used for the pure rolling mode as described in Reference 10.

For the present application, the combination of the LAHPMM techniques and the HSMB offers the following advantages over existing wind tunnel techniques such as employed by the Stability Tunnel located at VPI and the oscillation techniques described in References 34 to 44:

1. The ability of the LAHPMM to independently select the frequency of operation (0.01 Hz to 0.20 Hz), yawing amplitude, and swaying amplitude in combination with the towing carriage velocity can be used to produce:
  - (a) pure yawing motion over a range of frequencies for a constant yawing amplitude, or
  - (b) pure yawing motion over a range of amplitudes for a constant frequency, or
  - (c) combined yawing motion over a range of amplitudes and frequencies.
2. The LAHPMM can produce a pure swaying velocity and acceleration over a range of amplitudes and frequencies.
3. The LAHPMM can produce a pure yawing motion combined with a constant angle of sideslip on the model.
4. The LAHPMM can be used to evaluate the static stability coefficients over a range of sideslip angles of  $\pm 30$  degrees.
5. The LAHPMM can produce pure pitching and heaving motions by rotating the model 90-degrees and using a strut-sting support system.
6. Pitching and yawing can be performed at angles of attack up to 70-degrees without using bent stings.
7. The support systems are designed to provide minimal strut interference in accordance with the criteria described in Reference 48.
8. Accurate, repeatable, and direct measurement of model velocity.
9. Low turbulence environment.
10. Large test section (13 feet and 25 feet) and therefore minimal boundary corrections.
11. Operation at high dynamic pressure resulting in large forces and moments (see Table 1), and in better resolution than achievable in many wind tunnels.
12. High Reynolds Number due to lower kinematic viscosity.

Thus, the HSMB in combination with the LAHPMM System provides the aeronautical community with a powerful and unique tool for determining all of the stability derivatives of aircraft required by the equations of motion. In addition, the HSMB and associated flow visualization techniques provide the researcher a means to study and evaluate basic flow phenomena.

## 5.0 DESCRIPTION OF FACILITIES

The tests of the present investigation were made in the Tracor Hydronautics Ship Model Basin (HSMB®). The HSMB is the largest privately owned and operated ship model basin in the U.S.A. The facility is about 25-feet wide, 13-feet deep, and 420-feet long.



The specifications of the HSMB are presented in Figure 2(a) and a partial view of the tank is shown in Figure 2(b). As indicated in Figure 2(a), the HSMB is equipped with two towing carriages. The main Towing Carriage No. 1, shown in Figure 2(c), was used for the present study. The carriage is a servo controlled, electro-hydraulic powered platform that can be operated at controlled speeds of up to 20-feet per second. The carriage control room houses a DEC PDP 11/44 digital computer, associated graphics terminals, hard-copy readouts, various instrumentation and data acquisition systems in addition to the carriage speed controls and LAHPMM control system. The on-board systems provide a complete data acquisition and reduction center for immediate readout and processing to coefficient form of force, moment and displacement data produced by the six component balance and LAHPMM.

The Large Amplitude Horizontal Planar Motion Mechanism (LAHPMM) used for the present study is shown in Figure 3(a). As may be seen in Figure 3(a), the system consists of a steel-tubular frame mounted transversely across the carriage open-bay. The frame supports a swaying carriage assembly which incorporates a device for setting sideslip/angle-of-attack angles and provides a support for the yawing table and drive system. The LAHPMM can produce sinusoidal pure swaying/heaving motions having amplitudes up to  $\pm 3.0$  feet and frequencies of from 0.01 to 0.20 Hertz. Likewise the system can produce pure yawing/pitching motions having amplitudes up to  $\pm 30$  degrees and frequencies of from 0.01 to 0.20 Hertz.

The sinusoidal command signal for the two-axis servo control system is provided by a sine-cosine potentiometer. This function generator maintains the 90-degree phase angle between the sway/heave motion and the yaw/pitch motion required to produce pure yawing or pure pitching motions as shown in Figures 4 to 9.

The LAHPMM control unit shown in Figure 10 permits the test engineer to select the yaw/pitch amplitude, sway/heave amplitude and frequency prescribed by the test program to produce the pure motions. Also, for static tests, the command-system control can be used to remotely set the sideslip or angle-of-attack of the model. A complete detailed description of the LAHPMM system is presented in References 11 and 47.

#### 6.0 DESCRIPTION OF MODEL

The 60-degree delta-wing-fuselage model used in the present investigation is shown in Figure 11 and the geometric characteristics are presented in Table 2. The wing configuration was selected so that comparisons could be made with test data available in the literature. Thus, the wing has a flat-plate cross-section with a biconvex-leading edge to fix transition and a beveled-trailing edge. The wing was constructed using an aluminum center section with Hysol leading and trailing edges attached as shown in Figure 11. The fuselage is identical to a NASA-Langley existing fuselage which is part of a generic series. The cylindrical part of the fuselage was made using thin-walled stainless-steel tubing. The ogive nose was made from Hysol and is defined by the offsets presented in Table 3. The wing can be mounted in a mid, high, or low position. For the present program a high-wing position was chosen to simplify the wing construction and the wing-balance attachment. For the flow visualization tests the model was equipped with dye ports. As shown in Figure 11, two ports were located just forward of the intersection of the wing apex and fuselage. Also, dye ports were located at the fuselage nose and on the high pressure side of the ogive nose as shown in Figure 11.

The model was ballasted so that the model C.G. was coincident with the balance center and the model mass was measured. Also, the model moment of inertia about the Y and Z axes was measured using a bifilar pendulum system.

#### 7.0 MODEL SUPPORT SYSTEMS

Two separate model support systems were required for performance of the static and dynamic longitudinal and lateral tests. The two support systems and their attachment to the LAHPMM are shown in Figures 12 and 13.

As shown in Figure 12, the longitudinal support system consisted of an 8-inch diameter stainless-steel strut which supported a 4-inch and 3-inch diameter sting. The sting is supported in a roll-bearing-block assembly which can permit the forced-rolling of the model about the model-body axis. The sting supports a balance-holder tube which in turn supports the six component balance and model. A typical arrangement of the longitudinal system on the carriage is shown in Figure 14(a). With the arrangement shown in Figures 12 and 14(a), the model angle-of-attack can be varied from 0 to 68 degrees, in two-degree increments, using the LAHPMM servo-command system. The support system also permits the balance center and the model  $1/4$  MAC to be located on the center of rotation of the LAHPMM and at a constant depth in the towing tank. This allows the model to perform pure heaving and pure pitching motions without introducing additional model mass and moment of inertia tares.

The arrangement for the lateral tests is shown in Figure 13. The system consists of a single tubular 6-inch diameter strut having an internal lead-screw-nut arrangement attached through an  $\alpha$ -connecting link to the rear end of the balance-support tube. The forward end of the balance-support tube is supported by the strut using a ball-bearing yoke assembly. A typical arrangement of the lateral system on the carriage is shown in

Figure 14(b). With the arrangement shown in Figures 13 and 14(b) the angle of attack of the model can be infinitely varied between  $-4$  to  $70$ -degrees by driving the lead screw with a d.c. servo motor. The balance center and the  $1/4$  MAC are maintained on the LAHPMM center of rotation and at a constant depth in the HSMB. This allows the model to perform pure swaying and pure yawing motions without introducing additional model mass and moment of inertia tares. The lateral support system is similar to one that was used at the Langley Stability Tunnel as described in Reference 32.

Two NASA type six-component strain-gage balances were used for the present investigation. The balance characteristics are summarized in Table 4. A sketch showing a typical internal arrangement of the balance with the model is presented in Figure 15. The balance gages and connectors were waterproofed so that the balance could be operated submerged in the HSMB. The balances were calibrated using dead weights as shown in Figure 16. The resulting calibrations, including interactions between components, were fitted with a  $6 \times 6$  matrix and stored on the PDP 11/44 computer.

#### 8.0 DATA ACQUISITION AND PROCESSING SYSTEM

An integral part of the basic LAHPMM System is the means used to process and record the data transmitted from the six-component balance. The LAHPMM Data Acquisition System shown in Figures 17 and 18 is described in detail in Reference 17. Briefly, as shown in Figure 18, each channel is designed to operate in either the static or dynamic modes. In the static mode, the gage signal is processed through a signal conditioner unit (SCU) and the output is fed directly into the A-to-D converter of the data logger to obtain a single value integrated over a selected time base. In the dynamic mode, the "sinusoidal" output signal from each SCU is impressed across a sin-cos potentiometer and fed into a force component separator (FCS) which resolves the signal into in-phase and quadrature components. The output of the FCS is then fed into the A-to-D converter of the data logger and integrated over a discrete number of cycles to obtain a single reading for each component as shown in Reference 17. The output of the data logger is serially fed to the DEC PDP 11/44 which stores the data on disc as well as automatically reducing the data to nondimensional form on a run-by-run basis. The mathematical operation performed by the data acquisition system is discussed in Section 10.0.

#### 9.0 TEST PROGRAM

The majority of the tests were conducted in the HSMB at a dynamic pressure of  $34.8$  pounds per square foot. This corresponds to a Reynolds number of  $1.2 \times 10^6$  based upon the mean aerodynamic chord of the wing.

The longitudinal tests consisted of statics, pure heaving, pure pitching and combined pitching tests performed with respect to the body axes. The statics covered a range of angles of attack of from  $0$  to  $68$  degrees. The pure heaving tests were conducted for amplitudes of  $\pm 4$ ,  $\pm 6$ , and  $\pm 8$  degrees, corresponding reduced frequencies  $\frac{u_c}{2U}$  of  $0.0635$ ,  $0.0846$ ,  $0.1058$ , and  $0.1270$ , and a range of angles of attack of from  $0$  to  $56$  degrees. Both the pure pitching and combined pitching tests were conducted for  $\theta_m$  amplitudes of  $\pm 4$ ,  $\pm 6$ , and  $\pm 8$  degrees, corresponding reduced frequencies  $\frac{u_c}{2U}$  of  $0.0846$ ,  $0.1058$ ,  $0.1270$  and  $0.1480$ , and a range of angles of attack from  $0$  to  $34$  degrees.

The lateral tests consisted of statics, pure swaying, pure yawing and combined yawing tests performed with respect to the stability axes. The statics covered a range of sideslip angles of  $0$ ,  $\pm 4$ , and  $\pm 8$  degrees for angles of attack from  $0$  to  $68$  degrees. The pure swaying tests were conducted for  $\theta_w$  amplitudes of  $\pm 4$ ,  $\pm 6$ , and  $\pm 8$  degrees, corresponding reduced frequencies  $\frac{u_b}{2U}$  of  $0.110$ ,  $0.147$ ,  $0.184$ ,  $0.220$ , and  $0.257$ , and an angle of attack range of from  $0$  to  $68$  degrees. The pure yawing and combined yawing tests were conducted for  $\psi_m$  amplitudes of  $\pm 4$ ,  $\pm 6$ , and  $\pm 8$  degrees, corresponding reduced  $\frac{u_b}{2U}$  frequencies of  $0.110$ ,  $0.147$ ,  $0.184$ ,  $0.220$ , and  $0.257$ , and a range of angles of attack from  $0$  to  $68$  degrees. In addition, pure swaying, pure yawing and combined yawing tests were performed with respect to the body axes. Amplitudes of  $\theta_w$  and  $\psi_m$  of  $\pm 4$ ,  $\pm 6$ , and  $\pm 8$  degrees were used for reduced frequencies of  $\frac{u_b}{2U}$  of  $0.184$  and  $0.220$ . The angle of attack range for these tests was  $0$  to  $32$  degrees.

A series of flow visualization tests were conducted at Reynolds numbers from about  $0.2 \times 10^6$  to  $1.6 \times 10^6$ . During these tests dye was ejected from selected points on the wing and fuselage. Orthogonal views of the dye traces of the wake were photographed by NIKON 35mm sequencing cameras and VHS video cameras. For several of the tests an upstream view of the wake was photographed using a Nikonos underwater camera. The underwater cameras and underwater lights were attached to the towing carriage and towed with the model.

A short series of pitchup tests were conducted which simulated the maneuver of a typical fighter operating at  $26000$  feet of altitude, initial speed of  $500$  feet per second and pitching up at a rate of  $30$  degrees per second. Time histories of the forces, moments, linear and angular displacements and forward velocity were measured.

## 10.0 REDUCTION OF DYNAMIC DATA

The mathematical operations that the LAHPMM data acquisition system performs automatically is illustrated herein for the pure swaying case, shown in Figure 7, as follows:

The lateral position on the model is monitored by the sway feedback potentiometer, and is represented by a voltage which can be expressed as:

$$y = y_m \sin \omega t \quad [1]$$

A Y-force gage on the model also will produce an oscillatory signal during the test, which can be presented by:

$$Y_R = Y_* + Y_O \sin (\omega t - \phi) \quad [2]$$

Equation [2] can be written as

$$Y_R = Y_* + [Y_O \cos \phi] \sin \omega t + [-Y_O \sin \phi] \cos \omega t \quad [3]$$

$$\text{or} \quad Y_R = Y_* + Y_{IN} \sin \omega t + Y_{OUT} \cos \omega t \quad [4]$$

The designations "IN" and "OUT" have been adopted to identify force terms of Equation [4] which are oscillating in-phase and out of phase (quadrature) with the motion defined by Equation [1].

The voltages given by Equations [1] and [4] are impressed across a resolver consisting of individual sine-cosine potentiometers which are ganged together and which are rotating at the fundamental frequency. The sine wipers of the resolver are aligned in-phase with the sway feedback signal. The resulting voltage output from the sin-cos pot resolver can be expressed as:

Sway motion signal:

$$y \sin \omega t = \frac{1}{2} [y_m \sin^2 \omega t] \quad [5]$$

$$y \cos \omega t = \frac{1}{2} [y_m \sin \omega t \cos \omega t] \quad [6]$$

Y-force signal:

$$Y_R \sin \omega t = \frac{1}{2} [Y_* \sin \omega t + Y_{IN} \sin^2 \omega t + Y_{OUT} \cos \omega t \sin \omega t] \quad [7]$$

$$Y_R \cos \omega t = \frac{1}{2} [Y_* \cos \omega t + Y_{IN} \sin \omega t \cos \omega t + Y_{OUT} \cos^2 \omega t] \quad [8]$$

The factor  $\frac{1}{2}$  appears because the sin-cos pots act as voltage dividers.

The signals represented by Equations [5] to [8] are fed into the HI-DASDL-12 data logger shown in Figure 18. The DASDL provides an A-to-D converter and a time integration algorithm which is started and stopped by a pulse from an LED triggered by the same function generator which drives the sway motion. The following integrations are performed:

Sway motion signal: in-phase:

$$\int_0^{nT} y_m \sin \omega t \, dt = \int_0^{nT} \frac{1}{2} y_m \sin^2 \omega t \, dt = \frac{nT}{4} y_m \quad [9]$$

Sway motion signal: quadrature:

$$\int_0^{nT} y_m \cos \omega t \, dt = \int_0^{nT} \frac{1}{2} y_m \sin \omega t \, dt = 0 \quad [10]$$

Y force signal: in-phase:

$$\begin{aligned} \int_0^{nT} Y_R \sin \omega t \, dt &= \int_0^{nT} \frac{1}{2} Y_* \sin \omega t \, dt \\ &+ \int_0^{nT} \frac{1}{2} Y_{IN} \sin^2 \omega t \, dt \\ &+ \int_0^{nT} \frac{1}{2} Y_{OUT} \cos \omega t \sin \omega t \, dt \\ &= \frac{nT}{4} Y_{IN} \end{aligned} \quad [11]$$

Y-force signal quadrature:

$$\begin{aligned} \int_0^{nT} Y_R \cos \omega t \, dt &= \int_0^{nT} \frac{1}{2} Y_* \cos \omega t \, dt \\ &+ \int_0^{nT} \frac{1}{2} Y_{IN} \sin \omega t \cos \omega t \, dt \\ &+ \int_0^{nT} \frac{1}{2} Y_{OUT} \cos^2 \omega t \, dt \\ &= \frac{nT}{4} Y_{OUT} \end{aligned} \quad [12]$$

The integrations are performed both as indicated (NORMAL mode) and with a reversed polarity to the sin-cos potentiometers, (REVERSE mode). This process effectively cancels any bias voltage which might exist across the sin-cos pots. If the symbols N and R are used to designate "normal" and "reverse", and if the calibration constant be "K" volts/pound (force) or volts/foot (sway), then the integration results can be written as:

Sway motion signal: in-phase:

$$SA_{IN} = \frac{4}{nT} \cdot \frac{1}{KSA} \cdot \left[ \frac{N - R}{2} \right] \quad [13]$$

Sway motion signal: quadrature:

$$SA_{OUT} = 0 \quad [14]$$

Y-force signal: in-phase:

$$Y_{IN} = \frac{4}{nT} \cdot \frac{1}{KY} \cdot \left[ \frac{N - R}{2} \right] \quad [15]$$

Y-force signal: quadrature:

$$Y_{OUT} = \frac{4}{nT} \cdot \frac{1}{KY} \cdot \left[ \frac{N - R}{2} \right] \quad [16]$$

The Tracor Hydronautics Force Component Separator and the DASDL are designed to simplify the data reduction process, and automatically scale the output by the factor of  $4/2nT$  when used in DYNAMIC IN/QUAD mode. Thus, the actual output displays on the DASDL represent:

Sway motion signal: in-phase:

$$SA_{IN} = \frac{N - R}{KSA} \quad [17]$$

Sway motion signal: quadrature:

$$SA_{OUT} = 0 \quad [18]$$

Y-force signal: in-phase:

$$Y_{IN} = \frac{N - R}{KY} \quad [19]$$

Y-force signal: quadrature:

$$Y_{OUT} = \frac{N - R}{KY} \quad [20]$$

A similar analysis can be made for all the dynamic cases shown in Figures 4 to 9. The operation performed by the LAHPMM data acquisition system is equivalent to determining the Fourier coefficients of the fundamentals of the motion and force gage signals.

## 11.0 RESULTS AND DISCUSSION

For the present paper, the static and dynamic results, which have been analyzed to date, are presented in Figures 19 through 26 as curves of the various parameters plotted against angle of attack. Typical results for the pitchup maneuver and the flow visualization studies are presented in Figures 28 and 29, respectively.

### 11.1 Static Longitudinal Characteristics

The lift, drag and pitching moment coefficients are plotted against angle of attack in Figure 19. The results are compared with data from Reference 32 for a similar 60-degree delta-high-wing-fuselage configuration. As shown in Figure 19 the agreement of the results with data from Reference 32 is very good. The experimental lift curve slope of the wing through zero angle of attack is 0.043 per degree compared to a theoretical value of 0.042 per degree.

### 11.2 Pure Heaving Characteristics

The variation of the derivatives ( $C_{N_{\alpha \omega}}$ ) and ( $C_{m_{\alpha \omega}}$ ) with angle of attack for several reduced frequencies is presented in Figure 20. The results are compared with the data from the static tests. As shown in Figure 20, the dynamic results agree quite well with the static data at low angles of attack. However, at angles of attack above stall, both ( $C_{N_{\alpha \omega}}$ ) and ( $C_{m_{\alpha \omega}}$ ) exhibit large variations with angle of attack and reduced frequency.

The variation of the acceleration derivatives  $C_{N_{\alpha}}$  and  $C_{m_{\alpha}}$  with angle of attack for several reduced frequencies is presented in Figure 21. As shown in Figure 21, the magnitude of the derivatives undergoes very large changes at high angles of attack. Also, at the high angles of attack the changes in magnitude of the derivatives are dependent strongly upon the reduced frequency.

### 11.3 Pitching Characteristics

The variation of the derivatives  $C_{N_q}$  and  $C_{m_q}$  with angle of attack for several reduced frequencies, obtained from pure pitching tests, is presented in Figure 22. The results are compared with data from curved flow tests for a similar delta wing model presented in Reference 34. As can be seen from Figure 22, the agreement is quite poor except at zero angle of attack. In addition, the measured values of  $C_{m_q} - C_{m_{\alpha}}$ , determined from combined pitching tests are presented in Figure 22. It can be seen that the measured values of  $C_{m_q} - C_{m_{\alpha}}$  are equal to the algebraic sum of  $C_{m_q}$  and  $C_{m_{\alpha}}$  presented in Figure 21 for angles of attack up to 34 degrees.

### 11.4 Static Lateral Characteristics

The variation of ( $C_{Y_{\beta s}}$ ), ( $C_{N_{\beta s}}$ ), and ( $C_{l_{\beta s}}$ ) with angle of attack is presented in Figure 23. These derivatives were determined by taking the slopes of the coefficients over a range of  $\beta = \pm 8$  degrees. These derivatives were determined with respect to the stability axes. Therefore, it was necessary to transfer the yawing and rolling moments to the stability axes since they were measured with respect to the body axes. The results are compared with NACA data from Reference 32 obtained for high-wing fuselage configurations having similar diameter-span ratios. As can be seen from Figure 23 the comparison is quite good for angles of attack up to 36 degrees. Beyond stall, all the derivatives have large excursions with angles of attack.

### 11.5 Pure Swaying Characteristics

The variation of ( $C_{Y_{\beta \omega}}$ ), ( $C_{N_{\beta \omega}}$ ), ( $C_{l_{\beta \omega}}$ ),  $C_{Y_{\dot{\beta}}}$ ,  $C_{N_{\dot{\beta}}}$ , and  $C_{l_{\dot{\beta}}}$  with angle of attack is presented in Figure 24 for a reduced frequency  $\frac{\omega b}{2U} = 0.184$ . Results were obtained at other reduced frequencies but are not presented at this time. The results presented in Figure 24 are compared with data obtained from pure swaying tests performed, at a reduced frequency  $\frac{\omega b}{2U} = 0.218$ , in the NACA Langley Stability Tunnel using a mid-wing, delta-wing fuselage model.<sup>50</sup> In general the comparison is good.

### 11.6 Yawing Characteristics

The variations of the pure yawing derivatives,  $C_{Y_r}$ ,  $C_{N_r}$ , and  $C_{l_r}$  with angle of attack is presented in Figure 25 for a reduced frequency  $\frac{\omega b}{2U} = 0.184$ . These derivatives were obtained with respect to the stability axes. Therefore, it was necessary to transfer the yawing and rolling moments, measured with respect to the body axes, to the stability axes. The results in Figure 25 are compared with data from curved flow tests and pure yawing tests performed in the NACA Langley Stability Tunnel at  $\frac{\omega b}{2U} = 0.16$  using a mid-wing, delta-wing fuselage model.<sup>33 44</sup> In general, the results are in good agreement with the NACA pure yawing data but the trends and magnitude of the data are in poor agreement with the curved flow results. This indicates that substantial difference probably occur in the basic aerodynamic flow phenomena acting on the model under oscillatory conditions.

The acceleration derivatives  $C_{Y_{\ddot{r}}}$ ,  $C_{N_{\ddot{r}}}$ , and  $C_{l_{\ddot{r}}}$  were also determined from the pure yawing tests. In addition, all the derivatives were determined for a range of reduced frequencies. However, these results are not presented at the present time.

A limited series of pure swaying, pure yawing and combined yawing tests were performed with respect to the body axes for  $\frac{\omega b}{2U} = 0.184$ , and 0.220 and angles of attack up to 32 degrees. The results of these tests are presented in Figure 26. The curved flow results from Reference 33 for a similar delta-wing model are presented for comparison. The results presented in Figure 26 show clearly that the algebraic summation of the pure

swaying and pure yawing derivatives give results which are, in general, in good agreement with the results obtained from combined yawing tests. The following comparison made at  $\alpha = 32$  degrees illustrates this point.

(1) Pure Swaying	$C_{Y_{\dot{\beta}}}$	$C_{n_{\dot{\beta}}}$	$C_{l_{\dot{\beta}}}$
	-0.25	0.16	-0.50
(2) Pure Yawing	$C_{Y_r}$	$C_{n_r}$	$C_{l_r}$
	-0.75	-0.14	0.18
(3) Combined Yawing	$C_{Y_r} - C_{Y_{\dot{\beta}}}$	$C_{n_r} - C_{n_{\dot{\beta}}}$	$C_{l_r} - C_{l_{\dot{\beta}}}$
	-0.35	-0.28	0.70
(4) Item (2) - Item (1)	-0.50	-0.30	0.68

The LAHPMM system supports can be modified easily so that tests can be performed with respect to the body axis up to angles of attack of 45 degrees. In addition, the future implementation of the forced rolling system would provide the rolling derivatives needed to transfer the dynamic data from the stability axes system to the body axes system.

#### 12.0 SIMULATED PITCHUP TESTS

The LAHPMM and HSMB carriage control systems were programmed to simulate an aircraft pitchup maneuver. The full-scale and model conditions of the maneuver for a typical fighter aircraft operating at 26000 feet altitude is shown in Figure 27. Also, Figure 27 presents the typical variation with time of the forward velocity, angle of attack and heaving velocity simulated in the test. During these tests, the carriage velocity, heave displacement, pitch angle displacement, and the forces and moments acting on the model were recorded by the DEC PDP 11/44 A to D as a function of time. The length of a typical run was about 18 seconds. This is equivalent to about a 1.8 seconds full-scale maneuver. The results of a typical test are presented in Figure 28. The  $C_Y$ ,  $C_n$ , and  $C_l$  coefficients all exhibit a spike at about  $t = 10$  seconds. This point corresponds to an angle of attack of about 28 degrees. At  $t = 18$  seconds, corresponding to the end of the maneuver, the  $C_Y$ ,  $C_n$ , and  $C_l$  coefficients all exhibit large excursions in magnitude. In fact the rolling moment coefficient  $C_l$  exhibits an oscillation which might be related to wing rock.

#### 13.0 FLOW VISUALIZATION TESTS

An extensive series of flow visualization tests were performed over a range of model speeds from 1.0 to 8.0 feet per second, corresponding to Reynolds number based on the MAC of the wing of  $0.2 \times 10^6$  to  $1.6 \times 10^6$ , respectively. The dye ports were connected via tygon tubing to a pressurized supply tank containing the dye. Control manifolds and solenoid-operated valves were used to release various combinations of continuous dye traces from the model. The dye wakes were photographed using three 35mm Nikon cameras and two JVC VHS video cameras. All the cameras were encased in watertight boxes fitted with spherical lenses to correct for the difference in index of refraction between air and water. The camera supports and underwater lights were mounted on the HSMB carriage and were towed with the model. Two of the 35mm cameras and two VHS cameras provided orthogonal views of the dye traces from the model along the y- and z-axes of the HSMB. In addition, a third 35mm camera provided a view of the wake along the x-axis of the HSMB. It is impossible within the scope of the present paper to present all the data acquired during these tests. A typical example presented in Figure 29 shows three views of the flow around the fuselage nose and the interaction with the wing vortex system.

#### 14.0 CONCLUSIONS

Based on a comprehensive series of experiments conducted in the Tracor Hydraulics Ship Model Basin (HSMB®) to determine the subsonic static and dynamic stability characteristics of a 3.5-foot span, 60-degree delta-high-wing fuselage model operating at high Reynolds number and angles of attack up to 68 degrees, the following conclusions can be drawn:

1. The results of the investigation have demonstrated that the HSMB in conjunction with the Large Amplitude Horizontal Planar Motion Mechanism System (LAHPMM) can determine experimentally all the individual subsonic longitudinal and lateral static and dynamic stability derivatives, required by the equations of motion, for angles of attack up to 68-degrees.
2. Comparison of the static and dynamic results of the present study with data obtained during the 1950's in the NACA Langley Stability Tunnel for a similar wing-fuselage configuration is, in general, quite good.
3. For angles of attack up to 32 degrees, the algebraic summation of the component longitudinal and lateral dynamic derivatives give results which are in good agreement with derivatives obtained from combined oscillations.

4. The HSMB in combination with underwater still and video cameras can be used effectively for performance of flow visualization studies.

5. The HSMB and LAHPMM can be programmed to perform simulated pitchup tests. The results of such tests in combination with dyed wakes can be used to analyze the dynamics of such phenomena as wing rock at high angles of attack.

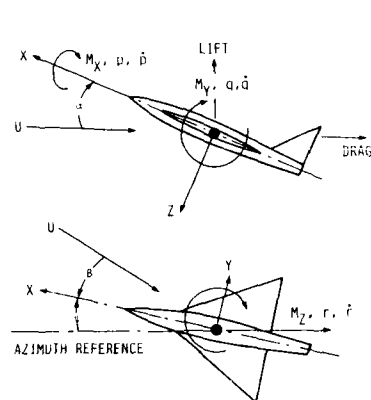
#### 15.0 REFERENCES

1. United States Air Force Contract No. F33615-85-C-3622 dated December 9, 1985.
2. Goodman, A. and Etter, R. J., "Experimental Determination of the Stability and Control Characteristics of a Proposed Rescue Submarine (DSRV) Using the HYDRONAUTICS High Speed Channel," HYDRONAUTICS, Incorporated Technical Report 511-4, November 1966.
3. Goodman, A., "Estimated Stability Control Characteristics and Other Hydrodynamic Coefficients of Two DSSV Configurations," HYDRONAUTICS, Incorporated Technical Report 850-1, May 1968.
4. Goodman, A. and Pepper, M., "Experimental Determination of the Hydrodynamic Coefficients for Computer Simulation Studies of Four Underwater Configurations," HYDRONAUTICS, Incorporated Technical Report 7654-1, April 1976.
5. Ankudinov, V., and Miller, E., "Predicted Maneuvering Characteristics of the Tanker "ESSO OSAKA" in Deep and Shallow Water," HYDRONAUTICS, Incorporated Technical Report 7778-1, June 1977.
6. Gertler, M., Miller, E. R., and Ankudinov, V., "Shallow-Water Maneuverability Characteristics of MARAD Systematic Series for Large Full-Form Merchant Ships," HYDRONAUTICS, Incorporated Technical Report 7568-1, August 1977.
7. Ternes, T., Miller, E. R., and Rudnicki, J., "Large Amplitude Horizontal Planar Motion Mechanism Test to Determine the Hydrodynamic Characteristics of a 670-Foot Single Screw Containership in Deep and Shallow Water (Revised)," HYDRONAUTICS, Incorporated Technical Report 7792-1, March 1978.
8. Miller, E., R., "Model Tests and Analytical Studies for the Development and Evaluation of Concepts for Improving the Inherent Controllability of Tank Vessels," HYDRONAUTICS, Incorporated Technical Report 7832-1, August 1979.
9. Goodman, A., "Experimental and Theoretical Investigation of Factors Affecting Fin-Body Interference (Final)," HYDRONAUTICS, Incorporated Technical Report 7927-1, August 1980.
10. Goodman, Alex, "Description and Operation of Sub Planar Motion Mechanism System," Tracor Hydronautics, Inc. Technical Manual 84070-1, June 1985.
11. Goodman, Alex, "Description and Operation of Large-Amplitude Horizontal PMM," HYDRONAUTICS, Incorporated Technical Manual 7730-1, November 1977.
12. Martin, Milton, "The Stability Derivatives of a Hydrofoil Boat, Part II," HYDRONAUTICS, Incorporated Technical Report 001-10(II), January 1963.
13. Wadlin, K. L., Ramsen, J. A., and Vaughan, V. L., Jr., "The Hydrodynamic Characteristics of Modified Rectangular Flat Plates Having Aspect Ratios of 1.0, 0.25, 0.125 and Operating Near a Free Surface," NACA Report 1246, 1955.
14. Goodman, Alex, Huang, T. T., and Etter, R. J., "Experimental Determination of the Dynamic Coefficients Applicable to Paired Cables," HYDRONAUTICS, Incorporated Technical Report 530-2, April 1967.
15. Brown, C. E., "The Use of Ship Model Basins for the Study of Vortex Wake Phenomena," HYDRONAUTICS, Incorporated Technical Report 7115-2, March 1973.
16. McGowan, William A., "NASA Aircraft Trailing Vortex Research," presented at the FAA symposium on Turbulence, Washington, D.C., 22-24 March 1971.
17. Kohl, R. E., "Model Experiments to Evaluate Vortex Dissipation Devices Proposed for Installation on or Near Aircraft Runways," HYDRONAUTICS, Incorporated Technical Report 7207-2 Final, August 1973.
18. Brown, C. E., "Measurements and Analysis of the Forces Acting on a Small Aircraft Flying in the Upwash Field of a Large Aircraft," HYDRONAUTICS, Incorporated Technical Report 7615, April 1978.
19. Miller, E. R., Jr. and Brown, C. E., "An Experimental Study of Trailing Vortex Wakes Using a Large Towing Tank," HYDRONAUTICS, Incorporated Technical report 7105-1, August 1971.

20. Kirkman, K. L., Brown, C. E., and Goodman, Alex, "Evaluation of Effectiveness of Various Devices for Attenuation of Trailing Vortices Based on Model Tests in a Large Towing Basin," HYDRONAUTICS, Incorporated Technical Report 7207-1, January 1973. (NASA CR2202, December 1973.)
21. Orlik-Ruckemann, K. J., "Techniques for Dynamic Stability Testing in Wind Tunnels," AGARD Dynamic Stability Parameters, Athens, Greece, 22-24 May 1978.
22. Bird, J. D., Jaquet, B. M., and Cowan, J. W., "Effect of Fuselage and Tail Surfaces on Low-Speed Yawing Characteristics of a Swept-Wing Model as Determined in Curved-Flow Test Section of Langley Stability Tunnel," NACA TN 2483, October 1951.
23. Chambers, Joseph R., Grafton, Sue B., and Lutze, Frederick H., "Curved-Flow Rolling-Flow and Oscillatory Pure-Yawing Wind Tunnel Test Methods for Determination of Dynamic Stability Derivatives," AGARD Dynamic Stability Parameters, NASA Ames Research Center, March 2-5, 1981.
24. Goodman, Alex and Feigenbaum, David, "Preliminary Investigation at Low Speeds of Swept Wings in Yawing Flow," NACA Research Memorandum L7109, February 1948.
25. Goodman, Alex and Brewer, Jack, "Investigation at Low Speeds of Effect of Aspect Ratio and Sweep on Static and Yawing Stability Derivatives of Untapered Wings," NACA Technical Note 1669, August 1948.
26. Goodman, Alex and Fisher, L. R., "Investigation at Low Speeds of the Effects of Aspect Ratio and Sweep on Static and Yawing Stability Derivatives of Untapered Wings," NACA Report 968, 1950.
27. Goodman, Alex and Jaquet, Byron, "Low Speed Pitching Derivatives of Low-Aspect Ratio Wings of Triangular and Modified Plan Forms," NACA Research Memorandum L50C02, April 1950.
28. Goodman, Alex, "Effect of Various Outboard and Control Fins on Low-Speed Yawing Stability of Derivatives of a 60 Deg. Delta-Wing Model," NACA Research Memorandum L50R12A, June 1950.
29. Goodman, Alex, "Experimental Investigation of the Low Speed Static and Yawing Stability Characteristics of a 45 Deg. Sweptback High-Wing Configuration with Various Twin Vertical Wing fins," NACA Technical Note 2534, 1951.
30. Goodman, Alex, "Effects of Wing Position and Horizontal-Tail Position on the Static Stability Characteristics of Models with Unswept and 45 Deg. Sweptback Surfaces With Some Reference to Mutual Interference," NACA Technical Note 2504, 1951.
31. Goodman, Alex and Campbell, J. P., "A Semiempirical Method for Estimating the Rolling Moment Due to Yawing of Airplanes," NACA Technical Note 1984, December 1949.
32. Goodman, Alex and Thomas, D. F., "Effects of Wing Position and Fuselage Size on the Low-Speed Static and Rolling Stability Characteristics of a Delta Wing Model," NACA Technical Report 1224, 1955.
33. Jaquet, B. M. and Fletcher, H. S., "Experimental Steady-State Yawing Derivatives of a 60° Delta-Wing Model as Affected by Changes in Vertical Position of the Wing and in Ratio of Fuselage Diameter to Wing Span," NACA Technical Note 3843, October 1956.
34. Fisher, L. R. and Wolhart, W. D., "Some Effects of Amplitude and Frequency on the Aerodynamic Damping of a Model Oscillating Continuously in Yaw," NACA Technical Note 2766, September 1952.
35. Fisher, L. R., "Some Effects of Aspect Ratio and Tail Length on the Contribution of a Vertical Tail to Unsteady Lateral Damping and Directional Stability of a Model Oscillating Continuously in Yaw," NACA Technical Note 3121, January 1954.
36. Lessing, H. C., Fryer, T. B., and Mead, M. H., "A System for Measuring the Dynamic Lateral Stability Derivatives in High-Speed Wind Tunnels," NACA Technical Note 3348, December 1954.
37. Fisher, L. F., "Experimental Determination of Effects of Frequency and Amplitude on the Lateral Stability Derivatives for a Delta, A Swept, and an Unswept Wing Oscillating in Yaw," NACA Report 1357, 1958.
38. Beam, B. H., "A Wind Tunnel Test Technique for Measuring the Dynamic Rotary Stability Derivatives at Subsonic and Supersonic Speeds," NACA Report 1258, 1956.
39. Riley, D. R., "Some Effects of Wing Fence on the Lateral Stability Derivatives of a 60 Degree Delta Wing Oscillating Continuously in Yaw," NACA RM L56D13, July 1958.
40. Campbell, J. P., Johnson, J. L., Jr., and Hewes, D. E., "Low-Speed Study of the Effect of Frequency on the Stability Derivatives of Wings Oscillating in Yaw with Particular Reference to High Angle-of-Attack Conditions," NACA RM L55H05, November 1955.

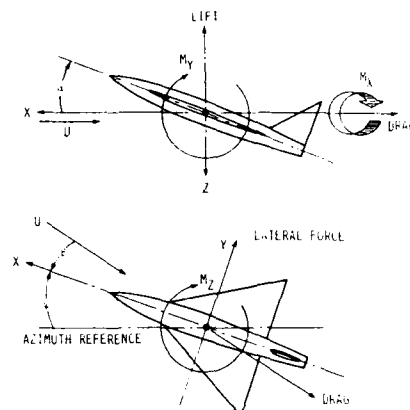


41. Queijo, M. J., Fletcher, H. S., Marple, C. G., and Hughes, F. M., "Preliminary Measurements of the Aerodynamic Yawing Derivatives of a Triangular, a Swept and an Unswept Wing Performing Pure Yawing Oscillations, with a Description of the Instrumentation Employed," NACA RM L55L14, April 1956.
42. Riley, D. R., Bird, J. D., and Fisher, L. R., "Experimental Determination of the Aerodynamic Derivatives Arising from Acceleration in Sideslip for a Triangular, a Swept, and an Unswept Wing," NACA RM L55A07, March 1955.
43. Lichtenstein, J. H. and Williams, J. L., "Effect of Frequency of Sideslipping Motion on the Lateral Stability Derivatives of a Typical Delta-Wing Airplane," NACA RM L57F07, September 1957.
44. Letko, W. and Fletcher, H. S., "Effects of Frequency and Amplitude on the Yawing Derivatives of Triangular, Swept, and Unswept Wings and of a Triangular Wing-Fuselage Combination With and Without a Triangular Tail Performing Sinusoidal Yawing Oscillations," NACA Technical Note 4390, September 1958.
45. Gertler, Morton, The DTMB Planar-Motion-Mechanism System," Proceedings of Symposium on Towing Tank Facilities, Instrumentation and Measuring Techniques, Zagreb, Yugoslavia, September 1959.
46. Goodman, Alex, "Experimental Techniques and Methods of Analysis Used in Submerged Body Research," Proceedings of the ONR Third Symposium on Navy Hydrodynamics, 1960.
47. Goodman, Alex, Gertler, Morton, and Kohl, Robert, "Experimental Techniques and Methods of Analysis Used at HYDRONAUTICS for Surface-Ship Maneuvering Predictions," HYDRONAUTICS, Incorporated Technical Report 7600-1, June 1976.
48. Johnson, Joseph L., Jr., Grafton, Due B., and Yip, Long P., "Exploratory Investigation of Vortex Bursting on the High-Angle-of-Attack Lateral-Directional Stability Characteristics of Highly-Swept Wings," AIAA Paper presented at 115th Aerodynamic Testing Conference, March 1980.



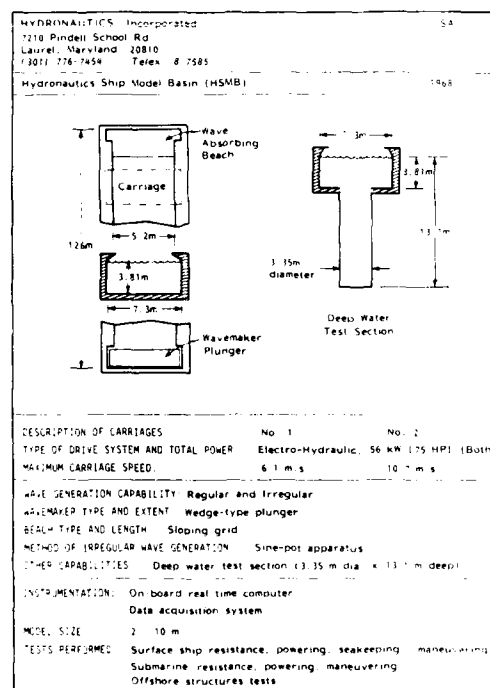
a. SYSTEM OF BODY AXES

FIGURE 1 - SYSTEM OF AXES USED. ARROWS INDICATE POSITIVE FORCES, MOMENTS, ANGULAR DISPLACEMENTS AND VELOCITIES



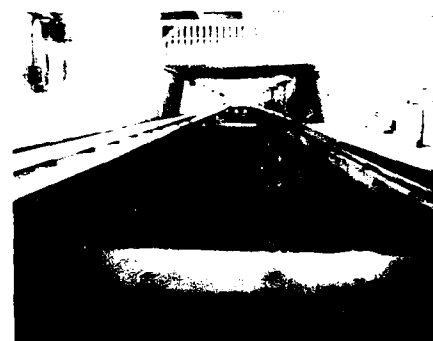
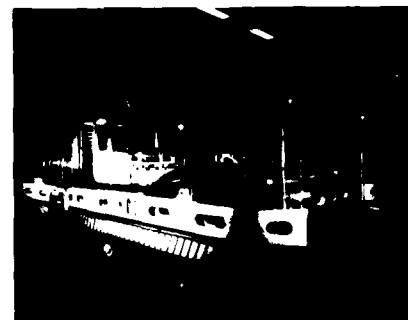
d. SYSTEM OF STABILITY AXES

FIGURE 1 - CONCLUDED



a. SPECIFICATIONS

FIGURE 2 - DESCRIPTION OF HSMB

b. PHOTOGRAPHIC PARTIAL VIEW OF HSMB  
FIGURE 2 - CONTINUEDc. HSMB CARRIAGE NO. 1  
FIGURE 2 - CONCLUDED

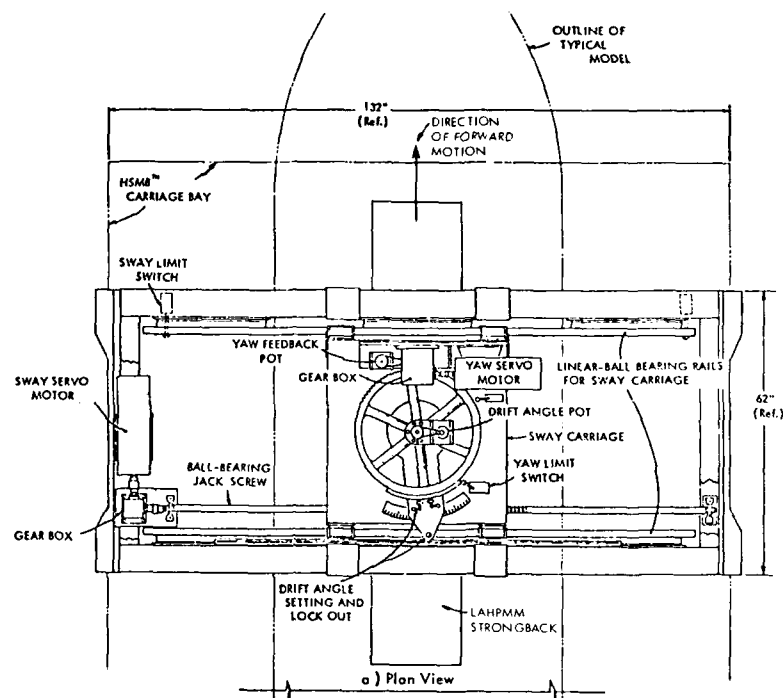


FIGURE 3 - SKETCH OF LAHPMM

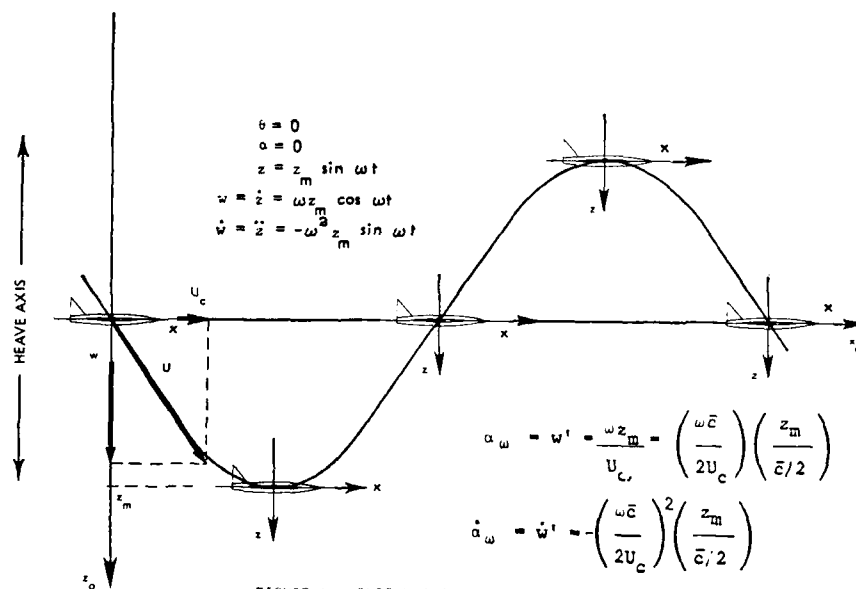


FIGURE 4 - PURE HEAVING TEST CONDITIONS

In general:  $\tan \theta = \frac{U_{z_0}}{U_{x_0}} = \frac{U_{z_0}}{U_c}$

and since:  $y = z_m \sin \omega t$

$\dot{z} = U_{y_0} = z_m \omega \cos \omega t$

$\therefore \tan \theta = \frac{z_m \omega}{U_c} \cos \omega t$  or  $\theta = \arctan \left[ \frac{z_m \omega}{U_c} \cos \omega t \right] = (\arctan \frac{z_m \omega}{U_c}) \cos \omega t = \frac{z_m \omega}{U_c} \cos \omega t$

$\dot{\theta} = \frac{d\theta}{dt} = - \left[ \frac{z_m \omega}{U_c} \right] \omega \left[ \frac{1}{1 + \left( \frac{z_m \omega}{U_c} \cos \omega t \right)^2} \right] \sin \omega t$

$= -\theta_m \omega \sin \omega t$

$\dot{q} = \dot{\theta} = - \frac{z_m \omega}{U_c} \omega^2 \left\{ \frac{1 + \left( \frac{z_m \omega}{U_c} \right) (1 + \sin^2 \omega t)}{\left[ 1 + \left( \frac{z_m \omega}{U_c} \cos \omega t \right)^2 \right]^{3/2}} \right\} \cos \omega t$

$= -\theta_m \omega^2 \cos \omega t$

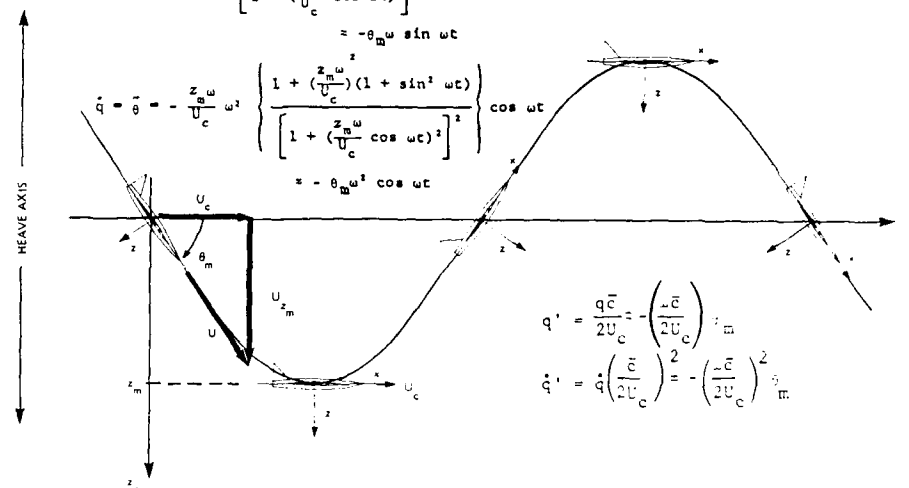


FIGURE 5 - PURE PITCHING MODE TEST CONDITIONS WITH AN ANGLE OF ATTACK = 0 DEGREES

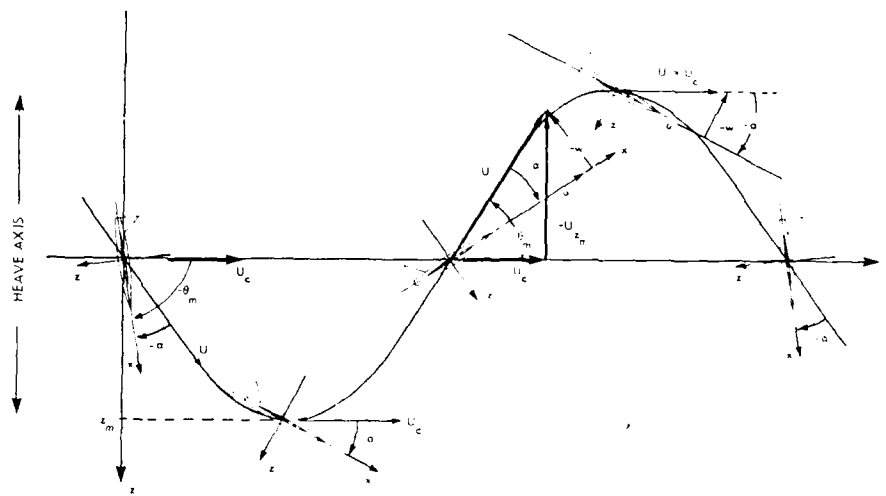


FIGURE 6 - PURE PITCHING MODE TEST CONDITIONS WITH AN ANGLE OF ATTACK = 0 DEGREE

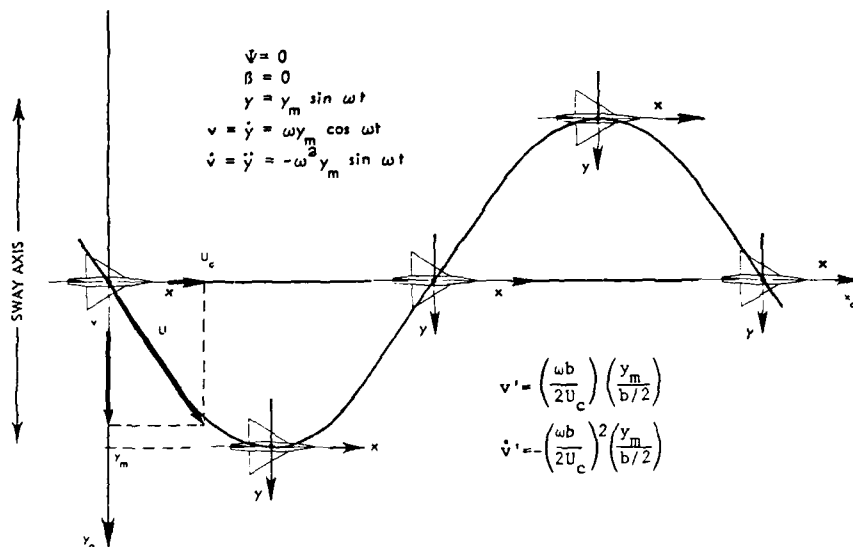


FIGURE 7 - PURE-SWAYING MODE TEST CONDITIONS

In general:  $\tan \psi = \frac{U_{y_o}}{U_{x_o}} = \frac{U_{y_o}}{U_c}$

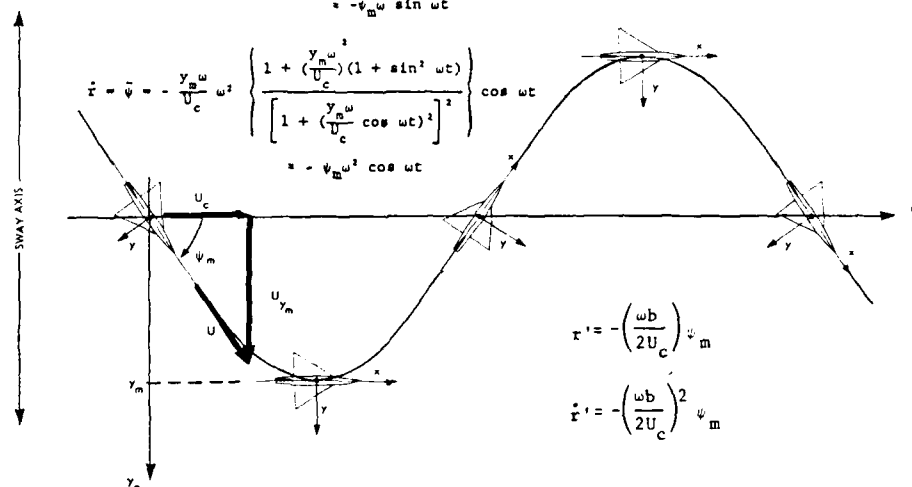
and since:  $y = y_m \sin \omega t$

$\dot{y} = U_{y_o} = y_m \omega \cos \omega t$

$\therefore \tan \psi = \frac{y_m \omega}{U_c} \cos \omega t$  or  $\psi = \arctan \left[ \frac{y_m \omega}{U_c} \cos \omega t \right] = \left( \arctan \frac{y_m \omega}{U_c} \right) \cos \omega t = \frac{y_m \omega}{U_c} \cos \omega t$

$\dot{\psi} = \dot{\psi} = -\left[ \frac{y_m \omega}{U_c} \right] \omega \left[ \frac{1}{1 + \left( \frac{y_m \omega}{U_c} \cos \omega t \right)^2} \right] \sin \omega t$

$\dot{\psi} = -\psi_m \omega \sin \omega t$

FIGURE 8 - PURE-YAWING MODE TEST CONDITIONS WITH AN ANGLE OF SIDESLIP  
 $\beta = 0$  DEGREES

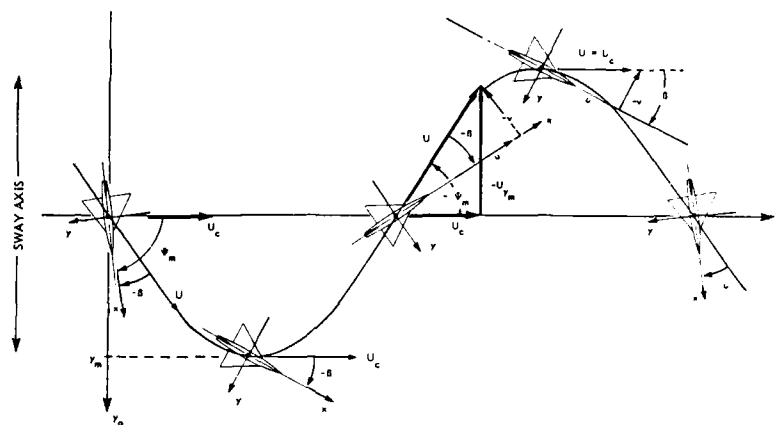


FIGURE 9 - PURE YAWING MODE TEST CONDITIONS WITH AN ANGLE OF SIDESLIP  $\beta > 0$  DEGREES

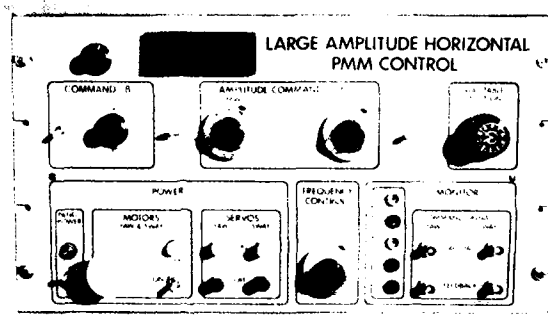


FIGURE 10 - HSMB LARGE AMPLITUDE HORIZONTAL PLANAR MOTION MECHANISM

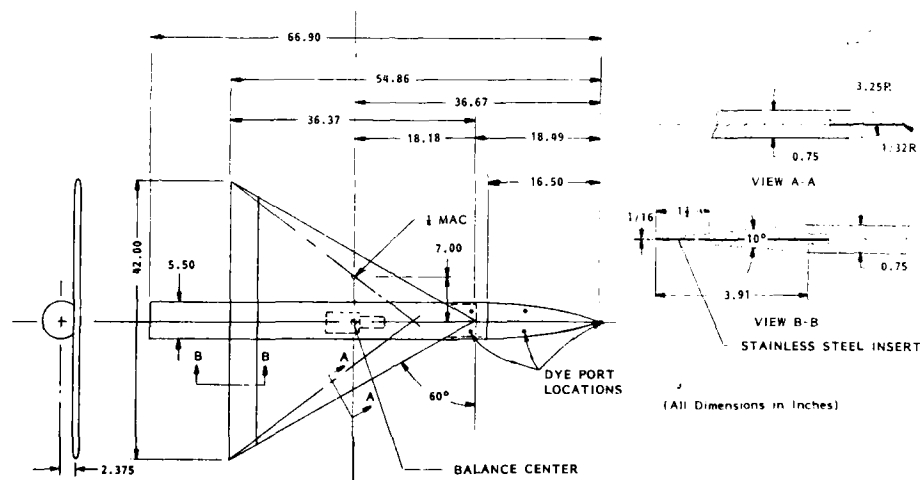


FIGURE 11 - 60 DEGREE DELTA-WING FUSELAGE MODEL

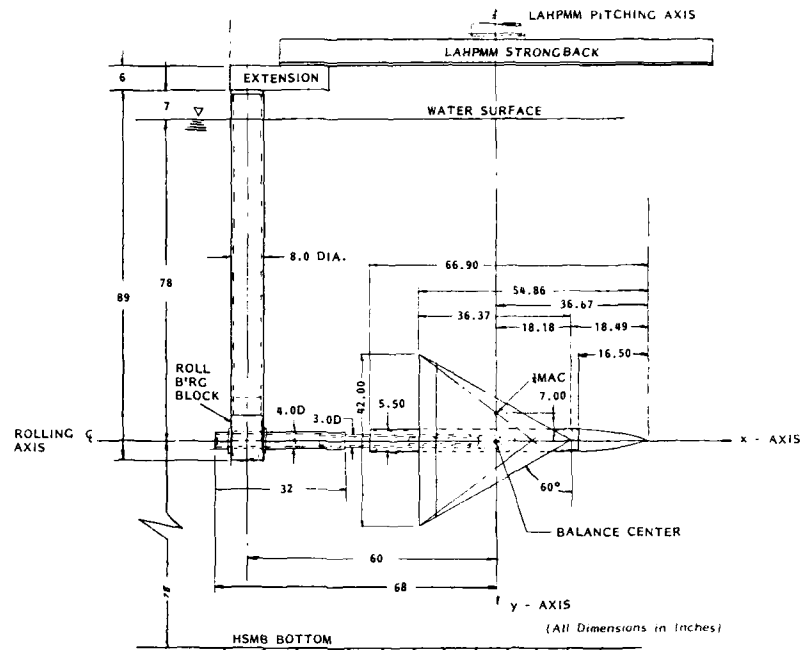


FIGURE 12 - LHPMM STRUT-STING SUPPORT AND MODEL ARRANGEMENT FOR STATIC AND DYNAMIC LONGITUDINAL TESTS

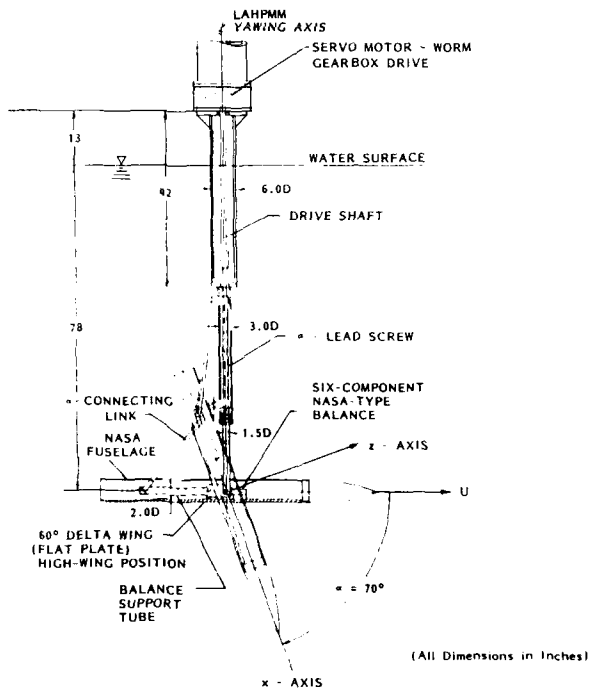
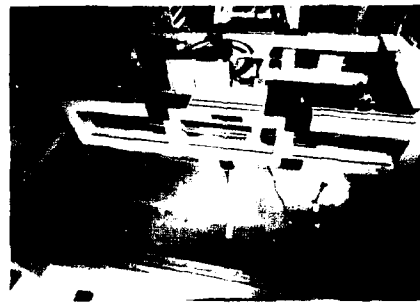


FIGURE 13 - LHPMM STRUT AND MODEL ARRANGEMENT FOR STATIC AND DYNAMIC LATERAL TESTS



a. LONGITUDINAL TESTS  
FIGURE 14 - LAHPMM WITH MODEL ATTACHED



b. LATERAL TESTS  
FIGURE 14 - CONCLUDED

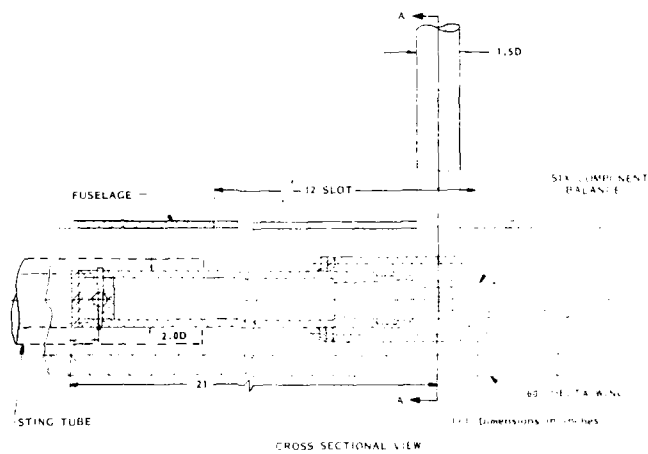


FIGURE 15 - ARRANGEMENT OF SIX-COMPONENT INTERNAL BALANCE



FIGURE 16 - CALIBRATION OF SIX-COMPONENT BALANCE

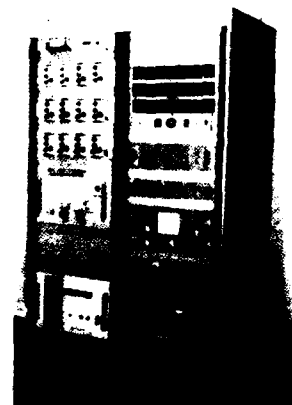


FIGURE 17 - PMM CONTROL AND DATA ACQUISITION SYSTEM



[illegible]

FIGURE 18 - CONTINUED

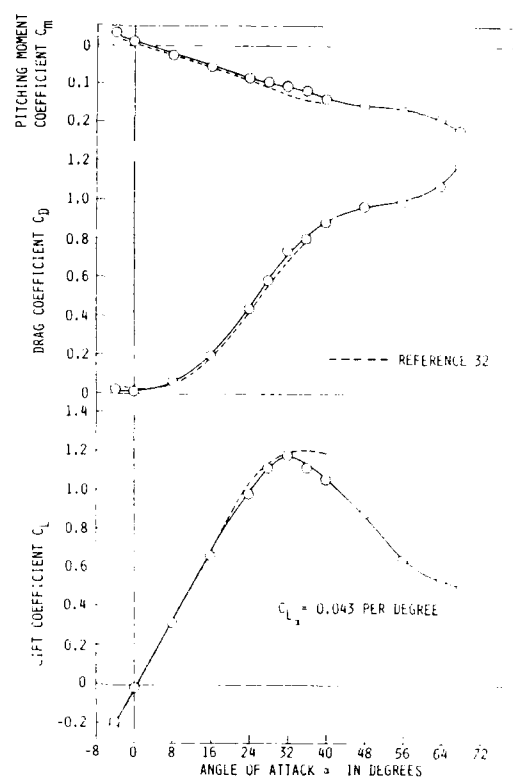


FIGURE 19 - COMPARISON OF  $C_L$ ,  $C_D$  AND  $C_m$  WITH NACA DATA FOR A SIMILAR HIGH WING-FUSELAGE CONFIGURATION

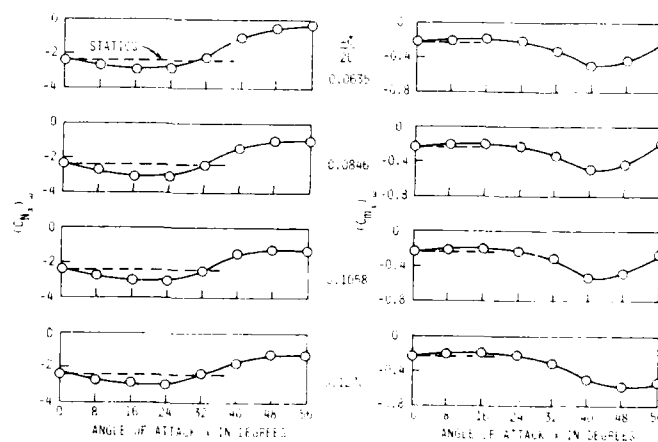


FIGURE 20 - VARIATION OF  $C_m$ ,  $C_L$  AND  $C_D$  WITH ANGLE OF ATTACK FOR SEVERAL FREQUENCIES

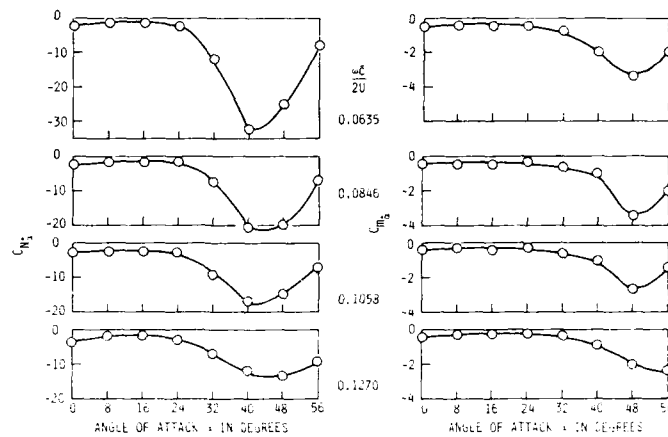


FIGURE 21 - VARIATION OF  $C_{N1}$  AND  $C_{m1}$  WITH ANGLE OF ATTACK FOR SEVERAL REDUCED FREQUENCIES

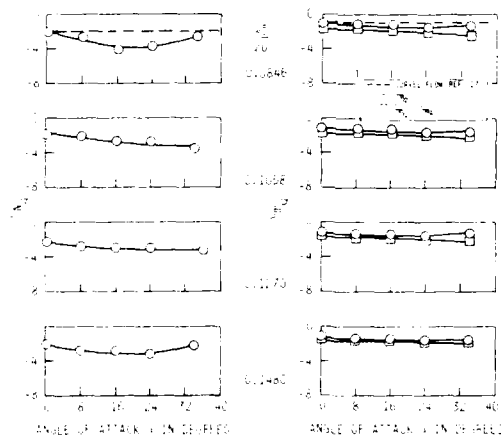


FIGURE 22 - VARIATION OF  $C_{N2}$  AND  $C_{m2}$  WITH ANGLE OF ATTACK FOR SEVERAL REDUCED FREQUENCIES

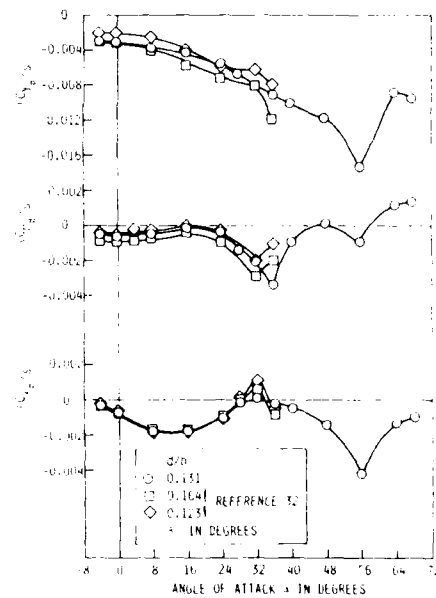


FIGURE 23 - COMPARISON OF  $C_{N1}$ ,  $C_{m1}$  AND  $C_{N2}$  WITH NACA DATA FOR A SIMILAR HIGH WING-FUSELAGE CONFIGURATION

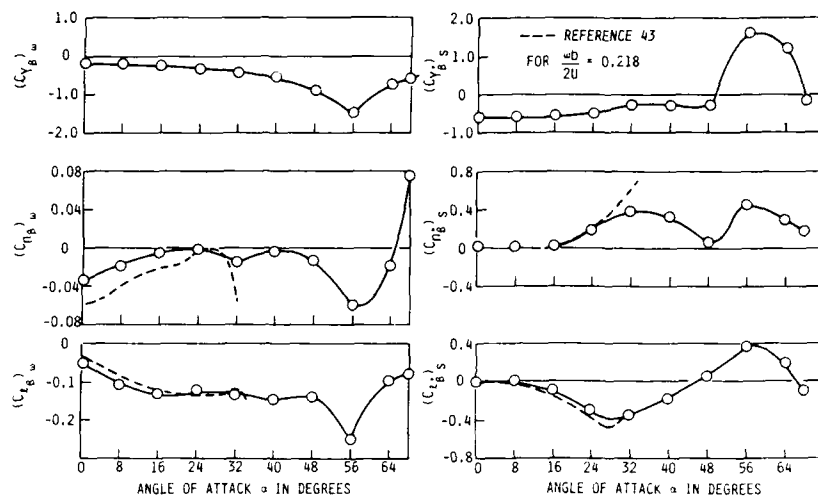


FIGURE 24 - VARIATION OF  $(C_v)_w$ ,  $(C_n)_w$ ,  $(C_t)_w$ ,  $(C_v)_s$ ,  $(C_n)_s$  AND  $(C_t)_s$  WITH ANGLE OF ATTACK FOR  $wD/2U = 0.184$

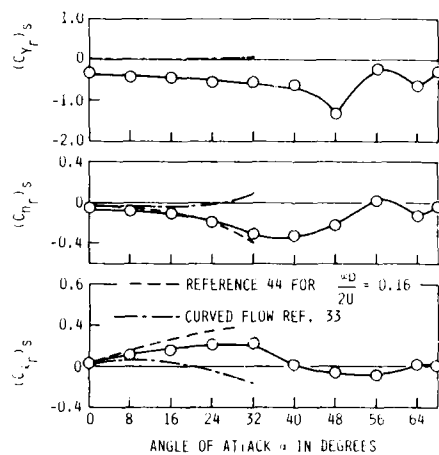


FIGURE 25 - VARIATION OF  $(C_v)_r$ ,  $(C_n)_r$  AND  $(C_t)_r$  WITH ANGLE OF ATTACK FOR  $wD/2U = 0.184$

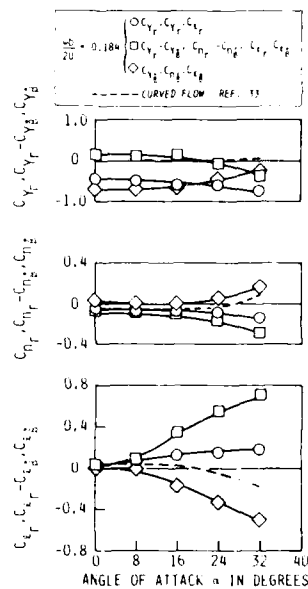


FIGURE 26 - VARIATION OF PURE YAWING, COMBINED YAWING, PURE SWAYING AND CURVED FLOW DERIVATIVES WITH ANGLE OF ATTACK

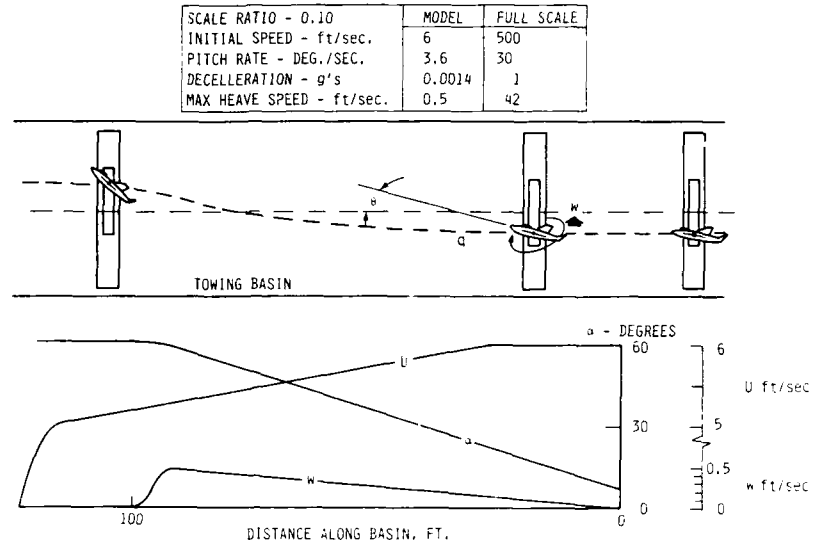


FIGURE 27 - TYPICAL SIMULATED PITCHUP MANEUVER

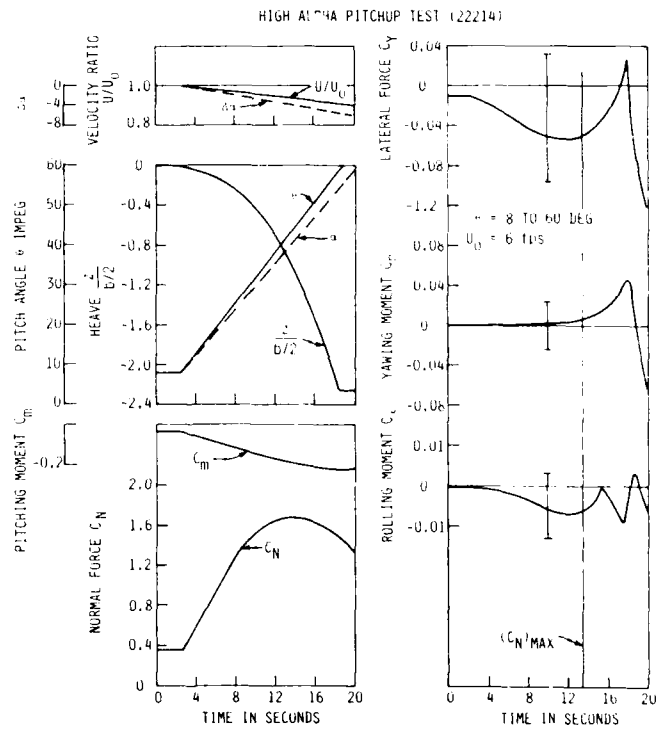


FIGURE 28 - RESULTS FROM PITCHUP TEST



FIGURE 29 - TYPICAL FLOW VISUALIZATION RESULTS

TABLE 1  
COMPARISON OF MAXIMUM LOADS  
FOR 60-DEGREE DELTA-WIND MODEL

Value of Coefficients	Langley Full-Scale Tunnel	HSMB
b, ft	3.5	3.5
U, fps	58.0	8.5
RN	$0.75 \times 10^6$	$1.72 \times 10^7$
q, psf	4.0	72.25
qS, lbs	21.2	382.93
qSb, lb-ft	74.2	1340.74
qSc, lb-ft	42.8	773.51
$\alpha$ , deg	34	34
$C_L = 1.25$	26.5	478.6 lbs
$C_D = 0.8$	17.0	306.3 lbs
$C_m = -0.2$	8.5	-154.7 lb-ft
Assume $\gamma = 0.175$ radians		
$C_{Y_F} = -0.2$	0.74	-13.4 lbs
$C_{n_F} = -0.2$	1.50	-27.1 lb-ft
$C_{l_F} = -0.2$	2.60	-46.9 lb-ft

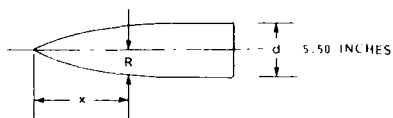
TABLE 2

MODEL CHARACTERISTICS

<u>WING:</u>	
Aspect Ratio	2.31
Taper Ratio	0
Leading-Edge Sweep Angle, Deg	60
Dihedral Angle, Deg	0
Twist, Deg	0
Airfoil Section	Flat Plate
Span, inches (ft)	42.0 (3.5)
MAC, inches (ft)	24.25 (2.02)
Root Chord, inches (ft)	36.37 (3.03)
Section Thickness, inches (%)	0.75 (3.1)
Area, Sq in. (sq ft)	763.77 (5.30)
<u>FUSELAGE:</u>	
Length, inches (ft)	66.90 (5.575)
Max Diameter, inches (ft)	5.5 (0.458)
Fineness Ratio	12.16
Diameter-Span Ratio	0.131
Ogive Nose (L/D)	3.0
<u>Note:</u>	Fuselage is identical to generic model used at NASA-Langley

TABLE 3

FUSELAGE NOSE OFFSETS

TABLE 4  
SIX-COMPONENT BALANCE CHARACTERISTICS

X	Y
Inches	Inches
0	0
0.825	0.275
1.650	0.523
2.475	0.770
3.300	0.996
4.950	1.403
6.600	1.760
8.250	2.335
9.900	2.310
11.200	2.640
16.500	2.750

Balance	Overall Dimensions	Design Loads					
		F <sub>N</sub>	F <sub>A</sub>	F <sub>V</sub>	M <sub>X</sub>	M <sub>Y</sub>	M <sub>Z</sub>
TRI 816	1.75-inch dia by 8.75-inch long	100	110	300	100	80	100
NASA 716	1.75-inch dia by 8.75-inch long	500	100	300	1000	500	100
Design Loads in lbs and lb-in.							

# FLOW VISUALIZATION STUDY OF VORTEX MANIPULATION ON FIGHTER CONFIGURATIONS AT HIGH ANGLES OF ATTACK

By

Gerald V. Malcolm  
Director, Research and Technology  
Andrew M. Skow  
President  
EIDETICS INTERNATIONAL, INC.  
Torrance, California 90505

## SUMMARY

Experiments were performed in a flow visualization water tunnel on a generic fighter model to explore vortex manipulation as an effective means of aircraft control by altering the natural state of the forebody and LEX vortices in the medium-to-high-angle of attack range with either small surface modifiers or blowing jets. Specifically, the forebody vortex system was examined with the clean forebody, with forebody strakes, and with forebody surface blowing. LEX vortices were examined with a clean LEX, with small geometric modifications near the apex, and with surface blowing, both in upstream and downstream directions at various locations on the LEX surface. The interactive effects of forebody and LEX/wing vortices and their response to the various methods of control were also examined.

Generally, it was concluded that the forebody vortices can be effectively controlled by either blowing or using strakes, but the effectiveness is very dependent on proper radial placement of the blowing port or strake. Geometric modifications and blowing at the LEX apex were not particularly effective in altering the trajectory of the LEX vortices or the burst points. Blowing aft of the mid-chord of the LEX was much more effective and could force the burst points to move forward significantly. Interactions between the forebody and LEX vortex systems were pronounced.

## SYMBOLS

$A_B$  = cross sectional area of model fuselage, 1.226 in<sup>2</sup>  
 $A_{Tube}$  = cross sectional area of blowing tube opening, 1.416x10<sup>-4</sup> in<sup>2</sup>  
 $b_L$  = LEX span (See Fig. 6)  
 $b_W$  = wing span (See Fig. 5)  
 $C_\mu$  = blowing coefficient,  $\dot{m}V_j/qA_B$   
 $l$  = LEX length (See Fig. 6)  
 $L_1$  = LEX No. 1, typical (See Fig. 6)  
 $l/d$  = fineness ratio of forebody  
 $\dot{m}$  = mass flow rate for blowing  
 $q$  = free-stream dynamic pressure  
 $R_b$  =  $(b_L/2)/(b_W/2)$   
 $R_s$  =  $1/(b_L/2)$   
 $V_j$  = jet velocity  
 $W_{50}$  = wing with 50° sweep, typical  
 $\alpha$  = angle of attack  
 $\Lambda$  = wing sweep angle (See Fig. 5)  
 $\phi$  = radial angle on forebody (See Figs. 10,11)

## 1. INTRODUCTION

Future air combat arenas will dictate requirements for fighter aircraft performance that will exceed the capabilities of present-day aircraft. One of the key technologies to advance the overall capability of the airplane is aerodynamic control. The flight envelope of current aircraft has been limited at least in part by controllability problems at high angles of attack, typically represented by sudden departures in roll and yaw and, in some cases, by pitchup or deep stall. Reduced controllability places undesirable limits on the maneuverability of the aircraft but, even worse, often leads to unrecoverable flight modes such as spins.



Several aerodynamic phenomena are known to contribute to the problem of uncontrolled flight.

- 1) Asymmetric vortex flows on the forebody, even at zero sideslip, produce large side forces with resulting yawing moments large enough to depart the aircraft in yaw. An example of asymmetric forebody vortices is shown in Figure 1 which is a photograph from a water tunnel test of a fighter airplane at high angles of attack.
- 2) Asymmetric vortex burst points in the vicinity of the LEX and wing causing asymmetric lift lead to roll departure. An example<sup>2</sup> is shown in Figure 2 with a generic and a real airplane model in the water tunnel at  $Q \neq 0$ .
- 3) Increased lift on the forebody and LEX results in a pitch-up or deep-stall condition that cannot be overcome with conventional horizontal tail control surfaces.

Alternate methods of controlling the flow field on a high-performance airplane that are effective at angles of attack beyond the range for effective conventional control surfaces need to be investigated. Such schemes as thrust vectoring and thrust turning vanes are currently being evaluated, but it is also possible, and perhaps more economical, to utilize novel aerodynamic controls. The typical flow field around a modern fighter aircraft is dominated by vortices. It is the existence of these complex vortex flows that eventually contributes to degraded control capability as the angle of attack is increased. It is reasonable to assume that if there were means to locally control these vortex flows on the airplane, one might be able to utilize this powerful force input to enhance the overall airplane controllability.

Several studies have been done to investigate non-conventional methods of aerodynamic control. The use of forebody strakes has been shown<sup>3-5</sup> to be an effective method of forcing naturally-occurring asymmetric forebody vortices at high angles of attack to be symmetric and therefore eliminate large yawing moments at zero sideslip. Use of deflectable forebody strakes that can be deployed asymmetrically has also been investigated<sup>6</sup>. Investigations of forebody blowing techniques to control the forebody vortex orientation have also been conducted in both water and wind tunnel experiments<sup>7-10</sup> where asymmetric forebody vortices were switched in orientation by blowing under the high vortex. Forebody vortex control becomes effective in the angle of attack range where rudder control decreases. Several studies have assessed the utility of moveable wing strakes (LEX) for roll and pitch control including strakes hinged at the root<sup>11</sup> and apex fences and flaps on delta wings<sup>12-15</sup>.

The purpose of this study was to explore methods of vortex manipulation requiring minimum physical input but resulting in maximum change to the vortex flow field to produce effective airplane control. The basic notion was to use the principal of "fluid amplification", or to achieve a large incremental change in the basic vortex structure around the airplane for minimal disturbance at the source of the vortices. The objective was to search for small deployable devices located close to the origins of the forebody or LEX vortices. These devices could be either mechanical or pneumatic. The mechanical devices might be small flaps, fences or strakes that could be hinged or popped out of the surface. Pneumatic devices could be small blowing ports or nozzles. Both are intrinsically low-energy devices, i.e., low hinge moments or low jet momentum. The first step was to visually assess the results of various schemes to deliberately alter the natural state of the vortices in the flow field of a typical fighter configuration. This was accomplished by performing water tunnel flow visualization experiments on a generic fighter model consisting of a cylindrical fuselage, tangent ogive forebody, clipped delta wings with different sweep angles and several wing LEX's. The approach was to document with photographs and video recordings, the behavior of the various vortices in response to as many "flow modifiers" as possible. Flow modifications were produced with strakes and blowing on the forebody and with blowing at various locations on the LEX. Geometry modifiers were applied only at the apex on the LEX. Several different configurations were also examined to assess the effects on the flow field of wing sweep angle, LEX size and longitudinal location of the LEX/wing with respect to the forebody.

## 2. TEST FACILITY AND CONDITIONS

The experiments were conducted in the NASA-Ames Dryden Flight Research Facility Flow Visualization Water Tunnel (Fig. 3). The tunnel is a continuous flow tunnel with a vertical test section 72 in. high and a cross section of 24 in. by 16 in. The test section is constructed with plexiglass on all four walls for ease in viewing the model. Although the flow speed is variable, the entire test was conducted at .25 ft/sec since this speed provides the optimum visualization conditions. The corresponding unit Reynolds number is  $3 \times 10^4$  per ft. The model was mounted on a bent sting so that the angle of attack could be continuously varied from 0 to 60°. Provisions for sideslip angles were available, but there was insufficient time to investigate sideslip effects in this initial test in preference to looking at more critical parameters.

## 3. MODEL

The generic model was designed to be a simple representation of the various fighter configurations now flying in this country and to be inexpensive to build. Figure 4 shows a photograph of the basic models. A cylindrical plastic body with an  $L/d = 3.5$  tangent ogive nose represents the fuselage. Wing planforms were clipped deltas with sweep angles of 30°, 40°, 50°, and 60°. Figure 5 shows a line drawing of the basic model. The wings were constructed from 1/16 in. thick sheet aluminum and were mounted with the bevel on the upper surface. The forebody section was a single piece 4.5 in. in length. The aft body section was split, and the wings were sandwiched between the two halves. The wing apex was removed as shown to allow the wing to be moved closer to the forebody piece. Up to four different sized LEX's (strakes) were available for each wing, depending on the sweep angle. The choice of a LEX planform shape for these tests was driven by a desire to generate a strong LEX vortex that would have a burst point as far aft as possible for a given angle of attack and whose burst point would be delayed as long as possible in moving forward with increasing angle of attack. Frirk and Lamar<sup>16-17</sup> performed an extensive theoretical study of LEX's (wing strakes) and conducted water tunnel experiments to document vortex burst characteristics. Based on their results, the strake identified in Ref. 16 as AD-17 was chosen as the basic LEX planform for the water tunnel model in this test. The base LEX geometry is specified in Refs.

16 and 17. Referring to Fig. 6, the dimensions were derived from

$$R_b = (b_L/2)/(b_W/2) = .212 \text{ and } R_S = 1/(b_L/2) = 7.77.$$

Using the specified span and slenderness ratios above, the base LEX is very large. Sub-scaled versions were designed and built for investigating various LEX sizes. The scaled configurations are 0.85, 0.60, and 0.50 of the base LEX. The table in Figure 6 shows the length and exposed half-span of each LEX and the ratio of exposed LEX area to wing reference area for each LEX/wing combination. The slenderness ratio,  $R_S$ , is a constant 7.77 for all LEX's. The coordinates of the four LEX's are shown in Figure 7. Figure 6 shows the LEX configurations actually tested. The No. 1 LEX (0.5-scale) was tested with wing sweeps of 40°, 50°, and 60°. The No. 2 and No. 3 LEX's (0.6 and 0.85-scale) were tested only with the 50° swept wing. The No. 4 LEX was not tested due to time constraints. The LEX's were constructed from 1/16 in. thick sheet aluminum and had a single-beveled 20° edge with the bevel on the upper side.

The positions of the LEX/wing combinations could be varied longitudinally in order to emulate configurations with either very long forebodies or with short coupling between the forebody and the

LEX/wing. The location limits were dictated by not allowing the wing trailing edge to be further aft than the body base and the LEX/body junction could not be forward of the nose/body tangent point.

Several candidates for LEX "modifiers" were tried to either enhance or spoil the vortex flow. These are shown in Figure 8. The premise for these modifiers was that modifying the flow near the LEX apex would be the most effective way of causing a change in flow over the entire LEX. Based on the experimental results discussed later, this may not be true.

Blowing on the LEX was achieved by simply placing a stainless steel tube on the upper surface of the model with the tube end located as desired. The various locations tried are sketched in Figure 9. Provisions were also made for blowing on the forebody. Blowing ports on the forebody were provided at the locations shown in Figure 10. Past experiments have shown that the most effective radial position for blowing to affect the forebody vortices at zero sideslip angle is  $\theta = 135^\circ$  to  $150^\circ$  from the windward stagnation line. The model was constructed so that each of these ports could be used independently. The blowing exit is perpendicular to the surface. Ports that were actually utilized will be discussed later. The dye ports on the forebody are also shown in Figure 10.

Blowing rate for the forebody was established based on the experience from past experiments. A blowing rate was calibrated to correspond to a maximum blowing coefficient,  $C_{\mu}$  of 1.5 based on the body cross sectional area of .00852 ft<sup>2</sup> where

$$C_{\mu} = \dot{m} V_j / \rho A_B$$

The quantity  $\dot{m} V_j$ , where

$$V_j = \dot{m} / \rho A_{\text{Tube}}$$

was measured directly in the test setup through all the tunnel and model plumbing. This was accomplished by measuring the volume rate of water displaced from the pressurized cannister supplying the blowing water for several different pressures. It was impossible to separately regulate the pressure for the blowing tubes from the dye lines with the test setup in the Dryden water tunnel facility, since the supply cannisters for both were pressurized by a single pressure source through a common manifold. The volume control on each of the dye lines, as well as the blowing lines, was regulated on the downstream side of the pressure cannister by a flow rate valve. Calibrating the blowing rate as a function of the valve position was nearly impossible. The approach taken was to set the pressure for the whole system based on the pressure needed to provide the maximum  $C_{\mu}$  with the control valve all the way open. Lower flow rates were obtained by opening the blowing valve for an estimated percentage of the maximum flow rate. For experiments where blowing rates were varied, the reference to blowing rates is light, medium and heavy, where heavy corresponds to the maximum. For these initial experiments, precise measurements of the blowing rate were not felt to be worth the time and effort. The LEX blowing was from the same size tube opening of .020 in. as the forebody, so blowing rates are nearly identical to those used on the forebody, i.e., the maximum  $C_{\mu}$  is approximately 1.5.

Forebody strakes were also investigated and are shown in Figure 11. Examples of water tunnel photographs obtained from this test are shown in Fig. 12a and a basic definition of the flow phenomena of interest to this study is illustrated in Fig. 12b.

#### 4. DATA ACQUISITION

Data consists of 35 mm photographs of the model in both planform and side views. Although they were not taken simultaneously, in most cases they were taken only a few seconds or minutes apart with two different cameras. In a few cases, the two views were taken at much different times, but this was not observed to be a problem since the flow at most attitudes is reasonably repeatable. Video tapes were also made with emphasis on planform views to show the dynamics of the observed flow phenomena.

Typically the angle of attack was varied as follows:

$$\alpha = 0, 3^\circ, 6^\circ, 9^\circ, 12^\circ, 15^\circ, 18^\circ, 21^\circ, 25^\circ, 30^\circ, 35^\circ, 40^\circ, 45^\circ, 50^\circ, 55^\circ, 60^\circ$$

Some results were obtained at only a few angles of attack such as forebody blowing, the interest for which is primarily at  $\alpha$  above 35° and LEX blowing which is only of interest at  $\alpha$  below 35°.

## 5. RESULTS

It is obvious that there are many combinations of model geometries and flow modifiers that could be tested. The priority for selecting the configurations that were eventually studied was to emphasize first the primary purpose of searching for effective means of vortex control on a "basic" configuration and secondly, to explore the effects of configuration changes such as sweep angle, LEX size and LEX/wing location. The basic model was chosen to be the configuration with a 50° swept wing, the smallest LEX (LEX No. 1) and with the LEX/wing in the most forward longitudinal position. In addition to the primary investigations of vortex control schemes, the sensitivity of the flow field to configuration differences were explored by testing the basic LEX/wing in the most aft longitudinal position, the 50° wing with the next two larger LEX's (LEX No. 2 and No. 3) in the forward position and the smallest LEX with the 40° and 60° swept wings in the forward position. The emphasis in this paper will be on the results of vortex control schemes for the basic model. Results on configuration effects can be found in Ref. 18.

Analysis of results has concentrated on evaluating the potential of various techniques as flow control devices and not so much on making detailed measurements of vortex positions and exact burst locations relative to the model surface.

The results will be briefly described and will cover the following:

- 1) Flow on the "Basic Model"
- 2) LEX Modifier Effects
- 3) LEX Blowing Effects
- 4) Interactive Effects of Forebody Strakes/Forebody Blowing/LEX Blowing

### 5.1 Basic Model

Figure 13 shows both planform and side views of the flow on the basic model at  $\alpha = 15^\circ, 25^\circ, 35^\circ, 45^\circ, 45^\circ$  and  $50^\circ$ . Vortices originating on the forebody, LEX and wing are clearly shown. Vortex trajectories and burst points are strongly dependent on angle of attack. At  $\alpha = 15^\circ$ , the vortex trajectories and burst points are nearly symmetric. The LEX vortices are further above the wing and burst further forward. They do not appear to interact as directly with the wing vortices as they do at lower angles of attack. Above  $\alpha = 35^\circ$ , the LEX vortices are asymmetric with the right forebody vortex higher above the body than the left one.

In general, on all the configurations it was observed that the LEX burst point is further aft on the same side as the high forebody vortex as compared to the LEX vortex on the side with the low forebody vortex. It was found in some of the blowing experiments, discussed later, that if one changed the forebody vortex asymmetry by blowing, the burst points for the LEX vortices would change as well. It appears that reduced vorticity in a forebody vortex results in an increase in vorticity in the LEX vortex on the same side resulting in a burst point further downstream. At  $\alpha = 50^\circ$ , both the LEX vortices are bursting at the apex of the LEX. In general, with the left forebody vortex close to the body and with the right LEX vortex burst point further aft, one would expect a nose-left and right-wing-up force contribution.

### 5.2 LEX Modifiers

Figure 14 shows planform and side views to compare various LEX modifiers. The intent was to try various minor modifications to the LEX apex in hopes of either enhancing the LEX vortex, i.e., delaying the vortex burst at a given wing location to higher angles of attack or to move the vortex burst point further aft at a given angle of attack. The alternative to enhancement is to spoil the vortex and cause it to burst sooner. These photographs show the flow field at  $\alpha = 12^\circ$  for a clean configuration in (a) and (b), for LEX Modifiers #1 in (c) and (d), #2 in (e) and (f) and #4 in (g) and (h). (LEX modifier configurations are shown in Figure 8.) The modifiers were all installed on the left LEX; the right LEX was used to try various LEX blowing schemes and will be discussed next. By comparing these four pairs of pictures, there do not appear to be significant differences in the vortex burst locations. In viewing the flow, it appeared that no matter what type of disturbance was created near the apex of the LEX, there was such a significant amount of LEX area behind the disturbed region that the flow appeared to quickly reestablish itself behind the disturbance, and a vortex was generated very similarly to the case with no disturbance.

For a smaller LEX, it may be that the disturbance near the apex would affect the LEX contribution more severely since there would be less area aft of the disturbance to generate a vortex. Since the LEX chosen for these experiments produces a very strong vortex, it is not unreasonable that a strong disturbance is required to disrupt it. No significant effects of LEX modifiers #3, #5, and #6 were observed in terms of changing the vortex trajectory or the burst point. The only exception was the "spoiler" used in (d) which was a small rectangular tab that was perpendicular to the LEX planform and created a turbulent wake approaching the LEX apex. This appeared to be effective as a spoiler at angles of attack up to about  $\alpha = 12^\circ$ , but at higher angles the wake disturbance had minimal impact on the development of the LEX vortex. To assess the real impact of the LEX modifiers on changing the aerodynamic forces on the model, one needs quantitative information in addition to the visualization results.

Similar results are shown in Figure 15 for  $\alpha = 21^\circ$ . The differences between the observed vortex locations and burst points with and without the spoiler are not significant. On the basis of the modifiers that were tried, it appears that, in general, to change the LEX flow significantly, particularly if the LEX is shaped to produce a strong vortex and is reasonably large in terms of percent wing area, one must introduce larger disturbances and perhaps locate them further downstream on the LEX to be more effective.

The notion that effective control can be gained by disturbing the vortex core at the apex of the LEX does not seem to be true. The strength of the vortex is not determined by the LEX apex geometry but by the entire edge of the LEX. This is seen to be true from the results of Frink and Lamar 16-17 where the vortex characteristics were shown to be extremely sensitive to the LEX shape. The most effective control would appear to be a manipulation of the vortex after it is fully formed or at least far enough aft on the LEX so that the generated disturbance cannot be overcome to any great extent by the remaining LEX surface. The LEX blowing experiments discussed next tend to support this observation.

### 5.3 LEX Blowing

Several different schemes for blowing on the surface of the right LEX were tried. The effects of varying the blowing location, blowing direction (upstream or downstream) and blowing rates were examined. The blowing schemes (location and direction) are illustrated in Figure 9. Figure 16 (a) through (d) shows planform views of LEX blowers #1, #3 and #7 with the model at  $\alpha=21^\circ$ . Blower #1 is blowing aft with the intent of energizing the vortex and moving the burst point further aft. It did not have much effect; the burst point is relatively unchanged. The same result was observed with LEX blower #3 (in Figure 16(c)) which used forward blowing near the LEX apex.

Figure 16 (d) shows LEX blower #7 and Figure 16 (e) through (h) show planform and side views of LEX blower #4. These two schemes also involve blowing forward, but the location of the blowing tube was much further aft than blower #3. The origin of LEX blower #7 is at the LEX leading edge approximately 1/3 of the LEX chord ahead of the LEX/wing junction. Comparing Figures 16 (d) and (a), the vortex burst point moved from mid wing to near the LEX apex. Figure 16 (g) and (h) shows planform and side views of LEX blower #4 with a blowing origin in the center of the LEX span just forward of the LEX/wing junction. In these photographs, the blowing is off. Figure 16 (k) and (l) shows the effect of blowing which is to move the burst point toward the apex. The location of the LEX vortex burst point can be controlled somewhat by varying the blowing rate. The tendency is for the vortex burst point to be stabilized at the location corresponding to no blowing. It appears that there must be some threshold blowing rate before the burst point changes, and then the burst point moves rapidly to a location just ahead of the blowing origin. It is possible that even though the burst point location does not change significantly with increasing blowing rate prior to some threshold, the vortex strength or influence on the wing lift may be more sensitive with changing blowing rates. Quantitative force measurements are needed to assess this.

In general, it was observed that to influence the vortex, one must introduce a disturbance somewhere between the midpoint on the LEX chord and the LEX/wing junction. It also appears to be more effective if one can disturb the origin of the vorticity, the LEX leading edge where the shear layer is generated when the flow separates, rather than to directly disturb the core. From a practical standpoint it would be easier to implement blowing at the surface than to blow into a core that might be located well away from an available mounting surface.

### 5.4 Forebody Strakes/LEX Blowing

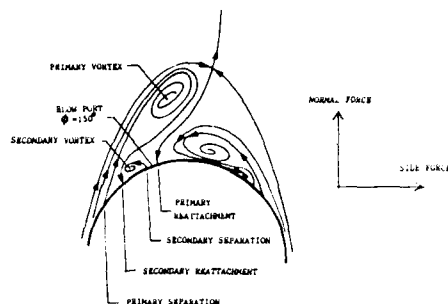
Figure 17 illustrates in planform and side views the effect of both a single strake on the forebody and the effect of blowing on the right LEX. All the photos are at  $\alpha=21^\circ$ . Frames (a) and (b) show the model without a strake and without blowing. Frames (c) and (d) show the configuration with a single strake (Strake #1) on the right forebody. The right forebody vortex is above the body, and the left vortex is pulled completely across the body ahead of the vertical tail. The effect on the rest of the flow field is significant. The right LEX vortex burst point is moved from the mid-wing location to the wing trailing edge and much further outboard. The left side LEX and wing vortices burst much further forward. The aerodynamic result of deploying a single strake as shown here would be increased lift on the right wing, decreased lift on the left wing and higher suction on the left forebody, resulting in yaw left and roll left (left wing down). Comparing (c) and (d) with (e) and (f), blowing on the right LEX causes the LEX vortex burst point to move from the trailing edge of the wing to a point forward of the blowing port. The left forebody vortex is pulled even further across the body to the right. The left LEX vortex bursts about the same place as before. In this case one would expect the lift on the right wing to decrease producing a change in the rolling moment in the direction of right wing down.

Adding a strake to the left forebody shown in (g) and (h) produces forebody vortex symmetry once again and the flow field is very similar to the case with no strake observed in (a) and (b). At this attitude, a asymmetric strake on the nose is seen to have very significant effects on the entire flow field. While symmetric strakes appear to have very little effect compared to the case with no strake, it is possible that even though the flow is symmetric with and without symmetric strakes, the nose lift contributing to the pitching moment may be different. Placement of the strakes can have a large influence on the contribution of the nose to the overall lift and pitching moment.

### 5.5 Forebody Strakes/Forebody Blowing

Figure 18 shows comparisons similar to Figure 17 except that the angle of attack is  $\alpha=40^\circ$ . Parts (a) and (b) without strakes or blowing show a very slight forebody vortex asymmetry and large asymmetry in the LEX vortex burst point. The right forebody vortex appears to be higher off the nose than the left one. Adding a strake on the right side shown in Parts (c) and (d) (note this strake, Strake #2, is somewhat shorter than the one shown at  $\alpha=21^\circ$  in Figure 17) forces the right-side vortex to be higher above the body and results in a larger forebody vortex asymmetry. Although not shown here, the effect of the small strake and the larger one shown in the previous figure at  $\alpha=21^\circ$  are nearly identical. It is logical to assume that the strakes could be made smaller yet and have nearly identical effects. Parts (e) and (f) show the effect of blowing on the right forebody. The vortex asymmetry switches, that is, the left forebody vortex is now higher off the body. The blowing location is at the second row of blowing ports at  $\theta=150^\circ$  (see Figure 10).

The sketch below



illustrates the relationship between the blowing port and the primary and secondary vortices. It appeared that the most effective location to blow was between the reattachment line of the primary vortex and the separation line for the secondary vortex. Blowing at  $\theta=135^\circ$  between the separation line for the primary vortex and the reattachment of the secondary vortex was not very effective in altering the asymmetric vortex patterns. The most effective method of blowing to switch the orientation of the forebody vortices was to blow at  $\theta=150^\circ$  on the side of the forebody where the primary vortex was farthest from the body. As a result of the forebody blowing and subsequent switching of forebody vortices, the LEX vortices burst points are nearly opposite from the non-blowing case. This illustrates the interactive nature of the forebody and LEX vortices since blowing on the nose affects more than just the nose vortices. Adding a matching strake to the left, (g) and (h), appears to make the forebody vortices symmetric again, and the LEX vortex burst points are asymmetric just as they were for the case with no strakes, (a) and (b).

## 6. CONCLUSIONS

The basic purpose of this effort was to explore the feasibility of manipulating the vortex flow field that naturally develops around a fighter aircraft in order to enhance its controllability. A generic fighter aircraft model was tested in a water tunnel at angles of attack from  $0$  to  $60^\circ$ . Several mechanisms for vortex control were examined on a baseline configuration including small modifications to the apex of the LEX, blowing on the LEX, blowing on the forebody, and strakes on the forebody. The results of these experiments can be summarized as follows.

- 1) Modifiers to the LEX apex had very little effect on the LEX vortex position or burst point.
- 2) Blowing on the LEX was ineffectual near the LEX apex, but very effective in forcing the LEX vortex burst point to move forward when applied aft of the LEX mid chord.
- 3) Blowing at the LEX edge appeared to be more effective in promoting the vortex to burst than blowing in the LEX vortex core location.
- 4) Forebody blowing was effective in switching the forebody vortex asymmetry when applied at a radial position of  $\theta=150^\circ$  from the windward stagnation line and perpendicular to the surface.
- 5) Single forebody strakes at  $\theta=150^\circ$  were very effective in producing asymmetric forebody vortices.

On the basis of the present experimental results and work by others, it can be concluded that there are a number of methods that appear to be effective for vortex manipulation.

### 6.1 Forebody

The introduction of strakes and/or local blowing at the proper location on the forebody has been shown in this investigation, as well as in others to be a powerful mechanism for altering the forebody vortex structure. Since the forebody has a large input in determining the airplane pitching and yawing moments, even small changes in the resulting forces on the forebody through vortex control can be very effective. The efficiency of the flow modifier, whether it be a strake or a blowing port or blowing nozzle, is very dependent on the longitudinal and radial location of the flow disturbance.

### 6.2 LEX/Wing

Modification of the vortices generated by the LEX, particularly by influencing the vortex burst point over the wings on each side independently, can have a significant impact on the rolling moment. A number of methods of influencing the LEX vortices were investigated. Minor modifications to the LEX apex, and blowing on the LEX near the apex did not have a large impact on the vortex burst location. It appears that to alter the vortex on a LEX which is designed for a strong vortex with a burst point as far aft as possible requires a local disturbance on the LEX surface aft of the apex. Local blowing aft of the mid chord was shown to be very effective in forcing the natural burst point to move forward. Regulating the blowing rate and proper placement of the blowing jet appears to have merit as a control mechanism. Further experiments will be required to assess the precision of control that can be achieved and the sensitivity of the actual force inputs to the LEX/wing with angle of attack and sideslip.

# REFERENCES

1. Skow, A. M. and Erickson, G. E., Modern Fighter Aircraft Design for High-Angle-of-Attack Maneuvering, AGARD/VK1/NASA/DFVLR, Lecture Series No. 12, March 1982.
2. Moore, W. A., Erickson, G. E., Lorincz, D. J. and Skow, A. M., Effects of Forebody, Wing and Wing-Body LEX Flowfields on High Angle of Attack Aerodynamics, SAE Paper No. 791082, Aerospace Meeting, Los Angeles, CA, December 1979.
3. Chapman, G. T., Keener, E. R. and Malcolm, G. N., Asymmetric Aerodynamic Forces on Aircraft Forebodies at High Angles of Attack - Some Design Guides, AGARD CP-139, Conference on Stall/Spin Problems of Military Aircraft, Rhode Saint Genese, Belgium, November 1975.
4. Skow, A. M. and Titiriga, A., A Survey of Analytical and Experimental Techniques to Predict Aircraft Dynamic Characteristics at High Angles of Attack, AGARD CP-235, Conference on Dynamic Stability Parameters, Athens, Greece, May 1978.
5. Headley, J. W., Analysis of Wind Tunnel Data Pertaining to High Angle-of-Attack Aerodynamics, AFFDL-TR-78-94, Volume I, July 1978.
6. Rao, D. M. and Murri, D. G., Exploratory Investigation of Deflectable Forebody Strakes for High-Angle-of-Attack Yaw Control, AIAA Paper No. 86-0333, AIAA 24th Aerospace Sciences Meeting, Reno, Nevada, January 1986.
7. Skow, A. M., Moore, W. A. and Lorincz, D. J., Forebody Vortex Blowing - A Novel Concept to Enhance the Departure/Spin Recovery Characteristics of Fighter Aircraft, AGARD CP-262, Conference on Aerodynamics of Controls, Naples, Italy, May 1979.
8. Moore, W. A., Skow, A. M. and Lorincz, D. J., Control of the Forebody Vortex Orientation by Asymmetric Air Injection - Application to Enhance Departure/Spin Recovery, Paper No. 80-0173, AIAA 18th Aerospace Sciences Meeting, Pasadena, CA, January 1980.
9. Peake, D. J. and Owen, F. K., Control of Forebody Three-Dimensional Flow Separation, AGARD-CP-242-15, May 1979.
10. Peake, D. J., Owen, F. K. and Johnson, D. A., Control of Forebody Vortex Orientation to Alleviate Spin Forces, AIAA-80-0183, January 1980.
11. Rao, D. M. and Huffman, J. K., Hinged Strakes for Enhanced Maneuverability at High Angles of Attack, AIAA Journal of Aircraft, Vol. 19, No. 4, April 1982, pp. 278-282.
12. Moss, F. C., Some UK Research Studies of the Use of Wing-Body-Strakes on Combat Aircraft Configuration at High Angles of Attack, AGARD CP-247, Conference on High Angle of Attack, London, UK, Norway, October 1978.
13. Wahls, R. A., Vess, R. J. and Moskovitz, C. A., An Experimental Investigation of Apex Fence Flaps on Delta Wings, AIAA Paper No. 85-4055, October 1985.
14. Rao, D. M. and Buter, T. A., Experimental and Computational Studies of a Delta Wing Apex-Flap, AIAA Paper No. 83-1815, AIAA Applied Aerodynamics Conference, Danvers, Mass., July 1983.
15. Hoffer, K. D., Rao, D. M. and Frassenelli, M. C., Basic Studies on Delta Wing Flow Modifications by Means of Apex Fences, Unpublished work under AFRL contract no. FY1456-85-00032.
16. Frink, N. T. and Lamar, J. E., Water Tunnel and Analytical Investigation of the Effect of Strake Design Variables on Strake Vortex Breakdown Characteristics, NASA TP-1676, August 1980.
17. Lamar, J. E. and Frink, N. T., Experimental and Analytical Study of the Longitudinal Aerodynamic Characteristics of Analytically and Empirically Designed Strake-Wing Configurations at Subcritical Speeds, NASA TP-1803, June 1981.
18. Malcolm, G. N. and Skow, A. M., Improved High Angle of Attack Controllability through Vortex Manipulation, Eidetics International TR 86-101, January 1986.

# ACKNOWLEDGEMENTS

We are indebted to NASA-Ames Dryden Flight Research Facility for making their water tunnel flow visualization facility available to us for these experiments. We would particularly like to thank Mr. John Del Frate and Mr. Carl Barnes, who are responsible for the operation of the facility, for their technical advice and assistance in conducting these tests.

This research was sponsored by the U.S. Air Force Flight Dynamics Laboratory, WPAFB, Ohio under Contract No. F33615-85-C-3619. A final report (Ref. 18) was submitted to the Air Force.

AD-A199 357

AERODYNAMIC AND RELATED HYDRODYNAMIC STUDIES USING

2/3

WATER FACILITIES (U) ADVISORY GROUP FOR AEROSPACE

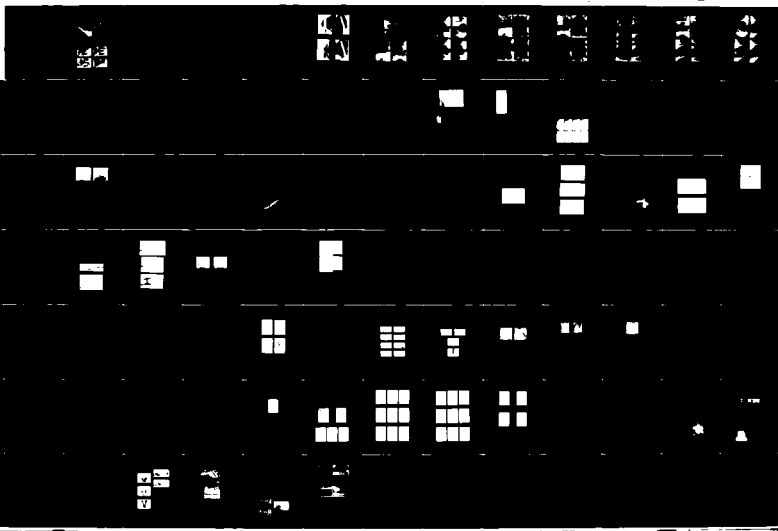
RESEARCH AND DEVELOPMENT NEUILLY-SUR-SEINE (FRANCE)

UNCLASSIFIED

JUN 87 AGARD-CP-413

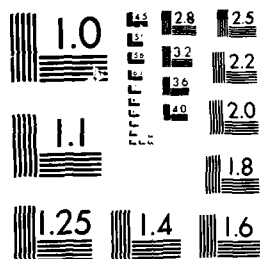
P/G 28/4

NL



111  
END

111  
END



MICROCOPY RE. CLIP



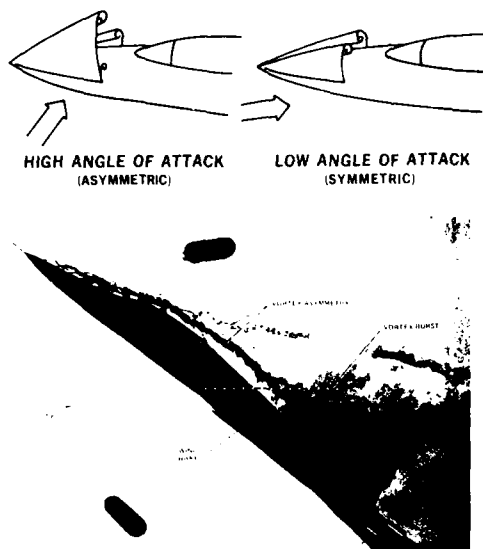


Fig. 1 - Asymmetric forebody vortices at zero sideslip (Ref. 1)

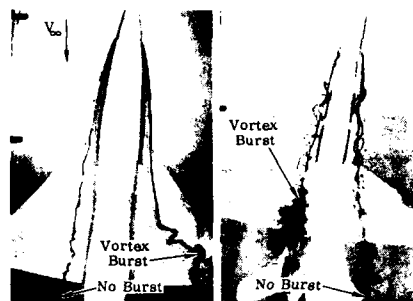


Fig. 2 - Asymmetric LEX vortices at non-zero sideslip (Ref. 2)

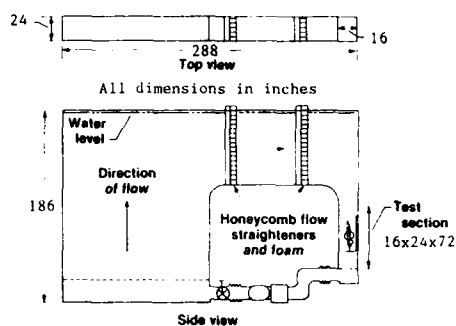
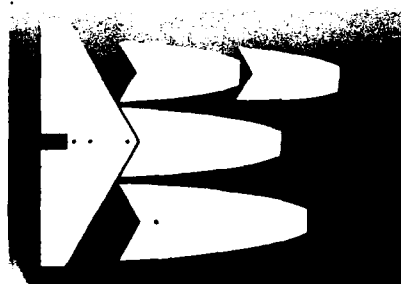
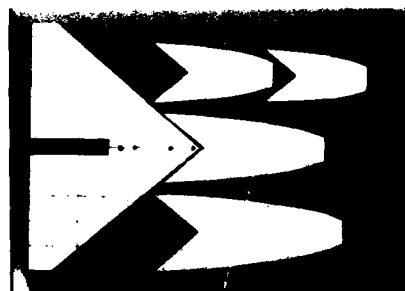


Fig. 3 - NASA Ames-Dryden Flow Visualization Water Tunnel



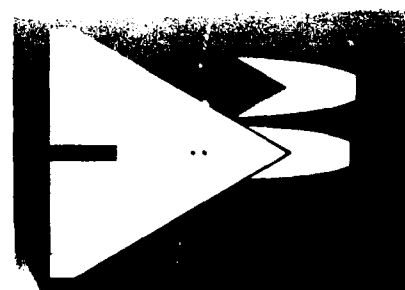
(a) 30° swept wing



(c) 50° swept wing



(b) 40° swept wing



(d) 60° swept wing

Fig. 4 - Water tunnel model components

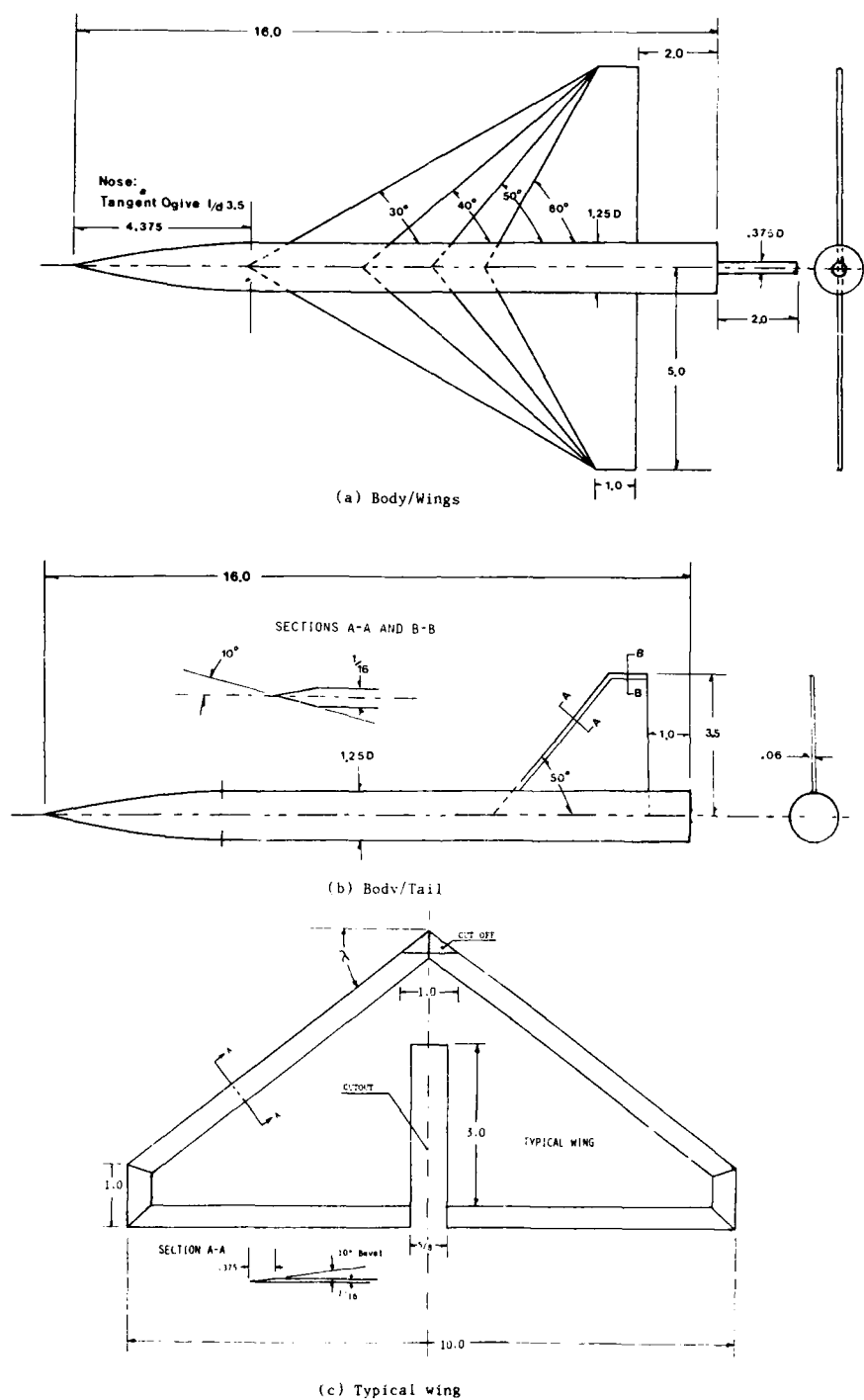


Fig. 5 - Basic model

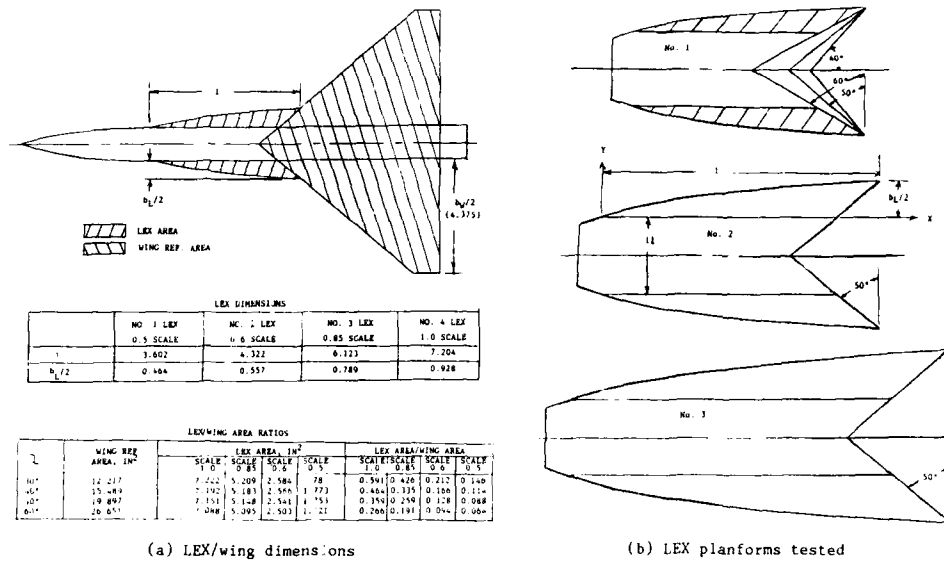


fig. 6 - LEX/wing geometries

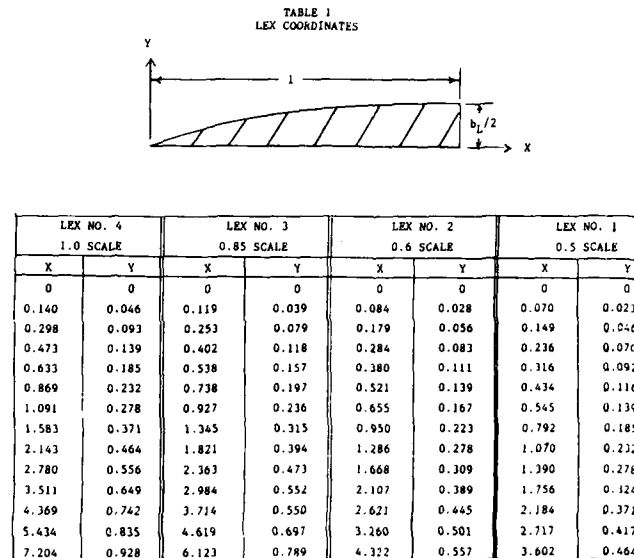


Fig. 7 - LEX Coordinates

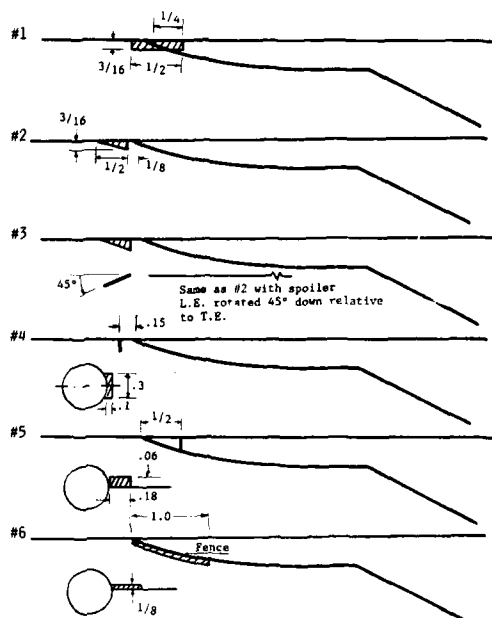


Fig. 8 - LEX modifiers

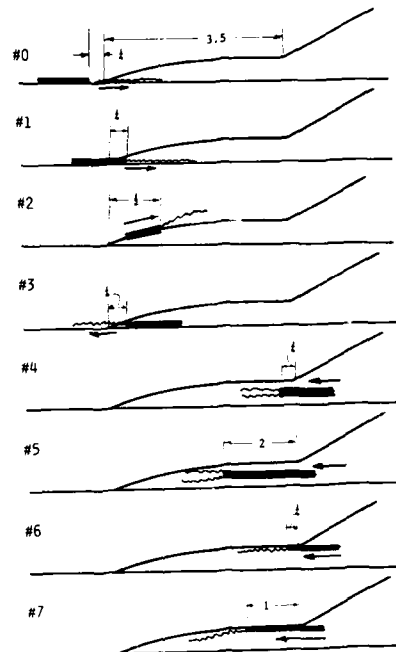


Fig. 9 - LEX blowing locations

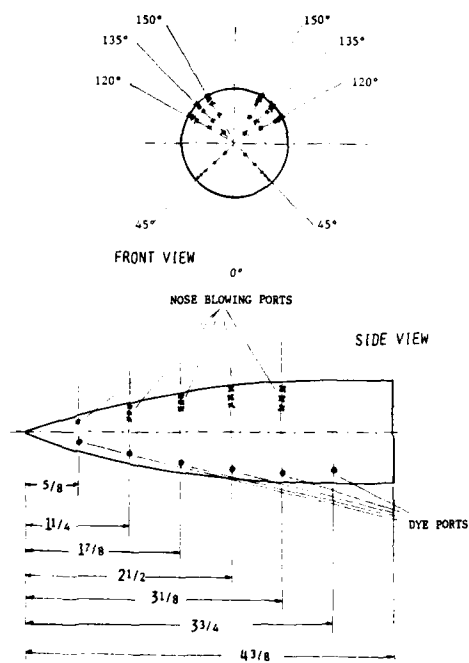


Fig. 10 - Forebody blowing and dye port locations

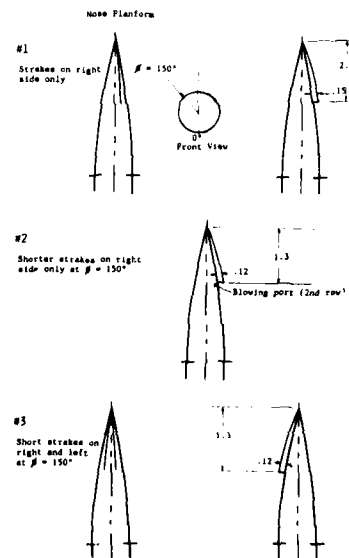


Fig. 11 - Forebody strake configurations



i) Configuration W40L1,  $\alpha = 18^\circ$



ii) Configuration W60L1,  $\alpha = 18^\circ$

Fig. 12a - Sample water tunnel photographs.

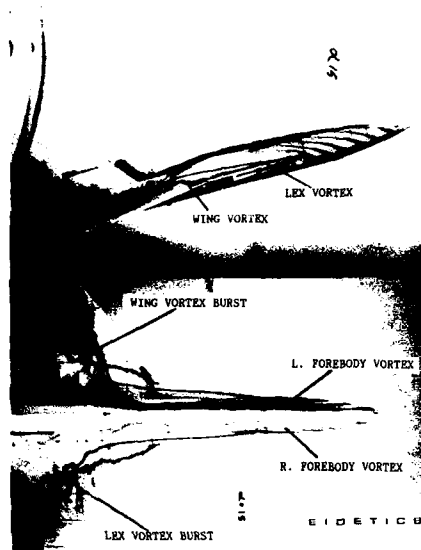
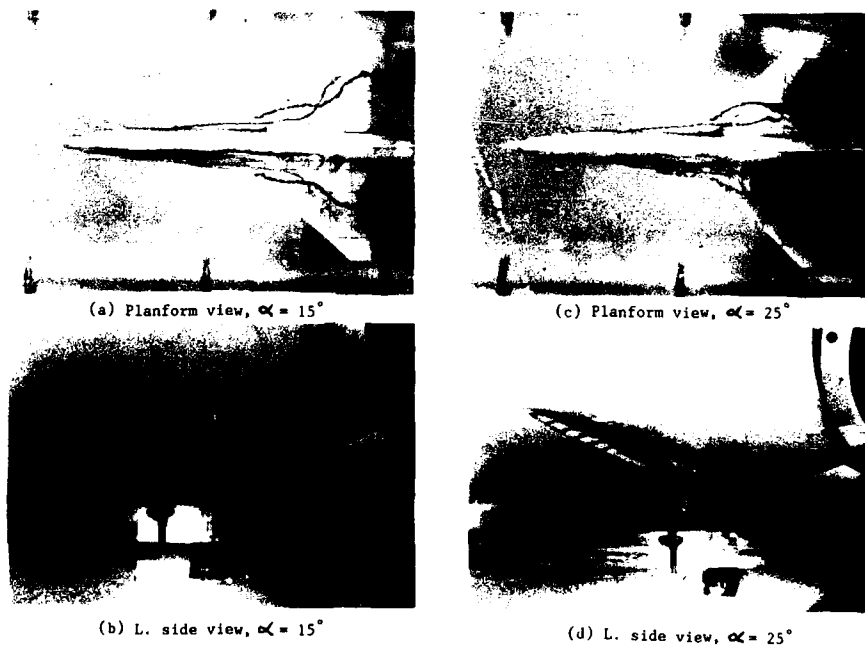


Fig. 12b- Sample photo of flow characteristics

Fig. 13 - Basic configuration,  $W_{50}L_1$



(e) Planform view,  $\alpha = 35^\circ$



(g) Planform view,  $\alpha = 40^\circ$



(f) L. side view,  $\alpha = 35^\circ$



(h) L. side view,  $\alpha = 40^\circ$



(i) Planform view,  $\alpha = 45^\circ$



(k) Planform view,  $\alpha = 50^\circ$



(j) L. side view,  $\alpha = 45^\circ$

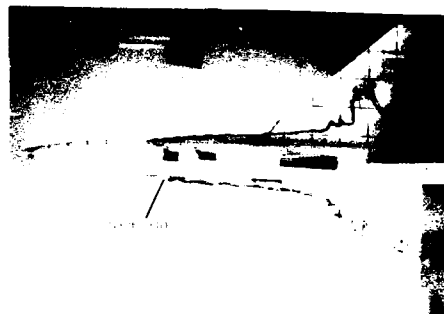


(l) L. side view,  $\alpha = 50^\circ$

Fig. 13 - concluded



(a) No modifier, planform view



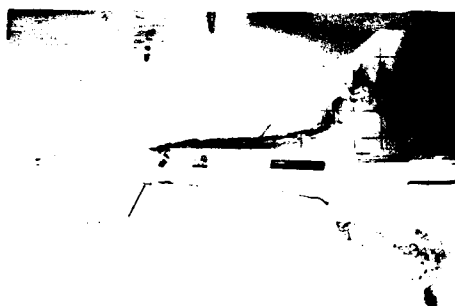
(c) Modifier #1, planform view



(b) No modifier, side view



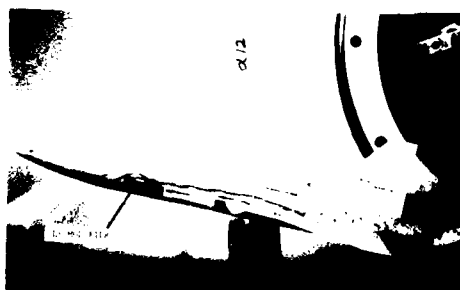
(d) Modifier #1, side view



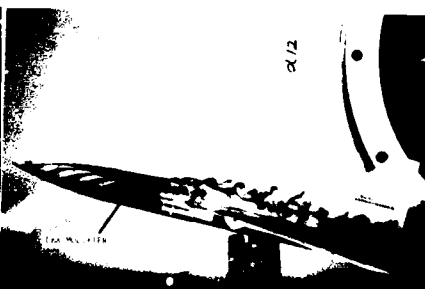
(e) Modifier #2, planform view



(g) Modifier #4, planform view



(f) Modifier #2, side view



(h) Modifier #4, side view

Fig. 14 - LEX modifiers (Left LEX only),  $\alpha = 12^\circ$

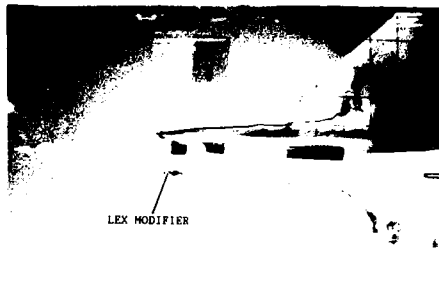




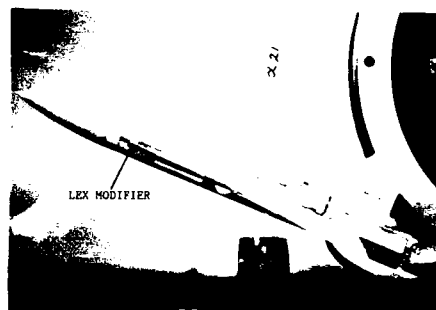
(a) No modifier, planform view



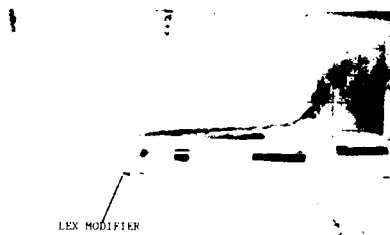
(b) No modifier, side view



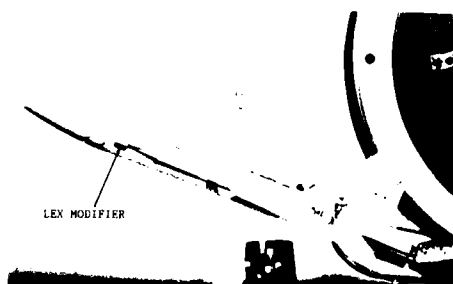
(c) Modifier #1, planform view



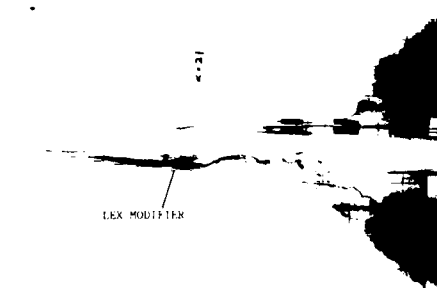
(d) Modifier #1, side view



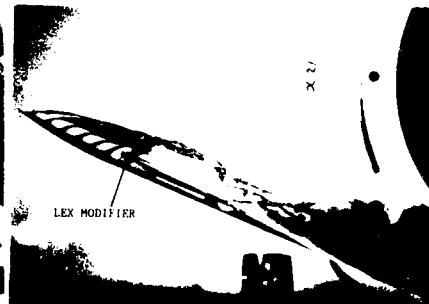
(e) Modifier #2, planform view



(f) Modifier #2, side view



(g) Modifier #4, planform view



(h) Modifier #4, side view

Fig. 15 - LEX modifiers (Left LEX only),  $\alpha = 21^\circ$

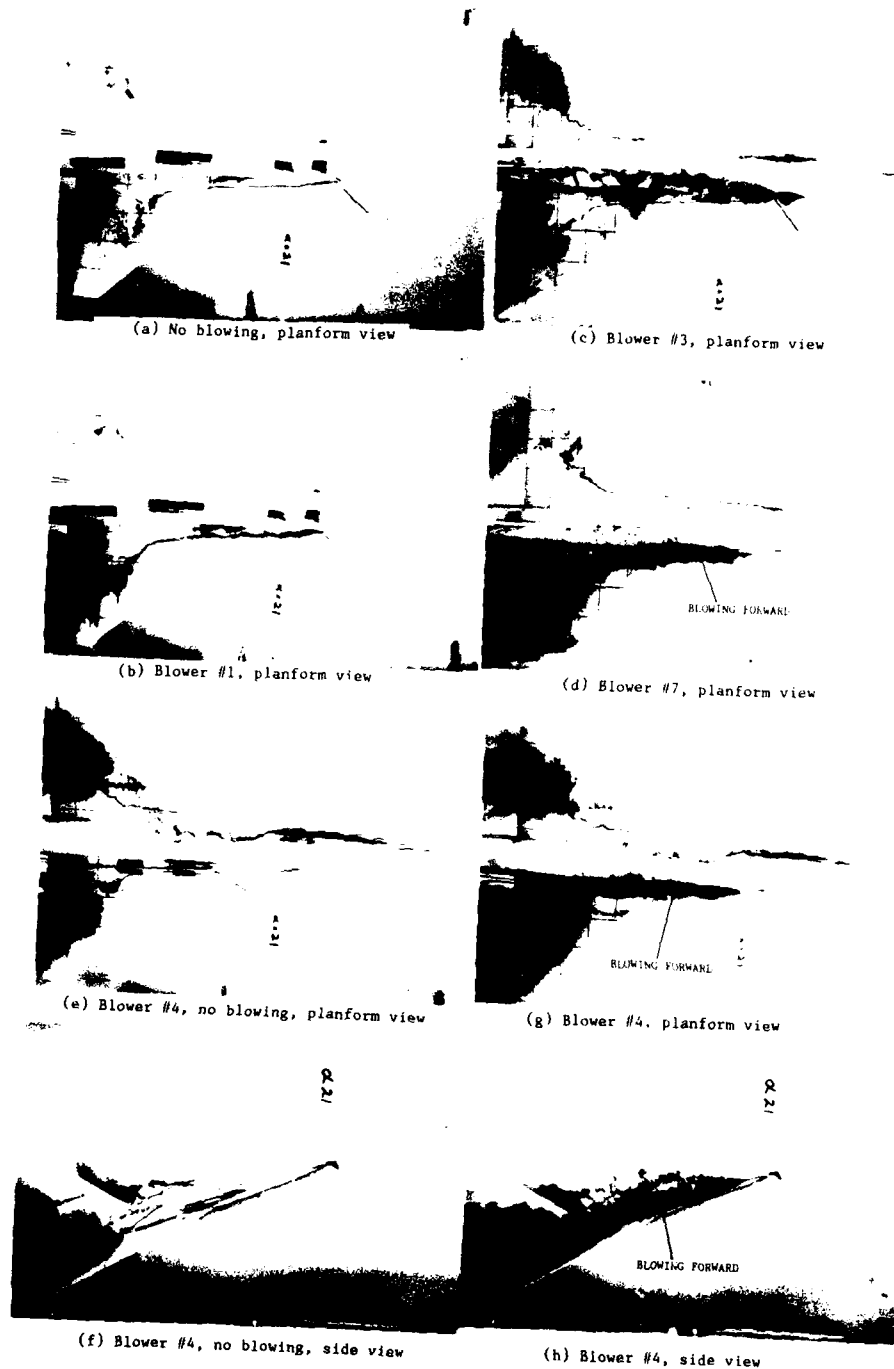


Fig. 16 - LEX blowing effects (Right LEX only),  $\alpha = 21^\circ$



(a) No strakes, no LEX blowing, planform view



(c) Strake #1 on forebody, no LEX blowing, planform view



(b) No strakes, no LEX blowing, side view



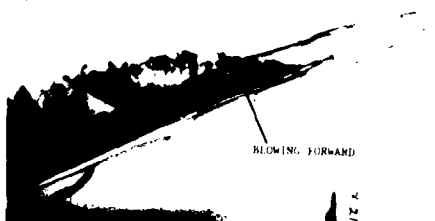
(d) Strake #1 on forebody, no LEX blowing, side view



(e) Strake #1 on forebody, LEX blower #7, planform view



(g) Strakes #3 (pair), no LEX blowing, planform view



(f) Strake #1 on forebody, LEX blower #7, side view



(h) Strakes #3 (pair), no LEX blowing, side view

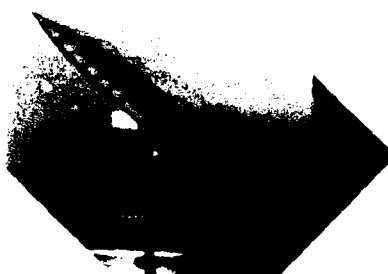
Fig. 17 - Effects of forebody strakes and LEX blowing,  $\alpha = 21^\circ$



(a) No strakes, no blowing, planform view



(c) Strake #2 on forebody, no blowing, planform view



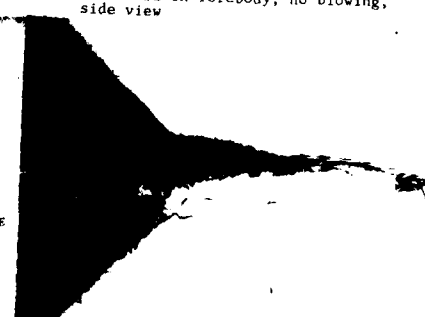
(b) No strakes, no blowing, side view



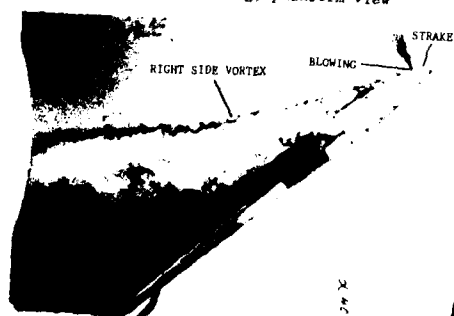
(d) Strake #2 on forebody, no blowing, side view



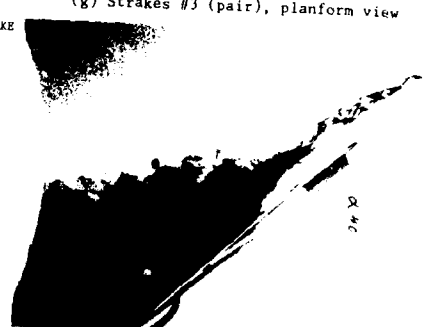
(e) Strake #2, blowing, planform view



(g) Strakes #3 (pair), planform view



(f) Strake #2, blowing, side view



(h) Strakes #3 (pair), side view

Fig. 18 - Effects of forebody strakes and forebody blowing,  $\alpha = 40^\circ$

# OSCILLATING FLOW OVER BLUFF BODIES IN A U-SHAPED WATER TUNNEL

by

**TURGUT SARPKAYA**

Department of Mechanical Engineering  
Naval Postgraduate School, Monterey, CA. 93943 U.S.A.

## SUMMARY

The studies described herein deal with sinusoidally oscillating separated and unseparated flows over various types of bluff bodies. First, the characteristics of a large U-shaped vertical water tunnel are described and then the numerical and experimental results obtained with circular cylinders are presented. It is shown that for two-dimensional, attached, and laminar-flow conditions the data are, as expected, in good agreement with the Stokes [1]-Wang [2] analysis. The oscillatory viscous flow becomes unstable to axially periodic Taylor-Görtler vortices above a critical Keulegan-Carpenter number  $K$  ( $K = U_T D / \nu$ ) for a given  $\beta$  ( $\beta = D^2 / \nu T$ ). For larger values of  $K$  the effects of separation and vortex shedding become increasingly important, eventually leading to a very interesting half Karman vortex street in the transverse direction in the range  $8 < K < 13$ . The discrete vortex model of the separated oscillating flow is shown to provide a reasonably satisfactory explanation of the transverse vortex street. Finally, an attempt is made, through the use of an idealized vortex model, to explain the observed flow modes and the cycle-to-cycle variations in forces and pressures in terms of their sensitivity to small stochastic variations in the position of the vortices.

## 1. INTRODUCTION

The problem of separated flow about a bluff body remains theoretically unresolved even for a unidirectional steady flow where the vortices interact with each other and with the counter-sign vorticity generated at the base of the body. Page and Johansen's pioneering work [3], Gerrard's [4] vortex formation model, and Roshko's [5] numerous contributions, followed by a large number of important papers, have provided extremely useful insights into the mechanism of vortex shedding. It became clear that a two-dimensional body does not give rise to a two-dimensional wake and only a fraction (about 60% for a circular cylinder) of the original circulation survives the vortex formation.

Many flows of practical interest are unsteady, i.e., the characteristics of the ambient flow are time-dependent. In the past 20 years or so a large number of theoretical and experimental studies have been carried out. These dealt primarily with unseparated laminar flows, the early stages of impulsively started flow over plates and cylinders (numerical and experimental studies), and oscillating flows with zero or non-zero mean (on an infinite flat plate and over a cylinder with streaming flow, all under laminar flow conditions) for the purpose of studying the effects of flow unsteadiness on the transition mechanism and turbulence development (see e.g. [6]). Very little has been attempted either theoretically or experimentally to analyze the wake-boundary-layer interaction in time-dependent flows. Most of the numerical studies based on the use of the Navier-Stokes equations and some suitable spatial and temporal differencing schemes are limited, out of necessity, to low Reynolds number flows about cylinders and airfoils. The subject of separated time-dependent flow at large Reynolds numbers is lesser developed but of greater practical importance (particularly to marine related topics) relative to other classical component disciplines of fluid mechanics.

A number of unsteady flow machines and their use in the investigation of unsteady turbulent boundary layers have been reviewed and documented by Carr [7]. These included flat plate, diffuser, pipe, airfoil, and cascade flows. The results have shown that (i) the time-averaged mean velocity profile is almost always the same as the velocity profile that would occur in a steady flow having an equivalent mean external flow velocity; (ii) the turbulent structure in the oscillating flow is not changed from the equivalent steady-state counterpart; and (iii) the unsteady effects are often confined to a thin layer near the wall, while the outer region of the boundary layer is not strongly affected.

The numerical solution of unsteady incompressible Navier-Stokes equations in their vorticity-stream-function formulation has been investigated by numerous researchers through the use of various finite-difference techniques. These studies concern mostly the separated flow about circular cylinder and prisms at relatively low Reynolds numbers (see e.g., Davis & Moore [8]). In an attempt to obtain solutions at higher Reynolds numbers and to provide a more natural and efficient description of the vortices, various versions of the discrete vortex model have been used. These models differ from each other in their treatment of the representation of the body, boundary layer, viscous diffusion, separation points, generation of counter-sign vorticity, etc. (see e.g., Chorin [9], Sarpkaya & Shoaff [10], Sarpkaya & Ihrig [11]). Two other methods, namely, the finite element and spectral methods have also received increasing attention.

It appears that the existing numerical methods cannot yet treat the high Reynolds number flows with sufficient accuracy for a number of reasons. The finite difference schemes require a very fine grid, a turbulence model, and a very large computer memory. The grid-free vortex methods suffer from a number of shortcomings (no discernable Reynolds number dependence, need to introduce circulation reduction, difficulties associated with the treatment of laminar or turbulent boundary layers and separation points, etc.). It seems that the modelling of the turbulent stresses in the wake, particularly in time-dependent flows, will be the major source of difficulty in all future calculations. As the methods of calculation are refined, one will need detailed data for quantitative comparison since the qualitative agreements between the calculated results and flow visualizations will not suffice. However, measurements of turbulent quantities in separated unsteady flows present numerous difficulties and there is clearly a requirement for redundant measurements through the use of suitable intrusive and non-intrusive instrumentation.

The separated unsteady flow situations involving wake return, as in the case of a sinusoidally oscillating flow about a cylinder, are an order of magnitude more complex and there has not yet been a satisfactory application of either the finite-difference methods or the discrete vortex models to their analysis.

In steady flow the position of the separation points is nearly stationary, except for small excursions of about  $\pm 3$  degrees (on a circular cylinder). Furthermore, the interference between the vortices and the body is confined mostly to the vortex formation region.

For oscillating flows the net effect of the shed vortices is twofold. Firstly, their return to the body dramatically affects the boundary layer, outer flow, pressure distribution, and the generation and survival rate of the new vorticity. Secondly, they not only give rise to additional separation points (during the early stages of the flow reversal) but also strongly affect the motion of the primary separation points. These effects are further compounded by the diffusion and decay of vortices and by the three-dimensional nature of the flow (all of which give rise to cycle-to-cycle variations, numerous flow modes, etc.). The stronger and better correlated the returning vortices, the sharper and more pronounced the changes are in the pressure distribution on the body and in the integrated quantities such as lift, drag, and inertia coefficients. Nevertheless, the increased correlation does not entirely eliminate the consequences of the stochastic variations in the motion of vortices.

In periodic flow, the mobile separation points (when they are not fixed by sharp edges), undergo large excursions (as much as 120 degrees during a given cycle of oscillating flow over a circular cylinder). This experimental fact renders the treatment of boundary layers on bluff-bodies subjected to periodic wake return extremely difficult, particularly when the state of the boundary layer changes during a given cycle. Furthermore, the classical criterion of separation for steady flow, i.e., the vanishing of skin friction on the body, is no longer valid for unsteady flow. According to the MRS criterion (Moore [12], Rott [13], and Sears [14]), it is the simultaneous vanishing of the shear and the velocity at a point within the boundary layer that determines the separation point. Furthermore, the time rate of change of circulation is no longer given by  $\partial \Gamma / \partial t = 0.5U^2$ , as in steady flow, where  $U$  is the outer flow velocity at separation, but by  $(0.5U^2 - UU_s)$  where  $U_s$  is the speed of the separation point.

It is clear from the foregoing that there is little hope of devising a satisfactory theoretical model before something is understood of the unsteady processes associated with the formation and reversal of the wake, spanwise coherence, the sensitive dependence of the motion of vortices on small changes in the previous conditions, nature of transition in oscillating flow about smooth and rough cylinders, etc.

The practical needs, coupled with the complexity of the problem, led to the proposal of an empirical equation, known as the MOJS equation (Morison, O'Brien, Johnson, & Schaff [15]) to predict the time-dependent in-line force acting on a vertical cylinder immersed in waves and other unsteady flows. Its justification is strictly pragmatic and rests with experimental confirmation. The MOJS equation has been examined in great detail and its limitations have been pointed out numerous times during the past ten years (see e.g., Keulegan & Carpenter [16], Sarpkaya [17, 18], Sarpkaya & Isaacson [19]).

Prior to 1975, the only data obtained under controlled laboratory conditions were those of Keulegan and Carpenter [16] with smooth cylinders and plates normal to the flow. In 1976, Sarpkaya [17] presented the results of a comprehensive study of the hydrodynamic forces on both smooth and rough cylinders in a sinusoidally oscillating planar flow in a U-shaped water tunnel and introduced the parameter  $\beta = D^2/\nu T$  into the analysis of separated time-dependent flows. Since 1976, a number of laboratory and ocean experiments have been carried out (for a detailed discussion of these see Sarpkaya & Isaacson [19]).

## 2. U-SHAPED VERTICAL WATER TUNNEL

The tunnel (the largest of its kind in the world) consists of thirteen modules. Each module is made of 3/8 inch (10 mm) aluminum plates which are reinforced with 1/2

in. x 4 in. x 22 in. (1.3 cm x 10 cm x 56 cm) aluminum flanges welded to the plates. The modules were assembled using an air drying silicon-rubber seal between the module frames. The flanges were held together with one inch steel bolts spaced six inches (15 cm) apart. The interior of each module was precision machined so that the largest misalignment was approximately 0.04 in. (1 mm). A sketch of the tunnel interior is shown in Fig. 1. The inside cross-section of the two risers is 6 ft x 3 ft. (1.83 m x 0.91 m) and that of the horizontal section is 4.67 ft x 3 ft. (1.42 m x 0.91 m). The size of these areas is dictated by such conditions as the available ceiling height, pressures to be encountered, amplitude and period of the oscillations, desired range of Reynolds and Keulegan-Carpenter numbers, boundary layer thickness on the walls, etc. The length of the horizontal test section was made twice as large as the maximum amplitude to ensure fully developed uniform flow at the test section. The corners of the tunnel are carefully streamlined to prevent flow separation.

The ancillary equipment for the tunnel consists of plumbing for filling and draining the tunnel with hot and cold water (50° to 160°F) (10° to 71°C), a heat exchanger and an air supply system (see Fig. 2). A three horsepower motor drives a centrifugal fan and supplies air to the tunnel. The air from the fan passes through an air control box and into a duct. The control box has two gate valves, one at the box entrance and one on top of the box. The entrance valve is raised and lowered vertically by a threaded rod attached to a manually operated gear and allows for a fine adjustment of the air flow. The top valve is opened and closed by sliding the hatch horizontally and provides a coarse adjustment of the air flow. The air then flows through the vertical duct to the three-way valve. The control valve permits the air to flow into the tunnel at prescribed time intervals. Figure 3 shows the details of the three-way control valve. The valve body is a drum which is two feet (61 cm) in diameter and four feet long (122 cm). Four openings were cut into the drum as shown in Fig. 3. The vane inside the drum is used to direct the motion of the air to-and-from the tunnel. The vane rocks about a mean position by means of a connecting rod through a sprocket wheel and chain mechanism (see Fig. 3). The chain is driven by a variable speed motor and gear. The speed of the motor is controlled by an electronic feed-back control system. It increases or decreases the speed of the motor so as to maintain the period of oscillation within  $\pm 0.001$  second about the natural period of the fluid in the tunnel. To insure smooth and uniform rotation of the system, one flywheel is attached to the drive shaft of the connecting rod and another flywheel to the motor drive shaft. Air flows from the duct into the entrance port (marked A in Fig. 3) and is directed by the vane into the tunnel (port B) or to the atmosphere (port D). The vane and the plastic flap also provide a smooth flow path for the air escaping from the tunnel (port C) when the supply air is vented to the atmosphere.

To oscillate the fluid in the tunnel, the three-way control-valve motor is activated and the centrifugal fan is turned on. The vane rocks back and forth (at a period of  $T = 5.3512 \pm 0.0010$  seconds, where 5.3512 seconds is the natural period of the tunnel for the amount of water admitted into the tunnel), supplying air to the tunnel and then exhausting it to the atmosphere. The amplitude is controlled by the amount of air supplied to the tunnel by opening or closing the gate valves on the control box. The amplitude, once set, remains constant as long as desired with a maximum variation of less than 0.2% per setting over at least 1000 cycles of oscillation. The small variation is primarily due to the voltage fluctuations at the generating plant.

## 2.1 Force Measurements

Depending on the type of bluff body tested (circular cylinders, prisms, spheres, cables, submarine-like bodies of revolution, etc.), one or two force transducers (shear gages) are used to measure the instantaneous force. The force transducers can measure both the in-line and transverse forces. One typical gage has a 50 pound (212 N) capacity with an overload capacity of 200 percent. With a 50 pound load, the gage deflection is about 0.01 inches.

The bellows which protects the strain gages is water-proofed by filling it with liquid silicon without bringing the liquid rubber into contact with air during the filling operation. Then the ends of the bellows are sealed air tight with clamps. The silicon rubber remains in its liquid form and protects the gages when they are subjected to approximately 20 feet (6 m) of water pressure at temperatures ranging from 50° to 160° F (10° to 71°C) (for additional details see [18]).

## 2.2 Acceleration, Elevation, and Velocity Measurements

During the past ten years, various methods have been used to determine the characteristics of the ambient flow at the test section. These consisted of (i) the visual observation and recording of the maximum and minimum water levels in both legs of the tunnel; (ii) the use of calibrated platinum capacitance wires in both legs of the tunnel; (iii) the measurement of the instantaneous acceleration by means of a differential-pressure transducer (see [17] for additional details) connected to two pressure taps on the legs of the tunnel; (iv) the measurement of the path of neutrally buoyant particles through the use of motion pictures; (v) measurement of the path of a few particles falling in the Stokes regime, again through the use of motion pictures; and (vi) the measurement of the velocity in the test section through the use of an LDV system at selected amplitudes of flow oscillation. These methods yielded the ambient flow acceleration, velocity, and displacement with an error less than 1%. The signals generated by the transducers were entirely free from noise and were never filtered.

### 2.3 Data Acquisition System

The actual electronic circuitry varied from one experiment to another depending upon the type of bluff body tested and the type of conditions to which the body is subjected. The following circuits are described for a typical circular cylinder experiment.

The outputs of the two force transducers are amplified by carrier and low-gain amplifiers and then sent to a multichannel recorder for simultaneous analog recording and to a computer system via an A/D converter for analysis and magnetic recording of the digitized data. The signal sampling rate was chosen to be 720 samples per cycle per channel (i.e., about 135 samples/second/channel or a sample for every 0.5 degrees). The data were recorded for 50 cycles of flow oscillation for each specific experiment and stored on floppy disks and analyzed partly during the experiments (for a quick look) and partly after the experiments (for more detailed analysis of the data).

### 2.4 Circular Cylinders

Each cylinder was made of three pieces: two fixed dummy ends and one active central piece with  $L/D = 2$ . A spacing of approximately  $1/32$  in. (0.8 mm) was maintained between the active and dummy pieces. The active segment was mounted concentrically on a supporting cylinder whose ends were in turn connected to two force transducers. The ends of the active cylinder were sealed so that the space between the supporting cylinder and the active segment was kept unflooded. The cylinders were first mirror polished and maintained clean during the smooth cylinder experiments. The cylinder surface was wiped clean at the end of each day in order to prevent the development of water marks on the surface. Subsequently, all three parts of a given cylinder were covered with sieved sand (using an epoxy resin [17, 18]) so as to obtain the desired relative surface roughness.

## 3. DISCUSSION OF RECENT INVESTIGATIONS

During the past ten years, the oscillating flow facility has been used to investigate the in-line and transverse forces on smooth and rough cylinders at high Reynolds numbers [17-20], the hydroelastic oscillations of elastically-mounted cylinders in harmonic flow [21], the flow about Bilge keels [22], oscillating flow about various rectangular prisms [23], and the behavior of oscillatory turbulent boundary layers. In this paper only the most recent investigations are described briefly.

### 3.1 Taylor-Görtler-Hall-Honji Instability

Stokes [1] was the first to show that the force acting on a cylinder or sphere oscillating sinusoidally in a viscous fluid is dependent on both  $K$  and  $Re$  (or  $\beta = Re/K$ ). In the case of a fixed circular cylinder in a sinusoidally oscillating flow Stokes force may be expressed in terms of the MOJS equation [15] given by,

$$F(t) = (1/2)C_d \rho D |U(t)| U(t) + (1/4)C_m \rho \pi D^2 dU(t)/dt \quad (1)$$

where

$$C_d = (3\pi^3/2K) [(\pi\beta)^{-1/2} + (\pi\beta)^{-1} + O(\pi\beta)^{-3/2}] \quad (2)$$

and

$$C_m = 2 + 4(\pi\beta)^{-1/2} + O(\pi\beta)^{-3/2} \quad (3)$$

in which  $C_d$  and  $C_m$  represent the Fourier-averaged drag and inertia coefficients. Equations (2) and (3) are valid only for large values of  $\beta$ . Wang [2] extended this analysis to  $O[(\pi\beta)^{-3/2}]$  using the method of inner and outer expansions. His solution, valid for  $K \ll 1$ ,  $Re.K \ll 1$ , and  $\beta \gg 1$ , may be reduced to

$$C_d = (3\pi^3/2K) [(\pi\beta)^{-1/2} + (\pi\beta)^{-1} - (1/4)(\pi\beta)^{-3/2}] \quad (4)$$

and

$$C_m = 2 + 4(\pi\beta)^{-1/2} + (\pi\beta)^{-3/2} \quad (5)$$

The expressions (2) and (3) differ from (4) and (5) only in the last terms. Stokes and Wang's solutions yield virtually identical results in the range of their validity, i.e., for large  $\beta$ .

Relatively few experiments have been carried out with sinusoidally oscillating cylinders at low Keulegan-Carpenter numbers. Honji [24] oscillated a circular cylinder in water at rest in the range  $70 < \beta < 700$  and  $0 < K < 4$ , and investigated the stability of the flow. He has delineated three regions in the  $(K, \beta)$ -plane: a region (corresponding to relatively small  $K$ ) in which no streaks formed because the flow remained attached, stable and two-dimensional; a second region in which the flow became unstable to axially periodic vortices; and a third region in which no clear streaks formed because the flow became turbulent.



Figure 4 is a sample picture of the streaked flow along a cylinder (obtained in the present investigation through the use of electrolytic precipitation from a thin strip of solder placed along the cylinder). The streaks are nearly equally spaced along the cylinder (about 0.6-0.7 D). The vortex sheets forming on the cylinder on each side of the streak wrap up into a pair of vortices of opposite sign, giving the streak a mushroom-shaped cross-section. The roll-up of the vortex sheets is known to be accompanied by Helmholtz instability which produces turbulence. It was not possible to observe Helmholtz instability in the present tests owing to a number of difficulties associated with the small size of the streaks.

Hall [25] carried out a stability analysis of the oscillating flow, valid only in the limit  $\beta \rightarrow \infty$  and  $K \rightarrow 0$ , and showed that 'oscillatory viscous flows interacting with rigid boundaries of convex curvature can become unstable to Taylor-Görtler vortices'.

Hall's critical Keulegan-Carpenter number may be written as

$$K_{cr} = Re_{cr}/\beta = 5.778\beta^{-1/4}(1 + 0.205\beta^{-1/4} + \dots) \quad (6)$$

according to which the critical Reynolds number  $Re_{cr}$  increases with increasing  $\beta$  (e.g.,  $Re_{cr} = 6433$ ,  $K_{cr} = 0.57$  for  $\beta = 11,240$ ).

Recently, Sarpkaya [18, 26] presented data (see Figs. 5-7) for a number of smooth and rough cylinders over a large range of  $\beta$  and has shown that (i) the theoretical values of the inertia coefficient agree quite well with those obtained experimentally for  $K$  smaller than that corresponding to the inception of boundary-layer transition; (ii) the drag coefficient predicted by the Stokes-Wang analysis agrees well with that obtained experimentally for  $K < K_{cr}$  at which the flow becomes unstable (Taylor-Görtler-Hall-Honji instability) (see Fig. 5); (iii) the critical regime is followed either by separation and transition or by transition and delayed separation. In either case, separation and minimum drag occur almost simultaneously; (iv) roughness precipitates instability and transition to turbulence in the boundary layers. Its net effect is to increase  $C_d$ , relative to the Stokes-Wang prediction, and to delay separation (see Fig. 6). These findings have established a connection between the Stokes-Wang analysis, Honji's observations, and Hall's stability analysis.

Figure 7 shows the dependence of the inception of the TGH instability and the onset of separation and turbulence on  $K$  and  $\beta$ . According to this figure,  $K_{cr} = 1.06$ ,  $Re_{cr} = 1097$ ,  $K_s = 1.5$ , and  $K_t = 1.7$  for  $\beta = 1035$ . In Fig. 5,  $C_d$  deviates from the Stokes-Wang prediction between  $K_{cr} = 0.7$  and  $0.8$  ( $Re_{cr} = 725$  and  $825$ ). The minimum  $C_d$  in Fig. 5 is seen to occur at  $K = 1.6$ . Thus, it appears that the minimum drag occurs shortly after separation and when the boundary layer becomes turbulent. Figure 6 shows representative data obtained with a rough cylinder ( $k/D = 0.01$ ) for  $\beta = 1800$ . According to Fig. 7, the instability should begin at  $K_{cr} = 0.4$  (probably at a smaller  $K$  on the basis of Fig. 5), a value which was unattainable in the present experiments. Apparently, the boundary layer has become unstable by the time  $K$  reached a value of about 0.45 (lowest  $K$  in Fig. 6). Subsequently,  $C_d$  decreases rapidly, while remaining on a line nearly parallel to the Stokes-Wang line, and reached its minimum value at  $K = 2.4$ . In summary, the transition at  $K_s = 1.1$  is followed by separation at  $K_s = 1.9$  ( $Re = 3,400$ ) and minimum drag at  $K = 2.4$ . The delay in separation is attributed to the earlier transition in the boundary layer.

It is evident from the foregoing that the sinusoidally-oscillating planar flow becomes unstable to axially periodic vortices at a critical value of the Keulegan-Carpenter number for a given  $\beta$  and  $k/D$  (relative roughness). The effect of roughness is to precipitate instability and transition. For smooth cylinders and for  $\beta$  smaller than about 2,600, separation precedes transition to turbulence in the boundary layers. In this case, the minimum drag and transition occur at about the same  $K$ . When the transition precedes separation, then the separation is delayed to a higher  $K$ -value. In this case too the minimum drag nearly corresponds to the occurrence of separation,  $K_s$  being slightly smaller than  $K_{md}$  ( $K$  for minimum drag).

### 3.2 Transverse Vortex Street in Oscillating Flow

Figures 5 and 6 show that for  $K > K_{md}$  the drag coefficient increases gradually as the effects of flow separation and vortex shedding become increasingly important. Extensive flow visualization experiments have shown that a half Karman vortex street develops in the transverse direction in the range  $8 < K < 13$ . Figures 8a through 8h show a sequence of eight photographs of the vortex motion resulting from the sinusoidal oscillation of a cylinder in a fluid otherwise at rest. Clearly, the vortex street is transverse to the direction of motion of the cylinder. There is no preferred transverse direction and the vortex street in Fig. 8 could have occurred to the right of the cylinder, with equal probability, depending on the initial conditions. However, once the street is formed, it is very stable and stays in that direction for an indefinite period of time (Bearman [27], Sarpkaya [28], and Williamson [29]).

The reason for the occurrence of the transverse vortex street in the said range of  $K$  values (corresponding to the amplitude-to-diameter ratios of  $A/D = 1.27$  to  $2$ ) is, as expected, the formation of two asymmetric vortices during a given half cycle and the effect of the returning vortices on the formation of the new vortices. This is

illustrated through the use of the discrete vortex model in Figs. 9a through 9f (the details of the numerical model will not be described here for sake of brevity. A detailed description of the discrete vortex model may be found in [10, 11]).

Figure 9a shows the flow towards the right, as it decelerates, (see the magnitude and the direction of the arrow at the center of the circle) and the vortex pattern which has evolved during the previous cycles of flow oscillation. As the flow reverses (see Figs. 9b-9d), the large vortex at the upper right-hand side of the cylinder gives rise to earlier separation and establishes, by its sense of rotation, a preferred position for the next dominant vortex (Figs. 9e and 9f). As the flow reverses once again, the counter-clockwise rotating vortex to the left of the cylinder in Fig. 9f, begins to move towards the cylinder, as in Fig. 9a, and the events of the previous half-cycle repeat, giving rise to the transverse vortex street. The creation, shedding and backward convection of the dominant vortex in this flow situation, where there are only a few vortices, strongly affect the pressure distribution about the cylinder. This is one of the most important reasons as to why the MOJS equation [Eq. (1)] fails to represent the in-line force acting on the cylinder with reasonable accuracy. Additionally, the growth and shedding of the dominant vortices from the same side of the cylinder gives rise to a net transverse force on the cylinder. Finally, the side from which the dominant vortex sheds may become switched either by the action of random disturbances in the flow or by stopping and restarting the tunnel.

At larger  $K$  values ( $15 < K < 25$ ) (see Fig. 10), the stronger of the two vortices formed during the previous half cycle (I) is shed and convected away as the flow reverses. It forms a couple with the new vortex generated downstream (III) and together they leave the immediate wake region. This allows the next dominant vortex (IV) to form on the lower (opposite) side of the cylinder (Fig. 10c) since it continues to grow following the premature shedding of vortex III. Vortex V grows only slightly prior to the next flow reversal. As the flow reverses (Fig. 10d), vortex IV is convected to the left and forms a new pair with vortex VII. These two vortices are then swept away in a manner similar to the convection of vortices I and III. This pattern repeats each half cycle.

The rapid motion of the vortex pairs, therefore, occurs on opposite sides of the flow and cylinder, i.e., vortices I and III move up and towards the right side while vortices IV and VII move down and towards the left (at roughly  $45^\circ$  to the direction of the ambient fluid motion). Thus, the location from which the stronger of the vortices sheds alternates between the top and bottom of the cylinder. In this range of Keulegan-Carpenter numbers, then, the generation of asymmetric vortices and the convection of the dominant vortex over the cylinder (once from the top and once from the bottom) gives rise to a cyclic transverse force. This cyclic lift force, however, has zero mean value. The direction of the vortex trails could be switched by stopping and restarting the tunnel. Occasionally, the trails were observed to switch while the flow was oscillating with a constant amplitude.

For larger Keulegan-Carpenter numbers ( $K > 25$ ), additional vortices form during a half cycle and an array of vortices more closely resembling a Karman vortex street is found on each side of the cylinder. The flow visualization and the discrete vortex analysis have shown that some of the vortices are destroyed by mixing with others of oppositely-signed vorticity as the flow reverses each half cycle. However, this process is not perfectly repeatable, i.e., the effects of the small changes in the strengths and positions of the vortices are sometimes so amplified by their mutual interactions that any finite-precision information about a particular instant provides no finite-precision information about the state of the flow at later times. In other words, sinusoidally oscillating flow about bluff bodies exhibits both a periodic and a stochastic behavior. Consequently, the quantification of the resulting in-line force as a linear sum of a velocity-square-dependent drag force and an acceleration-dependent inertial force [Eq. (1)] is at best a convenient engineering approximation with no obvious better alternatives.

### 3.3 Sensitivity to Slight Variations in Vortex Position

The study of the chaotic advection of particles through the use of highly idealized models has been the subject of numerous investigations. The model arises naturally from recent work on systems of a few point vortices, in particular the so-called restricted four-vortex problem [30-31] in which the advection of a single passive marker particle by three identical vortices is studied. The model described herein distills from these earlier investigations and considers the motion of a single vortex (and its image) in a sinusoidally oscillating flow about a circular cylinder.

A vortex of strength  $\Gamma/(\pi U_\infty D) = 0.5$  is placed at  $(0, y)$  at  $t = 0$  in the flow, oscillating with an ambient velocity  $U = U_\infty \sin \omega t$ , about a cylinder of diameter  $D$ . The Keulegan-Carpenter number is chosen to be  $K = 10$ . Then the path of the vortex, the lift and drag coefficients  $C_L$  and  $C_D$ , the magnitude  $Q$  as well as the  $x$ - and  $y$ -components of the advection velocity  $(u, v)$  of the vortex are calculated through the use of a 5th-order-accurate numerical scheme for various initial values of  $y$ . Figures 11-13 show that the results are dramatically dependent on the initial conditions. For  $y = 1.5054$  (Fig. 11) there are cycle-to-cycle variations in the calculated quantities. However, the vortex path does not come too close to the cylinder and the calculated quantities (e.g., the lift and drag coefficients) do not exhibit a chaotic behavior within 13 cycles of calculations. When  $y$  is decreased by 0.0001 ( $y = 1.5053$  in Fig. 12), the

vortex is 'captured' by the cylinder at the 9th cycle, giving rise to dramatic changes in all the computed quantities. In order to show that the observed behavior of the vortex is not a smooth function of  $y$ , the results shown in Fig. 13 were calculated using an intermediate value of  $y = 1.50535$ . Clearly, the path of the vortex and hence the behavior of all the other characteristics of unsteady flow about the cylinder depend critically on the initial conditions of the vortex. This highly idealized model suffices to show that any finite-precision information about the initial characteristics of a vortex (or of larger number of vortices) provides no finite-precision information about the characteristics of the flow at later times and that the lack of spanwise coherence of vortices is not the sole cause of cycle-to-cycle variations in the measured quantities. The motion of a larger number of vortices is expected to lead to similar conclusions. The extent to which the sensitivity of the flow to the conditions prevailing in the previous cycles is damped by finite core effects and viscosity is an important issue which cannot be dealt with through the use of idealized models.

#### 4. CONCLUDING REMARKS

The characteristics of sinusoidally oscillating separated and unseparated flows about a circular cylinder are discussed in as much detail as possible. It is shown that a large U-shaped vertical water tunnel is ideally suited for such an investigation. The oscillatory viscous flow becomes unstable to axially periodic Taylor-Görtler vortices above a critical Keulegan-Carpenter number  $K$  for a given frequency parameter  $\beta$ . For larger values of  $K$  the effects of separation and vortex shedding become increasingly important, eventually leading to a very interesting half Karman vortex street in the transverse direction. The discrete vortex model of the separated oscillating flow is shown to provide a reasonably satisfactory explanation of the transverse vortex street. Calculations based on an idealized vortex model suggest that the sensitivity of the characteristics of the flow to random disturbances superimposed on the motion of vortices at an earlier time (history effects) is the main flow feature responsible for the observed cycle-to-cycle variations.

Though much has been done towards the understanding of the behavior of time-dependent flow about bluff bodies, it will be necessary in the future to extend the geometrical shapes and parameters considered, to use ambient flows with more general time-dependence, and to devise sound theoretical models by including the effect of viscosity, so that the consequences of unsteadiness in flow in aerodynamics as well as in other branches of engineering can be better understood.

#### REFERENCES

1. Stokes, G. G., "On the Effect of the Internal Friction of Fluids on the Motion of Pendulums," *Trans. Cambridge Phil. Soc.*, Vol. 9, 1851, pp. 8-106.
2. Wang, C.-Y., "On High-Frequency Oscillating Viscous Flows," *Jour. of Fluid Mechanics*, Vol. 32, 1968, pp. 55-68.
3. Fage, A. & Johansen, R. C., "The Structure of Vortex Sheets," *Aeronautical Research Council, R&M*, No. 1143, 1928.
4. Gerrard, J. H., "The Mechanics of the Formation Region of Vortices behind Bluff Bodies," *J. Fluid Mech.*, Vol. 25, 1966, pp. 401-413.
5. Roshko, A., "On the Drag and Shedding Frequency of Two-Dimensional Bluff Bodies," *NACA Technical Note No. 3169*, 1954.
6. Bradbury, L. J. S., Durst, F., Launder, B. E., Schmidt, F. W., and Whitelaw, J. H. (Eds.), *Turbulent Shear Flows-III*, Springer-Verlag, New York, 1982.
7. Carr, L. W., "A Review of Unsteady Turbulent Boundary-Layer Experiments," in *Unsteady Turbulent Shear Flows* (Eds: R. Michael et al.), Springer-Verlag, N. Y., 1981, pp. 3-34.
8. Davis, R. W. & Moore, E. F., "A Numerical Study of Vortex Shedding from Rectangles," *J. Fluid Mech.*, Vol. 116, 1982, pp. 475-506.
9. Chorin, A. J., "Vortex Sheet Approximation of Boundary Layers," *J. Computational Phys.*, Vol. 27, 1978, pp. 428-442.
10. Sarpkaya, T. & Shoaff, R. L., "Inviscid Model of Two-Dimensional Vortex Shedding by a Circular Cylinder," *AIAA Journal*, Vol. 17, 1979, No. 11 pp. 1193-1200.
11. Sarpkaya, T. & Ihrig, C. J., "Impulsively-Started Steady Flow about Rectangular Prisms: Experiments and Discrete Vortex Analysis," *Journal of Fluids Engineering*, Vol. 108, 1986, pp. 47-54.
12. Moore, F. K., "On the Separation of Unsteady Laminar Boundary Layer," *UTAM Symposium, Boundary Layers*, Freiberg 1957, pp. 296-311, Berlin 1958.

13. Rott, N., "Unsteady Viscous Flow in the Vicinity of a Stagnation Point," **Quarterly Applied Mathematics**, Vol. 13, 1956, pp. 444-451.
14. Sears, W. R., "Unsteady Motion of Airfoils with Boundary-Layer Separation," **AIAA Journal**, Vol. 14, 1976, pp. 216-220.
15. Morison, J. R., O'Brien, M. P., Johnson, J. W., & Schaaf, S. A., "The Forces exerted by Surface Waves on Piles," **Petroleum Trans.**, AIME, Vol. 189, 1950, pp. 149-157.
16. Keulegan, G. H. & Carpenter, L. H., "Forces on Cylinders and Plates in an Oscillating Fluid," **Journal of Research of the National Bureau of Standards**, Vol. 60, No. 5, 1958, pp. 423-440.
17. Sarpkaya, T., "Vortex Shedding and Resistance in Harmonic Flow About Smooth and Rough Circular Cylinders at High Reynolds Numbers," **Technical Report No. MPS-59SL76021**, Feb. 1976, Naval Postgraduate School, Monterey, CA.
18. Sarpkaya, T., "In-Line and Transverse Forces on Smooth and Rough Cylinders in Oscillatory Flow at High Reynolds Numbers," **Technical Report No. MPS69-86-003**, July 1986, Naval Postgraduate School, Monterey, CA.
19. Sarpkaya, T. and Isaacson, M., **Mechanics of Wave Forces on Offshore Structures**, Van Nostrand Reinhold, New York, N. Y., 1981.
20. Sarpkaya, T., "In-Line and Transverse Forces on Cylinders in Oscillatory Flow at High Reynolds Numbers," **Journal of Ship Research**, Vol. 21, No. 4, Dec. 1977, pp. 200-216.
21. Sarpkaya, T., "Hydroelastic Response of Cylinders in Harmonic Flow," **Jour. of the Royal Institution of Naval Architects, The Naval Architect**, Vol. 3, 1980, pp. 103-110.
22. O'Keefe, J. L., "Time-Dependent Flow About Bilge Keels and Smooth and Rough Circular Cylinders," MS Thesis, Naval Postgraduate School, Monterey, CA. March 1986.
23. Heideman, J. C. and Sarpkaya, T., "Hydrodynamic Forces on Dense Arrays of Cylinders," **Proceedings of the Offshore Technology Conference**, OTC-5008, 1985, Houston, TX.
24. Honji, H., "Streaked Flow Around an Oscillating Circular Cylinder," **Jour. of Fluid Mechanics**, Vol. 107, 1981, pp. 509-520.
25. Hall, P., "On the Stability of Unsteady Boundary Layers on a Circular Cylinder Oscillating Transversely in a Viscous Fluid," **Jour. of Fluid Mech.**, Vol. 146, 1984, pp. 347-367.
26. Sarpkaya, T., "Force on a Circular Cylinder in Viscous Oscillating Flow at Low Keulegan-Carpenter Numbers," **Jour. of Fluid Mechanics**, Vol. 165, 1986, pp. 61-71.
27. Bearman, P. W., "Vortex Trajectories in Oscillating Flow," in **Proc. of Separated Flow Around Marine Structures**, Trondheim, Norway, 1985, pp. 133-153, The Norwegian Institute of Technology, Trondheim, Norway.
28. Sarpkaya, T., "Past Progress and Outstanding Problems in Time-Dependent Flow About Ocean Structures," in **Proc. of Separated Flow Around Marine Structures**, Trondheim, Norway 1985, pp. 1-36, The Norwegian Institute of Technology, Trondheim, Norway.
29. Williamson, C. H. K., "Sinusoidal Flow Relative to Circular Cylinders," **Jour. of Fluid Mechanics**, Vol. 155, 1985, pp. 141-174.
30. Aref, H. and Pomphrey, N., "Integrable and Chaotic Motions of Four Vortices," **Physics Letters**, A78, 1980, pp. 297-300.
31. Aref, H., "Stirring by Chaotic Advection," **Journal of Fluid Mechanics**, Vol. 143, 1984, pp. 1-21.

#### ACKNOWLEDGEMENTS

The work described in this paper represents part of a research program supported by the **National Science Foundation** under Agreement No. CEE-8210246. This support is gratefully acknowledged.

A special note of thanks is extended to LTCOL S. Mustafa for the discrete-vortex-model calculations, to LT T. Mc Coy for his assistance with the sensitivity analysis, and to Mr Jack Mc Kay for his most skilful and dedicated work in the design, construction and smooth operation of the test facilities.

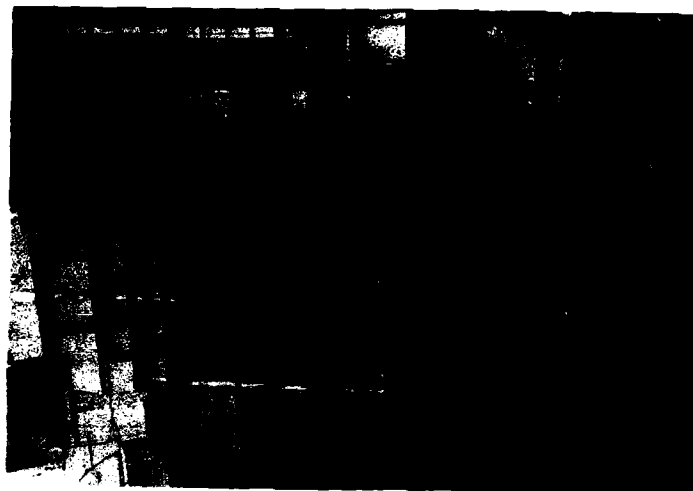


Fig. 1a A Photograph of the U-Shaped Vertical Water Tunnel

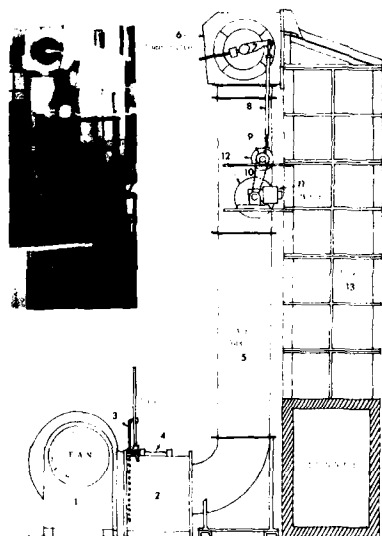


Fig. 2 Tunnel Air Supply System

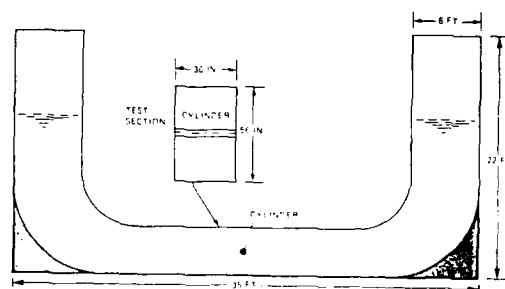


Fig. 1b Interior of the U-Shaped Water Tunnel

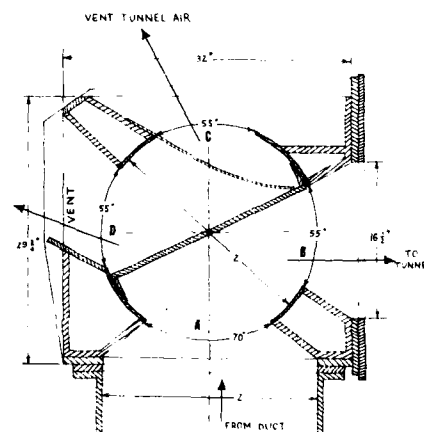


Fig. 3 Cut-Away Drawing of the Three Way Valve

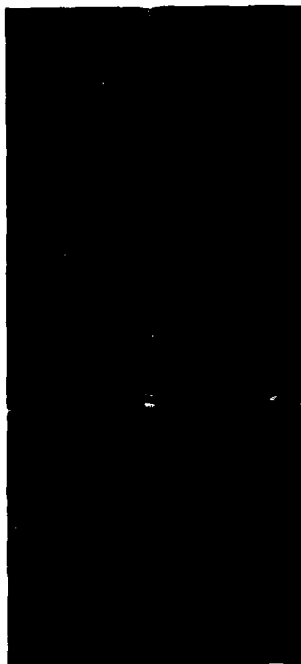


Fig. 4 Vortical Instability, Cylinder oscillation is parallel to this page ( $K = 1.1$  and  $\beta = 1380$ ).

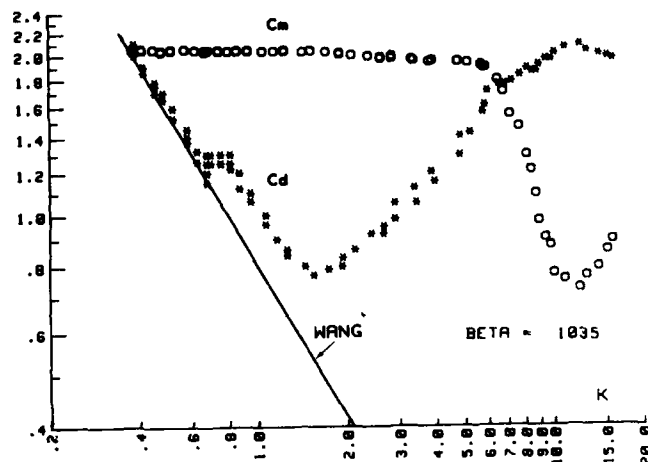


Fig. 5 Drag and Inertia Coefficients versus Keulegan-Carpenter Number. Experiment:  $\circ$ ,  $C_m$ ;  $*$ ,  $C_d$ ; Theory, —, ( $\beta = 1035$ ).

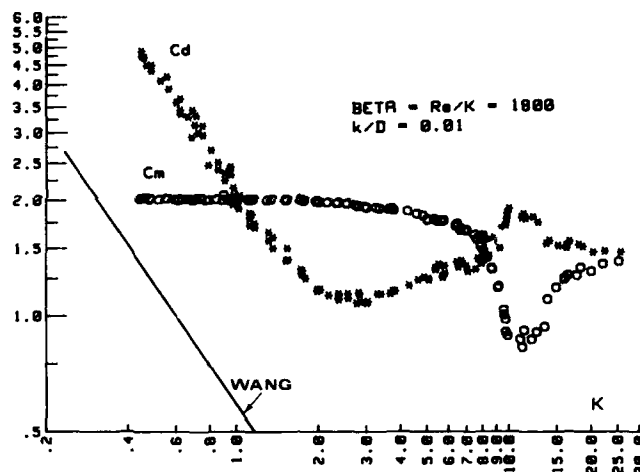


Fig. 6 Drag and Inertia Coefficients versus Keulegan-Carpenter Number. Experiment:  $\circ$ ,  $C_m$ ;  $*$ ,  $C_d$ ; Theory, —, ( $k/D = 0.01$ ,  $\beta = 1800$ ).

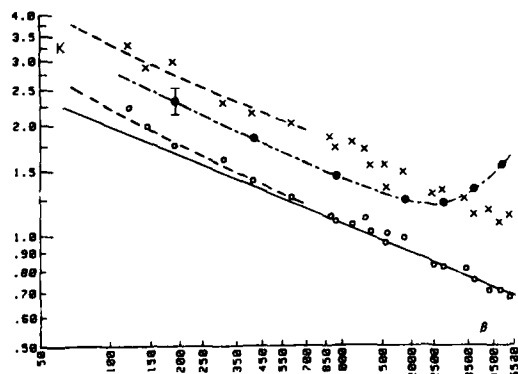


Fig. 7 Inception of Vortical Instability, Separation and Turbulence on an Oscillating Cylinder. Experiment:  $\circ$ , Vortical Instability;  $\bullet$ , Separation;  $\times$ , Turbulence; ----, Mean Line through Honji's Data (Lower line: instability, Upper line: Turbulence). Theory: —, Hall.

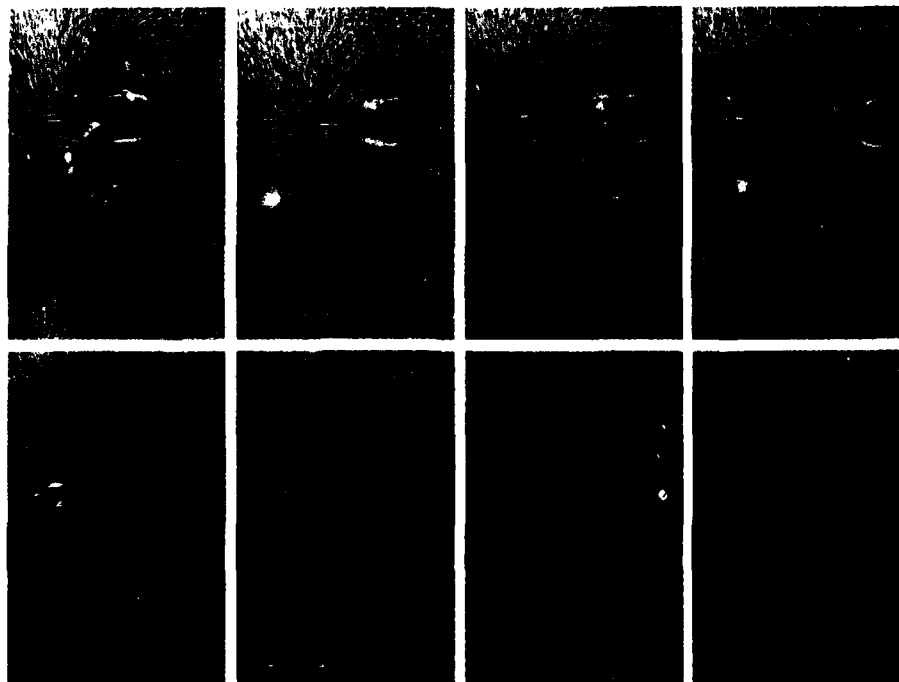


Fig. 8 Evolution of the Transverse Vortex Street,  
(top to bottom, left to right),  $K = 12.5$ .

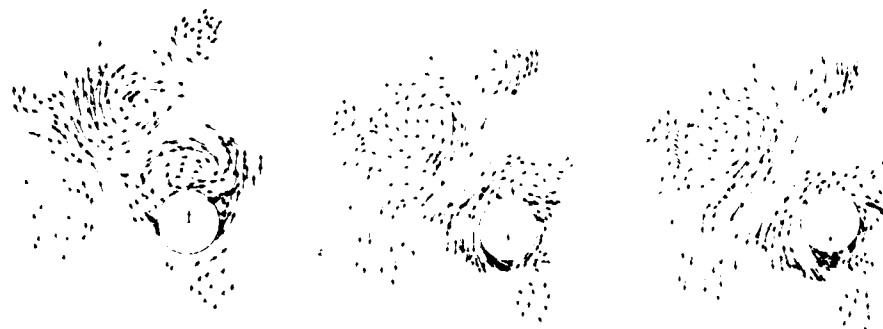


Fig. 9 Discrete  
Vortex Model of  
Oscillating Flow.

(a)  $U = 0.309$   
 $\dot{U} = -0.9511$   
 $K = 10$

(b)  $U = -0.309$   
 $\dot{U} = 0.9511$   
 $K = 10$

(c)  $U = -0.5878$   
 $\dot{U} = 0.8090$   
 $K = 10$

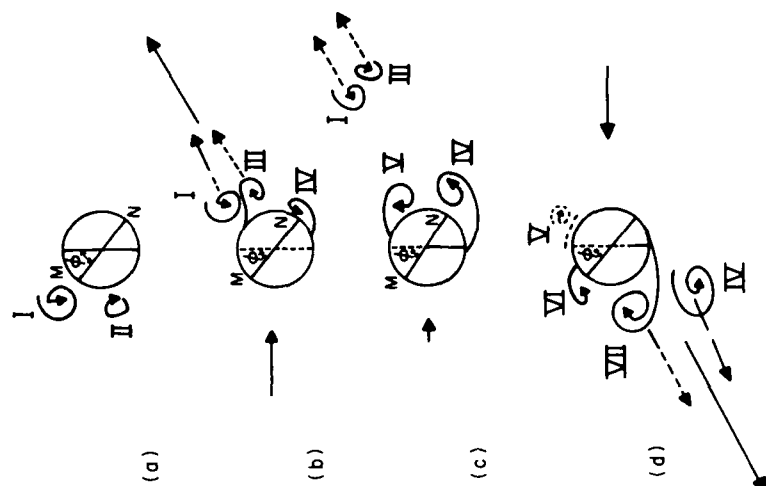
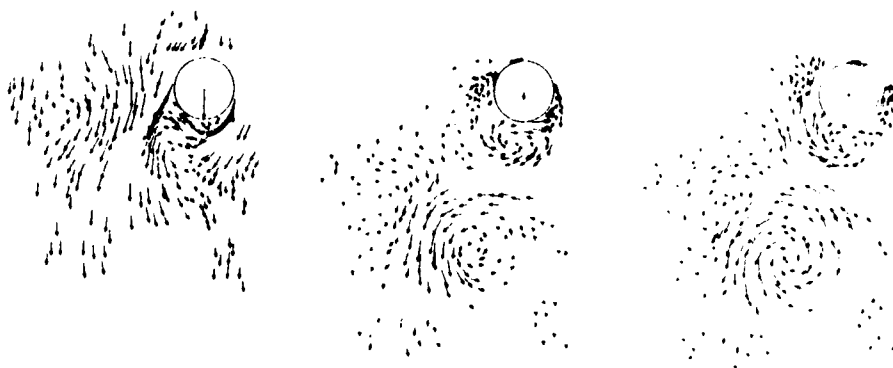
Fig. 10 Diagonal Vortex Shedding in the Range  $15 < K < 25$ .

Fig. 9 (Continued)

(d)  $U = -0.9877$   
 $\dot{U} = -0.1564$

(e)  $U = -0.309$   
 $\dot{U} = -0.9511$

(f)  $U = 0$   
 $\dot{U} = 1$





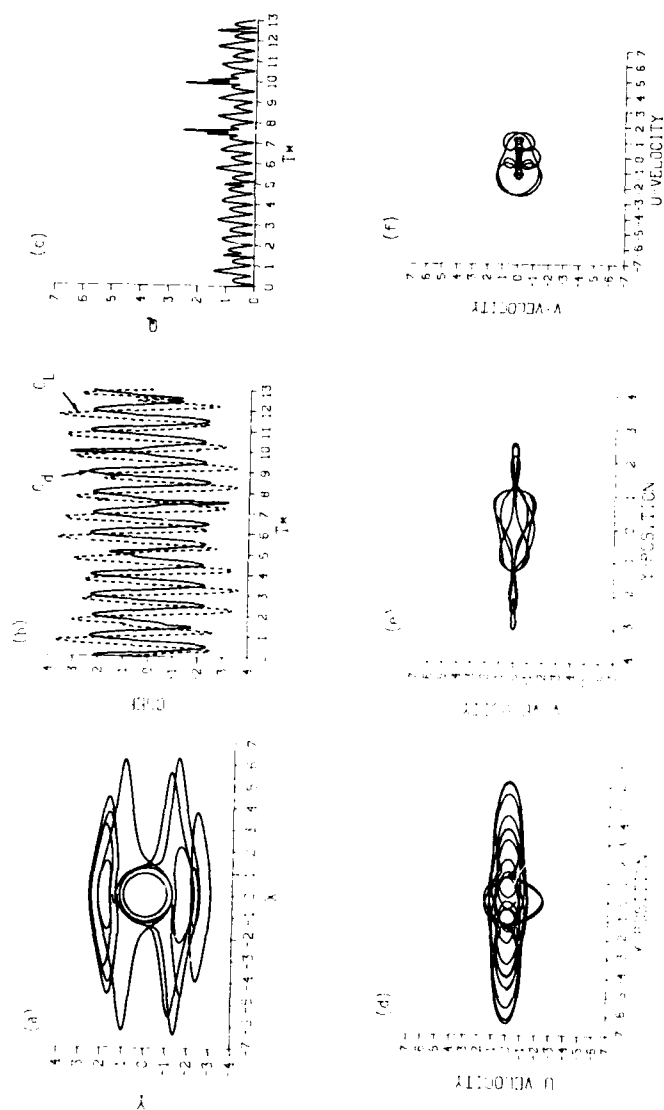


Fig. 11 Initial Position of the Vortex ( $\Gamma = 1.5054$ ). (a) Vortex Path, (b) Lift and Drag Coefficients, (c) Total Velocity, (d) x-component of the Velocity vs  $x$ , (e) y-component of the Velocity vs  $y$ , (f) y-component of the Velocity of the Vortex Center.  $T^*$  is the Time Normalized by Two Maximum (a) to (c) the Ambient Flow and the Cylinder Radius.

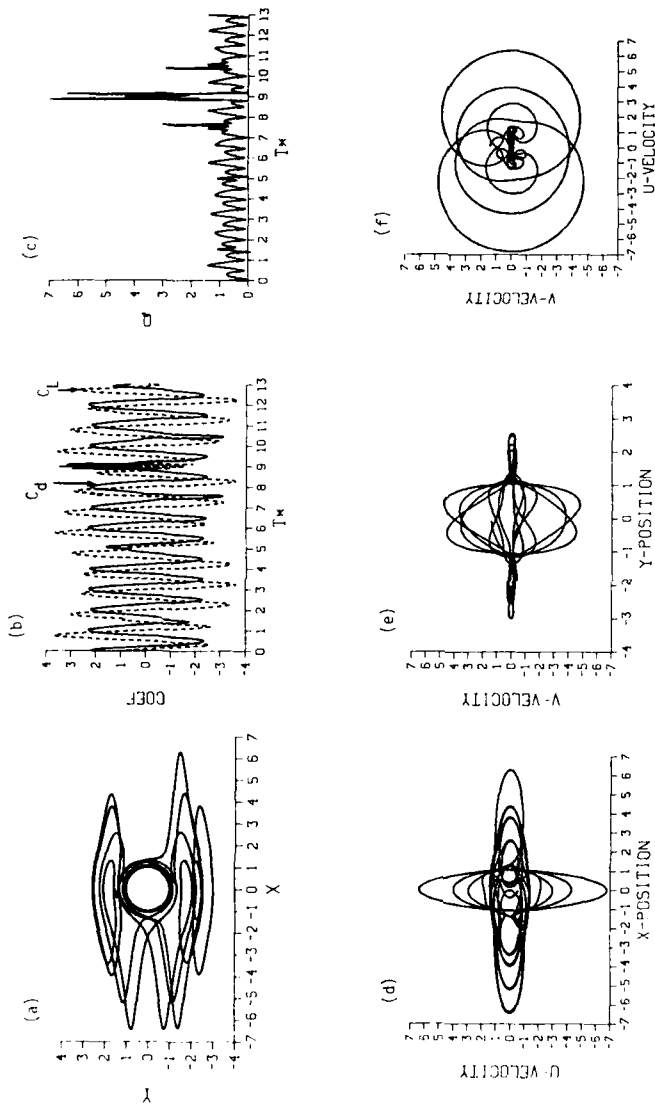


Fig. 12 Initial Position of the Vortex: (0, 1.5053). (a) Vortex Path, (b) Lift and Drag Coefficients, (c) Total Velocity, (d) x-Component of the Velocity vs. x, (e) y-Component of the Velocity vs. y, (f) y-Component of the Velocities of the Vortex Center.  $T^*$  is the Time Normalized by the Maximum Velocity of the Ambient Flow and the Cylinder Radius.

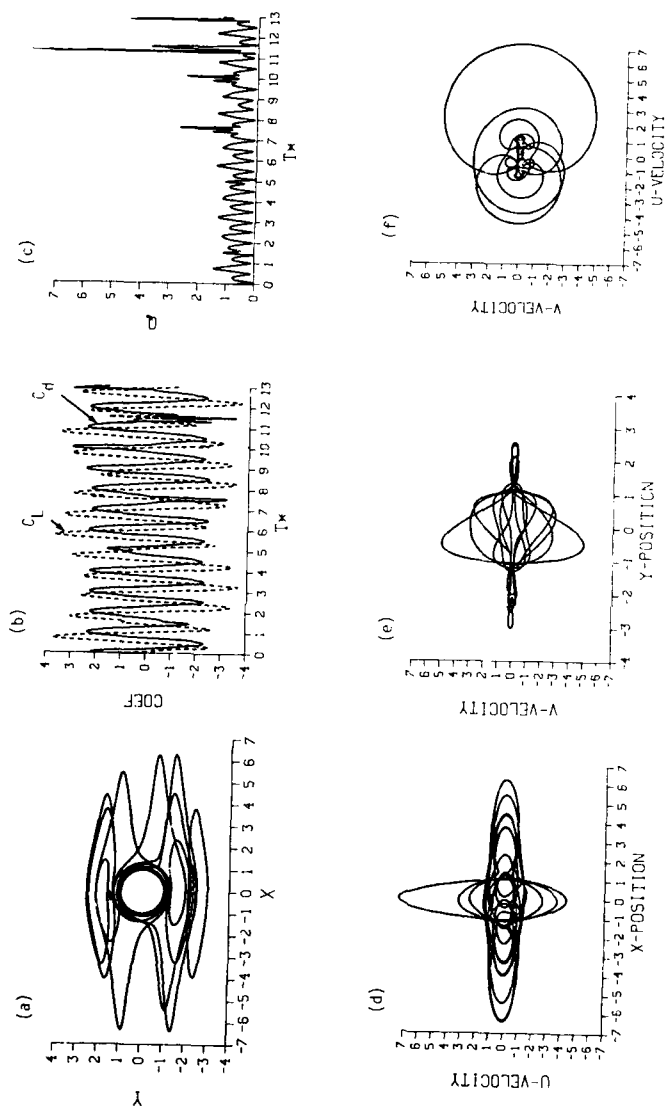


Fig. 13 Initial Position of the Vortex: (0, 1.50535). (a) Vortex Path, (b) Lift and Drag Coefficients, (c) Total Velocity, (d) X-Component of the Velocity vs. X, (e) Y-Component of the Velocity vs. Y, (f) Y-Component of the Velocities of the Vortex Center.  $T^*$  is the Time Normalized by the Maximum Velocity of the Ambient Flow and the Cylinder Radius.

7-1

The Use of the NRC/NAE Water Facilities in  
Canadian Aeronautical Research and Development

R.H. Wickens  
Low Speed Aerodynamics Laboratory  
National Aeronautical Establishment  
National Research Council  
Ottawa, Canada

N.E. Jeffreys  
Director, Institute of Marine Dynamics  
National Research Council  
St. John's, Newfoundland

**SUMMARY**

This paper describes some of the hydrodynamic facilities of the National Research Council in Ottawa and St. John's, Newfoundland. The NAE water tunnel, in particular, contributed to the understanding of the aerodynamics of various VSTOL concepts, and complex flows containing strong elements of vorticity and unsteadiness.

Several projects are described in which fundamental flow observations were made, and from which data was obtained in support of theoretical investigations.

The past and future potential of several water facilities of the NRC for pursuing aeronautical and marine research are described.

List of Symbols

b	Fuselage width	Q	Suction Quantity Cfs
$C_L$	Lift coefficient	u	Induced velocity normal to flight
$C_T$	Thrust coefficient	v	Local fluid velocity
$C_x$	Drag or wind axis coefficient	V	Tunnel velocity
$C_Q$	Suction coefficient, $\frac{2Q}{VS}$	$\alpha$	Angle of attack
D	Propeller diameter	$\lambda$	Body length
J	Advance Ratio, $\frac{V}{ND}$	$\Gamma$	Airfoil circulation
		(*)	Refers to stable flow on Zap Flap

**1.0 INTRODUCTION**

In the field of fundamental and applied fluid dynamics, particularly as related to the optimization of aerodynamic design, the techniques of flow visualization have proved useful in analysing complex flows of both a steady and unsteady nature. Flow visualization, with the use of indicators, wool tufts, smoke and the like have been standard in conventional wind tunnel testing for many years. For research, however, or in the discovery of new flow phenomena, the use of small scale models in water have proved invaluable aids to the imagination and to the solving of difficult flow problems. Water tunnel facilities, usually in the form of a water channel or water tunnel have played an important part in aerodynamic and hydrodynamic research and design, from the earliest work on the subject.

The flow visualization water tunnel at the NAE provides one experimental solution to the problem of analysing complex aerodynamic flows. By the use of flow indicators such as suspended aluminum particles, fluorescent dye or hydrogen bubbles, it has been possible to visualize various classical types of flow resulting from lifting systems, vortices, jets and other, more unusual flow configurations.

The history, and early use of this water tunnel is somewhat unclear, however it was designed and built at Goettingen, Germany, and used throughout World War II as a research facility in the services of the German aircraft industry. After the war it was procured by the National Research Council and has found a permanent place in the Low Speed Aerodynamics Laboratory. In this capacity, it has been used to provide a spur to the intuition and imagination of aeronautical research, and has contributed in some way to most of the major Canadian aeronautical projects, and also to many non-aeronautical problem areas.

Without flow visualization, it is sometimes hard to believe that the theoretical classical flows can actually exist in practice. One such example is shown in figure 1, the so-called "Toboggan" airfoil.

Here we have an unlikely-looking airfoil shape, which by means of suction, is able to contain a stable recirculating region whose upper boundary conforms to a thick airfoil shape. The flow was not only steady, but on the basis of the extreme streamline curvature evident in the photograph, was

producing considerable lift. Stable flow turning of 90 degrees has also been achieved. These types of flow are theoretically possible, however in the absence of direct observation, as the second photo shows, are somewhat unbelievable.



Fig. 1 "Tobboggan" Airfoil with suction

This paper will describe several areas of Aeronautical research in which the NAE water tunnel has played an important role in the development of aerodynamic design and in the understanding of flows which may characterize unusual configurations. In some cases, data were obtained from an analysis of the flow visualization patterns, and from the measurement of forces on the model. Theoretical comparisons in some cases provided excellent agreement with observation.

The utility of the NAE water tunnel will be continued and enhanced by modernization and possibly replacement, since it is now more than 40 years old. In addition, however, the National Research Council has other hydrodynamic facilities located at the Institute for Marine Dynamics at St. John's Newfoundland. These facilities, although used mainly for marine application, are, nevertheless appropriate and available for certain types of aeronautical research; (e.g. propellers, fuselage forms). The facilities of this institute, and some aerodynamic projects will be described in the final section of this paper.

## 2.0 DESCRIPTION OF THE NAE WATER TUNNEL

The water tunnel resembles a conventional closed circuit wind tunnel. It is constructed of mild steel sheeting and contains 350 gallons of water. The working section component spans the gap between the 4 to 1 contraction and the return leg duct. The working section dimensions are - width 10 inches, height 13 inches, length 32 inches. Glass plates form the front and the bottom sides, while the back wall contains a 10.25 inch diameter turntable, with a retaining ring, calibrated in degrees. Removable plates close the working section on top, thus preventing the surface disturbances from reaching the model. Figure 2 gives the general view of the facility with its ancillary equipment and control panel.

Water is circulated by a 15 inch diameter, four-bladed, propeller, situated in the return leg of the tunnel and driven by a 6.35 hp, 240v dc motor. Water velocities in the working section are infinitely variable from 0.2 feet per second to 10 feet per second, and accurately governed by means of a Ward Leonard motor speed control. These velocities correspond to a range of Reynolds numbers per foot of  $1.3 \times 10^4$  to  $6.5 \times 10^5$  at water temperature of 20°C. The light source, located below the working section volume consists of a 1200 watt high pressure quartz mercury vapour lamp. The light is emitted from within a moveable aluminum housing and is projected upwards through a lens in the form of a thin slit of illumination. This allows both longitudinal and cross flow planes of flow to be viewed. The alternating current electrical source results in a flashing illumination which leaves a row of dots or dashes when recorded on a photographic plate.

In most cases the models are mounted internally on the turntable, with the angle of attack adjusted from the outside. A sting attachment also mounted on the central turntable offers alternative support. For dynamic experiments this sting arrangement can be oscillated in pitch.

## 3.0 AERODYNAMIC INVESTIGATIONS

### 3.1 Circulation control for airfoils - the flapped airfoil

Early studies of the propeller-wing configuration for Vertical and Short Take Off performance, indicated that large chord multi-unit flaps were necessary in order to achieve appreciable slipstream deflection. The prevailing technology for these flaps were thought to be structurally difficult and mechanically complicated, and the use of a more simple flap form with suction or boundary layer control seemed an attractive alternative. One such simple configuration is the "Zap Flap", a trailing edge device which extends the effective chord of the wing as it deflects.

With sufficient suction in the "knee" of the flap at large deflection angles, it was thought possible to turn the oncoming flow, and to keep it attached on the reentrant surface. The success of the flow turning experiment of figure 1 seems to confirm this.

A model configuration conforming to the Zap Flap design was tested in the NAE water tunnel, and is shown in figure 3. The basic airfoil was an NACA 0012, with a 60% chord flap which extended rearwards as it deflected. The model chord and span were 7.00 and 2.00 inches respectively. End plates were provided. Circulation control was achieved by suction; the suction pipe was positioned in the acute angle between the airfoil and the flap.

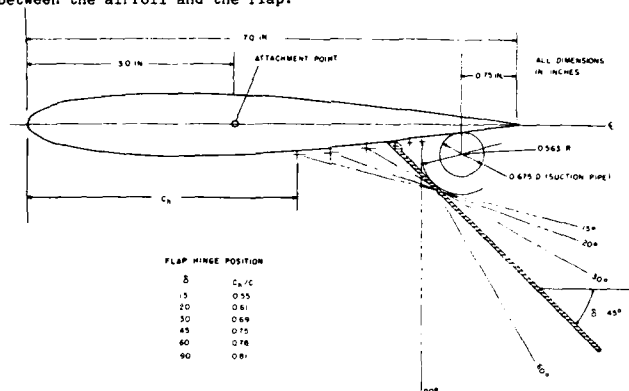
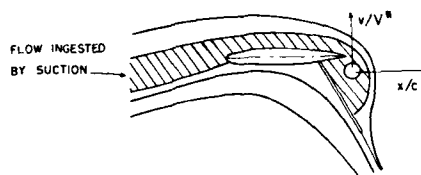


Fig. 3 NACA 0012 Airfoil with 60% Zap Flap

The separated region associated with normal operation of a Zap Flap without suction is shown in figure 4a at an angle of attack of 0 deg. and a flap angle of 30 deg. Figure 4b shows the effect of suction on the same configuration at an angle of attack of 10 degrees. A flow stagnation point now exists on the flap's upper surface. Its position depends on tunnel flow velocity, which for the constant suction flow of this experiment, also determined suction coefficient  $C_q$ . Unsuccessful attempts were made to position the stagnation point at the flap trailing edge. The resulting flow was not stable, and in time the stagnation point left the trailing edge, accompanied by considerable turbulence. Accordingly it was decided to investigate the effect of model incidence and flap setting with the flow stagnation point located as close as possible to the flap trailing edge, commensurate with flow stability.

In all cases of successful flow deflection and stable reattachment on the flap, the streamline characteristics exhibited two main features. 1) The oncoming, off-body streamline flow is deflected significantly by the lifting system and passes down stream. 2) The flow ingested by suction is separated from the main flow by dividing streamlines, and is always accompanied by a standing vortex in the flap cavity. This vortex is positioned just aft of the suction pipe, and is the main mechanism for turning the flow (Figure 4b).



Some extreme levels of stable flow deflection were achieved in this manner, and Figure 4c shows the deflected flap at a 60 degree setting, with flow turning over the upper surface reaching values greater than 90 degrees.

The method of flow visualization consisted of fine aluminum particles suspended in water, illuminated by a high intensity flashing light of 120 Hz frequency. This explains the characteristic patterns of the flow photographs, but also provided a method of determining local flow velocity, by counting time intervals on the photographic plate.

Measurements of this type were made in the flow surrounding the airfoil around a circuit which conformed to upper and lower streamline boundaries, remote from the airfoil. In this way, airfoil circulation was determined as follows:

$$\Gamma = \oint v \cos \theta \, d\ell \quad (1)$$

where  $\theta$  is the inclination of the local velocity vector to the elemental length  $d\ell$ . For airfoils in a real fluid, having a finite wake, or regions of separated flow, circulation escapes as vorticity, and may result in a large error.

Notwithstanding these reservations, airfoil lift coefficient has been determined for various model configurations. The accuracy of the method depends on the circuit being taken as far away from the airfoil as possible. A summary of airfoil performance is shown in Figure 5, in which suction

coefficient  $C_Q^*$  is plotted against  $C_L^*$  for all of the flap deflections. The suction required to produce high lift coefficients and large flow turning for stable flow reaches very high levels, as flap deflection increases. Figure 6 shows maximum lift coefficient achieved by suction for increasing flap angle.

The data achieved in this way was useful although not of high accuracy; they indicated the levels of suction coefficient which would be required to stabilize such a flow, and to produce high lift. The flow visualization also confirmed the streamline pattern which had been predicted by classical potential flow methods. Ref. (3) is a potential flow analysis in which the airfoil and split flap were represented by line segments, with a point vortex placed in the cavity between them. The Kutta conditions were established at the two trailing edges, and the resulting solution furnished the strength of the vortex, for a given model incidence and suction. The resulting streamline configuration confirmed in a general way what was seen by flow visualization; however a computation of lift indicated an over-estimation, which was attributed to the fact that vortex strength increased with incidence (Fig. 7).

The potential flow zero streamline divides the ingested flow field inside the cavity into two separate regimes: one chiefly controlled by the action of the vortex, and another influenced by the sink. This usually results in a third stagnation point on the interior surface of the flap, but which is not visible from the flow visualization photographs. The analytical model also does not include any flow separation which was clearly visible on the lower surface of the wing-flap boundary, and in some cases from the nose.

### 3.2 Aerodynamics of Lifting Propellers

The propeller has been used as a means of thrust generation for many years, and its operation and design in conventional attitudes is well understood for high rates of advance. During the transition of a V/STOL aircraft however, propellers may be inclined at large angles relative to the flight direction, and will be operating at very low advance ratios. Under these conditions both lift and induced drag are produced, and the nature of the induced velocities in both the propeller plane and the trailing wake are three-dimensional and non-steady. Distinct regions of propulsive flow and vortical flow co-exist and the resulting final wake is much more complex than for either a simple propeller or a wing.

The NAE water tunnel was used to explore and quantify the intake flow field and trailing wake of a propeller inclined to 90 degrees, and operating at low advance ratios in the "Helicopter" mode. The propeller model was a conventional fixed pitch, three-bladed design, of 3.5 in. diameter. It was positioned at the centre of the working section, approximately 2.5 diameters above floor level. The axis of rotation was vertical, and speed was controlled by means of a small air turbine (Fig. 9).

The investigation covered an advance ratio range ( $\frac{V}{ND}$ ), from 0.5 to 1.0. At very low advance ratios, propeller thrust, or in this case, lift, results mainly from the momentum change of the flow through the propeller disc. Thrust will at first decrease as flight speed increases, due to an unloading of the blade elements. As advance ratio  $\frac{V}{ND}$  continues to increase however, lift reaches a minimum, but thereafter continues to increase almost linearly with speed. At the same time, drag becomes significant and also continues to increase with speed. These increases of lift and drag are coincident with the appearance of wake trailing vortices and with the alteration of inflow velocities at the propeller plane. Figure 9 shows the variation of lift and drag with advance ratio for a propeller inclined 90 degrees to the flow.

It was the purpose of this flow visualization study to focus in on the vortical nature of these wake flows, and also the velocity distributions which they induce at the propeller.

Velocities were inferred by counting the time intervals of the illuminated aluminum particles. While this method is satisfactory for two-dimensional flow, they are thought to be least accurate in the propeller inflow, where local velocities were high, and where flow was curved; and also in the rolled-up wake, where the flow is three-dimensional.

#### Flow at the propeller plane

The onset of forward speed has been shown to produce changes in propeller lift and drag; large changes are also evident in the magnitude and distribution of the induced velocities at the intake plane. The fluid approaching the edges of the propeller is first subjected to an upwash and then a downwash as it passes through the propeller plane. The fluid above the retreating blades has a small component of induced velocity, whereas that above the advancing blade side is deflected almost normal to the propeller plane (Figure 10).

Figure 11a shows the general flow field above and upstream of the propeller plane, visualized using fluorescent dye. The advancing side is to the viewers' right. It is evident in this view that a large sidewash or lateral inflow exists over the forward portions of the propeller plane.

Figure 11b shows the filaments originating from a position slightly below the propeller plane. The two inner filaments are deflected outwards along the spanwise axis, before being dispersed by the passage of the propeller blades. The outer filaments, however, show that fluid which does not immediately pass through the propeller is subjected to a rotating motion at the edges of the disc, which brings fluid above the propeller plane; this fluid then passes through the propeller into the slipstream.

The normal induced velocity component  $\frac{U}{R}$ , inferred from the photographic plates, is shown in Figure 12 for an advance ratio,  $\frac{V}{ND} = .56$ . The  $\frac{U}{R}$  contours indicate that the highest normal induced velocities occur on the advancing side of the propeller plane. This is also reflected in the longitudinal variations of  $\frac{U}{R}$  of Figure 13, measured in three representative longitudinal planes

through the disc for an advance ratio of 0.56. These graphs indicate an upwash ahead of the disc, a high downwash over the rear portion of the disc, and a nearly constant downwash in the trailing wake.

#### Flow in the Trailing Wake

In this experiment, vortex-like motions, originating from advancing and retreating portions of the propeller disc, were observed when viewed from a cross flow plane behind the rotor. The vortices appeared to be of different sense and strength; the vortex with the larger angular rotation was associated with flow from the advancing blade side. The vortex was also displaced lower than that from the retreating blade side, due probably to the higher average downwash through that side of the propeller plane.

In some respects, this trailing vortex flow is similar to that behind a conventional or slender finite wing; an observation which has been made before with regard to helicopter wakes (Ref. 11). In the present case, however, at stations further downstream, there was evidence of a third, smaller vortex lying close to the vortex from the advancing side, but rotating in the opposite sense, and located on the advancing side of the flow. Figure (14) is a photograph of a plane 1.5 diameters behind the propeller, which shows three areas of concentrated vorticity ( $J=0.56$ ).

A quantitative explanation for this flow is shown schematically in figure (15). The single-bladed rotor advances with velocity  $V$  and rotates with angular velocity  $\Omega$ . The advance ratio and mean wake deflection corresponds to figure (11) approximately. The trailing wake consists of vortex filaments of variable strength, shed from both the tip and root portions of the blade. Since the move with the fluid, the wake consists of continuous loops and sinuous filaments which move past a fixed observer.

The sense or direction of rotation of the induced flow is indicated on the diagram, and it can be seen that relative to the blade, there has been no change in the direction of the induced motion from advancing to retreating side; continuous filaments are produced, varying only in strength.

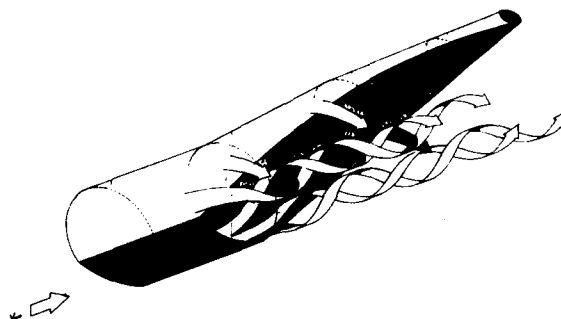
The observer, positioned downstream, sees different portions of the same filament, and the fluid on the retreating side appears to be rotating in the opposite direction to that on the advancing side. The central filament, originating near the hub, forms a third area of fluid motion similar to that seen in Figure 15.

#### Calculations of Propeller Wake Vortex Flow

Using a relatively simple theoretical model, calculations have been made by the cross-flow streamline pattern in which the third area of vorticity is represented. The model consists of a rectangular array of horseshoe vortices which lie in the rotor plane, and which induce downwash velocities in the retreating and advancing portions of the disc. The trailing arms of the vortices stream from the advancing and retreating edges of the array, and also from the central position. If measured downwash values are specified at locations on the lattice, then the calculation furnishes lift, rolling moment, and vortex strength. If the deflection of the trailing arms are computed downwind of the rotor, then cross flow streamlines of the equivalent potential flow can be computed. This type of calculation is shown in figure (16) for a rotor advance ratio of 0.56; these streamlines can be compared with Figure 14. Measured downwash contours of  $\frac{u}{R}$  are shown in (16C).

### 3.3 Vortex Separations from Upswept Fuselage Shapes

A wake, composed of clearly defined vortices, similar to those shed behind slender lifting bodies, or wings, is known to exist behind aircraft whose fuselages are highly cambered or swept up to accommodate rear-loading cargo doors.



SCHEMATIC DRAWING OF FLOW SEPARATION & VORTEX SHEDDING FROM A REAR-LOADING FUSELAGE

It has been suggested that the vortex wake may be the cause of certain undesirable flight characteristics, such as the deterioration of handling characteristics at low speeds, and an increase in cruising drag. The former effect is thought to be due to an alteration of fuselage longitudinal pressures and stability due to the lateral movement of the vortex cores during gusty crosswind landing approaches. The problem was under investigation by DeHavilland during the development of their Caribou and Buffalo aircraft. Further investigations of fuselage aerodynamics, with particular regard with vortex separation, interference and cross-coupling were addressed in Reference (7).



In most of these investigations, the NAE water tunnel provided the initial understanding of separation, rollup and movement of the vortex wake, on fuselage forms typical of current transport aircraft.

The model, which was a 1/72 scale representation of a DeHavilland design, is shown in figure (17)). Fluorescent dye, which was emitted from the interior at various locations along the fuselage, was used to visualize the vortices. The Reynolds number was 5000-7000 based on fuselage length. For higher tunnel speeds ( $Re = 87000$ ), aluminum particles were used.

The vortex separations for the lower, upswept portion of the fuselage produced a very clear image of the rotational nature of the separated, rolled up wake, as figure (18) shows. In cross-section; the two vortices lie below the fuselage lower surface, and the dye filaments exhibit a typical rolled-up appearance.

The location of the vortex core relative to the after fuselage mean line can be determined from flow photographs for various angles of attack and Reynolds number. In general, the vortex core is inclined at half the local fuselage incidence; thus conforming with similar observation made on slender wing configurations.

The development of the separated fuselage flows commences with the separation of the boundary layer on the bottom of the after-fuselage. Figure 18 shows the gradual development of three-dimensional separation lines and vortex shedding on the bottom of the fuselage at an angle of attack of 2. As the inner boundary layer filaments gradually deform, the separation lines become more pronounced, and the vortex cores began to exhibit their characteristic spiral formation.

The location of vortex cores beneath the fuselage was affected not only by fuselage incidence, but also by yaw. On the windward side, the windward vortex moved only slightly, and remained in the vicinity of the fuselage bottom. The leeward vortex however, moves relatively further away from the fuselage after body.

The loci of vortex cores, for two Reynolds Numbers is shown in Figure 19 for constant yaw. Various methods were tried in an attempt to control and possibly limit the vortex movement. Strakes were placed along the longitudinal chines of the after fuselage. The main result of the strakes at zero yaw was to restrict the vertical movement of the vortex core with incidence. The lateral location relative to the model centreline was unchanged. The effect of adding strakes on the general motion of the vortices with both incidence and yaw is shown by the cross flow envelopes of figure 20b and 20c. At low Reynolds Numbers, the strake changes the vortex movement boundaries considerably, by fixing a definite separation line and altering the shedding of vorticity. At the higher Reynolds Number 87000, the vortex movement region is much smaller, and not much affected by the presence of strakes.

A second method of vortex alteration was by the use of suction along the bottom centreline of the after fuselage. This provided an effective means of weakening the separated vortices, while encouraging the flow to remain attached for most of the incidence range. Reference (9) shows loci of vortex equilibrium positions in the vicinity of a cylinder with suction or blowing at the rear stagnation point. Corresponding streamlines and cylinder pressure distributions are also computed. In general, suction causes the vortices and their momentum stream tube to approach the cylinder, while blowing tends to cause detachment, and movement away from the cylinder. The flow visualization photograph shows vortex streamlines in the cross flow of a circular cylinder with suction on the lee side (Figure 21).

### 3.4 Forebody Vortices on Oscillating Configurations

The formation and shedding of forebody vortices on an aircraft configuration flying at a moderate angle of attack is well documented. As the angle of attack increases, these vortices become asymmetrical, even if the aircraft continues flying into the wind (i.e. has zero sideslip). This gives rise to non-zero lateral forces and moments.

On a configuration performing an oscillation in pitch around an angle of attack close to the onset of asymmetry, the forebody vortices oscillate to and from between their symmetrical and asymmetrical positions. The aerodynamic reactions are therefore a function of the motion of the vortices and can be described in the form of stability derivatives.

Because of the time lag between the motion of the vortices and the motion of the configuration of the aerodynamic reactions have components that are in phase as well as out of phase with the motion of the configuration. The resulting stability derivative will therefore comprise both static and dynamic derivatives. The derivative of lateral aerodynamic reactions due to a motion in a longitudinal plane (such as pitching) represent cross-coupling effects.

Figure (22) shows the pattern of vortices emanating from the nose cone of a slender cone-wing configuration oscillating in pitch. The spiral formation of the dye filaments indicate that the vortices are rolling up into concentrated cores, and are symmetrically placed relative to the model centre line. At a certain critical angle of attack  $\alpha_a$ , depending on the model reduced frequency  $\frac{W}{2U}$ , a definite and sudden asymmetry occurs in which both vortex cores are displaced to one side of the model centre line. This is illustrated in Figure 22b, in which the model is pitching slowly to a maximum angle of 45 degrees. As the model completes its pitch cycle and begins its downward travel, the vortex cores return to symmetry, but the angle of attack  $\alpha_s$  at which this occurs is considerably less than for  $\alpha_a$ . Figure 23 shows observations of the differences in angle of attack for the onset of asymmetry  $\alpha_a$ , and for the return to symmetry  $\alpha_s$  for a model oscillating in pitch. The phase lag depends strongly on reduced frequency; the rate of convection of the vortices are approximately 0.6 - 0.7 of free stream velocity.

At the highest end of the reduced frequency range, Figure 23 illustrates just the beginning

of the expected cyclical variation with reduced frequency, of  $a_2$  and  $a_3$ ; for a particular conitudinal location, and a particular reduced frequency there will be a point where the flow will be lagging by one or more full oscillation cycles, making it similar to that of the cycle before.

It has also been confirmed by tunnel experiments that it is indeed possible to control the direction of the vortex asymmetry by the use of blowing or mechanical disturbance near the nose of the model.

A more appropriate presentation of these phenomena is available in the form of a ciné film showing asymmetric motions of the vortex cores and clearly indicating the effects of the time lag.

#### 4.0 THE INSTITUTE FOR MARINE DYNAMICS

The Institute of Marine Dynamics, now located at St. John's, Newfoundland, stemmed from the Marine Dynamics and Ship Laboratory in Ottawa.

IMD is a National Facility which carries out research in response to the needs of the ship building and off shore industries across Canada. The research programs are developed in close cooperation with representatives of Industry and Government agencies such as Transport Canada. Its location in St. John's puts it at the centre of important marine oriented research and educational organizations. IMD also has close ties with other divisions of NRC such as the NAE.

IMD ranks as one of the world's largest hydrodynamic research Institute. Its laboratories include an ice tank, seakeeping and manoeuvring tank, towing tank, cavitation tunnel and associated workshops for the manufacture of models and their instrumentation. Specifications of these facilities are listed in Table I.

##### Ice Tank

The large scale ice tank, located in a refrigerated building allows the simulation of ship passage through a simulated Arctic Environment. Sensors mounted on the model or on the towing carriage spanning the tank, measure the ice-going properties of various designs.

##### Seakeeping Tank

The seakeeping tank is equipped with a sophisticated wave-making system, to simulate the multi-directional waves found in nature. Large scale models of structures may be moored or self-propelled under radio control and their motions measured by an optical tracking system. Research carried out in this facility includes the verification of the behaviour of a semi-submersible platform under extreme environmental conditions, and studies of seakeeping capabilities of ships in oblique waves.

##### Towing Tank

The towing tank at IMD is used for research into ship resistance, propulsion and seakeeping. Tests carried out include resistance measurements, flow visualization and wake surveys, measurements of propulsive power and seakeeping in head or following waves.

##### Cavitation Tunnel

The cavitation water tunnel, whose specifications are listed in Table I has been used to study the relationship between propeller design and cavitation, the generation of noise by cavitation and the effects of cavitation on appendages such as stabilizer fins.

The cavitation tunnel played an important part in the design of an under water towed body. A shape, including the design of stabilizing fins was evaluated which satisfied the requirements of static and dynamic stability in pitch, and appropriate towing forces. Water tunnel tests of various combinations of fin design on a streamline body provided initial evaluation of the static stability.

A computer simulation of the motion of the towed body and cable was performed to solve the coupled heave and pitch equations, using water tunnel data. The results predicted heavily damped pitch motion at all speeds with pitch damping increasing as towing speed increased. The simulation also provided steady-state towing forces, and showed the effect of the cable on body motion.

This work was followed by tests, in the towing tank, in which drag and static derivatives were measured. Dynamic derivatives were also determined.

The final full scale tests of the towed body were made in calm water; both the towing platform and the model were gyro-stabilized, and measurements were made of the three components of acceleration and angular displacement.

The conclusions of this development program showed that the design met all of the hydrodynamic requirements, the dynamic response was especially good, the tracking in severe ship manoeuvres was excellent, steady towing took place at predicted depths, and the agreement between predictions based on the model tests and the full-scale sea trial measurements were most satisfactory.

Future plans for the new laboratory in St. John's include the installation of a planar motion mechanism on the 200 m long 7 m deep Clearwater Towing Tank for use in submarine motion experiments. The Water Tunnel will continue to be used for flow visualization work. A large Wind Generator is being designed to produce the vertical variation of atmospheric winds over a water surface, including the presence of wind gusts and their spectral distribution of energy. The Wind Generator will be used with the Clearwater Towing Tank and the Wave Basin primarily for tests on offshore structures. The Variable

Density Wind Tunnel will be used for the further development of hotfilm anemometers and flow direction probes.

## 5.0 CONCLUSIONS

This paper has described the aerodynamic and hydrodynamic facilities of the National Aeronautical Establishment and the Marine Dynamics Institute of the NRC. Results have been presented of investigations of various aerodynamic configurations which were related to the development of Canadian aircraft or useful to the development of marine technology.

The aerodynamics projects described in this paper contributed in their time, significantly to the discovery and understanding of complex V/Stol and vortex flow phenomena. In the current context however, they are mainly of historical interest, while demonstrating the utilization of a water facility to its maximum extent.

The NAE water tunnel is currently continuing to contribute to aerodynamic knowledge in both the aeronautical and industrial aerodynamic fields. The projects investigated range from the dynamic stall characteristics of Wind Turbine blade sections, aerodynamic flow over spray nozzles and booms for aerial pest control, to the investigation of separated flows on wing-nacelle configurations typical of current propeller-driven aircraft.

It is obvious that water tunnel facilities will continue to be significant in the preliminary design and development of new aerodynamic concepts and techniques. The use of new technologies, measurement methods and computer-aided analysis will advance both hydrodynamic research and aerodynamic research. The ultimate aim would be to develop both facilities and methods to the stage where an interchange of marine and aeronautical skills could be mutually beneficial.

## ACKNOWLEDGEMENTS

The authors wish to acknowledge G.A. Dobrodzicki, Technical Officer in charge of the NAE Water Tunnel. They also wish to acknowledge K. Orlik-Ruckemann and C. Williams (IMD) for contributions to this paper.

## REFERENCES

1. Dobrodzicki, G.A. - Flow visualization water tunnel - its construction and capabilities. NRC LR-610, No. 20235.
2. Wickens, R.H.; Okapwu, U.; Clifford, R.R. - Water tunnel experiments on a Zap Flapped airfoil. NRC LR-294, Dec. 1960.
3. Mandl, P. - Effect of standing vortex on flow about suction airfoils with split flaps. NRC LR-239, Jan. 1959.
4. Wickens, R.H.; Gartshore, I.S. - Observations of the flow near a lifting propeller. NRC LR-325, Dec. 1961.
5. Templin, R.J. - Calculation of the vortex field downstream of a Rotor with its axis of Rotation perpendicular to the free stream flow. NRC Lab. Memo AE-114g, 1961 (limited distribution).
6. Peake, D.J. - The flows about rear fuselages of Typical Cargo Aircraft, NRC/DME QB No. 1968(3), Oct. 1968.
7. Rainbird, W.J.; Crabbe, R.S.; Peake, D.J.; Meyer, R.F. - Some examples of separation in three-dimensional flows. CASI J, Vol. 12, No. 10, Dec. 1966.
8. Wickens, R.H. - Observations of the vortex wake of a lifting fuselage similar to those on rear-loading aircraft. NRC LR-395, Jan. 1964.
9. Wickens, R.H. - Calculation of the equilibrium locations of a vortex pair behind a circular cylinder with a source or sink placed at the rear stagnation point. NRC LR-380, March 1963.
10. Orlik-Ruckemann, K.J. - Aerodynamic aspects of aircraft dynamics at high angles of attack. Journal of aircraft Vol. 20, No. 9, Sept. 1983.
11. Heyson, H.H. - A Note on the Mean Value of Induced Velocity for a Helicopter Rotor. NASA TN D-240, May 1960.
12. Wickens, R.H. - Reduction of aerodynamic drag of external spray booms and nozzles used on DC-6 aircraft. CASI Journal, Vol. 26 No. 1, 1980.
13. Wickens, R.H. - A technique for simulating the motion and ground effect of aircraft wake vortices. CASI Journal, Vol. 26, No. 2, 1980.
14. Newman, B.G. - Water flow investigation of static and dynamic stall on the NACA 0018 airfoil, and a flat plate airfoil. NRC/TM-WE-124, Aug. 1985.
15. Wickens, R.H. - Viscous three-dimensional flow separations from high-wing propeller-turbine nacelle models. AGARD CP-342 (16) - Aerodynamics of Vortical-Type Flows in Three Dimensions, April 1983.

TABLE I

Ice Tank	90 m x 12 m x 3 m Maximum ice thickness 15 cm Towing carriage maximum speed 4 m/s
Seakeeping Tank	75 m x 32 m x 3.5 (depth variable to 0.4 m) Multi-element wavemaker for long or short-crested regular or irregular waves
Towing Tank	200 m x 12 m x 7 m Towing carriage maximum speed 10 m/s Wavemaker for regular or irregular waves
Cavitation Tunnel	Working section 2.5 m x 0.5 m x 0.5 m Maximum flow speed 12 m/s

## IN OTTAWA

Towing Tank	137 m x 7.6 m x 3 m Maximum carriage speed 12 m/s Wavemaker for regular waves
Maneuvering Basin	122 m x 61 m x 3 m Wavemaker for regular waves

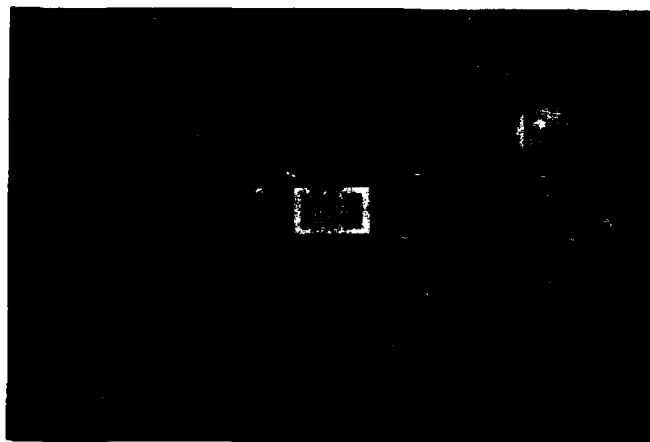
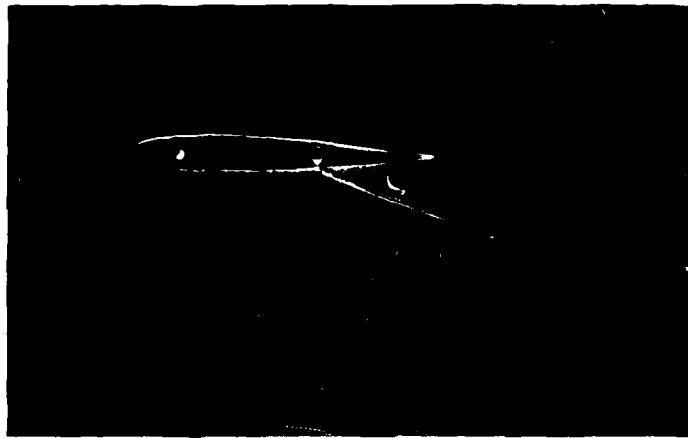


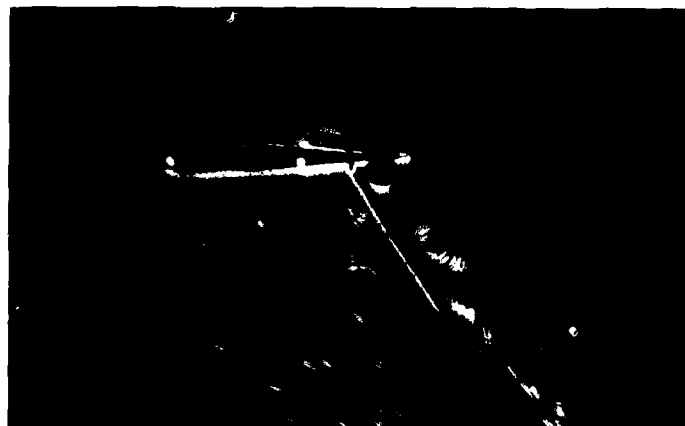
FIGURE (2) NATIONAL AERONAUTICAL ESTABLISHMENT'S WATER TUNNEL



a)  $\alpha = 0^\circ$ ,  $\delta = 30^\circ$ ,  $C_Q = 0$



b)  $\alpha = 10^\circ$ ,  $\delta = 30^\circ$ ,  $C_Q = 0.30$



c)  $\alpha = 0^\circ$ ,  $\delta = 60^\circ$ ,  $C_Q = 0.52$

FIGURE (4) ZAP FLAP AIRFOIL WITH SUCTION

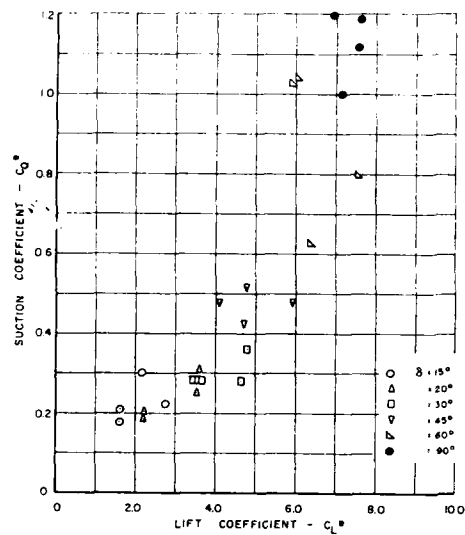


FIGURE (5) PERFORMANCE OF ZAP FLAP AIRFOIL

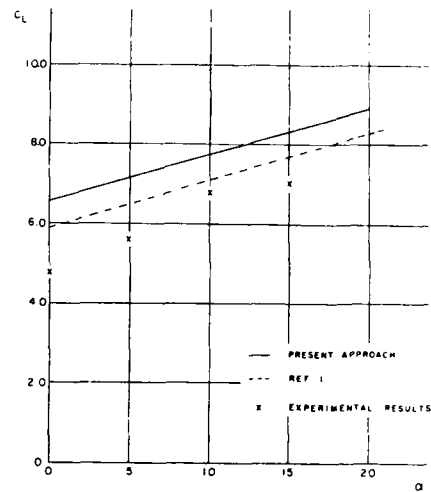


FIGURE (7) THEORETICAL VARIATION OF LIFT COEFFICIENT

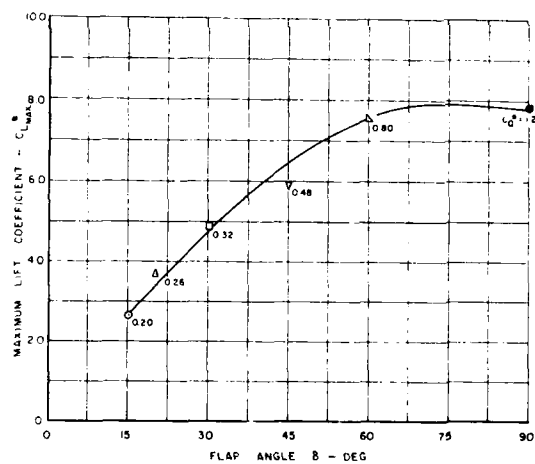


FIGURE (6) MAXIMUM LIFT COEFFICIENT FOR ZAP FLAP AIRFOIL



FIGURE (8) PROPELLER MODEL

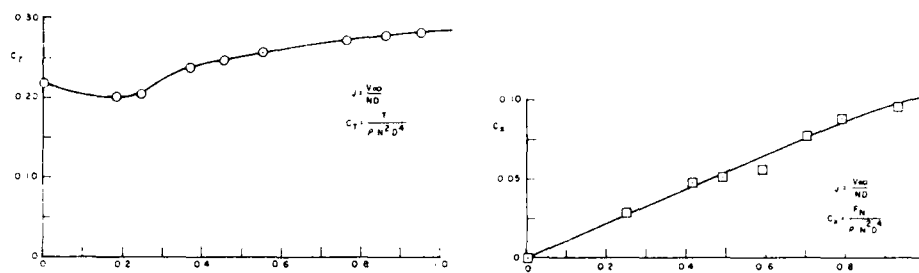


FIGURE (9) VARIATION OF PROPELLER LIFT AND DRAG WITH ADVANCE RATIO

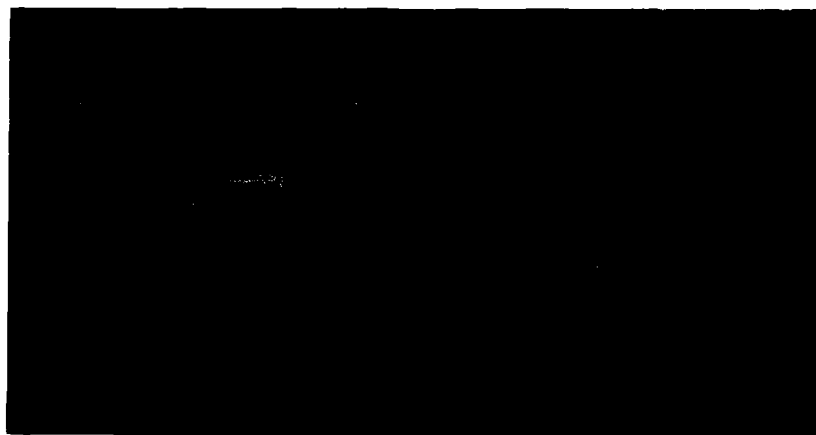
FIGURE (10a) PROPELLER INFLOW RETREATING BLADE  $\frac{V}{ND} = 0.56$ FIGURE (10b) PROPELLER INFLOW ADVANCING BLADE  $\frac{V}{ND} = 0.56$



FIGURE (11) FLOW STREAMLINES IN THE PROPELLER INTAKE PLANE,  $\frac{V}{ND} = 0.56$

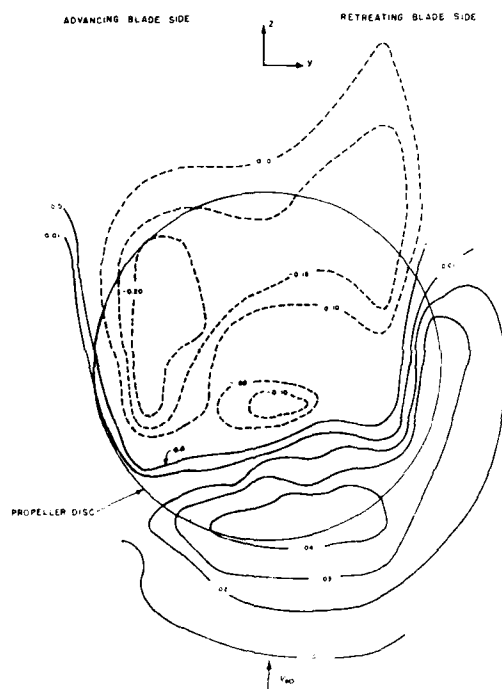


FIGURE (12) CONTOURS OF NORMAL INDUCED VELOCITY  $\frac{U}{R}$  in the propeller plane,  $\frac{V}{ND} = 0.56$



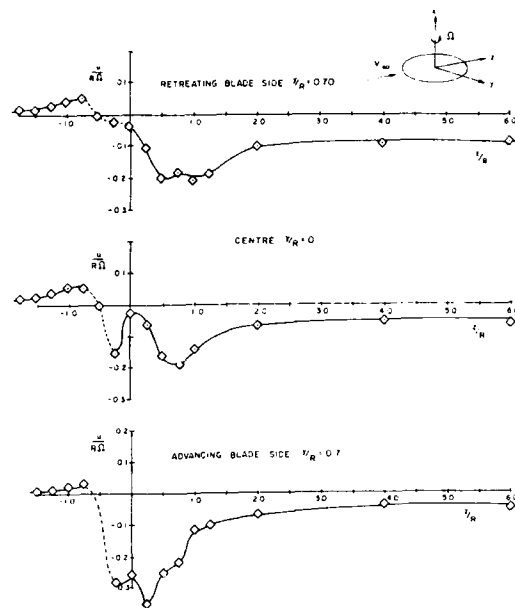


FIGURE (13) LONGITUDINAL VARIATION OF NORMAL INDUCED VELOCITY,  $\frac{V}{ND} = 0.56$

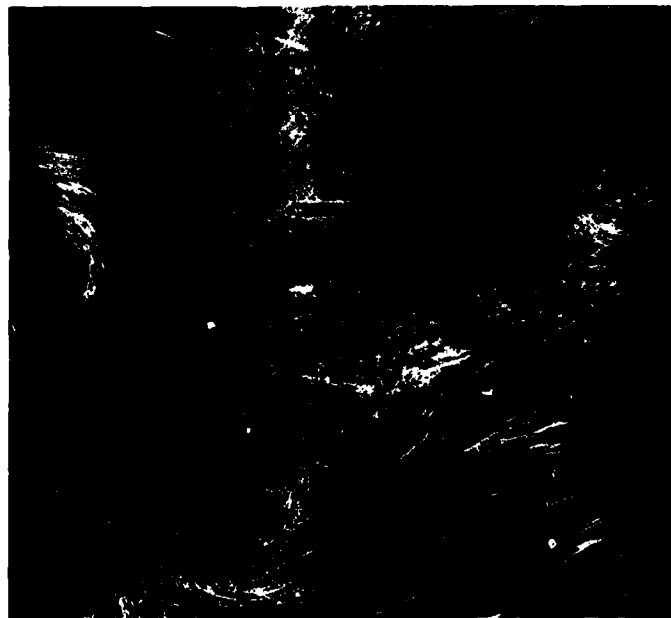


FIGURE (14) FLOW IN THE TRAILING WAKE, SHOWING THREE AREAS OF VORTICITY,  $\frac{V}{ND} = 0.56$

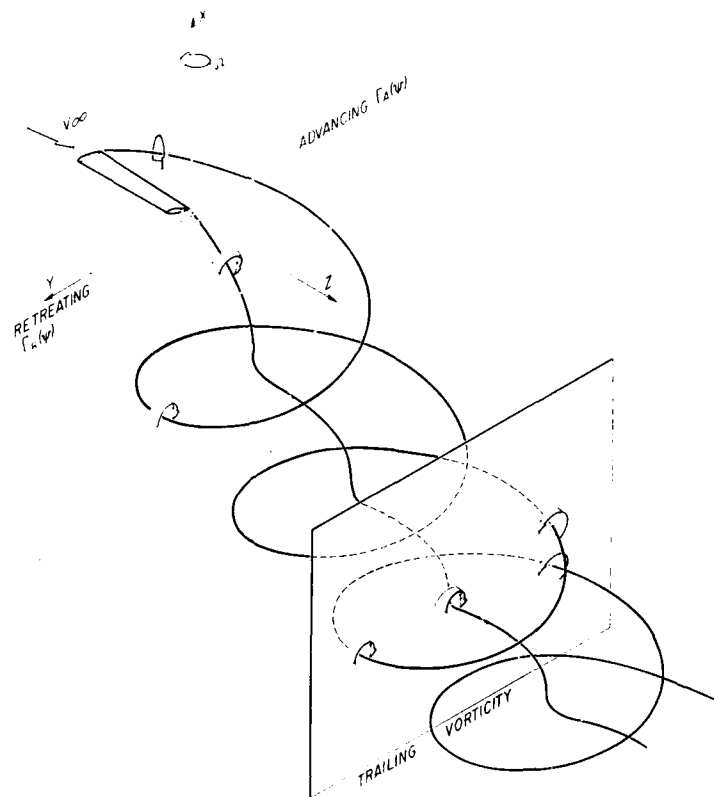


FIGURE (15) SCHEMATIC DRAWING OF THE WAKE FROM A SINGLE-BLADED PROPELLER

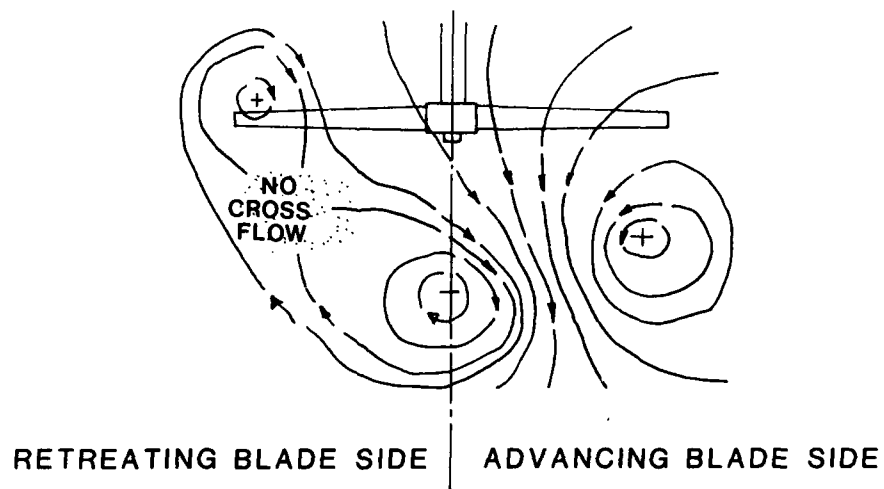
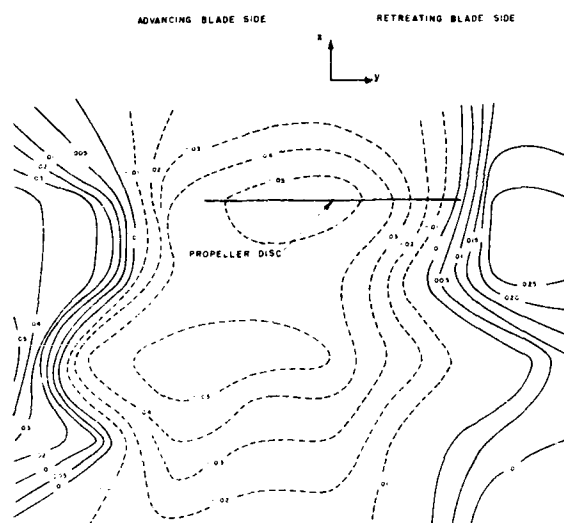


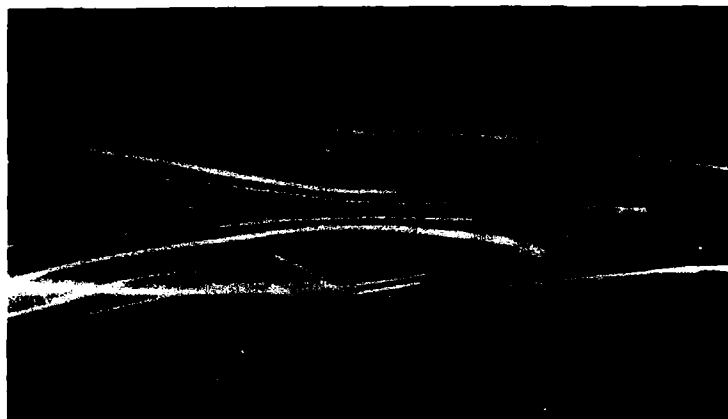
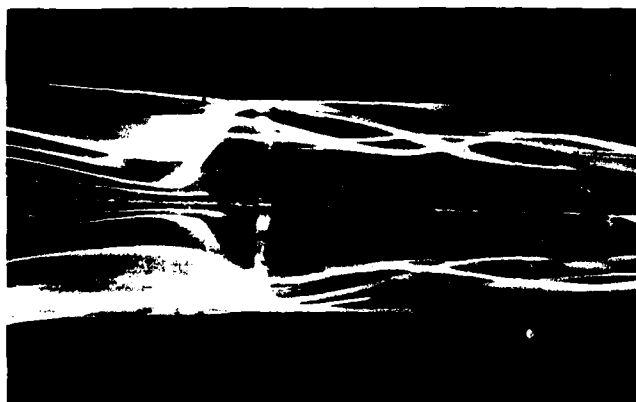
FIGURE (16a) THEORETICAL MODEL FOR THE VORTEX WAKE DOWNSTREAM OF A LIFTING PROPELLER



(16b) MEASURED DOWNWASH CONTOURS,  $\frac{V}{ND} = 0.56$



FIGURE (17) UPSWEPT FUSELAGE MODEL WITH VORTICES VISUALIZED BY DYE

 $\alpha_{FB} = 10$  DEGREES $\alpha_{FB} = 6$  DEGREES $\alpha_{FB} = 2$  DEGREESFIGURE (18) DEVELOPMENT OF THE TRAILING VORTEX WAKE ON THE BOTTOM OF THE FUSELAGE, ( $R_e = 5000$ )

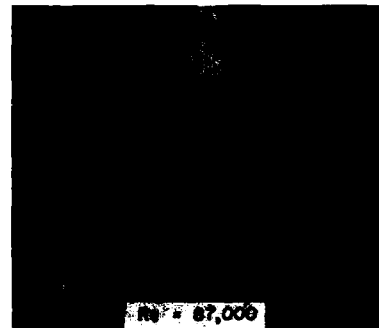
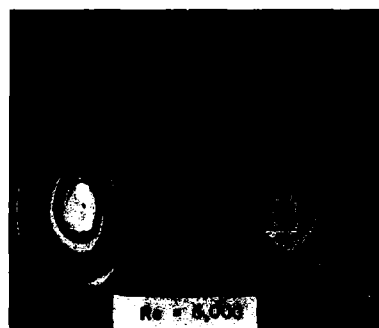
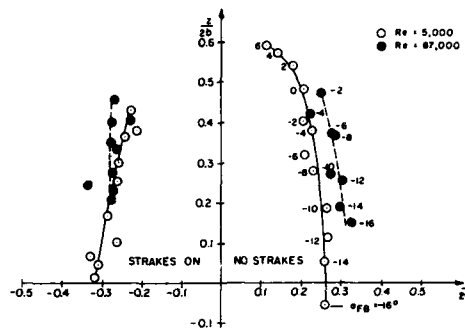
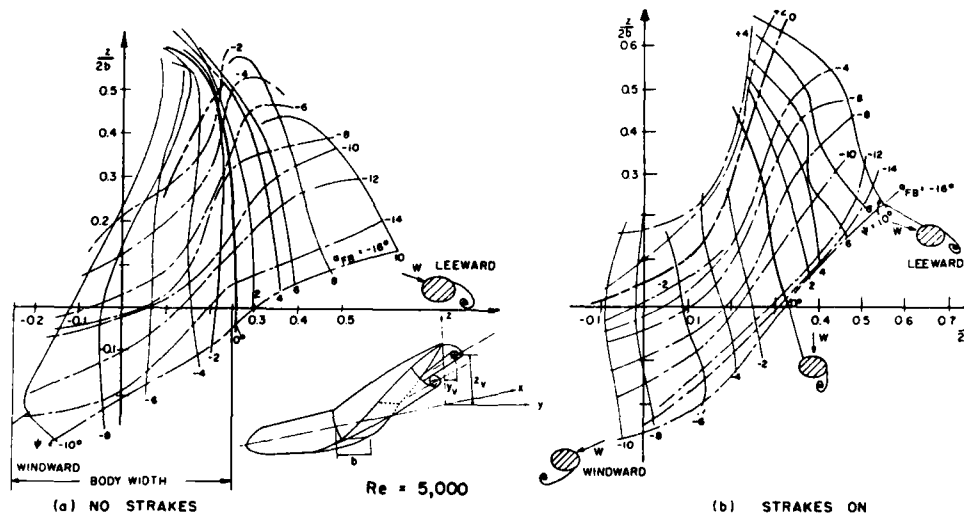
FIGURE (19) LOCATION OF VORTEX CENTRES IN THE FUSELAGE CROSS FLOW PLANE - YAW ANGLE =  $0^\circ$ 

FIGURE (20)

ENVELOPES OF THE MOTION OF A STARBOARD VORTEX DUE TO  
MODEL PITCH AND YAW

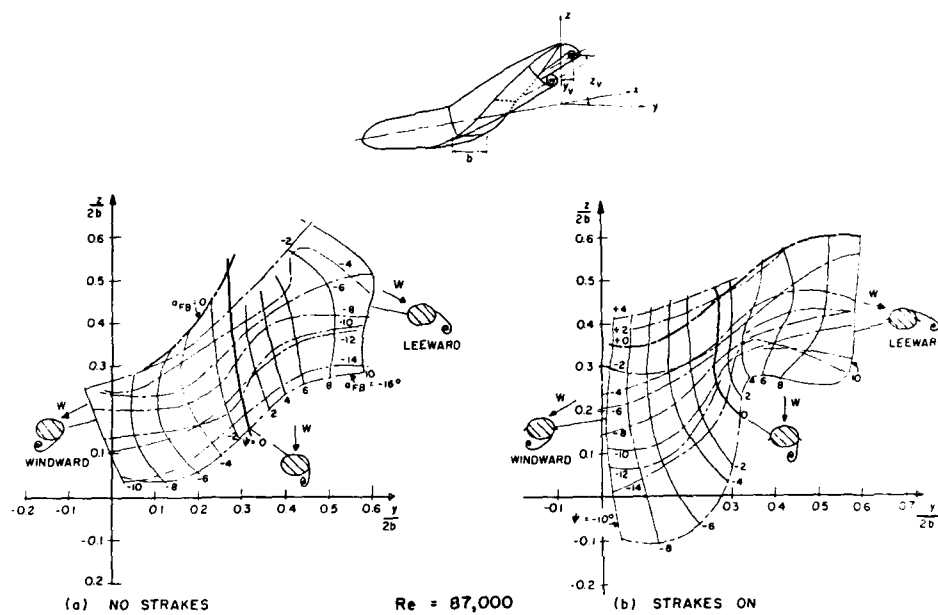
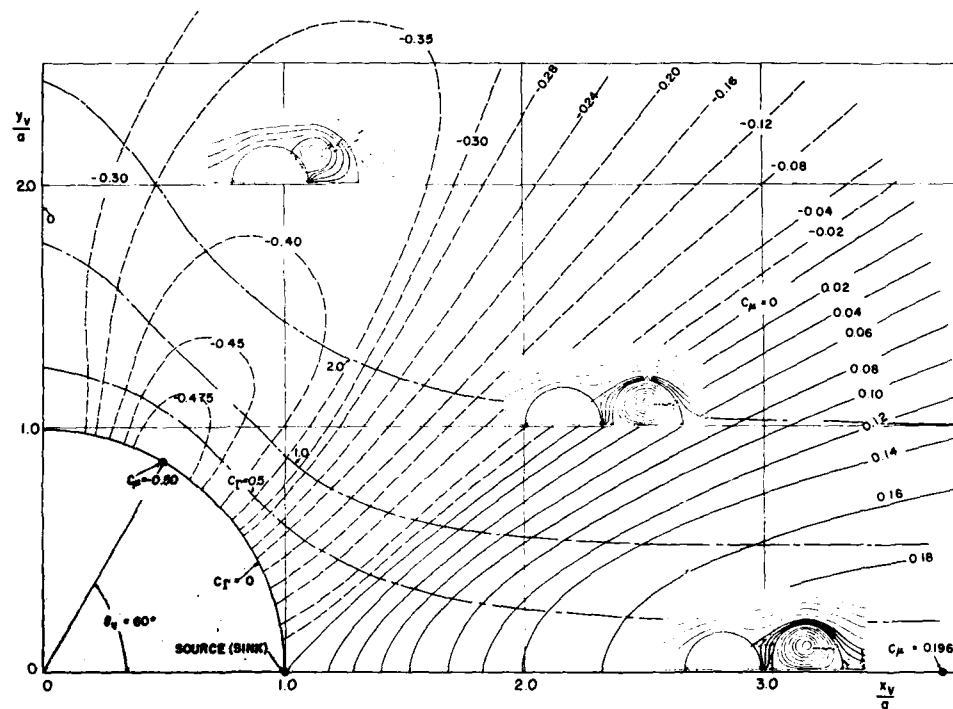


FIGURE (20)

ENVELOPES OF THE MOTION OF A STARBOARD VORTEX DUE TO  
MODEL PITCH AND YAW



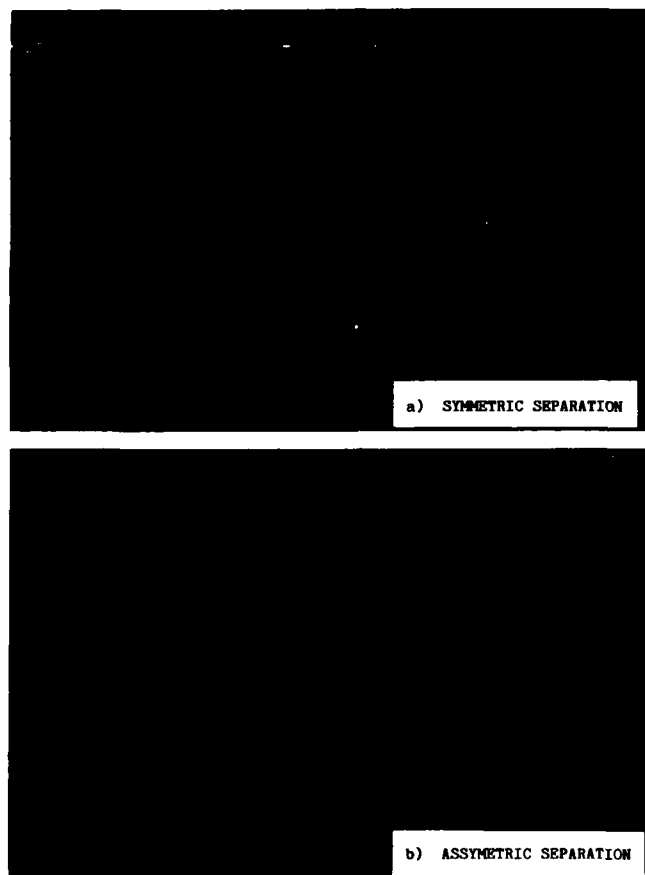


FIGURE (21) VORTEX SEPARATIONS FROM A SLENDER CONICAL WING-BODY CONFIGURATION

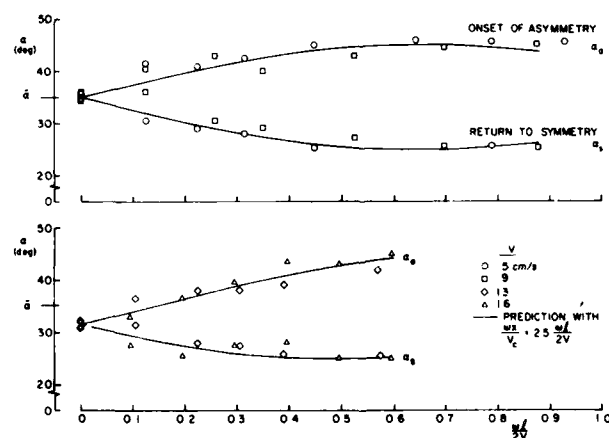


FIGURE (22) PHASE LAG ON MODEL OSCILLATING IN PITCH IN THE NAE WATER TUNNEL

## PRESENTATION D'UN BASSIN HYDRODYNAMIQUE

### ETUDE D'UN MISSILE AUX GRANDES INCIDENCES

par J. PERINELLE et A. LUPIERI  
S.A. MATRA Service Aérodynamique  
B.P. n° 1 78140 VELIZY (France)

### RESUME

Nous présentons, en premier lieu, le bassin hydrodynamique qui est une installation originale dans laquelle se font des essais en pesées et en visualisation d'écoulements sur des missiles en étude ou des recherches appliquées. Pour valider la technique d'essais, des comparaisons entre des résultats d'essais de soufflerie et du bassin hydrodynamique sont produites dans quelques cas caractéristiques. En visualisation, l'éclatement des tourbillons sur une aile delta en incidence fait aussi l'objet de recoupement avec des résultats fournis par d'autres constructeurs.

En second lieu, nous nous intéressons aux caractéristiques d'un missile en configuration partielle dans le domaine des grandes incidences, en subsonique. Deux aspects retiennent notre attention :

- tout d'abord l'apparition des phénomènes en latéral au delà d'une certaine incidence avec la corrélation essais pesées (soufflerie et bassin hydrodynamique) - visualisation d'écoulements,
- ensuite, faisant appel à des résultats d'essais en soufflerie, où une aile du missile est pesée en présence du fuselage et les trois autres ailes, nous faisons une nouvelle corrélation pesées - visualisation ; elle met en évidence la forte dépendance de la portance d'une aile, de sa position en roulis sur le missile.

### ABSTRACT

A presentation is made first of the water tank facility of MATRA in which measurements with a balance and visualizations are done to study the flows past missiles or perform other types of applied research. To assess the experimental techniques used, comparisons with wind tunnel results are shown for some typical situations. In term of visualizations, the phenomena of vortex breakdown on a delta wing at incidence is checked against other installation.

Secondly, the characteristics of a simplified missile configuration are considered in subsonic flow at large incidences. Emphasis is put on two aspects :

- the occurrence of side forces for angles of attack beyond a certain value, and how it is possible to correlate wind tunnel tests with the visualization of such flows,
- and, using wind tunnel data obtained with an instrumented model with a wing mounted on a balance in presence of the three other wings fixed to the body, a new correlation between measurements and visualization is made. It indicates the strong dependancy of the wing lift with its roll angle attitude on the missile.

### A - PRESENTATION D'UN BASSIN HYDRODYNAMIQUE

#### Historique

La première installation hydrodynamique que nous avons exploitée a été construite en 1967, époque à laquelle notre société s'est engagée dans la compétition automobile. Plusieurs équipes ont été sollicitées dans leur discipline pour participer au programme, parmi elles l'équipe aérodynamique. Nous n'avions pas ou peu d'expérience en ce domaine ; notre premier souci a été de définir un moyen d'étude pour répondre efficacement et dans les meilleurs délais à la demande qui nous était faite. C'est en grande partie sur un moyen expérimental que nous avons pensé appuyer les études de voiture. Le cas particulier des véhicules routiers a orienté notre choix sur les critères suivants :

- le moyen d'essais doit respecter les mouvements relatifs du véhicule par rapport au sol, avec la rotation des roues. S'agissant de véhicules très rapides, la sécurité, le comportement routier demandent une connaissance précise des charges ramenées aux trains avant et arrière : leur mesure doit se faire dans des conditions réalistes,



- possibilité de faire des visualisations spatiales d'écoulements, sans se limiter aux seules visualisations pariétales,
- pouvoir disposer d'un moyen d'essais autonome, de mise en oeuvre rapide, utilisant des maquettes à échelle réduite qui se prêtent à des modifications aisées, sur le site d'essais. L'aspect discrétion qui entoure généralement les essais d'automobiles doit être pris en compte.

La première installation - construction originale - était un bassin hydrodynamique constitué d'une cuve à eau de 10 mètres de long et de section carrée, 1 x 1 mètre à surface libre. La maquette du véhicule à étudier, maintenue rigidement par un dard - balance en montage aval, était déplacée ses roues en contact avec le sol en respectant la garde au sol et l'assiette nominales. Les mouvements relatifs décrits ci-dessus étaient correctement respectés : fluide au repos, sol immobile, déplacement de la maquette avec rotation de ses roues en contact avec le sol.

Il est apparu par la suite que l'installation pouvait être aussi utilisée dans des applications plus centrées sur nos activités traditionnelles, c'est-à-dire l'étude des missiles et armements conventionnels. Son intérêt général confirmé, elle connût par la suite de nombreuses évolutions et améliorations.

Une autre installation a remplacé la première en 1979 à l'occasion d'un déplacement géographique du laboratoire. L'expérience acquise a été répercutée dans la conception de ce nouveau bassin mieux adapté pour répondre aux besoins qui avaient évolué. Aujourd'hui, c'est un banc d'essais à caractère industriel ; la plupart des travaux qui s'y déroulent sont des essais sur des produits en projet ou en développement. Nous y faisons des études de recherche appliquée d'intérêt général pour l'ensemble de l'aérodynamique des missiles. Ces activités viennent en complément aux essais en soufflerie. Les résultats représentent le domaine incompressible.

#### DESCRIPTION DU BASSIN HYDRODYNAMIQUE (Fig. n° 1, planche 1)

Le bassin est une cuve à surface libre dans laquelle l'eau est au repos, c'est la maquette à étudier qui se déplace maintenue dans son attitude d'essai sous un chariot aérien.

Les dimensions intérieures de la cuve sont 12 mètres pour la longueur, 1 mètre pour la largeur et 1,2 mètre pour la profondeur. Les deux extrémités et une surface latérale sont vitrées pour l'observation visuelle, l'éclairage et la prise de vues au cours de visualisations. L'axe longitudinal de la cuve est à hauteur d'yeux. L'eau provient d'alimentation générale ; elle est à la température ambiante du bâtiment. Une station de filtrage autonome donne à l'eau une limpidité propice à l'observation tout en limitant dans le temps les développements de mousses sur les parois. Elle peut être stockée plusieurs mois entre deux vidanges.

Les équipements rentrent dans deux catégories distinctes selon leur utilisation pour les essais de pesées ou les essais de visualisation.

#### 1 - Les équipements pour les pesées

##### 1.1. Le chariot

C'est un chariot aérien coulissant sur deux glissières sur toute la longueur du bassin qui maintient la maquette dans l'eau dans son attitude d'essai. Le chariot est une plateforme très rigide qui peut être considérée comme indéformable sous les charges hydrodynamiques qui apparaissent sur la maquette pendant son déplacement. Le guidage en translation est particulièrement soigné, avec jeu réduit exempt de vibration. C'est un moteur-réducteur, à une extrémité du bassin, qui met en mouvement le chariot par l'intermédiaire d'une courroie crantée.

En marche avant, la vitesse est asservie : partant de l'arrêt, le chariot est uniformément accéléré jusqu'à la vitesse nominale d'essai ; elle est maintenue constante sur une distance de 6 à 7 mètres, plage sur laquelle se fait l'acquisition des mesures ; au-delà le chariot est uniformément décéléré jusqu'à l'arrêt. En marche arrière pour revenir au point de départ, la vitesse est réduite ; c'est un déplacement qui ramène le chariot à l'extrémité du bassin avant d'engager l'essai suivant.

##### 1.2. Le dispositif de mise en incidence

Sur le chariot, prend place un dispositif de réglage de l'attitude maquette : par deux mouvements combinés - une rotation et une translation - il règle l'incidence de la maquette et la maintient sensiblement sur l'axe de la cuve à égale distance du fond et de la surface libre. L'incidence apparaît dans le plan vertical. La maquette est tenue au culot par un dard - balance selon un montage classique de soufflerie. Entre le bras plongeur, sous le chariot et le dard balance s'intercale un dispositif de mise en roulis (rotation de la maquette autour de son axe). Les trois degrés de liberté décrits ci-dessus sont motorisés avec télécommande ; les deux rotations - incidence et roulis - sont mesurées par des capteurs avec relecture sur la baie de mesure. Ainsi, l'opérateur a, en essais, à partir des dispositifs embarqués sur le chariot aérien les moyens pour régler en télécommande l'incidence, le roulis de la maquette et sa position sensiblement axiale dans la cuve avec l'affichage numérique des valeurs d'angles à la baie de servitude.

##### 1.3. Les capteurs

Les balances - dard de mesures à jauges de contrainte sont monobloc et multicomposantes (4, 5 ou 6 composantes). La structure adoptée leur confère à la fois une grande sensibilité et une bonne rigidité. Leurs capacités de mesure sont adaptées au domaine d'efforts et de moments rencontrés en essais compte-tenu de la pression dynamique de la taille des maquettes et leurs coefficients aérodynamiques. Il y a intérêt à diminuer le poids des maquettes de façon à ce que celui-ci reste faible vis-à-vis des efforts aérodynamiques. La mesure des coefficients de traînée et de roulis pose quelquefois des difficultés liées au faible niveau des efforts et moments correspondants comparés aux quatre autres composantes. La qualité des étalonnages de balance - particulièrement la connaissance des termes d'interaction - a une répercussion immédiate sur la précision de ces deux coefficients. C'est un point qui a longtemps retenu notre attention

avant de pouvoir obtenir des résultats jugés fiables et précis. Une autre difficulté consiste à rendre étanche la balance qui séjourne dans l'eau pendant de longues périodes d'essais.

#### 1.4. La chaîne de mesure et les servitudes

L'ensemble des commandes, servitudes et la chaîne de mesure sont regroupés dans une double-baie avec un pupitre de mise en oeuvre, du chariot et des télécommandes de réglage de l'attitude maquette.

La chaîne, pilotée par un calculateur - contrôleur, comporte huit voies de mesures constituées de conditionneurs - amplificateurs. Un convertisseur assure le passage de l'analogique au numérique, chaque voie lui étant successivement connectée par un multiplexeur. En essais, pendant la phase d'acquisition, toutes les données sont recueillies en mémoire pour un traitement ultérieur qui débute dès la fin de l'acquisition. Les lectures d'incidence, angle de roulis et indication d'un chronomètre, sont faites sur des entrées particulières sur le calculateur. La pression dynamique est calculée à partir de la vitesse moyenne du chariot, elle-même se déduisant par chronométrage du temps de passage du chariot entre deux points.

#### 2 - Les équipements pour les visualisations

Un deuxième chariot aérien semblable au premier dans sa conception et utilisant le même chemin de glissement constitue une plateforme sur laquelle on embarque tous les matériels nécessaires aux essais de visualisation :

- générateurs de lumière (projecteur, projecteur à fente, flash, ...)
- générateurs de micro-bulles,
- matériel de prise de vues (appareil photographique, caméra cinéma, caméra vidéo ...)

Plusieurs montages pour la fixation des matériels sont disponibles sur la plateforme, soit à la partie supérieure du bassin (éclairage, générateur de micro-bulles), soit sur le côté vitré de la cuve (appareil photographique, caméras, ...). Les degrés de liberté pour régler ces matériels par rapport à la maquette d'étude, sont assurés par ces montages.

Le projecteur à fente est un matériel standard, légèrement adapté à notre besoin. Il éclaire en lumière blanche selon une tranche dont la largeur est de 60 cm et l'épaisseur de 1 cm environ. Grâce à un système optique, l'intensité lumineuse, dans la zone éclairée, est élevée avec des frontières franches, sans zone de pénombre.

#### 3 - Les maquettes d'essais

Leur taille est choisie en prenant en compte plusieurs contraintes :

- le domaine d'incidence à couvrir. Dans le cas d'essais aux grandes incidences, jusqu'à  $\alpha \leq 90^\circ$  il faut éviter de s'approcher soit du fond, soit de la surface libre d'où une limitation de la longueur maximum de la maquette. Mais c'est aussi l'envergure qui peut donner la taille de la maquette pour éviter que les extrémités d'ailes s'approchent des parois latérales.
- les capacités de mesure des balances disponibles. La taille de la maquette doit rester telle que les efforts et moments à mesurer soient à l'intérieur du domaine d'utilisation de la balance.
- l'obstruction doit rester faible pour pouvoir considérer que la maquette est en champ infini.

L'ensemble de ces contraintes est tel qu'en général les maquettes de missile ont une longueur d'environ 0,60 m pour un calibre de 0,03 à 0,04 m.

Les efforts et moments à mesurer sont suffisamment faibles pour pouvoir adopter des techniques de construction simplifiées plus économiques que celles des maquettes de soufflerie, avec des durées de fabrication plus réduites. Par exemple, les surfaces de contrôle (gouvernes, volets, ...) ont un axe lisse, pour s'encasturer dans le corps, maintenues en position braquée par une vis pointeau. Les réalisations sont de qualité, chaque élément de la maquette est une représentation fidèle de l'élément correspondant du missile. C'est une condition pour que les résultats d'essais représentent correctement l'aérodynamique étudiée. C'est aussi l'assurance de résultats répétitifs quand un essai est repris plusieurs fois au cours de campagnes successives dans le temps.

Les matériaux sont des alliages légers (facilité d'usinage, poids des maquettes réduit). De nombreuses maquettes de soufflerie ont une taille telle qu'elles se prêtent très bien à un montage au bassin. Il est fréquent que des essais soient faits au bassin ou en soufflerie avec les mêmes maquettes ; c'est une situation intéressante ne serait-ce que sous l'aspect des recoupements entre plusieurs essais en limitant les sources d'imperfections.

#### 4 - Domaine d'essais en pesées et technique de mesure

##### 4.1. Domaine de vitesse

La vitesse du chariot aérien - vitesse stabilisée pendant les acquisitions de mesure - est réglable entre  $V = 0$  m/sec. à 1,80 m/sec., c'est-à-dire, traduite en pression dynamique  $q \sim 1600$  pa. La vitesse usuelle retenue pour les pesées est de l'ordre de 1,3 m/sec. soit  $q \sim 850$  pa. Le nombre de Reynolds à la température de  $20^\circ\text{C}$  calculé sur une longueur de 1 mètre est  $Re \sim 1,25.10^6$ , soit, sur la longueur de référence moyenne  $l_{\text{réf}} = 0,035$  m,  $Re \sim 0,5.10^5$ .

##### 4.2. Domaine d'incidence

Le dispositif de réglage d'attitude de la maquette sur le chariot aérien a un débattement en incidence de l'ordre de  $45^\circ$ . En insérant des pièces intermédiaires dans la ligne de dard on décrit, en deux fois, la plage d'incidence -  $2^\circ \leq \alpha \leq 90^\circ$ .

4.3. Roulis

Le dispositif de roulis permet toutes les positions  $0 \leq \theta \leq 360^\circ + 2\pi$

Le dérapage est une combinaison de l'incidence et du roulis. Il est aussi possible de faire apparaître du dérapage par rotation autour d'un axe vertical du dispositif de réglage d'attitude de la maquette. La première technique s'applique davantage aux missiles, la seconde aux véhicules en présence du sol.

Un essai se déroule selon le schéma suivant :

- la maquette immergée est dans la configuration du point de mesure à faire :

- . braquage des gouvernes, volets ...
- . incidence du point de mesure,
- . position en roulis

- le chariot est à l'extrémité du bassin.

- les "zéros" de la balance sont enregistrés et mis en mémoire. Ils représentent les indications des ponts de mesure de la balance en l'absence d'efforts aérodynamiques et traduisent les "zéros" électriques et les poids morts des balance et maquette dans la configuration d'essais. Ensuite le chariot se déplace d'une extrémité à l'autre du bassin avec acquisition de points de mesure sur toutes les voies pendant la course à vitesse constante. La chaîne de mesure prend approximativement 100 points par seconde. En fin d'acquisition, c'est 500 points de mesure environ qu'il faut traiter pour élaborer les coefficients aérodynamiques de la configuration d'essais. Soulignons qu'au cours d'un passage, tous les paramètres d'essais sont figés : les braquages, l'incidence, le roulis ... sont constants. C'est dire qu'une polaire établie en 20 points s'obtient après 20 passages successifs différents au cours desquels on aura fait varier le paramètre d'essais.

5 - La technique de visualisation

Retenons ici la méthode de visualisation qui a fait l'objet de travaux de mise au point les plus importants. Elle consiste à ensémençer l'eau de micro-bulles d'hydrogène par électrolyse soit immédiatement en amont de la maquette, soit à partir de la maquette même. Ce sont des fils d'acier de 0,08 mm de diamètre mis sous une tension électrique de 60 volts, qui génèrent les bulles. Un fil tendu, déplacé dans l'eau à faible vitesse ( $V \sim 0,20$  m/sec.) dégage derrière lui un plan ou rideau de bulles dont le diamètre ( $\sim 0,05$  mm) est suffisamment faible pour pouvoir considérer leur mouvement ascensionnel négligeable vis à vis du mouvement de translation de la maquette. La déformation du rideau de bulles par le champ aérodynamique de la maquette donne une visualisation des écoulements. Comme les phénomènes sont tridimensionnels, l'utilisation d'un éclairage annexe particulier simplifie la compréhension en isolant de l'ensemble ce qui se passe dans une tranche d'écoulement : le laboratoire est plongé dans l'obscurité ; on éclaire localement la maquette à l'aide d'un projecteur à fente muni d'une optique dans la direction moyenne du plan dans lequel la visualisation est souhaitée. Toutes les bulles en dehors de la tranche éclairée sont invisibles ; seules celles dans le champ du projecteur apparaissent très clairement. Si l'ensemble maquette - projecteur - générateur de bulles est déplacé simultanément, l'observateur voit, dans l'espace éclairé, les bulles qui, par mémoire rétinienne, lui apparaissent sous forme de trajectoires lumineuses selon les lignes de courant : les bulles jouent le rôle de traceur dans l'écoulement. Si la tranche éclairée est perpendiculaire à l'axe de la maquette, l'observation par l'arrière permet de voir les développements tourbillonnaires d'extrados. Si elle est parallèle à l'axe, sur un profil d'aile, il est possible de visualiser des décollements d'extrados, etc .... A l'œil de l'observateur, peuvent se substituer un appareil photographique, une caméra cinéma, une caméra vidéo, etc ... pour enregistrement des images.

6 - Validation des résultats de pesées

Les essais de pesées constituent l'activité principale du bassin hydrodynamique ; il faut y voir une conséquence de la mise en oeuvre rapide de l'installation allée à un coût de fabrication maquette et d'exécution d'essais modique. Nous rappelons que le bassin est utilisé pour des travaux sur des produits en projet ou développement et en recherche appliquée, en amont par rapport aux essais en soufflerie. C'est au bassin qu'ont lieu les validations subsoniques des configurations issues du calcul et que sont obtenues les premières caractéristiques aérodynamiques réalistes utilisables en simulation. Il est essentiel que ces résultats représentent correctement les caractéristiques du missile ; c'est à cette condition que le bassin est utilisable en tant que moyen d'essais. L'aspect recoupement entre essais bassin - soufflerie dès que possible est un souci permanent au même titre que celui de faire des comparaisons entre souffleries, campagnes, maquettes, etc ...

Plusieurs cas de comparaisons figurent ci-dessous :

6.1. Le premier est relatif à une configuration de missile à ailes de faible allongement ( $\lambda \sim 0,24$ ) (figures n° 2 à 4).

Le nombre de Mach des essais en soufflerie est  $M = 0,90$  ; le nombre de Reynolds, calculé sur la longueur de référence du missile, est  $Re \sim 0,25.10^6$ . Au bassin hydrodynamique, la vitesse est  $V = 12$  m/sec. et le nombre de Reynolds  $Re \sim 0,4.10^5$ . C'est la même maquette qui est utilisée dans les deux cas. Nos comparaisons portent sur les coefficients de force normale  $C_N$  et de moment de tangage  $C_m$  pour des incidences allant jusqu'à  $40^\circ$  en soufflerie,  $90^\circ$  au bassin hydrodynamique. La figure n° 3 fait apparaître des écarts de portance au delà de  $25^\circ$  d'incidence qui atteignent approximativement 6 % à  $40^\circ$ .

En moment de tangage, les divergences sont plus importantes dans la zone centrée sur l'incidence de  $30^\circ$  mais nous constatons deux points :

- les recoupements sont corrects autour de l'origine (incidence nulle),
- les allures des courbes sont les mêmes en fonction de l'incidence.

Pour justifier ces écarts, il faut évoquer la différence de nombre de Mach (domaine incompressible au bassin hydrodynamique, domaine transsonique en soufflerie) d'autant plus sensible que les caractéristiques sont mesurées aux grandes incidences.

6.2. Le deuxième cas de comparaison concerne une configuration de missile canard, qui a la particularité, en subsonique - transsonique, de saturer précocement en portance au niveau de l'aile ( $\alpha$  sat.  $\sim 15^\circ$ ) (fig. n° 5 à 7).

Les conditions de soufflerie se résument à :

nombre de Mach = 0,7  
nombre de Reynolds  $Re = 2.10^5$  calculé sur la longueur de référence

Pour le bassin hydrodynamique :

nombre de Reynolds  $Re = 0,33.10^5$

La maquette est commune aux deux essais.

Tout comme précédemment, dans le domaine d'incidence exploré, les écarts de portance restent modérés avec un niveau maximum de 10 % dans la zone de saturation de l'aile ; de part et d'autre, la concordance des résultats est très bonne.

Les moments de tangage accentuent les écarts ci-dessus par le bras de levier de l'aile et la comparaison des résultats est moins satisfaisante au delà de la saturation ; visiblement il y a divergence des comportements qui laissent supposer un fonctionnement aérodynamique différent de l'aile dans les deux moyens d'essais après saturation.

C'est dans ces situations, où le nombre de Reynolds prend plus d'importance que les différences se font jour ; des tentatives de déclenchement de transition couche limite ont été faites ; elles connaissent plus ou moins de succès selon les cas. Signalons les excellents résultats obtenus sur un profil épais NACA où le déclenchement par fil sur le bord d'attaque a permis de retrouver les caractéristiques connues du profil, notamment au voisinage de la saturation. Sur des profils minces, symétriques, l'efficacité du déclenchement est moins certaine ; en tout cas, elle n'améliore pas de façon évidente les caractéristiques mesurées au bassin.

6.3. Le troisième cas est celui de la traînée d'une sphère de diamètre  $\emptyset$  200 mm (planche n° 4, fig. n° 8) tracée en fonction du nombre de Reynolds. SF. HOERNER dans son ouvrage "Résistance à l'avancement dans les fluides" (Fluid dynamic drag) signalait que les vitesses critiques dans l'eau sont, d'une façon générale, inférieures à celles dans l'air ; sans pouvoir justifier ce résultat par une loi physique et s'appuyant sur diverses expérimentations, il arrivait à la conclusion prudente que le nombre de Reynolds critique  $R'$  dans l'eau peut être approximativement moitié de celui dans l'air. Or, nous arrivons pratiquement à cette même conclusion puisque nous situons sur la courbe de la fig. 8 le Reynolds critique à  $R' \sim 2.2.10^5$ .

6.4. Le dernier cas de comparaison est celui obtenu au cours d'essais de visualisation pour déterminer le point d'éclatement des tourbillons sur une aile delta mince, en fonction de l'incidence.

La fig. n° 9, planche n° 4, regroupe les résultats de NORTHROP, de l'ONERA et ceux que nous avons obtenus avec les nombres de Reynolds correspondants. On remarquera la cohérence de tous ces résultats. La planche n° 5 est un recouplement de photos de visualisation à la base du recouplement sur les éclatements de tourbillons.

## B - ETUDE D'UN MISSILE AUX GRANDES INCIDENCES

### 1 - Introduction

Nous proposons ci-dessous des résultats d'une étude faite en parallèle en soufflerie et au bassin hydrodynamique sous le double aspect pesées et visualisation d'écoulements.

Le choix de la configuration du missile répond aux critères suivants :

- les possibilités d'emports simultanés sous avion de matériels de plus en plus nombreux, le respect des gabarits de sécurité restreignent les dimensions transversales des voilures. Pour les missiles stockés et tirés à partir d'un container, les problèmes d'encombrement se posent aussi et la tendance générale constatée est une diminution des envergures des missiles avec éventuellement un allongement des fuselages.
- les performances souhaitées en facteur de charge sont plus élevées et dans deux parties du domaine de vol, ce facteur de charge est difficile à réaliser. C'est tout d'abord le domaine des hautes altitudes, en vol supersonique où l'interception d'une cible rapide et faiblement manoeuvrante requiert, du fait du faible niveau de la pression dynamique, des coefficients de portance élevés. C'est ensuite le vol à faible vitesse, basse altitude, conditions rencontrées au moment du tir d'un missile. C'est le cas des missiles sol-air, tirés verticalement à partir d'un puits et qui doivent très vite relater l'horizontale, à basse altitude, en direction de la cible. Dans ce cas on trouve aussi les missiles air-air de combat rapproché ; dès les premiers instants du vol, ils doivent faire une rotation rapide à leur vecteur vitesse dans la direction du futur point d'interception. C'est la phase de vol appelée couramment "basculement". La faible pression dynamique due à la vitesse est à compenser par des coefficients de portance élevés.

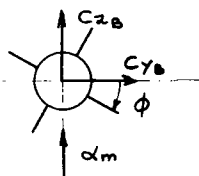
Les limitations en envergures évoquées plus haut sont telles que les caractéristiques de portance linéaire ne peuvent pas assurer, dans le domaine d'incidence usuel, les coefficients de portance attendus. Il faut alors envisager d'autres solutions à savoir utiliser les caractéristiques non-linéaires des fuselages et surfaces portantes en les amenant dans le domaine des grandes incidences où ces caractéristiques sont très développées.

L'ensemble ailes + fuselage cruciforme symétrique proposé ici satisfait les critères énoncés. En le complétant avec des gouvernes appropriées, nous obtiendrions un missile capable d'évoluer à des incidences de l'ordre de  $40^\circ$  à  $45^\circ$ . Comme de nombreuses études l'ont montré ces dernières années, dans le domaine des grandes incidences et basses vitesses (de  $M = 0$  jusqu'au transsonique), apparaissent des efforts et moments en latéral et en roulis ; quoique bien identifiés, ils sont difficiles à prévoir, en signe et amplitude, ainsi que la gamme d'incidence où ils se manifestent. Les configurations à comportement non-linéaire sont particulièrement sensibles à ces phénomènes pour plusieurs raisons. La première tient au fait que la majeure partie de la portance est d'origine tourbillonnaire ; elle se développe à l'extrados du fuselage, des ailes, ... Nous estimons, pour des configurations proches de celle étudiée ici, qu'elle représente environ 80 % de la portance totale à  $\alpha \sim 40^\circ$ . Quand le système de tourbillons devient dissymétrique, voire instable au delà d'une certaine incidence, ce sont des variations d'efforts et moments importants qui sont mises en jeu ; dans les pesées globales de maquette, l'apparition de dissymétries de tourbillons s'accompagne de l'apparition de coefficients  $C_y$ ,  $C_n$  et  $C_l$ .

En second lieu, les dimensions transversales réduites vis-à-vis des cordes d'aile et longueur totale du corps, font que chaque point du missile est concerné par les dissymétries dont les effets s'intègrent sur des surfaces importantes.

## 2 - Résultats de pesées

Les cinq coefficients du missile (pas de mesure de la traînée) sont tracés planche n° 6 dans un trièdre mixte dit "pseudo-lilienthal" ; c'est un trièdre qui suit le missile en incidence mais pas en roulis.



Missile vu de l'arrière

L'incidence  $\alpha_m$  - angle entre le vecteur vitesse infinie amont et l'axe du missile - est représentée par la composante transversale de la vitesse. L'angle  $\theta$  caractérise la position en roulis de la maquette. Trois positions sont explorées :  $\theta = 0^\circ$ ,  $22,5^\circ$ ,  $45^\circ$ . A  $\theta = 0^\circ$  une paire d'ailes est dans le plan défini par le vecteur vitesse et l'axe missile, l'autre lui étant orthogonale.

La première constatation faite à propos du coefficient de portance se rapporte à l'influence de l'angle de roulis sur le niveau du coefficient en fonction de l'incidence ; dès  $\alpha \sim 10^\circ$ , les trois caractéristiques se séparent nettement et, vers  $40^\circ$  d'incidence, il y a un rapport voisin de 2 entre les valeurs extrêmes. On peut noter l'allure pratiquement linéaire de la courbe à  $\theta = 0^\circ$  pour  $20^\circ \leq \alpha \leq 40^\circ$ . Ce comportement est moins évident pour les deux autres angles de roulis ; sur les trois courbes, il y a absence d'accident, comme il s'en trouve sur les autres coefficients.

Les coefficients de moment de tangage dont le signe positif traduit l'instabilité du missile sans ses gouvernes, sont déjà moins faciles à qualifier ; selon la gamme d'incidence, le comportement en roulis est différent : il semble qu'aux incidences les plus fortes, il y ait tendance à destabilisation pour  $\theta = 22,5^\circ$  et  $45^\circ$  par rapport à  $\theta = 0^\circ$ . La confrontation des coefficients de portance et moment avec l'évolution en roulis indique que les pertes de portance se situent vers l'arrière du missile.

Les coefficients en latéral  $C_y$ ,  $C_n$  et en roulis  $C_l$  à  $\theta = 22,5^\circ$ , avec une valeur bien définie dès les faibles incidences, sont dus aux non-linéarités du missile ; dans cette position non symétrique par rapport à la vitesse il y a une composante transversale aux efforts et moments sur le missile. Par contre, à  $\theta = 0^\circ$  et  $45^\circ$ , positions symétriques par rapport à la vitesse, les coefficients qui apparaissent au delà de  $\alpha \sim 30^\circ$  ont une signification moins évidente : les évolutions en incidence sont à variation très rapide, avec éventuellement changement de signe tandis que les points extrêmes atteignent des amplitudes qui représentent une fraction non négligeable des termes correspondants en tangage. Il se dégage de cette observation un caractère erratique accentué par la dispersion des résultats quand un même point de mesure est refait plusieurs fois consécutivement pour recouplement.

## 3 - Visualisation d'écoulements le long du missile

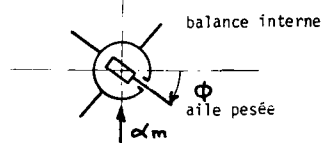
La première série de photos représente les écoulements autour du missile dans douze sections numérotées de 1 à 12 à partir de l'avant (fig. 13, planche n° 7). Les cinq premières sections sont sur le corps en amont des ailes, les sept suivantes sur les ailes avec une concentration au voisinage de l'avant de l'aile. La série de visualisations est faite à l'incidence  $\alpha = 30^\circ$  à un angle de roulis  $\theta = 0^\circ$ . Les essais de pesées et de visualisation ne sont pas simultanés d'où l'éventuelle difficulté à corréler correctement les pesées avec les visualisations, spécialement si on veut relier une dissymétrie d'écoulement au sens de variation des coefficients sensibles.

Les différentes vues des planches n° 7 et 8 montrent les tourbillons d'ogive dès leur naissance à l'avant, leur développement sur le corps cylindrique et l'apparition du bord d'attaque des ailes en section 6. En section 7, les tourbillons d'extrémité d'ailes commencent à se développer ; jusqu'en section 10, ils coexistent avec les tourbillons d'ogive qu'ils absorbent peu à peu et ces derniers ont

perdu leur identité en section 11. On peut dire que jusqu'à cette abscisse, la symétrie d'ensemble paraît conservée ; ce n'est plus vrai en section 12 où les noyaux des tourbillons occupent des positions dissymétriques par rapport au plan d'aile vertical. A posteriori, on peut s'interroger sur la réalité de la symétrie en section 11 où un léger glissement des tourbillons est perceptible. Il est probable que cette configuration d'écoulement s'accompagne, en pesée, d'efforts et moments parasites en latéral - roulis.

Les comparaisons entre les données quantitatives issues des pesées et les schémas d'écoulements sont certes très instructives et facilitent l'interprétation des phénomènes en latéral en configuration symétrique, mais il est clair que la seule pesée globale du missile est une information d'exploitation limitée. La compréhension dans le détail de toutes les implications des dissymétries d'écoulement demande au minimum une décomposition sur le missile des efforts et moments, élément par élément pour affecter à l'ogive, au corps, à chacune des quatre ailes leur participation respective aux caractéristiques aérodynamiques. Ce qui se passe en tangage, dans le même temps, retient aussi notre attention même si les caractéristiques globales du missile en portance et moment de tangage sont beaucoup moins sensibles que les autres composantes.

Pour aller plus avant dans l'étude, faisons appel à d'autres résultats acquis en soufflerie ; la maquette est identique en définition géométrique à celle des essais au bassin hydrodynamique ; mais au lieu d'une pesée globale, nous avons cette fois une balance interne, dans le fuselage de la maquette, pour mesurer les caractéristiques d'une aile en présence des trois autres ailes et du fuselage :



Le programme de soufflerie prévoit des évolutions en incidence ( $0^\circ \leq \alpha_m \leq 45^\circ$ ) de la maquette pour des angles de roulis donnés et des évolutions en roulis ( $0 \leq \theta \leq 360^\circ$ ) pour des incidences données. Le réseau de courbes disponible est tel qu'avec une seule aile pesée, on peut reconstituer la portance de chacune des quatre ailes dans tout le domaine ( $\alpha_m, \theta$ ) exploré.

Les conditions de soufflerie sont :

nombre de Mach  $M = 0,70$   
nombre de Reynolds  $Re = 1,1.10^6$

#### 4 - Corrélation entre les visualisations et les pesées d'ailes et de missile

La section d'observation d'écoulement est unique : c'est la section 11 et seul un nombre très restreint de visualisations en incidence est fourni. Nous retenons trois cas typiques en roulis :  $\theta = 0^\circ$ ,  $22,5^\circ$  et  $45^\circ$ .

##### 4.1. Etude à roulis nul - $\theta = 0^\circ$

Sur la planche n° 9, figurent deux visualisations à l'incidence  $\alpha = 30^\circ$  (déjà produite précédemment) et  $\alpha = 45^\circ$ . Sur cette dernière, la dissymétrie d'écoulement est particulièrement visible et un troisième tourbillon apparaît au-dessus de deux précédents. L'ensemble de l'écoulement extrados qui, loin de la maquette à la partie supérieure, gardait une symétrie à  $\alpha = 30^\circ$ , cette fois est entièrement déformé.

Reportons-nous aux pesées d'ailes, fig. n° 18. Les portances des quatre ailes sont tracées en fonction de  $\alpha$ , la flèche sur chaque aile indiquant le sens des portances positives.

En premier lieu, nous relevons la similitude des coefficients dans le domaine des incidences faibles à modérées ( $\alpha \leq 20^\circ$ ) pour les deux ailes du plan de lacet ; puis un écart très important se creuse entre les deux courbes qui se rejoignent enfin vers  $\alpha = 40^\circ$ . Au delà, les perturbations de mesure empêchent de conclure. Au maximum du ventre entre les deux courbes, il y a pratiquement un rapport 1,8 entre les portances de l'aile gauche et de l'aile droite. Ce phénomène est entièrement occulté en pesée globale (fig. 12).

Les ailes verticales du plan de tangage sont soumises à des efforts en latéral ; l'aile d'intrados est peu chargée, celle d'extrados l'est davantage à partir et au delà de  $\alpha = 30^\circ$ . Dans la plage de dissymétrie, la différence des portances des ailes du plan de lacet crée un couple en roulis ; la géométrie de l'aile attribue un bras de levier d'environ 0,75 calibre en envergure à la portance ; c'est un couple de roulis  $Cl \sim 2,3$  qui est créé. Les efforts en latéral des ailes du plan de tangage compensent ce couple ; il est probable que le signe du roulis résultant variera selon l'angle d'incidence considéré puisque les écarts maxima - de valeur équivalente sur les deux plans - sont décalés en abscisse. Le roulis résultant est la différence entre deux termes élevés : on comparera le niveau de  $Cl$  cité ci-dessus à celui obtenu en mesure globale fig. 12.

##### 4.2. Etude à roulis $\theta = 45^\circ$

Les deux visualisations à  $\alpha_m = 30^\circ$  et  $45^\circ$  (planche n° 10) comme ci-dessus montrent dans le premier cas une symétrie d'ensemble de l'écoulement qui disparaît dans le second cas ; seul le tourbillon latéral droit est organisé entre les ailes inférieure et supérieure ; à l'extrados du missile, l'écoulement est désorganisé ; il n'y a plus de tourbillon qui apparaît nettement.

Les coefficients de portance des quatre ailes conservent davantage la symétrie, se regroupant deux à deux avec des écarts minimes entre les courbes, comparés à ceux constatés à  $\theta = 0^\circ$ . On remarque

le faible niveau de portance des deux ailes supérieures qui, en moyenne, s'établit à une valeur proche de zéro. Les deux ailes inférieures ont une portance plus élevée, par endroit de 20 % supérieure à celle des ailes de la configuration  $\theta = 0^\circ$  ci-dessus.

#### 4.3. Etude à roulis $\theta = 45^\circ$ (planche n° 11)

La visualisation à  $\alpha = 30^\circ$  montre l'agencement des différents tourbillons d'aile ; celui de l'aile en position inférieure se distingue à peine : l'éclairage venant par le haut, le corps opaque de la maquette empêche la vision de ce qui se passe à l'intrados. Cette configuration en roulis non symétrique par rapport à la vitesse transversale, conduit naturellement à une architecture d'écoulement elle-même non symétrique. Et les portances des ailes s'établissent à des niveaux nettement différenciés. L'aile repérée 1 (roulis  $22,5^\circ$ ) a une portance jusqu'à 50 % supérieure à celle de l'aile à roulis nul ci-dessus. L'aile n° 2 est à portance négative dès les incidences modérées.

4.4. La portance d'une aile varie selon sa position en roulis sur le missile. Les douze coefficients que nous venons d'observer, regroupés en roulis pour l'incidence  $\alpha_m = 30^\circ$  indiquent le type de variation de portance d'une aile en fonction de  $\theta$ . La courbe de la figure n° 23 situe vers  $\theta \sim 30^\circ$  la position de l'aile où sa portance atteint son maximum, supérieur de 70 % à sa valeur à  $\theta = 0^\circ$ . A l'inverse, elle est négative pour  $270^\circ \leq \theta \leq 315^\circ$ , position où l'aile est à l'extrados du missile.

4.5. Un autre regroupement des portances consiste à tracer pour  $\theta = 0^\circ$ ,  $22,5^\circ$  et  $45^\circ$  la somme des portances des quatre ailes projetées dans le plan formé par le vecteur vitesse et l'axe missile. On obtient les trois courbes de la fig. n° 24, à confronter avec les pesées globales en portance de la fig. n° 12. Nous avons remarqué, observant ces dernières, que les pertes de portance sont élevées puisqu'entre la courbe à  $\theta = 0^\circ$  (portance maximum) et celle à  $\theta = 45^\circ$  (portance minimum) elles atteignent jusqu'à 45 %. Dans le même temps, la portance reconstituée des quatre ailes varie dans des proportions nettement plus faibles, avec une zone en incidence où les écarts disparaissent ( $\alpha_m \sim 34^\circ$  à  $38^\circ$ ).

Sur le missile d'étude, constitué d'un corps et quatre ailes, nous décomposons la portance en plusieurs parties :

- la portance du fuselage, sans la présence des ailes. Comme il est axisymétrique, sa portance est indépendante de l'angle de roulis.
- la portance de l'ensemble constitué par les quatre ailes et la partie du fuselage qu'elles interactionnent. A son tour, cette portance se décompose en la portance nette des ailes - celle étudiée pour chacune des quatre ailes ci-dessus - et la portance induite sur le fuselage.

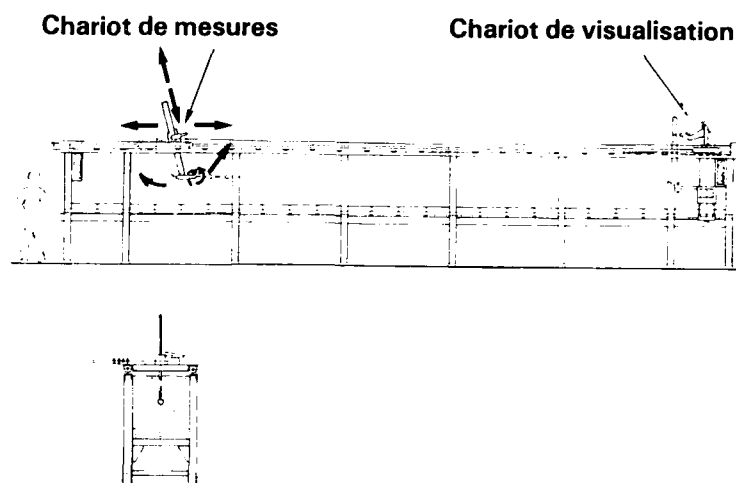
De ces trois composantes de portance, nous avons mesuré la somme (fig. n° 12) et la portance nette des ailes (fig. n° 24) et nous savons que la portance du fuselage est indépendante de l'angle de roulis. De la confrontation des pesées globales et des pesées d'aile, nous déduisons que c'est principalement sur la portance d'interaction des ailes sur le fuselage que se fait la modulation de portance en fonction de l'angle de roulis.

#### CONCLUSIONS

Les pesées globales au bassin hydrodynamique, les visualisations d'écoulements et les pesées d'ailes en soufflerie, constituent autant d'éléments qui facilitent la compréhension des phénomènes particuliers aux grandes incidences. Nous soulignons plus particulièrement les points suivants :

- sur le missile en incidence, la portance des ailes en position extrados est faible, voire négative. A l'intrados, elle passe par un maximum vers  $\theta \sim 30^\circ$  et est nettement supérieure à la portance de la position  $\theta = 0^\circ$ .
- la modulation de portance du missile en fonction du roulis apparaît essentiellement sur le terme d'interaction des ailes sur le corps,
- quand des coefficients apparaissent en latéral, les dissymétries d'écoulement se manifestent aussi sur les coefficients du plan de tangage, même si en pesée globale il n'y a pas d'effet apparent.
- enfin, ce ne sont pas les dissymétries d'écoulement les plus spectaculaires qui conduisent aux effets les plus importants sur les coefficients aérodynamiques ; quand l'écoulement a un aspect entièrement désorganisé, les coefficients retrouvent un niveau faible en latéral et symétrique en tangage. C'est d'avantage quand la dissymétrie s'amorce, qu'elle a les effets les plus grands.

## BASSIN HYDRODYNAMIQUE



### CARACTERISTIQUES

LONGUEUR :	12 m
LARGEUR :	1 m
HAUTEUR :	1,2 m
VITESSE DE DEPLACEMENT :	0 à 1,8 m/s

FIG. 1 : SCHEMA D'ENSEMBLE DU BASSIN HYDRODYNAMIQUE ET  
CARACTERISTIQUES PRINCIPALES



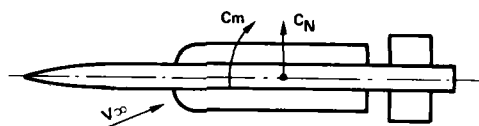


FIG. 2 : MISSILE CONFIGURATION « AILES LONGUES »

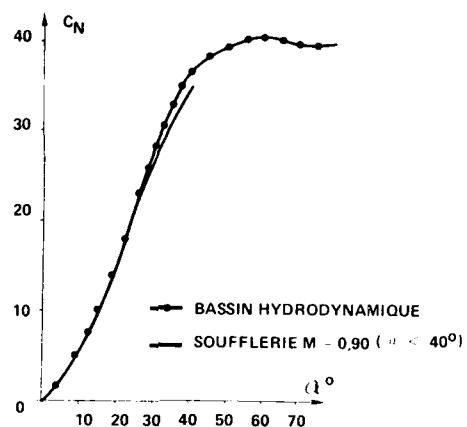


FIG. 3 : RECOUPEMENT EN PORTANCE

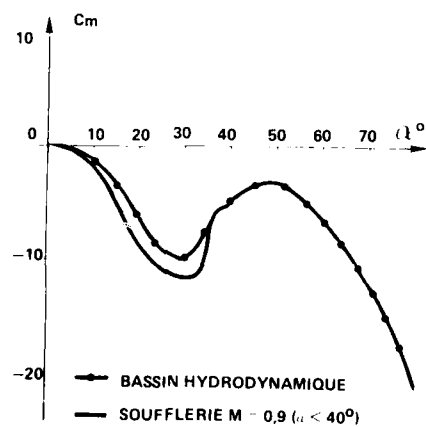


FIG. 4 : RECOUPEMENT EN MOMENT DE TANGAGE

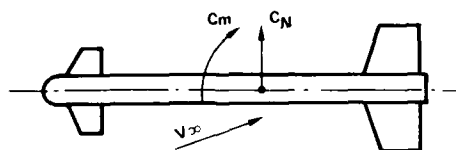


FIG. 5 : MISSILE DE CONFIGURATION CANARD

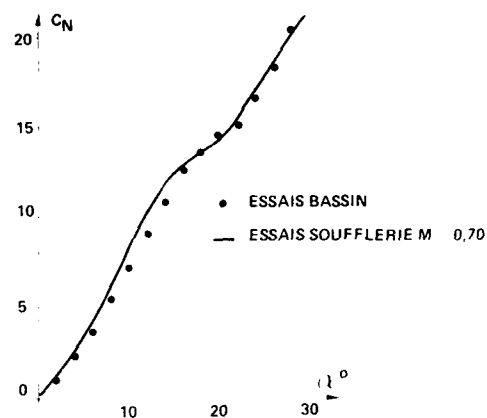


FIG. 6 : COMPARAISON DES COEFFICIENTS DE PORTANCE

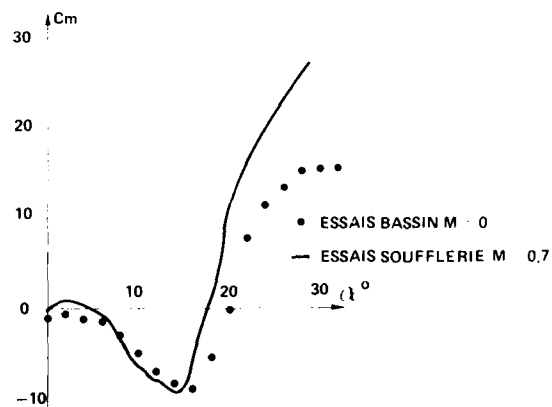


FIG. 7 : COMPARAISON DES COEFFICIENTS DE MOMENT DE TANGAGE

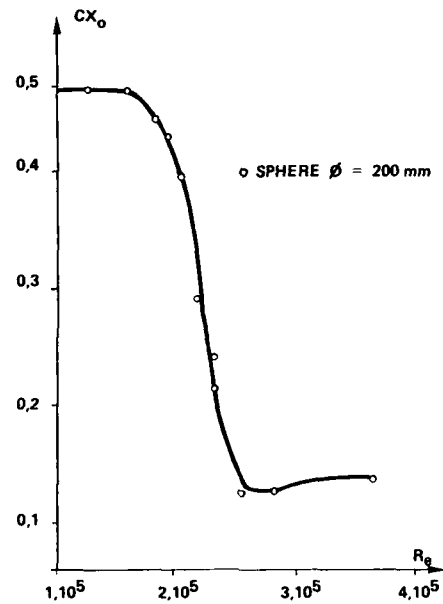


FIG. 8 : TRAINEE D'UNE SPHERE DANS L'EAU

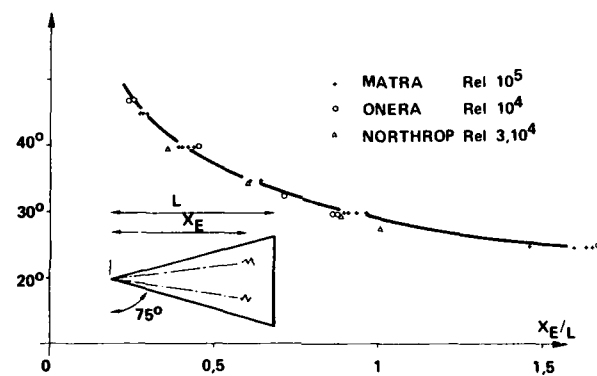
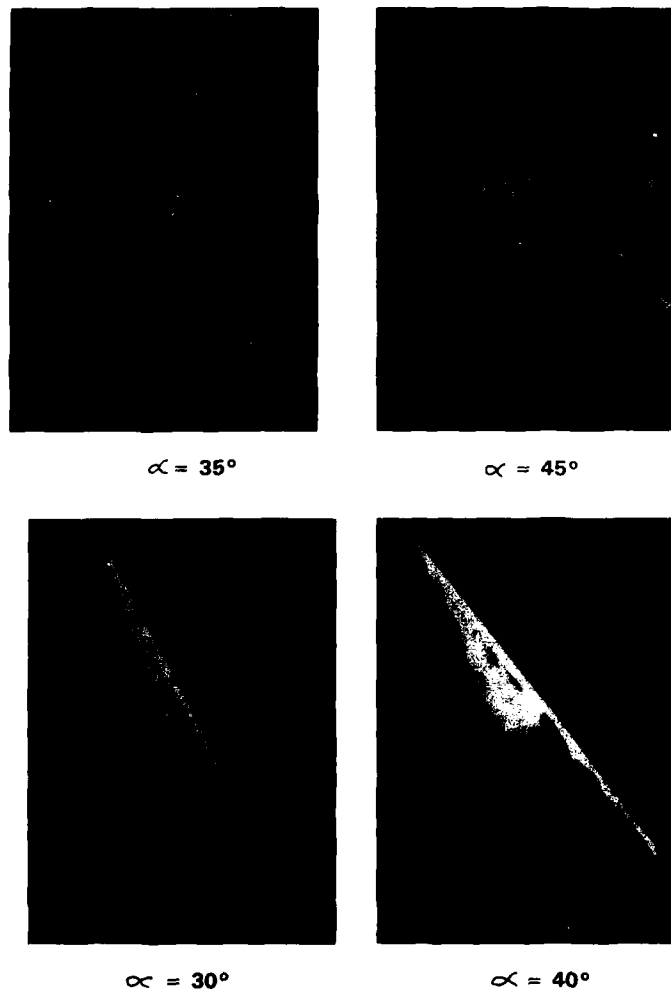


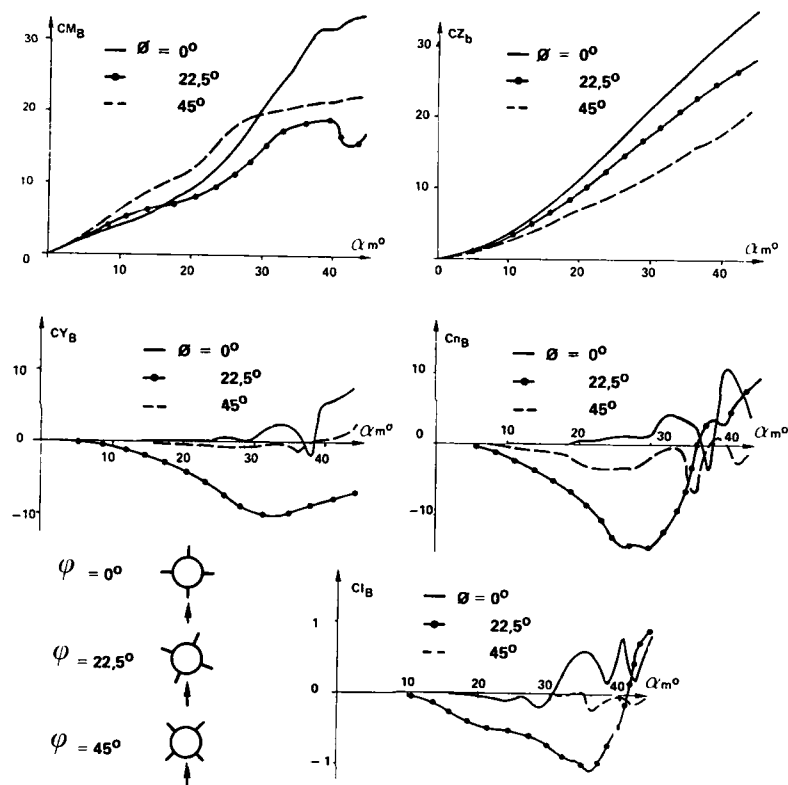
FIG. 9 : POINT D'ECLATEMENT DE TOURBILLONS SUR UNE AILE DELTA

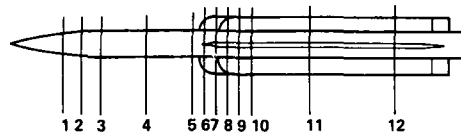


**FIG. 10 : EVOLUTION DE LA POSITION DU POINT D'ECLATEMENT  
DES TOURBILLONS D'UNE AILE DELTA MINCE EN FONCTION  
DE L'INCIDENCE**

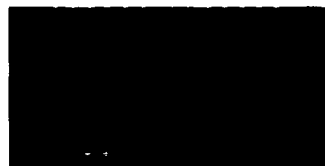


FIG. 11 : MISSILE D'ESSAIS

FIG. 12 : COEFFICIENTS AERODYNAMIQUES DU MISSILE  $M \approx 0$   
(Pesées au bassin hydrodynamique)



**FIG. 13 : MISSILE D'ESSAIS AVEC PLANS DE VISUALISATION**



**SECTION 1**



**SECTION 2**



**SECTION 3**



**SECTION 4**



**SECTION 5**



**SECTION 6**

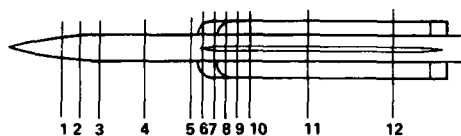


**SECTION 7**



**SECTION 8**

**FIG. 14 : EVOLUTION DES TOURBILLONS D'OGIVE ET DE VOILURE LE LONG DU MISSILE  $\alpha = 30^\circ$**



SECTION 9



SECTION 10



SECTION 11



SECTION 12

FIG. 15 : EVOLUTION DES TOURBILLONS DE VOILURE LE LONG DU MISSILE  $\alpha \approx 30^\circ$

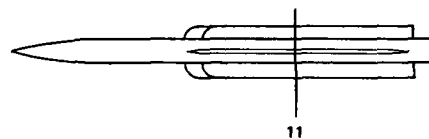


FIG. 16 : SECTION TRANSVERSALE N° 11 DE VISUALISATION SUR LE MISSILE



$\alpha = 30^\circ$

$\alpha = 45^\circ$

FIG. 17 : EVOLUTION DES TOURBILLONS DE VOILURE EN FONCTION DE L'INCIDENCE

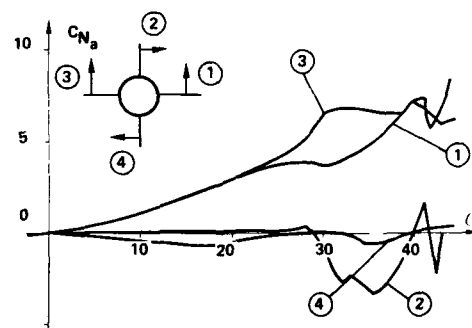


FIG. 18 : PORTANCE DE CHAQUE AILE DU MISSILE





$\alpha = 30^\circ \quad \phi = 45^\circ$



$\alpha = 45^\circ \quad \phi = 45^\circ$

FIG. 19 : EVOLUTION DES TOURBILLONS EN FONCTION DE L'INCIDENCE

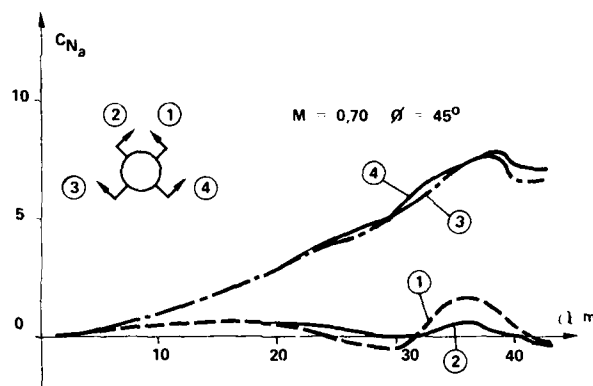
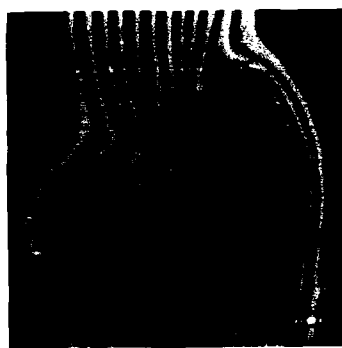


FIG. 20 : PORTANCE DE CHAQUE AILE DU MISSILE



$$\alpha = 30^\circ \quad \varnothing = 22.5^\circ$$

FIG. 21 : TOURBILLONS D'AILE EN POSITION DISSYMETRIQUE

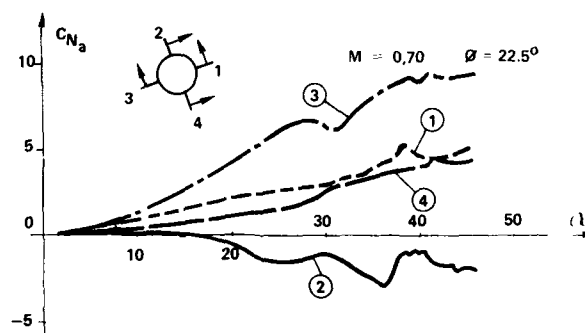


FIG. 22 : PORTANCE DE CHAQUE AILE DU MISSILE

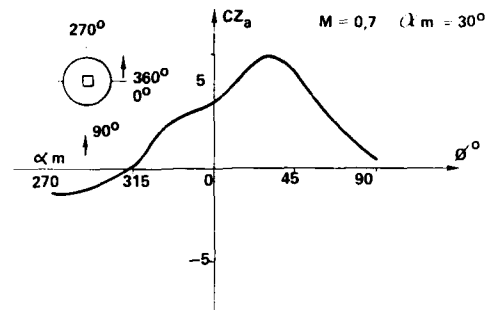


FIG. 23 : EVOLUTION DE PORTANCE D'UNE AILE EN FONCTION DE SA POSITION EN ROULIS SUR LE MISSILE

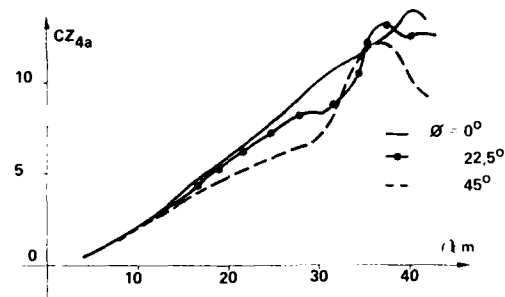


FIG. 24 : EVOLUTION DE LA RESULTANTE DE PORTANCE DES QUATRE AILES POUR DIFFERENTS ANGLES DE ROULIS

# Short Duration Flow Establishment on a Profile in a Water-Ludwig-Tunnel

W. Kerres and H. Grönig

Stoßwellenlabor, Rheinisch-Westfälische Technische Hochschule Aachen, 5100 Aachen,  
Federal Republic of Germany

## Symbols

A = cross section area	Subscripts:
c = chord length	H = high pressure chamber
h = height of the fluid column in the tunnel	L = low pressure chamber
p = pressure	M = test section at the place of the model
$\Delta p$ = accelerating pressure difference	0 = condition at the water surface
s = teeth distance of the chopper disk	s = sliding valve
t = absolut time	$\infty$ = undisturbed flow in the test section
T = exposure time	Superscript:
v = velocity	* = dimensionless value
x' = coordinate of the tunnel in flow direction	
x = coordinate of the model in flow direction	
y = coordinate normal to x	
$\rho$ = density of the fluid	
$\tau$ = characteristic starting time	

## Summary

This paper deals with the time dependent establishment of the flow field on an airfoil in unsteady flow. The impulsive start of the flow is achieved in a Water-Ludwig-Tunnel. By using a coded particle tracing method for flow visualization, the detailed flow establishment on a NACA 0012 airfoil at  $30^\circ$  angle of attack is shown from the beginning where potential flow exists with zero circulation to a "quasi-steady" formation of the vortex street.

## 1. Introduction

Experiments in unsteady flow, especially impulsively started flows, are difficult to realize because of the needed high acceleration in the beginning in order to reach a steady flow velocity in a short time. Continuously working channels, especially water channels, have acceleration times in the range of seconds to minutes. The intermittent working Water-Ludwig-Tunnel proposed by Akamatsu /1/ has an acceleration time in the range of tens of milliseconds. This facility allows experiments in an almost impulsively started flow with a following steady velocity for a few seconds. A second acceleration step of the flow is possible. A number of interesting flow problems may be studied in this channel, e.g. the unsteady Kutta condition, the development of the starting vortex, the development of the flow and the flow forces on an airfoil. The visualization technique proposed in this paper represents a modified particle tracer method, which yields the location of the photographed particles as a function of time with a resolution of less than one millisecond. This means, that the flow direction of the particles can be determined. By this coded-tracer technique, which is described below, the flow establishment on a NACA 0012 profile is observed.

## 2. Test facilities

### 2.1 Water-Ludwig-Tunnel

A channel of this type was built in 1984 in the Stoßwellenlabor of the RWTH Aachen. A sketch of the Water-Ludwig-Tunnel (Fig. 1) shows the principle of the channel: the high pressure section including the 750 mm long vertical test section ( $75 \times 150 \text{ mm}^2$ ) is separated from the low pressure section by a fast acting sliding valve. This valve opens the tunnel within 5 ms, and the pressure difference between high and low pressure chamber plus gravity forces accelerate the fluid.

The velocity history in the test section is determined with the equation of Bernoulli for unsteady incompressible flow:

$$(1) \quad \rho \int_0^h \frac{\partial v(x,t)}{\partial t} dx + p_L + \frac{\rho}{2} v_s^2 - \rho gh = p_H + \frac{\rho}{2} v_0^2$$

Under the assumption, that the flow velocity in the water tank is low ( $v_0/v_s \ll 1$ ) the velocity in the test section as a function of time follows from Eq.(1) as

$$(2) \quad v_M = v_{M\infty} \tanh \left( \frac{t}{\tau} \right)$$

with the steady velocity

$$(3) \quad v_{M\infty} = \frac{A_s}{A_M} \sqrt{\frac{2\Delta p}{\rho}}$$

the pressure difference

$$(4) \quad \Delta p = p_H - p_L + \rho g h$$

and the characteristic starting time

$$(5) \quad \tau = \frac{2 A_s \cdot \int_0^h \frac{dx}{A(x)}}{\sqrt{\frac{2\Delta p}{\rho}}}$$

In Fig. 2 the measured flow velocity in the Water-Ludwig-Tunnel is shown in comparison with the calculated values as a function of time. For these measurements a NACA 0012 airfoil with a chord length of 50 mm was installed at an angle of attack of  $30^\circ$  in the test section. In these tests the channel was driven by the hydrostatic pressure only. The experimental results give a characteristic starting time of  $\tau = 57$  ms (theoretically  $\tau = 53$  ms) and a steady velocity of 0.62 m/s (theoretically  $v_{M\infty} = 0.65$  m/s).

The difference between the theoretical and the measured values are due to the fact, that the calculation neglects the effect of the mounted airfoil and the turbulent flow e.g. at the sharp edges of the sliding valve. Another effect, not taken into account, is the finite opening time of 5 ms for the sliding valve, which causes a displacement of the measured velocity to greater times.

The static pressure  $p_M$  in the test section as a function of time is shown in Fig. 3 for a run of the channel of about two seconds. The pressure drop at the start indicates the acceleration of the flow, followed by the steady flow. The small decrease of the static pressure is caused by the sinking water level in the water tank.

If additionally to the hydrostatic forces the chambers are operated with a pressure difference, the characteristic starting time according to Eq.(5) decreases. If the tunnel is operated with the maximum possible pressure difference of  $\Delta p = 1.15$  bar, Eqs. (3-5) yield a characteristic starting time of  $\tau = 20$  ms and a steady velocity of  $v_{M\infty} = 1.8$  m/s.

## 2.2 Coded-tracer-method

The flow visualisation was realised by a modified tracer method, which enables one to find the exact position of the particles on the photograph as a function of time.

Generally the method of photographing traces of particles is a very simple one for measuring velocities in a two-dimensional flow. The flow field is visualized and shows the macroscopic velocities for the instant of the exposure time. It has been used previously in many steady flow problems, and also in such unsteady flows, where the changes of the flow field are small within the exposure time (3,4,5). If the exposure time is too long, the velocity can only be measured as an average over the exposure time, or it even cannot be detected at all if the traces are strongly bent. For short exposure times it is difficult to measure the length of the traces which are in this case identical with the streamlines. The simple tracer method shows no evolution of the flow field and gives no information about the direction of the flow.

There are different methods to measure the velocity changes during the exposure time: first, to mark the traces in equal time intervals by periodic exposures (6,7), or by stroboscopic laser light for high velocities (8), and secondly making series of photographs. The flow direction can only be determined, when at least two photos are taken (9) or when the traces are marked additionally with a second flash light (10) or a second laser (7).

In recent studies the velocities of tracer particles are measured with the help of computers connected to video cameras. By digitizing stored pictures (11), or even working with a three-dimensional on-line system (12) the velocities and directions are obtained.

With the coded-tracer-method applied in this paper the particle traces are provided with marks, yielding both direction and velocity. In Fig. 4 the facility for this visualization technique is shown: By means of a cylindrical lens the laser produces a light sheet of 2 mm thickness in the test section and illuminates plastic particles in the water (Vestamid, Chemische Werke Huls AG, diameter = 0.2 mm). In front of the lens a chopper disk rotates, which interrupts the beam according to the pattern of broad and small teeth on the circumference. The distances between the opening sides of the teeth are constant, so that the exact time of the coded traces can be determined, if the starting time of the pattern  $t$  and the time interval  $\Delta t$  are known. The photograph shows

the trailing edge of the NACA 0012 in the starting flow, taken by the camera as indicated in the sketch.

A photodiode receives the signal of the coded light. A transient recorder is triggered by the opening of the channel. If the camera shutter is released, the signal of the photodiode is digitized and stored. The computer prints the signal code in form of long (L) and short (K) characters and additionally the starting time of the pattern and the time interval between two consecutive dashes.

In this example, the photo is taken with an exposure time of 33ms ( $T = 1/30$ s). The same pattern of the traces is visible on the photograph and on the signal code. The position of the particles can be measured as a function of time, from which velocity and flow direction may be calculated. An example of the amount of information, which is stored in the flow photograph of Fig. 4, is demonstrated by drawing the flow velocities as arrows at the beginning (Fig. 5a,  $t = 10$ ms) and at the end of the exposure time (Fig. 5b,  $t = 40$ ms). The streamlines are superimposed qualitatively in the figures. The development from a flow with a stagnation point on the suction side of the airfoil to the stage with the separated starting vortex is obvious.

### 3. Flow establishment on an airfoil in unsteady flow

The airfoil consists of a NACA 0012 profile made of perspex (Fig. 6). It is mounted in the 75mm x 150mm rectangular test section with an angle of attack of  $\alpha = 30^\circ$ . The velocity history for the start and the following steady flow under these conditions is already shown in Fig. 2. The Reynolds number calculated with the chord length and the steady velocity  $v_{M\infty}$  is  $Re = 3.1 \times 10^4$ .

The photographs are taken with a 35mm camera. The beginning of the exposure time is given by  $t$  and made dimensionless with the velocity  $v_{M\infty}$  and the chord length  $c$ :  $t^* = v_{M\infty} \cdot t / c$ . In all photographs the exposure time is  $T = 1/30$  sec.

In Figs. 7-11 the flow development during the acceleration period of the fluid is photographed. In the very first instant after the start of the tunnel, potential flow with zero circulation exists around the airfoil (Fig. 7). The stagnation point is located on the suction side of the profile. To demonstrate the location of the stagnation point clearer Fig. 7 is chosen with an angle of attack of  $45^\circ$  (all others have  $30^\circ$ ) and with a larger scale than the following figures. The exposure time began before the channel started and is therefore negative. For  $\alpha = 30^\circ$  the hooked traces at the trailing edge in Fig. 8 indicate the same flow development: In the beginning a stagnation point is located on the suction side of the airfoil, and later the velocity direction is tangential to the profile's surface. At  $t^* = 0.3$  (Fig. 9), the flow on the airfoil stays tangential to the surface, and there is no separated flow region. In Fig. 10 the starting vortex is carried away from the airfoil. The particle traces are cycloides due to the rotating and translating fluid. Near the leading edge a separated flow area appears.

The further flow establishment takes place under the condition of a steady outer flow with  $v_{M\infty} = 0.62$  m/s. The first leading edge vortex has its origin at the nose of the profile (Fig. 11) in the separated flow region. This vortex increases to such a size, that it not only induces an almost complete backflow on the suction side, but also a secondary counterrotating vortex with its core at the quarterline and another vortex at the leading edge, rotating in the same direction (Fig. 15). The flow around the trailing edge leads to small disturbances in the shear layer between the fluid coming from the pressure and suction side of the airfoil (Figs. 12 - 14), until it is strongly influenced by the first leading edge vortex (Fig. 15). This vortex amplifies the shear flow in the shear layer giving birth to the first trailing edge vortex (Fig. 16, reduced scale for Figs. 16-33). This latter vortex grows until the first leading edge vortex starts to move away with the outer flow and pulls the trailing edge vortex away from the airfoil (Fig. 18). These two vortices are carried away as a vortex pair.

A separated flow region with highly turbulent flow stays on the suction side of the airfoil (Fig. 19). In this region the second leading edge vortex develops (Fig. 20) and a similar process as described before begins: the second trailing edge vortex is growing (Fig. 21), the second vortex pair swims away (Fig. 24) and the third leading edge vortex increases (Fig. 25), induces the trailing edge vortex (Fig. 26); the fourth vortex pair can be seen in Fig. 30, the fifth in Fig. 33 etc..

The experiments show that the mechanism of the formation of the vortex pairs is always the same. An exception is the starting vortex, which has its origin in the motion of the stagnation point together with the separation at the trailing edge. The first vortex pair has the biggest size compared with the following ones, which grow in turbulent flow regimes.

In Figs. 34-36 the path of the vortex cores are plotted in the dimensionless  $x^*-y^*$ -plane ( $x^* = x/c$ ,  $y^* = y/c$ ). The starting vortex is carried away by the flow almost parallel to the  $x$ -axis of the coordinate system. The leading edge vortex is formed in the separated flow at the nose of the airfoil, it increases on the suction side and swims away followed by the trailing edge vortex. The paths of the vortices cross at  $x^* = 0.8$ . The second leading edge vortex moves close to the airfoil towards the trailing edge. Its way is crossed by the corresponding trailing edge vortex at  $x^* \approx 4$ . The measured paths of the third vortex pair show a diverging behaviour.

The measured time intervals elapsed between the formation of the vortex pairs are shown in Fig. 37. The figure shows on the abscissa the time when the leading edge vortices are observed first, on the ordinate the time difference between the formation of the leading edge vortex and the corresponding, i.e. from itself induced, trailing edge vortex. This plot shows a decrease in the times between the formation of the corresponding vortex pairs. With the appearance of the third vortex pair the formation time differences become nearly constant. For the here described experiments, the time to this steady formation of the vortex street amounts to  $t \approx 700$  ms, corresponding to the flow situation given in Fig. 24.

A similar flow situation has been experimentally observed by Daube et al. [4]. There a NACA 0012 airfoil was towed vertically in a water tank with an angle of attack of  $34^\circ$  and a Reynolds number of  $Re = 1000$ . The dimensionless time  $t^*$  was defined in the same way, however, the flow stages related to  $t^*$  are different compared to the ones measured in the Ludwig-Tunnel: e.g. the origin of the first induced trailing edge vortex was observed at  $t^* \approx 3.0$  in the Ludwig-Tunnel, whereas it is found for times  $t^* \geq 5$  in the experiments of Daube et al. [4].

Reasons for this discrepancy lie probably in the different values of accelerating times, angles of attack and Reynolds numbers. The study of these influences will be a part of our future work.

#### 4. Conclusions

An intermittent working Water-Ludwig-Tunnel is described, which represents a facility to investigate models in impulsively accelerated flows. Its characteristics are a short acceleration time (5100 ms) and subsequently a steady velocity for about three seconds in the test section.

A coded-tracer-method is demonstrated as a simple facility to measure the velocity in magnitude and direction, especially its changes during the exposure time in contrast to the usually applied tracer technique. The resolution of this flow field measuring technique is shown in an example, where two different flow stages are stored on one photo: the starting flow with the stagnation point on the suction side of the airfoil and the starting vortex carried away by the outer flow.

The flow establishment on the NACA 0012 airfoil in an impulsively started flow with a Reynolds number of  $3.1 \times 10^4$  has been investigated. The starting vortex develops which has its origin in the motion of the stagnation point together with the vortex originating in the separation area at the trailing edge. The first vortex from the leading edge initiates the process of forming the vortex street, which is well known for the steady flow on an airfoil at a high angle of attack. The measured time intervals for the formation of the corresponding vortices allowed to determine a characteristic time, after which a constant frequency for the separation of the vortices is achieved.

#### Acknowledgment

This work was partially supported by the Sonderforschungsbereich 25, "Wirbelströmungen in der Flugtechnik", sponsored by the Deutsche Forschungsgemeinschaft. This support is gratefully acknowledged.

#### References

1. Akamatsu, T.: Applications of shock tube technology to studies of hydrodynamics. In: Shock Tube and Shock Wave Research (Ed's Ahlborn, Hertzberg, Russell), 24-35, University of Washington Press, Seattle and London 1979.
2. Kerres, W.: Konstruktion, Bau und Erprobung eines Wasser-Ludwig-Kanals zur Untersuchung instationärer Strömungsvorgänge, Diplomarbeit, Stoßwellenlabor Rheinisch-Westfälische Technische Hochschule Aachen, 1984.
3. Prandtl, L.: Ergebnisse der Aerodynamischen Versuchsanstalt zu Göttingen, III, Lief., S. 6-9, Verlag Oldenbourg München-Berlin, 1927.
4. Daube, O.; La Plume, Loïc; Monnet, P.; Contanceau, M.: Écoulement instationnaire décollé d'un fluide incompressible autour d'un profil: une comparaison théorie - expériences, AGARD Conference Proceedings no. 386, p. 3.1 - 3.14, 1985.
5. Honji, H.; Taneda, S.: Unsteady Flow Past a Circular Cylinder, J. Phys. Soc. Japan, Vol. 27, No. 7, p. 1668-1677, 1969.
6. Breslin, J.A.; Enrichi, R.L.: Precision Measurement of Parabolic Profile for Laminar Flow of Air between Parallel Plates, J. Fluid Mech., Vol. 10, No. 11, p. 2289 - 2292, 1967.
7. Ren, Z.G.: Orbital Path and Velocity of Particles in Wave-Current Motion Field, In: Flow Visualization III, Ed. W.J. Yang, University of Michigan, Ann Arbor, Michigan, USA, 1983.

/8/ Philbert, M.; Boutier, A.: Methodes Optiques de Mesure der Vitesses de Particules entrainees dans les ecoulements. La Recherche Aerospatiale, No.3, p. 171-184, 1972

/9/ Kobayashi, T.; Ishihara, T.; Sasaki, N.: Automatic Analysis of Photographs of Trace Particles by Microcomputer System. In: Flow Visualization III, Ed. W.J. Yang, University of Michigan, Ann Arbor, Michigan, USA, 1983.

/10/ Mezaris, T.M.; Telionis, D.P.; Jones, G.S.: Visualization of Separating Oscillatory Laminar Flow. In: Flow Visualization II, Ed. W. Merzkirch, Ruhr-Universitat Bochum, West Germany, 1980.

/11/ Marko, K.A.; Rimai, L.; Klick, D.: Digitized Track Image Recording with Silicon Intensified Vidicon and Digital Oscilloscope for Automated Trajectory and Velocity Measurements. In: Flow Visualization III, Ed. W.J. Yang, University of Michigan, Ann Arbor, Michigan, USA, 1983.

/12/ Doi, J.; Miyake, T.: Three-Dimensional Flow Analysis by On-Line Particle Tracking. In: Flow Visualization III, Ed. W.J. Yang, University of Michigan, Ann Arbor, Michigan, USA, 1983.

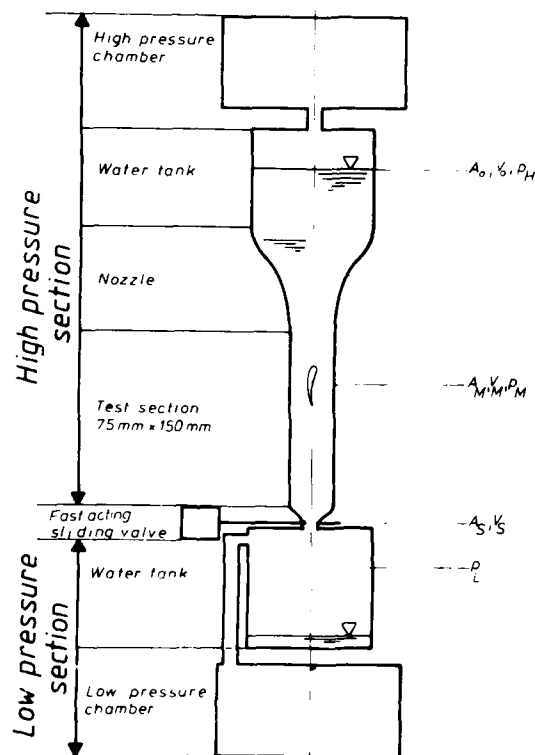


Fig. 1: Sketch of the Water-Ludwig-Tunnel



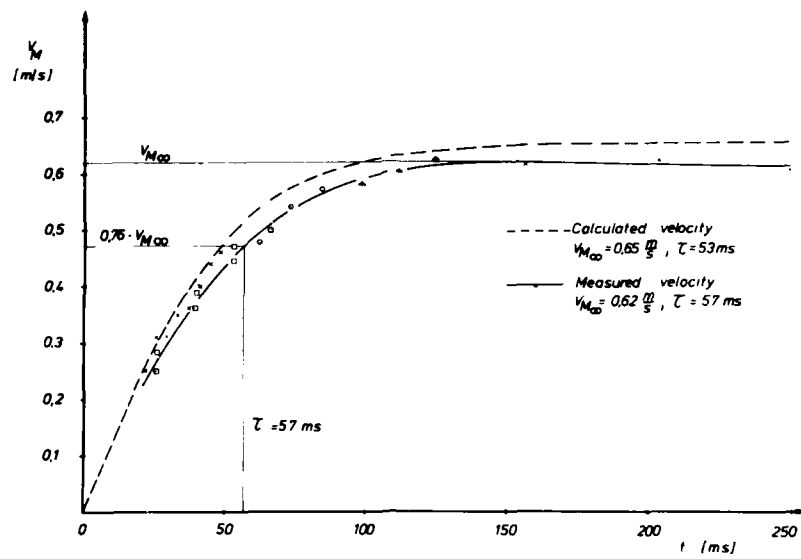


Fig. 2: Velocity in the test section as a function of time

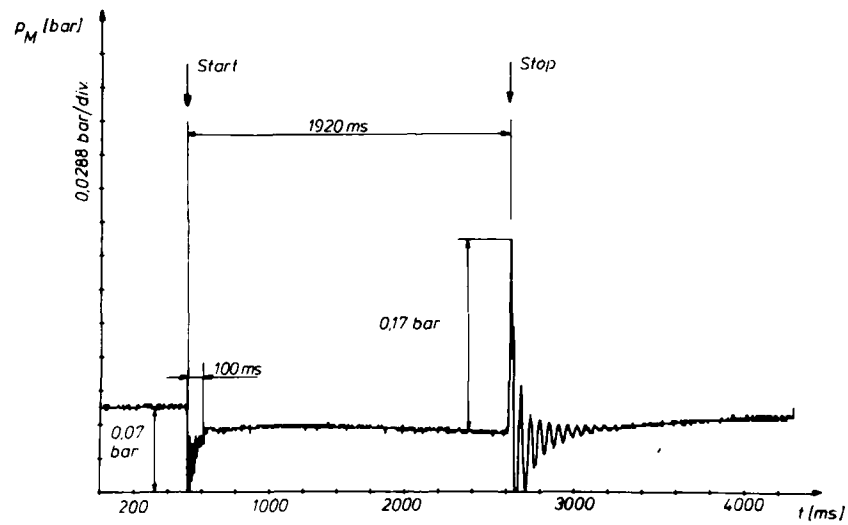


Fig. 3: Static pressure in the test section as a function of time

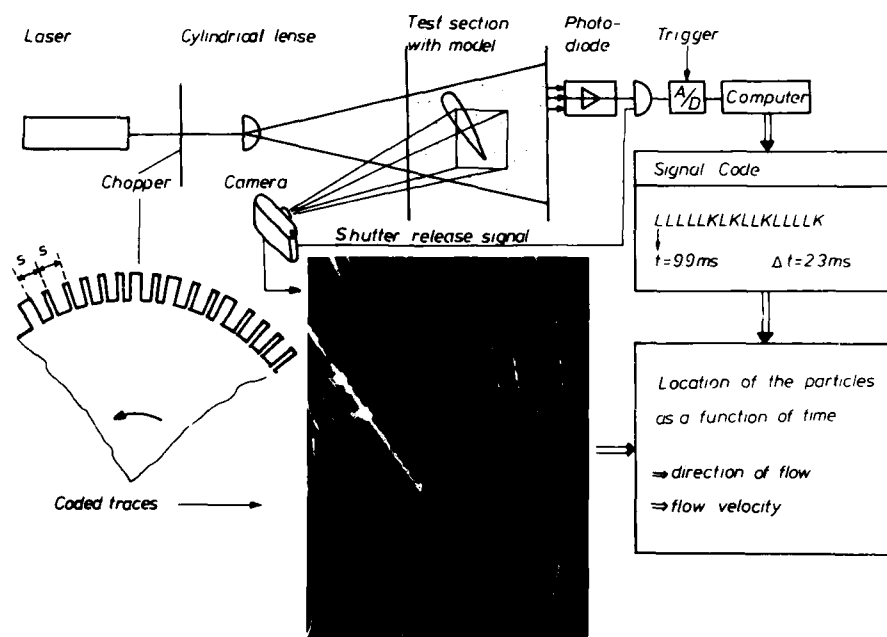


Fig. 4: Principle of the coded-tracer-method

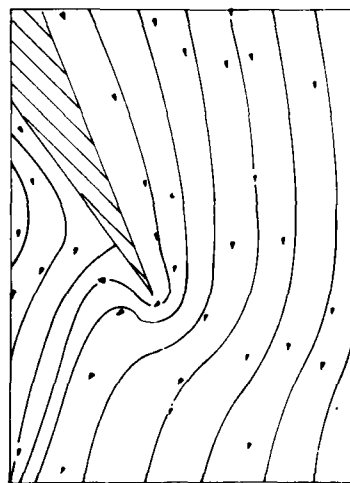


Fig. 5a

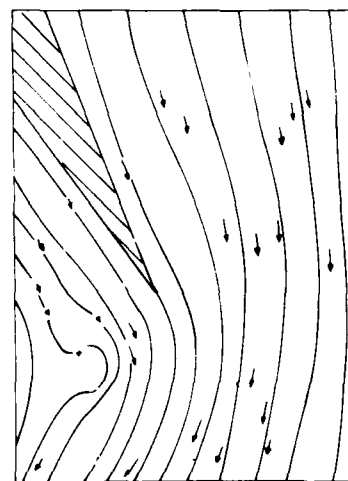


Fig. 5b

Fig. 5: Flow field at the trailing edge of a NACA 0012 airfoil in the starting flow; a)  $t = 10\text{ ms}$ , b)  $t = 40\text{ ms}$

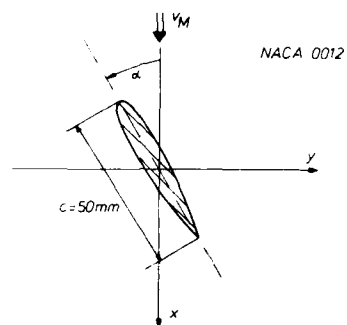


Fig. 6: Geometry of the airfoil

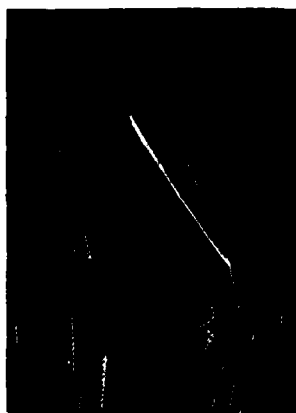
Fig. 7:  $t = -15 \text{ ms}, t^* = 0.2$   
( $\alpha = 45^\circ$  only in this figure)Fig. 8:  $t = 0 \text{ ms}, t^* = 0.4, 30^\circ$ Fig. 9:  $t = 21 \text{ ms}, t^* = 0.3$ Fig. 10:  $t = 52 \text{ ms}, t^* = 0.6$ Fig. 11:  $t = 97 \text{ ms}, t^* = 1.2$

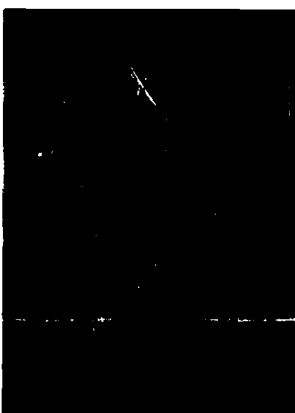
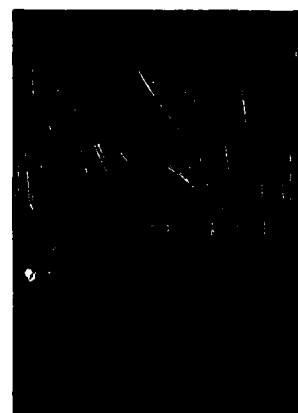
Fig.12:  $t = 113 \text{ ms}, t^* = 1,4$ Fig.13:  $t = 175 \text{ ms}, t^* = 2,2$ Fig.14:  $t = 192 \text{ ms}, t^* = 2,4$ Fig.15:  $t = 218 \text{ ms}, t^* = 2,7$ Fig.16:  $t = 248 \text{ ms}, t^* = 3,1$ Fig.17:  $t = 300 \text{ ms}, t^* = 3,7$ Fig.18:  $t = 330 \text{ ms}, t^* = 4,1$ Fig.19:  $t = 410 \text{ ms}, t^* = 5,1$ Fig.20:  $t = 470 \text{ ms}, t^* = 5,8$



Fig.21:  $t = 535 \text{ ms}, t^* = 6,6$



Fig.22:  $t = 583 \text{ ms}, t^* = 7,2$



Fig.23:  $t = 635 \text{ ms}, t^* = 7,9$

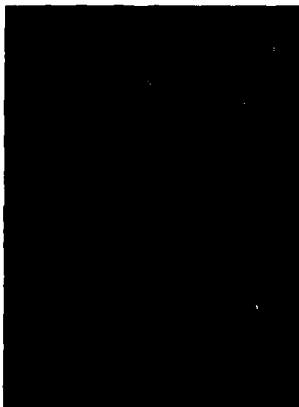


Fig.24:  $t = 695 \text{ ms}, t^* = 8,6$



Fig.25:  $t = 750 \text{ ms}, t^* = 9,3$



Fig.26:  $t = 805 \text{ ms}, t^* = 10,0$

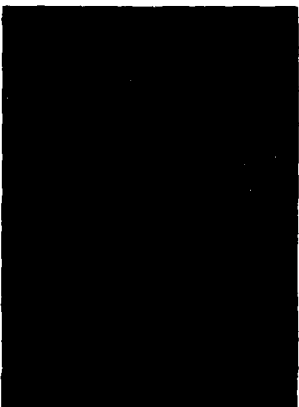


Fig.27:  $t = 925 \text{ ms}, t^* = 11,5$



Fig.28:  $t = 985 \text{ ms}, t^* = 12,2$



Fig.29:  $t = 1045 \text{ ms}, t^* = 13,0$

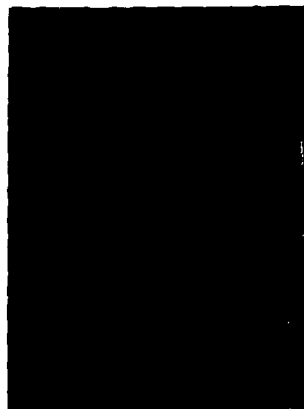
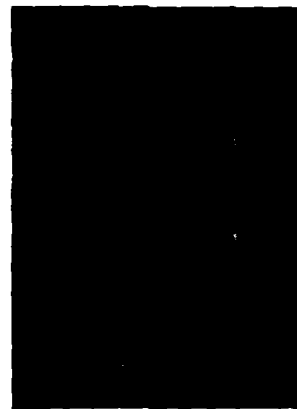
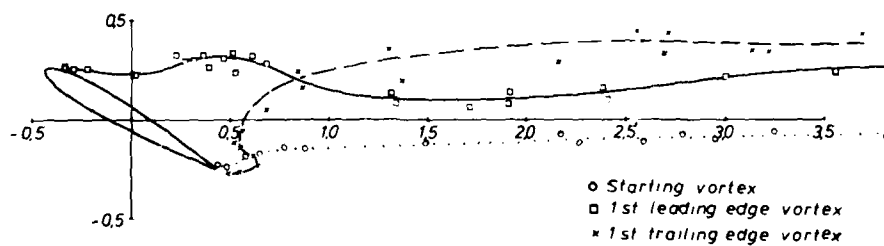
Fig.30:  $t = 1100 \text{ ms}, t^* = 13,6$ Fig.31:  $t = 1160 \text{ ms}, t^* = 14,4$ Fig.32:  $t = 1220 \text{ ms}, t^* = 15,1$ Fig.33:  $t = 1280 \text{ ms}, t^* = 15,9$ 

Fig.34: Paths of the vortex cores of the starting vortex and the first vortex pair

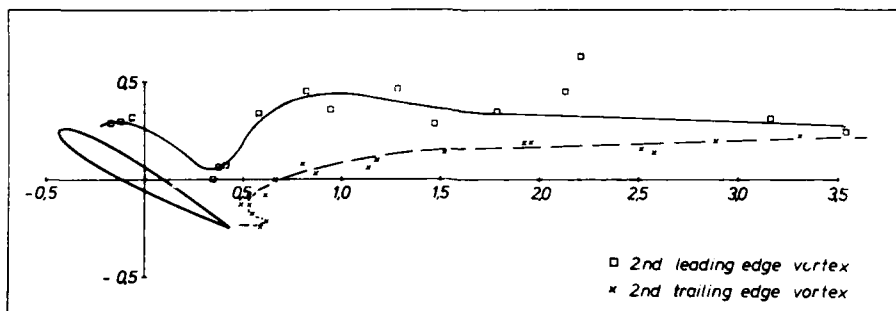


Fig.35: Paths of the cores of the second vortex pair

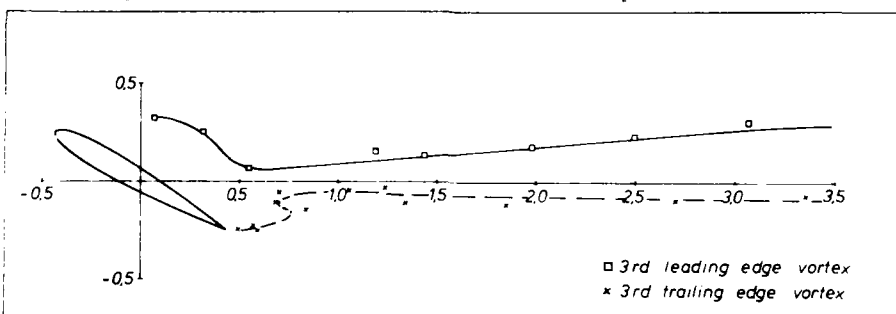


Fig.36: Paths of the cores of the third vortex pair

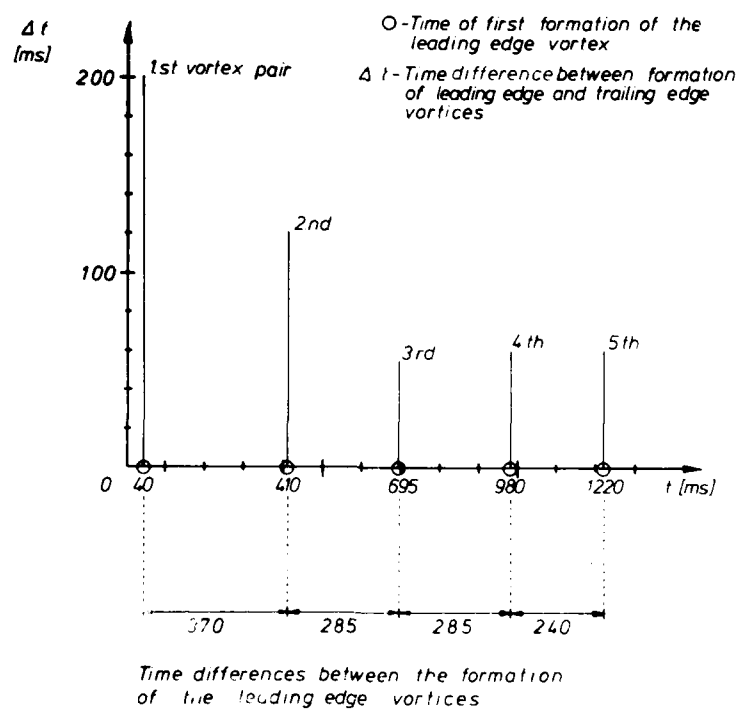


Fig.37: Times of the formation of the vortex pairs

**EXPERIMENTAL INVESTIGATION OF HOVER FLOWFIELDS IN WATER  
AT THE MCDONNELL DOUGLAS RESEARCH LABORATORIES\***

K. R. Saripalli<sup>†</sup>, J. C. Krout<sup>††</sup> and J. R. Van Horn<sup>†††</sup>  
McDonnell Douglas Research Laboratories  
P. O. Box 516, St. Louis, MO 63166

**ABSTRACT**

A new experimental facility, called the Hover Research Facility (HRF), is designed to study the flowfields generated by hovering vertical take-off and landing (VTOL) aircraft and helicopters. Water is used as the working medium because of its inherent advantages in flow visualization and laser Doppler velocimeter (LDV) measurements. The applications of the Hover Research facility include: (1) experimental investigation of twin-jet impingement flow with application to VTOL aircraft, (2) visualization of the flowfield around a fully contoured, model supersonic fighter/attack short-take-off and vertical landing (STOVL) aircraft, and (3) performance testing of a No Tail Rotor (NOTAR) helicopter in hover mode by use of a scaled model. Flow-visualization and quantitative LDV data on these experiments are presented.

**NOMENCLATURE**

A, B, C	Constants
D	Exit internal diameter of the nozzle or the exit jet diameter
H	Height of the nozzle exit above the ground plate
M	Constant
Re	Reynolds number based on the exit jet diameter and the exit jet velocity
S	Center distance between the jet exit
S <sub>i</sub>	Distance between the points of impingement on the ground (for inclined jet impingement)
U <sub>i</sub>	Instantaneous velocity in the streamwise (Z) direction
V <sub>i</sub>	Instantaneous velocity in the cross stream (X) direction
W <sub>i</sub>	Instantaneous velocity in the Y direction
U	Mean velocity in the streamwise direction
V	Mean velocity in the cross-stream direction
u	Fluctuating component of the velocity in the streamwise direction
v	Fluctuating component of the velocity in the cross-stream direction
U <sub>j</sub>	Jet centerline velocity at the exit
U <sub>max</sub>	The local maximum streamwise velocity in the fountain
X <sub>1/2</sub>	The fountain half-width where $U = \frac{1}{2} U_{max}$
X	Distance parallel to the line connecting the nozzle centerlines
Y	Distance perpendicular to the line connecting the nozzle centerlines and parallel to the ground plane
Z	Perpendicular distance from the ground plane

**1. INTRODUCTION**

Helicopters and vertical take-off and landing (VTOL) aircraft employing powered lift-jets produce complicated flowfields while hovering in and out of ground effect. These three-dimensional hover flowfields, shown schematically in Fig. 1, involve strong interactions between the lift-generating flow, the airframe surface, and the ground.

In the case of a VTOL aircraft powered by lift jets (Fig. 1a), the axisymmetric radial wall jets created by the impinging lift jets collide with each other to form a fountain upwash flow. The fountain is fan-shaped, spreading radially in all directions with increasing width away from the ground. The fountain is an important flow feature because its impingement on the aircraft undersurface increases lift, elevates skin temperatures, and increases the possibility of reingestion of exhaust gases into the inlets. Literature survey on fountain flows indicates a need for a reliable, detailed mean-velocity and turbulence data base on realistic 3-D fountain producing configurations. The helicopter rotor downwash (Fig. 1b) is a complex flow featuring tip and hub vortices and wake contraction. Certain elements of this flowfield, such as blade/blade-wake interaction, lift distribution along the blade in a multibladed rotor, interaction between the downwash and the fuselage, and the interaction between the downwash and the ground are not well defined.

This paper describes experimental work conducted in the Hover Research Facility (HRF) at McDonnell Douglas Research Laboratories (MDRL) on generic and configuration-oriented flowfields generated by hovering VTOL aircraft and helicopters. The HRF is specially designed for the study of such hover flowfields

\*This research was conducted under the McDonnell Douglas Independent Research and Development program.

<sup>†</sup>Scientist, McDonnell Douglas Research Laboratories

<sup>††</sup>Section Chief, Laboratory, McDonnell Douglas Research Laboratories

<sup>†††</sup>Project Engineer, McDonnell Douglas Helicopter Company



by use of water as the working medium. Flow visualization and quantitative experimental data on multiple-jet-impingement (VTOL aircraft) and rotor-downwash (helicopters) flowfields are presented. Visualization studies of the simulated flows around complex VTOL aircraft and helicopter models hovering in air, but of ground effect are described.

## 2. WORKING MEDIUM

As a working medium, water offers specific advantages over air: the tracers suitable for flow visualization in water are more numerous and have better light-reflecting characteristics. In addition, aerodynamic phenomena can be observed at a relatively slow speed in water (1/15th of that in air) at the same Reynolds number and model scale because of the difference in kinematic viscosities of air and water. Moreover, for laser Doppler velocimetry, the seeding of the flow is normally unnecessary in water because the natural suspended particles act as light scatterers. If seeding is necessary, it can be accomplished more easily in water than in air by adding neutral-density plastic particles of the proper size based on light-scattering requirements.

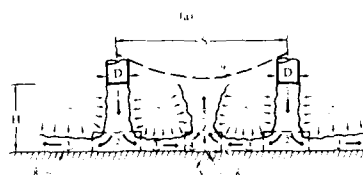
## 3. EXPERIMENTAL APPARATUS

Figure 2 shows the MDRI Hover Research Facility designed to conduct experimental studies of hover flowfields generated by VTOL aircraft and helicopters. The primary components are: 1. the main Plexiglas tank, 2. the header tank, 3. the nozzle units, and 4. the ground plate. The large transparent-walled Plexiglas main tank (11.48 x 1.62 x 1.17 m) has an approximate capacity of 350 liters.

The main tank houses the ground plate and either the nozzle units or model aircraft/helicopter, depending on the type of experiments to be conducted. It has bottom drains at all four sides and the bottom through which the section, fill, and drain lines are provided. The pressurized stainless-steel cylindrical header tank (91.4-cm diam.) supplies water to the nozzle units and also as a plenum to damp fluctuations produced by the pump.

The function of the Plexiglas nozzle units is to generate a source jet flow with acceptable levels of turbulent or non-uniformity; they are primarily used for basic fluid flow investigations. Studies with fountain (Fig. 1a) formation. Each nozzle unit, shown in detail in Figure 3, consists of a flow distributor, diffuser for conditioning the flow, a set of perforated plates, a honeycomb section of screens to establish a uniform flow with low turbulence, and a nozzle (1.6-cm exit diam.) for conditioning the flow.

The transparent Plexiglas ground plate is held at a fixed height above the bottom of the main tank and acts as an impingement surface for the jets with sufficient edge clearance for passage of the flow. The flow nozzles can be positioned by a traversing unit mounted in the main tank. The ground plate also draws off water from under the ground plate and pumps it into the header tank, thus supplying water to the jets through a series of flow control devices. With the available pumping capacity, jet Reynolds numbers up to 30,000 can be obtained in a typical 1.6-cm exit diam. impingement configuration.



- 1 Jet jet flow
- 2 Jet impingement region
- 3 Wall jet flow
- 4 Fountain formation region
- 5 Fountain up-wash flow
- 6 Wall jet interaction stagnation line
- 7 Entrainment
- 8 Ground plane
- 9 Fuselage undersurface

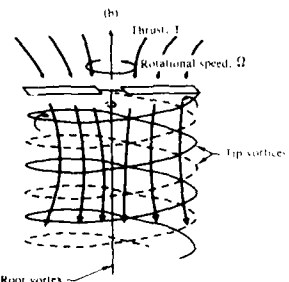
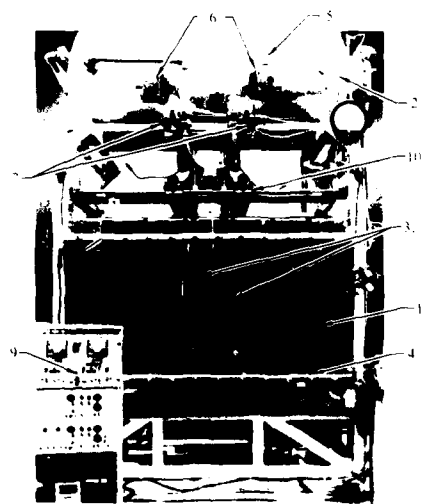


Fig. 1 Typical hover flowfields (a) multi-jet impingement flow in VTOL aircraft (b) Helicopter rotor downwash.



- 1 Main Plexiglas tank
- 2 Header tank
- 3 Nozzle units
- 4 Ground plate
- 5 Turbine flow meter
- 6 Motor-operated flow control valve
- 7 Sign-off valves
- 8 Settling chamber
- 9 Control panel

Fig. 2 Hover Research Facility

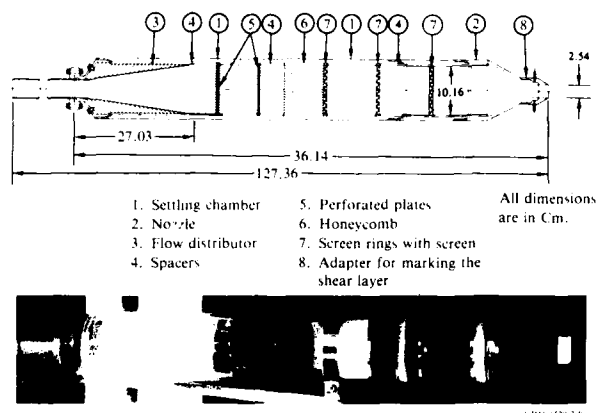


Fig. 3 Schematic of the nozzle units.

For VTOL aircraft model testing, the water is drawn through the inlets, circulates through the system, and exits through the jet nozzles on the model. The aircraft model is supported from the traversing system. The helicopter downwash is simulated by a scaled four-bladed rotor driven externally from above the main tank. For out-of-ground effect hover testing of helicopter models, the ground plate is replaced by a properly configured honeycomb with a hole (≈ 1 rotor-diameter in size) in the center to accommodate the unsteady rotor downwash. It should be mentioned here that an inexpensive small-scale pilot model facility shown in Fig. 4, was built to identify potential problems in the design of the large-scale Hover Research Facility and to develop the necessary flow-visualization techniques.

### 3.1 Flow-Visualization System

The HRF has a versatile flow-visualization system consisting of an injection system for introducing the tracer fluids (fluorescent dyes) into the required portions of the flow and an illumination system for producing a thin sheet of intense light, generated by an argon-ion laser, in any desired cross-section of the flow. Fluorescein-sodium, a dye that fluoresces a bright yellowish-green when excited with the 488-nm wavelength light of the argon-ion laser, is used extensively as a tracer fluid as it was found to be ideal for the present application. The laser beam from an argon-ion laser is steered through a series of optical components onto an optical scanner which in turn reflects the beam. The subject flows and are thus illuminated by the thin sheet of intense light generated by the oscillating laser beam.

### 3.2 Laser Doppler Velocimeter (LDV)

The nonintrusive nature of the LDV and its ability to sense the direction of flow are the primary reasons for selecting it as the primary measurement technique for the quantitative analysis of complex three-dimensional flows.

A two-color (two-component) TSI laser Doppler Velocimeter system was used in the dual-beam off-axis (about 30°) backward-scattering mode. Bragg-cell frequency shifting was used in both channels to detect the flow reversals. TSI counter-type signal processors were used to convert the Doppler signal into a form suitable for recording on a magnetic disk through a dedicated DEC MINC 11/23 computer. City water does not have enough particles to give good LDV signals in the backward-scattering mode; hence, the test medium is seeded with Dow Corning polystyrene particles (12 and 15  $\mu\text{m}$ ) to obtain good signal-to-noise ratios. Further details of the experimental apparatus and the flow visualization and measurement techniques are given in Ref. 1.

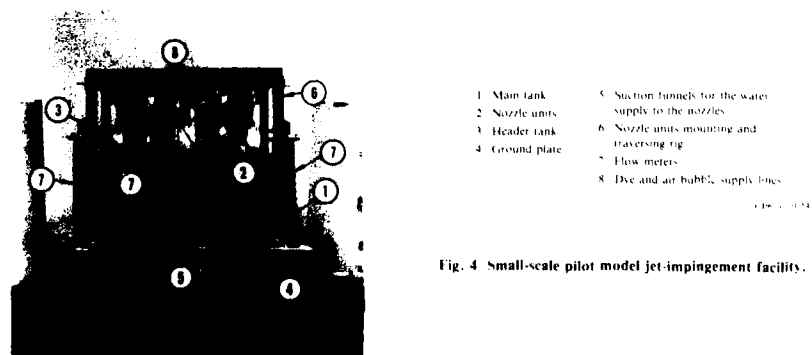


Fig. 4 Small-scale pilot model jet-impingement facility.

## 4. EXPERIMENTAL RESULTS

The application of the Hover Research Facility to the study of hover flowfields of VTOL aircraft and helicopters is described in the following.

## 4.1 Twin-Jet Normal Impingement

The upwash fountain flow (Fig. 1a) generated by the impingement of twin-jets is a flowfield common to all jet-powered VTOL aircraft configurations.

## 4.1.1 Flow Visualization Studies

Extensive flow-visualization studies were conducted on twin-jet fountain flows with the aid of dye, laser light-sheet technique. The first detailed view of the jet-impingement region, fountain formation region, and the fountain development was achieved. The effects of varying geometric parameters such as jet spacing, height of the jet exit, jet velocity, and jet diameter on the fountain flow were investigated through flow-visualization techniques. Stagnation-line patterns generated by multiple jet impingement were obtained by use of flow visualization with a sheet of light normal to the ground plane. Figure 5 shows some examples of these flow-visualization studies, some of which are replicated in the prototype facility; details are given in Refs. 2, 3 and 4. These flow-visualization studies were used to select the test cases for which detailed LDV measurements were made.

## 4.1.2 Laser Doppler Velocimeter Measurements

A two-component LDV was used to obtain mean-velocity and turbulence profiles for three different jet impingement configurations, shown in Fig. 6, with different jet spacing and height ratios from unity.

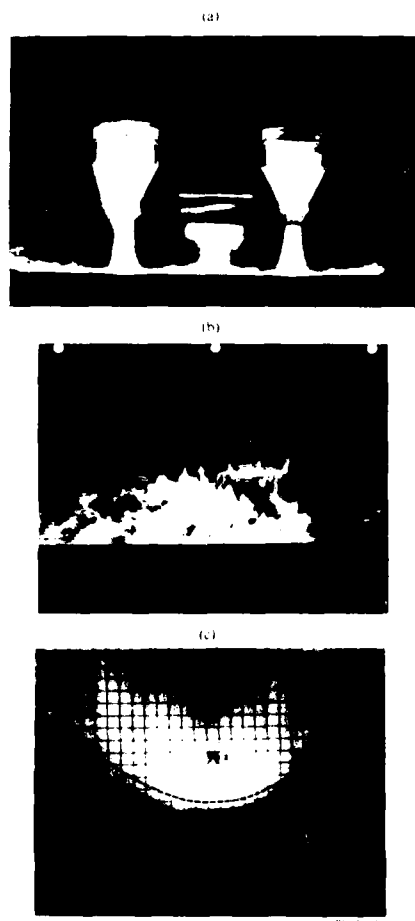


Fig. 5 Visualization of normally impinging twin-jet flow: (a) fountain upwash flow for equal strength jets, (b) radial flow in the fountain for equal strength jets, (c) stagnation line pattern for unequal strength jets.

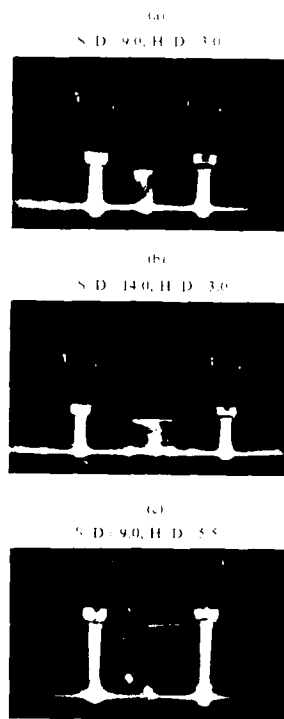


Fig. 6 Visualization of twin-jet impingement flow for three different configurations

The measurements were obtained in the symmetry plane connecting the nozzle centerlines. The distributions of mean-velocity components, turbulence intensities, Reynolds shear stress, and correlation function were derived from the basic data.

The distributions of mean-velocity and turbulence data across the fountain exhibit remarkable self-similarity for all configurations when non-dimensionalized with proper parameters. Figures 7, 8 and 9 show examples of the self-similar distributions of the non-dimensionalized data for the configuration for which  $S/D = 9$  and  $H/D = 3.0$ . The spreading of the fountain was found to be linear and the spreading rates were equal for all three jet-impingement configurations, as shown in Fig. 10. The decay of the streamwise maximum velocity in the fountain was found to be inversely proportional to the height above the nozzle; the rate of decay was equal for the three configurations, as shown in Fig. 11. The spreading time-scale and velocity decay characteristics closely resemble those of radial jets. The fountain was observed to be highly turbulent, with maximum turbulence intensities in the range of 50-60%. The data on the jet-impingement region and the majority of the fountain data, especially the turbulence data, are believed to be the final data reported on such flows. Details of the LDV measurements, specifically those in the impinging jet and fountain formation region, and those for other configurations are given in Refs. 1 and 6.

#### 4.2 Simulated VTOL Aircraft Flowfields in Hover

The fountain upwash flow (Fig. 1a) impinging along the underside of the fuselage of a VTOL aircraft, is a prime contributor to the near-field exhaust gas ingestion. Excessive ingestion of exhaust gas impairs propulsion system performance; the effect being more severe at higher exhaust gas temperatures. Also, impingement of the fountain on the fuselage undersurface increases skin temperatures.

One of the possible solutions to the exhaust gas ingestion problem is to annihilate the fountain by inclining the lift jets inward (Fig. 1b, Ref. 7), and accepting the associated decrease in the total lift. Alternatively, flow control devices such as deflectors may be used to redirect the fountain flow away from the inlets. These concepts were investigated in the Hover Research Facility through flow visualization studies on (a) an isolated twin-jet impingement flow, and (b) a full scale McDonnell Aircraft Company Model 274-1 ASTOL Advanced Short Takeoff and Vertical Landing aircraft.

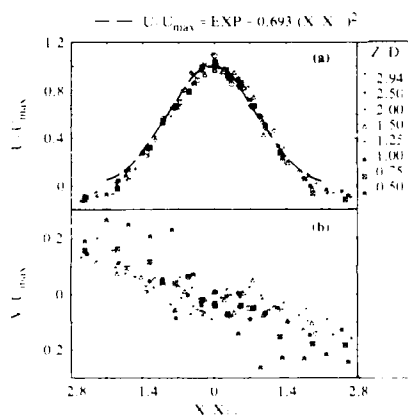


Fig. 7 Similar profiles of mean velocities ( $U, V$ ) across the fountain for the configuration:  $S/D = 9.0, H/D = 3.0$ .

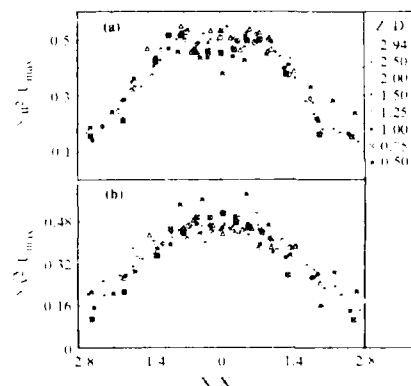


Fig. 8 Similar profiles of turbulence intensities in the fountain for the configuration:  $S/D = 9.0, H/D = 3.0$ .

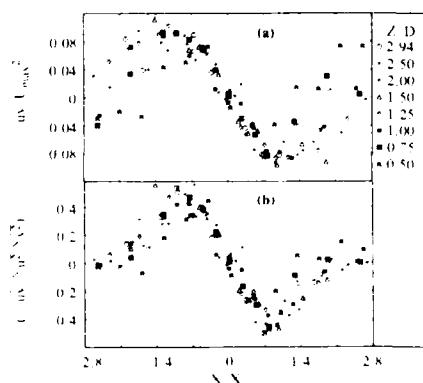


Fig. 9 Similar distributions of (a) Reynolds shear stress ( $-uv/u^2_{max}$ ) and (b) correlation function ( $-uv/\sqrt{u^2}\sqrt{v^2}$ ) across the fountain for configuration:  $S/D = 9.0, H/D = 3.0$ .

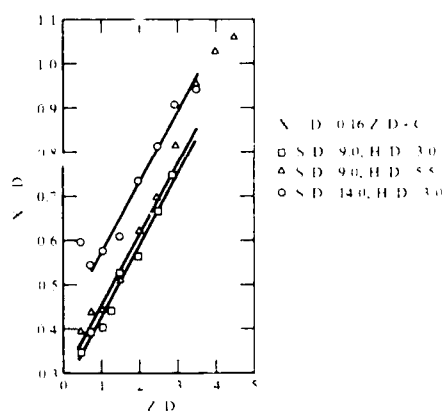


Fig. 10 Growth of the fountain half-width  $x_{1/2}$ .

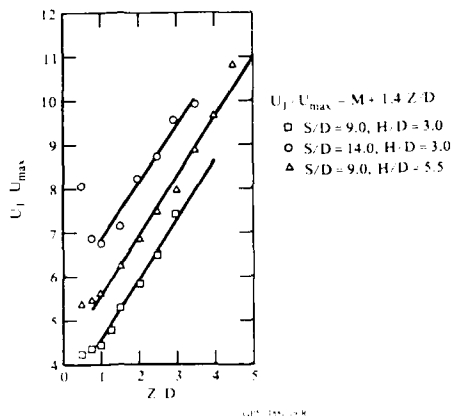
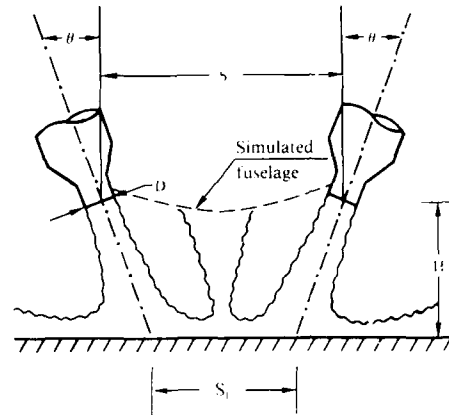
Fig. 11 Decay of the maximum velocity ( $U_{\max}$ ) in the fountain.

Fig. 12 Inclined twin-jet impingement flow.

#### 4.2.3. Inclined Twin-Jet Impingement

The flow field of the inclined twin-jet impingement flow was simulated with the impingement flow using the 3D-type turbulence model. The space between the two jets was divided into three regions: the upper region, the middle region, and the lower region. The upper region was divided into three regions: the upper region, the middle region, and the lower region. The middle region was divided into three regions: the upper region, the middle region, and the lower region. The lower region was divided into three regions: the upper region, the middle region, and the lower region. The flow field was simulated with the impingement flow using the 3D-type turbulence model. The space between the two jets was divided into three regions: the upper region, the middle region, and the lower region. The upper region was divided into three regions: the upper region, the middle region, and the lower region. The middle region was divided into three regions: the upper region, the middle region, and the lower region. The lower region was divided into three regions: the upper region, the middle region, and the lower region.

#### 4.2.4. Simulated Helicopter Flow

The flow field of the simulated helicopter flow was simulated with the impingement flow using the 3D-type turbulence model. The space between the two jets was divided into three regions: the upper region, the middle region, and the lower region. The upper region was divided into three regions: the upper region, the middle region, and the lower region. The middle region was divided into three regions: the upper region, the middle region, and the lower region. The lower region was divided into three regions: the upper region, the middle region, and the lower region. The flow field was simulated with the impingement flow using the 3D-type turbulence model. The space between the two jets was divided into three regions: the upper region, the middle region, and the lower region. The upper region was divided into three regions: the upper region, the middle region, and the lower region. The middle region was divided into three regions: the upper region, the middle region, and the lower region. The lower region was divided into three regions: the upper region, the middle region, and the lower region.

#### 4.3 Simulated Helicopter Flowfields in Hover

A NACA 0012 airfoil was used to simulate the helicopter flow field. The flow field was simulated with the impingement flow using the 3D-type turbulence model. The space between the two jets was divided into three regions: the upper region, the middle region, and the lower region. The upper region was divided into three regions: the upper region, the middle region, and the lower region. The middle region was divided into three regions: the upper region, the middle region, and the lower region. The lower region was divided into three regions: the upper region, the middle region, and the lower region. The flow field was simulated with the impingement flow using the 3D-type turbulence model. The space between the two jets was divided into three regions: the upper region, the middle region, and the lower region. The upper region was divided into three regions: the upper region, the middle region, and the lower region. The middle region was divided into three regions: the upper region, the middle region, and the lower region. The lower region was divided into three regions: the upper region, the middle region, and the lower region.

The flow field of the simulated helicopter flow was simulated with the impingement flow using the 3D-type turbulence model. The space between the two jets was divided into three regions: the upper region, the middle region, and the lower region. The upper region was divided into three regions: the upper region, the middle region, and the lower region. The middle region was divided into three regions: the upper region, the middle region, and the lower region. The lower region was divided into three regions: the upper region, the middle region, and the lower region. The flow field was simulated with the impingement flow using the 3D-type turbulence model. The space between the two jets was divided into three regions: the upper region, the middle region, and the lower region. The upper region was divided into three regions: the upper region, the middle region, and the lower region. The middle region was divided into three regions: the upper region, the middle region, and the lower region. The lower region was divided into three regions: the upper region, the middle region, and the lower region.

goal, experiments were conducted on a 9.49% geometrically scaled rotor and fuselage model of the NOTAH Helicopter in the Hover Research Facility. Figure 17 shows the NOTAH helicopter model in the Hover Research Facility.

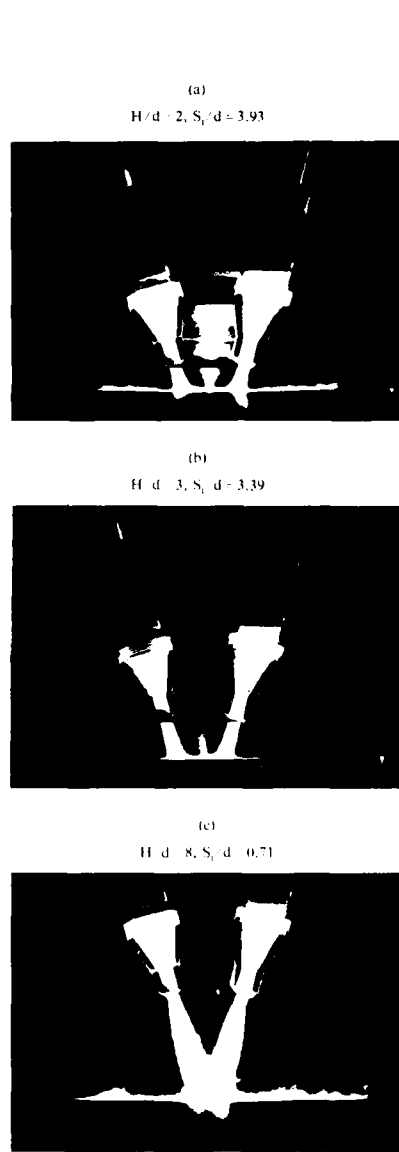


Fig. 13 Inclined twin-jet impingement flow at various heights above the ground.

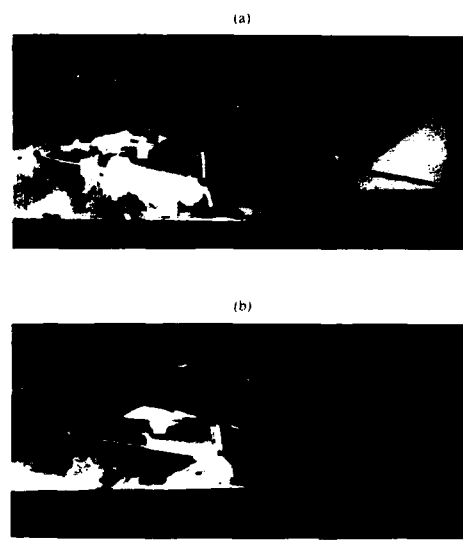


Fig. 14 Simulated exhaust gas flowfield (a) without (b) with the flow control devices around a model aircraft.

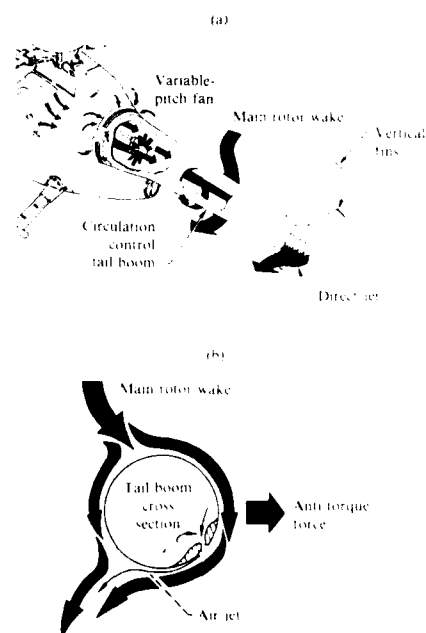


Fig. 15 NOTAH anti-torque system concept.



Fig. 16 NOTAR Flight demonstrator with fences.

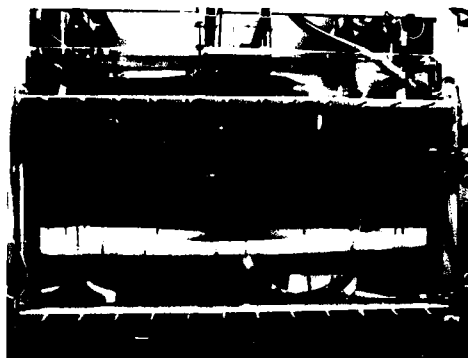


Fig. 17 NOTAR Helicopter model in the Hover Research Facility.

#### NOTAR Motor System

The purpose of the motor system was to provide the downwash with proper velocity distribution over the circulation control air boom. A four-bladed motor was used to provide one-half rotor diameter clearance along the upper side of the tank. NACA 0016 profile was used for the blade airfoils with different composite materials for the lower and upper blade halves to withstand compression and tension loads in the top and bottom halves, respectively. The motor was driven externally from above the main tank at 1750 rpm and was located 40 mm below the free surface to minimize the free-surface effects. The rotor rpm was established by scaling blade dynamic pressure. The unsteady rotor downwash was allowed to pass through a radially located hole (1/2 rotor diameter in size) in a plastic honeycomb (5-mm thick and 0.1 mm cell size) located 33 mm above the inside bottom of the main tank. The honeycomb replaced the ground plane in earlier jet impingement tests to simulate jet of ground hover testing of helicopter models. As the honeycomb eliminates large unsteady recirculation effects by allowing unrestricted passage of the downwash through the hole and smooth the flow as it returns through the honeycomb cell it is not to direct into the boom.

The downwash flow generated by the motor was validated by flow visualization studies and laser Doppler velocimeter (LDV) measurements. The downwash flow was visualized by seeding the tank with fine paint particles. Measurements were made during wind tunnel tests. The downwash was observed to pass through the hole in the honeycomb freely without impinging on it and exhibited the typical motor wake structure. The flow returning to the honeycomb was low velocity and did not disturb the natural flow pattern around the rotor. Figure 18 shows the velocity distribution in the downwash taken 50 mm below the plane of the rotor. The observed velocities were observed to be within 4% of the values for the full scale flight condition. Thus, the motor system was validated to give the desired downwash characteristics.

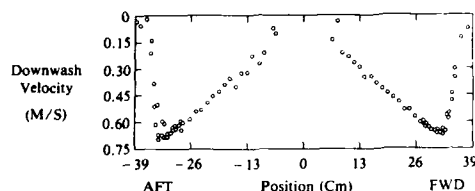


Fig. 18 Velocity distribution across the downwash.

#### 4.3.2 Flow Over the Tail Boom (Single Slot)

The scaled NOTAR fuselage was attached to the rotor. The fan inlet flow, the engine exhaust flow, and the flows from the jet thruster and the slot were simulated and scaled properly. The direct-jet thruster and the circulation control slot flows were metered individually. The slot momentum coefficient, a non-dimensional measure of the slot jet momentum was kept the same as for the NOTAR flight vehicle.

The flow over the tail boom was observed primarily by use of tufts. Figures 19a and 19c show the behavior of the flow over the tail boom as observed from the slot-side with and without the fences. Clearly, fences were necessary to keep the flow attached around the boom on the slot-side and to achieve the necessary circulation control (anti-torque) effects. Thus, the flow behavior exhibited on the exterior of the tail boom of the full-scale vehicle was duplicated in the tests conducted in the BHP. Figure 19c shows the attached flow around the tail boom in an end view obtained with the fluorescent dye/laser light sheet visualization technique.

#### 4.3.3 Solution to the Fence Problem

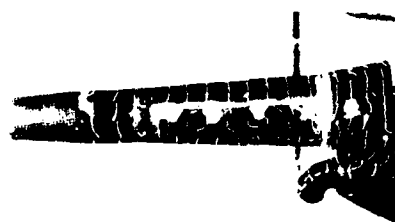
As stated earlier, the primary goal of the subject helicopter testing was to maintain attached flow around the boom without use of fences. Many configurational design modifications were tested but none was completely successful. The successful design that resulted in attached flow without fences is shown in Fig. 20. It consisted of a second slot added to the tail boom and was of the same length as the original slot. No additional flow was required and the total exit area of the original slot was divided between the two slots in the final configuration; the lower slot having a slightly larger cross-sectional area. Figure 21 shows the attached flow for the double slot-configuration without fences. Reference 4 gives full details of NOTAR helicopter model test results.

The NOTAR flight vehicle was modified to include the new slot design with an additional slot. The modified aircraft was flown successfully with improved performance characteristics of the NOTAR anti-torque system. Figure 22 shows the first flight of the modified NOTAR helicopter.

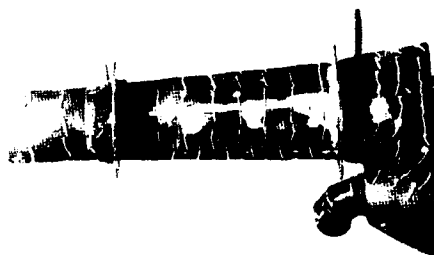
### 5. CONCLUSIONS

Water is shown to be an excellent working medium for flow visualization and LDV measurements. Detailed mean velocity and turbulence measurements were obtained on twin-jet fountain flows with application to VTOL aircraft. Mean velocity and turbulence profiles across the fountain exhibited self-similarity. The fountain was observed to be highly turbulent with maximum turbulence intensities in the range of 50-60%. The spread and mean velocity decay characteristics of the fountain closely resemble those of radial jets. Effective design solutions were obtained on engineering problems associated with VTOL aircraft and helicopters by use of flow-visualization techniques and through inexpensive scale-model testing in water.

(a) Fence "Off" (Side View)



(b) Fence "On" (Side View)



(c) Fence "On" (End View)



Fig. 19 Flowfield on the exterior of the tail-boom (single slot) (a) without fences, (b) and (c) with fences.



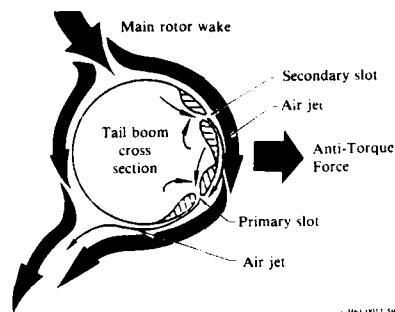


Fig. 20 Double-slot configuration.



Fig. 21 Attached flow for the double slot configuration without fences.



Fig. 22 First flight of the modified NOTAR Helicopter with two slots.

## 6. REFERENCES

1. Saripalli K. R., and Kroutil, J. C., "A Novel Experimental Facility for Conducting Jet Impingement Studies Related to VTOL Aircraft," AIAA 23rd Aerospace Sciences Meeting, Reno, NV, Jan. 1985; AIAA Paper 85-0052.
2. Saripalli, K. R., "Visualization of Multi-Jet Impingement Flow," AIAA/SAE/ASME 17th Joint Propulsion Conf., Colorado Springs, July 1981.
3. Saripalli, K. R., "Visualization of Multi-Jet Impingement Flow," AIAA J. 21, 483 (1983).
4. Saripalli, K. R., "Visualization Studies of Jet Impingement Flows at McDonnell Douglas Research Laboratories," Third Intl. Symp. on Flow Visualization, Ann Arbor, Sept. 1983.
5. Saripalli, K. R., "Laser Doppler Velocimeter Measurements in a 3-D Impinging Twin-Jet Fountain Flow," AIAA/AHS/ASCE Aircraft Design Systems and Operations Meeting, Colorado Springs, Oct. 1985; AIAA Paper 85-4036.
6. Saripalli, K. R., "Laser Doppler Velocimeter Measurements in 3-D Impinging Twin-Jet Fountain Flows," in Turbulent Shear Flows - 5: Selected Papers from the Fifth Symposium on Turbulent Shear Flows, Springer-Verlag 1986.
7. Lewis, W. J. and Hurd, R., "Augmented Vectored Thrust Engines and the Problem of Avoiding Hot-Gas Recirculation," J. Eng. Power 102, 61, 1980.
8. Kaemming, T. A. and Smith, K. C., "Techniques to Reduce Exhaust Gas Ingestion for Vectored Thrust V/STOVL Aircraft," AIAA Paper 84-2398, 1984.
9. Van Horn, J. R., "NOTAR (No Tail Rotor) Hover Testing Using a Scale Model in Water," 42nd Annual Forum and Technology Display, American Helicopter Society, June 1986.

## AN INVESTIGATION ON DUCTED PROPELLERS IN AXISYMMETRIC SHEAR FLOW

by  
J.A.C. Falcão de Campos (\*)  
Department of Mechanical Engineering  
Instituto Superior Técnico  
1096 Lisboa Codex  
Portugal

## SUMMARY

To improve the basic understanding of the complex interaction flow phenomena between ducted propeller systems and the ship's hull, the effects of radial non-uniformity of the inflow to the ducted propeller were investigated, both numerically and experimentally.

The mathematical model is based on the Euler equations for an inviscid, incompressible axisymmetric flow and on the representation of the propeller by an actuator disk. In a vorticity - stream function formulation, the problem is governed by two coupled integral equations, which express vorticity transport in the flow and the boundary conditions on the duct and hub surfaces. The numerical solution method employs a discretization of the vorticity field into vortex sheets, which are traced iteratively in a fixed grid.

The problem was also experimentally investigated in the Large Cavitation Tunnel of the Maritime Research Institute Netherlands. A five bladed propeller model, placed inside a duct, was tested behind wire screens, generating a wake velocity profile with axial symmetry. Laser-Doppler measurements of mean axial and radial velocities were carried out at various axial locations upstream and downstream of the ducted propeller. Detailed comparisons between the results of calculations and the experiments are presented and discussed.

## NOMENCLATURE

$C_p = (p - p_0) / (1/2 \rho U_0^2)$	- pressure coefficient
$\bar{C}_R = (2\bar{F}_R) / (1/2 \rho U_0^2 R^2)$	- duct radial force coefficient
$\bar{C}_{T_d} = T_d / (1/2 \rho U_0^2 R^2)$	- duct thrust coefficient
$\bar{C}_{T_p} = T_p / (1/2 \rho U_0^2 R^2)$	- propeller thrust coefficient
$E(k)$	- complete elliptic integral of the second kind
$\underline{F}$	- external force per unit mass
$F_R$	- duct radial force per unit radius
$F_x, F_r, F_\theta$	- components of $\underline{F}$ in the coordinate set $(x, r, \theta)$
$f_x, f_\theta$	- axial and tangential components of the concentrated force on the actuator disk
$G(x-x', r, r')$	- Green's function
$H = p/\rho + 1/2 u^2$	- total head
$H_0$	- total head of the undisturbed stream
$(\underline{i}_x, \underline{i}_r, \underline{i}_\theta)$	- unit vectors of coordinate set $(x, r, \theta)$
$\bar{J} = (U_0) / (U_\infty)$	- advance ratio
$K(k)$	- complete elliptic integral of the first kind
$K_{T_d} = (\pi/4) (T_d / \rho U_0^2 R^2)$	- duct thrust coefficient
$K_{T_p} = (\pi/4) (T_p / \rho U_0^2 R^2)$	- propeller thrust coefficient
$k, k_1$	- moduli of elliptic integrals
$k(s, s')$	- kernel function
$N$	- number of vortex sheets in the discretization of the non-uniform stream
$N_s$	- number of slipstream vortex sheets
$p$	- pressure

(\*) Present address: MARIN, 2, Haagsteeg, P.O. Box 28, 6700 AA Wageningen, The Netherlands.

11-2

$p_0$	- pressure at infinity upstream
$R$	- propeller radius, actuator disk radius
$R_0$	- radial extent of the inflow non-uniformity
$r_0$	- radius of the vortex sheet at infinity upstream
$r_\infty$	- radius of the vortex sheet at infinity downstream
$s, n$	- coordinates of the streamline based coordinate set $(s, n, \theta)$
$T_d$	- duct thrust
$T_p$	- propeller thrust
$U(r)$	- axial velocity of the undisturbed non-uniform stream
$U_0$	- uniform flow velocity outside the wake
$u, v, w$	- velocity components in the coordinate set $(x, r, \theta)$
$\underline{u}$	- velocity vector
$u_s, u_n, u_\theta$	- components of $\underline{u}$ in the streamline based coordinate set $(s, n, \theta)$
$x, r, \theta$	- cylindrical coordinates
$x$	- parameter of the complete elliptic integral of the third kind
$\Gamma$	- circulation on the actuator disk
$\gamma$	- strength of a vortex sheet
$\gamma_0$	- strength of the vortex sheet at infinity upstream
$\gamma_\infty$	- strength of the vortex sheet at infinity downstream
$\delta(x)$	- Dirac delta function
$\Pi(x^2, k_1)$	- complete elliptic integral of the third kind
$\rho$	- fluid density
$\psi$	- stream function
$\psi_{ij}$	- stream function value at a grid knot.
$\psi_\infty(x, r, r')$	- stream function induced by a semi-infinite ring vortex cylinder with unit strength
$\bar{\psi}$	- perturbation stream function
$\psi_d, \psi_p, \psi_w$	- stream function induced by the duct and hub surface vorticity, propeller vorticity and wake vorticity
$\psi_0$	- stream function of the undisturbed non-uniform stream
$\Omega$	- propeller angular velocity
$\underline{\omega}$	- vorticity vector
$\omega_x, \omega_r, \omega_\theta$	- components of $\underline{\omega}$ in the coordinate set $(x, r, \theta)$
$\omega_p, \omega_w$	- actuator disk vorticity, wake vorticity

#### SUBSCRIPTS

$(\underline{\quad})$	- vector
$d$	- duct
$p$	- propeller
$w$	- wake
$0$	- conditions at infinity upstream
$\infty$	- conditions at infinity downstream
$i, j$	- element or knot indices
$m$	- related to the $m^{\text{th}}$ vortex sheet
$k$	- related to the $k^{\text{th}}$ shipstream vortex sheet

## 1. INTRODUCTION

In marine applications, ducted propellers are frequently employed to achieve higher propulsive efficiency when the propeller is heavily loaded or to retard the occurrence of propeller cavitation, Ref. 1. In the first case, the duct is of the accelerating type and is acted by a positive thrust force in the same sense as the propeller thrust, while in the second case the duct is of the decelerating type and develops a negative thrust. One important aspect of the propulsive performance of ships fitted with ducted propellers relates to the way in which the interaction between the ducted propeller and the ship's hull is taken into account. In sympathy with conventional propeller practice, the usual interaction coefficients, known as thrust deduction, wake fraction and relative rotative efficiency, can be defined for ducted propellers. However, due to the presence of a third interacting element, the duct, which carries a force and induces a velocity field, such definitions are not straightforward. Basically, two extreme philosophies are possible and have been followed: the duct as a part of the hull and the duct as a part of the propulsor. Ref. 2 reviews both approaches and discusses alternative ones.

To improve the understanding of the interaction phenomena between duct, propeller and hull, more detailed analysis are required. Before attempting a complete analysis, the separate study of various aspects of the interaction phenomena is simpler from the theoretical point of view and is still a useful approach. One of the main aspects of interaction regards the interaction with the ship's wake, i.e., the interaction with the inflow non-uniformity to the propulsor. The study of this effect for conventional propellers has already deserved considerable attention in the last years (Refs. 3, 4, 5, 6 and 7). In all these studies the flow is assumed axisymmetric (i.e. only radial non-uniformity is considered) and inviscid, although rotational, with presence of vorticity in the incoming flow, assumed as a parallel shear flow.

The classical approach to the study of flow disturbances to parallel shear flows are based on inviscid flow theory (Euler equations of motion) and makes use of one of the approximations described by Bastien, (Ref. 8): the large shear-small disturbance approximation and the small shear-large disturbance, also known as secondary flow theory. Using the large shear-small disturbance theory, Weissinger (Refs. 9, 10) developed the linearised theory for two-dimensional airfoils in shear flows. Overlach in Ref. 11, extended this work to annular airfoils in axisymmetric shear flow. For the propeller interaction problem only the first approximation seems appropriate, considering the presence of strong shear in the ship's wake. Direct numerical solutions of the incompressible non-linear Euler equations for two-dimensional airfoils in shear flow have also been reported in the literature. Typical examples are the finite difference method of Chew et al (Ref. 12), the finite element calculations of Van der Vooren and Labrujère (Ref. 13) and the discrete vortex sheet method of Glück (Ref. 14).

In this paper the axisymmetric inviscid flow analysis is presented for a ducted propeller. The full non-linear problem, based on the Euler equations of motion, is first formulated in terms of vorticity and stream function, assuming the propeller to be represented by a lifting line model with infinite number of blades. Duct and hub surfaces are represented by vortex sheets and the boundary conditions are formulated considering the corresponding inner potential flow problems. Second, the problem is solved iteratively by a discrete vortex sheet method. The iteration proceeds from the previous approximation to the vorticity field to the next one, by computing the stream function induced at fixed grid knots and tracing the vortex sheets on the grid. The procedure allows the boundary conditions on the duct and hub to be treated in a rather natural way, but their statement is made in terms of velocity to improve accuracy.

Since no experimental data was available for comparison with the theoretical predictions, an experimental programme was conducted in the large Cavitation Tunnel of MARIN to obtain detailed information on the behaviour of a ducted propeller in a radially non-uniform flow. The test programme included force measurements on propeller and duct and detailed Laser-Doppler velocity measurements. A description of the experiments is given in Section 3. Finally, the comparison between the results of the theoretical calculations and the experimental data is presented and discussed.

## 2. THEORETICAL ANALYSIS

### 2.1 Formulation of the problem

Consider the flow of an inviscid and incompressible fluid through a ducted propeller system. The duct and hub are axisymmetric. The central body representing the hub is of finite extent. The propeller is represented by a lifting line model with infinite number of blades which exert axial and tangential forces on the fluid (actuator disk). The system is placed in a non-uniform axisymmetric axial stream with velocity  $U(r)$ .

The Euler equations of motion are

$$(\mathbf{u} \cdot \nabla) \mathbf{u} = -\nabla(P) + \mathbf{F}, \quad (1)$$

where  $\mathbf{u}$  is the fluid velocity,  $p$  the pressure,  $\rho$  the density and  $\mathbf{F}$  the external force per unit mass. The equation of continuity

$$\nabla \cdot \mathbf{u} = 0 \quad (2)$$

can be identically satisfied in axisymmetric flow introducing the Stoke's stream function  $\psi(x, r)$ . If  $(u, v, w)$  denote the velocity components in a cylindrical coordinate system  $(x, r, \theta)$ , then

$$u = \frac{1}{r} \frac{\partial \psi}{\partial r}, \quad v = -\frac{1}{r} \frac{\partial \psi}{\partial x}, \quad (3)$$

The vorticity vector  $\boldsymbol{\omega} = \nabla \times \mathbf{u}$  has components

$$\omega_x = \frac{1}{r} \frac{\partial(rw)}{\partial r}, \quad \omega_r = -\frac{\partial w}{\partial x}, \quad \omega_\theta = -\frac{1}{r} \left( \frac{\partial^2 \psi}{\partial x^2} - \frac{1}{r} \frac{\partial \psi}{\partial r} + \frac{\partial^2 \psi}{\partial r^2} \right) \quad (4)$$

In a curvilinear coordinate system  $(s, n, \theta)$ ,  $s$  being measured along the stream surfaces and  $n$  along the normal to the stream surfaces in a meridional plane, the vorticity vector has components

$$\underline{\omega} = \left( \frac{1}{r} \frac{\partial(rw)}{\partial n}, -\frac{1}{r} \frac{\partial(rw)}{\partial s}, \omega_\theta \right). \quad (5)$$

Using the vector identity

$$(\underline{u} \cdot \nabla) \underline{u} = \nabla \left( \frac{1}{2} \underline{u} \cdot \underline{u} \right) - \underline{u} \times (\nabla \times \underline{u}), \quad (6)$$

we obtain from (1), in the absence of external forces

$$\underline{u} \times \underline{\omega} = \nabla H, \quad (7)$$

where  $H = p/\rho + (1/2)u^2$  is the total head.

Eq. (7) shows that in the absence of external forces  $\partial H / \partial s = 0$  and  $\partial(rw) / \partial s = 0$ , i.e., the total head and the angular momentum are conserved along the meridional streamlines. Therefore, we may write

$$H = H(\theta), \quad rw = f(\theta). \quad (8)$$

The normal component of (7) writes

$$\frac{w}{r} \frac{\partial(rw)}{\partial n} - u_s \omega_\theta = \frac{\partial H}{\partial n}, \quad (9)$$

where  $u_s = (u^2 + v^2)^{1/2}$  is the meridional velocity. Using the relation  $d/d\theta = (1/ru_s) \partial/\partial n$  and Eq. (4), Eq. (9) becomes

$$\frac{1}{r^2} \left( \frac{\partial^2 \psi}{\partial x^2} - \frac{1}{r} \frac{\partial \psi}{\partial r} + \frac{\partial^2 \psi}{\partial r^2} \right) = \frac{dH}{d\theta} - \frac{(rw)}{r^2} \frac{d}{d\theta}(rw). \quad (10)$$

In the absence of swirl, Eq. (10) takes the form

$$\frac{\omega_\theta}{r} = -\frac{dH}{d\theta}, \quad (11)$$

which shows that  $\omega_\theta/r$  is constant along the meridional streamlines.

The Eq. (10) holds everywhere in the flow field, except at the disk itself, where an external force field is applied. Since the incoming flow is free of swirl, the particular form Eq. (11) holds everywhere in the field except inside the region occupied by the actuator disk and its slipstream. To determine the form of the right-hand-side of Eq. (10) in the disk slipstream, we have to consider the way in which the force field acts at the disk.

We assume the external force field at the disk to be of the form

$$\underline{F} = (f_x(\theta) \delta(s), 0, f_\theta(\theta) \delta(s)), \quad \theta \in (0, R), \quad (12)$$

where  $\delta$  is the Dirac delta function,  $R$  the disk radius and  $s=0$  denotes the point where the meridional streamline intersects the disk plane.

From

$$\underline{u} \times \underline{\omega} = \nabla H - \underline{F} \quad (13)$$

we derive

$$\frac{\partial H}{\partial s} = \frac{1}{u_s} (\underline{u} \cdot \underline{F}) \quad (14)$$

and

$$\frac{\partial}{\partial s}(rw) = \frac{r}{u_s} F_\theta. \quad (15)$$

Integrating (15) between  $s=-\infty$  and  $s=0$  and using (14), we get

$$rw = \begin{cases} 0 & \text{for } s < 0 \text{ (or } \theta > \theta(\infty, R)) \\ \frac{r}{u_s} f_\theta(r) & \text{for } s = 0 \text{ and } \theta \in (0, R), \end{cases} \quad (16)$$

which shows that  $rw$  has a jump at the disk. The jump in total head is found from a matching condition inside the blade row at the disk: the condition of normality between the force and the relative velocity to the blade. If the blade rotates with angular velocity  $\omega$ , such condition reads

$$(\underline{u} - \frac{1}{2}\omega \times \underline{r}) \cdot \underline{F} = 0, \quad (17)$$

which, with Eqs. (14) and (15), yields

$$\frac{dH}{ds} = \frac{\partial F}{\partial s} = -\frac{1}{2}\omega \frac{d}{ds}(rw). \quad (18)$$

Integrating Eq. (18) between  $s = -\infty$  and  $s = s = 0$ , we get

$$H(s) = \begin{cases} H_0(s) & \text{for } s < 0 \text{ or } s = 0, R \\ H_0(s) + \frac{1}{2}\omega rw & \text{for } s > 0 \text{ and } s = 0, R \end{cases} \quad (19)$$

where  $H_0 = p_0/\rho + 1/2 U^2$  is the total head before the disk and can be determined from the conditions at infinity upstream.

Substituting Eq. (19) in Eq. (10), we obtain for the flow in the slipstream:

$$\frac{1}{r^2} \left( \frac{\partial^2 \psi}{\partial x^2} - \frac{1}{r} \frac{\partial \psi}{\partial r} + \frac{\partial^2 \psi}{\partial r^2} \right) = -\frac{dH_0}{ds} + \left( -\frac{rw}{r^2} \right) \frac{d}{ds}(rw). \quad (20)$$

Eq. (20) extends to the non-uniform inflow case the equation presented by Wu (Ref. 13) for the uniform flow case. According to Eqs. (16) and (19), Eq. (20) applies outside the disk slipstream with the swirl term in the right hand side equal to zero.

Eq. (20) has to be solved subject to the particular boundary conditions of the present problem. The following boundary conditions may be imposed:

$$\frac{1}{r} \frac{\partial \psi}{\partial r} \rightarrow 0 \quad \text{as } x \rightarrow \pm \infty, \quad (21)$$

$$\frac{\partial \psi}{\partial x} \rightarrow 0 \quad \text{as } x \rightarrow \pm \infty \text{ or } r \rightarrow \infty, \quad (22)$$

$$\psi = 0 \quad \text{for } r = 0 \text{ and on the hub}, \quad (23)$$

$$\psi = C \quad \text{on the duct surface}, \quad (24)$$

In the boundary condition (24)  $C$  is an unknown constant which is related to the volume flow rate passing through the duct. The value of  $C$  depends on the circulation developed by the duct and can be determined by applying the Kutta condition at the duct's trailing edge.

For a full specification of the problem, the radial distribution of circulation

$$\Gamma(r) = 2\pi rw(s \rightarrow \infty) \quad (25)$$

is given at the disk.

For reasons of numerical convenience, the boundary conditions Eqs. (23) and (24) on the hub and duct surfaces are applied in a different way. Since we are only interested in the region external to the duct and hub surfaces, we may continue the flow field into the region bounded by these surfaces in an arbitrary way, provided these surfaces remain flow stream surfaces. If we assume the velocity to vanish identically inside this region, the velocity tangential to the surface is discontinuous and we obtain a representation of the duct and hub surfaces by vortex sheets. Then the boundary condition specifying zero tangential velocity on the inner side of the duct and hub contour is:

$$-\frac{1}{r} \left( \frac{\partial \psi}{\partial n} \right)_{\text{inn}} = 0 \quad \text{on the duct and hub}, \quad (26)$$

The strength of the vortex sheet  $\gamma(s) = -1/r(\partial \psi / \partial n)_{\text{out}}$  equals the discontinuity of tangential velocity at the surface.

The main difficulty in solving the problem governed by Eq. (20) with boundary conditions Eqs. (21) - (26) results from the fact that, although the differential operator on the left-hand side of Eq. (20) is linear, the right hand side is a non-linear function of  $\psi$ . For purposes of numerical solution, the boundary value problem, Eqs. (20)-(23) and Eqs. (25)-(26), is reduced to a coupled set of integral equations over the flow domain and its boundaries (duct and hub surfaces).

The stream function induced by a vorticity field  $\gamma_\omega(x, r)$  is:

$$\Psi(x, r) = \int_{\Omega} G(x-x', r, r') \omega_{\Omega}(x', r') dx' dr', \quad (27)$$

where the integration extends over the region where  $\omega_{\Omega}(x, r) \neq 0$ . The Green's function  $G(x-x', r, r')$  represents the stream function induced by a ring vortex with unit circulation. The expression in terms of elliptic integrals is given by Kücheman and Weber (Ref. 16):

$$G(x-x', r, r') = \frac{1}{2\pi} [(x-x')^2 + (r+r')^2]^{1/2} \left[ \left(1 - \frac{k^2}{2}\right) K(k) - E(k) \right], \quad (28)$$

with

$$k^2 = 4rr' / [(x-x')^2 + (r+r')^2]. \quad (29)$$

We write the stream function as a sum of three contributions

$$\Psi(x, r) = \Psi_w(x, r) + \Psi_p(x, r) + \Psi_d(x, r), \quad (30)$$

respectively associated with the wake vorticity

$$\omega_w = -rdH_0/dz, \quad (31)$$

the vorticity shed from the actuator disk

$$\omega_p = -(\dot{r} - \omega) \frac{d}{dz}(rw) \quad (32)$$

and the duct and hub vortex sheets  $\omega_d$ , Eqs. (27), together with Eqs. (30), (31) and (32), provides a non-linear integral equation in the flow domain.

The second integral equation expresses the boundary condition (26) on the duct and hub surfaces. When accounting for the velocities induced by the vorticity distributions (31) and (32), we get from Eq. (25):

$$-\frac{1}{2} \dot{r}(s) + \int_{\Omega} \frac{(\dot{r}(s') - \omega(s'))}{|D+1|} K(s, s') ds' = -\frac{1}{R} \left( \frac{\dot{r}_w}{n} + \frac{\dot{r}_p}{n} \right). \quad (33)$$

The kernel function is the velocity tangent to the contour induced on the point  $(x(s), r(s))$  by a ring vortex located on the point  $(x'(s'), r'(s'))$  of the duct and hub contour. As noted before, the integral equation (33) admits an infinite number of solutions with different circulation and theutta condition has to be added to uniquely specify the solution.

## 2.2 Numerical Solution

The problem formulated in the previous sub-section is solved numerically by a discrete vortex sheet method. The method is based on a discretization of the vorticity of the incoming flow and the vorticity shed from the actuator disk into a number of vortex sheets, (Fig. 1b).

We assume the wake region to be of finite extent and the velocity distribution  $\dot{r}$  is piecewise constant

$$\dot{r}(r) = \dot{r}_m \quad \text{for } r_{m-1} < r < r_{m+1}, \quad m=1, N, \quad (34)$$

with  $r_{01} = 0$ ,  $r_{0N+1} = R_0$  and  $\dot{r}_{N+1} = 0$ , being the constant velocity outside the wake. We further use  $\tilde{r}_m$  and  $\tilde{r}_{m+1}$  to define non-dimensional quantities, the stream function values at the radii of the vortex sheets  $r_{0m}$  and

$$\tilde{r}_m = \dot{r}_0(r_{0m}) = \sum_{j=1}^{m-1} \frac{1}{2} (\tilde{r}_{0j+1} - \tilde{r}_{0j})^2, \quad m=1, N. \quad (35)$$

The function  $H_0(\cdot)$  is constant between the vortex sheets. At the vortex sheets themselves, the function has a jump of magnitude

$$dH_0/dz = H_{0j+1} - H_{0j} = \frac{1}{2} (\tilde{r}_{0j+1}^2 - \tilde{r}_{0j}^2) = \tilde{r}_{0m}, \quad m=1, N, \quad (36)$$

where  $\tilde{r}_m = 1/2(\tilde{r}_{0m+1} + \tilde{r}_{0m})$  is the mean velocity at the sheet and  $\tilde{r}_{0m} = \tilde{r}_{0m+1} - \tilde{r}_{0m}$  is the strength of the vortex sheet at infinity upstream. The function  $dH_0/dz$  is

$$\frac{dH_0}{dz} = \sum_{m=1}^N \tilde{r}_{0m} \delta(\tilde{r} - \tilde{r}_m) \quad (37)$$

where  $\delta$  is the delta function of Dirac. The strength of the same vortex sheet at a general point in the

field is:

$$v_m(s) = \lim_{\epsilon \rightarrow 0} \int_{-\epsilon}^{+\epsilon} \omega_m \, dn = \lim_{\Delta t \rightarrow 0} \int_{t-\Delta t}^{t+\Delta t} \Delta H_{0m}^{-1} (z - z_m) \left[ -r/(z/\Delta n) \right] dz = \Delta H_{0m}^{-1} \left[ -\frac{1}{r} \left( \frac{z}{\Delta n} \right) \right]_{z=z_m}^{z=z_m+\Delta t}. \quad (38)$$

Since  $u_{sm} = -\frac{1}{r} \left( \frac{z}{\Delta n} \right)_{z=z_m}$ , from Eqs. (36) and (38) we get:

$$v_m(s) = \frac{\bar{v}_m}{u_{sm}} \cdot u_{sm}, \quad m = 1, N. \quad (39)$$

The same result could be obtained using the condition of equal pressure at both sides of the sheet and applying Bernoulli equation.

In a similar way, we discretize the vorticity shed from the actuator disk (Eq.12) into a number of vortex sheets by assuming a piecewise constant circulation distribution at the disk, i.e.,  $\Gamma(r) = \Gamma_k$  for  $r_k < r < r_{k+1}$ ,  $k=1, N$ . The first vortex sheet is assumed to be bound to the hub and the  $N$ th vortex sheet is shed from the edge of the actuator disk,  $r_{N+1} = 1$ . Following the same procedure as described for the wake vortex sheets, we derive for the strength of the  $k$ th slipstream vortex sheet

$$\gamma_k(s) = \left( \frac{1}{2J} - \frac{k+1}{2r_k} \right) \frac{\bar{v}_k}{u_{sk}}, \quad k=1, N, \quad (40)$$

where  $u_{sk} = -1/r(r/\Delta n)_{r=r_k}$  and  $(r/\Delta n)_{r=r_k} = (\bar{v}_k + \bar{v}_{k+1})/4$  are, respectively, the values of the meridional velocity and the angular momentum at the vortex sheets,  $J = (C_{L0})/(N)$  is the advance ratio and  $\Delta n = r_{k+1} - r_k$ . The same equation has been derived, in a slightly different way, by Greenberg (Ref.17) in his study of non-linear actuator disk theory.

The locations of the vortex sheets in the field are not known a priori and they have to be found by an iterative procedure, which we will describe further on. In each step of the iteration, the locations of the wake and slipstream vortex sheets are found by tracing in a fixed grid the stream surfaces  $\psi = \psi_m$ ,  $m=1, N$ , and  $\psi = \psi_k$ ,  $k=1, N$ . A grid of constant stepsize in the radial direction and of variable stepsize in the axial direction was employed in the present study (Fig.2). The constant stepsize in the radial direction was chosen to obtain higher accuracy in the computation of axial velocities from the knot values of the stream function by numerical differentiation. On each axial station  $x=x_i$ ,  $i=1, M$ , three point Lagrange interpolation is used to obtain from the knot values  $\psi_{ij}$  the radius  $r_{im}$  of the  $m$ th vortex sheet  $\psi = \psi_m$ .

In each iteration step the major effort of the computation goes into the calculation of the stream function induced at the grid knots by all the vortex sheets, including the hub and dust surface vortex sheets. For that purpose, each vortex sheet is further discretized into parabolic elements. The input points for fitting the parabolas are just the points  $(x_i, r_{im})$  obtained from the streamline tracing procedure. On each element the vortex sheet strength is assumed to vary linearly. Let  $x=x(t)$ ,  $r=r(t)$ ,  $t=0 \rightarrow 1$  be the parametric equations of a parabolic element,  $l$  being the total arc length measured from the parabola vertex,  $\gamma = \gamma(t) = \gamma(0) + \gamma(1)t$  the vortex sheet strength on the element. The stream function induced at the grid knot  $k = (x_i, r_j)$  by this single element is:

$$\psi_{ij}^{(e)} = \frac{\gamma(0)}{4\pi} \int_{-l}^{+l} \frac{r(t)}{r} dt + \frac{\gamma(1)}{4\pi} \int_{-l}^{+l} \frac{r(t)}{r} dt + \frac{\gamma(1)}{4\pi} \int_{-l}^{+l} \frac{r(t)}{r} dt + \frac{\gamma(1)}{4\pi} \int_{-l}^{+l} \frac{r(t)}{r} dt \quad (41)$$

The integrals in Eq.(41) are regular since  $r(t) \neq r$ , and they are evaluated numerically with Gaussian integration. A considerable number of Gaussian points is, however, required when the distance between the element and the grid knot is small. On the other hand, if the distance between the element and the grid knot is large in comparison with the typical arc length  $l$  of the element, multipole expansion of the Green's function about the parabola vertex are employed (Ref. 18).

Outside the computational grid  $x < x_1$  or  $x > x_M$  the vortex sheets are assumed to be of constant radius and are replaced by semi-infinite ring vortex cylinders of constant strength. The stream function induced by a ring vortex cylinder of radius  $r'$  extending from  $x' = 0$  to  $x' = \infty$  at a point  $(x, r)$  is given by Green's (Ref.19) in the form:

$$\psi(x, r, r') = \frac{r}{4\pi} \left[ A(\epsilon) + \frac{1}{\epsilon + \sqrt{\epsilon^2 + 1}} \right] - (1 - \epsilon) K(k_1) - (1 + \epsilon) E(k_1) + \frac{1}{\epsilon + \sqrt{\epsilon^2 + 1}} K(k_1) - E(k_1), \quad (42)$$

where

$$A(\epsilon) = \begin{cases} \pi & \text{for } \epsilon < 1 \\ 0 & \text{for } \epsilon > 1 \end{cases}$$

$$\epsilon = \frac{r}{r'} \quad \text{for } x < x'$$

$$k_1 = \frac{2\sqrt{r'}}{\sqrt{r^2 + r'^2 + 1}}, \quad \epsilon > 1, \quad \text{and } \quad \epsilon = \frac{r}{r'} \quad \text{for } x > x'. \quad (43)$$

and  $\epsilon = r/r'$ ,  $x > x'$ .



AD-A199 357

AERODYNAMIC AND RELATED HYDRODYNAMIC STUDIES USING  
WATER FACILITIES (US ADVISORY GROUP FOR AEROSPACE  
RESEARCH AND DEVELOPMENT NEUILLY-SUR-SEINE (FRANCE)  
JUN 87 AGARD-CP-413

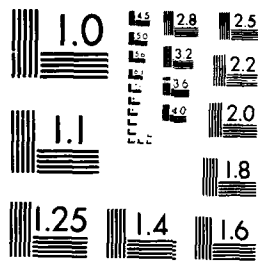
3/5

UNCLASSIFIED

1/6 2874

NL





MICROCOPY RESEARCH

Summing all the contributions from all the vortex sheets, the stream function at the grid knot  $(x_i, r_j)$  is:

$$\psi_{ij} = \sum_{(e)} \psi_{ij}^{(e)} + \sum_{m=1}^N \left[ \gamma_{om} \psi_{\infty}(-\zeta_{om}, \eta_{om}, r_{om}) + \gamma_{\infty m} \psi_{\infty}(\zeta_{\infty m}, \eta_{\infty m}, r_{\infty m}) \right] + \sum_{k=1}^{N_T} \gamma_{\infty k} \psi_{\infty}(\zeta_{\infty k}, \eta_{\infty k}, r_{\infty k}), \quad (44)$$

with  $\zeta_{om} = (x_i - x_1)/r_{om}$ ,  $\eta_{om} = r_j/r_{om}$ ,  $\zeta_{\infty m} = (x_i - x_m)/r_{\infty m}$ ,  $\eta_{\infty m} = r_j/r_{\infty m}$ ,  $\gamma_{om}$  and  $\gamma_{\infty k}$  are the asymptotic values of the wake and slipstream vortex sheet strength and  $r_{om}$  and  $r_{\infty k}$  the corresponding radii. In Eq.(44) the first summation is carried out over all the elements inside the computational grid, including the elements used to discretize the duct and hub surface vortex sheets.

The iterative procedure used to calculate the flow inside the computational domain can be described as follows:

- (1) We start from a first approximation to the locations of the vortex sheets, neglecting their deformation inside the computational domain, i.e., assuming the vortex sheets to be cylinders of constant radii. The constant strengths of the vortex sheets shed from the actuator disk are determined from moderately loaded theory.
- (2) The boundary conditions on the duct and hub surfaces are satisfied by solving (in discretized form) the Eq.(33) and applying the Kutta condition at the duct's trailing edge.
- (3) The values of the stream function at the knots of the computational grid are determined according to Eq.(44) and the vortex sheets are traced inside the computational domain.
- (4) The strengths of the wake and slipstream vortex sheets are determined from Eqs.(39) and (40) at the extremities of the elements, using the values of meridional velocities obtained by interpolation from axial velocity profiles and vortex sheet slopes on each axial station. As mentioned before, a linear variation of vortex strength between the values at the extremities is assumed on the element.

Steps 2 to 4 are repeated until convergence is achieved.

It must be noted that the strength of the hub and duct vortex sheets has much steeper gradients than the wake and slipstream vortex sheet strengths, due to the presence of stagnation points on the boundary. For that reason, the discretization of the boundary vortex sheets is not coupled to the computational grid and larger number of elements are placed near the stagnation points. Also from the point of view of numerical accuracy, Biot-Savart integration is preferred to numerical differentiation of stream function when evaluating the velocities on the right-hand-side of Eq.(33). Expressions for axial and radial velocities induced by a ring vortex can be found, for instance, in Ref.(16).

### 3. EXPERIMENTAL INVESTIGATIONS

To gather detailed experimental information on the performance of ducted propellers operating in a non-uniform flow and for comparison with the results of the theoretical calculations, a set of experiments was carried out in the Large Cavitation Tunnel of MARIN (test section 0.9 m x 0.9 m). A five bladed propeller model of 0.2 m diameter was placed at mid-chord inside a duct model (type NSMB 37, chord/diameter ratio = 0.5, Ref.(1)). Table 1 gives the main particulars of the propeller model. An axisymmetric wake field was generated ahead of the ducted propeller by means of a circular wire-mesh screen of 0.4 m diameter. To create a large velocity deficit at the axis of the wake a circular plate of 30 mm was placed in the center of the screen.

The velocity field at various planes upstream and downstream of the ducted propeller was measured with a Laser-Doppler velocimeter. The locations of the measuring planes are shown in Fig.3. Also shown in the figure are the locations of windows on the duct surface to allow Laser-Doppler measurements inside the duct. In the present investigation, with the propeller operating inside the duct, no such measurements were carried out. The velocimeter allowed the simultaneous measurement of velocity components in vertical (z) and axial (x) directions. The dimensions of the measuring volume are 0.214 mm in the vertical direction (z) and 16.34 mm in the horizontal direction (y). For this reason the velocity measurements were carried out by vertical traverses. Only mean velocity data was collected and no attempt has been made to measure turbulence quantities.

For various propeller loading conditions, the forces acting on the duct were measured. The axial force was measured with a strain gauge located in the fastening between duct and the tunnel wall. The radial force acting on the duct was deduced from the measurement of the force in the tangential direction, acting on the intersection of a meridional plane with the duct. For this purpose, the duct was cut into two parts in such a plane and the two parts were connected by force transducers with strain gauges. The force measurements were carried out for three propeller loadings with propeller rotational speeds of 645, 960 and 1600 r.p.m. at constant tunnel speed of 3.5 m/s. These conditions correspond to propeller thrust coefficients  $K_{Tp} = 0.101, 0.171$  and  $0.204$ , respectively.

### 4. RESULTS AND DISCUSSION

As a preliminary test case for the computational method and also for purposes of comparison, the ducted propeller in uniform flow was considered first. In this case only the slipstream vorticity needed to be discretized. The calculations were performed with 48 elements on the duct and 21 elements on the hub. The computational grid was chosen with 10 axial stations spanning the slipstream from the propeller disk  $x=0$  down to  $x=3$  (i.e., a distance downstream equal to three propeller radii) and 15 radial stations

with 0.175 as constant radial stepsize. This choice implied the discretization of each vortex sheet with 10 elements inside the computational domain. From preliminary calculations it appeared that to make the iteration process converge, relaxation was required. A relaxation factor of 0.5 was applied when computing new iterates to the stream function knot values. The convergence history of duct axial and radial forces is shown in Fig. 4. It is seen that 6 iterations were sufficient to get converged results within 1%. It can also be concluded in this case that the effect of the number of vortex sheets, used in the slipstream discretization, on the converged values of the duct forces is rather small.

In the case of the ducted propeller placed in the axisymmetric wake flow, the calculations were performed for the experimental conditions (propeller thrust coefficients  $K_{TP} = 0.101, 0.171$  and  $0.204$ ). The axial velocity profile measured behind the screen was discretized with 11 vortex sheets, as shown in Fig. 5. In this figure the wake velocity is given relative to the velocity measured outside the wake. It should be noted that this velocity,  $U_0 = 4.13$  m/s, outside the wake field generated by the screen, was considerably larger than the tunnel speed, which was set to 3.75 m/s. Such increase of velocity is thought to be due to the displacement of the screen inside the tunnel. In the calculations we used the velocity measured outside the wake to define the propeller advance ratio  $J = (U_0)/(nR)$  and the loading coefficient  $C_{TP} = T_P / (1/2 \rho U_0^2 \pi R^2)$ . No corrections for tunnel wall interference were applied to the results of the experiments.

To ascertain the effect of the propeller radial distribution of loading, two distinct distributions were used in the calculations. They are shown in Fig. 6 together with the corresponding piecewise constant discretizations. Due to the different curvature of the vortex sheets at different propeller loadings, two grids with different number of axial stations (implying different number of elements on the vortex sheets) were used. For the two higher loadings, where the vortex sheets are more curved, especially ahead of the ducted propeller, a grid with 24 axial stations was considered. For the smallest loading 15 axial stations were taken. In all cases the number of radial stations was 15.

Fig. 7 shows the convergence histories of the duct forces. It is seen that, in general, six iterations were sufficient to get converged results within 2% for the duct radial force and 1% for the duct thrust. Generally, the vortex sheets traced inside the computational domain appeared to be rather smooth and no difficulties were met in tracing vortex sheets in the close vicinity of the duct and hub surfaces. For the highest propeller loading the configuration of the vortex sheets, calculated with the disk circulation distribution 1, is shown in Fig. 8. It is to be remarked that the grid used to trace the vortex sheets is too coarse to enable an accurate approximation to the vortex sheet shape in regions of extreme streamline curvature or curvature gradient which occur near the duct stagnation points and near the hub nose.

The comparison between the calculations in uniform flow and in the shear flow at the same propeller loading (thrust identity) is shown in Figs. 9 and 10. Fig. 9 shows the locations of the slipstream vortex sheets calculated with the disk circulation distribution 1. The results show that there is a much lower rate of decrease of the radial velocity with the distance to the ducted propeller in the shear flow case. From Fig. 10 it can be concluded that, for the same propeller radial load distribution, the effect of shear tends to decrease the thrust ratio between propeller and duct.

The comparison between the calculated and measured axial velocity profiles at three different locations upstream and downstream of the ducted propeller are shown in Figs. 11 to 13. It may be concluded that the agreement between the calculations, assuming circulation distribution 1, and the measured profiles is reasonable at the highest propeller loading, but worsens as the propeller load decreases. Although the real circulation distributions of the propeller at various loadings have not been established in this work, it is known, from comparison with a companion study in uniform flow (Ref. 18), that the position of the maximum value of circulation moves radially inwards with decreasing propeller loading in the case of shear flow. To illustrate the sensitivity of the computed velocity field to the radial circulation distribution, the results of the calculations with the circulation distribution 2, are also shown in the figures. It can be seen that the effect of the circulation distribution on the induced velocities is very large inside the propeller slipstream. This result points out to the need for determining the correct radial circulation distribution of the propeller. It should be reminded that the traverse made upstream of the ducted propeller was performed at a very small distance from the duct leading edge. With the radial stepsize employed in the calculations, the axial velocity gradients near the leading edge could not be resolved. Also, the duct viscous wake has not been modelled, so that the calculations are not expected to be accurate in that region (region of strong velocity deficit, about  $r/R = 1.1$  in Figs. 12 and 13).

The comparison between the computed and measured duct forces is given in Table 2. The discrepancies are very large, even at the highest propeller loading in which the correlation for the velocity field is reasonable. Although the viscous effects on the duct are not known, there is a tendency toward a consistent overestimation of the duct forces by the theory. The uncertainty in the propeller circulation distribution cannot explain the discrepancies. In fact, although it has a considerable influence in the velocity field calculated inside the slipstream, it appears to have a much smaller effect on the duct forces. No clear-cut explanation of the discrepancies can be given, although two essential difficulties with the application of the present method may well be responsible for the found differences. The first relates to the particular discretization of the wake profile and the total head of the duct stagnation stream surface. In fact, the difference in duct force, obtained if the duct stagnation stream surface is traced in consecutive intervals of total head far upstream, is of the order of magnitude of the differences between the theoretical and experimental results. Second, the circulation around the duct contour is controlled by the Kutta condition at the duct's trailing edge. For this particular duct, which has a thick round trailing edge, the choice of the rear stagnation point (which was the particular form of the Kutta condition used in this study) remains arbitrary to a certain extent.

##### 5. CONCLUDING REMARKS

A theoretical model based on the axisymmetric Euler equation has been applied to study the effects of inflow radial non-uniformity on the performance of a ducted propeller. The two coupled integral equations governing the problem were solved numerically by a discrete vortex sheet method. Although the method was not applied to resolve in detail all flow regions, a characterization of the effects of axisymmetric

shear on the performance of the ducted propeller, has been given. The agreement with the measured velocity field is reasonable, considering the uncertainties of the propeller radial load distributions. Since for ducts with a round trailing edge, inviscid flow theory provides with no means of determining the duct circulation, an accurate prediction of the forces acting on the duct remains a difficult task.

#### 6. REFERENCES

1. Oosterveld, M.W.C., "Wake Adapted Ducted Propellers", Doctor's thesis, NSMB Publication N° 345, 1970.
2. Stierman, E.J., "Extrapolation Methods for Ships Fitted with a Ducted Propeller", Int. Shipb. Progr., Vol. 31, N° 356, April 1984, pp.3-10.
3. Huang, T.T., Wang, H.T., Santelli, N., Groves, N.C., "Propeller/Stern boundary layer interaction on axisymmetric bodies: theory and experiment", DTNSRDC Report 76-0113, Dec. 1976.
4. Huang, T.T., Groves, N.C., "Effective wake: theory and experiment", 13th Symp. Naval Hydrodynamics, Tokyo, ONR, 1980.
5. Goodman, T.R., "Momentum theory of a propeller in a shear flow", Journ. Ship Research, Vol. 23, N° 4, Dec. 1979, pp.242-252.
6. Dyne, C., "A note on the design of wake adapted propellers", Journ. Ship Research, Vol. 24, N° 4, Dec. 1980, pp.227-231.
7. Falcão de Campos, J.A.C., Van Gent, W., "Effective wake of an open propeller in axisymmetric shear flow", NSMB Report n° 50030-3-SN, May 1981.
8. Hawthorne, W.R., "On the theory of shear flow", Gas Turbine Laboratory, Report n° 88, MIT, Cambridge, Massachusetts, 1966.
9. Weissinger, J., "Linearisierte Profiltheorie bei ungleichförmiger Anströmung. I. Unendlich dünne Profile (Wirbel und Wirbelbelegungen)", Acta Mechanica, 10, 1970, pp.207-228.
10. Weissinger, J., "Linearisierte Profiltheorie bei ungleichförmiger Anströmung. Teil II: Schlanke Profile", Acta Mechanica, 13, 1972, pp.133-154.
11. Overlach, B., "Linearisierte Theorie der axialsymmetrischen Strömung um Ringflügel bei ungleichförmiger Anströmung", Dissertation, Karlsruhe, 1974.
12. Chow, F., Krause, E., Liu, C.H., Mao, J., "Numerical investigations of an airfoil in a non-uniform stream", Journ. of Aircraft, Vol. 7, N° 6, 1976, pp.531-537.
13. Van der Vooren, J., Labrujère, Th. E., "Finite element solution of the incompressible flow over an airfoil in a non-uniform stream", International Conference on Numerical Methods in Fluid Dynamics, Univ. of Southampton, 1973.
14. Glück, D., "Theoretische und experimentelle Untersuchungen von stationären Strömungsfeldern mit inhomogener Anströmung", Dissertation, Ruhr-Universität Bochum, 1979.
15. Wu, T.Y., "Flow through a heavily loaded actuator disk", Schiffstechnik Bd. 9, Heft 47, 1962, pp.134-138.
16. Kücheman, D., Weber, J., "Aerodynamics of propulsion", McGraw-Hill, 1953.
17. Greenberg, M.D., "Nonlinear Actuator Disk Theory", Zeitschrift für Flugwissenschaften, Bd. 20, Heft 3, pp.90-98.
18. Falcão de Campos, J.A.C., "On the Calculation of Ducted Propeller Performance in Axisymmetric Flows", Doctor's thesis, NSMB Publication N° 696, 1983.
19. Coesel, M.J.N., "Nonlinear Actuator Disk Model for Propeller and Windmill", Fourth Lips Propeller Symposium, Druenen, The Netherlands, 1979.

#### 7. ACKNOWLEDGEMENT

This study was performed during the author's stay at MARIN-NSMB, on leave from Instituto Superior Técnico. The financial support of Instituto Superior Técnico is gratefully acknowledged. The author would like to thank Dr. W. Van Gent and Ir. B.R.I. Luttmer for their interest and many helpful discussions.



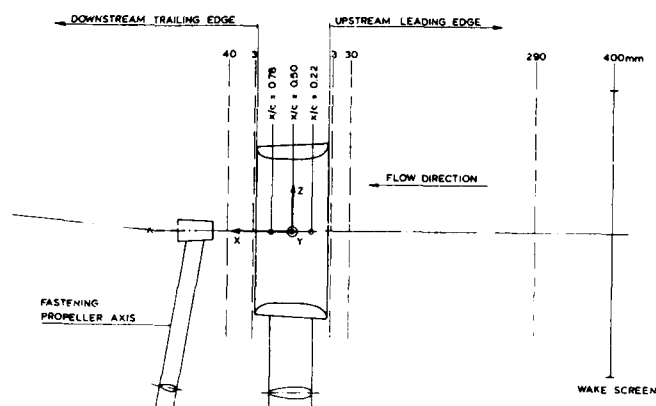
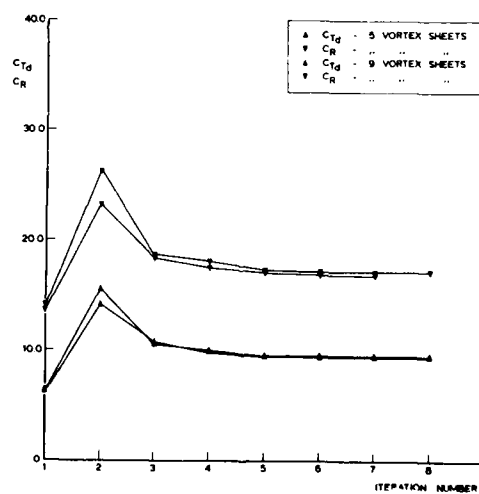


Fig. 3. Location of Laser-Doppler velocity traverses.

Fig. 4. Convergence history of duct forces. Duct propeller in uniform flow  $J = 0.208$ ,  $C_{T0} = 12.48$ .

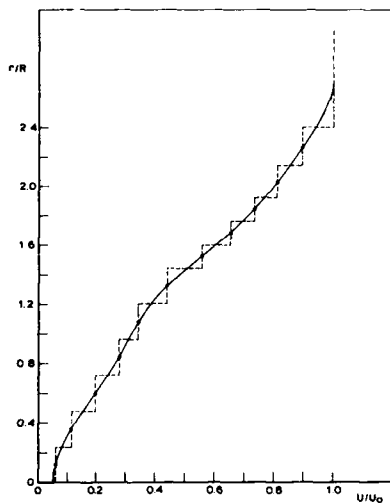


Fig. 5. Discretization of wake velocity profile.

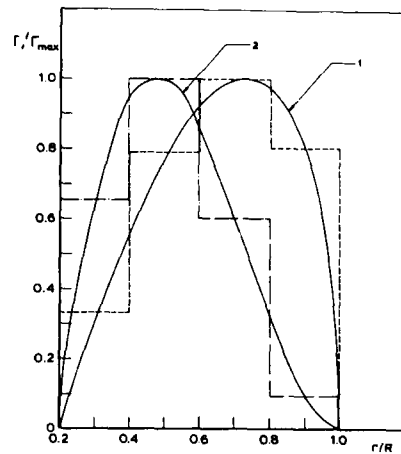


Fig. 6. Discretization of disk circulation distributions.

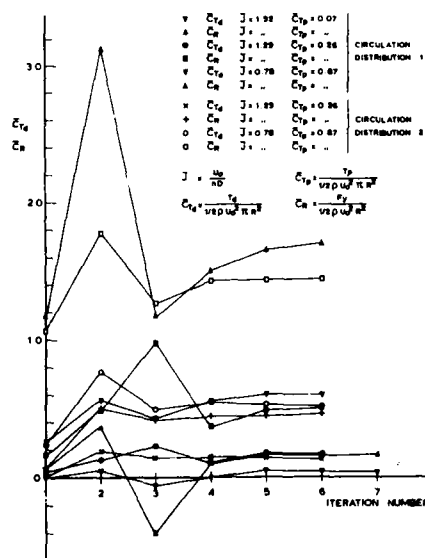


Fig. 7. Convergence history of duct forces. Ducted propeller in shear flow.



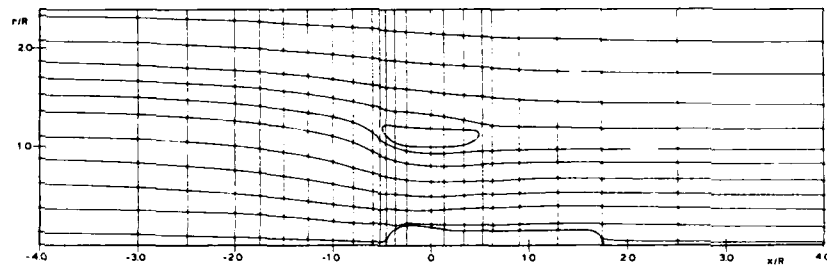


Fig. 8. Location of wake vortex sheets. Ducted propeller in shear flow.  $\bar{J} = 0.78$ ,  $\bar{C}_T \approx 0.87$ .

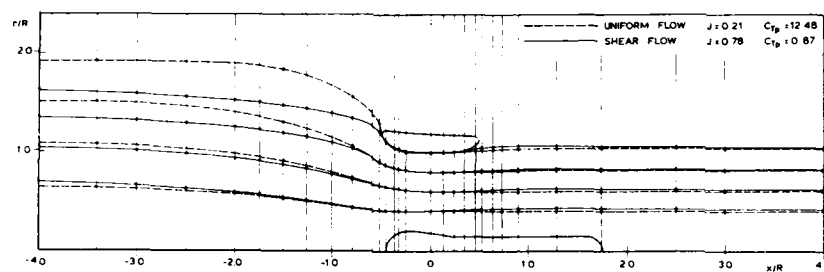


Fig. 9. Location of slipstream vortex sheets. Comparison between uniform flow and shear flow.

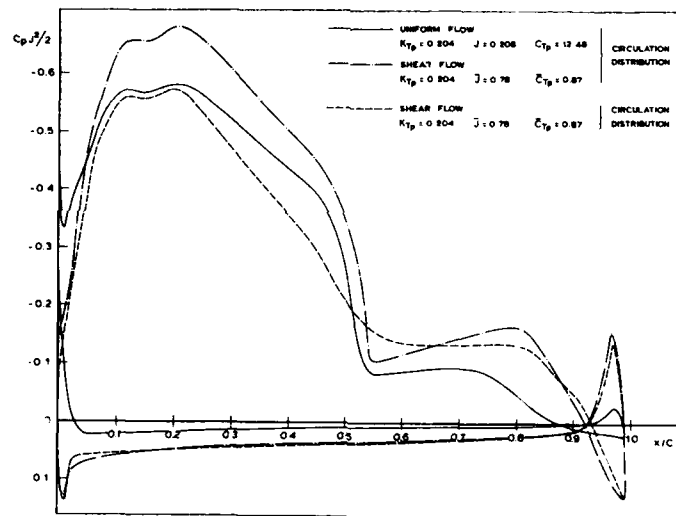


Fig. 10. Pressure distributions on the duct.

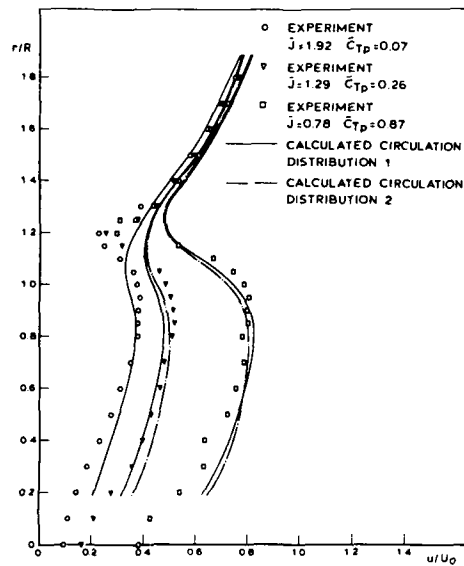


Fig. 11. Measured and calculated axial velocity profiles at  $x/R = -0.53$ . Ducted propeller in shear flow.

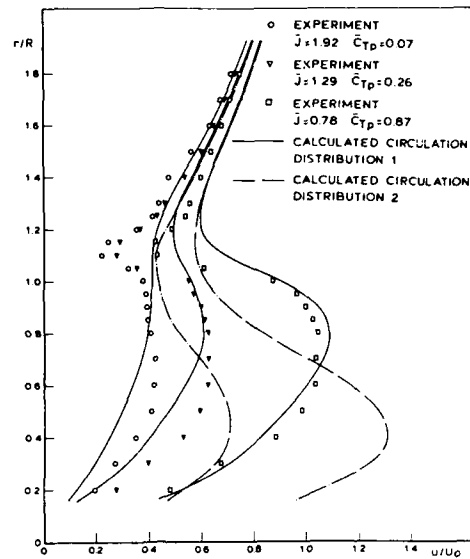


Fig. 12. Measured and calculated axial velocity profiles at  $x/R = 0.53$ . Ducted propeller in shear flow.

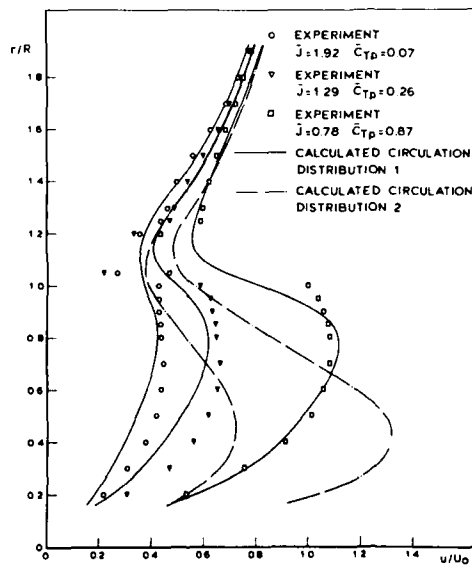


Fig. 13. Measured and calculated axial velocity profiles at  $x/R = 0.90$ . Ducted propeller in shear flow.

MEASUREMENTS OF AERODYNAMIC FORCES ON UNSTEADILY MOVING BLUFF  
PARACHUTE CANOPIES

by

D.J.Cockrell, R.J.Harwood and C.Q.Shen\*  
University of Leicester Engineering Department  
Leicester LE1 7RH, England

SUMMARY

Equations which describe the unsteady motion of bluff bodies through fluids contain certain components, termed added mass coefficients, which can only be determined by experiment. From the solutions to such equations the ways in which the shapes of parachute canopies influence the frequency of their oscillatory motion in pitch and their corresponding damping rates are required. Although a full-scale parachute canopy descends through air, oscillating in pitch as it does so, experiments necessary to determine these added mass coefficients have been performed under water, using for this purpose a large ship tank from the towing carriage of which the model parachute canopies were suspended. These experiments showed that the added mass coefficients for bluff parachute canopies differed appreciably from their corresponding potential flow values. The latter were obtained from the analysis of inviscid fluid flow round regular shapes which were representative of those parachute canopies. The significance for the prediction of the parachute's dynamic behaviour in pitch of these differences is outlined.

NOMENCLATURE

$a$	Dimensionless velocity-component of force
$C_N$	Total normal aerodynamic force coefficient developed on the immersed body
$C_T$	Total tangential aerodynamic force coefficient developed on the immersed body
$[C_T]_V$	Velocity-dependent component of the tangential aerodynamic force coefficient in unsteady flow
$D_0$	Nominal diameter of parachute canopy
$F(t)$	Instantaneous force acting on the immersed body
$F_i$	Inertia force acting on the immersed body
$F_T$	Total force acting on the immersed body
$k$	Added mass coefficient $k=a/\rho_f V$
$k_{11}$	Added mass coefficient in the canopy axis of symmetry direction, caused by linear motion in that direction
$k_{53}$	Added mass coefficient in the canopy transverse direction, caused by linear motion in that direction
$m$	Mass of system under consideration
$S$	Representative area of the immersed body
$T$	Period of oscillation
$V(t)$	Instantaneous velocity of the immersed body
$V_N$	Oscillatory velocity component in the transverse direction
$V_0$	Maximum amplitude of immersed body velocity
$V_R$	Resultant velocity of the immersed body
$V_S$	Steady descent velocity
$V_T$	Oscillatory velocity component in the axial direction
$\alpha$	Added mass of the immersed body also angle of attack
$\rho_f$	Density of the fluid in which the body is immersed
$V$	Representative volume of immersing fluid displaced by the body. For a parachute canopy $V=\pi D_0^3/12$

INTRODUCTION

In order to predict satisfactorily the amplitude and the frequency of the pitching oscillations accompanying the descent motion for a system comprising a parachute canopy and its payload, the relevant equations of motion must first be established. If for the purposes of simplicity the canopy and payload are considered as two rigidly-connected components of a single system then the dynamics of the latter can be expressed in six component equations, three of which represent translational motion and three rotational motion. Each equation of motion consists of terms which represent either aerodynamic, gravitational or inertial forces and moments. Though the latter two terms can be formulated readily, the aerodynamic forces and moments acting on an unsteadily-moving bluff body, with an instantaneous acceleration as well as an instantaneous velocity, are also required. For a bluff body like a parachute canopy, whose mass is of the same order as that of the fluid which it displaces, these unsteady aerodynamic forces and moments are not generally determinable analytically. Thus, the purpose of the experimental programme which is to be described is to determine these aerodynamic terms.

\* Honorary Visiting Fellow, University of Leicester. Permanent Address: Research Institute of the Hongwei Machinery Factory, Xiangfan, Hubei Province, China.

## 1. AERODYNAMIC FORCES AND MOMENTS ACTING ON UNSTEADILY-MOVING BLUFF BODIES

When an immersed body moves unsteadily through a real and incompressible fluid Iversen & Balent<sup>1</sup>, among others, have modelled the instantaneous component of the aerodynamic force developed in a given direction  $F(t)$  in terms of a component depending on the body's instantaneous resultant velocity  $V_R(t)$  together with a second component, termed the *added mass*, which depends on its instantaneous acceleration in a given direction,  $\dot{V}(t)$ . Thus:

$$F(t) = \frac{1}{2}\rho S a V_R^2(t) + k a_f V \dot{V}(t) \quad (1)$$

where  $\rho$  denotes the density of the fluid in which the body is immersed while  $S$  and  $V$  respectively denote a representative area and a representative volume of the immersed body. This expression, in which  $a$  and  $k$  are, as yet, two undetermined dimensionless coefficients, derives from the proportionality to  $V_R^2$  in steady flow of the component of aerodynamic force in a given direction and the proportionality to  $\dot{V}$  of a component of aerodynamic force which can be shown to be developed on an immersed body moving unsteadily through an ideal fluid.

For model parachute canopies the coefficients  $a$  and  $k$  are to be determined experimentally. However, in such an experiment the aerodynamic force  $F(t)$  is not the only force which acts on the system, comprising the canopy and its support. Because this whole system of mass  $m$  moves unsteadily, an inertia force,  $F_i = -m\dot{V}$ , also acts on it. Thus the total external force  $F_T$  to be applied to the system equals  $F + F_i$  and can be written:

$$F_T = \frac{1}{2}\rho S a V_R^2(t) + (k a_f V + m)\dot{V}(t) \quad (2)$$

Any experimental method of determining the coefficients  $a$  and  $k$  depends on measurement of instantaneous values of  $F_T$  together with corresponding instantaneous values of  $V_R$  and  $\dot{V}$ . The technique adopted is by mounting the model parachute canopy on to one end of a stiff sting, the opposite end of which is strain-gauged. To this latter end the desired instantaneous motion is imparted to the model. To determine the coefficient  $k$  it is first necessary to separate the effects of the two acceleration-dependent terms in Eq.(2). Even if the mass of the model were very small compared with its added mass,  $k a_f V$ , the mass of its supporting sting when compared with that of the representative volume of air displaced by the parachute canopy could not be considered to be negligible.

By testing the model canopy under water rather than in air and then by shrouding the support sting so that any aerodynamic forces which might be developed on it would be of no significance, the term  $k a_f V$  can be increased by nearly three orders of magnitude without materially altering the inertia force developed on the sting. Provided that these tests are scaled correctly, so that under water the model behaviour is properly representative of the prototype in air, the use of water facilities for these aerodynamic studies considerably simplifies the measurement technique to be adopted.

Once the decision has been taken to test the parachute models under water, the use of water facilities rather than a wind tunnel becomes increasingly attractive on the grounds of what is more readily available to an experimentalist concerned with the aerodynamic forces and moments developed on bluff parachute canopies. Probably the biggest single problem in determining aerodynamic forces developed on models of bluff bodies like parachute canopies is that of blockage constraint. It would be unwise to make measurements in a constrained environment in which the blockage area ratio, defined as the ratio of the cross-sectional area of the bluff body under test to the cross-sectional area of the fluid stream at the body location, exceeded about 7.5%, thus for a small model of a parachute canopy, having a projected diameter of 600 mm say, the appropriate minimum cross-sectional area for a wind tunnel working section would be about 3.5 m<sup>2</sup>, say 7.0 ft. diameter. To attain full-scale Reynolds number the working section wind speed would need to be about 60 ms<sup>-1</sup>, or about 200 ft.sec<sup>-1</sup>. It would be difficult to assess the power requirement adequately for such a facility but experience suggests it would be at least 90 kW (120 h.p.) and this exceeds the scope of most teaching establishments such as the University of Leicester.

By contrast, the power required to propel a bluff body through otherwise stationary water can be rather more modest. In the test programme to be described model parachute canopies were moved unsteadily under water in the 61.0 m.(200 ft.) long ship tank shown in Fig.(1). This ship tank is located at The Institute of Higher Education, Southampton, England. It has a cross-sectional area of 3.66 m.(12 ft.) x 1.83 m.(6 ft.). In such a facility full scale Reynolds number around model parachute canopies fixed to the ship tank towing carriage would be attained at carriage velocities of about 15 ms<sup>-1</sup>, with a power requirement dependent on the complexity of the towing carriage but of the order of only about one-half that required for the corresponding wind tunnel. The ship tank used was originally designed for the testing of streamlined ship hulls, thus considerably less power than this was available at the towing carriage. However, since early flow separation occurs from bluff parachute canopies, achievement of Reynolds numbers of about one-tenth full scale or greater was quite adequate for test purposes.

There are thus good reasons why the required experimental programme was undertaken under water in a ship tank rather than in a large and thus costly wind tunnel facility.

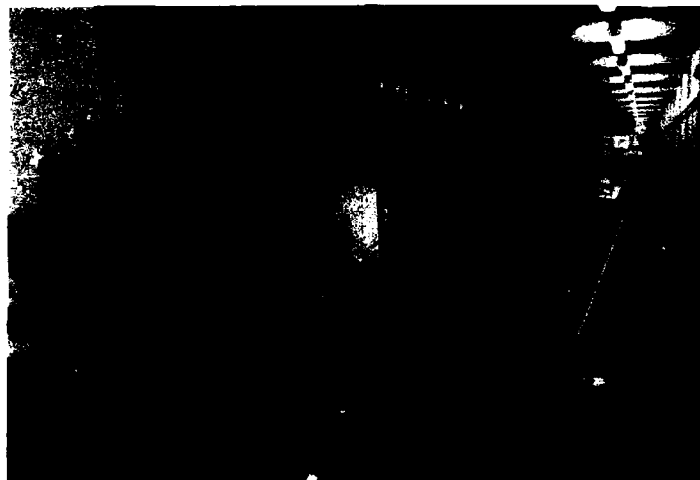


Fig.1 The Ship Towing Tank at the Institute of Higher Education,  
Southampton, England

## 2. SCALING MODEL TESTS

To obtain results which can be applied to the prototype parachute canopy, the model must be both geometrically and dynamically similar to the prototype. Geometric similarity implies accurate modelling of the full-scale canopy shape, inclusive of canopy flexibility and porosity. Achievement of the necessary porosity is discussed in Section 4. To measure aerodynamic forces and moments means must be found to transmit internal forces and moments from the parachute canopy to the strain gauge transducers. In these tests a rigid extension to the support sting was carried through a grommet at the apex of the canopy, at which point aerodynamic forces and moments could be transferred from the canopy to the sting extension, to the suspension line confluence point, where aerodynamic forces and moments transmitted through these suspension lines could be transferred. This sting extension undoubtedly constricted the model canopy, indeed in giving it rigidity it may well have helped to ensure geometric similarity of the otherwise flexible canopy. There is no evidence that it does so in a manner which is at all unrepresentative of the full-scale prototype canopy.

To achieve dynamic similarity not only must the model Reynolds number based on the towing carriage velocity be approximately that for the prototype motion but the oscillatory motion must also be to scale, that is, the ratio of towing carriage velocity to maximum oscillatory velocity, or reduced velocity, must be approximately scaled. For a scale model with scaled oscillation amplitude Sarpkaya and Isaacson<sup>2</sup> have shown that this reduced velocity is a function of the Keulegan-Carpenter number,  $V_0 T / D_0$ , where  $V_0$  is the maximum velocity amplitude for the immersed body and  $T$  is the oscillation period. For the tests here described the periodic motion mechanism applied sinusoidal oscillations to the system for which the reduced velocity was about 5:1. At this value, in transverse motion the model parachute canopy oscillated through angles of attack of about  $\pm 10$  degrees. Under these conditions, Sarpkaya and Isaacson indicated that both the velocity-dependent force components (first term on r.h.s. in Eq.(2)) and the inertia components (second term on r.h.s. in Eq.(2)) may well be significant.

## 3. METHODS OF MEASURING THE VELOCITY-DEPENDENT COEFFICIENTS IN UNSTEADY MOTION AND THE ADDED MASS COEFFICIENTS

By means of the strain-gauged stinger the parachute canopy model was connected via the simple harmonic motion generating mechanism shown in Fig.(2) to the ship tank towing carriage. The sting was rigidly attached to the U-shaped clamp shown on the right of this figure. In this way the steady velocity of the towing carriage was made to represent the canopy's steady descent velocity  $V_S$  and the oscillatory motion representative of the canopy's pitching motion during descent could be generated and superimposed on this steady velocity. By rotating the circular turntable shown in the figure, periodic motion could be imparted in any required direction to the canopy.

For the two-dimensional motion of a fully-inflated parachute canopy shown in Fig.(3), the resultant velocity  $V_R$  can be represented by a steady descent velocity  $V_S$  together with a periodic oscillatory motion which possesses a component  $V_T$  along the canopy axis of symmetry and a component  $V_N$  at right angles to this axis. First consider the canopy to be at zero angle of attack and the oscillatory motion to be entirely in the axis of symmetry direction.

Then:

$$V_R(t) = V_S + V_T(t) \quad (3)$$

and

$$\dot{V}(t) = dV_T(t)/dt \quad (4)$$

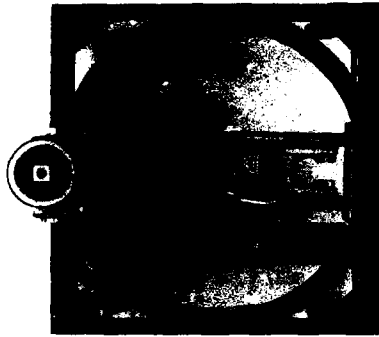


**Fig. 2 Mechanism Used to Impart Simple Harmonic Motion to the Strain-gauged Canopy Supporting Sling**

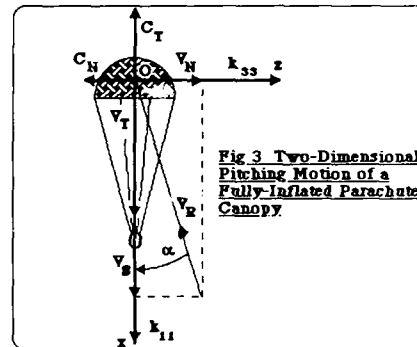


**Fig. 3 Two-Dimensional Pitching Motion of a Fully-Inflated Parachute Canopy**

A mean value of the coefficient  $a$ , which in this case represents the velocity-dependent part of the tangential force coefficient  $C_T$ , can be determined by multiplying through Eq.(1) by  $V_T(t)$  and integrating the resulting equation with respect to time, when since

$$\int_0^T [2V_T(t)\dot{V}(t)]dt = [V_T^2]_0^T = 0 \quad (5)$$

$$\text{then} \quad a = C_T = \int_0^T [F(t)V_T(t)]dt / \int_0^T \rho_f S \int_0^T V_R^2(t)V_T(t)dt \quad (6)$$

Similarly, the coefficient  $k$ , which in this case represents the added mass coefficient in the direction of the canopy axis of symmetry  $k_{11}$ , is given by multiplying Eq.(1) through by  $\dot{V}(t)$  before integrating with respect to time, for as

$$\begin{aligned} \int_0^T [V_R^2(t)\dot{V}(t)]dt &= \int_0^T [V_S^2\dot{V} + 2V_S V_T\dot{V} + V_T^2\dot{V}]dt \\ &= [V_S^2 V_T + V_S V_T^2 + V_T^3/3]_0^T = 0 \end{aligned} \quad (7)$$

$$\text{then} \quad k = k_{11} = \int_0^T [F(t)\dot{V}(t)]dt / \frac{1}{2} \rho_f S \int_0^T V_R^2(t)\dot{V}(t)dt \quad (8)$$

Now consider the parachute to be at zero angle of attack and the oscillatory motion to be entirely in the transverse direction, at right angles to the axis of symmetry.

Then

$$V_R(t) = [V_S^2 + V_N^2(t)]^{0.5} \quad (9)$$

and

$$\dot{V}(t) = dV_N(t) / dt \quad (10)$$

As the parachute canopy oscillates its instantaneous angle of attack  $\alpha(t)$  is given by:

$$\alpha(t) = V_N/V_S \quad (11)$$

and for small values of angle of attack

$$a = C_N = (\partial C_N / \partial \alpha) \cdot (V_N/V_S) \quad (12)$$

Then, by multiplying Eq.(1) through by  $V_N(t)$ :

$$(\partial C_N / \partial \alpha) = \int_0^T [F(t)V_N(t)]dt / \frac{1}{2} \rho_f S \int_0^T V_R^2(t)V_N(t)dt \quad (13)$$

In the same way, the coefficient  $k$ , which now represents the added mass coefficient  $k_{33}$ , is given by multiplying Eq.(1) through by  $V(t)$  before integrating with respect to time:

$$k = k_{33} = \int_0^T [F(t)\dot{V}(t)] dt / \rho_f \int_0^T V^2(t) dt. \quad (14)$$

#### 4. LACK OF GEOMETRIC SIMILARITY. THE POROSITY OF PARACHUTE CANOPIES

The nominal porosity of parachute canopy fabric is determined by measuring, at a known pressure difference, the discharge of air through unit area of the fabric. In Britain this pressure difference is 10 inches of water; in the United States and in mainland Europe it is 0.5 inches of water. Since this discharge will depend on the properties of the fluid flowing through the fabric, its porosity in water will differ significantly from its porosity in air.

The porosity of parachute fabric has a small effect on the magnitude of the tangential force coefficient  $C_T$  but a marked effect on the magnitude of the normal force coefficient  $C_N$ . The directions of these steady state aerodynamic coefficients are shown in Fig.(3). Since the magnitude of  $C_N$  will affect that of the rate of change of normal force coefficient with angle of attack, measured at zero angle of attack  $(dC_N/d\alpha)_{\alpha=0}$ , the selection of a canopy fabric having an appropriate porosity is an important way of ensuring that  $(dC_N/d\alpha)_{\alpha=0}$  is positive and thus that the canopy exhibits static stability in pitch. Because fabric porosity is influenced by the test medium, wrong conclusions about parachute stability can be drawn from tests on canopies performed under water.

This point is illustrated in Fig.(4). In this figure characteristics have been drawn showing the variation of the coefficient  $C_N$  with angle of attack for three different canopies, all of the same shape. In air, canopy (a) is of negligible porosity, canopy (b) of average porosity and canopy (c) is very porous. Whether determined in air or in water the characteristics of canopy (a) indicate static instability in pitch. Correspondingly, both in air and in water canopy (c) exhibits static stability. But canopy (b) exhibits static stability in air but static instability in water.

The reason for this difference is evident. For a given pressure difference laminar flow through the pores of the fabric is inversely proportional to the viscosity of the fluid flowing. Since the viscosity of water is some 50 times that of atmospheric air the discharge of water through canopy (b) will be negligible, making it effectively imporous. Dimensional analysis reveals that the conditions under which the discharge through the pores is inversely proportional to the viscosity are that the same material must be tested in the two effectively incompressible media, with the same applied pressure difference, at effectively identical Reynolds numbers and Euler numbers,  $\Delta p(1/2\rho_f V^2)$ . In the experiments described the dynamic pressure with water discharging did not differ appreciably from that made normally in airflow, thus the two Euler numbers were not dissimilar.

This observation illustrates that aerodynamic testing of models in other media than that in which the prototypes fly is not just a matter of ensuring that overall Reynolds number similarity has been maintained.

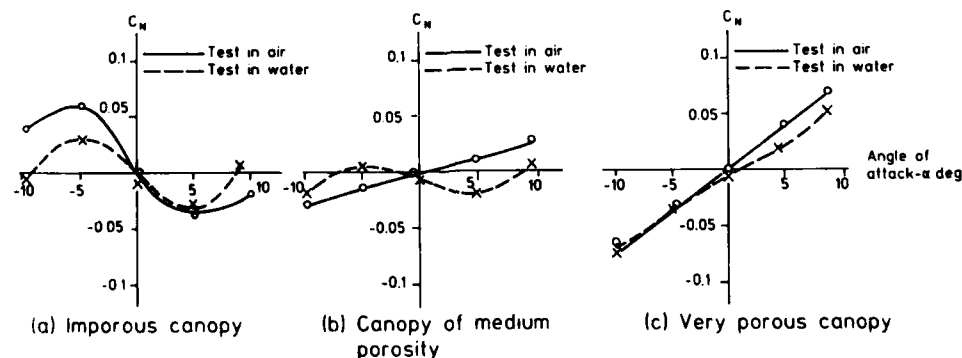


Fig. 4 Tests on porous parachute canopies in air and in water

## 5. ANALYTIC AND EXPERIMENTAL VALUES OF SIGNIFICANT ADDED MASS COEFFICIENTS

An analytical relationship concerned with parachute stability in pitch and originally produced by Doherr and Saliaris<sup>3</sup>, has been reproduced in outline in Fig.(5). The original relationship was based on the assumed characteristics of an 8.5 m.(28 ft.) nominal diameter parachute canopy with a mass of 6.7 kg. and a cylindrical payload of 127.3 kg. The canopy was assumed to be statically stable at an angle of attack of zero degrees and  $dC_N/da$  per radian at zero angle of attack could have any positive value from zero to infinity. No numbers have been assigned to the axes in the figure as these are functions of the parameters chosen for the canopy and its payload.

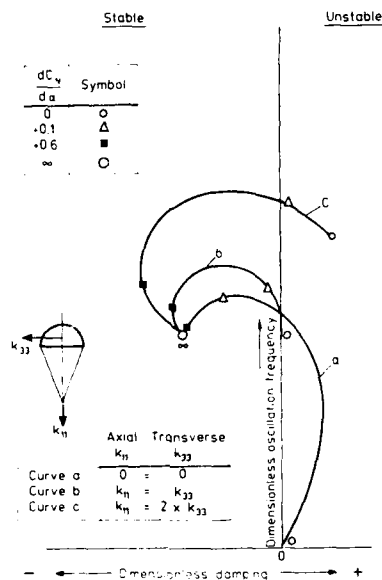


Fig. 5 Effect of added mass coefficients on dynamic stability after Doherr and Saliaris.

Provided that  $dC_N/da$  is positive, the figure makes clear that considering the ratio of  $k_{11}$  to  $k_{33}$  to be equal to 1.0 (curve b) rather than for each of these coefficients to be zero (curve a) results in a small destabilising tendency and increases the frequency of the pitching oscillations. If the ratio of  $k_{11}$  to  $k_{33}$  exceeds 1.0 (curve c) this destabilising tendency is increased. When  $dC_N/da$  is large and positive the added mass coefficients  $k_{11}$  and  $k_{33}$  have little effect on dynamic stability characteristics, but their values are of considerable significance when the value of  $dC_N/da$  is small and thus marginal. What constitutes a marginal value for  $dC_N/da$  is itself dependent on the relative sizes of the added mass coefficients,  $k_{11}$  and  $k_{33}$ .

The only values for  $k_{11}$  and  $k_{33}$  that can be established by analysis are those for potential flow around a shape representative of a parachute canopy. To determine these values is rather more difficult than might at first appear. A range of analytical values of from 1.6 to 2.1 has been determined for  $k_{11}$  and is given in the literature. A corresponding value for  $k_{33}$  is 1.3. From potential flow methods of analysis there are therefore grounds for supposing that for flow round a parachute canopy the added mass coefficient  $k_{11}$  is marginally larger than the coefficient  $k_{33}$ .

Some experimental values determined in the present test programme are given in Table 1. Values obtained for the velocity-dependent component of the tangential aerodynamic force coefficient in unsteady flow,  $[C_T]_V$  and for the rate of change with angle of attack of the velocity-dependent component of the normal force coefficient, measured at zero angle of attack,  $[dC_N/da]_{\alpha=0}$ , are sufficiently close to steady flow corresponding values for latter to be recommended for use in predictions of parachute dynamic motion in pitch that is, for this pitching motion to be considered to be quasi-steady.

For the added mass coefficients in the direction of the canopy axis of symmetry,  $k_{11}$ , experimental values obtained substantially exceed potential flow evaluations of from 1.6 to 2.1. The experimental values can be seen to vary in a predictable manner with the volume of air which is enclosed within the canopy. As the porosity of the canopy fabric is increased there are reductions of  $u_m$  to about 10% from imporous canopy values for  $k_{11}$ .

The measured added mass coefficients in the canopy transverse direction,  $k_{33}$ , are smaller by an order of magnitude at least from the corresponding values for  $k_{11}$ . In fact, in the programme of tests conducted they were of the same order of magnitude as the inertial forces developed on the canopy supporting sting, thus they could not be separated with precision from these inertial forces. However,



in future tests conducted in the Southampton ship tank measurements of the transverse added mass coefficient,  $k_{33}$ , will be made using parachute canopies that are of twice the present nominal diameter, increasing by eight times the added mass component in the transverse direction while only marginally increasing the corresponding inertial forces.

**Table 1: EXPERIMENTAL CHARACTERISTICS OF PARACHUTE CANOPIES  
IN STEADY AND UNSTEADY MOTION**

	$C_{T-}$ Steady State	$[C_T]_{V-}$ Unsteady Motion	$[dC_N/d\alpha]_{u,a=0}$ Steady State /radian	$[dC_N/d\alpha]_{u,a=0}$ Unsteady Motion /radian	Added Mass Coefficients $k_{11}$ $k_{33}$ Axial Transverse	
Round Canopies						
Without Drive Slots	0.54	0.57	- 0.33	- 0.17	5.5	Ne
With Drive Slots	0.58	0.51	- 0.34	-	5.5	gl
Cross Canopies						
3:1 Arm Ratio						
Imporous	0.74	0.63	- 0.17	- 0.29	3.9	ig
Very Porous, $\lambda = 23^*$	0.61	0.61	+ 0.37	+ 0.36	3.6	ib
4:1 Arm Ratio						
Imporous	0.79	0.69	+ 0.52	+ 0.42	3.2	le

\* cu ft /sq ft/sec, measured at 10 inches of water pressure

## 6. CONCLUSIONS

In these tests conducted on model parachute canopies in which water facilities were used rather than the air as the test medium, two advantages and one disadvantage are apparent:

### Advantages

1. In unsteady motion, testing under water rather than in air leads to easier separation of acceleration-dependent aerodynamic forces from inertial forces, since the former are dependent on the mass of the fluid displaced by the models while the latter, developed on both the immersed body and its support, depend on the mass of that immersed body and its support.

2. Ship towing tanks constitute large test facilities in which bluff bodies can be tested without significant blockage constraint. Because the model bluff bodies rather than the immersing fluid is moved by the power source, it is probable that these facilities use rather less power than do wind tunnels having working sections of corresponding sizes.

### Disadvantage

Since use of a fluid medium which differs from that in which the prototype flies can introduce unexpected scaling problems, when using water facilities care must be taken in considering the relevant dimensionless groups which influence the required aerodynamic characteristics. In the problems considered the Euler number,  $\Delta p / (1/2 \rho_f V^2)$ , is a significant but unexpected independent dimensionless parameter.

## 7. ACKNOWLEDGEMENTS

This work has been conducted with the support of the Procurement Executive, U.K. Ministry of Defence to whom the Authors express their thanks. They also thank the Principal and Staff of Institute of Higher Education, Southampton for permission to use the ship tank and for their ready assistance with the tests conducted.

## REFERENCES

- Iversen, H.W. and Balent, R.A. Correlating Modulus for Fluid Resistance in Accelerated Motion. *Journal of Applied Physics*, 22,3, March 1951, 324-326
- Sarpkaya, T. and Isaacson, M. *Mechanics of Wave Forces on Offshore Structures*. Van Nostrand Reinhold Co., 1981
- Doherr, K.-F. and Saliaris, C. On the Influence of Stochastic and Acceleration Dependent Aerodynamic Forces on the Dynamic Stability of Parachutes. AIAA-81-1941. *Proceedings of 7th Aerodynamic Acceleration and Balloon Technology Conference*, San Diego, 1981

# Water Flow Visualisation of a Ramrocket Combustion Chamber

by  
P. J. Boszko  
G. S. Owen  
IMI Summerfield  
Kidderminster  
Worcestershire DY11 7KZ  
England

## Summary

Flow within the combustion chamber of a ramrocket has been investigated using water flow visualisation with air bubbles as tracers. Configurations with four axisymmetric intakes entering the combustion chamber at either  $45^\circ$  or  $90^\circ$  have been considered. A region of stable recirculatory flow has been identified at the head end of the combustion chamber and estimates have been obtained of the amount flowing through the recirculation region. Based on this information fuel jets have been designed which it is believed will aid ignition, secure flame stability and improve combustion efficiency. The interaction between fuel jets and the recirculatory air flow has been tentatively investigated on flow visualisation tests using jets of coloured water.

## 1. Introduction

In recent years the application of the airbreathing concept to rocket propulsion has gained increasing prominence as a means of obtaining increased fuel efficiency. IMI Summerfield has considerable experience in research, development and production of solid propellant rocket motors, using the cast-double-base technique, and is currently engaged in a research programme on the integrated ramrocket as the design of this type of airbreathing motor requires expertise in solid propellant technology.

Airbreathing motors can basically be broken down into three types, according to the range of missile flight speeds within which each operates most effectively. Firstly there is the turbojet which operates within the high subsonic to low supersonic ( $M 0.7 - M 1.5$ ) regime. Next, in a group together, are the ramrocket (also known as a ducted rocket), the liquid fuel ramjet and the solid fuel ramjet which all operate at low to middle supersonic flight Mach number ( $M 2 - M 4$ ). Finally there is the so-called Scramjet which operates in the hypersonic regime ( $M 5 - M 7$ ).

By definition, an airbreathing missile takes in air from the atmosphere to provide oxygen necessary for combustion with fuel that is already stored within the missile. If the forward velocity of the missile is high enough ( $M > 2$ ) then the ram effect of the air will provide a combustion chamber pressure high enough to sustain combustion and produce a propulsive thrust, as in the ramrocket. For flight Mach numbers less than  $M 1.5$  a compressor is necessary to generate an adequate combustion chamber pressure, as in the turbojet.

This paper is concerned specifically with the design of a combustion chamber for a ramrocket having 4 axisymmetric side intakes mounted as shown in Fig. 1. Within this combustion chamber air from the atmosphere is mixed with hot, partially combusted, fuel obtained from the combustion in a separate chamber of a gas generator containing a solid fuel-rich propellant charge. To decouple the gas generator performance from the conditions within the ramrocket combustion chamber (ram combustor) the fuel supply is choked to sonic velocity on leaving the gas generator. The products of combustion from the ram combustor are exhausted to atmosphere at supersonic velocity through a convergent-divergent nozzle to produce motor thrust.

## 2. Design aims

The design aims of a ramrocket combustion chamber are to utilise the aerodynamics of its internal fluid flow to achieve efficiently and simply the following objectives:

- i) flame stability,
- ii) good combustion efficiency
- and iii) ignition between fuel and ram air within a short time, say 0.5s, of the two flows coming into contact. In the event of subsequent flame-out reignition is also a requirement. If at all possible, depending on the temperature and composition of the efflux from the gas generator, this requirement becomes one for autoignition.

## 3. Flow visualisation equipment

As a first practical step to achieving the objectives stated above water flow visualisation trials have been carried out to try to identify the basic flow pattern that ram air would have in the same design of chamber, for it is considered that there is some commonality in the design criteria for a ramrocket combustion chamber and a gas turbine combustor where water flow visualisation is a well established design tool used to identify the location and approximate strengths of stable recirculatory flow areas in the combustion chamber. Thus it is considered that the existence of any such flows in a ramrocket combustion chamber, if they exist, might be used in a similar manner to the gas turbine by designing the fuel flow to feed directly into suitable recirculation regions to give a favourable local fuel/air mixture ratio whilst at the same time enhancing the flow pattern. In this way good mixing will be achieved which is necessary for ignition and good combustion efficiency and the recirculation itself, provided it is stable, will act as a pilot zone and stabilise the flame. A water flow visualisation model was manufactured that could be used in the Flow Visualisation Facility at Cranfield Institute

of Technology. Part of this facility, shown in the diagrammatic view Fig. 2, is capable of supplying aerated water pumped from a large storage tank at variable flow rates up to 23 l/s (300 gal/min). The size of the entrained air bubbles can be varied to suit the conditions that are required. Large bore rigid pipework and flexible hose connects the storage tank to the model via control valves. Overflow water from the model is returned to the storage tank for re-use.

A view of the model with the pipework and control valves in the background is shown in Fig. 3.

The full scale model was made in Perspex, acrylic sheet and tube, and consists of a flow tank 381 mm (15") square x 711 mm (28") high which is mounted on a stand allowing the water supply to be fed into it through its 381 mm (15") square base plate. A perforated distribution plate was mounted 63.5 mm (2.5") above the base plate to stabilise and direct the flow of water. The body tube incorporating the appropriate inlet configuration is supported from the top plate by a mounting flange that enabled it to be removed from the flow tank and changed easily and quickly. The Perspex body tube is made in such a way that a plate in the lower end, the end simulating the forward closure of the ramrocket combustion chamber, can be moved up and down in the tube thus varying its distance from the fixed inlets. Holes through this plate allow coloured water to be forced, from pressurised storage tanks mounted on the support stand, into the body tube in different positions to simulate the injection of the fuel rich gas in the ramrocket combustion chamber. These features are considered necessary to determine the effect that each feature, and its relative position, has on the location, size and strength of the flow patterns within the model.

In order to visualise the flow patterns clearly in the required planes and to enable photographs to be taken for record purposes a bright light source was provided in the form of a slim elongated beam. Fig. 4 shows a sketch of the model with the light source. The beam of light illuminates the activity within its path by reflecting light off individual bubbles. It was found that by viewing the areas of interest in semi-darkness, at an approximate angle of 120° from the plane of the light beam the flow patterns showed up most clearly. Photographs and videos of the flow patterns in the areas of interest were taken for record purposes. The best photographs were obtained with long exposure times, individual bubbles while in the beam of light showing up as lines indicating very clearly the flow patterns that existed. Very good results were obtained with video, the flow patterns being seen more clearly than by normal visual observation.

#### 4. Flow visualisation results

The missile intake configurations that have been investigated are those shown in Fig. 5 with four axisymmetric intakes on a 120 mm diameter body and having dump angles of  $\alpha = 90^\circ$  and  $\alpha = 45^\circ$ . Circular intakes were considered at both 90° and 45° dump angles and square intakes at the 45° dump angle. The motor design was based on a requirement to produce thrust sufficient to overcome drag at a design point of M 2.1 at sea level and this resulted in fixing the ratio of intake internal diameter ( $d_i$ ) to ram combustor internal diameter ( $d_c$ ) at  $d_i/d_c = 1/3$ .

The flow visualisation trials showed for both intake configurations the existence of a toroidal recirculation region at the head-end of the ram combustor in a region forward of the inlet dump plane as shown in Figs. 5, 6 and 7. By observing the position of the dividing streamline within an inlet one can estimate the proportion of the total amount of fluid diverted into the head-end recirculation region; this was about 30% with the 90° inlet dump angle and about 20% with a 45° inlet dump angle. To investigate the stability of the flow pattern, tests were run with variations in water flow rate from 0.76 l/s (10 gal/min) to 7.6 l/s (100 gal/min) and numerous times at each flow rate with the flow being turned on as rapidly as possible. It was found that the same basic flow pattern established itself quickly each time, from which it was inferred that the flow pattern was stable. These flow rates correspond to Reynolds numbers of between 10 000 and 100 000 which, though significantly lower than the Reynolds number of the actual air flow, are high enough to ensure that the flow is fully turbulent.

The quantity of water diverted into the head end appears to be directly related to the flow area at the inlet station between the inlet jets and the motor body wall through which any flow passing into the forward end of the motor must pass as it returns down the motor tube. The situation for the 90° intake configuration is shown in Fig. 8 which is a cross sectional view of the motor at the intake dump plane. The shaded areas depict the incoming jets which meet to form a cruciform restriction to axial flow returning from the head end of the combustor. Thus, flow into the head end can subsequently flow into the main body of the combustor only through the unshaded areas in Fig. 8.

In Fig. 8 the ratio  $A_K$  of the unshaded to shaded area can be expressed very approximately as

$$A_K = 1 - \frac{4}{\pi} \left[ 2 \left( \frac{d_i}{d_c} \right) - \left( \frac{d_i}{d_c} \right)^2 \right] \quad (1)$$

where  $d_i$  = inlet internal diameter at the dump plane,  
 $d_c$  = combustor internal diameter.

In the present design  $d_i/d_c = 1/3$ , as stated earlier and fixed by other design considerations, which gives a value from equation (1) of  $A_K \approx 29\%$ . Thus, for the 90° intake configuration equation (1) provides a ready estimate of the amount of flow into the forward recirculation region.

A theoretical model of the flow field at the head end of this type of combustor with any intake dump angle has been developed at Cranfield Institute of Technology (Ref. 1) and has given results in good agreement with the observed figures stated above for both 90° and 45° intakes.

Another design parameter under investigation in the flow visualisation trials was the geometrical size of the head end of the combustor. Varying the size of this region from  $l/d_c = 0.2$  to 0.6 where  $l$  is the distance from the ram combustor head end to the leading edge of the air intake (see Fig. 3) had no apparent effect on the amount of fluid entering the recirculation region. However, with increasing

$L/dc$  the shape of the recirculation does become distorted to fill the available space, as seen on Fig. 10 for a square intake configuration at a  $45^\circ$  dump angle. As before, varying flow rates and sudden starting of the flow did not affect the basic flow pattern.

A value of  $L/dc \approx 0.5$  is desirable if one is to accommodate a boost charge in the ramcombustor to take the missile from launch up to a velocity at which the ramrocket will operate. Such a propulsion system is termed an integrated boost ramrocket and is shown in Fig. 9. The boost charge in such a system operates as a conventional rocket motor until the boost propellant has finished burning and then the boost combustion chamber becomes the combustor for the ramrocket. To facilitate a smooth transition from boost to ramrocket it is desirable to minimise boost debris, such as charge inhibition, in the combustor and this can be achieved by permitting the boost charge to burn on the forward face. At the same time it is desirable to protect the inlet port covers (see Fig. 9) from the boost motor environment. Both objectives can be met by a case-bonded boost charge design which has a burning web  $w$  of propellant between the forward end of the charge and the intake dump plane, as shown in Fig. 9, and this leads to the requirement for  $L/dc \approx 0.5$ .

Thus the flow visualisation trials indicated that the desirable dimension of  $L/dc = 0.5$  at the forward end is reasonable and the design not sensitive to small changes.

With the above information on the flow pattern within the combustor one can begin to design fuel jets which deliver a pre-determined amount of fuel into the recirculation region to give, for example, a local stoichiometric fuel/air mixture which will give the highest flame temperature and is most readily ignitable.

At the same time one can design the fuel jets to enhance, rather than disrupt, the basic air flow pattern in the combustor. This can be done, for example, by directing radial jets into the portion of the recirculation where the general direction of flow is the same as the direction of the fuel jet flow as shown in Fig. 5. Or, if some of the fuel is to be delivered directly into the main body of the combustor then a sensible design would be for the fuel jets to be directed axially in between the cruciform of the incoming air jets as shown in Fig. 8.

So far, however, these ideas for a combustor design have been based only on an assumed knowledge of how air alone will behave within the combustor. Yet this situation, with air alone flowing through the combustor, is probably only applicable momentarily at the start of the ramrocket phase prior to ignition of the gas generator, for after this there will be both air and fuel flowing in the combustor. Thus it would be desirable to obtain some confidence that injection of fuel, at sonic or greater velocities, will not adversely affect the basic air flow pattern.

To demonstrate this, pressurised coloured water jets, simulating the fuel jets, were fed into the combustor superimposed upon the basic intake flow. It was observed that the two flows appeared to mix well in the recirculation regions and flow together into the body of the combustor. It was noted also that there was a rapid disappearance of colour from the recirculation regions once the 'fuel' jets were turned-off indicating good flow out of the recirculation. Finally, the axial jets appeared able to penetrate the intake and recirculatory flows and deliver 'fuel' into the main body of the combustor.

However, since the simulated fuel jets were of water they could not attain the sonic velocity that the actual fuel jets would have achieved and thus the precise value of the above observations is questionable. Nevertheless as the trials did not highlight any adverse effect from the simulated fuel injection they necessarily provided some confidence, albeit small, that the fuel flow will operate as it has been designed to do and not seriously alter the basic air flow pattern.

#### 5. Ramrocket firing results

At this stage it was considered that there was sufficient confidence in the design to proceed to small scale static ramrocket motor firing trials. The fuel rich propellant for these trials had a flame temperature of 1500 K with which it was hoped to achieve rapid autoignition.

The trials to date have been successful and rapid autoignition, within the desired 0.5 s, has been achieved on all trials. It should be noted here that as these trials were of the ramrocket alone, without an integrated boost motor, there had been no pre-heating of the ram combustor walls by boost motor gases to help ignition. A typical set of pressure records are shown in Fig. 11 which show ramrocket ignition in relation to the ignition of the gas generator. In fact it can be seen that the ramrocket autoignited as the pressure, and hence the fuel flow, of the gas generator approached its design operating level. The elapsed time on Fig. 11 of approximately 1.0 s for the gas generator to reach its design operating pressure reflects the difficulty in igniting a fuel rich gas generator propellant, but improving on this ignition characteristic is not considered to be a problem.

All other aspects of the performance of the ramrocket appeared to be satisfactory and currently preparations are being made for a further series of static trials with a full size integrated boost motor to test the complete sequence of boost, transition and ramrocket.

#### 6. Reference

1. D. Gueroui, School of Mechanical Engineering, Cranfield Institute of Technology, Bedford, England, Ph.D thesis in preparation.

#### 7. Acknowledgement

This work has been carried out with the support of the Procurement Executive, Ministry of Defence.

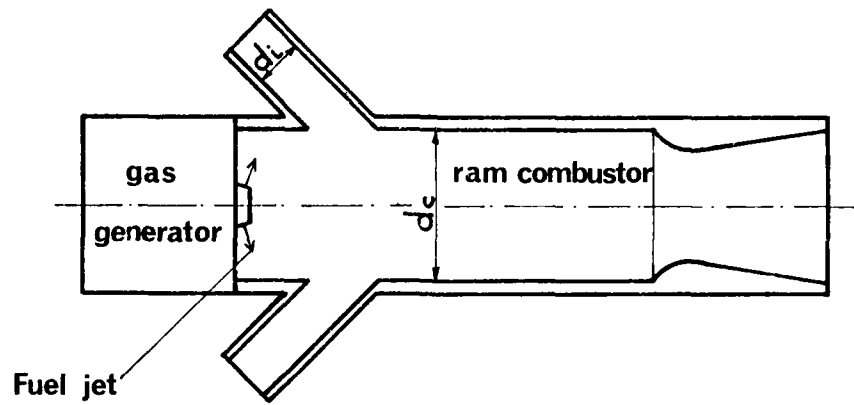


Fig. 1. Diagrammatic view of combustion chamber.

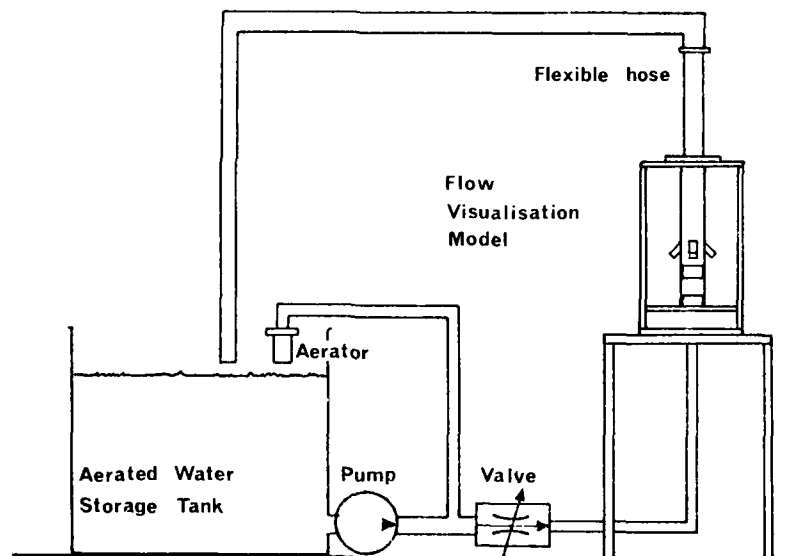


Fig. 2. Diagrammatic view of tank, pipework & model.

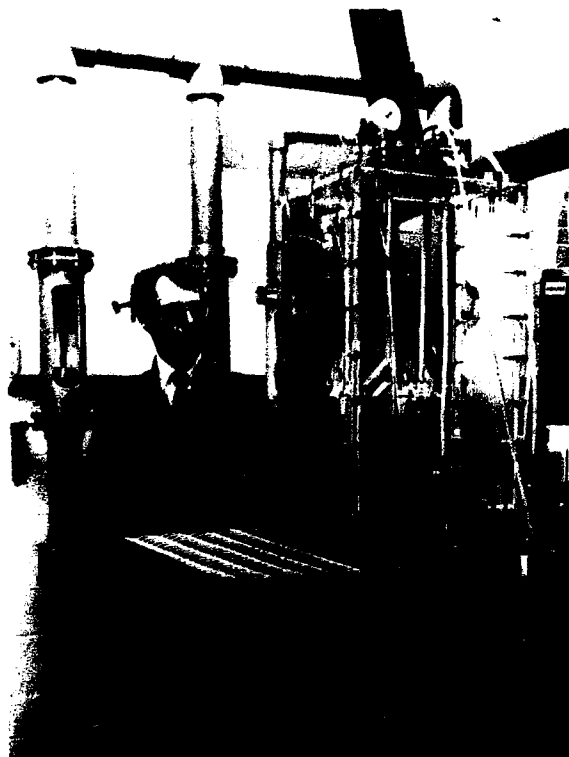


Fig. 3.

Flow visualisation  
model , pipework  
& control valves.

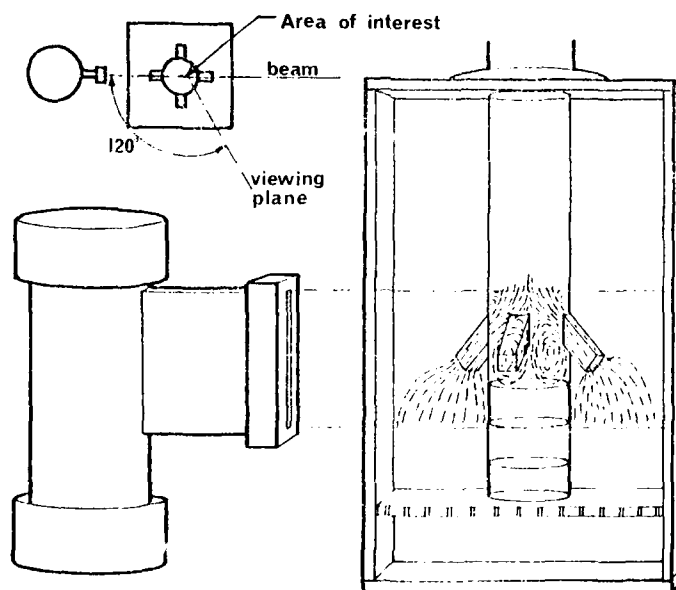


Fig. 4. Light source and model.

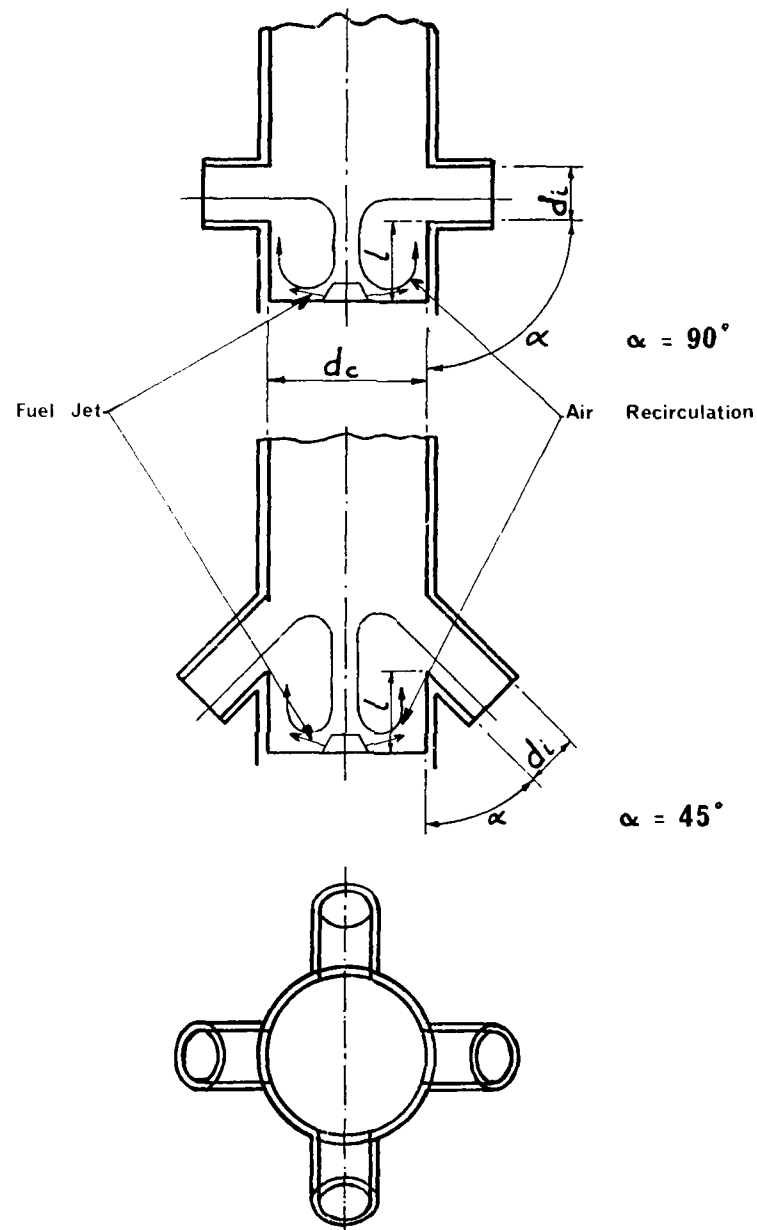


Fig. 5. Sections through  $90^\circ$  &  $45^\circ$  missile intake configurations.

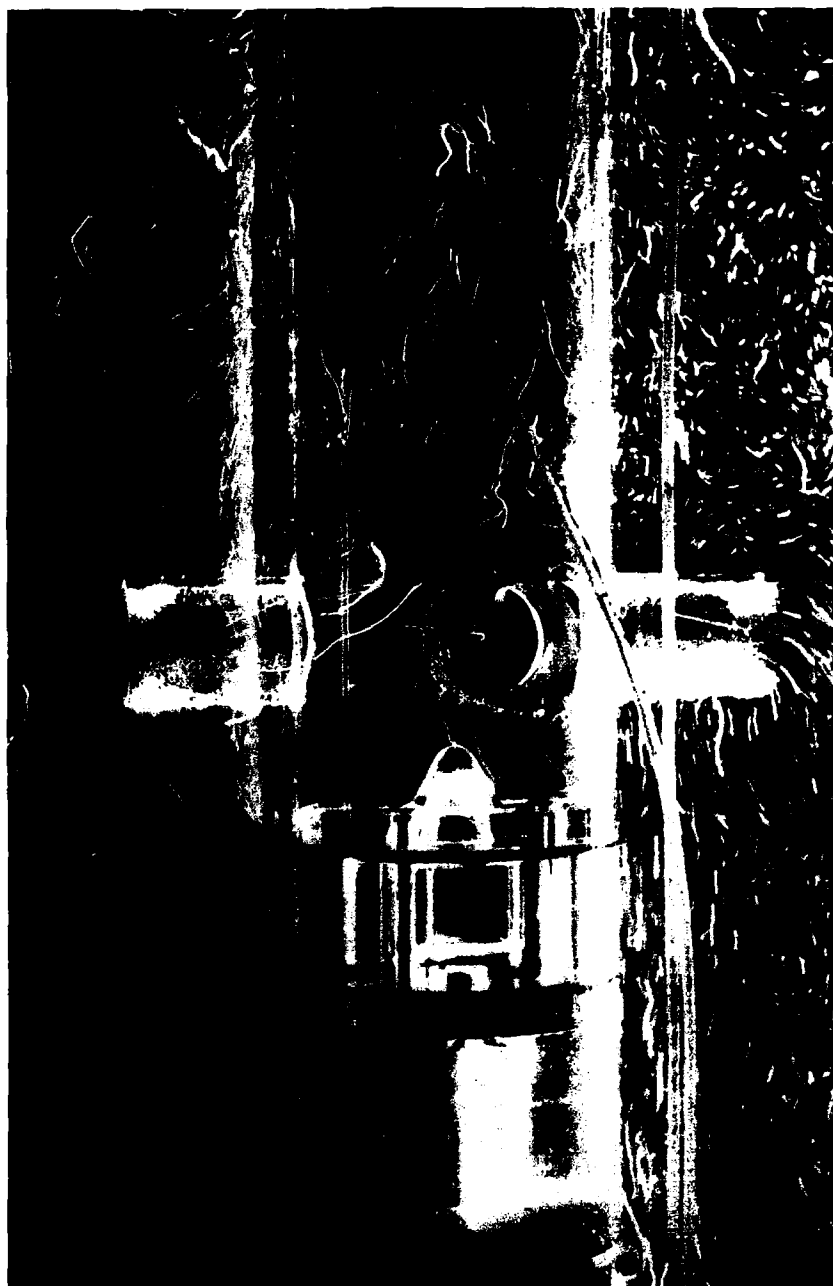


Fig. 6. Flow pattern with circular intakes  
and 90° dump angle.



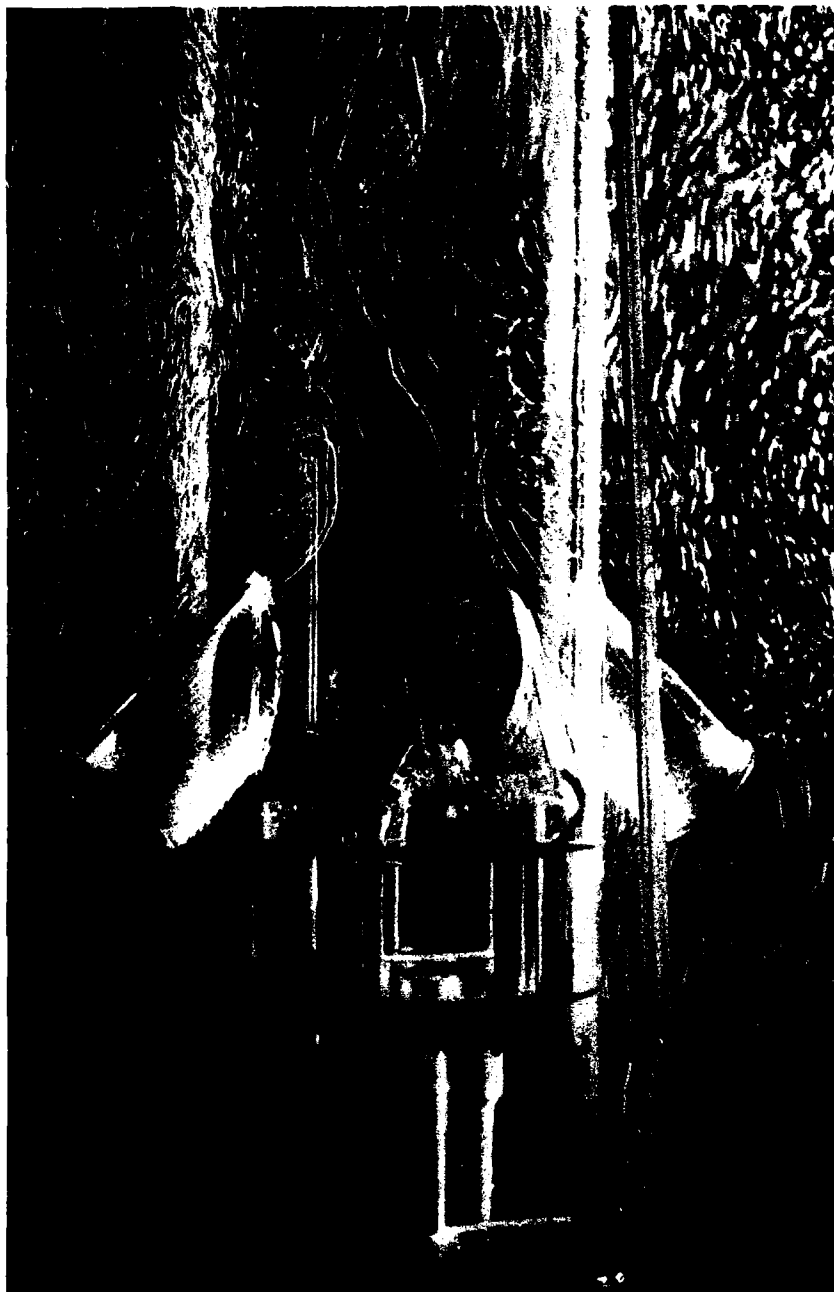


Fig. 7. Flow pattern with circular intakes and 45° dump angle.

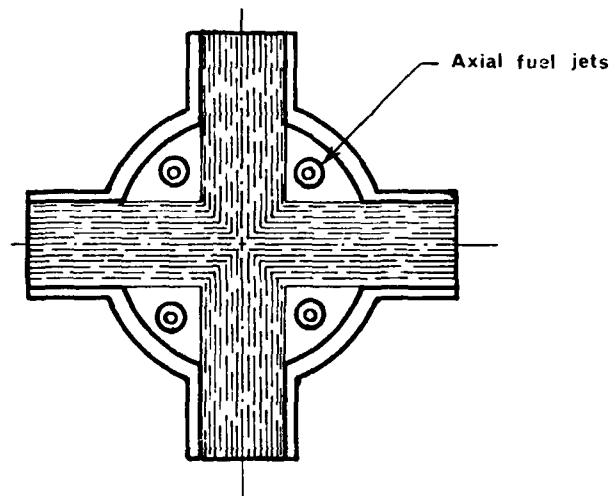


Fig. 8. Section through 90° inlet dump plane.

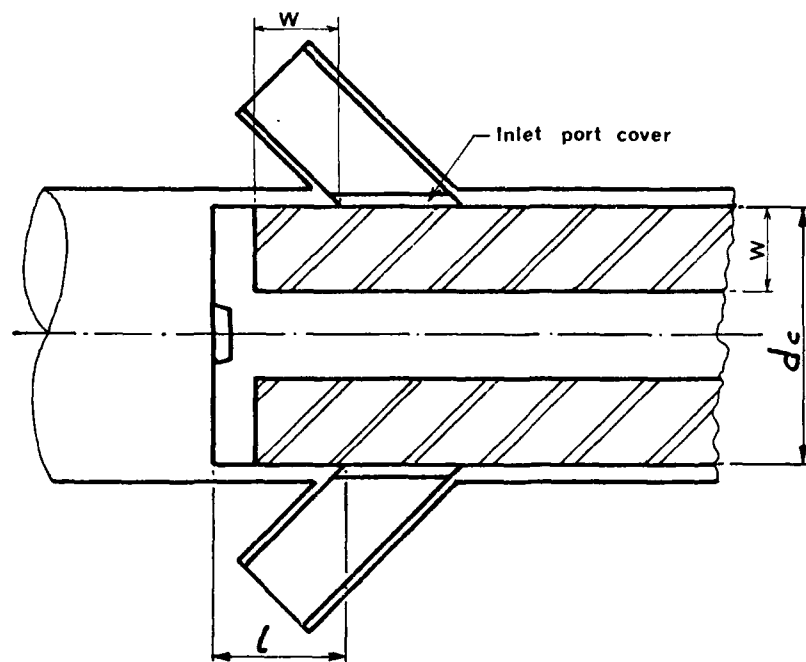
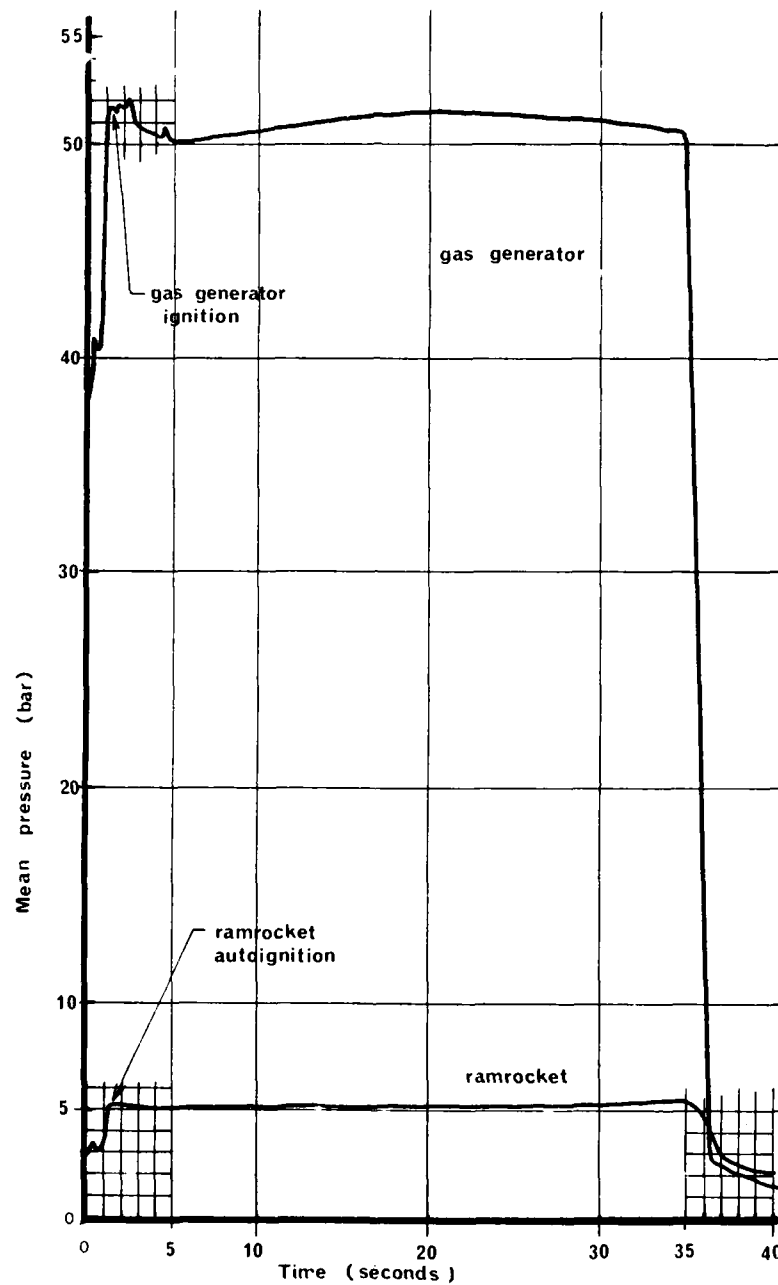


Fig. 9. Section through forward end of integrated boost combustion chamber.



Fig. 10. Flow pattern with square intakes and 45° dump angle .



**Fig. 11** Gas generator & Ramrocket pressure-time curves.

"POSSIBILITES D'ESSAI OFFERTES PAR LES TUNNELS HYDRODYNAMIQUES A VISUALISATION DE L'ONERA  
DANS LES DOMAINES AERONAUTIQUE ET NAVAL"

par

H. WERLE

Office National d'Etudes et de Recherches Aérospatiales (ONERA)  
BP 72, 92311 CHATILLON CEDEX (France)

RESUME -

Les tunnels hydrodynamiques de l'ONERA, qui ont longtemps joué le rôle de pionnier en ce qui concerne la visualisation des écoulements, disposent d'un ensemble de montages et de méthodes d'essai, qui sont en mesure de couvrir un vaste champ d'application.

Cette communication constitue une mise à jour de l'état actuel de la technique expérimentale et donne un aperçu sur les résultats les plus marquants qu'elle a permis d'obtenir dans les domaines aussi variés que la recherche fondamentale et les applications à l'aérodynamique et à l'hydrodynamique.

THE ONERA WATER TUNNELS TEST POSSIBILITIES  
FOR FLOW VISUALIZATION IN AERONAUTICAL AND NAVAL DOMAINS

SUMMARY -

The ONERA water tunnels, which for a long time were the pioneers in flow visualization, cover a large scope of test means and methods, encompassing a wide field of application.

This paper presents an up-to-date description of the experimental technique used for plane, axisymmetrical and three-dimensional flow, and gives a survey of the most notable results achieved in domains as varied as fundamental research and aerodynamics and related hydrodynamic studies.

INTRODUCTION -

Mis en service en 1952, le premier tunnel hydrodynamique (TH1) de l'ONERA [1] bénéficie d'une très longue expérience aussi bien en matière de technique expérimentale (moyens, montages, méthodes de visualisation), qu'en matière de résultats (écoulement aux faibles vitesses). Pour satisfaire les nombreuses demandes d'essais effectués non seulement dans le cadre de sa vocation aérospatiale, mais aussi au titre de l'assistance industrielle, ce premier tunnel a été complété en 1964 par une cuve à veine plus spacieuse pour les essais au point fixe [2], transformée en tunnel (THJ) par la suite, et enfin en 1981 par un grand tunnel (TH2), dont les performances plus élevées facilitent les essais aux grands angles d'attaque et ceux en régime turbulent. Rénovées, ces 3 installations ont été regroupées dans le nouveau laboratoire de visualisation hydrodynamique de la Direction de l'Aérodynamique à Chatillon [3].

Ce laboratoire consacre toute son activité à des études d'écoulements. La présente communication se propose de passer en revue les nombreuses possibilités offertes par ces installations en évoquant les différents types de montage et de maquettes qu'elles ont mis en jeu. Elles les illustrent par des exemples variés de visualisations [4] qu'elles ont permis d'obtenir et qui concernent de nombreux phénomènes fondamentaux de la mécanique des fluides, que l'on retrouve non seulement en aérodynamique appliquée à l'aéronautique, mais bien sûr aussi en hydrodynamique du domaine naval.

TECHNIQUE EXPERIMENTALE -

Avant de décrire quelques maquettes typiques (fig.1) et de préciser leur montage en veine (fig.2), rappelons brièvement que les 3 tunnels, qui équipent ce laboratoire, sont disposés verticalement et fonctionnent en circuit ouvert par vidange sous l'effet de la gravité : voir fig.3 qui précise leurs dimensions et performances. Chacune de ces installations comporte tous les dispositifs nécessaires (circuits de colorant, projecteurs à fentes, miroirs, etc.) pour la visualisation des écoulements par traceurs [5] : émissions de colorant de même densité et viscosité que l'eau (par ex. fig.4) et fines bulles d'air en suspension dans l'eau (par ex. fig.5).

D'autre part le laboratoire est équipé d'un ensemble de moyens d'essais annexes (circuits d'aspiration et de soufflage, pompes, moteurs, etc.) utilisés pour la simulation de certains éléments des maquettes, ou de leur montage, tels que prise d'air, piège à couche limite, fente de soufflage, sortie de jet, hélice ou rotor, sol, etc.

Comme c'est le cas en soufflerie, même les maquettes les plus simples, notamment les modèles "courant plan" (fig.1a), demandent souvent des montages soignés, si l'on veut éviter ou réduire les effets de phénomènes parasites, tels que les couches limites des parois de veine, ou celles des panneaux de garde entre lesquels le modèle se trouve disposé : ces couches limites finissent par décoller lors des essais à circulation élevée. D'autres problèmes se posent, lorsqu'il s'agit de visualiser tout le champ aérodynamique autour du modèle et nécessitent un panneau avant mince et transparent, un éclairage des deux côtés, un montage en porte à faux et des prises de vues délicates

en raison de l'envergure du modèle : voir schéma 2a.

A noter par exemple dans le cas du profil avec volet de courbure (fig.1a) que l'axe support, dont le prolongement en constitue la charnière, permet non seulement de régler l'incidence  $\alpha$  du profil, le braquage  $\delta$  du volet, mais sert aussi au passage des colorants et du fluide injecté (fente de soufflage tangentiel amont) ou prélevé (fente d'aspiration aval). On retrouve le même type de problème dans le cas d'une demi-maquette montée à la paroi (fig.1b).

Le montage sur dard arrière est souvent utilisé dans le cas de modèles axisymétriques, mais aussi dans celui de maquettes tridimensionnelles comportant un axe longitudinal, comme pour les essais d'hélice isolée (fig.1c). Ce dard supporte le moyeu fixe, transmet le mouvement de rotation à l'hélice et contient en outre les canalisations qui distribuent le colorant au bord d'attaque des différentes pales (fig.7c), le calage de ces dernières ne pouvant être modifié qu'à l'arrêt.

Le même type de montage a été utilisé pour une maquette de sous-marin (fig.1i) et l'on peut distinguer à l'extrémité de ce modèle la présence autour du dard, d'une prise d'air annulaire permettant de simuler l'effet d'aspiration de l'hélice : voir schéma 2b.

Une variante de ce dernier dispositif a été expérimentée récemment avec un autre type de sous-marin maintenu en veine par un mât profilé latéral (figs.9j, 10d). Cette maquette permettait d'ailleurs de faire passer le mât par le massif avant lorsque l'on voulait minimiser les sillages à l'arrière (fig.9k).

Un autre exemple de fixation sur dard arrière est celui d'une maquette complète d'avion, comme celle d'un avion VTOL à jets (fig.1g). Le dard utilisé groupe tous les circuits de colorant et de fluide pour les 8 prises d'air et sorties de jet des réacteurs de sustentation, ainsi que pour les 2 prises d'air latérales des réacteurs de propulsion (figs.8a-d). Un tel dard comporte parfois même à sa surface un soufflage tangentiel vers l'aval pour simuler les effets d'induction des jets de propulsion (voir fig.16a de la réf.[5]).

Cette disposition avec dard a aussi pour avantage de bien dégager le dessous du modèle (fig.8e), mais ne facilite pas la prise de vues, aux faibles incidences, de coupes transversales d'écoulement observées dans un miroir placé en aval du modèle : voir schéma 2b.

C'est pourquoi on lui préfère souvent un montage sur mât d'intrados, qui assure le développement régulier de l'écoulement d'extrados (le plus souvent étudié) et celui de son sillage, en minimisant les effets de supports sur le gradient de pression longitudinal.

On adopte, soit un mât d'intrados pour les essais aux faibles incidences ou au point fixe ( $V = 0$ ), comme par exemple sous une maquette motorisée d'hélicoptère (fig.1d) essayée en présence d'un plancher figurant le sol et pouvant coulisser le long de ce support [3], soit un mât profilé et incliné, mieux adapté au domaine des incidences élevées : voir schéma 2c. A noter que ce montage comporte une rotule qui permet dans le cas d'une maquette complète à la fois sa mise en incidence et en dérapage. Cette possibilité subsiste d'ailleurs dans le cas d'une maquette partielle comme celle d'un avion avec tout son fuselage équipé de prises d'air et sorties de jet et comportant une voilure à géométrie variable (fig.1f) : sur ce modèle, seule l'aile gauche est complète, mais avec possibilité de faire varier sa flèche même en cours d'essai [6].

Dans le cas d'une maquette d'avion, on utilise parfois un 2ème modèle fixé sur un mât latéral, mais comportant un fuselage complet. Dans ces conditions, les perturbations dues au support se limitent généralement à l'aile située côté support et l'on peut alors obtenir des vues de profil avec l'écoulement au-dessus et au-dessous du modèle, notamment lors d'essais effectués en présence d'un sol.

Pour simuler d'une manière réaliste les effets de sol autour de maquettes en translation (fig.1e) [7], différents tapis roulants se déplaçant à la vitesse  $V$  du courant ont été mis au point, mais ces dispositifs se révèlent assez fragiles à l'usage et restent limités aux faibles vitesses (fig.8e). Enfin, il reste à mentionner quelques montages spéciaux destinés à imprimer au modèle d'essai un mouvement d'oscillations périodiques ou de rotation uniforme simulant un tonneau ou une vrille (fig.1h). Ces essais en instationnaire [5] comportent bien entendu de nombreuses difficultés supplémentaires, qui concernent entre autres, l'alimentation en colorant de la maquette, les perturbations dues à la présence et au mouvement des supports, les jeux nécessaires au mouvement et l'observation des phénomènes (prises de vues rapides [8]), notamment depuis l'aval (montage nécessitant un support avec couronne : fig.1h).

#### EXEMPLES DE VISUALISATIONS OBTENUES -

La fig.4 qui est extraite de la fiche technique 1985 relative au nouveau tunnel TH2 groupe un certain nombre d'exemples de visualisations récentes effectuées à l'aide de colorant et concernant aussi bien les études fondamentales (vues 4a-g) que les recherches appliquées (vues 4A-E), parmi lesquelles figure notamment l'écoulement autour d'une maquette du train à grande vitesse (TGV) en présence d'un vent latéral (dérapage) : voir fig.4E. Mis à part cet exemple de véhicule terrestre sur lequel nous ne reviendrons plus, la suite de cet exposé va examiner tour à tour et dans l'ordre, les recherches à caractère fondamental, puis les applications du domaine aéronautique, enfin celles du domaine naval.

#### RECHERCHES FONDAMENTALES -

Des exemples variés de visualisations des phénomènes fondamentaux de la mécanique des fluides sont donnés par les figs.4a-g, 5 et 6. Ils permettent d'apporter quelques précisions sur l'emploi des traceurs liquides ou gazeux utilisés à cet effet.

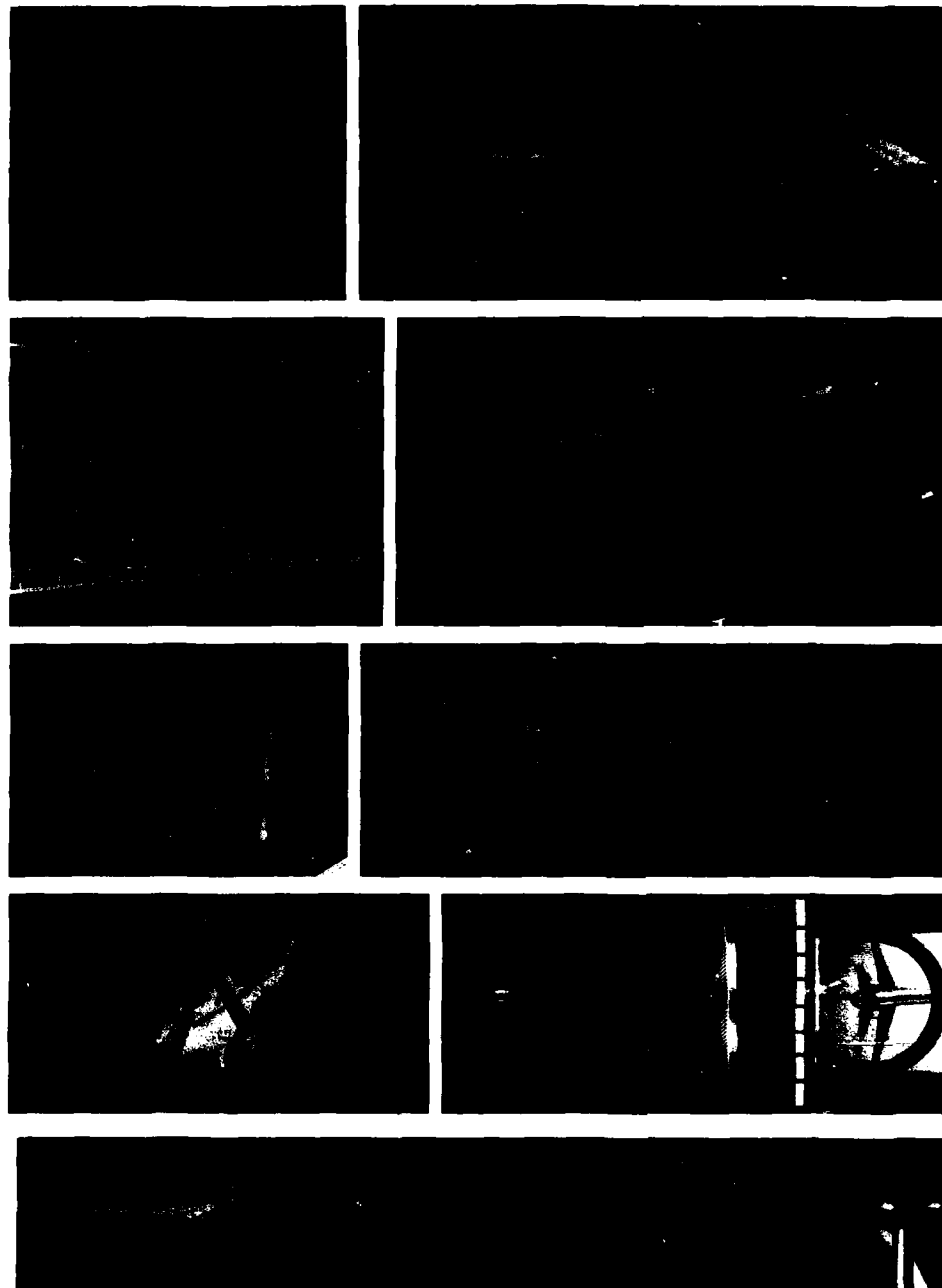
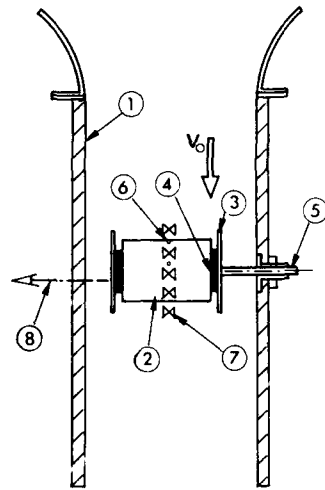
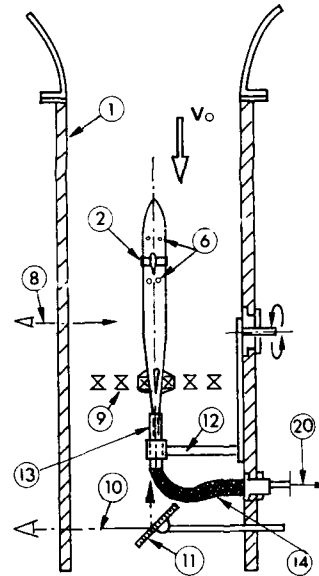


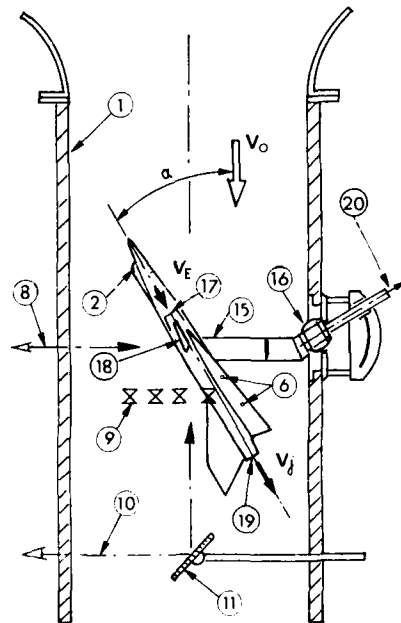
FIG. 1 - MAQUETTES ET MONTAGES D'ESSAI.

- a Profil monté entre panneaux avec soufflage ou aspiration à la charnière du volet (contrôle de la couche limite).
- b Montage sur panneau de garde d'une demi-maquette d'avion de transport.
- c Montage d'une hélice isolée sur moyeu axial fixé sur dard arrière.
- d Montage sur mât d'intrados d'une maquette complète d'hélicoptère avec prises d'air et sorties de gaz.
- e Montage sur mât latéral d'une aile delta avec simulation du sol par tapis roulant ou à l'aide d'une maquette image (tapis escamoté).
- f Montage sur mât d'intrados d'une maquette partielle d'avion avec aile à géométrie variable } avec prises d'air et sorties de jets.
- g Montage sur dard arrière d'une maquette complète d'avion VTOL à jets.
- h Montage sur couronne transmettant à une maquette d'avion un mouvement de rotation (tonneau ou vrille).
- i Montage sur dard arrière d'une maquette de sous-marin avec simulation de l'hélice par une prise d'air annulaire.

FIG. 2 - SCHEMAS DES PRINCIPAUX TYPES DE MONTAGE EN VEINE.

a) Maquette «courant plan» montée entre panneaux.  
(Même type de montage pour demi-maquette  
fixée sur un panneau).

b) Maquette de sous-marin montée sur dard arrière.

c) Maquette entière fixée sur mât profilé d'intrados  
(ou évent. latéral).

## LEGENDE :

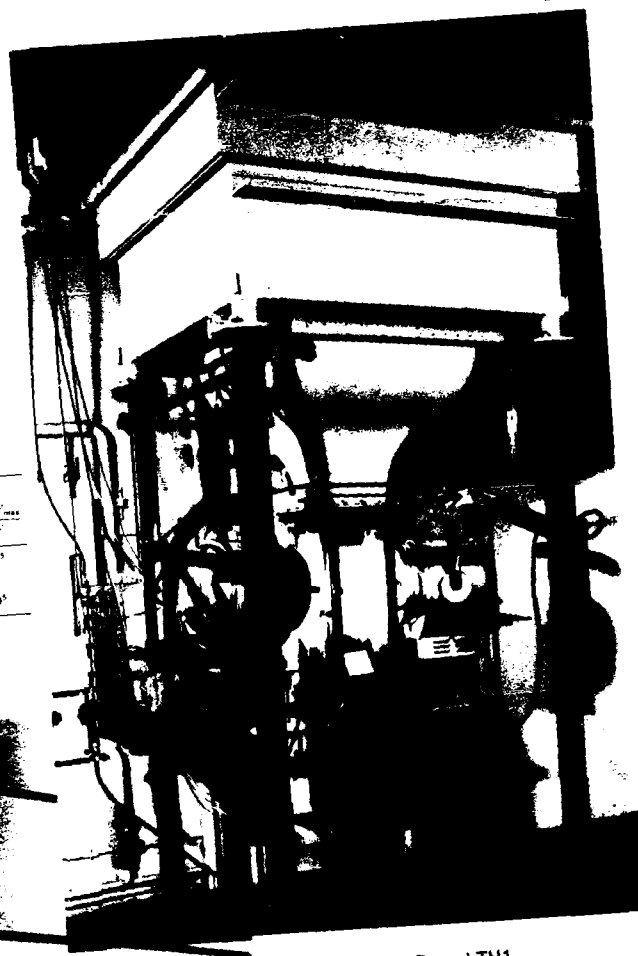
- 1 Paroi de la veine.
- 2 Maquette.
- 3 Panneau de garde.
- 4 Jeu réglable pour essais à circulation élevée.
- 5 Axe support servant de passage au colorant (évent. au circuit de soufflage ou d'aspiration) et au réglage de l'incidence  $\alpha$ .
- 6 Trous émetteurs de colorant.
- 7 Tranche de lumière longitudinale
- 8 Axe de prise de vues correspondant
- 9 Tranche de lumière transversale
- 10 Axe de prise de vues correspondant
- 11 Miroir aval réglable
- 12 Support manivelle servant au réglage de l'incidence  $\alpha$  ou du dérapage  $\beta$  des maquettes montées sur d'ard arrière.
- 13 Prise d'air annulaire autour du dard pour modifier le gradient de pression longitudinal (simulation d'un effet d'hélice, réduction d'un effet d'obstacle du support, etc.).
- 14 Conduites d'alimentation de colorant et d'aspiration
- 15 Mât support d'intrados (ou évent. latéral) servant de passage au colorant (évent. aux circuits de soufflage et d'aspiration).
- 16 Montage sur rotule servant au réglage de l'incidence  $\alpha$  et du dérapage  $\beta$  des maquettes.
- 17 Prise d'air de la maquette (débit  $Q_E$ ).
- 18 Plan canard.
- 19 Sortie de jet (débit  $Q_j$ ).
- 20 Vers les ensembles vanne-pompe-rotamètre pour le contrôle des débits  $Q_E$  et  $Q_j$ .

Visualisation  
par bulles d'air



FIG. 3 - VUES ET CARACTERISTIQUES PRINCIPALES DES TUNNELS HYDRODYNAMIQUES DE L'ONERA.

Tunnels	Section $L \times L$ de la veine (m)	Vitesse $V_{max}$ (m/s)	$Re = \frac{LV_{max}}{\nu}$
TH1	0,22 x 0,22	0,25	$0,5 \cdot 10^5$
TH2 { Circuit normal	0,45 x 0,45	0,25	$10^5$
TH2 { Circuit rapide		1,70	$7 \cdot 10^5$
TH3	0,80 x 0,80	0,065	$0,5 \cdot 10^5$



Tunnel TH1



Tunnel TH3

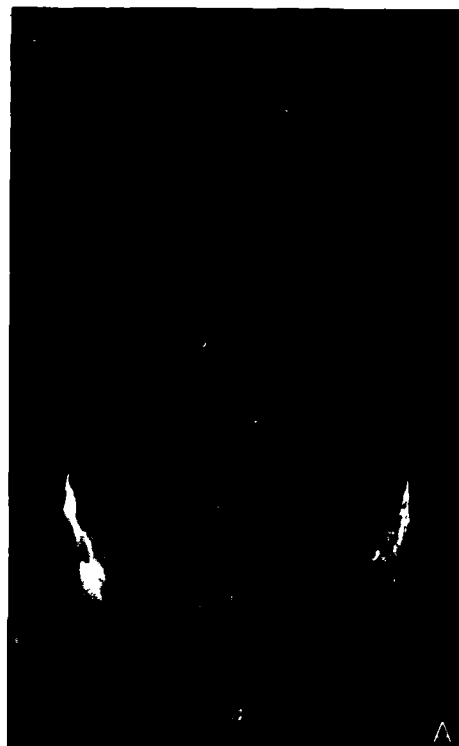
VOIR LA VUE DU TUNNEL TH2 EN HAUT  
DE LA PAGE SUIVANTE →

14-6

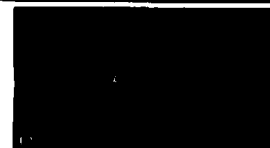
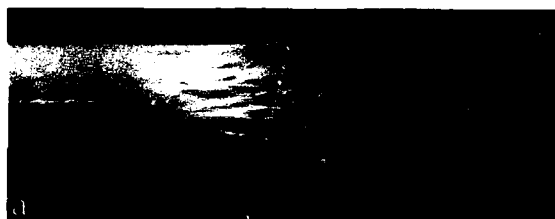
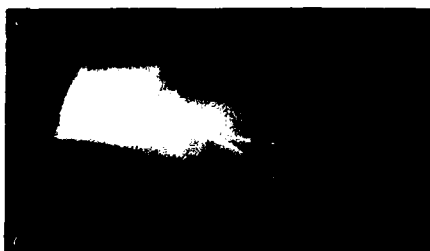


TUNNEL HYDRODYNAMIQUE TH2  
WATER TUNNEL TH2

FIG. 4



VISUALISATION PAR ÉMISSIONS DE COLORANT  
VISUALIZATION BY DYE EMISSIONS



**RECHERCHES****APPLIQUÉES :**

avions complets (A)  
 sous-marins (B)  
 missiles (C)  
 hélicoptères complets (D)  
 véhicules (E)

**APPLIED****RESEARCH :**

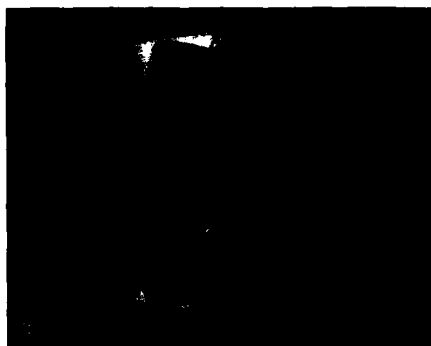
complete aircraft (A)  
 submarines (B)  
 missiles (C)  
 complete helicopters (D)  
 vehicles (E)

**RECHERCHES  
FONDAMENTALES :**

couche limite et  
 transition (a)  
 écoulement sain (b)  
 décollement 2D (c)  
 tourbillon (d)  
 éclatement (e e')  
 décollement 3D (f) et  
 sillage (g g')

**FUNDAMENTAL  
RESEARCH :**

boundary layer and  
 transition (a)  
 unseparated flow (b)  
 2D separated flow (c)  
 vortex (d)  
 breakdown (e e')  
 3D separation (f) and  
 wake (g g')

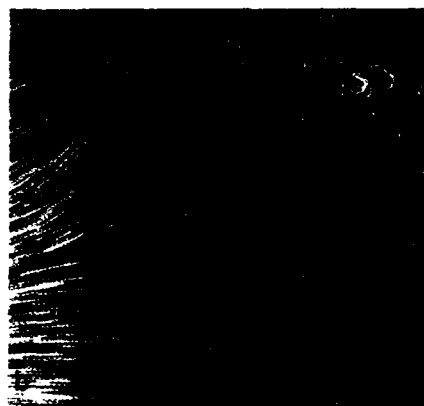


EXEMPLES DE RECHERCHES EFFECTUEES  
AU TUNNEL TH2 :

FIG. 4 - VISUALISATION PAR COLORANT  
(VOIR PAGES PRECEDENTES)

FIG. 5 - VISUALISATION PAR BULLES D'AIR  
(VOIR CI-DESSOUS)

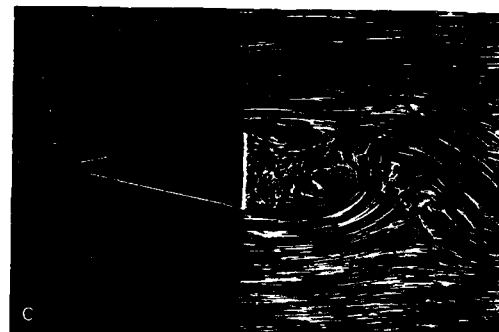
Ecoulement plan (coupes longitudinales)



Profil Naca 0012  $\alpha=20^\circ$   $Re_c \approx 2 \cdot 10^4$   
(Cliché avec effet chronophotographique)



Profil Naca 0012  $\alpha=10^\circ$   $Re_c \approx 5 \cdot 10^4$  (cliché à temps  
d'exposition long)

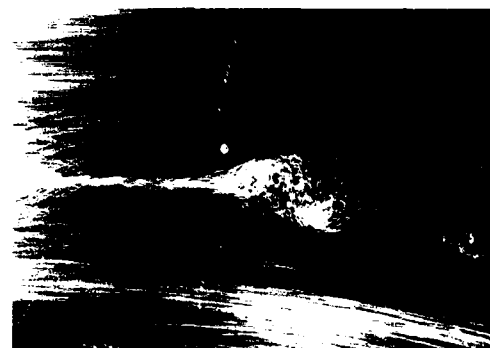


Profil pointu (dièdre)  $\alpha=0^\circ$   $Re_c \approx 0,5 \cdot 10^4$   
(Cliché à temps d'exposition court)



Coupe transversale  
située au bord de fuite  
( $Re_c \approx 0,5 \cdot 10^5$ )

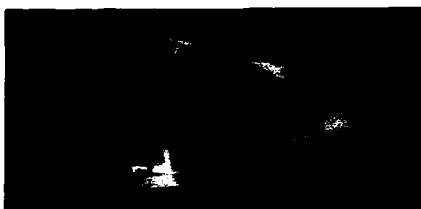
Tourbillon marginal d'une aile rectangulaire (profil Naca  
0012  $\alpha=12^\circ,5$ ) : coupes longitudinales suivant l'axe du  
tourbillon ( $Re_c \approx 2 \cdot 10^5$ )



Eclatement  
du tourbillon  
devant un obstacle

FIG. 6 -  
AUTRES  
EXEMPLES  
DE RECHER-  
CHES FONDA-  
MENTALES

$Re_L \approx 3.10^5$



Décollement sur le retrait courbe d'un fuséau  $Re_L \approx 6.10^5$   
cylindrique sans incidence

Effet des cannelures longitudinales

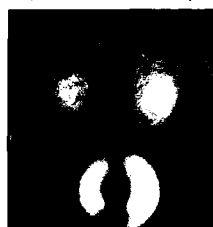


Tourbillons d'extrados sur maquettes élancées (coupes transversales)

Ellipsoïde de révolution  
 $L = 6D_{MAX}$   $\alpha = 30^\circ$



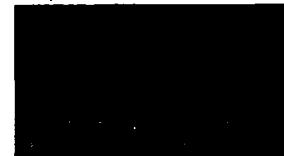
$Re_L = 1.2.10^5$  (coupe à 0,5L)  $Re_L = 7.2.10^5$  (coupe à 1,04)



Ogivo-cylindre: coupe arrière  
 $L = 15D$   $\alpha = 50^\circ$   $Re_L \approx 10^5$



$\alpha = 20^\circ$   
Aile delta mince :  $q = 75^\circ$   $Re_c \approx 2.10^4$   
(Coupes transversales au bord de fuite)



Noyaux éclatés  $\alpha = 30^\circ$



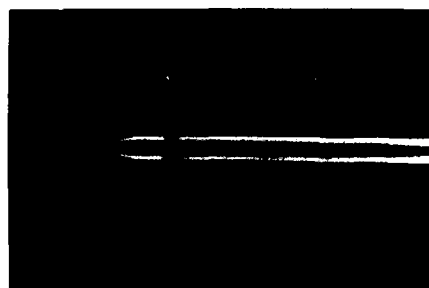
Jet isolé émis dans  
le sens du courant  
Jet plan Jet de  
révolution  
 $\bar{V}_j \approx 20 V_0$   
(écoulement moyen)



Jet plan de faible  
allongement  
 $\bar{V}_j \approx 2 V_0$   
(écoulement  
instantané)  
Effet d'un nid d'abeille  
disposé dans la sonde  
sur la structure du jet



Hélice isolée (écoulement moyen).



Coupes  
diamétrales

$\gamma = 0,2$   
 $N = 6 \text{ tr/s}$

$V_0 = 0$   
 $N \neq$

Démarrage d'un rotor d'hélicoptère (écoulement instantané)

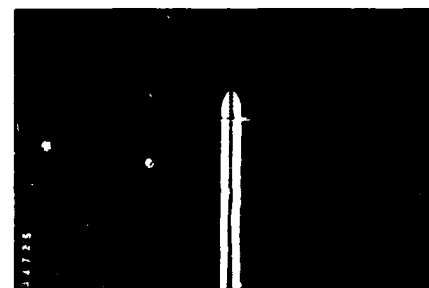
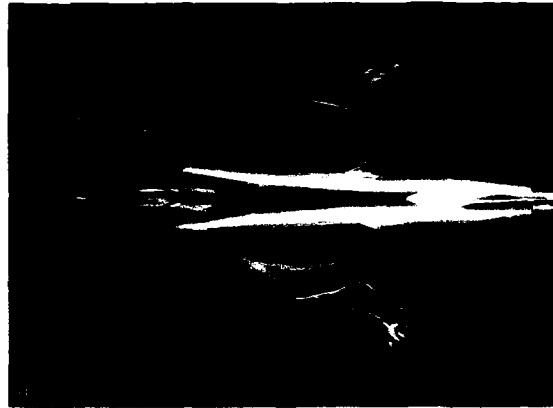
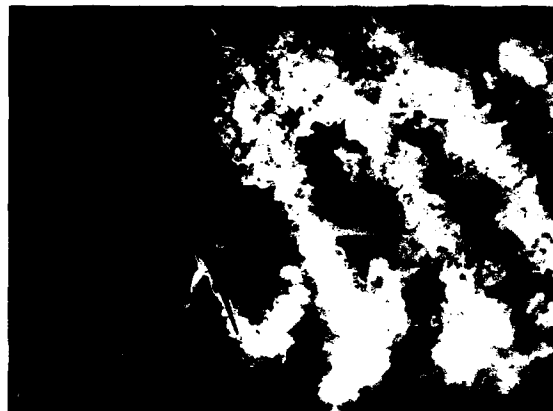


FIG. 7 - EXEMPLES DU DOMAINE AERONAUTIQUE



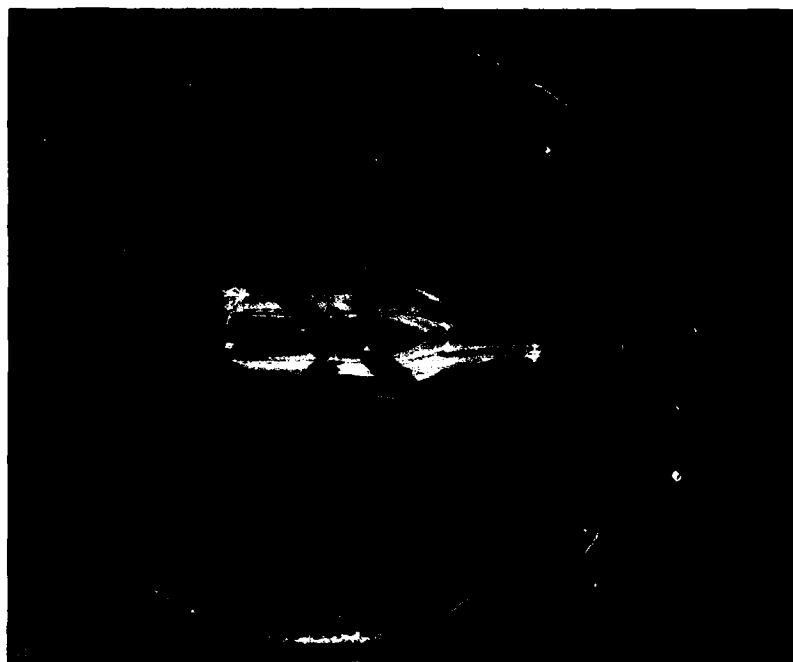
Ecoulement sur l'extrados d'une maquette  
schématique d'avion de combat avec plan canard  
( $\alpha = 10^\circ$   $\beta = 0^\circ$   $Re_c \approx 10^4$ )



Ecoulement instantané autour d'une  
hélice tractrice  $\gamma = 0,7$   $N = 1 \text{ tr/s}$   
 $\alpha_m = 0^\circ$   $Re_D \approx 1,8 \cdot 10^4$



Ecoulement  
autour d'une  
tête de lanceur  
du type  
"Ariane"  
 $\alpha = 35^\circ$   
 $L = 11 D$   
 $Re_L \approx 3 \cdot 10^4$



Ecoulement  
instantané  
au point fixe  
( $V_0 = 0$ )  
autour d'une  
maquette motorisée  
d'hélicoptère  
 $\Lambda = 0$   $N = 0,6 \text{ tr/s}$   
 $\alpha_B = 0^\circ$   $Re_c \approx 10^4$

En courant plan ou axisymétrique, le colorant peut être émis à la surface d'un modèle lisse sous la forme d'une nappe pariétale, continue en régime laminaire et devenant instable en régime transitionnel (ondulations, puis spots de turbulence) comme par exemple sur un fuseau cylindrique sans incidence ( $Re_{xL} \approx 1,5.10^5$  : fig.4a). Cette nappe décolle dans le cas d'une sphère ( $Re_D = 40^5$  : fig.4g) et la transition retarde ce décollement ( $Re_D = 3.10^5$  : fig.4g'). Dans le cas d'un fuseau cylindrique muni d'un rétreint courbe de pente modérée, la transition a pour effet d'éviter le décollement (figs.6ab). On note que la présence de cannelures longitudinales permet de retarder le décollement pour un régime proche de la transition (figs.6ac) [9].

Dans la plupart des essais, le colorant est émis à la surface des modèles sous la forme de filets isolés, plus ou moins pariétaux suivant leur débit. En stationnaire, ils représentent des lignes de courant, qui révèlent l'absence de décollement (fig.4b), la présence de courant de retour dans un décollement (fig.4c), la structure organisée de tourbillons marginaux (fig.4d) ou longitudinaux (fig.4f). Soumis à un gradient de pression longitudinal adverse, ces tourbillons éclatent [10] et ce phénomène peut être visualisé aussi bien en régime laminaire (fig.4e) qu'en turbulent (fig.4e'). Dans ce dernier cas, on observe la diffusion rapide du colorant sauf au voisinage de l'axe du tourbillon. Il en est de même pour le colorant émis à la surface des modèles qui ne subsiste en tant que filet qu'au voisinage de son trou d'émission (figs.4bc). Le colorant sert parfois aussi à teinter un jet turbulent et se dilue alors rapidement dans la zone de mélange (figs.6ij). Des prises de vues rapides [8] permettent alors d'observer les grosses structures tourbillonnaires qui se forment le long de sa frontière (fig.6k), et l'on peut ainsi noter par exemple les effets dus à une grille disposée dans la sonde émettrice (fig.6l). Rappelons enfin en ce qui concerne les décollements [11], qu'une réduction du débit des émissions de colorant permet parfois de faire apparaître les singularités de l'écoulement pariétal : ligne de décollement ou de partage, foyer, noeud, col, etc (voir figs.4Bgg' et 7b).

Les mêmes phénomènes fondamentaux ont été visualisés par des bulles d'air, dont les trajectoires révèlent l'allure des lignes de courant (fig.5a), l'étendue des décollements (fig.5b) et le caractère des sillages (fig.5c). En courant plan, des prises de vues rapides à une seule exposition (fig.5c) ou plusieurs (fig.5b) précisent l'allure du champ de vitesse. Rappelons aussi qu'aux nombres de Reynolds élevés, une accumulation des bulles d'air (effet centripète) met en lumière l'axe des tourbillons longitudinaux intenses (fig.5d) jusqu'à leur éclatement (fig.5f). Enfin les coupes transversales visualisées par les mêmes traceurs révèlent la présence, la position, la structure organisée, le caractère et la stabilité des tourbillons longitudinaux, tels que tourbillon marginal isolé (fig.5e), tourbillons symétriques issus de corps fuselés (figs.6de) ou devenant axisymétriques aux incidences extrêmes (fig.6f à rapprocher de fig.4C), tourbillons d'ailé delta organisés (fig.6g) ou éclatés (fig.6h) [11]. Enfin, deux derniers exemples concernent l'écoulement instationnaire autour d'un rotor qui n'est peut être plus tout à fait un cas fondamental : les bulles d'air visualisent l'écoulement moyen dans une coupe diamétrale d'une hélice tractrice (fig.6m), et notamment la forme convergente du tube de courant laminaire intéressé par l'hélice et celle divergente du flux turbulent l'ayant traversée et à la frontière duquel se déplacent les tourbillons hélicoïdaux issus de l'extrémité libre des pales. Une vue prise au flash (fig.7c) fige ces tourbillons visualisés par colorant et fait apparaître en outre la présence d'un bulbe décollé fixé au bord d'attaque des pales relativement minces ainsi qu'un effet de centrifugation du colorant pariétal.

Le deuxième exemple est celui de l'écoulement instantané observé dans le plan diamétral d'un rotor isolé d'hélicoptère au moment de sa mise en rotation au point fixe (fig.6n) : les bulles d'air visualisent non seulement le tourbillon de démarrage torique se formant à l'extrémité libre des pales, mais aussi celui qui se forme près du moyeu central dans l'espace annulaire balayé par le pied non profilé des pales.

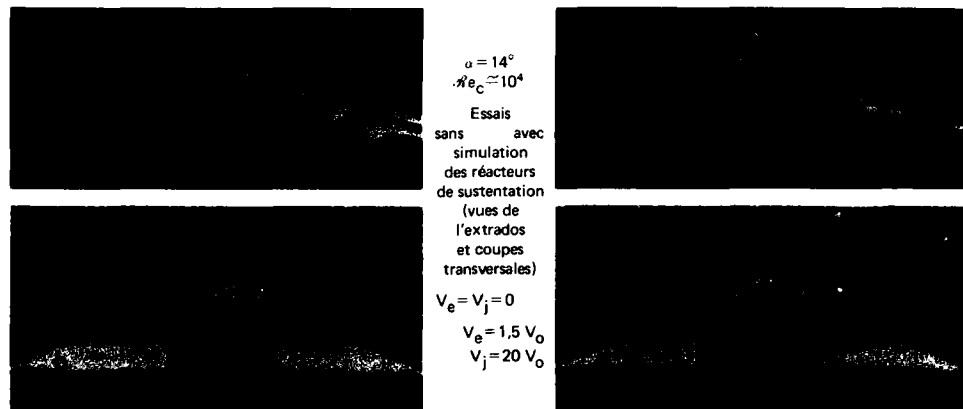
#### EXEMPLES DE VISUALISATIONS DU DOMAINE AERONAUTIQUE -

Dans ce domaine, on peut distinguer deux familles de modèles : les avions et les hélicoptères, si l'on met à part le cas limite de la maquette du lanceur ARIANE (fig.7b) et celui d'un missile schématisé déjà mentionné (fig.4C), qui se rattachent peut être plus ou moins au domaine spatial : leurs essais aux grands angles d'attaque, ce qui correspond aux conditions de lancement d'engins en présence d'un fort vent latéral, font apparaître des décollements comportant des tourbillons d'extrados axisymétriques [12]. On sait que ce phénomène se traduit par des forces latérales à l'avant du modèle et pouvant poser de délicats problèmes de stabilité et de contrôle.

En ce qui concerne les avions, les tunnels ONERA disposent de nombreux résultats d'essais [10, 13, 14], dont quelques exemples de maquettes ont été donnés par la fig.1. Dans le cadre restreint de cet exposé, on se contentera d'en donner un exemple typique et d'évoquer les tendances actuelles des essais en cours.

Les visualisations obtenues avec la maquette d'avion delta à décollage vertical à jets décrite ci-dessus, aussi bien en translation [14] qu'au point fixe [2], confirment les effets sur l'écoulement autour du modèle dus à la simulation des prises d'air et sorties de jets des 8 réacteurs de sustentation : leur mise en service fait apparaître une composante verticale de vitesse descendante. Ainsi, sur le modèle en translation à incidence moyenne, les tourbillons d'extrados observés sans jets (figs.8ab) se résorbent (figs.8cd), conséquence de la diminution de l'incidence effective de la voilure.

En présence d'un sol (fig.8e), l'écoulement se complique par suite de la formation d'un tourbillon "effet de sol" [15], incurvé en fer à cheval et se formant sur le sol en amont de la zone d'impact des jets. Ce tourbillon n'occupe sa position correcte que lorsque le sol est simulé d'une façon réaliste par un tapis roulant. En effet, sur un plancher fixe se produit inévitablement le décollement de la couche limite parasite devant l'obstacle constitué par les jets, et ce décollement déplace le tourbillon "effet de sol" et peut modifier l'incidence locale.



Maquette d'avion VTOL à jets

Essai près du sol  
 simulé par un  
 tapis roulant  
 (coupe longitudinale)

$$\begin{aligned}
 \alpha &= 0^\circ \quad Re_c = 0,5 \cdot 10^4 \\
 V_e &= V_0 \quad V_j = 20 V_0 \\
 V_{TR} &= V_0
 \end{aligned}$$

Maquette d'avion delta avec plan canard

Coupe située à la hauteur  
du plan canard

$$\alpha = 20^\circ \quad \beta = 0^\circ \quad Re_c \approx 2 \cdot 10^4$$

(coupes transversales)



Coupe à la mi-corde de l'aile



Coupe au bord de fuite de l'aile

Maquette motorisée d'hélicoptère (coupes transversales)



Essai au point fixe  $\Lambda = 0$   
 $(\omega_B = 0 \quad Re_c = 10^4 \quad N = 0,67 \text{ tr/s})$

Essais en translation  $\Lambda = 0,2$   
 $(\alpha_B = -10^\circ \quad Re_c \approx 10^4 \quad N = 1 \text{ tr/s})$

Coupes au voisinage du moyeu et coupe aval



FIG. 8 - EXEMPLES D'ÉCOULEMENTS DU DOMAINE AÉRONAUTIQUE

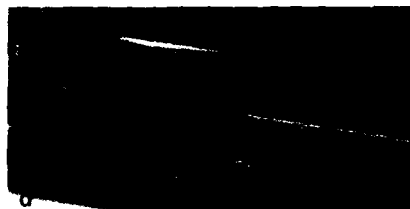




Maquette de sous-marin avec pont  
( $Re_L \approx 0,4 \cdot 10^5$ )

$\alpha = \beta = 0^\circ$

à gauche : coupes suivant le plan de symétrie



à droite : coupes transversales  $\alpha = 8^\circ$   $\beta = 0^\circ$   
situées à mi-longueur du massif et du pont arrière



Vue de dessus

$\alpha = 8^\circ$   $\beta = 8^\circ$

Maquette de sous-marin avec coque axisymétrique ( $\alpha = \beta = 0^\circ$ )



Coupe transversale arrière ( $Re_L = 7 \cdot 10^5$ )

Coupe arrière suivant le plan de symétrie  
essai avec prise d'air (coefficient de débit  
 $\epsilon = 3$ ) simulant le fonctionnement de l'hélice  
( $Re_L \approx 0,7 \cdot 10^5$ )

FIG. 9 — EXEMPLES D'ÉCOULEMENTS  
DU DOMAINE NAVAL

On peut remarquer sur ce modèle, la simulation des deux prises d'air latérales en écoupe des réacteurs de propulsion. On sait [14] qu'un blocage de ces prises d'air peut avoir pour effet de perturber la formation de l'écoulement tourbillonnaire sur la voilure, du fait de la proximité de l'apex, origine du tourbillon principal d'extrados, notamment aux grandes incidences.

Les essais de maquettes d'avion, effectués dans les tunnels ONERA depuis un certain temps, concernent principalement ces grands angles d'attaque [5], pour lesquels les tourbillons d'apex se trouvent affectés du phénomène d'éclatement (fig.4A). Comme l'on montré des essais antérieurs [3], le soufflage latéral, une voilure prolongée à l'amont par des strakes à forte flèche, et surtout des plans canards disposés au-dessus de l'apex permettent de retarder dans certaines conditions cette désorganisation des tourbillons principaux.

Le cas d'un modèle schématique avec plan canard est évoqué par les figures 7a et 8fgh : on notera la complexité du schéma tourbillonnaire d'extrados, par suite de la présence de tourbillons supplémentaires de canard et de fuselage, et même de dérive en cas de dérapage, et l'on imagine les interactions qui en résultent. La tendance actuelle des essais n'est pas sans compliquer encore les phénomènes, puisqu'elle envisage des formules de canard orientable, et même différemment de chaque côté en cas de dérapage, et des voilures munies de bec de bord d'attaque et de volets de bords de fuite. Par contre, on enregistre des effets de plus en plus négligeables des prises d'air que l'on tend à faire passer de la position latérale à la position ventrale.

La deuxième famille de maquettes concerne les hélicoptères : les essais de la maquette motorisée décrite précédemment (fig.1d) ont été effectués successivement au point fixe sans et avec sol dans la veine du tunnel TH3 [3,10] et en translation (vol horizontal, vols de montée et de descente) au tunnel TH2 [8,10] ; en raison de leur caractère instationnaire, ils constituent un des exemples de visualisation hydrodynamique parmi les plus complexes qu'il soit.

Au point fixe (figs.7d et 8i), les visualisations mettent en évidence non seulement l'écoulement induit par la rotation du rotor principal et le déplacement des tourbillons marginaux issus des pales et d'allure hélicoïdale, mais aussi la déformation imposée par cette rotation aux tubes de courant captés par les prises d'air et aux panaches de colorant émis par les sorties de gaz, enfin les décollements sur l'avant côté droit et l'arrière côté gauche du fuselage ainsi que les effets plus localisés dus à la rotation du rotor de queue.

En vol d'avancement, le colorant (fig.4D) révèle la forme en plan cycloïdale des tourbillons (issus du rotor principal et emportés par le courant, le dérapage de l'écoulement moyen à la hauteur du fuselage, d'autre part, les bulles d'air confirment dans des coupes transversales (figs.8jk) que le disque balayé par le rotor se comporte comme une aile portante avec formation sur les bords latéraux de tourbillons marginaux concentrés. A signaler, d'ailleurs, qu'en raison de la taille du modèle, le rotor principal est rigide et sans variation cyclique du pas des pales.

#### EXEMPLES DE VISUALISATIONS DU DOMAINE NAVAL -

Ce domaine, qui n'entre pas exactement dans le cadre habituel de l'activité des tunnels ONERA, peut cependant être illustré par deux exemples.

Le premier concerne les essais d'une maquette de la turbovoile imaginée par L. MALAVARD [16]. Cette voile cylindrique rigide, mais orientable, peut être utilisée pour la propulsion d'un bateau grâce à la force aérodynamique résultant du vent relatif et particulièrement importante en raison du contrôle de l'écoulement d'extrados au moyen d'une aspiration. Les visualisations au tunnel TH1 (figs.10ab) [17] soulignent l'efficacité du procédé, qui permet d'obtenir une résorption notable de la zone décollée et une augmentation importante de la circulation autour de la voile, qui est confirmée par le net déplacement du point d'arrêt amont.

Le deuxième exemple est celui d'une maquette de sous marin. Dans un premier cas, il s'agit d'un modèle schématique à coque axisymétrique et comportant un avant court. Les visualisations révèlent l'étendue des décollements libres se produisant devant les différents obstacles (massif avant, barres) et la structure en fer à cheval des tourbillons qui les caractérisent (figs.4B et 10c).

Il en est de même autour des ailerons arrière, où l'on peut observer en outre les perturbations dues au sillage du massif (fig.9k) ainsi que les effets d'un gradient de pression longitudinal favorable, tel que celui qui résulterait d'une hélice propulsive simulée ici par une prise d'air disposée à l'arrière et fonctionnant avec un coefficient de débit  $E > 1$  (voir figs.9j et 10d).

Dans un deuxième cas, il s'agit d'un modèle plus complet avec pont (fig.1f) [18]. Les visualisations obtenues précisent à nouveau le mécanisme de l'écoulement autour du massif avant (décollement au pied du massif, zone de circulation à l'arrière) et le caractère tourbillonnaire organisé ou non de son sillage (figs.9a-c), mais aussi leur évolution lors d'une mise en incidence (figs.9d-f) et en dérapage (figs.9g-i). Cette évolution est marquée par l'accentuation du caractère tourbillonnaire organisé des sillages et décollements, ces derniers se développent en venant se fixer le long des arêtes du pont.

#### CONCLUSION -

Comme on vient de le voir, pour visualiser les écoulements, analyser finement leur mécanisme et préciser leur évolution en fonction de nombreux paramètres, l'ONERA exploite depuis près de 35 ans des installations hydrauliques consacrées à des études aérodynamiques et hydrodynamiques apparentées, sans avoir épuisé toutes les possibilités de recherche dans ces domaines.

La preuve en est que les deux dernières décennies ont vu la mise en service de telles installations dans la plupart des pays faisant de la recherche aérospatiale ou navale, et bien souvent ces nouvelles installations ne se limitent pas à la visualisation, mais effectuent aussi des mesures

 $C_d = 0$ Maquette de turbo voile (cylindre profilé avec aspiration)  $\alpha = 15^\circ$   $Re_L = 6000$  $C_d = 0,15$ Maquette de sous-  
marin avec coque  
axisymétrique  
( $\alpha = \beta = 0^\circ$ ).Vue du massif  
 $Re_{x_{MASSIF}} \approx 0,35 \cdot 10^5$ Vue de l'arrière  
 $Re_{x_{AILERON}} \approx 0,7 \cdot 10^5$ Essai avec prise d'air  
( $\epsilon = 1$ ) simulant le  
fonctionnement de  
l'héliceFIG. 10 -  
EXEMPLES  
D'ECOULEMENTS  
DU DOMAINE  
NAVAL

quantitatives.

Loin de mettre en cause ce type d'expérimentation, le développement des ordinateurs, qui intervient après celui des souffleries, crée lui aussi tout un courant de demandes d'éléments de comparaison que peuvent lui fournir ces essais effectués dans l'eau.

Enfin, en ce qui concerne plus particulièrement la visualisation des phénomènes, la grande facilité offerte par l'eau devrait lui assurer encore de beaux jours à notre époque marquée par la diffusion universelle de l'image couleur imprimée et télévisée ; c'est tout au moins ce que l'on ressent devant l'ampleur que prennent les symposiums internationaux [19] ou les colloques nationaux [20] entièrement consacrés à la visualisation des écoulements.

#### REFERENCES -

- [1] H. WERLÉ (Oct. 1960) - Méthodes d'étude, par analogie hydraulique, des écoulements subsoniques, supersoniques et hypersoniques - AGARD Rep.399.
- [2] H. WERLÉ et M. GALLON (Mars 1969) - Cuve hydraulique pour la visualisation des écoulements au point fixe - La Rech. Aérop. n°129.
- [3] H. WERLÉ et M. GALLON (Sept.1982) - Le nouveau laboratoire de visualisation hydrodynamique de la Direction de l'Aérodynamique. La Rech. Aérop. 1982-5.
- [4] Film ONERA 1067 (1986) présenté au cours du symposium.
- [5] H. WERLÉ (Mars 1982) - Flow visualization techniques for the study of high incidence aerodynamics - AGARD - VKI Lecture Series 121.
- [6] J. MIRANDE, V. SCHMITT et H. WERLÉ (Oct. 1978) - Système tourbillonnaire présent à l'extrados d'une aile en flèche à grande incidence - AGARD CP 247 mémoire n°12.
- [7] H. WERLÉ (Mars 1970) - Visualisation de l'effet de sol à basse vitesse autour d'une maquette d'avion - La Rech. Aérop. 1970-2.
- [8] H. WERLÉ (Août 1984) - Etude de courants fluides à l'aide de photographie et cinématographie rapides - 16è congrès Photographie Rapide Strasbourg.
- [9] F.G. HOWARD and W.L. GOODMAN (June 1985) - Axisymmetric Bluff-body drag reduction through geometrical modification - J. Aircraft vol.22 n°6.
- [10] H. WERLÉ (Avril 1983) - Visualisation des écoulements tourbillonnaires tridimensionnels - AGARD CP 342 mémoire n°8.
- [11] H. WERLÉ (Mai 1975) - Ecoulements décollés - Etude phénoménologique à partir de visualisations hydrodynamiques - AGARD CP 168 mémoire n°39.
- [12] H. WERLÉ (Nov. 1979) - Tourbillons de corps fuselés aux incidences élevées. L'Aéron. et l'Astron. 1979-6.
- [13] H. WERLÉ (1974) - Le tunnel hydrodynamique au service de la recherche aérospatiale - ONERA Publ. n°156.
- [14] H. WERLÉ (Oct. 1977) - Application of hydrodynamic visualization to the study of low speed flow around a delta wing aircraft (symposium TOKYO). in Flow Visualization: voir [19].
- [15] R.E. KUHN and J. ESHLEMAN (Oct. 1985) - Ground effect on V/STOL and STOL Aircraft - A survey AIAA 85-4033 COLORADO Springs.
- [16] L. MALAVARD (1984) - Un nouveau propulseur éolien de navire - La vie des Sciences, C.R. Ac. Sc., n°1.
- [17] H. WERLÉ (Juil. 1984) - Visualisation hydrodynamique de l'écoulement autour d'un cylindre profilé avec aspiration, maquette de la turbovoile COUSTEAU MALAVARD - La Rech. Aérop. 1984-4.
- [18] H. WERLÉ (1975) - Applications aérospatiales, industrielles et maritimes de la visualisation hydrodynamique des écoulements - ATMA (session 1975).
- [19] Intern. Symp. - Flow Visualization I - TOKYO (Oct. 1977). Flow Vis. II - BOCHUM (Sept. 1980). Flow Vis. III - ANN ARBOR (Sept. 1983). Flow Vis. IV - PARIS (Août 1986). Hémisphère Publ. Corp.
- [20] 1er Colloque national de visualisation et de traitement d'images - NANCY (Janv 1985) - Univ. NANCY I.

THE USE OF A WATER TOWING TANK FOR AERODYNAMIC TESTING AND  
METHODS FOR QUANTITATIVE EVALUATION OF PHOTOGRAPHS

H. Bippes

DFVLR Institute for Experimental Fluid Mechanics  
D-3400 Göttingen, Bunsenstr. 10, F.R. Germany

SUMMARY

The use of the water towing tank of the DFVLR for fluid dynamic testing is briefly described. The capability of measuring techniques is discussed. Among the various techniques the quantitative evaluation of photographs of visualized flow proved to be most effective for the use in a water towing tank. Two methods enabling the survey of three-dimensional flow fields are dealt with in detail. The first method based on photogrammetric techniques has already been applied to the investigation of three-dimensional disturbances in an unstable laminar boundary layer and to the study of a free vortex flow. The second one is based on holographic techniques. Its feasibility for supplying quantitative data is discussed.

1. INTRODUCTION

For aerodynamic testing purposes the water towing tank has proved to be a useful means for supplementing the simulation possibilities of wind tunnels. The principle of moving the model through a stagnant fluid and the relative ease of flow visualization in a liquid favours certain special experimental studies.

These are:

1. Slowly decaying wake flows far downstream of the model where wind tunnel testing is restricted by the length of the test section.
2. Ground effects and gap flows generated by moving the model relative to fixed walls or obstacles.
3. Laminar and turbulent boundary layers as well as the development of instabilities in transitional boundary layers. - Due to the low disturbance level in the stagnant water some additional transition features could be detected.
4. Unsteady flows with particular reference to the possibility of accelerating and decelerating the model in a prescribed manner.
5. Flows in stably stratified fluids.
6. Complicated subsonic flows by means of flow visualization.

For the acquisition of quantitative data principally the same measuring techniques can be used as in wind tunnels. In many cases the higher density and heat transfer of water in comparison with air leads to a corresponding increase of accuracy. On the other hand the comparatively high electrical conductivity of water requires significant modifications. The shortcoming of intermittent testing and the inevitable settling times between successive test runs in a towing tank necessitate measuring techniques which provide as much information per test run as possible. A powerful means in this regard is flow visualization and photography. The flow pattern is stored on a film or plate and can be mapped therefrom at any time after the test.

The required testing time is reduced to the duration of the exposure of the photographs. Thus, the flow need not be retained for a long time. Another point of view is that the benefits of flow visualization can be combined with the acquisition of quantitative data.

In the following a method is described which supplies quantitative data from flow photographs by means of a stereo-photogrammetric method. Main emphasis is placed on three-dimensional flow fields. In addition an attempt is described to use holographic techniques for recording and surveying flow fields.

2. PHOTOGRAMMETRIC METHOD

Photogrammetry as a spatial surveying method is applied in different fields of civil engineering and appropriate evaluation methods have been elaborated. However, in fluid mechanical testing photogrammetry has hardly penetrated. For experiments in a water towing tank the refraction of the image light beams on the air-water interface must be taken into account (the cameras being in air or water).

The postulate of accurate measurements sets certain standards on the photographic and visualization techniques as well.

## 2.1 SUITABLE FLOW VISUALIZATION TECHNIQUE

Most suitable for photogrammetric evaluation of photographs are suspensions of particles which can be identified and traced in the photographs. It is necessary that the particles are small enough to follow the flow at any time so that they represent fluid markers.

A visualization method which satisfies the described condition to a large extent is the hydrogen bubble method. For this reason and because of its simple handling this technique has been chosen. In order to facilitate the tracing on the photographs discrete bubble lines (known as time lines) are produced by pulsing the electrical current in the hydrogen generating electrolysis process (Schraub et al. [1]). Averaging effects in unsteady flows are minimized by doubly exposing the photographs, so that each fluid marker is imaged twice on each photograph (Fig. 1). While the recording of the time between two successive exposures can easily be done, the main problem is the determination of the spatial displacement of the fluid markers from their images on the photographic plates.

## 2.2 TWO-MEDIUM PHOTOGRAMMETRY

The photogrammetric procedure of determining the spatial location of object points from their images on the photographs is to reconstruct the imaging light rays at the instant of photography. This can be done either in an analogue manner, i.e. with the aid of an analogous restitution apparatus or analytically. The first method allows direct mapping of the object with the aid of a plotter and is therefore commonly used. In commercially available apparatus, however, the refractive interface water-air cannot be modelled so that the less convenient analytical evaluation procedure had to be chosen.

The geometric relations between object and image points in the stereoscopic model of a two-medium space can be derived from Fig. 2.  $O_1$  and  $O_2$  located at distance  $b$  from one another are the perspective centres of the two cameras.  $\psi_1$  and  $\psi_2$  are the image planes. The homologous perspective rays  $X_{E1} + g_1$  and  $X_{E2} + g_2$  \* centred in the bundle of rays, which image object points  $P$  in their images  $P'_1$  and  $P'_2$  on  $\psi_1$  and  $\psi_2$ , are refracted at the water surface  $\pi$ .

If the inner and outer orientations of the cameras are known, i.e. the camera geometry and the orientations of the cameras in a given spatial coordinate system, then each object point can be reconstructed with the aid of the coordinates  $(x_1, y_1)$  and  $(x_2, y_2)$  of a pair of homologous image points  $P'_1$  and  $P'_2$  in the image plane. Hence, the first problem is to determine the orientation. If cameras with known inner orientation are used, the outer orientation is determined in two steps:

1. A geometrical model of the relative orientation of the two cameras and their orientation to the refractive surface is established.
2. The geometrical model is transformed in real scales into a given spatial coordinate system.

Reconstruction of a photogrammetric model:

The orientation parameters establishing a photogrammetric model, i.e. a model of the image rays as existing at the photographing process, are: three rotations  $(\phi_1, \phi_2, \phi_3)$  for each camera, the base-altitude ratio  $v = b/h$ , and the inclination  $\epsilon$  of the base  $b$  against the plane water surface (all the orientation parameters are depicted in Fig. 2). There are 8 unknowns altogether.

The relation between the coordinates  $(x_1, y_1)$  and  $(x_2, y_2)$  of the image plane and the orientation parameters is given by the "intersection condition" of the image rays established by Rinner [2]:

$$\bar{X}_{E1} + \bar{\lambda}_1 \bar{g}_1 = b + \bar{X}_{E2} + \bar{\lambda}_2 \bar{g}_2 \quad (2.1)$$

The orientation problem is solved if for each homologous pair of image rays a pair of parameters  $\bar{\lambda}_1$  and  $\bar{\lambda}_2$  can be found for which the intersection condition is fulfilled. Hence, for determining the 8 unknowns of the relative orientation the image coordinates of 8 pairs of homologous image points are required. This leads to the solution of a system of 8 algebraic and transcendental equations (2.2) where the intersection condition (2.1) is expressed in the orientation parameters and the coordinates of the image points in the image system

$$[\cos \epsilon + v(\frac{u_2}{w_2} - \frac{u_1}{w_1}) + \frac{u_2}{w_2} \sin \epsilon] [v_1(e_2 p_2 - w_2) - v_2(e_1 p_1 - w_1)] - \quad (2.2)$$

$$[v(\frac{v_2}{w_2} - \frac{v_1}{w_1}) + \frac{v_2}{w_2} \sin \epsilon] [u_1(e_2 p_2 - w_2) - u_2(e_1 p_1 - w_1)] = 0$$

\* Letters marked with bars denote vectors

where

$$e_i p_i = w_i \left( 1 - n \sqrt{1 + \frac{n^2 - 1}{n^2} \frac{u_i^2 + v_i^2}{w_i^2}} \right) \quad i = 1, 2$$

and  $n$  denotes the refractive index air - water.

$$u_i' = x_i \cos \lambda_i - y_i \sin \lambda_i$$

$$v_i' = y_i \cos \lambda_i + x_i \sin \lambda_i$$

$$w_i' = f_i \cos \omega_i - v_i' \sin \omega_i$$

$$v_i = v_i' \cos \omega_i + f_i \sin \omega_i$$

$$u_i = u_i' \cos \phi_i - w_i' \sin \phi_i$$

$$w_i = w_i' \cos \phi_i + u_i' \sin \phi_i$$

$u_i, v_i, w_i$  are the coordinates of the image points in the coordinate system of the photogrammetric model centred in  $O_1$ .

The orientation parameters being known, the position of the object points in the coordinate system  $(u, v, w)$  of the photogrammetric model, positioned in  $O_1$ , can be calculated from eq. (2.3):

$$U = \left( \frac{b}{w_1} + \gamma_1 \right) u_1 \quad (2.3)$$

$$V = \left( \frac{b}{w_1} + \gamma_1 \right) v_1$$

$$W = b - \gamma_1 (e_1 p_1 - w_1)$$

with

$$\gamma_1 = \frac{u_s v_2 - u_2 v_s}{u_1 v_2 - u_2 v_1}$$

and

$$u_s = b \left[ \cos \sigma + v \left( \frac{u_2}{w_2} - \frac{u_1}{w_1} \right) + \frac{u_2}{w_2} \sin \sigma \right]$$

$$v_s = b \left[ v \left( \frac{v_2}{w_2} - \frac{v_1}{w_1} \right) + \frac{v_2}{w_2} \sin \sigma \right]$$

Transformation of the photogrammetric model into the given spatial coordinate system:

The transformation of the coordinates  $(U, V, W)$  of the photogrammetric model into the coordinates of the given spatial coordinate system  $(X, Y, Z)$ , Fig. 3, requires two "pass points", i.e. two points of known position. The transformation can be written as:

$$\begin{pmatrix} X \\ Y \\ Z \end{pmatrix} = \begin{pmatrix} X_0 \\ Y_0 \\ Z_0 \end{pmatrix} + \underline{A} \begin{pmatrix} u \\ v \\ w \end{pmatrix} \quad (2.4)$$

where  $(X_0, Y_0, Z_0)$  are the coordinates of  $O_1$  in the given spatial system.

For the special case of one coordinate normal to the refractive surface - as in the coordinate system of the photogrammetric model the transformation matrix  $\underline{A}$  is:

$$\underline{A} = \begin{bmatrix} \cos \sigma & \sin \sigma & 0 \\ -\sin \sigma & \cos \sigma & 0 \\ 0 & 0 & 1 \end{bmatrix}$$

the scaling factor  $m$  is:

$$m = \sqrt{\frac{(x_2 - x_1)^2 + (y_2 - y_1)^2}{(u_2 - u_1)^2 + (v_2 - v_1)^2}} \quad (2.5)$$

where the indices 1 and 2 denote the coordinates of the two pass points in the scale model and the given spatial coordinate system.

Numerical solution of the orientation problem:

For the numerical solution of the orientation problem an iterative approximation procedure is applied. The use of more than the required number of image points and pass points, respectively, enables the application of a least squares procedure to improve the accuracy of the numerical solution.

Error bounds of the photogrammetric measurement:

Assuming that the orientation parameters are precisely known, then the main error results from the measurement of the image coordinates. Since in the two-medium case in conventional optical restitution instruments a stereoscopic view is not guaranteed for the whole imaged object, the error derives from the inaccuracy of the monocular measurement of image coordinates  $\Delta x = \Delta y \leq 0.01$  mm. The error in the depth of object points caused by  $\Delta x$  may then be deduced from Fig. 4 as follows:

$$\gamma \approx \frac{b}{z}$$

the differential deviation of  $\gamma$

$$\Delta \gamma \approx \frac{b}{z^2} \Delta z \quad (2.6)$$

for small angles  $\alpha$  this can be written as:

$$\Delta \gamma \approx \frac{1}{f} \Delta x \quad (2.7)$$

with (2.6) and (2.7) the error in the depth of the object is

$$\Delta z \approx \frac{z^2}{b f} \Delta x \quad (2.8)$$

Assuming  $b = 185$  mm,  $z = 650$  mm and  $f = 380$  mm as in our case, the error in the image measurement  $\Delta x \leq 0.01$  mm causes a photogrammetric error in the depth survey of

$$\Delta z \leq 0.14 \text{ mm.}$$

The errors in X and Y direction are smaller.

In order to avoid that this photogrammetric error is not further increased by errors in the orientation parameters the latter must be recalculated for each stereo-photograph.

A comparison between the survey of a spatial model by means of theodolites and the photogrammetric method proved that the estimated accuracy is achieved.

## 2.3 PHOTOGRAPHY

For photogrammetric purposes basically any camera can be used. For a regular camera, however, the inner orientation (i.e. the position of the perspective centre of the objective with respect to the image coordinate system) has to be found for each photograph. This can be done with the aid of a spatial system of pass points which must be imaged and measured on each photograph (Jacobi [3]). In order to avoid this effort, stereometric cameras are generally used, i.e. cameras with fixed inner orientation. Frame markers in the image plane, when imaged on the photographs, allow the image coordinates to be given with respect to the perspective centre. Such cameras cannot be focussed and are therefore not appropriate for photographs at close but different range as is necessary for resolving small bubbles of 20  $\mu$ m in diameter. Hence, a stereometric camera was constructed which is adapted to our special application (Fig. 5, Bippes [4]). Both objectives are incorporated in a common housing. The focal length, the base length, an inclination of the common image plane, and the section of it chosen for the photograph can be adjusted mutually by means of micrometers. The camera is mounted parallel to the water surface with the optical axes normal to it. With the aid of the described arrangements the number of orientation parameters to be calculated and the number of pass points required for it is reduced.

## 2.4 ON THE FEASIBILITY OF THE METHOD

As already emphasized the photogrammetric method described combines the benefits of flow visualization with the possibility of providing quantitative data. The measuring process does not exceed the time of exposure. The locations of interest for measurements can be chosen in the visualized flow field at any time after the test. On the other hand some efforts have to be made to create a system of pass points the relative locations of which must be surveyed very precisely. Extensive microscopic image analysis can be tiresome and finally the measuring equipment for this special application is not commercially available.

The effectivity of the method may be shown in two examples. The first one stems from measurements of the axial velocity in the core of the trailing edge vortices (Bippes [5]). Such vortices undergo an apparently random wandering which is also influenced by



the downstream development of instabilities. Hence, the position of fixed hot-wire probes relative to the vortex axis varies with time. Fig. 6 shows for comparison profiles of the axial velocity in the vortex core measured with the photo-optical method and with hot-wire anemometer (Baker [6]). It is suggested that the pointed shape of the profile is missed in the hot-wire measurements, because of the uncertainty of the probe position with respect to the vortex axis.

The second example shows a result of the investigation of the unstable laminar boundary layer flow along a concave wall (Bippes [4]). In such a flow, Taylor-Görtler vortices develop as primary instability. In Fig. 1 this instability manifests itself by the sinusoidal deformation of the time lines (in undisturbed laminar flow the time lines are straight lines). Further downstream the originally straight vortices undergo an oscillating motion so that the position of the hot-wire probes again becomes uncertain (Fig. 7a). This is illustrated by the irregularity of the instantaneous hot-wire signal of probe 1 in Fig. 7b which displays the existence of travelling waves with maximum amplitude in the streamwise zones of low velocity (zone b in Fig. 1). For measuring the disturbance profiles (Fig. 8) and the amplification rate of Taylor-Görtler vortices (stationary waves) the photogrammetric method again proved to be adequate because it allows to identify the streamwise zone a or b (Fig. 1) along which the measurements have to be taken.

In the literature there are some examples where quantitative data were taken from mono-photographs. Such a procedure is only admissible in the ideal case of plane flows. As an example, Fig. 9 shows the deformation normal to the wall of the time lines displayed in Fig. 1. It is obvious that without any knowledge of this deformation, boundary layer measurements may be misleading.

### 3. DISCUSSION OF A HOLOGRAPHIC DEVICE FOR RECORDING AND SURVEYING THREE-DIMENSIONAL FLOW FIELDS

A further method for recording three-dimensional flow fields on two-dimensional photographic plates is holography. In contrast to conventional photography not only the intensity distribution of the light scattered by the object is stored, but also the phase relations. Thus, it is possible to reconstruct the wave fronts emanating from the object in real scales. This quality also facilitates the quantitative evaluation. It allows the reconstructed three-dimensional object to be viewed under a range of angles which is only restricted by the size of the hologram. Any motion of the object can be recorded with the aid of holographic interferometry, a property which can also be utilized for velocity measurements.

The limitation of holography for recording and reconstructing flow fields visualized with the aid of hydrogen bubbles is the limiting resolving power of the hologram. For the same reasons as for the stereo-photogrammetric method the hydrogen bubble technique is proposed for flow visualization.

#### 3.1 RECORDING ARRANGEMENT

The design concept of the holographic arrangement has to be adapted to the given application. The testing facility sets bounds to the geometry of the holographic device. The size of the fluid markers prescribes the required resolving power.

Basically, for recording the transparent hydrogen bubbles, the simpler in-line arrangement with only one beam path could have been chosen (the reference wave being that part of the initial beam, which is not distorted by the object). In this case, however, the viewer of the hologram has to look into the expanded light beam. For this and some other practical reasons the off-axis arrangement shown in Fig. 10 has been used. The light beam is divided by a beam splitter (T) into an object and a reference beam. The object beam falls on the hologram (H) after being scattered by the hydrogen bubbles (fluid markers) whereas the reference beam passes directly onto the hologram. A diffusing screen (M) illuminates the entire area of the hologram, and, conversely, light scattered by all points on the screen impinges on every portion of the hologram. As a result, every part of the hologram carries information concerning light waves that have passed through every part of the object at all different angles. In this way the full size of the hologram contributes to the resolution (Sect. 3.3) and facilitates the depth observation.

As coherent light source a pulsed ruby laser is used. The pulse duration is 30 ns, i.e. a time scale in which all motion is essentially frozen. Thus, holograms of moving objects are possible and the expenditure for stabilizing equipment is reduced. All optical components are mounted on positioners on an assembly of aluminium profiles of high mechanical quality which provide translation of the positioners with the optical components as on optical rails. Supporting wheels facilitate the transport of the complete assembly.

The laser system used provides two-pulse operation. It is therefore possible to superimpose two holograms so that any motion of the object between two pulses separated in time by a known amount, can be observed as a series of interference fringes, which are frozen into the holographic plate. This technique allows a detailed study of motion.

## 3.2 RECONSTRUCTION ARRANGEMENT

For practical reasons the holograms are reconstructed in a separate device with the aid of a He-Ne laser as continuous light source (Fig. 11). Most important for the resolving power in the reconstruction process is the use of a point source for illumination and the exact geometric reconstruction of the reference beam. The first condition is approximated by introducing a microscope objective-pinhole diaphragm (S) into the beam path. The realization of the second condition is facilitated by using a plane wave front for the reference beam. The angle  $\alpha_{RP}$  between reference and object beams (Fig. 10) has to be modified in the reconstruction arrangement according to the difference in wave length of the ruby and He-Ne lasers. For the simplest case, where the object beam falls normal on the holographic plate, the modified angle is:

$$\alpha_{RP} = \arcsin\left(\frac{\lambda_{\text{He-Ne}}}{\lambda_{\text{ruby}}} \sin \alpha_{RP}\right) \quad (3.1)$$

As sketched in Fig. 11 two images are generated by the reconstruction of the object wave, the so-called virtual and real images. The latter, produced by the conjugate light beam can be imaged on a diffusing screen or on a film in real scales (if the above mentioned geometrical conditions are satisfied). By shifting the diffusing screen or film plane through the real image it can be seen in different sections. Thus, an object can be surveyed laterally as well as in depth.

## 3.3 RESOLVING POWER

As already mentioned the most critical problem for the use of holography is the resolution of the small particles needed for adequate flow visualization.

Corresponding to the Raleigh criterion the limiting resolving power of a hologram is determined by the diffraction of light by the smallest aperture (Kiemle und Röss [7]). The lateral resolution is then:

$$\Delta s = 1.22 \frac{\lambda z}{d} \quad (3.2)$$

where  $\lambda$  denotes the wave length of the coherent light source,  $z$  is the distance from object to hologram and  $d$  is the smallest aperture.

The depth resolution is

$$\Delta z = 2 \lambda \frac{z^2}{d^2} \quad (3.3)$$

In our recording arrangement (Fig. 10) the smallest aperture is given by the hologram size  $d = 100 \text{ mm}$ , the optical length between object and holographic plate is  $851 \text{ mm}$  (it must be modified by the refractive index air - water), and the wave length of the light source is  $694.3 \text{ nm}$ . With these data the resulting lateral resolution calculated from Eq.(3.2) is:

$$\Delta s = 7.2 \text{ } \mu\text{m}$$

and the depth resolution corresponding to Eq.(3.3) is:

$$\Delta z = 100.5 \text{ } \mu\text{m}.$$

Thus, the limiting resolving power calculated from Eq.(3.2) is sufficient for the resolution of hydrogen bubbles which are about  $20 \text{ } \mu\text{m}$  in diameter. Usually, however, the limiting resolving power can not be achieved for a number of reasons, namely, the degree of coherence of the light source and insufficient coherence length, respectively, and imaging errors such as spherical aberration, coma and astigmatism.

The holographic device described so far has been tested by a simple object. It is a water tank with a resolution target and hydrogen bubbles in it, the hydrogen bubbles being generated on a helically deformed wire of  $20 \text{ } \mu\text{m}$  in diameter. Fig. 12 shows the object photographed from the virtual image (comp. Fig. 11). Fig. 13 displays details of the same object now photographed from the real image with the image plane in different sections of the reconstructed interference pattern. It becomes evident that only the object points in close proximity to the film plane are well focussed. Thus, the depth of the object can be traced within the resolution calculated in Eq.(3.3).

Fig. 14 stems from a test in the water towing tank. It shows a concentrated vortex shed from the tip of a rectangular wing photographed from the virtual image of a reconstructed hologram. It can be seen that the resolution of the hydrogen bubbles is poorer than in Fig. 13. The reason is that the distance between the object and the ho-

lographic plate is increased by about 200 mm. Hence, the limiting resolving power calculated above is not fully achieved. An improvement can be accomplished either by optimizing the degree of coherence of the light source and by minimizing imaging errors or by enlarging the hologram (see Eq. 3.2). The latter remedy is the most simple and effective but also the most expensive one.

#### 4. CONCLUSIONS

The principle of moving the model through a stagnant fluid in a water towing tank and the relative ease of flow visualization favours some special experiments. The intermittent operation and the resulting settling times between successive runs demand measuring techniques which provide as much data per test run as possible. Flow visualization and photography have proved to be a powerful means. The flow pattern is frozen on a photographic plate and can be analysed in detail at any time after the test. The required testing time is reduced to the exposure time.

For quantitative data reduction from the photographs a stereo-photogrammetric method has been developed. It allows to reconstruct analytically the imaged object in real scales. For flow visualization the hydrogen bubble technique has been used. The photographs are doubly exposed within a defined time interval so that each fluid marker is imaged twice. Thus, the displacement of the fluid markers within the time of successive exposures and therewith the velocity vector can be determined. The feasibility of the method is shown by two examples.

A second method for recording three-dimensional flow fields on two-dimensional photographic plates is holography. With the aid of holographic techniques not only the distribution of intensity but also the phase distribution of the light scattered by an object is stored. Thus, it is possible to reconstruct the wave front in real scale. A holographic device for recording and surveying three-dimensional hydrogen bubble patterns is described. Some examples of first tests are shown. The resolving power has proved to be the main problem for recording hydrogen bubbles at larger distances.

#### 5. REFERENCES

- [1] Schraub, F.H.; Kline, S.J.; Henry, J.; Runstadler, P.W; and Litell, A.: "Use of Hydrogen Bubbles for Qualitative Determination of Time Dependent Velocity Fields in Low Speed Water Flows", Stanford University, Thermosc. Div. Mech. Eng. Dept., Report MD-10, 1964.
- [2] Rinner, K.: "Abbildungsgesetz und Orientierungsaufgaben in der Zweimedienphotogrammetrie", Österr. Zeitschr. f. Verm. Wesen, Sonderheft 5, 1948.
- [3] Jacobi, O.: "Kalibrieren gewöhnlicher Photoapparate und deren Verwendung als Meßkammern", Bildmessung u. Luftbildwesen, Heft 2, pp. 59-70, 1968.
- [4] Bippes, H.: "Experimentelle Untersuchung des laminar-turbulenten Umschlags an einer parallel angeströmten konkaven Wand", Sitzungsber. d. Wiss., Math.-naturwiss. Klasse, 3. Abh., Springer Verlag Berlin, Heidelberg, New York, 1972.  
English Translation: Experimental Study of the Laminar-Turbulent Transition on a Concave Wall in a Parallel Flow, NASA TM-75243, 1978.
- [5] Bippes, H.: "Experimente zur Entwicklung der freien Wirbel hinter einem Rechteckflügel", Acta Mech. 26, pp. 223 - 245, 1977.
- [6] Baker, G.R.; Barker, S.J.; Botak, K.K.; and Saffman, P.G.: "Laser Anemometer Measurements of Trailing Vortices in Water"; J. Fluid Mech. 65, Part 2, pp. 325-336, 1974.
- [7] Kiemle, H.; Röss, D.: "Einführung in die Technik der Holographie", Techn.-Phys. Sammlung, Bd. 8, pp. 94-116, Herausg. D. Röss und R. Sewid, Akad. Verlagsgesellsch. Frankfurt am Main, 1969.

#### 6. ACKNOWLEDGEMENTS

The author wishes to thank Dr. W. Hentschel of the University of Göttingen who elaborated and tested the design concept of the holographic equipment.

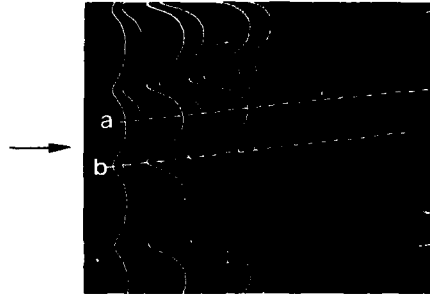


Fig. 1: Doubly exposed time line pattern. Lines a and b are stream-wise zones of maximum disturbance velocity in the unstable laminar boundary layer on a concave wall (top view)

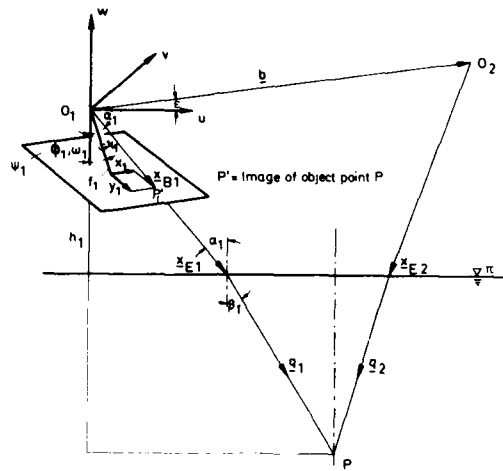


Fig. 2: Basic geometry of two-medium photography.  $O_1$  and  $O_2$  are projection centres,  $\pi$  is the image plane of one camera,  $\pi$  is the refractive surface,  $\phi, \omega, \chi, \epsilon, b, f, h$  are orientation parameters,  $x_{E1}$  and  $q_1$  are image rays,  $x_{B1}$  is the vector to the image point  $P'_1$

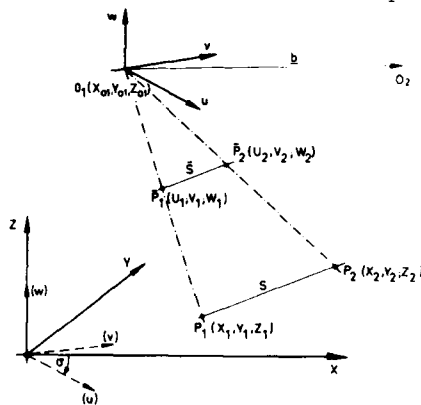


Fig. 3: Transformation of the photogrammetric model (coordinate system  $\{u, v, w\}$ ) with object points  $P$  into the given spatial coordinate system  $\{X, Y, Z\}$  with object points  $P$

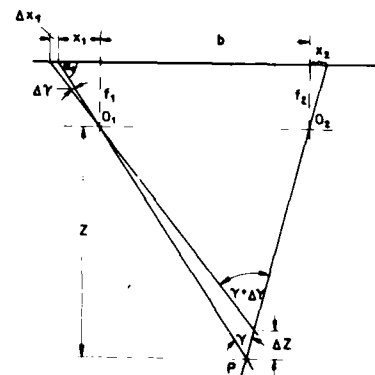


Fig. 4: Principle of estimating the photogrammetric error



Fig. 5: Stereometric camera mounted on the trolley of the water towing tank

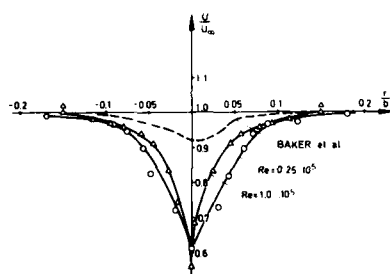


Fig. 6: Velocity profiles of the axial flow in a trailing edge vortex, measured 10 wing chords behind the trailing edge of a rectangular wing which was set at an angle of incidence of  $10^\circ$ .  $U$  = axial velocity,  $r$  = radial distance from the vortex axis, and  $b$  = distance between a pair of trailing vortices

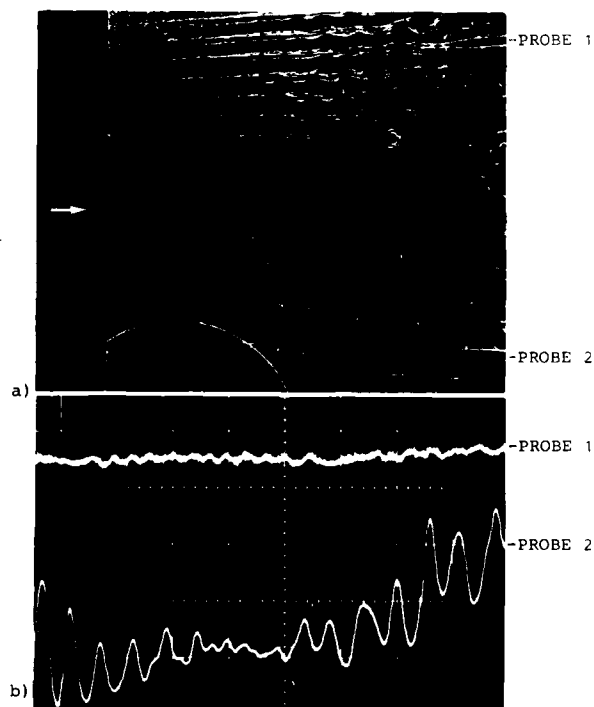


Fig. 7: Uncertainty of hot-wire measurements due to the unsteadiness of the Taylor-Görtler instabilities in the unstable laminar boundary layer along a concave wall  
a) flow pattern with hot-wire probes in streamwise zones of fast and low velocity (top-view). The hydrogen bubbles are generated continuously in contrast to Fig. 1  
b) hot-wire time signals

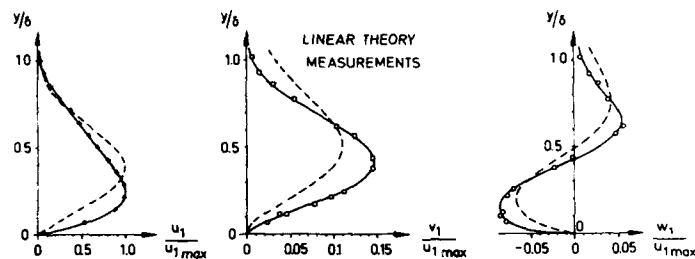


Fig. 8: Disturbance profiles in the unstable laminar boundary layer on a concave wall

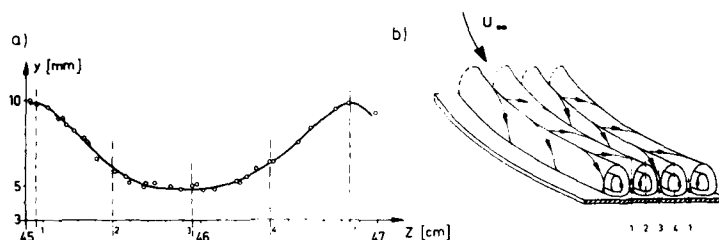
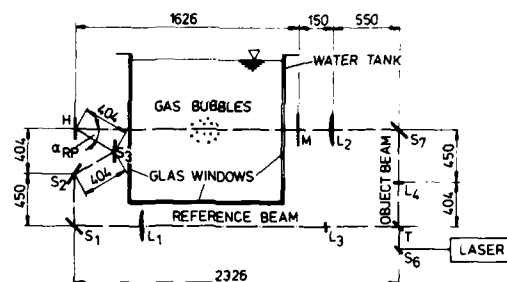
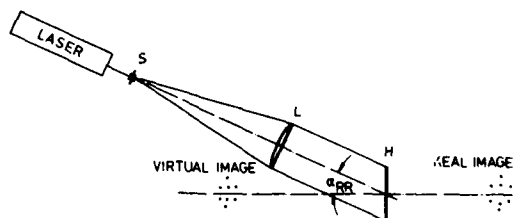


Fig. 9: a) Deformation of the time lines in Fig. 1 by Taylor-Görtler vortices.  $y$  and  $z$  are the coordinates normal to the wall and in the spanwise direction, respectively  
b) sketch of a system of Taylor-Görtler vortices



$S_6$  = DIELECTRIC MIRROR       $S_{1,2,3,7}$  = AL-MIRROR  
 $T$  = BEAM SPLITTER       $H$  = HOLOGRAPHIC PLATE  
 $L_{3,4}$  = DIVERGING LENS       $M$  = DIFFUSING SCREEN  
 $L_{1,2}$  = COLLIMATING LENS

Fig. 10: Recording arrangement of the holographic system



$H$  = HOLOGRAPHIC PLATE  
 $L$  = COLLIMATING LENS  
 $S$  = MICROSCOPIC OBJECTIVE PINHOLE DIAPHRAGM

Fig. 11: Reconstruction arrangement of the holographic system

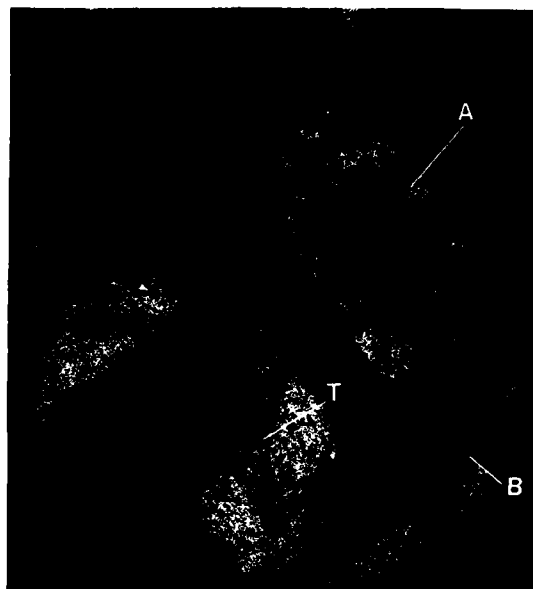


Fig. 12: Photograph of the virtual image of the reconstructed wave front. The hydrogen bubble sheet (H), the resolution target (T), and the air bubbles (A) are situated in different depths

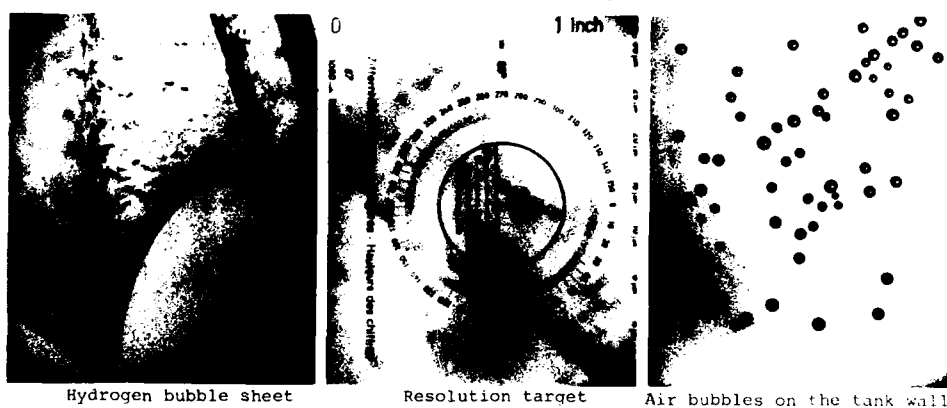


Fig. 13: Photographs of the real image of the reconstructed wave front as appearing in different depths



Fig. 14: Trailing edge vortex visualized by a continuous bubble sheet in the water towing tank, real image of streak surface generated from a straight bubble wire oriented across the vortex axis

# Flow Measurements in a Water Tunnel Using a Holocinematographic Velocimeter\*

Leonard M. Weinstein and George B. Beeler  
NASA Langley Research Center  
Hampton, VA 23665  
USA

## SUMMARY

Dual-view holographic movies were used to examine complex flows with full three-space and time resolution. This approach, which tracks the movement of small tracer particles in water, is termed a holocinematographic velocimeter (HCV). A small prototype of a new type water tunnel was used to demonstrate proof-of-concept for the HCV. After utilizing a conventional flow visualization apparatus with a laser light sheet to illuminate tracer particles to evaluate flow quality of the prototype tunnel, a simplified version of the HCV was employed to demonstrate the capabilities of the approach. Results indicate that a full-scale version of the water tunnel and a high performance version of the HCV should be able to check theoretical and numerical modeling of complex flows and examine the mechanisms operative in turbulent and vortex flow control concepts, providing an entirely unique instrument capable, for the first time, of simultaneous three-space and time measurements in turbulent flows.

## NOMENCLATURE

D	tracer particle diameter
n	index of refraction
N	number of far-field distances
Re/m	Reynolds number per meter, $U/v$
Re <sub>D</sub>	Reynolds number, $UD/v$
t	time
U	streamwise velocity
$\vec{V}$	net velocity vector of tracer particle
x	longitudinal dimension (streamwise)
y	vertical dimension
z	depth-wise dimension (focal direction)
$\nu$	kinematic viscosity
$\lambda$	wavelength of laser light

## 1. INTRODUCTION

Fluid flows with turbulence, vortices, and other time-varying three-dimensional features are still poorly understood.<sup>1</sup> The physics of these flows cannot be studied adequately since experimental data are currently limited to temporal evolution of small spatial regions. One highly promising approach to obtaining more complete experimental data for such flows is the holographic velocimeter.

Most of the previous versions of holographic velocimeters use multiple exposures on each hologram to determine tracer particle motion.<sup>2,3</sup> One version used a sequence of multiple exposures on several frames to obtain a time history of the velocity field.<sup>4</sup> For this holographic velocimeter, the frame-time-separation was large compared to the flow dynamics examined resulting in incomplete temporal resolution. All of the previous reasons, which either measured particle displacement or used interference fringe information to determine the velocity field, lacked spatial and temporal resolution. The study by Hentschel and Lauterborn,<sup>5</sup> however, described a high-speed holographic movie technique which was able to take up to 4,000 single-exposure holograms up to 300 kHz. Although this system was limited in both resolution and field of view, it allowed much higher temporal resolution than even the present HCV for limited samples. None of the previous studies addressed the data-handling problem for the high frequency case, and this limited the quantity of available reduced data.

The holographic velocimeter described in the current paper and used with a low-speed water flow facility, overcomes most of the limitations of the previous studies. Recent developments in laser technology, computer capability and mass data storage, along with a slightly different approach to determining the velocity field, makes possible a system with significantly improved capability compared to previous efforts. Moderately high-

\*Use of trademarks or names of manufacturers in this paper does not constitute an official endorsement of such products or manufacturers, either expressed or implied by the National Aeronautics and Space Administration.



speed single-frame holographic movies allow high tracer particle density and frame rates adequate to resolve turbulent flow details in low-speed water flow. Since particle locations can be measured accurately in two dimensions, but less accurately along the focal axis,<sup>6</sup> a simultaneous second view of the flow field is used to obtain equal accuracy in all three spatial dimensions. Particle locations are found with an automatic image-processing system. Particle motion, determined from successive frames in the movie, is used to obtain the velocity field. This system is called a holocinematographic velocimeter (HCV). Figure 1 provides a simple demonstration of this technique.

A new type of water tunnel has been developed for use with the HCV. With cavitation and free surface effects kept negligible, the tunnel and HCV can be used to examine the basic physics of many important flows. To demonstrate the performance of the new water tunnel design, a small prototype was built. Laser light-sheet flow visualization was used to examine the flow behind a circular cylinder at Reynolds numbers just below and just above that required to generate a von Karman vortex street. This prototype tunnel was also used with a limited-performance version of the HCV to demonstrate proof-of-concept of the HCV. Results of these tests and details of the planned full-scale water tunnel and high performance HCV system are the subject of this paper.

## 2. EXPERIMENTAL SETUP

Table 1 has a comparison of the prototype water tunnel and HCV used herein with the large water tunnel and higher speed HCV planned for the near future. In either version, a trade-off between field of view, resolution, and frame speed can be made; therefore, specifications given are nominal values only.

### 2.1 Water Tunnel

A prototype of the water tunnel was constructed to demonstrate flow performance and for proof-of-concept for the HCV. A sketch of this facility is shown in Figure 2. This is a one-fourth scale version of the facility described in Reference 7. The tunnel consists of a vertical water-filled pipe that is lowered by a hydraulic cylinder past a stationary model. The model is supported by wires, and guided by side constraints. Since this flow has no sidewall boundary layer or flow history, it has very low free-stream disturbance levels. The run time of several seconds is sufficient for operation of the HCV. Another distinct feature of this facility design is that the optical system is stationary; in tow tank testing, the moving carriage often creates a vibration problem.

The test section has a 7.5 cm square cross section and the entire tunnel is 1 meter long. The tunnel is constructed of acrylic plastic and has four optical glass windows 5 cm wide by 25 cm high that start 25 cm from the top. Linear slide bearings are used to constrain the tunnel laterally. The tunnel is supported by a hydraulic cylinder which is connected to an oil sump through an adjustable throttle valve. The sump is pressurized with air to raise the tunnel, then lowered by venting the air. A combination velocity and position transducer allows the velocity to be set to  $\pm 0.3$  mm/sec. and the height to be measured to within  $\pm 0.1$  mm. Figure 3 shows a photo of the tunnel with cameras positioned on each side.

### 2.2 Cylinder Model

The model used for the current study was a 0.6 cm diameter circular cylinder. The model support frame is mounted diagonally across the tunnel and is supported by two wires going through clearance holes in the top of the tunnel. The wires are attached to a stationary support directly above the tunnel. A cross section of the tunnel with model and support frame are shown in Figure 4; a sketch showing the model mounted on the support is also shown. A second cylinder is needed for rigidity, but is small enough and far enough downstream so as not to disturb the flow being examined. The measured flow field covers the center one-third of the tunnel and extends from the base of the cylinder model downstream to approximately 3 cm. The flow velocity was adjusted such that flow with and without von Karman vortex streets could be examined.

### 2.3 Tracer Particles

Small hollow glass spheres about 40  $\mu$  in diameter were used to trace the flow. These particles were flotation separated to obtain uniform size. The particles had a specific gravity of about 0.4, a rise rate of nearly 0.1 cm/sec. Since the motion of the tunnel was vertical, the particle rise rate can simply be subtracted from the model velocity to obtain the correct local flow velocity. The tracer particles were injected at the top of the tunnel, then pulled down and dispersed with a pump, which draws water from the bottom of the tunnel and injects it at the top. Recirculating the water also eliminated thermal

gradients. When the pump was shut off, flow currents damped within a few minutes, and then a run was made.

The size of the tracer particles used resulted from a compromise between image quality and spacing required. In Reference 8, the recommendation was made for far-field in-line holograms that the particles should be kept at or below 80 far-field distances ( $N$ ), where:  $Z = ND^2/\lambda$ . For the present case,  $\lambda = .50 \mu$ ,  $N = 80$ ,  $Z = 22 \text{ cm}$  and  $D = 40 \mu$ . The tracer spacing was further limited by the total projected area blockage. For the present case, a 1 mm spacing through the tunnel would result in about 10 percent area blockage, which was near the maximum usable.<sup>9</sup>

#### 2.4 Laser Light Sheet

Flow visualization, using a laser light sheet to illuminate the tracer particles, was used to evaluate the tunnel flow quality. A 25 mw cw beam with  $\lambda = .51 \mu$  was obtained from an air cooled argon ion laser. The setup shown in Figure 5 used a 3 mm glass rod to obtain a vertical light sheet. The light sheet entered the tunnel normal to the wall and thus cut the cylinder model and flow at  $45^\circ$  (due to the model being mounted diagonally). A video camera with close-up lens was positioned perpendicular to the light sheet. The video camera provided 60 partial frames (30 full frames) per second which were recorded on a VCR. The video record was enhanced to improve sharpness and contrast. Polaroid photographs were made from the enhanced images to show the flow. The streak length (due to finite exposure and camera persistence) indicated the velocity for each tracer particle.

#### 2.5 Holographic Camera

A simplified version of the HCV described in Reference 7 was used for proof-of-concept tests. Two orthogonal in-line holographic cameras were used with the set up shown in Figure 6. The same argon ion laser (25 mw at  $\lambda = 0.51 \mu$ ) was used for this system as for the laser light sheet study. The laser beam passed through a motor driven chopper disk with a single slot 3 mm wide. The beam was chopped at a radius of 10 cm, with the motor running at 900 rpm (15/sec); this resulted in an exposure of 1/2 ms. An opto-interruptor set at the edge of the disk was used to advance the 35 mm flight research pin registration cameras between exposures. The cameras held the film stationary during the exposure. The only motion during an exposure was due to tunnel flow, and for the low tunnel speeds used here ( $< 2 \text{ cm/sec}$ ) resulted in  $< 10 \mu$  image smear, which was not believed to be significant for the present study.

Kodak LPF-4 film was used in the present study. This film requires about 10 ergs/cm<sup>2</sup> to obtain good holograms. The resolution is about 800  $\ell/\text{mm}$ , but in-line holograms have far lower resolution requirements than large angle reference beam holograms. Thus, acceptable holograms were obtained for the current study.

#### 2.6 Holographic Reconstruction

The reconstruction setup is shown in Figure 7. A He-Ne laser was used for the current study. The laser beam was collimated to 5 cm diameter. The difference in reconstruction wavelength (632 nm) compared to recording wavelength (514 nm) only changed length scale of the optical axis. Since the index of refraction of water also change length scale of the optical axis, the two effects were combined in a single length scale. The measured particle optical axis locations were corrected by multiplying by  $\frac{633}{514} \times n$ , where  $n = 1.333$  for water at  $22^\circ\text{C}$ .

The developed roll of holographic movie film was placed in a computer-controlled film advance, which positioned each successive hologram and then clamped a glass cover down to keep the film stationary. This resulted in a real image of the tracer particles about 15 cm beyond the film. A precision three-axis positioner moved a video camera to image the field of view in small sections to obtain the desired positional accuracy. A microscope objective mounted on an adaptor tube imaged approximately a 2 mm square area at a time. The image quality of reconstructed holograms of the particle fields tended to be poor due to speckle and images of out of focus particles, therefore a spatial filter was used to improve image quality. The filter with an adjustable holder is illustrated in the sketch in Figure 8. A band-pass filter was selected to remove high frequency noise and also to enhance particle contrast.

The hologram was examined in small area sections as previously mentioned, and also in 1 mm steps along the focal axis. Each video image was digitized and reduced by an image analysis system which detected the particle edges to determine the particle centroid coordinate. Brightness level and size criterion were used to separate particle images

from the noise remaining after spatial filtering. Details of the data reduction tasks and procedures are given in Reference 7.

### 3. RESULTS AND DISCUSSION

#### 3.1 Laser Light Sheet

The flow directly behind the circular cylinder model was examined at two flow speeds. Results of the laser light-sheet flow visualization are shown in Figure 9. In the top photo,  $U_{\infty} = 0.6$  cm/sec, which resulted in  $Re_D = 30$ . This was below the eddy shedding velocity, although a separated region did extend nearly one cylinder diameter downstream. The left photo is a 1/60 sec exposure (1 video frame) while the right photo is a 1/8 sec exposure. The total field of view is approximately 2 cm square. Even the shorter exposure had image smear due to Videcon persistence corresponding to several video frames. With the exposure of 1/8 sec, ( $\approx 7$  frames) the velocity field was more clearly defined. The lower two photos were made at  $U_{\infty} = 2$  cm/sec which corresponded to  $Re_D = 100$ . Again 1 video frame and 7 video frames are shown. Again the flow is much more clearly defined for the longer exposure. The eddy shedding was time dependent, and had a period of approximately 1.3 sec for  $U_{\infty} = 2$  cm/sec. If longer than 1/8 sec exposures were used, the detail was smeared by variation in the pattern, hence a compromise between streak length and pattern change had to be attained. The  $Re_D$  at which eddy shedding started was found from other runs to be between 40 and 50, which is in good agreement with the literature. The flow quality was obviously very good even at these very low speeds, and it should be even better at the higher speed planned for the larger scale facility. Once the mixing currents have completely damped, the only disturbances in the flow were due to the impulse start (which disappear in just over 5 length-scale time constants) and model guide accuracy (which can be controlled to desired tolerances).

Discreet tracer particles, which show up as sharp individual lines of finite length, allowed streamlines rather than streak lines to be observed. Use of dye visualization for the same flow would have shown loops of flow created in the near-base region of the cylinder which remain as loops as they convect further downstream. Laser light-sheet visualization of particles can thus be used to obtain quantitative velocity field information, but is restricted to a two-dimensional slice. An example of other uses of this technique was shown in Reference 10.

#### 3.2 Holographic Velocimeter

Proof-of-concept thus far has focused on obtaining holographic movies of the flow examined by the laser light sheet, and reducing the holograms to a set of particle coordinates. The flow structures observed in Figure 9 were  $> 0.4$  cm in diameter with a simple structure. This allowed a larger particle spacing for the HCV than the minimum possible. For the present case, a mean spacing of just under 2 mm was selected. This results in fewer particles and simplified data reduction.

Dual view holographic movies were made at 15 frames/sec for  $U_{\infty} = 2$  cm/sec. The time steps corresponded to 1.33 mm movement in the mean flow per frame, which gave temporal resolution slightly better than spatial resolution. Since movement was slightly less than the mean spacing, tracking of the particles from frame to frame was possible. The reversed flow region just behind the cylinder also exhibited lower speeds than the mean flow, hence tracking was still possible as long as a frame to frame movement was less than one-half the particle spacing. To reduce the particle coordinates to a common frame of reference for the two views, a short strip of exposure was made before the tunnel run with a small pointed tube penetrating into the common field of view. The pointed tip of the tube was used to initialize the coordinate system so that all results were referenced to a known common origin. The reference tube was removed before the run began.

A data run lasting about 10 sec. was made. This would cover several cycles of eddy shedding. After the data run, the film was processed and loaded into the reconstruction optical setup. A typical video frame from the reconstructed image is shown in Figure 10. The image quality without the spatial filter is shown for comparison at the left side of the figure. The image has a lot of speckle and fringe noise, and particle images are not smooth. The automatic data reduction system had difficulty finding all of the particles and registered false readings. When the band pass spatial filter was used the image looked like the right side photograph. Sharply focused particles appeared as smooth round easily-seen images. As the particle went out of focus, it got larger (but dimmer) and developed a diffused region around it. Even more out of focus, and only a few small blobs remained. The use of brightness and size thresholds allowed only fairly sharply-focused particles of the correct size to be reduced. Good agreement between the automatic data reduction system and operator judgement was obtained, and proof-of-concept was therefore demonstrated to this point.

### 3.3 Planned Efforts for the HCV

Both views of the data from the phototype system will be reduced to a magnetic tape record of particle coordinates. The merge and track procedures described in Reference 7 will be used to generate a velocity data base. This data will then be compared to the laser light sheet, and also examined for any three-dimensionality. If all procedures work correctly, the full-scale water tunnel and high-speed version of the HCV will be started.

## 4. CONCLUSIONS

A dual view holographic movie technique has been developed to study complex flows with three-space and time resolution. A prototype of a new type water tunnel was developed for use in evaluating the holographic movie technique as well as the conventional laser light-sheet flow visualization. Results of the effort include:

1. The water tunnel was demonstrated by examining the flow behind a circular cylinder. Conventional laser-light sheet visualization showed good flow quality, even at very low speeds.
2. The HCV prototype system was demonstrated for a 15 frame/sec movie rate.
3. Use of a band pass spatial filter to improve holographic image quality resulted in a clear, easy to reduce data image.

When the larger water tunnel and higher speed version of HCV are completed, the system should be able to check theoretical modeling of complex flows and examine the mechanisms operative in turbulent and vortex flow control concepts.

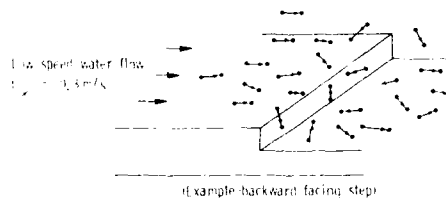
## 5. REFERENCES

1. Bushnell, M. D.: Turbulent Drag Reduction for External Flows. Paper No. AIAA 83-0227, 1983.
2. Trolinger, J. D.; Belz, R. A.; and Farmer, W. M.: Holographic Techniques for the Study of Dynamic Particle Fields. AEDC TR-68-215, Nov. 1968.
3. Trolinger, J. D.; and O'Hare, J. E.: Aerodynamic Holography. AEDC-TR-70-44, August 1970.
4. Belz, R. A.; and Menzel, R. W.: Particle Field Holography at Arnold Engineering Development Center. Optical Engineering, Vol. 18, No. 3, June 1979, pp. 256-265.
5. Hentschel, W.; and Lauterborn, W.: High Speed Holographic Movie Camera. SPIE, Vol. 491, August 1984.
6. Shofner, F. M.; Webb, R. O.; Menzel, R. W.; and Heifner, R. L.: Optical Processors for Holographic Velocimetry Data. AFFDL-TR-69-100, Feb. 1970.
7. Weinstein, L. M.; Beeler, G. B.; and Lindemann, A. M.: High-Speed Holocinematographic Velocimeter for Studying Turbulent Flow Control Physics. AIAA Shear Flow Control Conference, March 12-14, 1985, Boulder, Colorado. Paper No. AIAA 85-0526.
8. Malyak, P.; and Thompson, B. J.: In-Line Far-Field Holographic Velocimetry. Under Grant No. NAG-1-312 for NASA Langley Research Center, November 1983.
9. Trolinger, J. D.: Particle Field Diagnostics by Holography. AIAA 18th Aerospace Sciences Meeting, Pasadena, CA, January 1980. Paper No. AIAA 80-0018.
10. Coutanceau, M.; and Texier, A.: Experimental Investigation of the Creeping Motion of a Drop in a Vertical Tube. Experiments in Fluids, Vol. 4, No. 5, pp. 241-246, 1986.

Table 1

## Comparison of Prototype HCV System to Planned HCV System

	Prototype HCV	Planned HCV
Cross Section of Tunnel	7.5 x 7.5 cm	25 x 25 cm
Length of Tunnel	1 m	4 m
Maximum Flow Speed	0.1 m/s	1 m/s
Water Temperature	20°C	20-60°C
Maximum Reynolds No. per Meter	$1.1 \times 10^5$	$2.2 \times 10^6$
Type Laser Used	Argon Ion	Copper vapor
Laser Pulse Rate	(chopped) 15 pps	7,000 pps
Laser Pulse Duration	0.5 ms	30 ns
Film Exposure Rate	15 fr/sec	700 fr/sec
Camera Used	35mm pin registration framing camera (Flight Research)	35mm continuous film transport (Hytax)
Field of View	2 cm x 3 cm	2.5 cm x 4 cm



- Make holographic movie of 3-d flow with tracer particles
- First in each sequential pair of frames  $\rightarrow X, Y, Z$  at  $t$
- Second in pair is located  $\rightarrow \Delta X, \Delta Y, \Delta Z$  at  $\Delta t$
- Data reduction for entire movie yields (in real time)  $V(X, Y, Z, t)$

Fig. 1. - The determination of time-varying velocity fields with HCV.

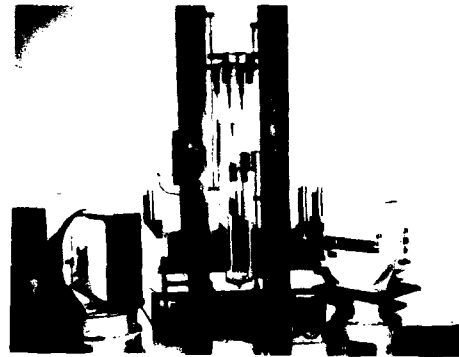


Fig. 3. - Photo of prototype vertical water tunnel.

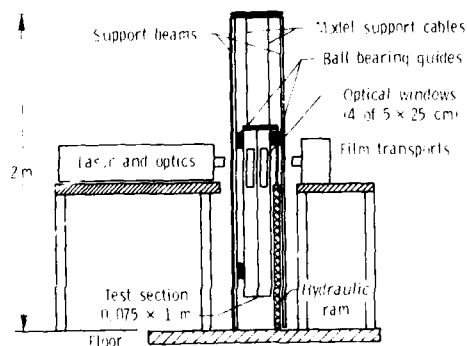


Fig. 2. - Prototype vertical water tunnel.

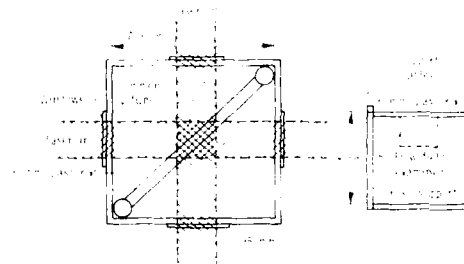


Fig. 4. - Details of tunnel cross section and model.

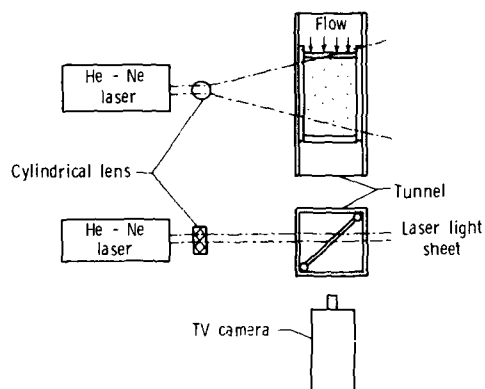


Fig. 5. - Laser light-sheet flow visualization setup.

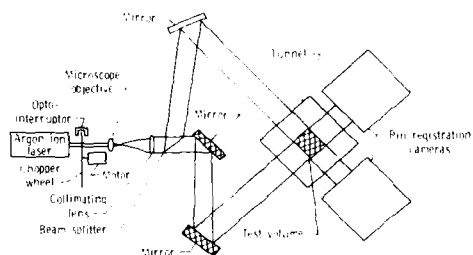
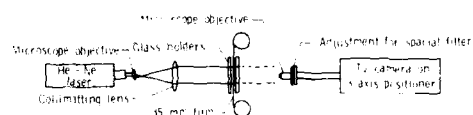
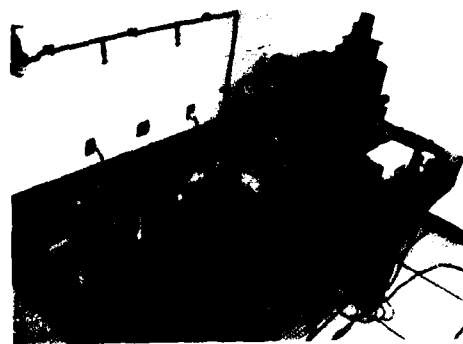


Fig. 6. - Dual view holographic camera.



(a) Optical reconstruction setup.



(b) Photo of setup.

Fig. 7. - Reconstruction optical setup.

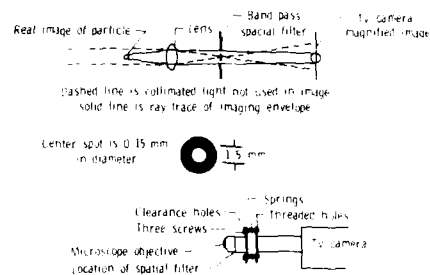


Fig. 8. - Spatial filter for image improvement.

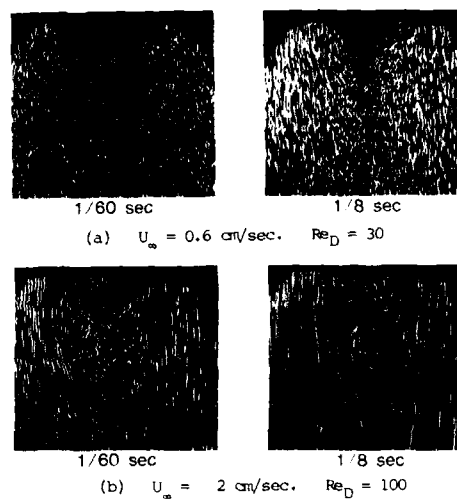


Fig. 9. - Laser light-sheet visualization behind 0.6 cm circular cylinder.

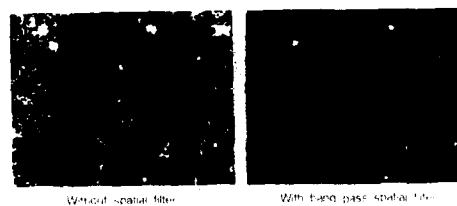


Fig. 10. - Particle images from PKV of flow behind 0.6 cm cylinder.  $U_{\infty} = 2$  cm/sec.

## ETUDE EXPERIMENTALE DE NAPPES TOURBILLONNAIRES EN ECOULEMENT PLAN

par Christian BERGER, Magali BOURGEOIS, Gérard LAVERGNE, Christine LEMPEREUR,  
Jean-Michel MATHE

OFFICE NATIONAL D'ETUDES ET DE RECHERCHES AEROSPATIALES

CENTRE D'ETUDES ET DE RECHERCHES DE TOULOUSE

Département d'Etudes en Mécanique et Energétique des Systèmes (DERMES)

2, Avenue Edouard Belin. 31055 TOULOUSE CEDEX

FRANCE

RESUME :

Dans le but d'une étude expérimentale des instabilités de cisaillement en écoulement laminaire, un canal hydraulique vertical a été réalisé de façon à générer une confluence de deux écoulements bidimensionnels à vitesses différentes. Cette étude consiste à caractériser les instabilités se développant en aval du culot droit à partir de relevés de profils de vitesse par anémométrie laser et de différentes techniques de visualisations et de traitement d'images. Le nombre de Reynolds calculé sur la largeur du culot et la moyenne des deux vitesses est inférieur à 600. La modélisation de ce type d'écoulement à l'aide de nappes tourbillonnaires émises aux extrémités du culot permet la restitution de lignes d'émission comparables à celles observées sur l'expérience.

I - INTRODUCTION

La couche cisaillée est un des écoulements fondamentaux dont la description sert de base à des modèles de turbulence et à la compréhension des mécanismes d'instabilité. L'étude qui en est faite ici, s'appuie essentiellement sur une analyse quantitative par visualisations couplée à des techniques anémométriques classiques. L'interprétation s'effectue en associant aux valeurs instantanées les configurations correspondantes de l'écoulement. Les essais sont réalisés en tunnel hydrodynamique à nombre de Reynolds modéré où les instabilités, à la frontière du laminaire et de la turbulence, sont suffisamment propres pour une observation directe et lentes pour permettre un traitement en temps réel par des moyens vidéo classiques. L'intérêt d'une telle approche est, d'une part de transformer en s'aidant de la microinformatique, les techniques de visualisation en instruments de mesures, et d'autre part de fournir directement aux numériciens des bases de données autres que le champ de vitesses.

L'identification d'un calcul numérique par le champ de vitesses ou de pression reste délicate pour les écoulements turbulents tant que les modèles nécessitent une fermeture dont la généralité n'est pas assurée.

Les logiciels dont dispose le numéricien permettent maintenant des représentations graphiques en couleur et en variables Lagrangiennes dont l'interprétation est plus rapide qu'un listing et qui rapprochent les simulations numériques des observations expérimentales. L'étude présentée dans cet article qui comprend trois parties principales (visualisations, mesures, calculs) décrit une instabilité quasi bidimensionnelle derrière une plaque plane d'épaisseur non négligeable dont le sillage propre vient interférer avec la couche de mélange. En liaison avec les numériciens de la turbulence, une étude a été faite sur l'influence d'une préturbulence de grille sur le développement de l'instabilité (Réf. 1).

II - MOYENS D'ESSAISII.1. Canal hydrodynamique

L'installation a été spécialement réalisée pour générer une confluence d'écoulements bidimensionnels. L'ensemble de l'installation présentée sur la figure 1 se compose de :

- Deux réservoirs d'alimentation de  $1m^3$  chacun munis de différents trop-pleins qui assurent la régulation en charge.
- La chambre de tranquillisation équipée de filtres et grilles et le convergent sont divisés par une cloison étanche qui vient affleurer à l'entrée de la veine d'essais.
- Une veine d'essais en plexiglass de section d'entrée 20 cm x 30 cm et de sortie 22 cm x 30 cm pour une hauteur utile de 1 m. Ce canal est légèrement prismatique pour atténuer les effets de couches limites sur les faces latérales. L'extrémité de la cloison de séparation est aménagée pour recevoir différentes formes de culot (culot rectangulaire, culot droit, culot évidé...).

Les conduites d'alimentation de la chambre de tranquillisation sont équipées de débitmètres et de vannes. Un circuit d'asservissement permet d'afficher le rapport de vitesses désiré. Les performances de l'installation autorisent une vitesse maximum de 7 cm/s. Le nombre de Reynolds calculé sur la largeur du culot et la moyenne des vitesses reste inférieur à 600.

La qualification de la veine d'essais par sondage L.D.A. a permis de vérifier l'uniformité du profil de vitesses avant l'implantation de la cloison de séparation.

II.2. Moyens de visualisations

Les visualisations sont effectuées à partir de différents traceurs :

- injection de colorant : soit localement par filets colorés, soit globalement en colorant l'un des écoulements.
  - injection de particules de polystyrène non expansées de densité voisine de celle de l'eau qui peuvent être introduites une à une par un injecteur ou en amont, par paquets, de façon à les répartir dans l'écoulement.
  - génération de bulles d'hydrogène : les bulles d'hydrogène sont produites par un fil de nickel (cathode) tandis qu'une plaque de cuivre placée en fond de cuve constitue l'anode.
- L'application d'une tension continue permet l'électrolyse de l'eau et la production de bulles d'hydrogène.

Ces traceurs sont éclairés par une tranche lumineuse placée transversalement à l'écoulement.

Les traceurs sont choisis en fonction de l'analyse recherchée. Les particules sont utilisées pour une étude Lagrangienne permettant de calculer les vitesses locales. Les colorants liquides forment des lignes continues qui matérialisent des lignes particulières de l'écoulement (lignes d'émission, interfaces, etc.).

### II.3. Moyens d'acquisition

Les systèmes d'acquisition et de traitement d'images ont été développés au département et sont présentés en détail dans la référence (2). Ils se composent essentiellement de : (Fig. 2)

- un capteur optique : magnétoscope, caméra vidéo ou matricielle de type C.C.D de résolution 488 par 384,
- une interface permettant le suivi de particules ou l'extraction de contours,
- un microcalculateur BFM 186 organisé autour d'un microprocesseur 8086 associé à un processeur arithmétique 8087.

Le système de trajectographie a pour fonction d'acquérir la position de traceurs particulières à chaque instant. Ces particules diffusent la lumière incidente et apparaissent comme des taches brillantes facilement détectables par un dispositif à seuil. Les positions des particules sont acquises à la fréquence de la caméra (50 ou 60 Hz) puis sauvegardées sur mémoire de masse. La durée d'un essai peut atteindre plusieurs milliers de trames. Le système d'extraction de contours réalise l'acquisition d'images codées sur 1 à 4 bits avec une définition de 256 x 256 éléments d'images. La numérisation et la sauvegarde dans la mémoire centrale du calculateur ont lieu en temps réel vidéo (ici à la fréquence de 50 Hz) permettant d'acquérir en continu plusieurs trames successives.

#### II.3.1. Acquisition de trajectoires

Des logiciels de traitement restituent en temps différé les trajectoires des particules et les vitesses ou accélérations correspondantes. Un lissage récursif à nombre de points variable peut éventuellement être effectué sur ces trajectoires. La présence de trois trajectoires suffisamment proches permet une évaluation à chaque instant du rotationnel moyenné sur le triangle formé par ces particules.

#### II.3.2. Extraction de contours

Le signal vidéo est envoyé sur une interface qui analyse les gradients de luminance suivant huit directions autour de chaque pixel. On mémorise ainsi le numéro de la trame (temps), les coordonnées de l'origine du contour et les valeurs des vecteurs directionnels qui le définissent. A partir de l'acquisition brute du contour, des logiciels permettent d'améliorer la restitution du contour (lissage, continuité de la ligne,...) (Figure 3)

### III - DESCRIPTION DE L'ÉCOULEMENT

Les résultats présentés dans cet article concernent la configuration avec le culot droit qui s'est avérée la plus intéressante du point de vue de la stabilité. Ce type d'écoulement représente un équilibre entre l'effet de sillage et l'effet de cisaillement. Les visualisations ont fait apparaître deux structurations différentes de l'écoulement (Fig. 4, 5).

Pour des vitesses voisines, le sillage domine et on observe la configuration caractéristique en tourbillons alternés. Pour des rapports de vitesses plus élevés, le cisaillement impose une seule allée tourbillonnaire qui caractérise la couche de mélange. Cet écoulement est à rapprocher de l'écoulement cisaillé pur rencontré derrière une plaque mince. Un rapport de vitesse critique de 1,5 a mis en évidence une bifurcation différenciant très nettement les deux régimes. Les figures 4 et 5 illustrent cette différence de structuration.

### IV - CARACTÉRISATION DE LA ZONE DE MÉLANGE

L'évolution d'une couche de mélange se développant derrière une plaque mince est généralement linéaire. Ce résultat est d'ailleurs confirmé par les théories analytiques de couches limites (Réf. 3) qui permettent de relier le taux d'expansion de la zone de mélange au rapport de vitesses. Dans le régime à deux nappes la superposition des contours à différents instants donne une enveloppe que l'on a cherchée à comparer au sillage déterminé par les relevés de vitesses (méthodes classiques).

L'extraction de contours montre de façon évidente la périodicité du phénomène. Un des problèmes importants des modélisations en écoulement turbulent est la liaison entre le mécanisme de diffusion (dispersion statistique) et la convection. Ainsi le problème de la liaison entre la périodicité spatiale et temporelle est une question importante de l'instabilité laminaire (Réf. 4).

L'aspect périodique dans l'espace est directement observable mais il est important dans cette analyse de préciser l'évolution de la période spatiale. Trois techniques différentes ont été confrontées pour indiquer l'évolution de cette période :

- par film chaud
- par colorimétrie (Réf. 5). Variation de la luminance moyenne dans une fenêtre d'analyse
- par extraction de contours.

Ces trois techniques indiquent une division du sillage en deux ou trois zones (Fig. 6) :

- une zone de formation proche du culot
- une zone correspondant à l'enroulement des tourbillons (zone principalement étudiée)
- une région où la diffusion est terminée et seule la convection d'ensemble réside (tourbillons fossiles ou formes passives)
- cinématique de la zone de mélange.

Les techniques de visualisation décrites dans le paragraphe précédent fournissent une restitution à partir des acquisitions des trajectoires ou des lignes particulières qui permettent une étude de



la cinématique des grosses structures. En particulier, la régularité des formes observées autorise, non seulement le calcul des vitesses mais aussi les rayons et centres de courbure instantanés. La figure 7 montre des centres de courbure calculés à partir de l'interface directrice. Ce dépouillement ne peut être transposé en écoulement tridimensionnel turbulent. Le filtrage de ces acquisitions (centre de courbure unique) peut servir de comparaison directe à une méthode numérique. Dans ce contexte la comparaison avec des modèles macroscopiques permet la validation de calculs des grosses échelles.

Des exemples de trajectoires sont présentés sur les figures 8 et 9 pour les deux cas d'écoulement. Une évaluation du rotationnel moyen peut être effectuée à partir du suivi de trois particules voisines formant un triangle pendant plusieurs trames successives. Un exemple de résultat est indiqué sur la figure 10. Cette technique peut être appliquée à l'ensemble de l'écoulement et peut permettre de déterminer les limites de l'écoulement irrotationnel.

L'enregistrement successif de plusieurs trajectoires permet la restitution à posteriori de champ de vitesse moyenné en phase si l'acquisition est effectuée avec une référence de temps liée à l'écoulement. Ce repérage de phase est ici donné par un signal lumineux délivré par une diode couplée à un film chaud situé dans le sillage, proche du culot. La fluctuation sinusoïdale de la vitesse mesurée par le film chaud conditionne l'éclairage de la diode. Périodiquement ce signal lumineux est acquis en même temps que les particules. A partir de ce repérage de phase, il est ensuite aisé d'effectuer un dépouillement et de restituer des champs de vitesses instantanées.

Des exemples de champs obtenus à différents instants dans le cas du régime à une nappe sont présentés sur la figure 11.

Un très grand nombre d'acquisition de trajectoires est nécessaire pour obtenir un champ de vitesses avec une bonne résolution.

A partir de l'acquisition brute du contour de l'interface obtenu par coloration de l'un des deux écoulements, des logiciels permettent d'une part, un prétraitement et, d'autre part, la détermination de paramètres géométriques (calcul des coordonnées  $x, y$ , détermination des centres de rotation, forme de l'enveloppe moyenne de l'interface). (Figure 12). L'erreur commise lors de l'acquisition est de l'ordre du pel.

L'interface reproduite est légèrement "tronquée" au niveau de l'enroulement le plus prononcé, ceci est dû à une légère diffusion du colorant.

Calcul du champ de vitesses à partir de l'interface.

Les interfaces numérisées peuvent être sensiblement superposables en les décalant de la vitesse moyenne de convection. Cette observation permet de considérer l'interface comme une ligne de glissement. L'interface est discrétisée en segments tourbillonnaires dont les intensités sont calculées à partir de l'hypothèse précédente. Ce type de calcul fournit une estimation du champ de vitesses instantanées. (Fig. 13), le champ moyen est obtenu par superposition de plusieurs champs de déformation. (Fig. 14).

#### V - SIMULATION NUMERIQUE DE L'ÉCOULEMENT

On définit un domaine de calcul limité par les parois de la veine, une portion du culot et les sections d'entrée et de sortie de l'écoulement. La section d'entrée est à 5 cm en amont du bord de fuite du culot, la section de sortie est à 25 cm en aval.

La frontière est discrétisée en segments :

- 10 segments sur les parois de la veine
- 6 segments pour chaque section d'entrée
- 9 segments pour représenter le culot.

Chaque segment est porteur d'une singularité de type source ou puits, d'intensité constante. Sur les parois solides, on impose la condition d'imperméabilité  $V_n = 0$  et sur les sections d'entrée la vitesse correspondant au rapport de fonctionnement choisi. Les intensités inconnues  $X$  vérifient une équation linéaire de la forme  $A.X = B$  où  $A$  représente la matrice des coefficients d'influence mutuels et  $B$  le vecteur colonne des vitesses normales. Ce système est résolu à l'instant initial pour calculer l'écoulement potentiel qui constitue la première étape pour le développement du calcul.

A l'instant  $t = 0$ , on injecte des singularités de type tourbillon en deux points situés de part et d'autre du culot. Ces points sont légèrement décalés des parois pour tenir compte des couches limites sur la cloison de séparation. (Fig. 15).

L'injection se fait alternativement d'un point à l'autre avec des signes opposés, à une fréquence correspondant à celle de l'instabilité. L'intensité des tourbillons est imposée suivant les valeurs des vitesses d'entrée. Sur chaque période, l'intensité varie à chaque pas de temps, suivant une loi exponentielle de la forme  $\Gamma = \Gamma_0 \exp(-t/\tau)$  où  $\Gamma_0$  représente l'amplitude et  $\tau$  la constante d'amortissement. Une ligne d'émission est calculée en injectant sur l'axe de symétrie (ou en tout autre point de l'écoulement) un marqueur passif dont il suffit de suivre l'évolution. La figure 16 représente un exemple de ligne d'émission pour le régime à deux nappes.

#### VI - INFLUENCE D'UNE PRÉTURBULENCE

On étudie dans ce paragraphe l'influence d'une prétrouble sur la formation et le développement des instabilités. La turbulence est générée par une grille du côté de la vitesse la plus faible et située à 3,5 cm en amont du culot.

La turbulence devient homogène et isotrope au delà d'une distance de l'ordre de 40 à 50 fois la dimension de la maille. Le niveau de turbulence décroît en fonction de la distance aval selon une loi de la forme (Réf. 6)

$$\frac{U'}{U} = K_1 + K_2 \frac{X}{M}$$

avec U module de la vitesse  
 U' fluctuation de la vitesse  
 X abscisse à partir de la grille  
 M dimension de la maille  
 K<sub>1</sub>, K<sub>2</sub> constantes

Trois grilles métalliques à mailles carrées et à fils ronds sont utilisées :

G1	M = 1 mm	D <sub>f</sub> = 0.5 mm
G2	M = 3.5 mm	D <sub>f</sub> = 0.75 mm
G3	M = 5 mm	D <sub>f</sub> = 1.3 mm

En colorant un des deux écoulements en présence de la grille, on peut visualiser la formation et le développement des instabilités qui restent bien observables comme dans le cas sans grille. Mais, pour une même vitesse moyenne, le rapport de vitesse critique séparant les deux régimes est d'autant plus faible que la maille de la grille est petite, comme l'indique le tableau ci-dessous.

	Sans grille	G3	G2	G1
$\frac{V1}{V2}$	1.4	1.26	1.23	1.13

Pour préciser l'influence de la grille sur la zone de mélange, des spectres d'amplitude de vitesses ont été établis dans différentes sections de l'écoulement. La figure 17 montre un spectre obtenu dans la section du culot, à 10 mm de l'axe de symétrie. On observe une raie basse fréquence ( $f = 0.6$  Hz) correspondant au fondamental du détachement tourbillonnaire. Son amplitude décroît lorsqu'on s'éloigne du culot. On retrouve dans le spectre, au delà du fondamental, l'influence de la grille autour de 12 Hz qui reste la même dans toute section.

La vitesse de l'écoulement décomposée sous la forme  $u = \bar{u} + \tilde{u} + u'$  avec  $\bar{u}$  vitesse moyenne,  $\tilde{u}$  vitesse moyenne cohérente,  $u'$  fluctuation, peut être observée sur les spectres de sillage et hors sillage. La figure 18 montre la comparaison avec et sans grille faisant apparaître le remplissage du spectre et l'émergence de la raie fondamentale.

Le tableau ci-dessous résume l'influence de la maille sur l'amplitude du fondamental

	Sans grille	G3	G2	G1
$u'$				
(mm/s)	0.425	0.380	0.35	0.17

On remarquera que malgré la faible influence de la grille sur la qualité des visualisations que l'on peut effectuer, la présence de la grille modifie les mécanismes fins de l'écoulement dans la zone de mélange et qu'il s'avère nécessaire de compléter le dépouillement macroscopique par une analyse au film chaud pour explorer l'écoulement.

#### VII - CONCLUSION

Cette étude a montré la possibilité d'analyser, par techniques vidéo banalisées, la structure instantanée d'un écoulement instationnaire lent. L'écoulement analysé ici, une couche de mélange bidimensionnelle, a pu être observé par les techniques de visualisation classiques et le dépouillement des évolutions de forme a permis une bonne comparaison avec les techniques classiques par anémométrie et a conduit à une modélisation simple des instabilités de cisaillement. Ces études effectuées en écoulement laminaire bidimensionnelles sont actuellement étendues aux cas turbulents et tridimensionnels.

#### REFERENCES

- 1 - Etude expérimentale et modélisation de couche de cisaillement  
Rapport CERT n° 2209.00. Mars 1985
- 2 - LEMPEREUR, MATHE  
Application de techniques d'acquisition et de traitement d'images à l'étude des instabilités de nappes tourbillonnaires en cuve hydraulique  
Colloque de visualisations Nancy. Janvier 1985.
- 3 - ABRAMOVITCH  
The theory of turbulent jets. Pergamon Press.
- 4 - GASTER M.  
A note on the relation between temporality increasing and spatially increasing disturbances in hydrodynamic stability. J. Fluid. Mech. n° 14, 1962, P. 222 - 224.
- 5 - TOULOUSE G.  
Electroniques et traitement d'images. Rapport CERT 1980.
- 6 - COMTE BELLOT, CORSIN  
The use of a contraction to improve the isotropy of grid generated turbulence. J. Fluid Mech. 1965.

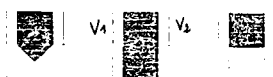
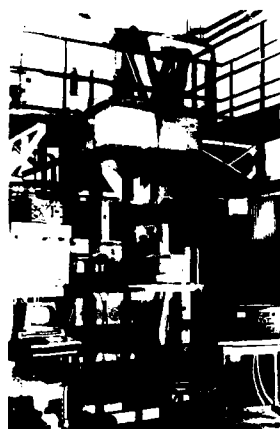


Fig. 1 Vue générale de l'installation avec différents types de culots étudiés.

CAPTEUR OPTIQUE (CAMERA OU MAGNETOSCOPE)

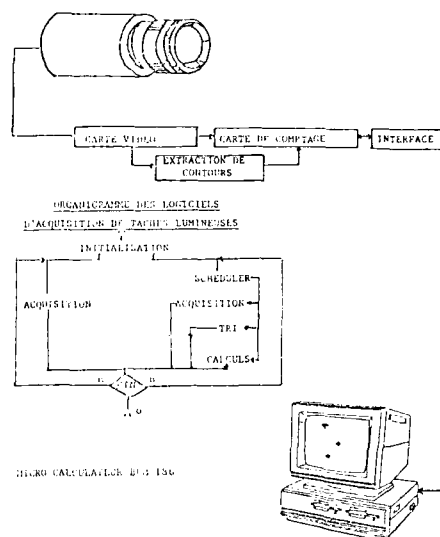


Fig. 2 Système d'acquisition.



Fig. 3 Acquisition brute de contours.



Fig. 4 Régime à une nappe.



Fig. 5 Régime à deux nappes.

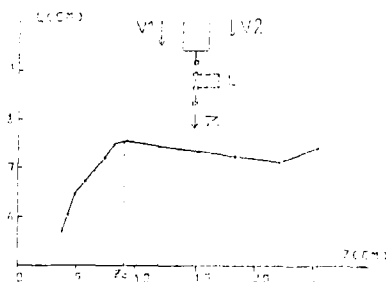


Fig. 6 Période spatiale, régime à une nappe  
 $\frac{V1}{V2} = 2.2$  (culot rectangulaire)



Fig. 7 Exemples de calcul de centre de courbure.

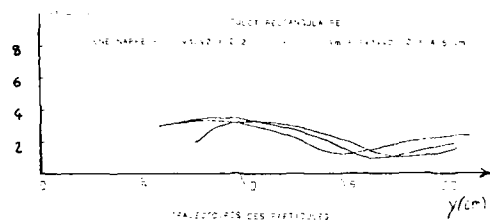
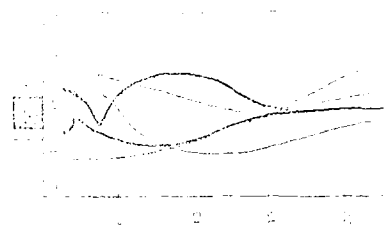
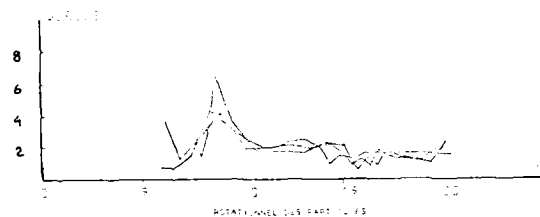
Fig. 8 Exemples de trajectoires  
(Régime à une nappe).Fig. 9 Exemples de trajectoires  
(Régime à deux nappes).

Fig. 10 Calcul du rotationnel.

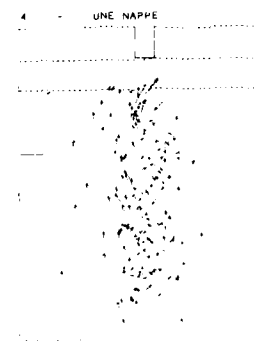
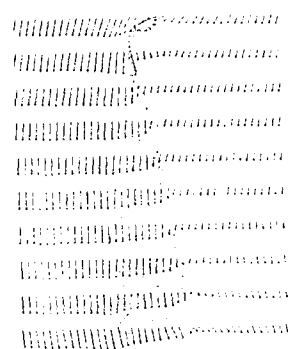
Fig. 11 Restitution du champ instantané  
de vitesses.

Fig. 12 Acquisition des interfaces.

Fig. 13 Restitution du champ instantané  
à partir de l'interface.  
(Une nappe)Fig. 14 Restitution du champ moyen de vitesse  
à partir de l'interface.

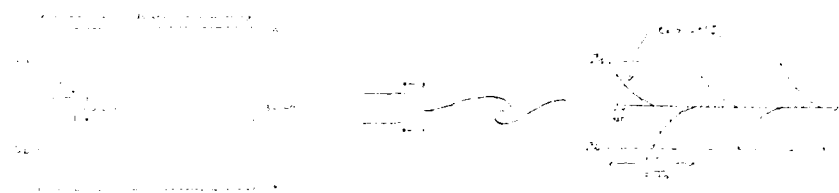
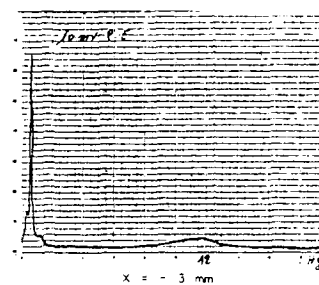
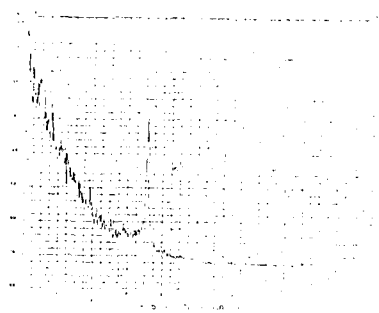
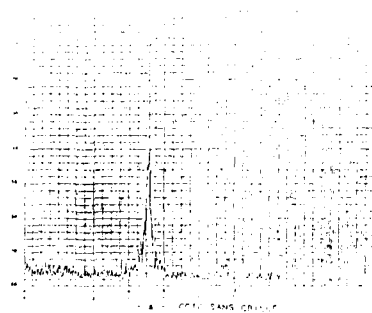


Fig. 15 Domaine de calcul - évolution de l'intensité des tourbillons.

Fig. 16 Exemple de ligne d'émission calculée  
(deux nappes)Fig. 17 Spectre obtenu dans le sillage de la  
grille.Fig. 18 Comparaison des spectres obtenus côté grille et côté sans  
préturbulente.

## THREE-DIMENSIONAL FLOW VISUALIZATION USING LASER-SHEET SCANNING

D. M. Nosenchuck  
M. K. Lynch  
Department of Mechanical and Aerospace Engineering  
Engineering Quadrangle  
Princeton University  
Princeton, N.J. 08544

It has been demonstrated that the conventional technique of fixed-laser-sheet flow visualization can be extended to include three-dimensional visualization by means of a scanning laser sheet. This system was implemented using a rotating mirror in conjunction with appropriate fixed optics. A space-filling three-dimensional data base was digitally obtained from the imaging and recording units, and was processed to yield a variety of three-dimensional views of the flow field in addition to obtaining quantitative results regarding mixing levels and velocities. Laser-sheet scanning was first applied in a study of boundary-layer turbulence in which active control was implemented. The flow visualization readily indicated the near-wall instabilities present in turbulent spots and synthetic turbulent boundary-layers. When control was attempted using an array of surface heating elements, the visualization technique graphically illustrated the attenuation of the near-wall sub-layer "streak" and resultant quiescent outer flow.

## INTRODUCTION

Flow visualization has historically provided a great deal of vital information concerning the complex flows associated with turbulence. Passive dye, injected at the plate wall, provides for a reasonable picture of the overall flow field. Due to limits in the perceptual abilities of the observer, it is nearly impossible to obtain any information concerning internal structures using this method. Conventional laser-induced fluorescence of a dye injected into the water flow provides for an intricate nonsteady visualization of a fixed cross-section of the flow. What is lacking, however, is a representation of the flow normal to the sheet, an essential ingredient if the topology is to be mapped and understood. Ideally, one would like to observe a continuous representation of the three-dimensional flow field. This would provide valuable qualitative and quantitative information which would allow the researcher to map out the entire flow field.

The technique of laser-induced fluorescence is attractive in that it is capable of resolving very small scales normal to the sheet, as well as within the sheet (based on the limitations of the imaging optics), and has the essential feature of being capable of generating three-dimensional space-filling data sets. This is due to the characteristic of the laser probing the field in a localized manner, without influencing adjacent regions. By taking a series of "cuts" through the field, a complete image may be reconstructed. This is in contrast to using passive dyes and imaging the flow field stereoscopically, observing only surfaces. It is essential that the internal nature of complex flow events (e.g. turbulent structures) be diagnosed if an adequate understanding is to be realized. The role that vorticity plays is complex, and generally undecipherable when conventional flow visualization techniques are involved. Having a complete space-filling data base would permit detailed observation of the interaction and evolution of discrete vortices, as well as distributed vorticity in the flow. Thus, it was decided to extend the technique of laser-induced fluorescence to include rapidly moving sheets, synchronized with imaging and recording optics.

## SCANNING LASER SHEET FLOW VISUALIZATION

Scanning laser-sheet flow visualization was accomplished by rapidly traversing a laser sheet through the flow field in a period small compared to the time scales of interest in the flow. The resultant data consisted of a series of two-dimensional sheets which represented a space-filling three-dimensional volume. The process is roughly analogous to a very high-speed CT scan, where a series of tomographs is obtained. The net effect is to record the entire laser-dye field each time the sheet is traversed through the flow. The resultant images provide a qualitative picture of the flow, as well as quantitative information concerning the degree of turbulent mixing which has occurred. The setup, shown in Figure 1, provides for a complete three-dimensional visualization of the boundary layer flow field.

This technique has proven effective in providing a three-dimensional picture of the interactions between high and low speed fluid in turbulent flows. Disodium fluorescein dye was injected into the flow using a slot which was flush with the flat plate. Since the dye is injected at the wall, it "tags" the low speed fluid. During the bursting process this low speed, high vorticity fluid moves away from the wall and mixes with the outer flow. This process, which produces a large portion of the turbulent energy, can be examined using the laser sheet scanning technique.

There are several critical parameters which must be defined and specified before an appropriate system can be designed. The spatial resolution normal to the laser sheet can be determined knowing the scales present in the flow. The global extent of the imaging volume and the period of the scan may easily be specified, knowing the spatial extent of the flow field and the temporal scales present in the flow. Secondary parameters involve the planform imaging area and laser energy density within the area.

The desired global extent (height) of the imaging volume divided by the spatial resolution yields a rough indication of the required number of laser sheets needed to reconstruct the field. For example, in one of the present experiments, it was desired to image a 2.0 cm portion of the boundary layer with approximately 1.0 mm resolution in the  $z$  direction. A minimum of 20 sheets was required to fill the volume, but 32 sheets were used (being a convenient power of 2 for the controlling electronics to deal with). The intersheet normal separation is then 0.62 mm, setting a rough maximum on the laser sheet thickness.

The period of a scan must be less than that associated with  $1/2$  of the period of the highest frequencies present in the flow. This is to reduce bias between the upper and lower portions of the scan and also to ensure that repetitive scans accurately capture the nonsteady nature of the flow. If the highest frequency is 20 Hz, then a scan must be completed in 25 ms. Given the previous example this requires that 1300 sheets be generated each second (neglecting the time taken to reposition the starting sheet after each scan). In our experiments, we used a system capable of 2000 steps/sec, but were limited by our imaging video recorder to 30 steps/sec.

The laser sheet was produced by appropriately expanding and focussing an Argon-ion laser beam (501 nm) with a series of vertically and horizontally oriented cylindrical lenses as shown in Figure 2. A rotating mirror was placed in the optical path to deflect the defocussed beam in the  $\pm y$  direction. The optics ensured that a thin sheet was formed which, when deflected, remained parallel to itself over a height of up to 10 cm.

The mirror was mounted on a low-inertia stage which was rapidly rotated in discrete amounts by a stepper motor. Electronics were designed and fabricated to permit  $2^N$  ( $0 < N < 8$ ) sheets to be scanned in succession at arbitrary heights over the plate (with the net scan range limited to 10 cm). A  $45^\circ$  front surface mirror was mounted on a traverse spanning the water channel. This allowed a video camera, positioned beside the channel, to record the images and a step/frame counter (Figure 3). The vertical synchronization pulse from the videotape machine was used to drive the stepper motor which resulted in a single step of the laser sheet for each frame recorded. This greatly aided in the processing of the recorded images, but limited the scanning rate to 30 steps/sec. A block diagram of the stepper motor control electronics is shown in Figure 4. The images were then digitized off-line using a video frame grabber, and stored on disk.

Several representative sheets from a single rapid scan of the laser sheet through a turbulent spot may be seen in Figure 5. These digitized images may be processed in multiple ways to yield both qualitative and quantitative insights into the nature of the flow. For example, the degree of mixing (most of which is attributable to turbulence) can be determined by distinguishing between gray-levels (thus dye concentration) in a single sheet. Also, movies can be made which show time evolutions at one or more discrete sheet locations in the flow (revealing the movement of the cross-section(s) of the structures). For complete spatial and temporal diagnosis, three-dimensional image-processing routines can be applied to the data obtained from high-speed scan(s) through the flow (digitally reconstructing the three-dimensional image using appropriate data). Several views from a single scan, created using this reconstruction technique, can be seen in Figure 6. The images were processed from a 32-sheet scan (several sheets of which are shown in Figure 5). This technique permits, for the first time, *quantitative three-dimensional visualization and quantitative flow visualization of complex flows.*

#### APPLICATION OF FLOW VISUALIZATION TECHNIQUE

The laminar-turbulent transition process and the mechanisms involved in turbulence energy production have been the focus of much work, due to the role these factors play in issues concerning viscous drag. Several methods of controlling boundary layer flows have emerged which make significant drag reductions possible.<sup>1-6</sup> Flow control has also proven to be a useful tool for gaining insight into the dynamic processes involved in transition and fully turbulent flows. A variety of views exists regarding the organized structure in turbulent boundary layers. Existing theories seem to agree on several points, however. Flow in the viscous sublayer seems to separate itself into high and low speed regions called "streaks".<sup>8</sup> This longitudinal low-speed area is traditionally called a streak because dye injected at the wall accumulates in this region. It is generally agreed that the average spanwise spacing between these streaks is  $z^+ = 90$  to 100 wall units. The liftup, sudden oscillation, and breakup of these streaks is referred to as "bursting". Experimental evidence<sup>9</sup> has shown that most of the production of turbulent energy near the wall occurs during the bursting process.

Some preliminary work has been done<sup>2</sup> which indicates that localized, active, feedback control may be used to cancel the naturally occurring, three-dimensional disturbances which lead to bursting in turbulent flows. Since these bursts appear to be the source of a large percentage of the energy produced in turbulent flows, control of this process seems to be the most logical and efficient flow control alternative.

The experiments presented herein involve active control of three-dimensional disturbances which lead to turbulence in boundary layer flows. The research was conducted on a flat-plate model in the Moody Water Channel at Princeton University. The relatively low maximum free-stream velocity of 9.6 cm/sec, and the large size of the facility, combined to create a flow with long temporal and large spatial scales. The overall experimental layout is shown in Figure 7. An array of streamwise heating elements was used to introduce disturbances into the flow and, as active control actuators, to cancel these disturbances. Heating strips were selected as actuators due to the solid state nature, ease of control, and efficiency of these devices in introducing small disturbances. The heating strips, when activated, increased the velocity of the fluid above them, which decreased the velocity of the flow between the heaters. A typical arrangement of heaters is shown in Figure 8. In the active control experiments, the front row of heaters was used to introduce a disturbance and the back row was activated spatially and temporally out of phase to cancel the disturbance. The dimensions, lateral spacing, and activation times of the heating strips were scaled with the flow parameters to produce high and low speed regions similar to those found in naturally occurring turbulent flow.

The disturbances and the resulting flow field were studied using a variety of techniques. Constant temperature anemometry and thermocouples were used to measure the temperature and velocity in the vicinity of the heaters as well as at several points downstream of the heater array. The laser sheet flow visualization technique, described in this report, was used to investigate the resulting flow field more closely. The data collected using this technique was processed in many ways to study the three-dimensional nature of the flow. These images made observations of the bursting process and the interactions between the input and control disturbances possible.

It was essential to characterize the response of the heaters in order to evaluate their performance as actuators for control. Thus, a complete study was made of the temperature and velocity fields present in the flow surrounding a single longitudinal heating element. This was followed by a survey of the flow field downstream of the heaters following the pulsing of a single row of heating elements. The experiments were repeated using the front and back rows of heaters individually. The power and pulse duration of each row of heaters were adjusted to produce a significant velocity disturbance, without introducing buoyant instabilities. These results were then applied to the use of heater arrays as actuators in a control scheme to cancel three-dimensional disturbances in the flow, thus delaying the onset of turbulence.

Heating at the wall introduces a temperature gradient into the flow which acts to locally increase the velocity of the fluid in the near wall region. A comprehensive study was conducted of the velocity field along the centerline of the heaters in order to better understand the temperature-velocity interaction. The velocity field above a heating strip may be found using temperature measurements from a thermocouple and the output from a hot-film probe located at the same point. The effect of temperature on the velocity signal can be removed by manipulating the hot-film calibration equations and making use of the measured temperature. Figure 9 shows the temperature and compensated velocity traces at several locations downstream of a heating element. The maximum overheats, measured near the wall on the centerline of the heating element, were from 2 - 3°C. The dissipation of the temperature disturbance and emergence of a velocity disturbance can be seen clearly.

In order to create the low-speed streaks (shown to be a major factor in turbulence production) several longitudinal heating elements were activated at the same time. Independent disturbances were created, using first two heaters in the front row of the array, followed by similar disturbances created using three heaters in the back row. The lateral spacing between the centerlines of the heaters in a given row was approximately  $x^+ = 90$  wall units. This spatial configuration was chosen due to its similarity to the spacing of streaks occurring in naturally turbulent boundary layer flows. The hot-film probe was used to study the velocity field 0.6 m downstream of the heaters for the cases with and without control. A lateral traverse was made of the central region of the flow, at a height of  $y^+ = 15$ , for each configuration of the heater array. When no control was applied, high-speed regions could be seen downstream of the heated areas while, due to continuity, low-speed streaks were evident between them. When control was applied, small velocity fluctuations could be seen, but the magnitude was greatly diminished. Surface plots of the resulting velocity fields are shown in Figure 10. The mean velocity at this point in the flow ( $y^+ = 15$ ) was 3.0 cm/sec. The maximum deviation from this mean was reduced from 1.0 cm/sec to 0.4 cm/sec when control was applied.

The turbulent spots which form as a result of open-loop pulsing of the heaters were studied using measurements taken at an observation point 2 m downstream of the heater array. The effectiveness of the control scheme was tested by making these same measurements when the control heaters were activated. Hot-film measurements, used to determine the increase in drag, were taken on the centerline at a  $y^+ = 15$  and, in order to gain an insight into the structures present in the flow, pictures were taken of the flow using the scanning laser sheet technique. The heater pulses, and resulting average velocity trace corresponding to the pulsing of each row of heaters individually and both rows when control was applied can be seen in Figure 11. The velocity traces are ensemble averages of 15 runs made for each case. The drag increases 60% over the undisturbed case when using the front heaters and 40% when using the rear heaters. The velocity and drag decrease below the nominal (no heat) value when active control is applied. The laser-sheet scanning technique described in the previous section was used to examine the physical nature of the flow at this location. Pictures depicting the flow at two different heights for each of the above mentioned cases can be seen in Figure 12. The interactions between high and low speed regions which are characteristics of turbulent flow can be seen in Figures 12a and 12b. Figure 12c, which



represents the flow when control is applied, reveals a flow which is indeed laminar at the 2.0 m observation point.

Longitudinal surface heating has been demonstrated to introduce controlled, three-dimensional, velocity disturbances into laminar boundary layer flows. When the spanwise heater spacing is approximately 90 wall units, these velocity disturbances are observed to be similar to the low-speed streaks seen in naturally occurring turbulent flows. In addition to inducing velocity disturbances, the heating elements have proven effective as control actuators to attenuate these disturbances. Control was applied by introducing a perturbation which was temporally and spatially out of phase with the initial disturbance. Low-speed streaks were weakened significantly using this technique. The growth of inflectional instabilities was delayed, which reduced the incidence of bursting in the flow, thus lowering the drag. The combination of hot-wire probes, thermocouples, and the sophisticated flow visualization technique described in this paper provided a complete data set to study these flows.

#### CONCLUSIONS

It has been demonstrated that the conventional technique of fixed-laser-sheet flow visualization can be extended to include three-dimensional visualization by means of a scanning laser sheet. This system was implemented using a rotating mirror in conjunction with appropriate fixed optics. Various alternative schemes based on linear mirror displacements, optical shutters, and several other mechanical and electro-optic techniques were considered, but were found not to satisfy the basic criteria of a viable three-dimensional flow visualization scheme. Such criteria include:

- (1) accuracy of temporal and spacial imaging
- (2) capability of dealing with highly complex, nonsteady flows
- (3) is robust in operation
- (4) adaptable to imaging a wide variety of flow fields.

The approach taken to meet these needs used four cylindrical lenses and a single rotating mirror controlled by a custom stepper motor controller. The controller was synchronized to a video system to permit each discrete sheet to be imaged and stored on a single field of videotape. It was found that this system was very easy to align and implement. The resulting three-dimensional space-filling data base was digitized and readily manipulated for graphical display and preliminary quantitative analysis (e.g. velocity and vorticity field generation using time-of-flight techniques and spectral analysis of dye species concentration for diffusion and mixing studies).

The technique was first applied to image turbulent spots occurring on a flat plate. The unexpectedly high incidence of high and low speed streaks which were clearly evident in the flow prompted us to implement an array of surface heaters biased towards perturbing the flow in the streamwise direction. This array of surface heaters was used to control the flow, delaying the onset of turbulence, and reducing the incidence of bursting. The three-dimensional imaging technique was used to validate the control scheme.

#### REFERENCES

- 1) Bushnell, D. M., Turbulent Drag Reduction for External Flows, AIAA 21st Aerospace Sciences Meeting, Reno, Nevada, 1983, Paper No. 83-0227.
- 2) Nosenchuck, D. M., Lynch, M. K., Active Control of Low-Speed Streak Bursting in Turbulent Spots, AIAA Shear Flow Control Conference, Boulder, Colorado, March 1985.
- 3) Liepmann, H. W., Brown, G. L., and Nosenchuck, D. M., Control of Laminar Instability Waves Using a New Technique, *J. Fluid Mech.*, 1982, vol. 118, 187-200.
- 4) Liepmann, H. W., and Nosenchuck, D. M., Active Control of Laminar-Turbulent Transition, *J. Fluid Mech.*, 1982, vol. 118, 201-204.
- 5) Nosenchuck, D. M., Passive and Active Control of Boundary Layer Transition, Ph.D. Thesis: California Institute of Technology, 1982.
- 6) Maestrello, L., and Ting, L., Analysis of Active Control by Surface Heating, *AIAA Journal*, vol. 23, no. 7, 1985.
- 7) Miller, P. L., A Laser Scanning System: Flow Visualization in Water Using a Laser Pumped Fluorescent Dye, Internal Report, Princeton University, 1985.
- 8) Kline, S. J., Reynolds, W. C., Schraub, F., and Runstadler, P. W., The Structure of Turbulent Boundary Layers, *J. Fluid Mech.*, 1967, vol. 30, 741-773.
- 9) Blackwelder, R. F., The Bursting Process in Turbulent Boundary Layers, *Lehigh Workshop on Coherent Structures in Turbulent Boundary Layers*, ed. C. R. Smith, D. E. Abbott, 1978, 211-227.

## ACKNOWLEDGEMENTS

We would like to thank Paul Miller for ideas he supplied in the initial stages of this research. The excellent three-dimensional image software support provided by Gregory Russell was also greatly appreciated. Special thanks go out to Robert Bogart for his skilled craftsmanship and hours of help on the water channel. In addition, we would like to thank Donna Biddulph, Mark Guire, Thomas Frobose, and Lou Procrocos for sharing their knowledge and skills of electronics.

The research described in this report was supported by ONR Contract N00014-85-K-0352 and NSF Young Investigator Award MSM-8352175.

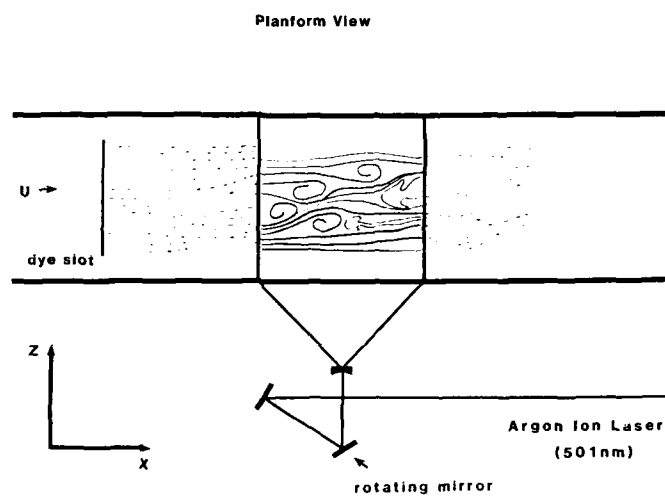


FIGURE 1: Planform View of Scanning Laser Sheet Setup

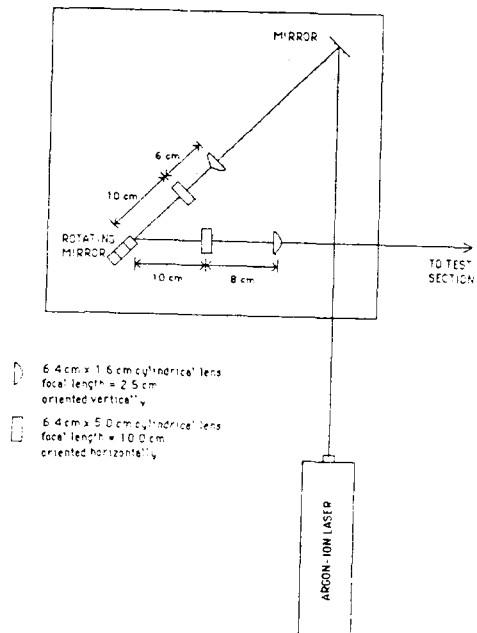


FIGURE 2: Detailed Schematic Diagram

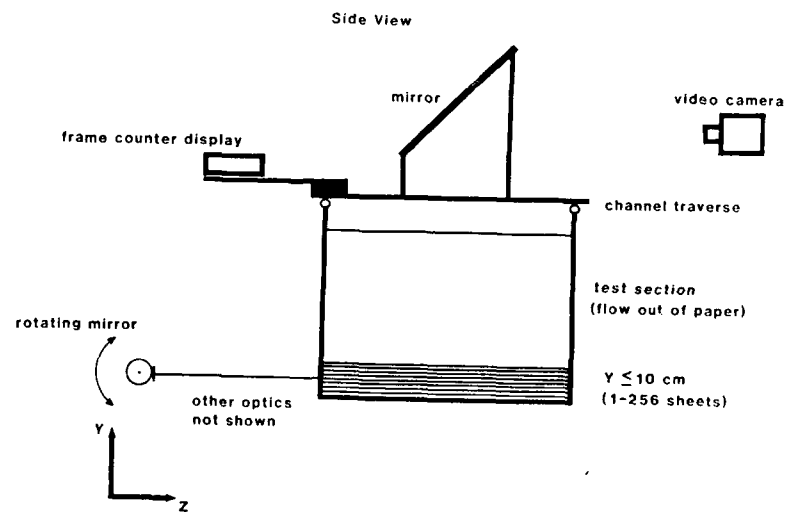


FIGURE 3: Side View of Detailed Schematic Diagram

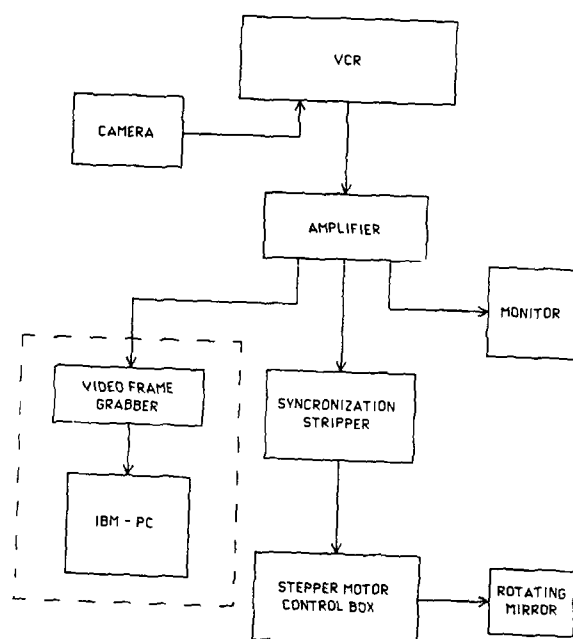


FIGURE 4: Block Diagram of Stepper Motor Control Electronics

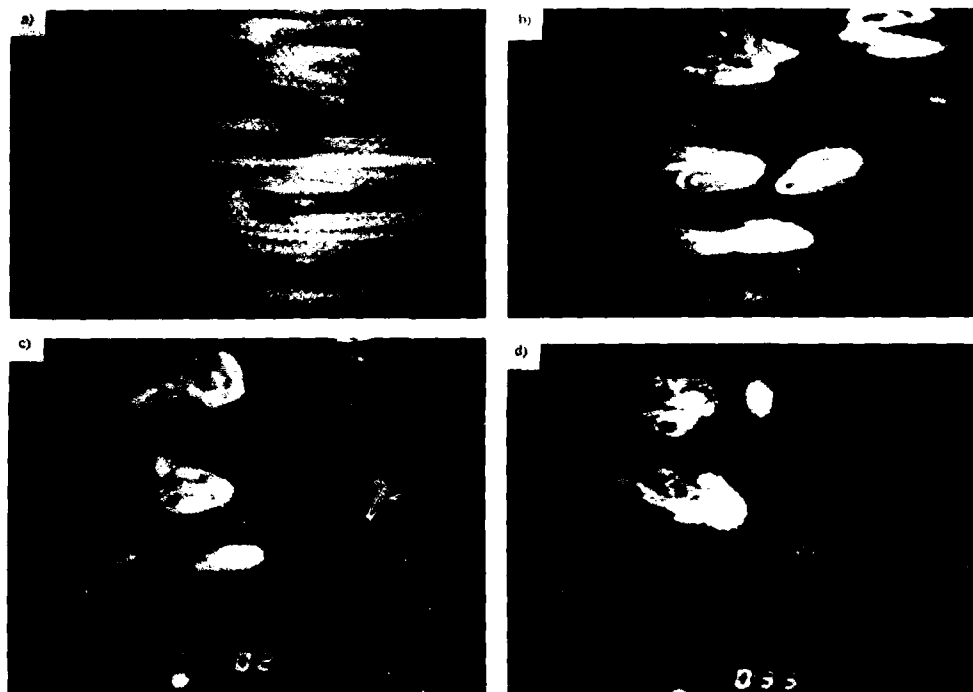


FIGURE 5: Representative Sheets from a Single Laser Scan of a Turbulent Spot

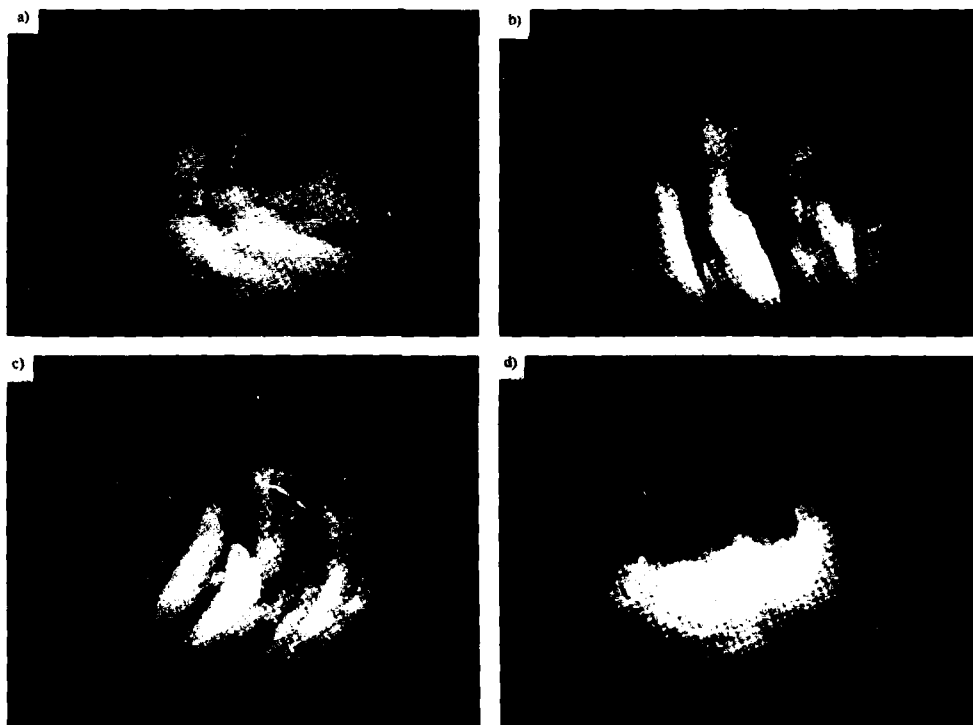


FIGURE 6: Several Views of a Turbulent Spot - Reconstructed from Scan Shown in Figure 16

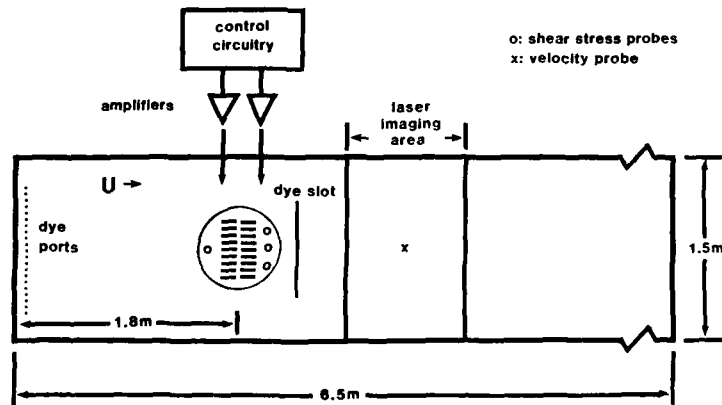


FIGURE 7: Experimental Layout

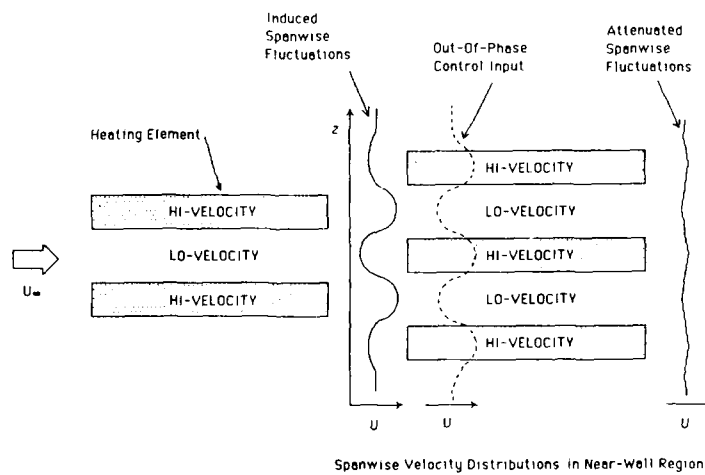


FIGURE 8: Proposed Control Scheme - Configuration of Heating Elements

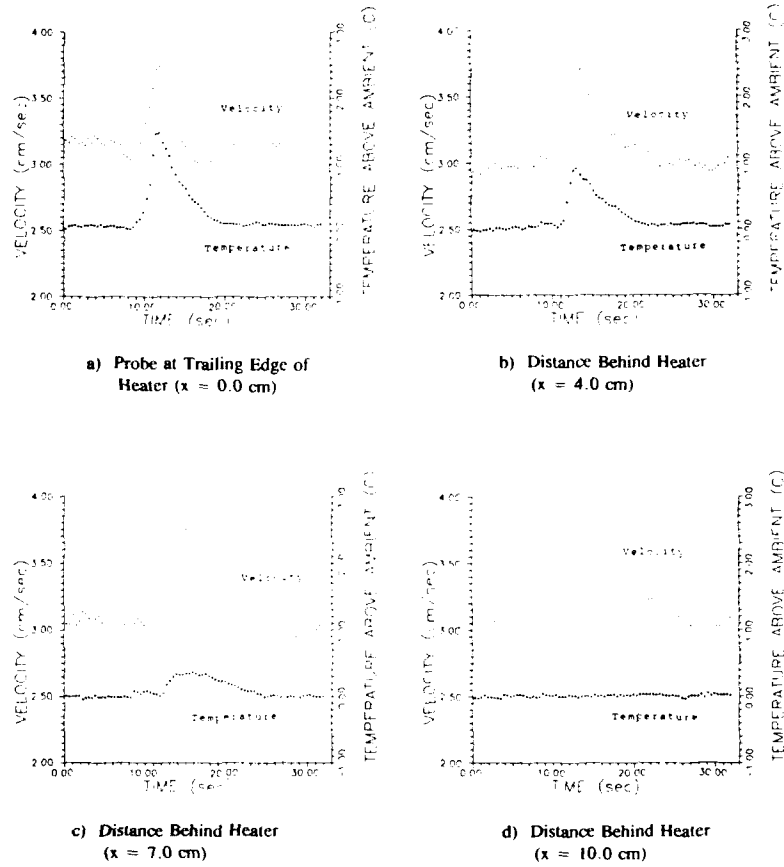


FIGURE 9: Evolution of Temperature and Velocity Disturbances

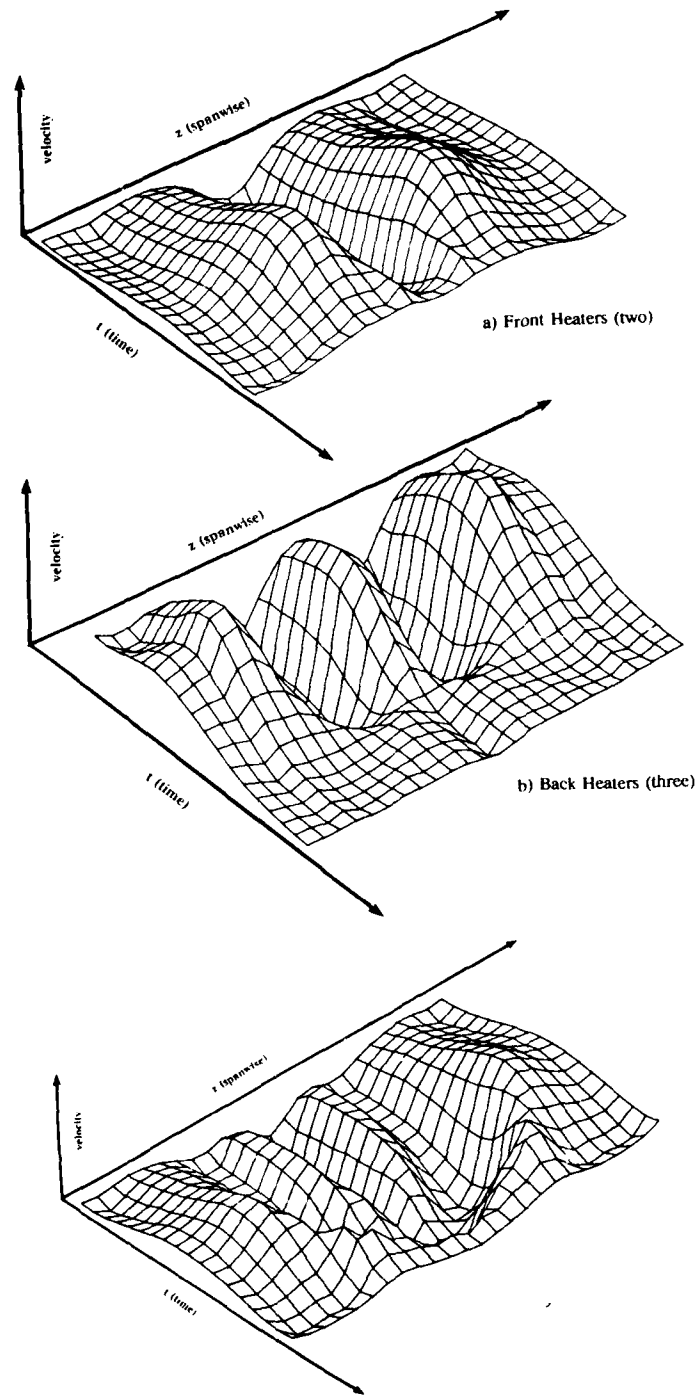


FIGURE 10: Velocity Field at a Location 0.6 m Downstream of the Heater Array at a Height of  $y^+ = 15$  (Open-Loop Pulsing a,b and With Control c)



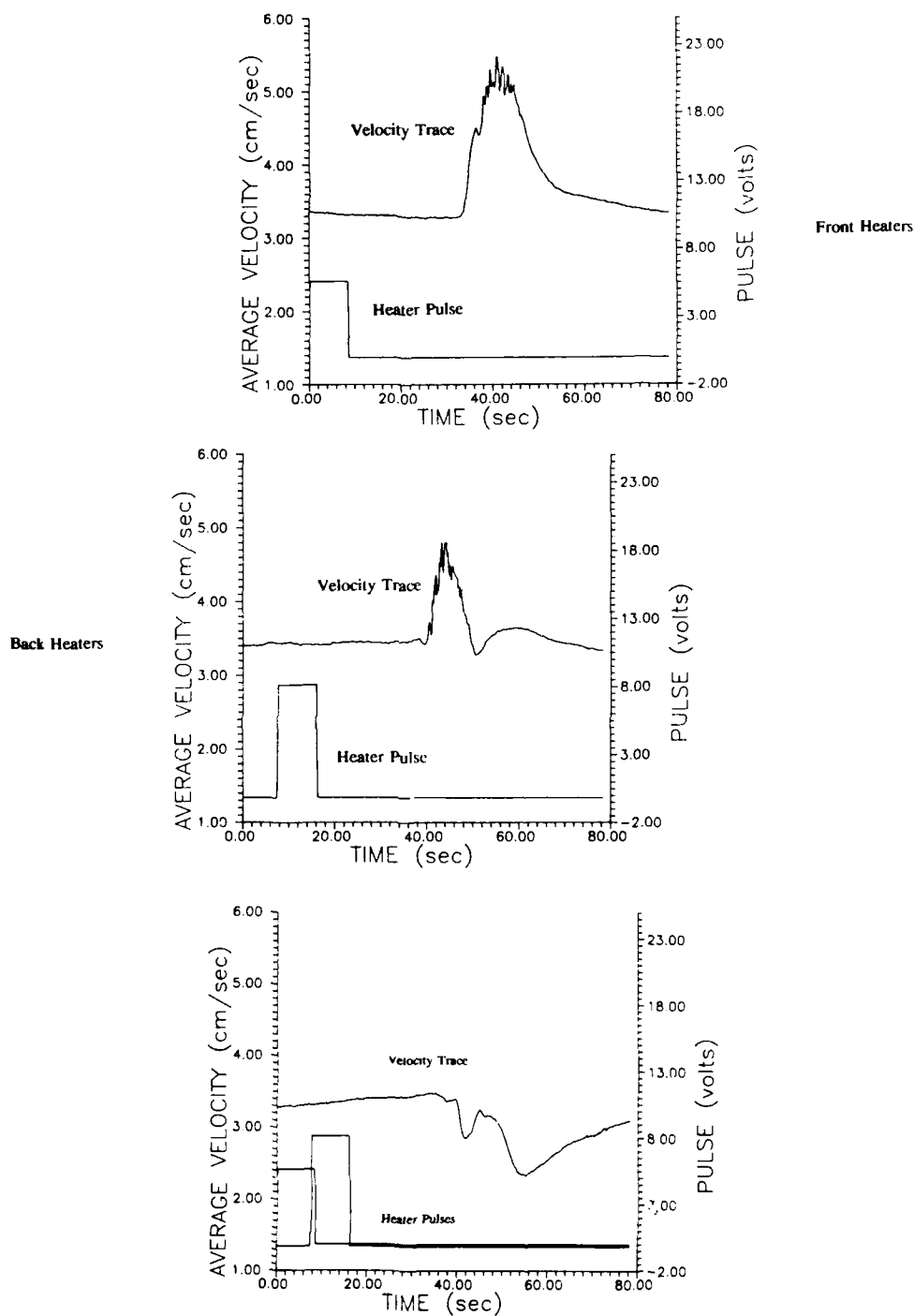


FIGURE 11: Averaged Velocity Traces 2.0 m Downstream of Heaters at a Height of  $y^+ = 15$  (Open-Loop Pulsing a,b and With Control c)

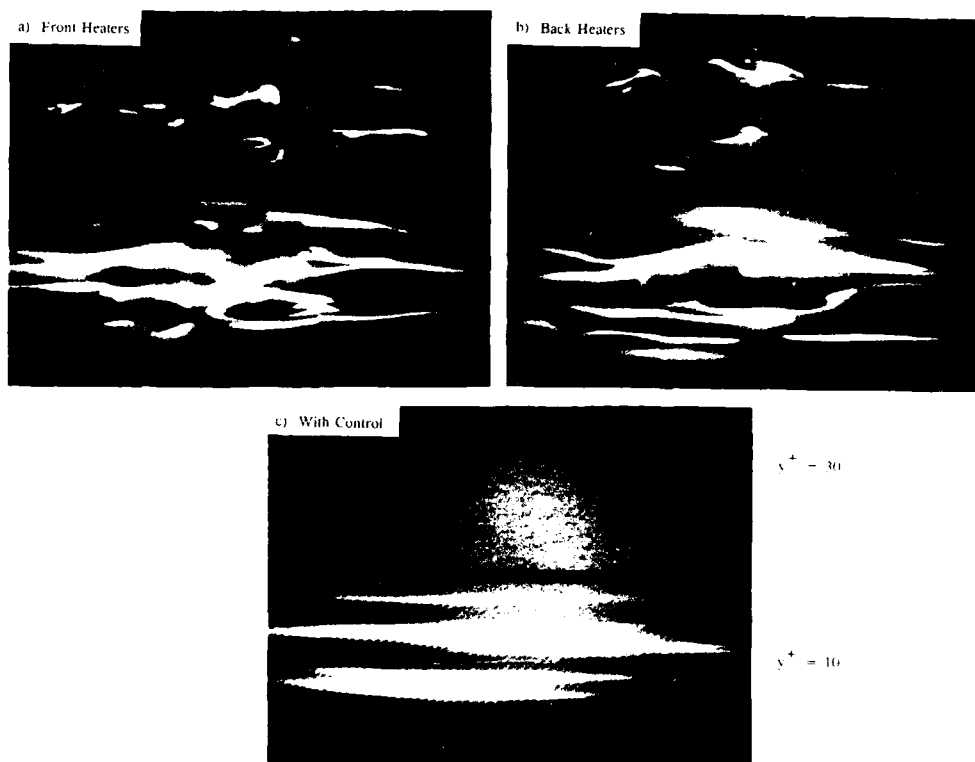


FIGURE 12: Comparison of Flow at Two Heights (Open-Loop Pulsing a,b and With Control c)

# APPLICATION OF HIGH SPEED HOLOGRAPHY TO AERODYNAMIC AND HYDRODYNAMIC THREE-DIMENSIONAL VELOCIMETRY.

M. Stanislas, O. Rodriguez, M. Dadi, F. Beluche

Institut de Mécanique des Fluides de Lille,  
5 Bvd Paul Painlevé, 59000 LILLE, FRANCE.

An application of holography to the measurement of fluid velocity in 3-D domains is proposed. After a short description of the method, an example of application to the water flow around a circular cylinder at low Reynolds number is presented. Then, the main limitations of the method are discussed and solutions are proposed to overcome them.

## 1/ INTRODUCTION

In 1948, D. GABOR proposed a new method for the formation of images in two steps without lenses, which he called wave front reconstruction /1/. This invention, later called holography, is mostly known, nowadays, for its ability to produce three dimensional images of objects, that is, to reconstruct wave fronts in amplitude and phase. At the end of the sixties, the appearance of lasers as coherent light sources, has led to a large development of the technique and its applications. Let us mention for example interferometry which is now widely used for flow investigation.

An other field of applications which is closer to Gabor's original purpose, is the use of micro-holography for particles measurements. A complete state of the art on this topic is proposed by B.J. THOMPSON /2/. The work to be presented here deals with the application of holography to the velocity measurement in fluid flows. First we present a description of the method, then an example of application is given, and finally the main drawbacks are detailed and solutions proposed to overcome them.

## 2/ DESCRIPTION OF THE METHOD.

Figure 1a presents a sketch of the experimental set-up. The output beam of a pulsed ruby laser is passed through a diverging lens before crossing the seeded flow to finally illuminate an holographic plate. The laser can produce from 1 to 4 pulses of 25 mJ each, with time intervals varying from 5  $\mu$ s to 10 s. Thus 1 to 4 holograms can be recorded on the same plate. After processing, the hologram is mounted on a reconstruction set-up (fig. 1b). An Helium-Neon continuous laser is used to reproduce the reference beam. A motorized table allows the motion of the hologram in the three coordinates directions with a step of 1  $\mu$ m. A magnifying optic and a video camera are used to observe the real reconstructed image. Thus, the size and successive positions of each particle present in the field can be measured and the knowledge of the time intervals gives the velocity of the particle. Let R and R' be the distance from the laser to the hologram respectively in the object and image space and  $\lambda$  and  $\lambda'$  the wavelengths of the lasers. The origin being on the hologram, the coordinates x,y and z of a particle in the object space and the coordinates x',y',z' of the real image are linked by the following relations:

$$\frac{1}{z} = \frac{1}{R} - \frac{\lambda}{\lambda'} \left( \frac{1}{z'} - \frac{1}{R'} \right)$$

$$z = \frac{R-z'}{R} z'$$

$$y = \frac{R-z'}{R} y'$$

The quality of the image obtained depends on the diffraction of the system, on the geometric aberrations introduced by the hologram and on the resolution of the video camera. A typical case, representative of our experimental set-up is that of a 20  $\mu$ m particle located at 20 cm from the hologram. In this case, the accuracy on length measurements using the formula given above is about  $\pm 2.5 \mu$ m in the plane normal to the

beam axis. This has been verified experimentally, using micrometric length scales. It corresponds to a precision better than 1% on the measurement of this velocity component. For the component parallel to the beam axis, the accuracy is about 10 times worst, due to the focusing uncertainty. Thus, with this method, it is possible to get the size and velocity of all particles present in the 3D domain recorded on the hologram. If the particles have the same velocity as the fluid, 3D instantaneous velocity charts of the flow can be obtained.

### 3/ EXAMPLE OF APPLICATION.

Figure 2 presents the experimental set-up for an application in water. The aim of the experiment is to get instantaneous velocity charts of the flow around a cylinder at low Reynolds number in order to compare them with computations using direct Navier-Stokes solvers [3/]. The experiment is built in a vertical water tunnel. The test section is 140x140 mm<sup>2</sup> and has a length of 1 m. The free stream velocity can be varied from 2 to 7 cm/s. The model is a circular cylinder of 10 mm in diameter and 240 mm in length. It passes through two glass windows which allow velocity measurements 15 diameters upstream and 25 diameters downstream. The Reynolds number based on the diameter can be varied from 160 to 600. The flow is seeded with non expanded polystyrene particles of density 1.02 and diameter 10 to 80  $\mu$ m. Figure 3 presents a photograph of the monitor screen in the case of a 3 exposures hologram. Figures 4 and 5 show two velocity charts obtained for  $Re = 210$  and 500. They are the projection on a plane normal to the cylinder's axis of the velocities measured in a slice of 4 cm in span, located in the middle of the test section. One can clearly see the oscillation of the wake of the cylinder. Comparisons with LDV measurements done on the same experiment give an agreement better than 3% on the velocity upstream of the cylinder.

### 4/ ACTUAL LIMITATIONS AND POSSIBLE DEVELOPMENTS.

As any measurement technique, multiple exposure holography presents some limitations which have to be studied and overcome when possible. We shall point out three of them, which are the most critical for the type of applications we have in mind: optical limitations, particles behaviour and data analysis.

#### 4-1 Optical limitations.

As can be seen from figure 1, in a Gabor hologram the reference beam passes through the object. Thus, this object has to be transparent enough to disturb only slightly the reference. This is not the case when the seeding is too dense or when gradients of the refraction index exist. Furthermore, the object beam is part of the reference light diffracted by each particle, so that, when the size of the particle diminishes, the diffracted intensity vanishes and, for particles smaller than 10  $\mu$ m, no image can be obtained by this method.

One solution to obtain an hologram when the reference beam is perturbed or when the particles are too small, is to split the reference and object beams. This permits to make the reference beam pass outside of the flow if it is not transparent enough. It also permits to adjust the intensity ratio between the two beams, so that smaller particles can be detected. In fact, in aerodynamic, the first case is included in the second one for, if gradients of refractive index exist in the flow, they are usually due to compressibility, which means high velocity gradients. This implies that very small particles must be used if they are supposed to follow the flow (see 4-2).

H. ROYER [4/] has proposed different solutions to apply the separated reference method. He showed that an intensity ratio of  $10^4$  to  $10^6$  is necessary to detect submicron particles. This ratio depends on the geometry of the set-up and on the size and nature of the particles. This implies anyway an important reduction of the spatial size of the useable domain. In practice, with the energy currently delivered by pulsed ruby lasers, it has to be reduced to a slice of a few centimeters height and a few tenth of a millimeter thickness.

Figure 6 presents different experimental set-up that can be used in aerodynamic studies. The main difficulty in choosing a set-up is to minimize the geometric optical aberrations introduced by the hologram. This can be done by using a set-up derived from GABOR original one. This is the case of the set-up proposed on figure 6 a, b and c. The first is the simplest one which permits to detect particles smaller than the diffraction limit, but it implies a transparent object. Set-up 6b is designed to be used in the case of a flow with refraction index gradients but, due to the fact that the reference and object beams come on both sides of the hologram, films with more resolution and less sensitivity must be employed and thus, the useable field is reduced. The last set-up makes also the reference beam pass outside the object but it implies the use of a splitting plate of the size of the hologram and it increases the distance between the hologram and the object. In the case where none of these pseudo in-line set-up can be used, an off-line hologram must be realized. The set-up 6d has been shown by ROYER [5/] to minimize the geometrical aberrations which can become very important in other cases. A calculation in the case studied in 2/ gives a precision of the same order. The main source of error is the astigmatism which in this case is of the order of 3  $\mu$ m.

As an example, figure 7 presents a picture of the video screen in the case of smoke particles of the order of 1  $\mu$ m in diameter in a jet. The hologram was recorded with the set-up 6a. A 4 pulses hologram was realized with time intervals of the order of 100  $\mu$ s.

## 4-2 Particle behaviour

As written above, to be detectable by in line holography particles must be bigger than about 10  $\mu\text{m}$ . This constraint is minor in liquid flows, because one can easily find particles of similar density. It can become critical in gas flows where the particle inertia is not negligible. This has been the subject of many theoretical developments since the original work of BOUSSINESQ /6/, but few experimental results are available. In order to test the various models and to get a reliable criterion for the influence of inertia forces on the accuracy of fluid velocity measurements, we have developed an experimental study on the flow along a 45° angle wedge /7/. Particles of different sizes and densities have been used to seed the flow and various models have been tested.

The most general model for a Reynolds number small compared to unity ( $Re_p$  is defined with the velocity discrepancy between the fluid and the particle and with the particle diameter), is due to GATIGNOL /8/:

$$\begin{aligned} \frac{4\pi a^3}{3} \rho_p \frac{d\vec{V}_p}{dt} = & -6\pi\mu a (\vec{V}_p - \vec{V}) - \frac{2\pi a^3}{3} \rho \left( \frac{d\vec{V}_p}{dt} - \frac{d\vec{V}}{dt} \right) \\ & - 6a^2 \sqrt{\pi\mu\rho} \int_{-\infty}^t \left( \frac{d\vec{V}_p}{dt} - \frac{d\vec{V}}{dt} \right) \frac{d\tau}{\sqrt{t-\tau}} \\ & + \frac{4\pi a^3}{3} \rho \frac{d\vec{V}}{dt} + \frac{4\pi a^3}{3} (\rho_p - \rho) \vec{g} \end{aligned}$$

In this formula,  $a$  is the particle radius,  $\rho$  and  $\rho_p$  are the fluid and particle densities,  $\vec{V}$  and  $\vec{V}_p$  the fluid and particle velocities and  $\mu$  the fluid viscosity. The first term on the right hand side is the Stokes drag. The second one corresponds to an added mass. The third term takes into account the time history of the motion. The fourth term is the effect of the pressure gradient due to the acceleration of the fluid. The last term is due to the gravity forces. When the Reynolds number is not small compared to 1, empirical generalizations have been proposed by many authors. Those of ODAR and HAMILTON /9/:

$$\begin{aligned} \frac{4\pi a^3}{3} \rho_p \frac{d\vec{V}_p}{dt} = & \frac{1}{2} C_D \pi a^2 \rho |\vec{V}_p - \vec{V}| (\vec{V}_p - \vec{V}) - C_A \frac{4\pi a^3}{3} \rho \left( \frac{d\vec{V}_p}{dt} - \frac{D^p \vec{V}}{Dt} \right) \\ & - C_H a^2 \sqrt{\pi\mu\rho} \int_{-\infty}^t \left( \frac{d\vec{V}_p}{dt} - \frac{D^p \vec{V}}{Dt} \right) \frac{d\tau}{\sqrt{t-\tau}} \\ & + \frac{4\pi a^3}{3} \rho \frac{D^p \vec{V}}{Dt} + \frac{4\pi a^3}{3} (\rho_p - \rho) \vec{g} \end{aligned}$$

$$C_D = \frac{24}{Re_p} (1 + .15 Re_p^{.687})$$

$$C_A = \frac{(\vec{V} - \vec{V}_p)^2}{\left| \frac{D^p \vec{V}}{Dt} - \frac{d\vec{V}_p}{dt} \right| 2a}$$

$$C_H = 1.05 + \frac{0.066}{A_C^2 + 0.12}$$

$$Re_p = \frac{|\vec{V} - \vec{V}_p| 2a \rho}{\mu}$$

$$C_H = 2.88 + \frac{3.12}{(A_C + 1)^3}$$

and of SHILLER AND NAUMAN /10/:

$$\frac{4\pi a^3}{3} \rho_p \frac{d\vec{V}_p}{dt} = \frac{1}{2} C_D \pi a^2 \rho |\vec{V}_p - \vec{V}| (\vec{V}_p - \vec{V})$$

$$C_D = \frac{24}{Re_p} (1 + .15 Re_p^{.687})$$

can be retained as the most representative. Figure 8 presents a comparison between measured and computed velocities in the case of 15 to 20 microns polystyrene particles of density 40 kg/m<sup>3</sup>. The flow velocity has been measured by LDV using submicron smoke particles. Computations are made using the model of SHILLER and NAUMAN /10/. The maximum

velocity difference between the fluid and the particles is 4%. The maximum difference between predictions and measurements is better than 2%. Figure 9 presents the relative difference  $\delta = |V_p - V|/|V|$  along a computed trajectory in the case of a water particle of 20  $\mu\text{m}$ . Comparisons are made between the 3 previous models and experimental results obtained by holography. One can see that the models /9/ and /10/ give a quite correct prediction of  $\delta$ . As conclusion, it appears that the simplest model which correctly describes the particle behaviour for Reynolds numbers lower than 100 is that of SHILLER and NAUMAN /10/ which retains only a corrected Stokes term to define the drag coefficient:

#### 4-3 Data analysis

The last but not least limitation of the method is the time necessary to extract the information contained in the hologram. Due to the magnification imposed by the size of the particles, the video screen represents typically about 1  $\text{mm}^2$  at the scale of the flow. This means that actually, a very long time is needed to get the complete information contained in an hologram. One way of reducing this acquisition time is to design an automatic assessment system. The basic principle is to connect the video camera to a digital image analyser. The holographic image is scanned using the motorized tables driven by the computer. The system has to detect the particles and to determine their position and size by periodically digitizing and analysing the video image. The main problem is to determine the in focus position of the image. Various authors /11/-/12/ have proposed solutions for this purpose. Figure 10 presents the solution tested by BEXON /11/. The image is thresholded at two levels 1 and 2 and the two images obtained are subtracted. One obtains a halo representative of the slope of the particle image border. When the surface of the halo is minimum, the image is considered to be focussed. Comparison with microscope measurements give a good agreement on the diameter for particles larger than 25  $\mu\text{m}$ . The combination of a Roberts cross operator and of a trapezoidal weighting function defined using the intensity histogram is shown by HAUSSMANN and LAUTERBORN /12/ to give, by computing the average of the resulting image, an efficient focussing criterion. In any case, the choice of a criterion has to be made on the basis of simplicity for the treatment of a volume of  $5 \times 5 \times 1 \text{ cm}^3$  with a step in depth of 500  $\mu$  implies the acquisition and treatment of at least 50.000 pictures.

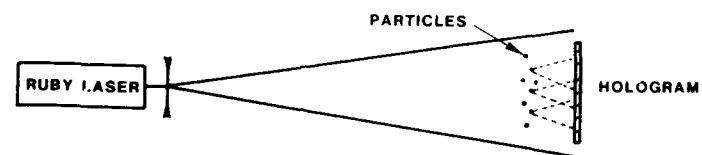
#### 5/ CONCLUSION

An application of holography to the velocity measurements in fluid flows has been presented. The method is interesting in the fact that it is non intrusive, it gives access to the three components of the instantaneous velocity in three dimensional domains. In this way, it appears to be quite complementary to the classical laser doppler velocimetry. As all measurements techniques, this method has its limitations. Solutions have been studied and proposed for each of them. The most limitative is the acquisition time. This is actually the object of our effort.

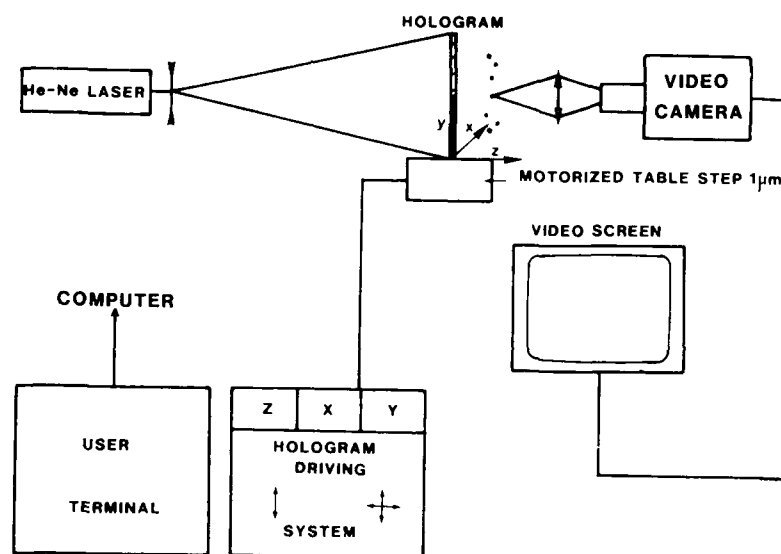
#### REFERENCES

- /1/ GABOR D. "A new microscope principle." Nature 1948.
- /2/ THOMPSON B.J. "Holographic methods of dynamic particulate measurements - Current status." SPIE vol 348 pp 626-633 High speed photography San Diego 1982.
- /3/ BRAZA M. "Simulation numérique du décollement instationnaire externe par une formulation vitesse pression. Application à l'écoulement autour d'un cylindre." Thèse de Docteur Ingénieur INPT Toulouse n°182.
- /4/ ROYER H. "Montages particuliers pour l'holographie des micro-particules." Rapport ISL R118/76 1976.
- /5/ ROYER H. "Holographie à grande distance. Application à la ballistique." Rapport ISL 113/85 1985.
- /6/ BOUSSINESQ J. "Sur la resistance qu'oppose un fluide indéfini en repos au mouvement varié d'une sphère solide." CRAS vol 100 pp 935-937, Paris, 1885.
- /7/ DADI M. Thèse de docteur ingénieur. (to appear) 1986.
- /8/ GATIGNOL R. "The Faxen formulae for rigid particles in unsteady non uniform Stokes flow" J. de Méca. Th. et App. vol 1 n°2 p 143-160, 1983.
- /9/ ODAR F. HAMILTON W. "Forces on a sphere accelerating in viscous fluid" J.F.M. vol 18 pp 302-314
- /10/ SHILLER and N. MAN A.Z. Ver. Deut. Ing. 77 p 318, 1933.
- /11/ BEXON R. GIBBS J. BISHOP G.D. "Automatic assessment of aerosol holograms." J. Aerosol Sci. vol 7 pp 397-407, 1976.
- /12/ HAUSSMAN G. and LAUTERBORN W. "Determination of the size and position of fast moving gas bubbles in liquids by digital 3-D image processing of hologram reconstructions." Applied Optics vol 19 n°20, 1980.

We are thankful to the French Ministry for Defense which, through the D.R.E.T., has sponsored most of this work.



1 a RECORDING



1 b RECONSTRUCTION

FIGURE 1 APPLICATION OF HIGH SPEED  
MICROHOLOGRAPHIC TO VELOCIMETRY

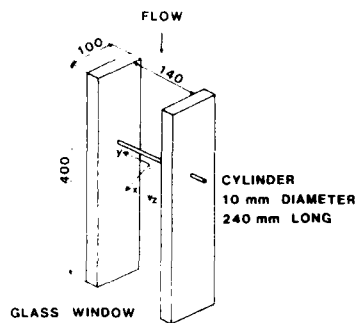


FIGURE 2 EXPERIMENTAL SET UP



FIGURE 3 3 EXPOSURES HOLOGRAM  
OF POLYSTYRENE PARTICLES IN WATER

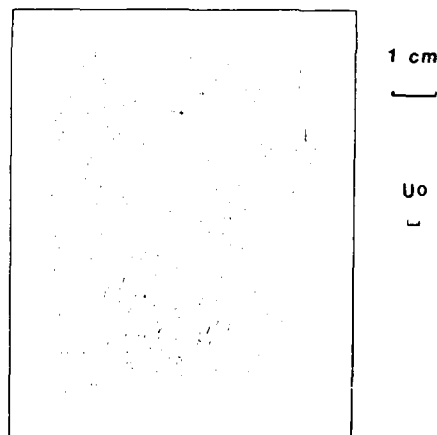


FIGURE 4 INSTANTANEOUS  
VELOCITY FIELD AT  $Re = 210$

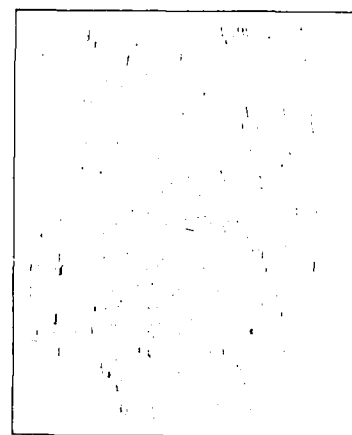
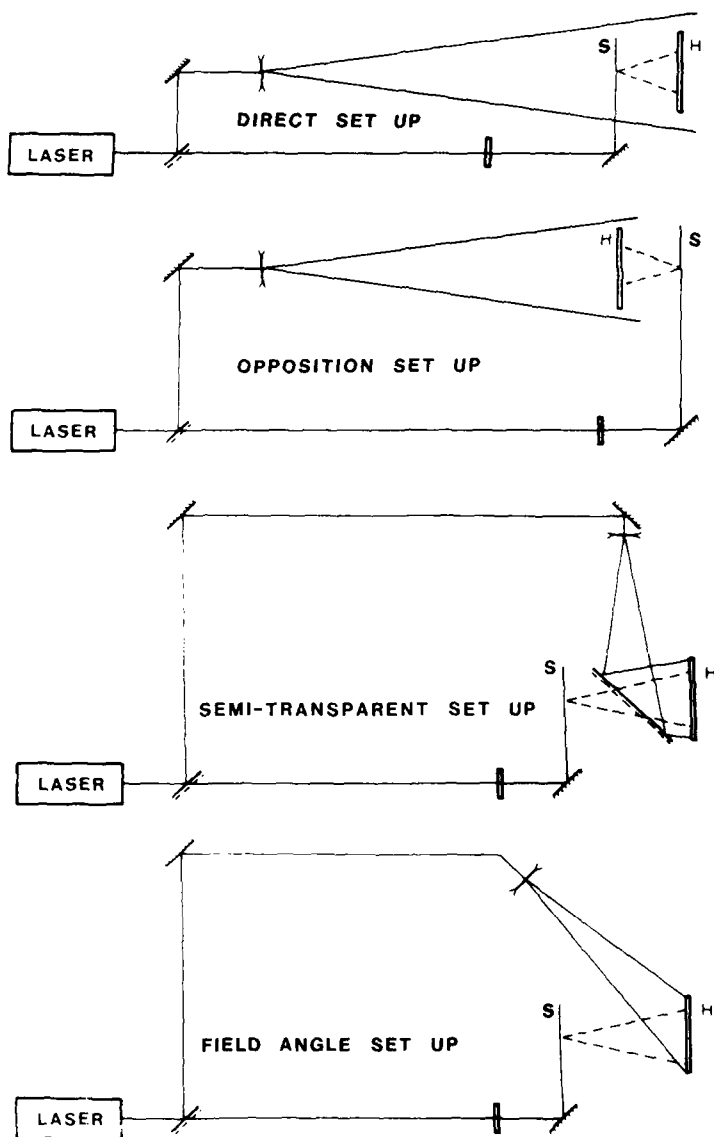


FIGURE 5 INSTANTANEOUS  
VELOCITY FIELD AT  $Re = 500$





**FIGURE 6      SEPARATED REFERENCE SET UP**



FIGURE 7

4 EXPOSURES HOLOGRAM OF MICRON SMOKE PARTICLES IN AIR

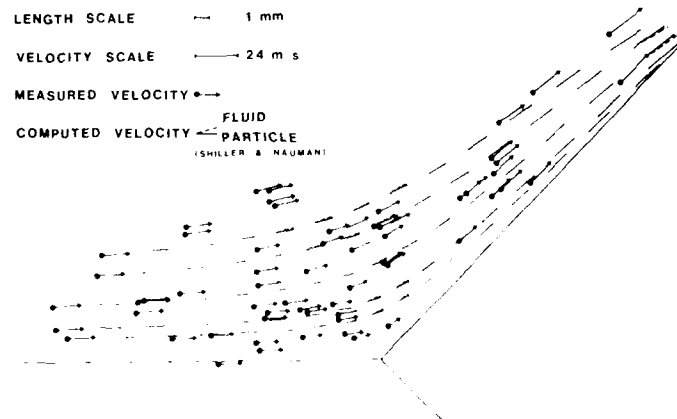


FIGURE 8 COMPARISON BETWEEN MEASURED AND COMPUTED  
PARTICLES VELOCITIES EXPANDED POLYSTYRENE 15-20 MICRONS

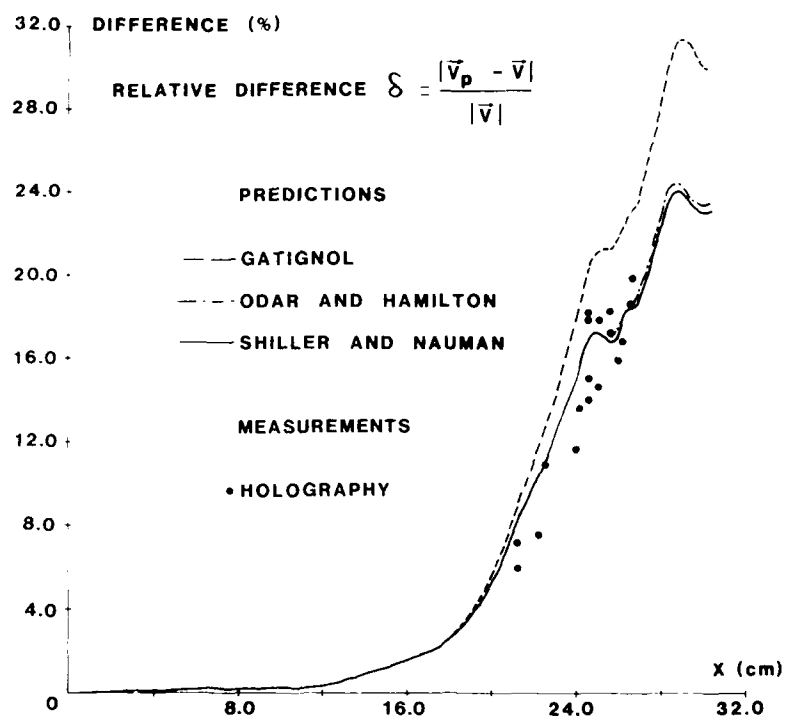


FIGURE 9 COMPARISON BETWEEN MEASURED AND COMPUTED VELOCITIES ALONG A TRAJECTORY WATER PARTICLES 15-20  $\mu$ m

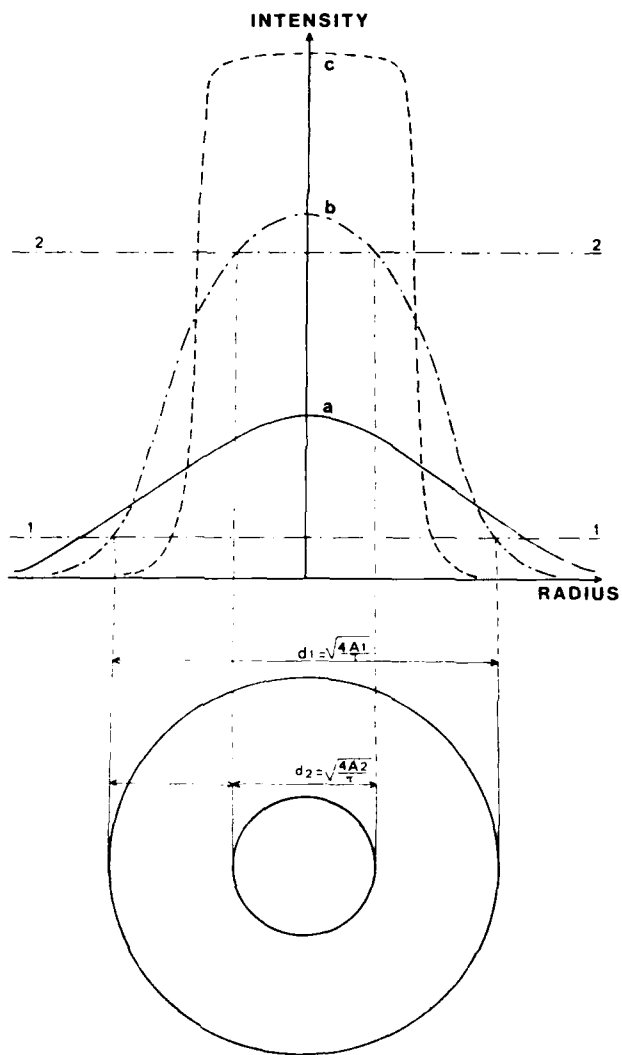


FIGURE 10 INTENSITY OF THE IMAGE OF A PARTICLE  
AS A FUNCTION OF THE FOCUS POSITION

# MATCHED INDEX LASER ANEMOMETRY SYSTEMS FOR FLOW STUDIES IN COMPLEX GEOMETRIES

by  
A. Dybbs, R.V. Edwards and E. Reshotko  
Case Center for Complex Flow Measurements, C<sup>3</sup>FM  
Departments of Mechanical and Aerospace Engineering  
and  
Chemical Engineering  
Case Western Reserve University  
Cleveland, Ohio 44106

## SUMMARY

Optical access to the flow is necessary if laser anemometry is to be used to map a given flow field. Often this access is difficult or impossible to obtain because of the shape of the object about which (or within which) the flow exists. Examples are flows in porous media, fluidized beds, heat exchangers or near sinusoidal surfaces. Making the object of transparent material such as of glass or plexiglas is not sufficient to provide a reliable, useable optical environment for laser measurements. It is often necessary to use a fluid whose index or refraction matches that of the object.

At the Case Center for Complex Flow Measurements, C<sup>3</sup>FM at Case Western Reserve University, we have constructed a matched index of refraction flow system. The purpose of this paper is to describe this system and present examples of measurements made with this system. In particular this paper will discuss

1. When index matching is needed.
2. How close the match has to be.
3. Practical details of operating an index matched facility.
4. Flow measurements made using an index matched facility to study boundary layer transition due to roughness, the flows within rod bundles and the flow regimes within porous media.

## INTRODUCTION

There are many flows for which velocity measurements within complex internal passages or near curved solid surfaces are required for improved understanding of flow and transport mechanisms. Examples of such flows include flows in porous media, flows in rod bundle heat exchangers, flows in fluidized beds, and flows near wavy walls. Often the dimensions of the important flow regions are such that hot wire anemometry or pitot probes are unacceptable. Laser anemometry being non-intrusive is a candidate for such measurements provided the problem of optical access can be solved. One solution to this problem is to build a scale model of the flow passage object from a transparent optical material whose index of refraction can be matched by a suitable fluid. The purpose of this paper is to describe such a matched index of refraction flow system and discuss some of the fluid mechanic results obtained.

## THEORETICAL CONSIDERATIONS

The effect of a mismatch in index of refraction will be discussed here primarily in terms of ray tracing and Snell's law. The calculations could be done totally in terms of Fresnel coefficients, but the computations are tedious and no real new insight results from this method.

Snell's law for a ray traversing a surface where there is a step change in the index of refraction is (see Figure 1):

$$n_1 \sin \theta_1 = n_2 \sin \theta_2 \quad (1)$$

where  $n_1$  is the index of refraction on side 1, and  $\theta_1$  is the angle of ray from the surface normal at the point of incidence. This rule applies for curved surfaces as well.

If  $n_1 > n_2$ , then there exists an incidence angle  $\theta_c$  where the ray does not traverse the surface at all. This is called the critical angle. That is to say,

$$\sin \theta_2 = \sin 90^\circ = 1 = \frac{n_1}{n_2} \sin \theta_c$$

$$\sin \theta_c = \frac{n_2}{n_1} \quad (2)$$

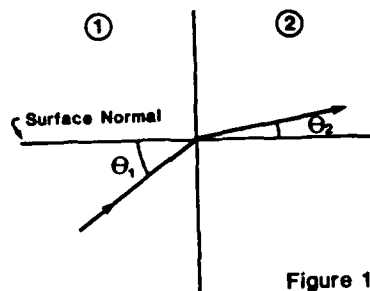


Figure 1

Fig. 1. Ray Traversing Between Two Media of Different Index of Refraction ( $n_1$  and  $n_2$ ).

For an example let  $n_1 = 1.44$  and let  $n_2 = 1.00$ . Then  $\theta_{1c} = 43.98^\circ$ . Any ray making a larger angle with the surface normal will not cross the surface. Therefore, even if the optical surfaces are flat, it may be necessary to adjust the indices of refraction in order to gain optical access.

#### FLAT INTERFACES

Consider now two rays at different angles traversing the plane interface between two media of different index of refraction (see Figure 2). This situation arises when one is using a laser fringe anemometer (normally referred to as a laser Doppler velocimeter or LDV).

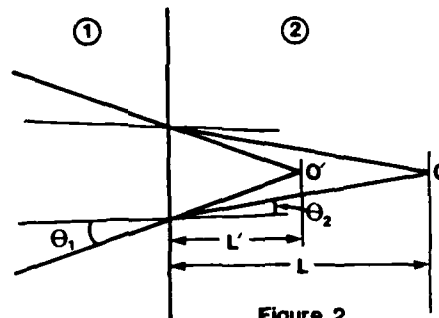


Figure 2

Fig. 2. Two Rays at the Same Angle ( $\theta_1$ ) Traversing the Plane Interface Between Two Media of Different Index of Refraction.

The rays would have intersected at point O' if there had been no interface. This is called the apparent intersection. The rays actually intersect at O. By geometry one can easily see that

$$\frac{L'}{L} = \frac{\tan \theta_2}{\tan \theta_1} = f\left(\frac{n_1}{n_2}, \theta_1\right) \quad (3)$$

The angle  $\theta_2$  is calculated by Snell's law. Further, if one attempts to move the intersection point while keeping the angle the same, one can see that

$$\frac{dL}{d\theta_1} = f\left(\left(-\frac{n_2}{n_1}\right), \theta_1\right) \quad (4)$$

The measurement volume of the LDV is displaced from its apparent intersection, and if one moves the intersection of the beams, the displacement is modified by the index of refraction mismatch.

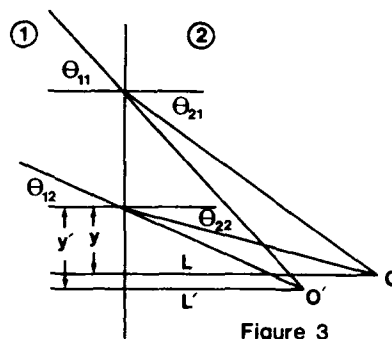


Figure 3

Fig. 3. Two Rays at Different Angles ( $\theta_{11}$  and  $\theta_{12}$ ) Traversing the Plane Interface Between Two Media of Different Index of Refraction.

The problem is more complicated if the angles that the two rays make with the walls are not equal (see Figure 3). Again the point of intersection of the two rays moves with respect to the apparent intersection. Basing the coordinate system on the intersection of the lower beam with the interface, it is easy to see that

$$\frac{L}{L'} = \frac{\tan \theta_{11} - \tan \theta_{12}}{\tan \theta_{21} - \tan \theta_{22}} \quad (5)$$

$$\frac{y}{y'} = \frac{\left( \frac{\tan \theta_{11}}{\tan \theta_{12}} - 1 \right)}{\left( \frac{\tan \theta_{21}}{\tan \theta_{22}} - 1 \right)} \quad (6)$$

$$\theta_{21} = \arcsin \left( \frac{n_1}{n_2} \sin \theta_{11} \right); \quad \theta_{22} = \arcsin \left( \frac{n_1}{n_2} \sin \theta_{12} \right)$$

Again  $\theta_{21}$  and  $\theta_{22}$  can be computed by Snell's law. The position of the intersection is a nonlinear function of the input angles even for a plane interface. Further, note that the bisection angle at the intersection is changed. This means that for a laser velocimeter, the velocity component measured is not the same one measured in the absence of the interface. The relation between the bisection angles is

$$\tan \theta'_s = \frac{L'}{L} \tan \theta_s + \frac{(y-y')}{L} \quad (7)$$

where  $\theta'_s$  and  $\theta_s$  are the bisection angles in the absence of the interface and in the presence of the interface, respectively.

There is one more complication caused by the mismatch of the index of refraction. If a third ray at a different angle is passed through the interface that would have intersected in the absence of the interface, it will not have a common intersection in the presence of the interface. Each pair of beams will intersect, but there will not be a common intersection. Therefore, a two-component LDV with three beam arrangement aligned with the intersection in medium 1 will not necessarily be aligned when the rays cross into medium 2.

It can be shown that to first order, the size of the beam waist of a laser beam focused through an interface:

1. is the same size as in medium 1.
2. has its position shifted along the beam by the ratio  $n_1/n_2$ . If  $n_2$  is bigger than  $n_1$ , the position of the waist is shifted further away from the intersection of the beam with the interface by  $n_1/n_2$ . The distance is shortened by the same amount if  $n_2 < n_1$ . Given the nonlinear behavior of the position of beam intersections, it is possible that the beam waists of a laser Doppler velocimeter may not be at the intersection point. Since the difference in angle of beams in a time of flight laser velocimeter (TLV) are typically much smaller than those of a LDV, the TLV is less affected by this latter effect.

The more common situation of having rays traverse two interfaces is somewhat more complicated. However, all the results previously derived apply except that the beams are displaced somewhat passing through the intermediate medium. The relation of the angles between the outer media is the same as before.

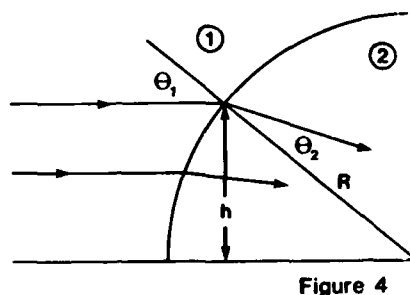


Figure 4

Fig. 4. Horizontal Rays Intersecting a Curved Interface of Radius of Curvature  $R$ .

## CURVED INTERFACES

Consider a set of horizontal rays intersecting a curved interface of constant radius of curvature  $R$  (see Figure 4). The interface acts like a poor lens, bending the rays toward or away from the axis depending on whether  $n_2$  is greater than  $n_1$  or not. The amount of bending also depends on the height of the intersection above the horizontal axis. In Figure 4, it is easy to see that

$$\sin \theta_2 = \frac{n_1}{n_2} \frac{h}{R} \quad (8)$$

Here rays that enter parallel may intersect in medium 2. However, no two pairs intersect at the same point. Rays that would have intersected if solely contained in medium 1 may still intersect in medium 2, but again the location of the intersection is altered. If  $n_1 > n_2$ , there are some rays that never enter the medium, since their angles with the surface normal are greater than the critical angle. The height above the axis  $h$ , above which no rays enter, is given by

$$h = R \frac{n_2}{n_1} \quad (9)$$

Likewise, if a ray is parallel to the horizontal axis in medium 2, it will not be able to exit at some heights if  $n_2 > 1$ . This height is given by the same formula:

$$h = R > \frac{n_1}{n_2} \quad (10)$$

The above calculations show that if a parallel set of rays intercepts the interface of a cylinder (or a sphere), there are regions of the surface where no rays cross the interface. The fraction of the radius outside of this zone is given by the appropriate ratio of indices of refraction - the ratio must be less than one.

For a simple curved surface, computation of the position of intersection (if any) of two rays can be complicated. For the more complicated curved surfaces encountered in some flows, the calculations are indeed formidable.

If a laser beam encounters a cylinder or sphere of diameter smaller than the laser beam, the beam will be severely distorted in a region corresponding to the critical angles discussed above. The beam's phase fronts will be distorted even in the region of the solid where there is no reflection due to critical angles being exceeded. This can result in distortion of the fringe pattern in a LDV causing a loss of velocity to frequency proportionality or an increase in bandwidth of the received signal.

EFFECTS OF  $n_1 / n_2$ 

All of the problems encountered above can be mitigated if one can make the ratio  $n_1 / n_2$  close to unity. The question is, how close is close enough?

## Example 1:

Suppose you have a flat interface with three beams crossing it (see Figure 3). You desire to have the intersection of the upper two beams with the lower beam be within 0.1 cm.



Consider that the intersection point with no interface would be given by the point  $O'$  whose coordinates are  $(7,0)$ , as shown in Figure 3. The tangents of the angle of incidence of the three beams at the interface are 0, 0.1 and 0.2, respectively. All the intersections are at  $y = 0$  (see equation (6)). We need only compute  $L$ . Using equation (5), we get Table 1.  $Y1$  is the intercept of the lower beam and the middle beam.  $Y2$  is the intercept the top and lower beam,  $Y4$  is the  $L$  intersection of the upper two beams.

Note that the intersections  $Y1$  and  $Y2$  are within 0.1 cm for  $n_1/n_2$  between 1.4 and 1.7. However, the intersection can be far from the apparent intersection at 7. Furthermore, the intersection of the upper pair of beams will be within 0.1 cm of the intersection with the lower beam only if  $n_1/n_2$  is between 1.01 and 0.99. Careful specification of the problem is obviously necessary.

TABLE 1.  
All lengths in cm.

$\frac{n_1}{n_2}$	$Y1$	$Y2$	$Y1-Y2$	$Y4$
1.4	4.993	4.976	0.01703	5.000
1.3	5.31	5.266	0.044	5.000
1.2	5.782	5.82	-0.03871	5.000
1.1	6.337	6.357	-0.0201	5.000
1.01	6.928	6.93	-0.002	5.000
1	7	7	0	5.000
0.99	7.074	7.071	-0.003	5.000
0.95	7.382	7.372	-0.01076	5.000
0.9	7.807	7.785	-0.0221	5.000
0.8	8.413	8.366	-0.0474	5.000
0.7	10.1	10.3	-0.2000	5.000

#### Example 2:

You have a cylindrical pipe filled with fluid of index of refraction  $n_1$ . The diameter of the pipe is 5 cm. The beams come in parallel to the horizontal axis. Up to a point, you would like to desire that the beams inside the pipe deviate by no more than  $90^\circ$  from horizontal inside the pipe.

From equation (8), we see that the angle from the horizontal is given by

$$\theta' = \arcsin \frac{h}{B} = \arcsin \frac{\frac{h}{n_1}}{\frac{h}{n_2}}; \quad \frac{h}{B} = \frac{n_1}{n_2}.$$

$$|90^\circ \text{ ends} - 0^\circ \text{ ends}| \geq |\arcsin \frac{n_1}{n_2} - \arcsin \frac{n_1}{n_2}|.$$

This inequality is satisfied by  $n_1/n_2$  between 1.004 and 1.01.

#### Example 3:

You have a rod of 1 cm diameter spheres of index of refraction  $n_1$  surrounded by a fluid of index of refraction  $n_2$ . You wish to focus a laser beam to a 1 cm diameter through the rod, keeping the critical region on the spheres less than 0.01 cm. Using equations (10) and (11), it can be immediately seen that  $n_1/n_2$  must be between 1.001 and 1.002.

It is appropriate for this example to consider distortion of the phase as the beam propagates. The maximum phase difference between that part of the beam that encounters a sphere and that part that bypasses the sphere is  $2\pi(n_1 - n_2)L$ . This makes a thick lens of focal length approximately  $L$  (see Reference 1):

$$P \approx \frac{1}{L} \frac{n_1 - n_2}{n_2} \quad (11)$$

If the propagation distance is to be 1 cm and there is the possibility of lengths of the beam must be kept much larger than the propagation distance. If the propagation distance is 1 cm, and there is the possibility of intersecting several spheres, the "thick lens" approximation to the focal length is  $L \approx \frac{1}{P} \approx \frac{n_2}{n_1 - n_2}$ . This condition gives a result comparable to just considering critical angles.

#### PRACTICAL CONSIDERATIONS

There are many commercial devices available to measure the index of refraction of a fluid. However, there are no devices known to the authors that will measure the index of refraction of a solid. We have found an immersion method that is quite satisfactory. A table of critical angles

and their indices of refraction is at the end of this section. A procedure for index matching is as follows:

1. Estimate the index of refraction of the solid. If there is no information from the manufacturer, the following table may help.

Material	Index of Refraction
Plexiglas (Perspex)	1.48 - 1.49
Optical Glass	1.47 - 1.55
Pyrex Glass	1.45 - 1.473

2. Find the temperature coefficient of the chosen fluid (or mixture) by measuring the index of refraction at several temperatures using a commercial refractometer.
3. Pass a laser beam (at the wavelength you want to use) through a clear container with the fluid inside. Let the beam propagate several meters to a wall (or other target). Mark the spot where the laser hits the target (see Figure 5).
4. Place the solid in the liquid and the laser beam. Note that the beam at the target has moved and/or become distorted. It is especially noticeable when the solid is moved.
5. Adjust the temperature and/or composition of the fluid until the distortion at the target is minimized. The indices of refraction are matched.

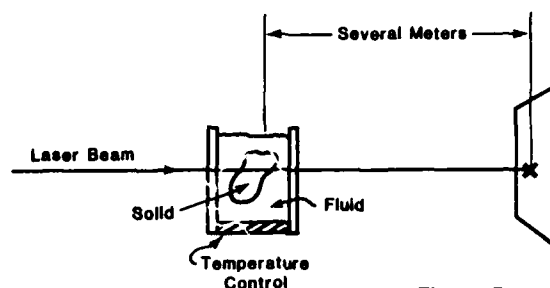


Figure 5

Fig. 5. Schematic of Index of Refraction Matching Procedure.

If the solid is a sphere or a cylinder, you can use equation (11) to estimate how well the indices match. If the beam size does not appear to have changed when the beam passes through the center of the solid, then the focal length of the equivalent lens is greater than the distance to the wall. Thus

$$n_1 - n_2 < L_w/R$$

Where ( $L_w$ ) is the distance to the target and  $R$  is the radius of the solid.

#### USEFUL SUGGESTIONS

It has been assumed all along that the solid has a single index of refraction. This is rarely true. First, the index of refraction is a function of wavelength; therefore, all matching must be done at the wavelength to be used. Note that if your refractometer does not use the wavelength of interest, you can match the index but you may not know the index of refraction at your wavelength. This is acceptable.

Second, most transparent solids have inclusions and/or index of refraction variations due to induced stresses. Inclusions (air bubbles or solids) should simply be avoided. The stresses can be greatly relieved by annealing the solid. This can be done by taking the solid up to about 80% of its melting temperature, holding it there for 10 hours or more, and then cooling to room temperature over several hours. Most glass shops have facilities to do this.

Some types of glass are made with a coating on them. This is particularly true for glasses used for reflectors or costume jewelry. These coatings usually do not have the same index of refraction as the interior solid. These coatings should be avoided.

The properties of the fluids should be checked from time to time. We have found that some fluid mixtures "age" and the viscosity and index of refraction shift noticeably over the period of a year.

If you find a suitable mixture, note the batch numbers of the components. Always use the same batch if possible. Remember, the manufacturer is not making the fluids for index matching; some "improvement" may be detrimental. Our original silicone oils were made to thicken nail polish. When we ordered a second batch (without specifying batch number), we found the oils were suddenly immiscible.

AD-A199 357

AERODYNAMIC AND RELATED HYDRODYNAMIC STUDIES USING  
WATER FACILITIES (U) ADVISORY GROUP FOR AEROSPACE  
RESEARCH AND DEVELOPMENT NEUILLY-SUR-SEINE (FRANCE)  
JUN 87 AGARD-CP-413

4/5

UNCLASSIFIED

P/G 2874

NL

==  
==

0

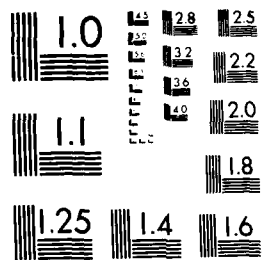
==  
==

==  
==

==  
==

==  
==

==  
==



MICROCOPY DE 1010A

Temperature control is essential if you want to keep  $|n_2 - n_1| < 0.001$ .

TABLE 2. Matched Index Materials

MATCH I:

Fluid: A mixture of:  
 Sohio's Mineral Seal Oil 58% by volume  
 Sohio's MOI-57 42% by volume  
 Solid: Optical Glass FK-3 Schott Inc.  
 Resulting properties at 31°C:  
 $n_d = 1.464$ ;  $\mu = 5.75 \text{ cp} \pm 0.2 \text{ cp}$   
 $\rho = 0.85 \text{ g/cm}^3$   
 $\nu = 6.76 \text{ cs}$

MATCH II:

Fluid: A mixture of: 73% by weight  
 Dow Corning 550 27% by weight  
 Union Carbide L42  
 Solid: Plexiglas  
 Resulting properties at 22°C:  
 $n_d = 1.4905$ ;  $\nu = 188 \text{ cs}$ ;  $\rho = 1.03 \text{ g/cm}^3$

MATCH III:

Fluid: A mixture of  
 Dow Corning 556 48.5% by weight  
 Dow Corning 550 51.5% by weight  
 Solid: Pyrex Glass Corning Glass Co.  
 Resulting properties at 28.1°C:  
 $n_d = 1.474$ ;  $\nu = 43.3 \text{ cs}$ ;  $\rho = 1.03 \text{ g/cm}^3$

MATCHED INDEX FACILITY AT C<sup>3</sup>FM-TYPICAL MEASUREMENTS

We have constructed a special index matched facility at Case Western Reserve University. The facility shown in Figure 6 is a closed flow loop with gravity head and a pump recycle. Various test sections up to two meters long can be mounted in the loop. The system has a capacity of 3.6 L/s and the flow rate can be held constant to 2%.

The special features of the system are:

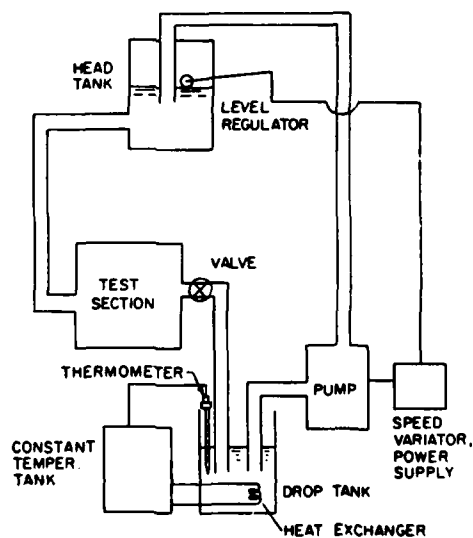


Fig. 6. Schematic of Matched Index of Refraction Flow System.

1. Splash guard in the head reservoir. This is essential to prevent small air bubbles from being entrained in the fluid. These bubbles can interfere with the laser beams and/or get trapped in the test section.
2. Temperature control in the loop. Some of the applications for the loop require a refractive index match of better than 0.01%. In addition, temperature control is necessary.
3. The system is sealed except for a vent to a fume hood. Some of the fluids used in the system are volatile and somewhat noxious.

The index matched facility has a one color two component three beam (polarization) TSI Inc. laser velocimeter mounted on it. A panoply of instrumentation is available on the system, most of which is interfaced to a computer. The usual mean moments of both components of velocity can be measured along with fluctuation spectra and cross correlations. A second laser velocimeter is planned for spatial cross correlation measurements.

This system has been used for velocity measurements:

1. inside porous media,
2. in rod bundle arrays,
3. inside surface roughness on a flat plate.

#### FLows IN POROUS MEDIA

The matched index of refraction flow system has been used to measure fluid velocities in porous media and rod bundles. The purpose of these studies is to provide a fundamental understanding of the physics of flow in these systems.

For the porous media model, results from one configuration are presented. Three dimensional velocity distributions are determined for liquids flowing through porous media. The porous media consists of glass and plexiglas rods arranged in a complex, fixed three dimensional geometry. The liquids used are water, silicone oils, Sohio MDI-57 oil and mineral seal oil. The Reynolds number based on average pore size and average pore velocity ranges from 0.16 to 700.

A model of the rod porous medium is shown in Figure 7. It is constructed of pyrex glass rods  $1.27 \pm 0.04$  cm in diameter and consists of vertical rods fixed symmetrically in a hexagonal shape. The space between these rods is filled by horizontal rods, some perpendicular to the side walls of the test section and the bulk flow direction and some at  $\pm 30^\circ$  angles to the side walls of the test section. A total of eighty-eight rods is used, thirty-three are fixed vertically by two 1.27 cm thick aluminum plates and the remaining fifty-five fill the void spaces. Wall effects are eliminated by cutting the horizontal rods and fitting them along the walls. Such an arrangement of rods needs no glue. This porous structure has an inhomogeneity in porosity in the bulk flow direction that varies from 0.33 to 0.79 [see References 2 and 3 for more details].

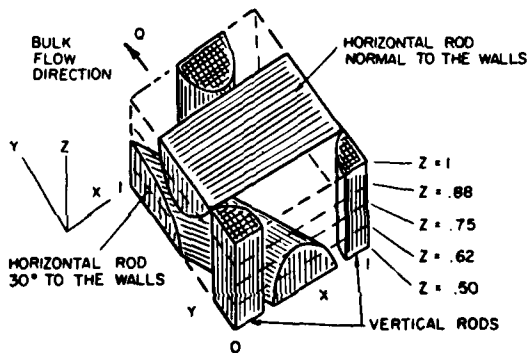


Fig. 7. Structure of cell measured in complex rod bundle structure.

Figure 8 shows the velocity component,  $U_y$ , in the bulk flow direction for  $Re = 0.8$ . Each of the plots in Figure 8 corresponds to a horizontal "slice" of the representative cell at constant  $z$ -coordinate.

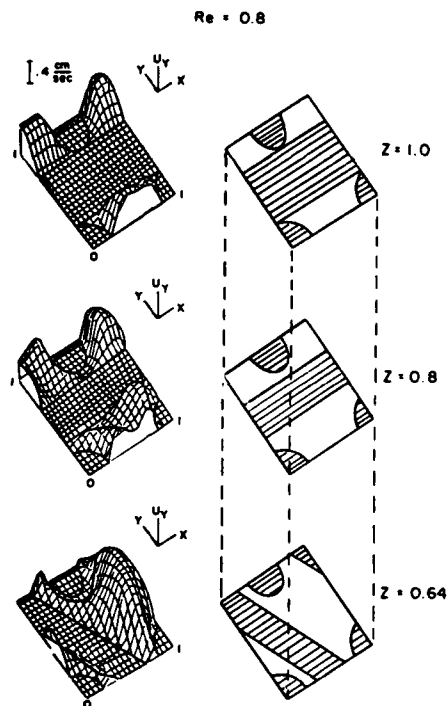


Fig. 8. Measured velocity in component in bulk flow direction  $U_y$  at  $Re = 0.8$  (see Fig. 7).

Figure 9 shows the vertical component of velocity,  $U_z$ , in the  $Z$  direction. The positive and negative areas of the velocity profiles can be distinguished.

Figure 10 shows the velocity component,  $U_y$ , in the bulk flow direction for three different  $Re$  numbers at  $Z = 0.93$ .

Figure 11 shows the vertical component of fluid velocity for the same  $Re$  number as shown in Figure 10.

Over 30,000 velocity pairs were recorded for each Reynolds number. This would not have been possible without the computer interfaced instrumentation.

#### FLows IN ROD BUNDLES

Flows in rod bundles are studied to gain a better understanding of the physical processes involved in various flow regimes. The Reynolds number based on the hydraulic diameter and average velocity in the rod bundle varies from 1 to 1500.

The staggered rod bundle arrangement used is constructed of cylindrical pyrex glass rods  $1.27 \pm 0.04$  cm in diameter. A schematic of the test section is shown in Figure 12. Seven rows are used. Wall effects are eliminated by cutting rods in half axially and placing these half rods in the appropriate row. Thirty-nine rods and six half rods are used. All of the rods are annealed to relieve any thermal stresses and to insure a uniform refractive index. The test section (see Figure 12) is constructed as a rectangular box 13.5 cm x 9.55 cm x 22 cm long. It is made of aluminum with optical quality pyrex glass windows. In practice the test section is angled so the laser beams will not have to pass through the ends of the rods. The transverse spacing  $S_n$  is fixed at 1.59 cm and the longitudinal spacing  $S_p$  is varied from 2 cm to 2.5 cm to 3 cm (see Figure 12). This is accomplished by providing the side walls of the test section with

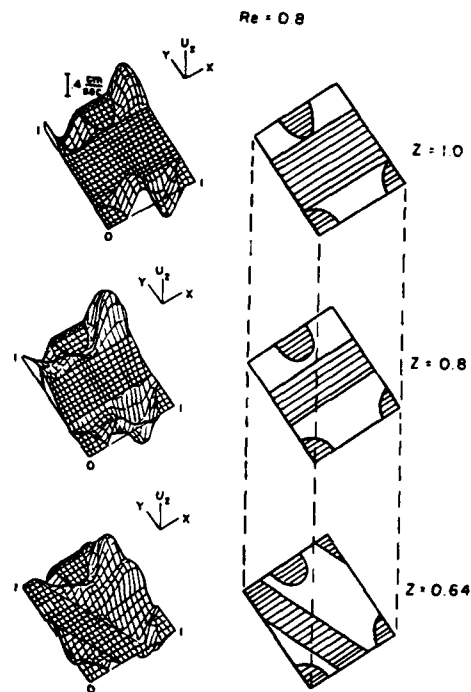


Fig. 9. Measured velocity component in vertical direction  $U_z$   $Re = 0.8$  (see Fig. 7).

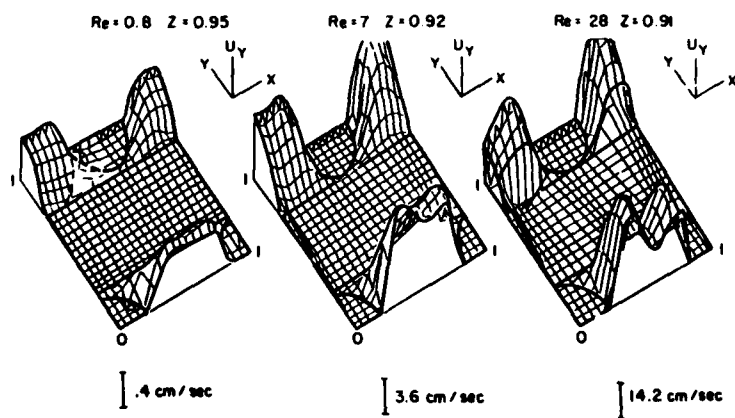


Fig. 10. Developing boundary layers and core flow for  $Re = 0.8, 7$  and  $28$ .  $U_y$  is bulk flow component.



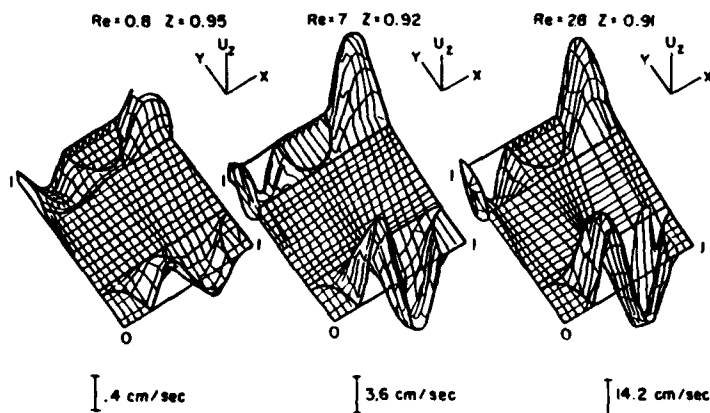


Fig. 11. Measured vertical component of velocity  $U_z$  for  $Re = 0.8, 7$  and  $28$ .

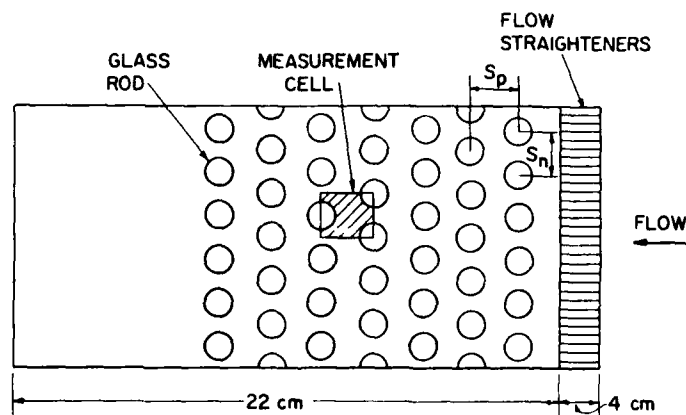


Fig. 12. Schematic of Rod Bundle Test Section. Top View.

plates of different hole spacings. Both the top and bottom walls of the test section are removable for changing the rod spacings.

Two velocity components are measured for three longitudinal spacings  $S_p = 2$  cm,  $2.5$  cm and  $3$  cm of the staggered rod bundle shown in Figure 12. One component of the velocity is in the bulk flow direction, and the other is perpendicular to the bulk flow direction. Detailed velocity measurements are made between the fourth and fifth row of rods in the cell shown in Figure 12. The cell is in the mid-plane perpendicular to the rod axis and is  $1.9$  cm  $\times$   $3$  cm. Typical flow patterns are shown in Figures 13 and 14. Figure 13 shows the direction of the velocity in the measuring cell at  $Re = 97$ . The flow is turbulent and there is evidence of backflow and eddies. Figure 14 shows the magnitude of the velocity for the same flow shown in Figure 13. Flow reversals are again evident. Figure 13 and 14 show steep gradients near walls, backflows and eddies.

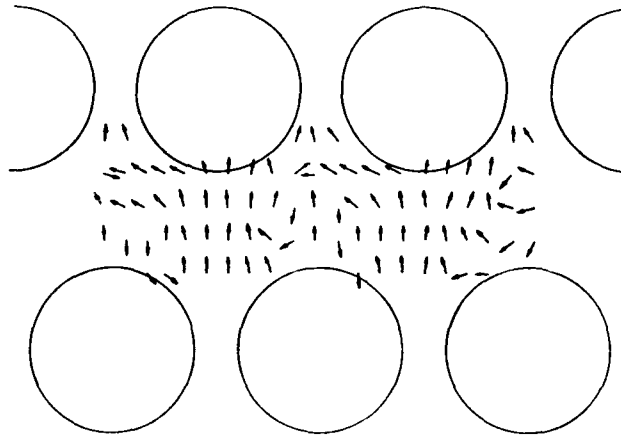


Fig. 13. Direction of velocity between the fourth and fifth rows in rods for  $S_p = 2.0\text{cm}$ ,  $Re = 97$ . The arrows indicate only velocity direction.

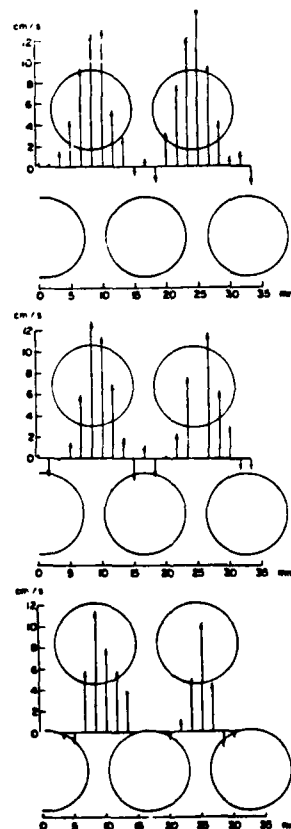


Fig. 14. Magnitude and position of the velocity for the flow shown in Fig. 13.  $S_p = 2.0\text{ cm}$ ,  $Re = 97$ . The flow is between the fourth and fifth row of rods

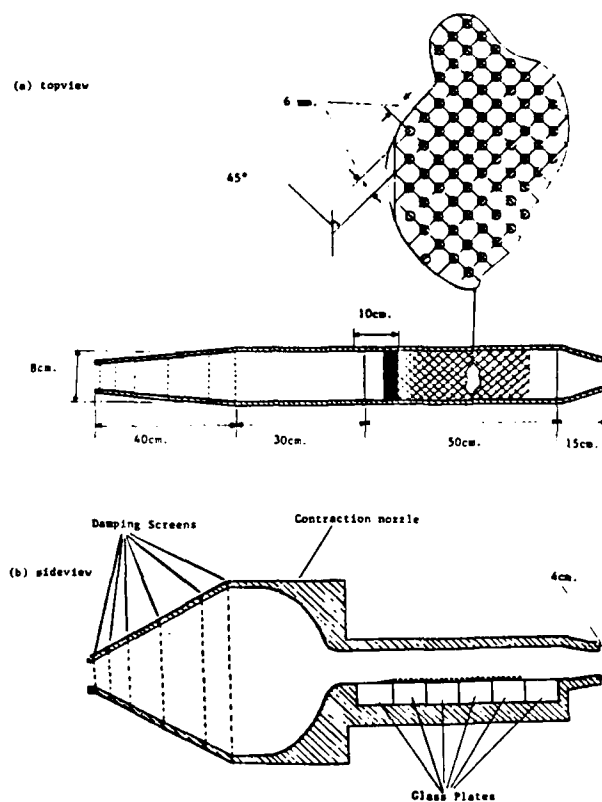


Fig. 15. Schematic of the test section for boundary layer studies. Patterns of distributed roughness is shown in (a) The turbulence intensity of tunnel is less than 0.03

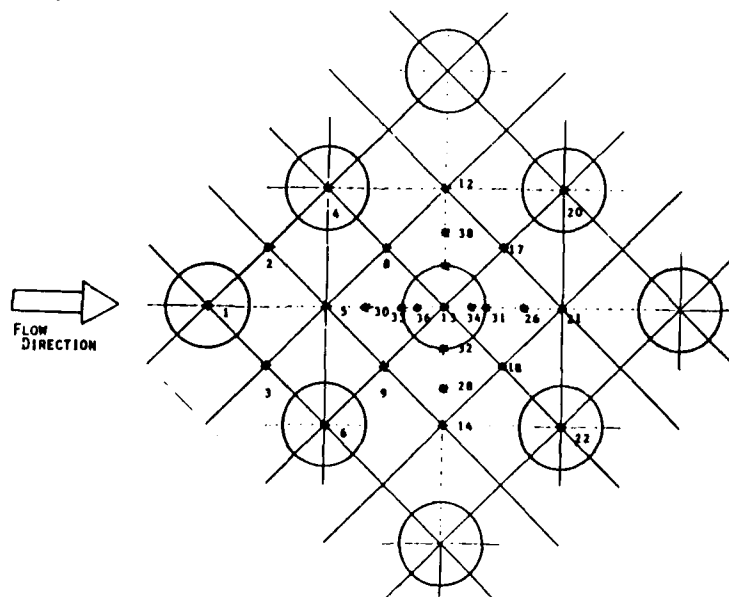


Fig. 16. Schematic of roughness indicating measurement locations.

# FLOWS INSIDE AND ABOVE DISTRIBUTED ROUGHNESS IN BOUNDARY LAYERS

The purpose of this study is to obtain a better understanding of the effects of distributed roughness on the transition from laminar to turbulent flow in the boundary layer on a flat plate. The roughness is modeled as a two dimensional array of 3 mm diameter glass beads arranged in a square grid pattern aligned  $45^\circ$  to the flow, as shown in Figure 15. The beads are affixed to a flat glass plate, which forms the bottom wall of a flow channel 40 mm high by 80 mm wide as shown in Fig. 15. The mean and fluctuating streamwise and vertical velocity components are measured using the C<sup>3</sup>FM matched index of refraction flow system.

Figure 16 shows a plan of the roughness and indicates various locations where two component velocity profiles are measured. The velocity vector profiles are shown in Figs. 17-19 and the corresponding single component vorticity contours are shown in Figs. 20-22. These profiles are for a plane passing through locations #1, #5, #30, #33, #36, #13, #34, #31, #26, and #21 as shown in Figure 16. See Ref. 7 for more details.

The data was processed using the Quantitative flow Visualization, QFV, program developed by Tjan and Dybbs [8]. The resulting velocity vector plots are shown in Figs. 17-19. These plots are for laminar flow  $Re_\delta = 160$ , transitional flow  $Re_\delta = 315$  and post transitional flows. The results show the presence of vortical structures within the roughness layer.

Single component of vorticity contour plots are shown in Figs. 20-22. The purple regions are of high vorticity and the white regions are of low vorticity.

## DISCUSSION AND CONCLUSIONS

The purpose of this paper is to present the rationale and techniques for index of refraction matching along with some example measurements. While the experimental techniques are emphasized, the fluid mechanical results obtained from these measurements provide important new insights to each of the flows. These results are:

## FLOW IN POROUS MEDIA

The results of the measurements indicate that there are four flow regimes in a porous medium.

1. The Darcy or creeping flow regime where the flow is dominated by viscous forces and the exact nature of the velocity distribution is determined by local geometry. This type of flow occurs at  $Re < 1$ . At  $Re \approx 1$ , boundary layers begin to develop near the solid boundaries of the pores.
2. The inertial flow regime. This initiates at  $Re$  between 1 and 10 where the boundary layers become more pronounced and an "inertial core" appears. The momentum defect due to the solid surface has not penetrated to the center of an interstitial space. "Core" flow refers to flows where the inertial aspects of the flow appear to dominate the viscous aspects. The developing of these "core" flows outside the boundary layers is the reason for the nonlinear relationship between pressure drop and flow rate. As the  $Re$  increases, the "core" flows enlarge in size and their influence becomes more and more significant on the overall flow picture. This steady nonlinear laminar flow regime persists to a  $Re \approx 175$ .
3. An unsteady laminar flow regime in the Reynolds number range of 175 to 300. At a  $Re \approx 175$ , the first evidence of unsteady flow is observed in the form of laminar wake oscillations in the pores. These oscillations take the form of traveling waves characterized by distinct periods, amplitudes and growth rates. In this flow regime, these oscillations exhibit preferred frequencies that seem to correspond to specific growth rates. Vortices form at  $Re \approx 250$  and persist to  $Re \approx 300$ .
4. A highly unsteady and chaotic flow regime, a turbulent flow regime for  $Re > 300$ .

These results indicate new parameters are important for the understanding of transport phenomena in porous media. In particular a new characteristic length, the passage length, is important in the Darcy and inertial flow regimes, and the Stokes number is important in the unsteady laminar flow regime. These parameters have been used to develop new models for pressure drop and heat transfer in porous media [see References 2-5]

## FLOWS IN ROD BUNDLES

These results are used to gain a better understanding of low  $Re$  number flows in rod bundles. In particular, the various flow regimes are characterized and a prediction of the onset of back-flow is made as a function of  $Re$  number and spacing. These results have important implications for low Reynolds number heat exchangers. See Reference 6 for more details.

## FLOW INSIDE AND ABOVE DISTRIBUTED ROUGHNESS IN BOUNDARY LAYERS

The results of these measurements provide important insights as to the mechanism of boundary layer transition in the presence of roughness. The interpretation of the flow measurements shows:

1. The velocity profiles in the presence of the roughness can be divided into two regions
  - A. An outer region from  $1 - 1\frac{1}{2}$  roughness heights to the outer edge of the boundary layer (outside of the roughness), and
  - B. An inner region from the wall to  $1 - 1\frac{1}{2}$  roughness heights.

For each type of boundary layer the outer region profiles are identical. The inner region profiles differ depending on  $Re_k$  and their relative position to a roughness element. For example, for the boundary layer at the beginning of transition the outer region profile is laminar ( $H=2.35$ ) while both the inner region  $u$  and  $v$  velocity profiles are significantly different from those found in the inner region of the laminar boundary layer (see Figs. 17-19).

2. The mean inner region velocity profiles (both  $u$  and  $v$ ) show a transfer of high momentum fluid from the outer region into the inner region along a plane going through the sides of the roughness. These profiles also show a transfer of low momentum fluid from the inner region into the outer region along a plane going through the center of the roughness. These momentum transfers intensify in approaching the transition region. In addition a separation region of one roughness diameter was observed behind the roughness element in the boundary layer near the beginning of transition.
3. There is no evidence of Tollmien-Schlichting instability waves in the flow. Near the beginning of transition a single frequency oscillation of  $18.75 \pm 1.25$  Hz was measured in both  $u'$  and  $v'$ . While maintaining the same narrow band frequency content, this oscillation amplified rapidly as it moved downstream. When regarded as a disturbance of  $18.75 \pm 1.25$  Hz frequency, the corresponding nondimensionalized frequency  $[B_v/U_0^2] = 1017 \times 10^{-6}$  is well above the neutral stability boundaries for infinitesimal disturbances in the boundary layer. Considering the narrow band, constant frequency content of this oscillation, its high non-dimensionalized value and the subcritical thickness Reynolds number of the boundary layer, it is unlikely that it is a Tollmien-Schlichting instability wave.

The results of these measurements suggest that a possible mechanism for transition under the conditions studied is similar to that observed by Mochizuki [9-10] for a single spherical element. In Mochizuki's experiments hairpin and horseshoe vortices are observed. The hairpin vortices appear as a spiral pair behind the sphere and the horseshoe vortices appear in front and to the side of the sphere.

In this work the general upward movement of the flow along an axis in the downstream direction going through the center of the roughness elements, and the general downward movement of the flow in an axis in the downstream direction going through the sides of the roughness elements (see Fig. 16), may indicate a pair of vortices generated behind the roughness and rotating in the same direction as the hairpin vortices observed by Mochizuki, flanked by the weak horseshoe vortices due to the vorticity upstream of the roughness element.

For the distributed roughness studied the hairpin vortices are stronger than the horseshoe vortices. The hairpin vortex energy comes from the downwash of the flow from the high velocity fluid at the top of the roughness (high momentum region) while the horseshoe vortex energy comes from the stagnation of the fluid in front of the roughness element (low momentum region). As is the case with Mochizuki's observations, the hairpin vortices generated behind the roughness lift up and penetrate the boundary layer. The contributions of the downstream roughness elements would thus increase the strength of the vortices toward the eventual transition.

The single frequency oscillation measured could be attributed to shedding of these hairpin vortices, which appear at an  $Re_k = 315$ . As a comparison with the work of Mochizuki [9-10] and Gupta [11] for a single spherical roughness element, the Strouhal number based on the velocity at the roughness height of the undisturbed laminar profile and the Strouhal number based on velocity at roughness height at point 30 in the distributed roughness was calculated. These numbers were  $0.08 \pm 0.005$  and  $0.23 \pm 0.015$  respectively. They are in the same range as those found by Mochizuki and Gupta.



Fig. 17  
Laminar Boundary Layer

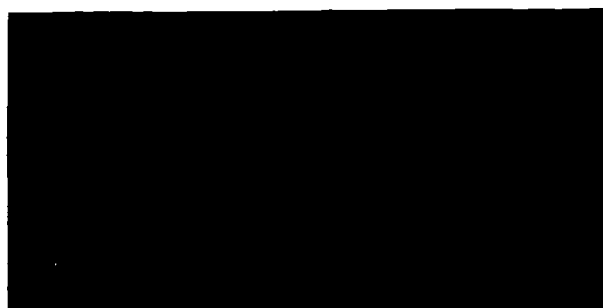


Fig. 18.  
Transitional Boundary Layer



Fig. 19.  
"Turbulent" Boundary Layer

Figs. 17-19. Vector velocity plots of flow within distributed roughness in laminar transitional and post transitional ("turbulent") boundary layers. These plots are of two velocity components in the mid-plane (see Fig. 16) of a typical roughness structure. The plots were constructed using a Quantitative Flow Visualization Scheme (QFV).

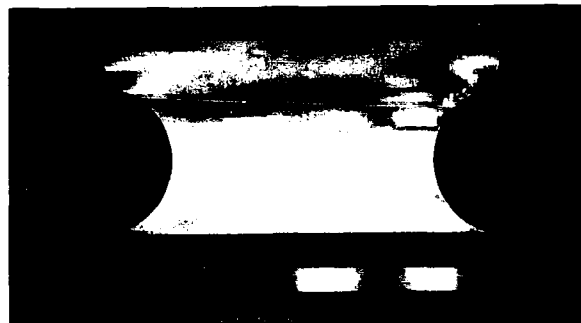


Fig. 20.  
Vorticity map of laminar boundary layer.

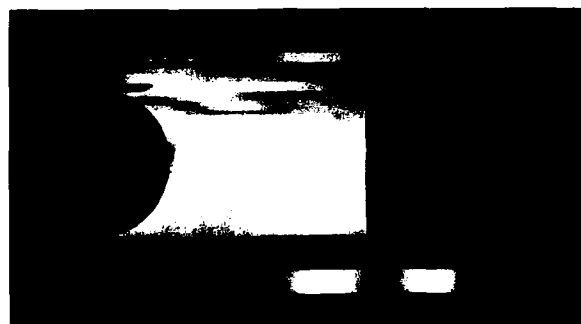


Fig. 21.  
Vorticity map of transitional boundary layer.



Fig. 22.  
Vorticity map of turbulent boundary layer.

Figs. 20-22. Single vorticity contour plots for corresponding vector plots of Figs. 17-19 in the mid-plane of the roughness (see Fig. 16) for laminar transitional and post transitional ("turbulent") boundary layers. These plots were constructed using a Quantitative Flow Visualization Scheme (QFV).

## REFERENCES

1. Jenkins, Frances A. and White, E. Harvey, "Fundamentals of Optics, 3rd ed. McGraw Hill Book Co. in New York, New York, 1967.
2. Rosenstein, N.D., Dybbs, A. and Edwards, R.V., "Non-Linear Laminar Flow in A Porous Medium," Ph.D. Thesis, Case Western Reserve University, 1980.
3. Dybbs, A. and Edwards, R.V., "A New Look at Porous Media Fluid Mechanics - Darcy to Turbulent", and invited keynote paper at the NATO Advanced Study Institute on Mechanics of Fluids in Porous Media, 1982. Also published in Fundamentals of Transport Phenomena in Porous Media, eds. J. Bear, M.Y. Corapcioglu and M. Nijhoff, Netherlands, 1984.
4. Dybbs, A. and Edwards, R.V., "An Index Matched Flow System For Measurements of Flow in Complex Geometries", in Laser Anemometry in Fluid Mechanics pp. 171-181, ed. D.F.G. Durao, Lodon 1984.
5. Edwards, R.V. and Dybbs, A. "Refractive Index Matching for Velocity Measurements in Complex Geometries", TSI Quarterly, Volume X, Issue 4, October - November 1984.
6. Nowshirivani, S.A., Dybbs, A., Edwards, R.V. and Farrokhalaei, R., "Velocity Measurements in Rod Bundles", in Proceedings International Symposium on Applications of Laser-Doppler Anemometry to Fluid Mechanics, ed. D.F.G. Durao, 1982.
7. Tadjfar, M., Reshotko, E., Dybbs, A. and Edwards, R.V., "Velocity Measurements Within Boundary Layer Roughness Using Index Matching" in International Symposium on Laser Anemometry FED Volume 33, pp. 59-73, eds A. Dybbs and P.A. Pfund, ASME press (book #G00328).
8. Tjan, W. and Dybbs, A., "Quantitative Flow Visualization for Laser Anemometry" Third International Symposium on Applications of Laser Anemometry to Fluid Mechanics, ed D.F.G. Durao, 7-9 July 1986, Lisbon.
9. Mochizuki, M., "Smoke Observation on Boundary Layer Transition Caused by a Spherical Roughness Element", J. of the Phys. Soc. of Japan, Vol. 16, No. 5, 1961.
10. Mochizuki, M., "Hot-wire Investigations of Smoke Patterns caused by Spherical Roughness Element". Natural Science Report, Ochanomizu University, Tokyo, Japan, 1961.
11. Gupta, A.K., "Some Observations in the Wake of a Small Vertical Cylinder Attached to a Flat Plate", Phys. of Fluids, Volume 23, No. 1, January 1980.

## ACKNOWLEDGEMENTS

The authors would like to thank their graduate students, Dr. Rosenstein, Dr. Farrokhalaei, Mr. Bilardo, Mr. Nowshirvani, Mr. Tadjfar and Mr. Tjan for their contributions to this work. Also, we appreciate the useful discussions with our colleagues. The partial financial support of the National Science Foundation through grant #CME 79-13389, the office of Naval Research through grant #N00014-84k-0294 and the support of the Case Center for Complex Flow Measurements, C<sup>3</sup>FM, is appreciated.



MESURES EN TUNNEL HYDRODYNAMIQUE  
PAR METHODE ELECTROCHIMIQUE

C. TOURNIER - P. FLORENT  
Laboratoire de Mécanique des Fluides  
Université de Valenciennes  
59326 VALENCIENNES - FRANCE

RESUME

Cet exposé présente la méthode polarographique de mesure du frottement pariétal. Cette méthode permet de faire dans un liquide approprié des mesures en écoulement tridimensionnel et instationnaire sans apporter de perturbations. Pour la mise en oeuvre, un canal hydraulique de grande capacité a été conçu ( $Re = 1,5.10^6$ ). Il est entièrement réalisé en matériaux électriquement neutres et chimiquement inertes.

Des exemples de mesures par la méthode polarographique sont enfin donnés. Ils ont été choisis pour mettre en évidence l'intérêt de cette méthode dans des cas typiques d'écoulements fortement tridimensionnels ou instationnaires. La possibilité de mesure en transfert de masse est aussi présentée.

I. INTRODUCTION

La difficulté essentielle du traitement des couches limites tridimensionnelles réside dans la connaissance des profils de vitesse, par rapport à la direction locale de l'écoulement extérieur. L'étude expérimentale de la configuration des lignes de courant pariétales est une méthode très puissante pour analyser la validité des traitements mathématiques qui sont appliqués aux écoulements tridimensionnels, soit comme conséquence des traitements classiques, soit pour utiliser des calculs dans un repère triplement orthogonal à la paroi. En effet le repère généralement utilisé est basé sur les lignes de courant de l'écoulement extérieur et la normale à la surface. Ce repère n'est quasi-orthogonal que pour les faibles courbures de la paroi et des couches limites de faible épaisseur.

Les techniques de visualisation sont alors d'un emploi assez général. Cependant lorsque l'écoulement n'est pas permanent, les lignes de courant ne se confondent plus avec les trajectoires des marqueurs. D'autre part, lorsque l'écoulement devient turbulent, les mouvements aléatoires de petite échelle et l'effet de diffusion qui en résulte, viennent encore compliquer l'interprétation des clichés. Les techniques de visualisation pariétales sont, de plus, perturbatrices à cause d'accumulation en paroi ou de granulométrie trop importante.

L'intérêt de la technique électrochimique que nous utilisons est de fournir directement des valeurs instantanées du frottement pariétal. Ces valeurs sont indépendantes de l'histoire antérieure des particules de fluide. Cette technique permet également, par des méthodes de traitement de signal appropriées, de reconstituer les configurations instantanées de l'écoulement, indépendamment des perturbations locales introduites par la turbulence.

Le canal hydraulique que nous avons conçu et réalisé, permet d'associer sur une même installation les techniques classiques de visualisation, la technique polarographique de mesure instantanée du frottement pariétal et la vélocimétrie LASER.

Nous rappelons dans un premier temps les principes de la polarographie. Ensuite nous décrirons le canal hydraulique et nous terminerons par des exemples d'études menées par cette technique.

II. METHODE POLAROGRAPHIQUE

La méthode de mesure de frottement pariétal que nous utilisons est dérivée d'une méthode d'analyse électrochimique bien connue : la polarographie qui est basée sur la mesure du coefficient de transfert d'une électrode en régime de diffusion contrôlée.

Pour un système REDOX en présence d'une électrode inattaquable dans un fort excès d'électrolyte indifférent, la réaction de réduction a lieu au niveau de l'électrode.



Si cette réaction est suffisamment rapide la concentration de l'ion actif est nulle à la surface de l'électrode et l'apport de courant est uniquement limité par le déplacement des ions au sein de la solution, déplacement qui se fait par diffusion et par convection. Ainsi les courbes de polarisation présentent un palier qui ne dépend que des conditions hydro-dynamiques au voisinage de l'électrode. (Figure 1). Ce palier est régi par l'équation de la diffusion contrôlée :

$$\frac{\partial C}{\partial t} + \vec{V} \cdot \vec{\text{grad}} C = DC \quad (2)$$

avec les conditions aux limites de concentration nulle  $C=0$  sur l'électrode et  $\frac{\partial C}{\partial Y} = 0$  sur les parois inertes. ( $D$  est le coefficient de diffusion de l'espèce active).

Dans la méthode polarographique, ces conditions hydrodynamiques en général complexes sont fixées une fois pour toute, et la hauteur du palier permet d'identifier l'espèce ionique.

De nombreux travaux en régime de diffusion contrôlée ont été réalisés ensuite par des électrochimistes pour étudier le courant limite, l'effet de la température ou les coefficients de diffusion des solutions, mais les électrodes utilisées sont de grandes dimensions et ne permettent que des mesures de coefficient de transfert moyen. L'interprétation des résultats est alors très délicate car toutes les conditions hydrodynamiques ne sont pas explicitées et les formules déduites des expériences ne font pas apparaître les paramètres importants.

Inversement les résultats obtenus par voie théorique sont difficilement comparables aux résultats expérimentaux faute de pouvoir reproduire correctement les mêmes conditions hydrodynamiques.

### 1. Fondements métrologiques

Le coefficient de transfert d'une électrode d'aire  $A$  :  $K = \frac{D}{4C_0} \iint \left( \frac{\partial C}{\partial y} \right)_{y=0} dA$  est déterminé à partir de l'équation (2). Il dépend en général d'une infinité de variables qui sont les vitesses dans tout le champ de diffusion. Inversement à partir d'une mesure du coefficient de transfert il est impossible d'en déduire ces variables qui sont les paramètres physiques à mesurer. Pour un usage métrologique, il faut faire correspondre autant de signaux que de paramètres physiques.

Cette constatation ne fut faite qu'en 1962 par l'équipe du Professeur HANRATTY de l'Université de l'Illinois. L'apport fondamental fut fait par REISS et HANRATTY [1] qui, constatant la très faible épaisseur de couche limite de diffusion vis-à-vis de celle de la couche limite dynamique, montrent que l'on peut réduire le nombre de paramètres physiques en utilisant des micro-électrodes.

Considérons une électrode affleurant à la paroi supposée chimiquement inerte. Le champ des vitesses au voisinage de la paroi peut-être développé perpendiculairement à la paroi selon la formule de TAYLOR. ( $x$  et  $z$  sont dans le plan tangent à la paroi).

$$U(x,y,z,t) = y.S_x(x,z,t) + \frac{y^2}{2!} \frac{\partial S_x}{\partial y}(x,z,t) + \dots$$

$$W(x,y,z,t) = y.S_z(x,z,t) + \frac{y^2}{2!} \frac{\partial S_z}{\partial y}(x,z,t) + \dots$$

(3)

et d'après l'équation de continuité :

$$V(x,y,z,t) = -\frac{y^2}{2} \left[ \frac{\partial S_x}{\partial x} + \frac{\partial S_z}{\partial z} \right] - \frac{y^3}{6} \left( \frac{\partial^2 S_x}{\partial x \partial y} + \frac{\partial^2 S_z}{\partial z \partial y} \right) + \dots$$

En dehors des points de frottement nul, pour une électrode suffisamment petite l'épaisseur de la couche limite de concentration est suffisamment faible pour pouvoir se limiter au premier terme du développement de TAYLOR. Ainsi le champ tridimensionnel de vitesse ne dépend plus que de deux champs bidimensionnels  $S_x(x,z,t)$  et  $S_z(x,z,t)$  dans toute la couche limite de concentration.

Si de plus le champ du gradient de vitesse dans la couche limite de concentration est homogène, c'est-à-dire si les électrodes sont de petites dimensions vis-à-vis des longueurs d'ondes des plus petites perturbations spatiales du champ de vitesses et si l'amplitude de ces perturbations relativement à la valeur ponctuelle au centre de l'électrode est petite, il est possible de négliger les variations spatiales de  $S_x$  et  $S_z$  relativement à leur valeur au centre de l'électrode. Ainsi le problème ne dépend plus que de deux paramètres  $S_x(t)$  et  $S_z(t)$  (Figure 2).

$$\begin{cases} U = y.S_x(t) \\ W = y.S_z(t) \end{cases} \quad (4)$$

L'équation (2) s'écrit :

$$\frac{\partial C}{\partial t} + y \frac{\partial C}{\partial x} + \frac{\partial C}{\partial z} = \frac{1}{(S_x)^{2/3}} \left( \frac{\partial^2 C}{\partial x^2} + \frac{\partial^2 C}{\partial z^2} \right) + \frac{\partial^2 C}{\partial y^2} \quad (5)$$

en faisant le changement de variable ( $\ell$  : longueur caractéristique de l'électrode).

$$\begin{aligned} \bar{C} &= \frac{C}{C_0}, \quad \bar{x} = \frac{x}{\ell}, \quad \bar{z} = \frac{z}{\ell}, \quad \bar{y} = S_x^{1/3} \frac{y}{\ell}, \quad \bar{n} = n \cdot \frac{\ell^2}{D} \cdot \frac{1}{S_x^{2/3}} \\ S_x &= \frac{S_x \ell^2}{D}, \quad S_z = \frac{S_z \ell^2}{D}, \quad K = \frac{S_x}{A} \int \frac{\partial C}{\partial y} dA \end{aligned} \quad (6)$$

et les conditions aux limites s'écrivent :

$$\begin{cases} \bar{C} = 0 \text{ sur l'électrode} \\ \bar{C} = 1 \text{ au loin} \\ \frac{\partial \bar{C}}{\partial \bar{y}} = 0 \text{ sur les parois inertes} \end{cases}$$

Si le gradient pariétal  $\bar{S}_x$  est suffisamment grand, il est possible de négliger la diffusion longitudinale et pour des électrodes d'allongement grand dans la direction  $z$ , l'équation (5) se réduit à :

$$\frac{\partial \bar{C}}{\partial \bar{t}} + \bar{y} \frac{\partial \bar{C}}{\partial \bar{x}} = \frac{\partial^2 \bar{C}}{\partial \bar{y}^2}$$

et le coefficient de transfert est [1]

$$K = 0,807 |S_x|^{1/3}$$

$S_x$  intervient par sa valeur absolue car l'électrode n'est pas sensible à la direction de l'écoulement (Figure 3).

Cette solution asymptotique est, selon LING [2] valable dès que  $S_x = 5000$  ce qui est presque toujours vérifiée car le nombre de Schmitt  $S_c = \frac{V}{D}$  est grand ( $S_c = 1000$ ).

## 2. Mesure en écoulement tridimensionnel.

Plusieurs arrangements d'électrodes ont été proposés pour faire des mesures en écoulements tridimensionnels [3]. Nous développons la technique des électrodes scindées introduites par PY [4]. Cette technique permet de faire des mesures en grandeur et direction même dans des zones fluctuant très largement.

La surface active de la micro-électrode étant de forme quelconque, et le champ de gradient de vitesse au voisinage étant homogène, le champ de concentration est donné par l'équation de la diffusion contrôlée (5) et le coefficient de transfert  $K_i$  d'une surface quelconque  $A_i$  de l'électrode est :

$$K_i = \frac{\dot{S}x^{1/3}}{A} \iint_{A_i} \frac{\partial \dot{C}}{\partial y_{y=0}} dA_i \quad (9)$$

Remarquons que ces coefficients de transfert sont additifs. Si on peut négliger les termes de diffusion tangentielle, c'est à dire si le gradient pariétal  $\sqrt{(\dot{S}x^2 + \dot{S}z^2)}$  est suffisamment grand, l'équation se réduit à :

$$\frac{\partial \dot{C}}{\partial t} + y \frac{\partial \dot{C}}{\partial x} + y \frac{\partial \dot{C}}{\partial z} \cotg \alpha = \frac{\partial^2 \dot{C}}{\partial y^2} \quad (10)$$

Cette équation définit un champ de concentration universel, indépendant du gradient pariétal, donc le terme  $\iint_A \frac{\partial \dot{C}}{\partial y} dA$  ne dépend que de la direction de l'écoulement pour une géométrie d'électrode donnée.

Nous utilisons des électrodes dont la surface active est formée de deux parties symétriques par rapport à un axe électriquement neutre (Figure 4).

$$\begin{aligned} K_1 + K_2 &= \frac{\dot{S}x^{1/3}}{A} \int_A \left( \frac{\partial \dot{C}}{\partial y_{y=0}} \right) dA \\ K_1 - K_2 &= \frac{\dot{S}x^{1/3}}{A} \left[ \int_{A_1} - \int_{A_2} \left( \frac{\partial \dot{C}}{\partial y_{y=0}} \right) dA \right] \\ \left[ \begin{aligned} \frac{K_1 - K_2}{K_1 + K_2} &= F(\sin \alpha) \\ \frac{K_1 + K_2}{\dot{S}x^{1/3}} &= g.G(\sin \alpha) \end{aligned} \right] \quad (11) \end{aligned}$$

La fonction  $K_1 - K_2 / K_1 + K_2$  ne dépend que de la géométrie des électrodes. Le coefficient de transfert de l'électrode entière est :  $K_1 + K_2 = g.G(\sin \alpha) \dot{S}^{1/3}$

La fonction  $G$ , elle aussi, ne dépend que de la géométrie de l'électrode.  $K_1 + K_2$  permet donc de déterminer le gradient pariétal une fois connue sa direction par  $K_1 - K_2 / K_1 + K_2$ .

Remarquons que le fait de ne pas avoir un axe neutre infiniment mince n'a aucune importance pratique car  $\iint_A \left( \frac{\partial \dot{C}}{\partial y} \right) dA$  ne dépend que de la géométrie des électrodes et peut facilement être déterminée par étalonnage.

La figure 4 donne un exemple de courbe d'étalonnage pour une électrode 2 fois (0,1 x 0,5 mm).

## 3. Réponse en fréquence

Les fluctuations du champ des vitesses entraînent l'existence des fluctuations du champ de concentration et des coefficients de transfert. Si on suppose que l'écoulement est permanent en moyenne, il est alors possible de faire la décomposition classique de chaque grandeur ( $G$ ) en faisant apparaître les termes moyens ( $\bar{G}$ ) et les termes fluctuants ( $g$ ).

En hypothèse quasi stationnaire il est possible de linéariser la réponse des sondes. Les deux cas pratiques importants sont (figure 5) :

$\alpha = \frac{\pi}{2}$  : l'écoulement moyen est perpendiculaire à l'axe neutre de l'électrode.

$$\frac{\sqrt{\frac{\dot{S}z^2}{S}}}{S} = \frac{\sqrt{\frac{(k_1 + k_2)^2}{\bar{K}_1 + \bar{K}_2}}}{\bar{K}_1 + \bar{K}_2} = \frac{\sqrt{\frac{(k_1 - k_2)^2}{\bar{K}_1 - \bar{K}_2}}}{\bar{K}_1 - \bar{K}_2}$$

$\alpha = 0$  : l'écoulement moyen est selon l'axe neutre de l'électrode.

$$\frac{\sqrt{\frac{sz^2}{S}}}{\bar{S}} = \frac{1}{P} \sqrt{\frac{(k_1 - k_2)^2}{\bar{K}_1 + \bar{K}_2}}$$

avec  $P = \left( \frac{\partial F}{\partial \sin \alpha} \right)_{\alpha=0}$

Inertie introduite par les sondes :

Lorsque les fluctuations du champ des vitesses sont petites, il est possible de linéariser l'équation de la diffusion. Le principe de superposition s'applique alors, le champ de perturbation  $c$  provoqué par  $s_x$  et  $s_z$  est la somme des champs de perturbations  $c_x$  et  $c_z$  qui seraient provoqués respectivement par  $s_x$  et  $s_z$  seul.

$c_x$  et  $c_z$  sont alors solution des deux équations :

$$\frac{\partial c_x}{\partial t} = \frac{1}{S_x^{2/3}} \left( \frac{\partial^2 c_x}{\partial x^2} + \frac{\partial^2 c_x}{\partial z^2} \right) + \frac{\partial^2 c_x}{\partial y^2} - \left[ y \frac{\partial c_x}{\partial x} + \frac{s_x}{S_x} y \frac{\partial c}{\partial x} \right] \quad (12)$$

$$\frac{\partial c_z}{\partial t} = \frac{1}{S_x^{2/3}} \left( \frac{\partial^2 c_z}{\partial x^2} + \frac{\partial^2 c_z}{\partial z^2} \right) + \frac{\partial^2 c_z}{\partial y^2} - \left[ y \frac{\partial c_z}{\partial x} + \frac{s_z}{S_x} y \frac{\partial c}{\partial z} \right] \quad (13)$$

L'équation (12) peut être rendue bidimensionnelle en négligeant les termes de diffusion longitudinale et transversale.

La deuxième équation ne peut pas être rendue bidimensionnelle de par la présence du terme  $y \frac{\partial c_z}{\partial x}$ , c'est pourquoi la détermination de la réponse des sondes aux fluctuations transversales nécessite exclusivement un traitement tridimensionnel [5].

La figure 6a représente la réponse fréquentielle aux fluctuations longitudinales en module et en phase.

La courbe est identique à celle obtenue dans le cas bidimensionnel par PY [6] qui a montré qu'une combinaison linéaire des signaux  $\{K_1 + K_2\} + \beta \{K_1 - K_2\}$  peut améliorer considérablement la réponse en fréquence.

La réponse aux fluctuations transversales est représentée sur la figure 6b. Elle est du même ordre que la réponse des sondes simples aux fluctuations transversales. Elle permet de prévoir désormais les limites d'utilisation des sondes.

### III. LE CANAL HYDRAULIQUE POLAROGRAPHIQUE

Pour mettre en oeuvre la technique polarographique nous avons conçu un tunnel hydrodynamique adapté.

A priori ce tunnel présente les mêmes qualités que tous les tunnels hydrodynamiques. Les principaux critères sont :

- le nombre de REYNOLDS,
- l'écoulement dans la veine (uniformité, turbulence, absence de cavitation...),
- les méthodes de visualisations,
- l'équipement de mesures disponible : Laser Doppler Anémométrie, Photogrammétrie etc...

Par rapport aux souffleries subsoniques traditionnelles les tunnels hydrodynamiques présentent toutefois quelques inconvénients liés essentiellement au confinement nécessaire de leur veine d'essais comme

- l'étanchéité indispensable de toutes les parties constitutives du tunnel,
- la protection des systèmes électriques...

On ne saurait néanmoins pas oublier qu'ils présentent des qualités tout à fait indéniables, notamment la possibilité d'associer facilement visualisations et mesures grâce à quoi le dégrossissage des problèmes aérodynamiques peut être effectué rapidement. En effet, les visualisations de mise en oeuvre plus aisée dans l'eau que dans l'air permettent une appréhension des écoulements fluides qui accélère l'orientation des recherches vers des configurations soit critiques, soit plus performantes. Signalons par ailleurs, que les tunnels permettent, compte tenu de la différence de viscosité et de masse volumique, l'utilisation de modèle plus petits et moins onéreux que ceux expérimentés dans les souffleries.

Les caractéristiques de fonctionnement du tunnel hydraulique polarographique de l'Université de VALENCIENNES sont les suivantes :

- veine de section carrée 300 x 300 mm
- vitesse supérieure à 4 m/s
- le nombre de Reynolds rapporté au côté de la veine est supérieur à  $10^6$ .

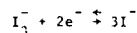
Parmi les nombreuses solutions polarographiques couramment utilisées, quelques unes sont plus

particulièrement adaptées à des usages de métrologie pariétale. Citons celles qui sont à base de ferri-cyanure, triiodure, quinone qui donnent autant de solutions que de solvants différents possibles.

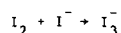
Il faut que la solution ait un comportement newtonien. La réaction chimique doit être réversible et très rapide. Elle doit donner le maximum de courant électrique pour un minimum d'ions transportés. Elle doit être stable et le polarogramme doit présenter un palier très net. Pour avoir de bonnes réponses en fréquence, le coefficient de diffusion doit être grand, sans toutefois permettre aux couches de diffusion d'être trop épaisses.

Nous avons choisi le système rédox iodure - triiodure dans une solution aqueuse d'iodure de potassium dont les principales caractéristiques polarographiques sont bien connues [7]

La réaction électrochimique est la suivante :



Le solvant est une solution à 100 grammes par litre d'iodure de potassium dans de l'eau permurée (résistivité supérieure à  $1M\Omega \times cm$ ). L'iode y est dissout à  $10^{-5}$  mole par litre environ. L'apparition de l'ion triiodure se fait en présence d'un excès d'ions  $I^-$  d'après la réaction :



La concentration en ion triiodure est largement inférieure à la limite d'apparition de la migration électrique. Les micro-électrodes de mesure et l'anode sont en platine. L'anode est de grande dimension et elle sert de référence de potentiel. Toutes les parties en contact avec le fluide autres que les électrodes doivent être électriquement neutres pour ne pas perturber les mesures. Elles doivent en outre être chimiquement inertes.

Nous avons choisi un canal à veine horizontale fonctionnant en circuit fermé à l'aide d'une hélice actionnée par un moteur (Figure 7). La géométrie des différentes parties a été définie pour optimiser la qualité de l'écoulement dans la veine d'expérience mais aussi pour réduire au maximum les volumes car l'iodure de potassium est relativement onéreux.

Les principales parties sont les suivantes :

#### Le convergent

Il a une section d'entrée circulaire et une section de sortie carrée de 300 x 300 mm. Le rapport de contraction vaut 17,1.

Il est réalisé en polypropylène toilé renforcé par un stratifié résine polyester armé de fibres de verre (figure 7).

#### La chambre de tranquillisation

Elle précède le convergent et a pour rôle d'homogénéiser l'écoulement.

La longueur est volontairement très faible pour minimiser la quantité de liquide polarographique. L'utilisation de déflecteurs s'avère indispensable (figure 8) Ils ont été optimisés par une étude préalable en soufflerie. Ils permettent une diminution sensible de la longueur de la chambre de tranquillisation et une réduction de moitié de la perte de charge singulière locale. La chambre de tranquillisation est en même matériau que le convergent. Elle se termine par un filtre en nylon et un nid d'abeille à mailles hexagonales.

#### La veine d'expérience

La veine est du type guidée de section carrée de 300 x 300 mm. Elle est réalisée en altuglas transparent et sa conception permet une visibilité intégrale sur les quatre faces (figure 9).

Sa longueur principale de 1140 mm peut être portée à 1800 mm. Des veines spéciales munies de piège à couche limite et de parois adaptables sont en cours de conception.

#### La propulsion

Le moteur à courant continu régulé de 13,25 KW entraîne une hélice quadripale réalisée en polyfluorure de vinylidène. L'étanchéité est assurée par une garniture en alumine-carbure de tungstène.

L'arbre est en acier gainé de polypropylène. Il est guidé par un palier interne en céramique et un palier externe avec roulement et butée à billes.

#### Le canal de retour

Il guide le fluide jusqu'à l'entrée de la chambre de tranquillisation. Il contient le tronçon de redressement et l'échangeur de chaleur. Les aubes directrices du redresseur convertissent les rotations induites par l'hélice. L'échangeur de chaleur réalisé en polypropylène assure une température constante du fluide.

### IV. MESURES EN TUNNEL POLAROGRAPHIQUE

#### 1. Ecoulement pariétal autour de cônes élancés à grande incidence [8]

Le travail que nous présentons a été mené grâce à l'aide de la D.R.E.T. dans un tunnel hydrodynamique de petites dimensions.

Dans un premier temps, nous avons mesuré les coefficients de transfert de sondes simples de surface active circulaire sur un cône idéal et sur un cône émoussé avec un rayon de 44 mm (figure 10).

Nous avons pu mettre en évidence plusieurs zones au comportement différencié (figures 11a et b):

Suite à la zone de couche limite proprement dite dont l'étendue azimutale diminue avec l'incidence et où les fluctuations sont très faibles, apparaît une zone où le gradient de vitesse présente un minimum très net et des fluctuations très importantes. La zone aval est caractérisée par des gradients de vitesse très intenses et des fluctuations assez importantes. Dans cette zone, apparaissent des structures gagnant en intensité avec l'incidence et lorsque l'on s'éloigne de la pointe. D'une façon générale, nous n'avons pas mis en évidence la dissymétrie particulièrement significative ; mais nous avons observé que l'instabilité de l'écoulement augmente avec l'incidence. Elle est particulièrement importante à 60°.

Le fait d'émousser la pointe permet de stabiliser les grosses structures tourbillonnaires tout en les intensifiant.

Dans un deuxième temps, nous avons déterminé les composantes transversales et longitudinales du gradient de vitesse à l'aide d'un cône muni de sondes doubles, de surface active rectangulaire (figure 12). L'évolution de la composante transversale permet de proposer une représentation schématisée de l'allure des lignes de courant au voisinage immédiat de la paroi (figure 12). Elle met en évidence la présence de nappes tourbillonnaires de plus en plus complexes quand on s'éloigne du sommet du cône, entre la zone de couche limite proprement dite et la zone "d'arrêt" aval. La composante longitudinale du gradient permet de suivre l'évolution du sens de l'écoulement aux différentes incidences. Cette composante est toujours faible, sauf dans toute la zone à l'aval de l'écoulement.

L'analyse spectrale n'a pas permis de mettre en évidence une fréquence privilégiée.

Les mesures permettent de se faire une idée globale sur l'écoulement pariétal autour d'un cône en incidence. Elles permettent en particulier une reconstitution de l'écoulement moyen. Sur la figure 13, nous avons représenté le vecteur gradient pariétal moyen de vitesse sur le cône développé en intensité et direction.

Globalement nous n'avons pas mis en évidence de dissymétrie significative des nappes tourbillonnaires expliquant des comportements aérodynamiques anormaux [9]. La cause en est peut être la forte obstruction de la veine d'expérience. (Section carrée de 150 x 150 mm par un cône dont le cylindre de base a un diamètre de 30 mm). Une étude de cet effet d'obstruction débute dans le canal de grande capacité que nous avons présenté.

## 2. Importance du positionnement du support des sondes de mesure dans les écoulements.

On sait [10] que la réponse d'une sonde anémométrique au voisinage d'une paroi dépend de la géométrie de la sonde et de l'angle  $\alpha$  fait par l'axe du support de cette sonde avec la paroi. Pour des géométries de sonde (figure 14), on note (figure 15), au voisinage de la paroi une augmentation avec cet angle de la vitesse moyenne enregistrée et une diminution de la valeur quadratique moyenne de la fluctuation turbulente. La sonde dite pariétale fournit des résultats comparables à la sonde droite inclinée à environ 10° (figure 16). Ce phénomène est dû à l'effet de sillage des broches lorsque celles-ci sont placées dans un gradient de vitesse. L'importance du gradient de vitesse dans lequel la sonde est placée peut être mis en évidence dans un jet pariétal plan, où nous avons observé le décalage des profils de vitesse avec une sonde orientée à 10° et 90°. C'est un effet de déplacement (figure 17) [11]. Dans une couche limite on a déjà remarqué [12] que la représentation de la loi logarithmique à la paroi

$$\frac{U}{U_\tau} = C \log y - \frac{U_\tau}{v} + D$$

fournit pour D une valeur qui dépend de cet angle  $\alpha$  alors que la constante C reste inchangée avec l'orientation de l'axe du support de la sonde.

La méthode polarographique nous permet de retrouver ces résultats. Nous avons reporté (figure 18) le gradient pariétal mesuré par une sonde polarographique, rapporté au gradient pariétal mesuré en l'absence de sonde. On y remarque bien l'effet de blocage de la sonde "type couche limite", l'augmentation du gradient avec la sonde droite, quand l'angle fait par son support avec la paroi augmente. Pour les angles de 45° et 90° on note que l'importance de l'effet de sillage du support et des broches a une incidence sur le gradient pariétal de vitesse même lorsque la sonde est en dehors de la couche limite.

L'utilisation de cette méthode de mesure pariétale non perturbatrice conjuguée à l'anémométrie laser permettra d'effectuer des mesures notamment dans les intractions de sillages et d'obtenir des résultats qui ne traduiront pas des erreurs expérimentales qui pourraient être réintroduites dans les modélisations.

## 3. Etude locale du transfert de masse sur un cylindre aileté

L'objectif de cette étude est la détermination de surface d'échange de chaleur à hautes performances dans les échangeurs à tubes ailetés par utilisation d'instationnarités créées par un écoulement fluctuant en direction. L'utilisation d'écoulement "battant" permet de prévoir une augmentation du transfert. La complexité des phénomènes nécessite une étude locale en deux parties :

La première partie consiste en la mesure par polarographie du gradient pariétal de vitesse, donc du frottement, sur un cylindre muni d'ailettes. La méthode polarographique permet des mesures locales en écoulement instationnaire sans perturbation.

Dans la deuxième partie nous mesurons directement le coefficient local de transfert de masse sur un cylindre aileté totalement actif. Bien que le nombre de Schmitt soit grand, il est possible de prévoir, par analogie, le transfert de chaleur [13] dans une configuration semblable pour des surfaces d'échange isothermes.

Les deux cylindres d'étude sont géométriquement identiques (figure 19). Le cylindre de mesure du frottement porte des sondes simples circulaires de diamètre 0,1 mm. Ces sondes ne mesurent donc que le module du gradient pariétal de vitesse et sont insensibles à la direction de l'écoulement. Une sonde est située sur le cylindre et d'autres sondes sont situées sur une ailette à différentes distances de l'axe.

Le cylindre de mesure du transfert de masse a une surface totalement active en platine. Les électrodes de mesure du transfert local sont situées aux mêmes endroits que pour les mesures du gradient pariétal. Elles sont formées d'une surface de platine de 0,4 mm de diamètre isolée du reste de la surface par un anneau isolant de largeur moyenne de 0,05 mm.

Pour recréer localement l'écoulement battant, c'est le cylindre qui est mis en oscillation selon son axe dans un écoulement perpendiculaire de vitesse uniforme au loin (figure 19). Le nombre de Reynolds rapporté au diamètre du cylindre est égal à 17 000. Les oscillations ont une amplitude variable de 0 à 8 mm et une fréquence de 0 à 50 Hz.

De l'étude complète [14] nous allons extraire quelques mesures typiques à titre d'exemple.

#### Mesures sur le cylindre :

La figure 20 présente l'évolution du coefficient de transfert de la sonde circulaire située sur le cylindre en fonction de l'azimut compté à partir du point d'arrêt amont. Les valeurs sont toujours positives car les sondes simples ne sont sensibles qu'au module du gradient pariétal de vitesse.

L'évolution est semblable aux mesures sur un cylindre isolé [15]. On distingue en particulier la zone de couche limite de 0 à 80° environ, la zone de décollement avec le courant de retour et la zone d'arrêt aval de grande étendue où le frottement moyen est quasi-nul.

Quand les pulsations varient de 0 à 50 Hz, on note une stabilité de la zone de couche limite. Ce résultat était prévisible malgré le caractère tridimensionnel dû à la présence des ailettes.

L'évolution notable après le point de décollement est principalement due à la mauvaise réponse des sondes simples en écoulement oscillant autour d'un frottement moyen nul.

Les mesures du transfert de masse (figure 21) montrent l'insensibilité remarquable de la zone de couche limite aux oscillations transversales. Après le décollement, le transfert qui augmente systématiquement avec la fréquence présente deux maxima, l'un à 90° environ et l'autre au point d'arrêt aval.

#### Mesures sur les ailettes :

Les mesures du gradient pariétal de vitesse sur les ailettes mettent en évidence la complexité de l'écoulement qui y est fortement tridimensionnel.

La figure 22 présente l'évolution du transfert de masse sur une ailette à 11 mm de l'axe du cylindre.

On note pour une fréquence donnée en fonction de l'azimut, une décroissance régulière du transfert sur la partie amont de l'ailette. La présence d'un pic très marqué est dû à l'interaction avec le sillage du cylindre. Quand la fréquence augmente jusqu'à 33 Hz le transfert augmente quelque soit l'azimut. On note ensuite un effet global d'amortissement pour la fréquence plus élevée. La fréquence a pour effet également de diminuer la largeur d'épanouissement du sillage du cylindre.

### V. CONCLUSION

Les quelques exemples de mesure par technique électrochimique que nous avons présentés montrent l'intérêt de cette méthode pour des études dynamiques pariétales dans des configurations fortement tridimensionnelles ou instationnaires. Les mesures directes de transfert sont aussi possibles et permettent de développer des analogies avec le transfert de chaleur. Ces analogies sont plus générales que l'analogie de Reynolds.

Cependant la mise en oeuvre est relativement compliquée car elle nécessite un liquide spécial et des installations électriquement neutres et chimiquement inertes.

Le Laboratoire de Mécanique des Fluides de l'Université de Valenciennes (France) s'est doté d'un canal hydraulique de grande capacité répondant à ces conditions.

La possibilité de faire des mesures en écoulement tridimensionnel du frottement pariétal instantané associé à des mesures par anémométrie Laser dans la masse du fluide et des visualisations par bulles d'hydrogène, font de cette installation un outil unique et très précieux.

### VI. REFERENCES

- [ 1 ] L.P. REISS, T.J. HANRATTY "An experimental study of the unsteady nature of the viscous sublayer". A.I.Ch. E. 9-p. 154 (1963).

- [ 2 ] S.C. LING "Heat-transfer characteristics of hot-film sensing element used in flow measurement".  
J. of Basic Eng. p. 629 Sept. 1960.
- [ 3 ] T.J. HANRATTY, J.A. CAMPBELL "Measurements of wall shear stress".  
In fluid Mechanics Measurements (Ed. R.J. GOLDSTEIN) HEMISPHERE (1983).
- [ 4 ] B. PY, J. GOSSE "Sur la réalisation d'une sonde polarographique sensible à la vitesse et à la direction de l'écoulement".  
C.R. Acad. Sc. Paris 269 p. 401 (1969).
- [ 5 ] C. TOURNIER, B. PY "The behaviour of naturally oscillating three-dimensional flow around a cylinder".  
J. Fluid. Mech. Vol. 85 p. 161 (1978).
- [ 6 ] B. PY "Etude tridimensionnelle de la sous couche visqueuse".  
Int. J. Heat Mass Transfer Vol. 16 p. 129 (1973).
- [ 7 ] D.P. GREGORY, A.C. RIDDIFORD "Transport to the surface of a rotating disk".  
J. Chem. Soc. London p. 3756 (1956).
- [ 8 ] A. MORTEVEILLE, C. TOURNIER "Comportement des cônes élançés à grande incidence".  
Rapport final DRET n° 83 - 1095 (1985).
- [ 9 ] AGARD "High angle of attack aerodynamics".  
Déc. 1982.
- [10] P. FLORENT, G. THIOLET "Importance de l'orientation du support de sonde à fil chaud par rapport à une paroi sur la détermination des vitesses moyennes dans une couche limite turbulente".  
C.R. Acad. Sc. Paris t. 269 Série A p. 405 (1969).
- [11] P. FLORENT, G. THIOLET "Contribution à l'étude du positionnement des fils chauds dans les écoulements".  
3ème Congrès Canadien de Mécanique CALGARY (1971).
- [12] P. FLORENT "Sur l'effet de déplacement des sondes anémométriques au voisinage des parois en fonction de leur orientation".  
C.R. Acad. Sc. Paris t. 271 Série A p. 388 (1970).
- [13] E.R. ECKERT, R.M. DRAKE "Heat and mass transfer".  
Mc. Graw-Hill N.Y.
- [14] L. DEHAY "Etude locale du transfert de masse sur un cylindre aileté".  
Université de Valenciennes - à paraître -.
- [15] C. TOURNIER "Etude de l'écoulement tridimensionnel instationnaire autour des cylindres par tribométrie électrochimique".  
Thèse d'Etat, Univ. Paris VI 1976.

#### VII. REMERCIEMENTS

Nous remercions la Région Nord - Pas-de-Calais et la D.R.E.T. qui par leur aide financière ont permis la réalisation du canal hydraulique.



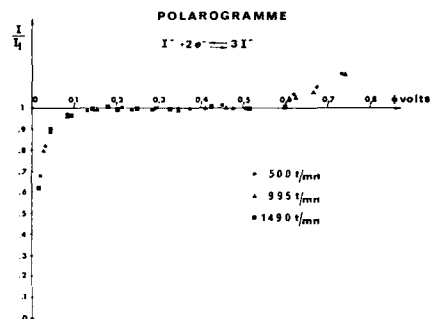


Figure 1 : Polarogramme

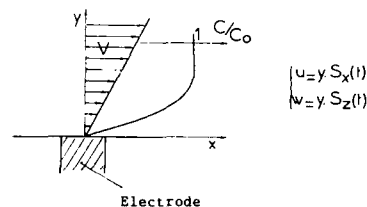


Figure 2 : Profil linéaire de vitesse

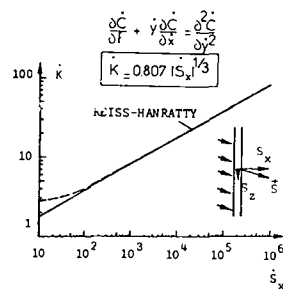
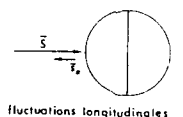
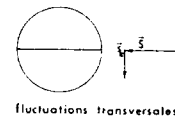


Figure 3 : Coefficient de transfert d'une électrode d'allongement infini.



$$\frac{\sqrt{S_z^2}}{S} = 3 \quad \frac{\sqrt{(k_1 + k_2)^2}}{K_1 + K_2} = 3 \quad \frac{\sqrt{(k_1 - k_2)^2}}{K_1 - K_2}$$



$$\frac{\sqrt{S_z^2}}{S} = \frac{1}{P} \quad \frac{\sqrt{(k_1 - k_2)^2}}{K_1 + K_2}$$

Figure 5 : Réponse aux fluctuations de vitesse : hypothèse quasi-stationnaire.

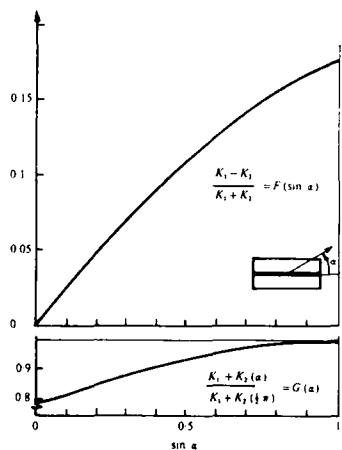


Figure 4 : Electrodes scindées-courbes d'étalonnage

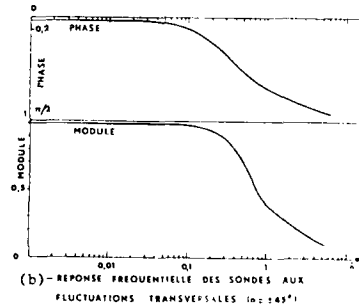
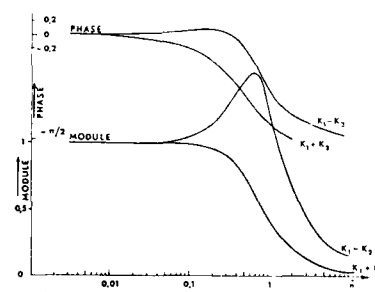


Figure 6 : Réponse fréquentielle

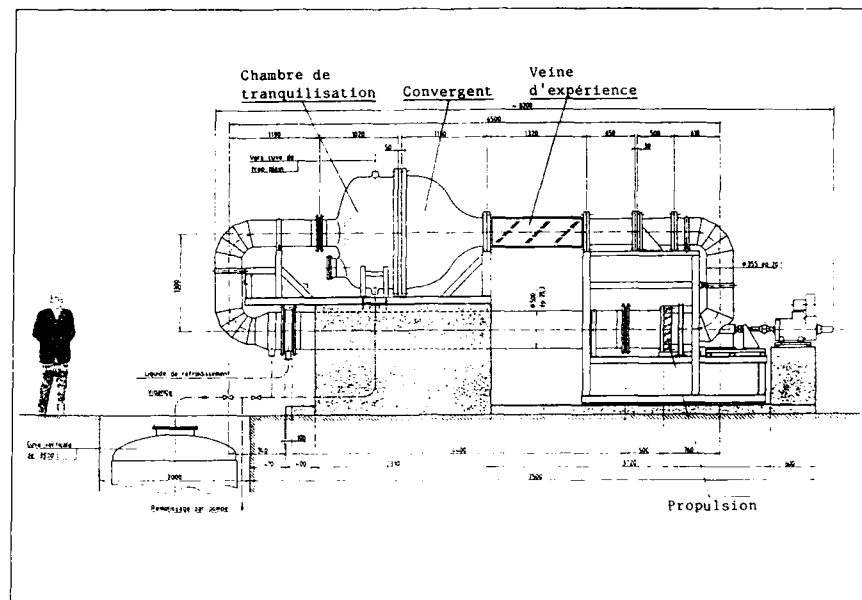


Figure 7 : Canal hydraulique polarographique



Figure 8 : Déflecteurs

COUPE TRANSVERSALE

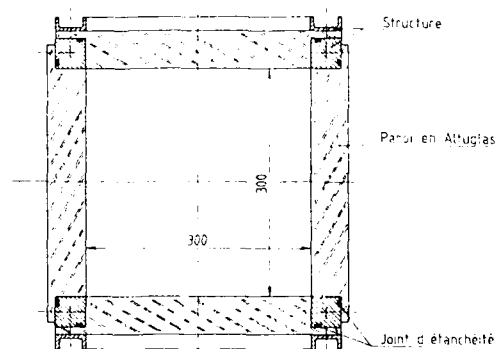


Figure 9 : Veine d'expérience à visibilité intégrale

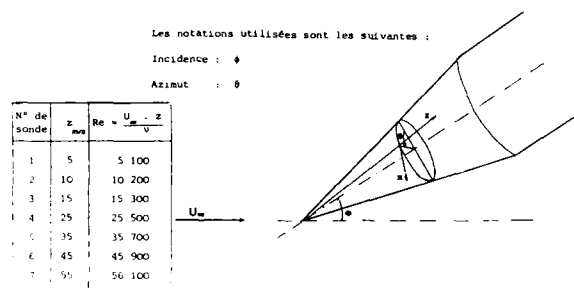


Figure 10 : Cône en incidence : géométrie et notations

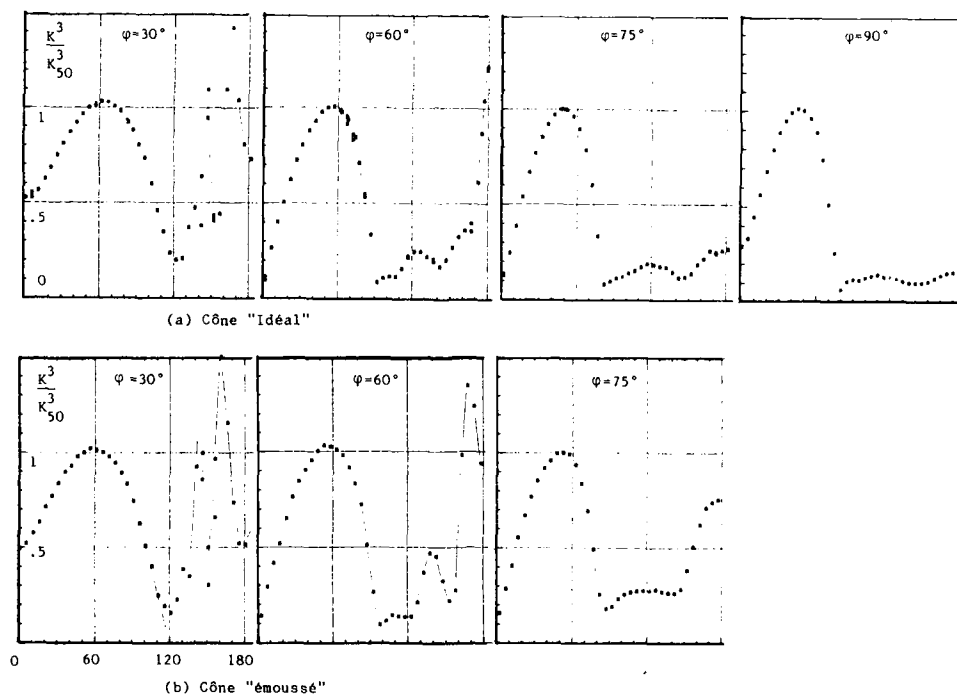


Figure 11 : Coefficient de transfert -électrode simple- à différentes incidences en fonction de l'azimut

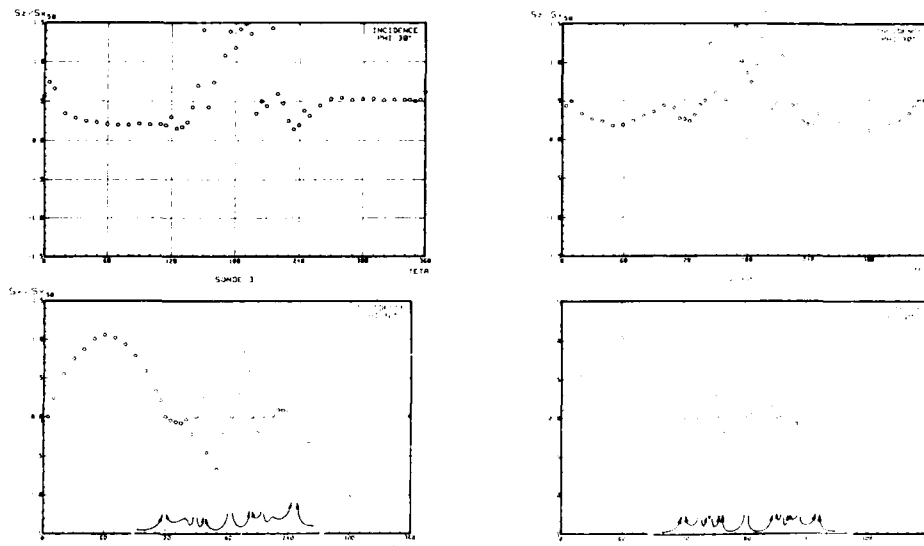


Figure 12 : Composantes longitudinale ( $S_z$ ) et transversale ( $S_x$ ) du gradient pariétal de vitesse

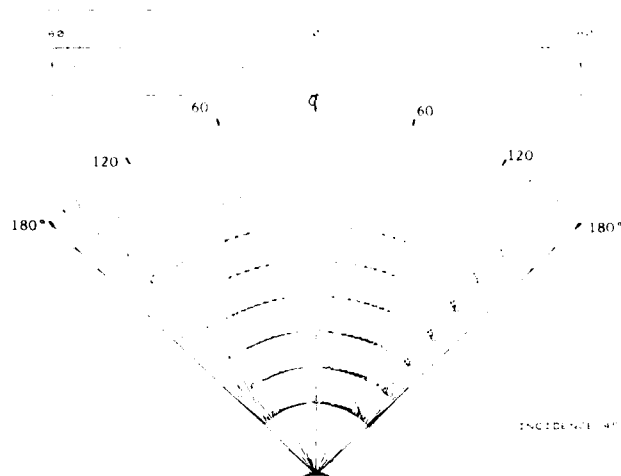


Figure 13 : Gradient pariétal de vitesse en grandeur et direction sur un cône développé



DISA 55R15

DISA 55R11

Elément sensible : film de nickel déposé sur un fil de quartz de 75μ de diamètre. Longueur sensible : 1,25mm

Figure 14 : Sondes anémométriques étudiées

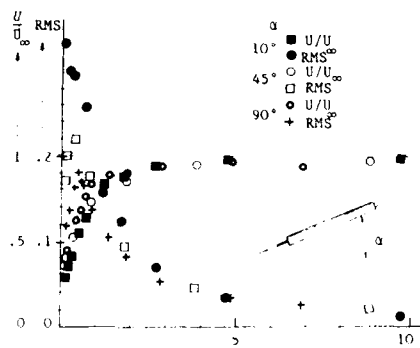


Figure 15 : Profils de vitesse mesurés : influence de l'inclinaison des sondes

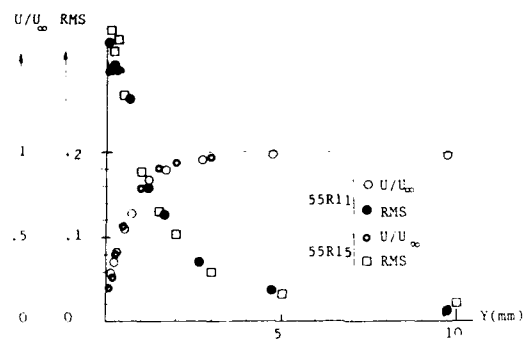


Figure 16 : Profils de vitesse : comparaison sonde "couche limite" sonde droite

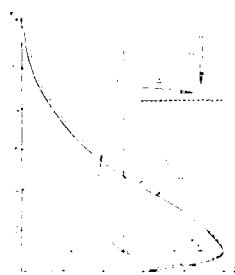


Figure 17 : Profils des vitesses dans un jet pariétal plan d'après [11]

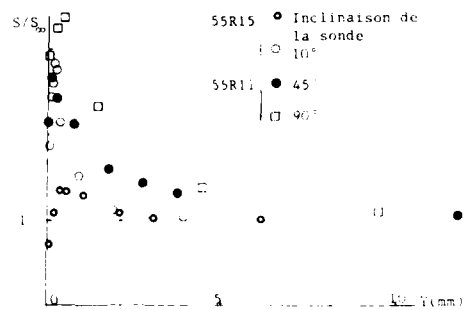


Figure 18 : Variation du gradient pariétal en fonction de la distance de la sonde anémométrique à la paroi

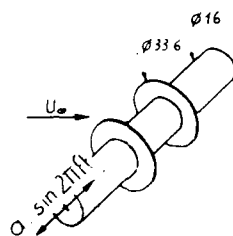


Figure 19 : Cylindre aileté

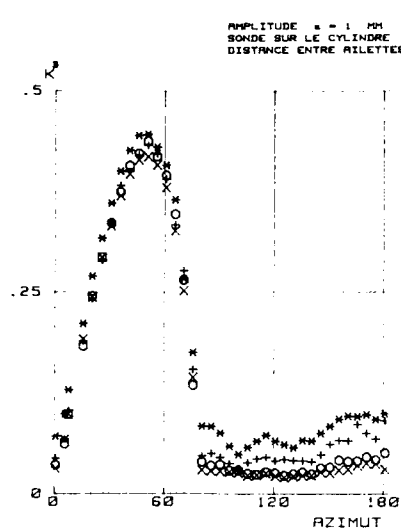


Figure 20 : Evolution du coefficient de transfert local sur le cylindre (échelle arbitraire)

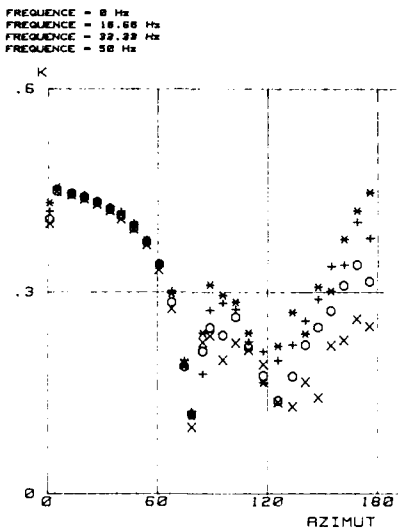


Figure 21 : Transfert de masse local sur le cylindre (échelle arbitraire)

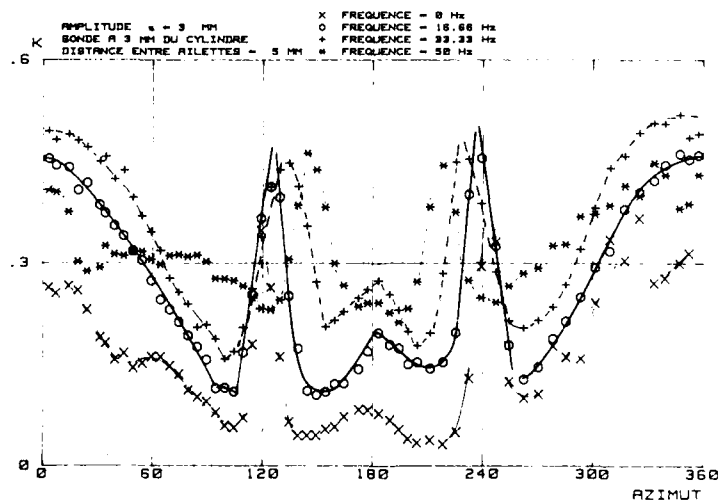


Figure 22 : Transfert de masse locale sur l'ailette à 11 mm de l'axe (échelle arbitraire)

# **FLOW VELOCITY MEASUREMENTS BY IMAGE PROCESSING OF OPTICALLY MODULATED TRACES**

by  
M. Gharib, B. Dyne, O. Thomas and C. Yap  
University of California, San Diego, B-010  
La Jolla, California 92093  
USA

## **SUMMARY**

A computerized flow visualization technique capable of quantifying the flow field automatically is described. The technique uses a time modulated illumination scheme to retrieve vectorial information from the pathlines of particles suspended in the flow. This technique has eliminated a major source of error in velocity reading which is common in conventional particle tracing techniques. Application of the present technique to the recirculating flow field of a two dimensional cavity is described. Velocity profiles obtained from the pathlines of the particles through the present technique show excellent agreement with the velocity profiles obtained using laser doppler velocimetry.

## **INTRODUCTION**

The human eye-brain system has excellent capability in recognizing patterns and structures which makes flow visualization a unique tool in obtaining a crucial physical understanding of complicated flow phenomena. Usually the nature of this understanding is qualitative. However, further progress depends upon the implementation of the obtained information to plan quantitative experiments by using techniques such as hot wire anemometry or laser doppler velocimetry. These two techniques are typically limited to simultaneous sampling at a few spatial locations.

In this respect, the global Lagrangian nature of the information contained in a single flow image makes the development of a quantitative flow visualization technique very attractive in principle. Such a technique has the potential of providing multi-point spatial and temporal information regarding the velocity or vorticity field.

Among many available flow visualization techniques, flow pictures produced by the pathlines (traces) of small particles suspended in fluid have been used in obtaining velocity field information (1,2). The velocity data (except the direction of the motion) is obtainable from the trace photographs by measuring lengths and positions of streaks. To obtain the sense of the motion, one can follow the trace particles on short-exposure photographs separated by short time intervals. But the difficulty of identifying the same particle on two photographs, especially for a high concentration of particles, makes the latter technique impractical.

A major drawback in using the conventional particle tracing technique has been the unacceptable amount of manual work required to obtain a velocity vector field from a large number of traces. In recent years, there have been several attempts to make the particle tracing technique less laborious by using image digitizers and computer image processing techniques (3,4,5). These attempts suffer from the fact that the lack of vectorial information requires the final judgement of an operator who should bear in mind the flow direction and assign a local velocity vector to each individual trace. This is usually done during the digitization process and requires both manual labor and a prior knowledge of the flow direction.

This paper will introduce a new combined illumination and image processing technique developed specifically to eliminate both the flow direction ambiguity and required manual labor. The developed technique is fully automated and has a general feature that can be easily adapted to various types of experiments. The intention of this paper is to present the detailed elements of this technique and demonstrate its potentials by reporting the results of its applications to a cavity flow field. However, the detailed experimental results will be reported elsewhere.

In the following sections, the schemes used in our technique for the generation of the variable intensity traces, image digitization, image processing, trace detection and flow computation are described.

## **GENERATION OF THE VARIABLE INTENSITY TRACES**

The information regarding the flow direction can be obtained by generating variable intensity traces. Gharib and Hernan (6) used after-glowing properties of optically activated phosphorescent particles to construct the velocity vector field of a transient free surface vortex. The practical difficulties of producing phosphorescent particles with the appropriate life times to resolve particular flow time scales, as well as the need for pulsed laser sources to obtain high quality flow images led us to develop a simpler method for generating variable intensity traces.

#### PARTICLE TRACING BY TIME MODULATION OF THE LIGHT SOURCE

By using an Argon-Ion laser and a fast laser beam scanner, a thin sheet of light (1-3 mm in thickness) can be generated in the plane of a desired flow cross-section. Prior to the beam scanner, the laser beam goes through a chopping filter (Fig. 1). This filter which is used as an intensity modulator can be designed to generate a variable laser beam intensity as it chops the beam. We tried two different filter designs. In the first design a filter with a variable density gradient is used to generate a continuous intensity variation on the entire trace length. Two small round openings at the two ends of the chopping filter's window generate two bright spots on each trace which will be used as the reference points. These reference points eliminate a major source of error which is usually undetected in the previous particle tracing techniques (3,4,5). To understand the problem, let us define the traveling time of the particle  $\Delta\tau$  as the total time that the particle has traveled through the laser sheet during the illumination period, ( $\Delta T$ ). In conventional particle tracing techniques  $\Delta T$  corresponds to the camera's exposure time and the basic assumption is that  $\Delta T = \Delta\tau$  and particle velocity is usually defined as

$$U_p = \Delta L / \Delta T$$

where  $\Delta L$  is the photographically registered trace length. However in a real situation, the particles that enter the sheet after starting of the illumination or exit earlier than ending of the illumination period will have a traveling time shorter than  $\Delta T$ . This problem usually causes erroneous velocity readings for particles with large velocity components normal to the plane of illumination. In the present technique, a particle that has remained in the sheet during the illumination period should have two bright reference points. Lack of one or both points on a trace disqualifies the trace for the velocity calculations.

Figure 2 represents a typical trace generated by using the first filter design. In the second design a uniform density filter is used between two reference points and an extension of this uniform filter past the second reference point is used to label it as the trace's ending point. Figure 3 represents a sample trace generated by the second filter configuration.

Note that in the chopping filter method, a desired flow time scale can be easily resolved by controlling the illumination period through the rotation rate of the filter. Also, another advantage of chopping the filter over the activated phosphorescent particle tracing technique is that regular solid or liquid particles (not necessarily luminescent) can be used. However by using luminescent particles and a proper laser emission line, one can excite trace particles at a desired color and therefore reduce the image background noise by eliminating the scattering particles through optical filtering. For most of our experiments we used 40  $\mu$ m polystyrene particles coated with Sodium Fluorescein or Rodamine. The 450 nm (blue) line of a 2 watt Argon-Ion laser was used to obtain yellow color traces from the particles coated with Sodium Fluorescein and red color traces from the Rodamine particles.

#### IMAGE ACQUISITION AND DIGITIZATION

The flow images were acquired with a 35 mm camera which was focused on the illuminated plane. The camera's recording time was synchronized with the chopping filter through a pulse generator and an electronic shutter. Each photographic positive print was digitized by a CCD (charge couple device) camera and an image digitizer. This process was controlled by a host computer (IBM AT). Each photographic plate was digitized into a 512 x 512 pixel matrix with a 256 (8 bits) gray level resolution.

#### SOURCES OF ERROR

Accuracy of the measurements and calculations of the described technique can be greatly influenced by several parameters including the conditions for the particles to reflect the real local velocity vector (7, 8), optical imaging error (9), accuracy of locating the particles (5) and non-uniformity of particle distribution. However, the most fundamental source of error that is removed with our technique is the erroneous trace length reading due to the lack of information regarding the entrance or the exit of the particle from the light sheet. The nature of this error reveals no indication of its frequency. Under estimation of the velocity magnitude as large as one hundred percent of the local mean velocity might occur in the conventional sheet lighting technique.

A second most important source of error is due to the fact that one tries to obtain an Eulerian velocity field from a Lagrangian measurement. The temporal and spatial evolution of the velocity will contribute to the inaccuracy of Eulerian velocity component obtained from the particle traces (10). However, a short illumination period which essentially results in short enough trace lengths to avoid large velocity changes in space and time or curvature in the traces will allow one to obtain a good estimate of the Eulerian velocity.



#### SOFTWARE STRUCTURE AND OPERATIONAL DETAILS

The resulting data were displayed on a monitor and also were stored on a hard disk for the subsequent processing. The software was designed to operate either on the displayed digital image or on the stored information on the hard disk.

The first step in the analysis of the digital images was to define the boundaries of each streak line. By pre-examination of a sample image, the operator inputs a gray level threshold that determines the minimum pixel value of what will be considered a trace. Due to the initial removal of the scattering light by the optical filtering, we had obtained images with a large signal-to-noise ratio. Figure 4 presents an example of the intensity distribution over a sample trace and its relative value to the background gray level. The quality of the images made it possible to identify the trace regions with usually a single threshold level. Once the threshold value was determined, it was applied to the remaining of the sequence of images. Using this threshold value, the processing program then sets any pixel below the threshold value equal to zero (black) and saves the thresholded image. In the next step, the program scans the screen, line by line, and detects the first pixel of any potential trace region. This pixel should have at least three neighboring pixels with a value above the set threshold level for the program to begin to define a region, otherwise the pixel is set to zero.

A region is defined by tracing around the boundary of the region and sorting the coordinates of the boundary pixels in an array. A boundary pixel, as is sketched in Figure 5 must have at least two neighboring pixels with a value above the threshold level. Using the described criterion the next boundary pixel has been found by a clockwise search in a  $3 \times 3$  matrix, centered at the current detected pixel, starting from the last detected boundary pixel. Once the region boundary is defined (Fig. 6), the gray level value of the entire region is set to zero, so that the region will not be defined again as the program continues to scan the screen. The scanning continues until all the trace regions are identified.

In the next step, an automatic search is conducted for the reference points inside the region by scanning the pixels inside each region and computing average and maximum gray level values of the defined region. A gray level with a given fraction between the average and maximum is then chosen as the reference point threshold. A value of .33 yields the best results to identify the reference point region (Fig. 7). Once the outline boundary of a reference point is defined in the same way that a region is defined, the centroid of it will be determined and assigned to the corresponding region. By counting the number of centroids in each region the program disqualifies any region with either one or more than two reference points. Therefore any region which was generated by an incomplete trace or by two crossing traces is eliminated from further processing (Fig. 8). In the next step, the program draws a line between the two centroids of each valid region and at a specified number of equally distanced points on this line draws normal lines to intersect the boundaries of the region (Fig. 9) and consequently to identify the mid-point of the trace region (Fig. 10). For the highly curved traces, the number of normals can be increased to achieve better resolution in constructing the trace. The distance that a particle travelled during  $\Delta T$  was equated to the sum of the segments that were generated by the mid-points (Fig. 10).

For the first type of chopping filter, where a continuous intensity variation was obtained on each trace, the local velocity direction is found by comparing the gray level values in surrounding neighborhood pixels of each reference points. For the traces which were obtained by the second method, the reference point that has the largest distance from the closest tail end is identified as the starting point. Finally, the velocity scalar, direction and mid-location of each trace is stored in a file for further processing. It is interesting to mention that despite the non-optimum nature of the current system, the net time for the image digitization, trace detection and velocity vector field construction of a single flow picture is approximately two minutes. A typical reported time for obtaining a similar information by conventional techniques is in the order of one hour (4,5).

In the next step a square grid system is imagined to cover the entire digitized field. The data for each trace is then read and assigned to the mesh square into which the mid-point of the trace falls. A vector summation of the all traces associated with a certain mesh square results in the mean velocity vector for that mesh square.

#### EXPERIMENTAL ARRANGEMENTS AND RESULTS

As part of an attempt to show the practicality of the present technique, we implemented it to construct the velocity vector field of a two dimensional cavity flow.

The experiments were performed in a water tunnel on a 7 cm deep two dimensional cavity as shown in Figure 1. The boundary layer at the upstream corner was laminar at the operational free stream velocity of 30 cm/sec.

For a small value of cavity width to depth ratio ( $b/h$ ), the flow inside the cavity is essentially a steady recirculating stream (11). For a large cavity width to depth ratio ( $b/h \gg 1$ ), the cavity flow becomes unstable on a large scale and shows strong three dimensional behavior.

Figure 11 presents the flow field for  $b/h=.8$  which was obtained from averaging 60 consecutive images. Figure 12 presents a similar flow field for  $b/h=1.15$  where the flow inside the cavity is strongly unsteady and three dimensional.

Both flow fields are indicative of the recirculating region inside the cavity. The information contained in these figures can easily be used to compute vorticity and the pressure field. However, our main goal was to compare these Lagrangian velocity information to the information obtainable from single point Eulerian measurement techniques such as laser doppler velocimetry (LDV). For this purpose, by using LDV, one traverse of the velocity field at the middle of the cavity with  $b/h=.8$  was obtained. Figure 13 shows an excellent agreement between this velocity profile and the one obtained from the particle tracing method. Such agreement can be seen only on the upper half of the velocity profile for the large cavity configurations with  $b/h=1.15$  (Fig. 14). The disagreement of the two velocity profiles can be attributed to the strongly three dimensional flow near the bottom of the cavity which drastically reduces the number of valid traces. However, this problem can be resolved by increasing the number of images to obtain better statistics of the mean velocity field.

#### CONCLUSION

The above results provide credence to the applicability of the developed method as a quantitative automatic flow visualization technique. It can be easily applied to complicated flow problems where single point measurements or laborious conventional particle tracing techniques cannot be considered feasible. The developed technique can provide fast multi-point flow information for analytical investigation. Therefore, in this respect, it can be considered as the only counterpart to multi-point numerical methods. In order to reduce the total time needed to obtain the velocity field, experiments are underway to eliminate the photographic steps of the technique by direct optical and electronic image recording of the flow field. The new experiments involve the three dimensional mapping of the velocity field by stereo imaging of the flow field by two cameras.

#### ACKNOWLEDGEMENT

The authors would like to thank Dr. L. Costa of the Kodak Research Laboratories in Rochester, New York for providing us with the experimental fluorescent particles. Also, we would like to extend our thanks to K. Stuber for her careful laser doppler measurements and to Dr. M. Hernan for his valuable suggestions during the early stages of the present work.

#### REFERENCES

1. Prandtl, L. & Tietjens, O.G. (1934), Applied Hydro-and Aeromechanics. McGraw-Hill, New York. 311 pp.
2. Ahlborne, F. (1902) "On the Mechanism of Hydrodynamic Drag", Abhandl. Geliete Naturuuss. 17 Hamburg.
3. Wiese Nielson, K. Th. (1970) "Vortex Formation in Two-Dimensional Periodic Wake", Ph.D. Thesis, Oxford.
4. Demotakis, P.D., Debussy, F.D. & Koochesfahani, M.M., (1981) "Particle Streak Velocity Field Measurements in a Two-Dimensional Mixing Layer", Physics. Fluid 24(6).
5. Imaichi, K. & Ohmi, K., (1983) "Numerical Processing of Flow-Visualization Pictures - Measurements of Two-Dimensional Vortex Flow", J. Fluid Mech. Vol. 129, 1983, pp. 283-311.
6. Gharib, M. & Hernan, M.A., (1985) "Flow Velocity Measurement by Image Processing of Optically Activated Tracers", AIAA 85-0172, AIAA 23rd Aerospace Sciences Meeting, Reno, NV 1985.
7. Merzkirch, W. (1974), Flow Visualization. Academic Press, New York.
8. Saffman, P.G. (1965) "The Left on a Small Sphere in a Slow Shear Flow", J. Fluid Mech. 22, 385-400.
9. Wolf, P. R. (1983), Elements of Photogrammetry, 2nd Edition. McGraw-Hill, New York, 628 pp.
10. Altman, D.B. (1985), "Laboratory Studies of Internal Gravity Wave Critical Layers", Ph.D. Thesis, University of California, San Diego.
11. Gharib, M. & Roshko, A. (1987) "The Effect of Flow Oscillations on Cavity Drag", J. Fluid Mech. Accepted for Publication.

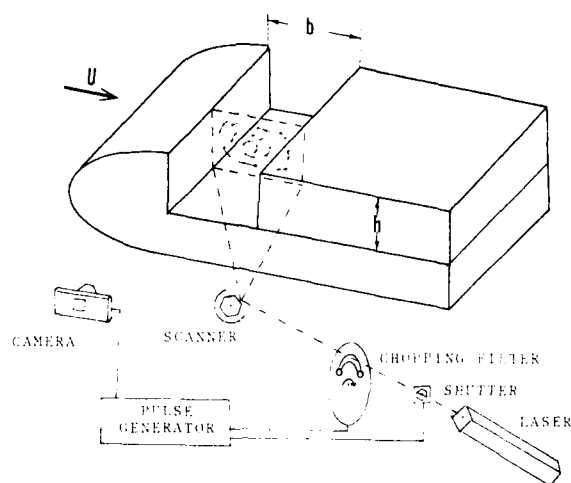


FIG.1 SCHEMATIC OF THE EXPERIMENTAL SET-UP



FIG.2 SAMPLE TRACE FROM CONTINUOUS GRADIENT FILTER



FIG.3 SAMPLE TRACE FROM UNIFORM FILTER

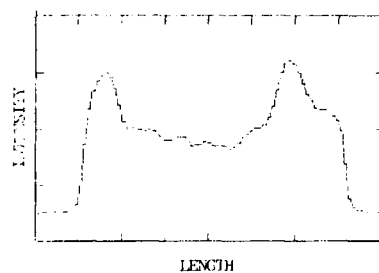


FIG.4 INTENSITY DISTRIBUTION FOR TRACE IN FIG.3

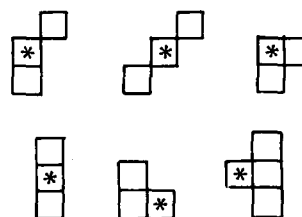


FIG.5 DEFINITION OF A BOUNDARY PIXEL

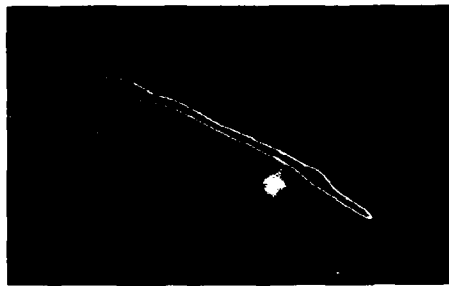


FIG. 6 REGION BOUNDARY

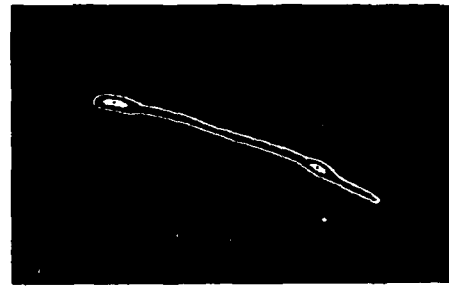


FIG. 7 REFERENCE POINTS DETECTION

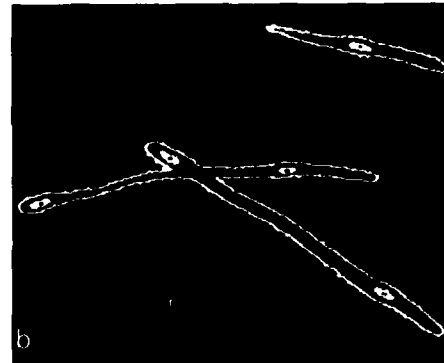


FIG. 8 SAMPLES OF INCOMPLETE AND CROSSED TRACES  
A) ORIGINAL IMAGE B) PROCESSED IMAGE

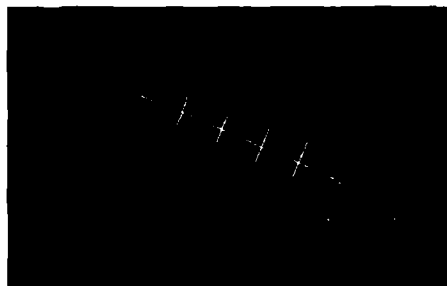


FIG. 9 NORMAL DRAWING PROCESS



FIG. 10 COMPLETION OF PROCESS IN FIG. 9  
SHOWING COMPLETED VELOCITY VECTOR

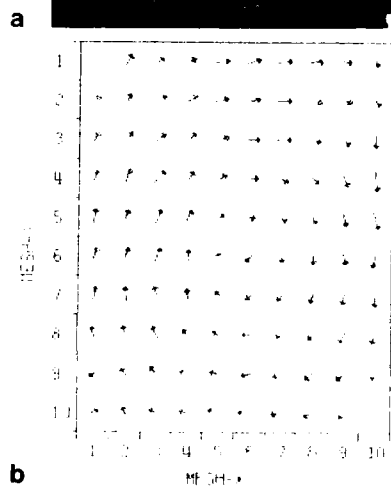


FIG. 11 A) SAMPLE FLOW FIELD FOR  $b/h = .8$   
B) AVERAGED VELOCITY FIELD FOR FIG. 11A

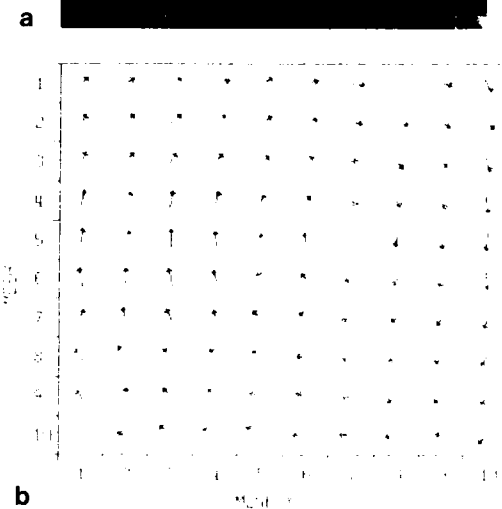
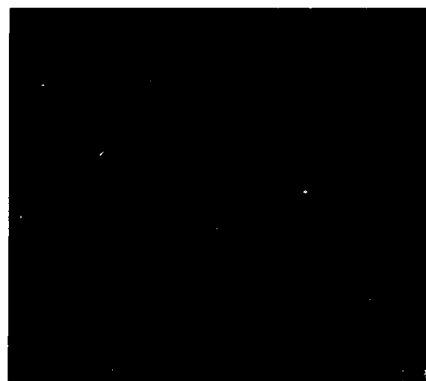


FIG. 12 A) SAMPLE FLOW FIELD FOR  $b/h = 1.15$   
B) AVERAGED VELOCITY FIELD FOR FIG. 12A

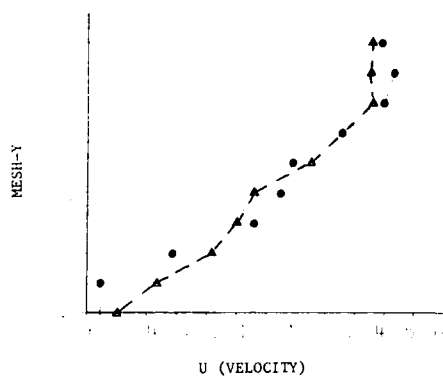


FIG. 13 COMPARISON OF IMAGE PROCESSING  
MEASUREMENTS ( $\Delta$ ) TO LDV MEASUREMENTS ( $\bullet$ )  
FOR  $b/h = .8$

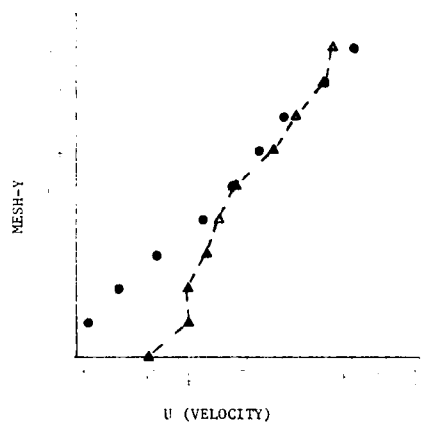


FIG. 14 SAME AS FIG. 13 FOR  $b/h = 1.15$

**A Non-invasive Experimental Technique for the Measurement of  
Unsteady Velocity and Vorticity Fields**

L. Lourenco and A. Krothapalli  
Florida State University, Tallahassee, Florida

and

J.M. Buchlin and M.L. Riethmuller  
von Karman Institute for Fluid Dynamics  
Rhode-St-Genese, Belgium

**SUMMARY**

A new velocity measurement technique is described that provides the simultaneous visualization of a two-dimensional streamline pattern and the quantification of the velocity field. The main advantage of this technique is that the velocity field can be measured with sufficient accuracy and spatial resolution so that the vorticity field can be readily obtained. This technique is ideally suited for the study of unsteady vortical flows, which occur in high angle of attack aerodynamics. The technique, some of the important parameters that affect its use, and some recent examples are described.

**NOMENCLATURE**

C	airfoil chord
d	cylinder diameter
Re	Reynolds number
t	time
U	streamwise velocity
V	lateral velocity
$\Delta x$	streamwise distance between scanning locations
$\Delta y$	lateral distance between scanning locations
$\omega$	vorticity

## 1. INTRODUCTION

Since the early works of Prandtl water facilities together with flow visualization techniques e.g. dy. injection, hydrogen bubbles, have been extensively used to provide a better understanding of complex flow phenomena, such as the ones occurring in high angle of attack aerodynamics. The advantage that water facilities have over conventional wind tunnels is that they provide an easy means to perform the flow visualization. In particular, when dealing with unsteady flows, because of the lower kinematic viscosity of water compared to that of air, it is possible to reproduce an aerodynamic flow in water with a lower free stream velocity to attain a Reynolds number comparable to that in air. Due to the lower velocities, the flow time scales become relatively larger thus leading to clearer observations of dynamic phenomena.

Even though conventional visualization techniques are an excellent means to understand the global flow features, they only provide qualitative information. A detailed description of flow fields can only be achieved through mapping of the entire flow field. However, the measurement of velocity in unsteady flows remains a challenging problem in experimental fluid mechanics. Available techniques such as hot-wire anemometry and Laser Doppler Velocimetry can only provide "one point" information. In order to obtain whole field data, measurements must be carried out sequentially one point at a time. Although this sequential method can be easily implemented in applications involving steady flows, it is of rather difficult application in unsteady flow phenomena.

Recently, a novel measurement technique commonly known as Laser Speckle or Particle Image Displacement Velocimetry became available. This technique permits the simultaneous visualization of the two-dimensional streamline pattern in unsteady flows and the quantification of the velocity field. The main advantage of this new technique is that the whole two-dimensional velocity field can be recovered with great accuracy and spatial resolution, from which the instantaneous vorticity field can be easily obtained. This constitutes a great asset for the study of a variety of flows that evolve stochastically in both space and time, and in the case of interest, to the study of unsteady separated flows, which occur in high angle of attack aerodynamics.

## 2. PRINCIPLE OF THE TECHNIQUE

The application of LSV or PIDV to fluid flow measurement involves several steps. First, it is necessary to "create" a selected plane or surface within the flow field. This is accomplished by seeding the flow with small tracer particles, similarly to LDV applications, and illuminating it with a sheet of coherent light, as shown in Figure 1. A pulsed laser such as a Ruby or a NdYag laser, or a CW laser with a shutter is normally used as the light source. The laser sheet is formed, for example, by focusing

the laser beam first with a long focal length spherical lens, to obtain minimum thickness, and then diverging the beam in one dimension with a cylindrical lens. The light scattered by the seeding particles in the illuminated plane provides a moving pattern. When the seeding concentration is low, the pattern consists of resolved diffraction limited images of the particles. When their concentration increases, the images overlap and interfere to produce a random speckle pattern. A multiple exposure photograph records this moving pattern. The lower particle concentration originates a mode of operation of the technique referred to as Particle Image Displacement Velocimetry, reserving the term Laser Speckle Velocimetry for the high particle concentration levels where a random speckle pattern is actually formed (reference 1). In a second step the local fluid velocity is derived from the ratio of the measured spacing between the images of the same tracer, or speckle grain, and the time between exposures.

Several methods exist to convert the information contained in the multiple-exposed photograph, or specklegram, to flow field data such as velocity or vorticity. The recorded image, whether formed by isolated disks, in the case of low particle concentration, or speckle grains for high particle concentration is a complicated random pattern. It would be very difficult to measure the local displacements by visual or computer-aided inspection. However, it is important to realize that the multiple exposure photograph results in a periodic random image from which the periodicity information can be retrieved using Fourier or Auto-correlation analysis. Basically, the multiple-exposed photographs or specklegrams can be analyzed either on a point-by-point basis, which yields measurements of the local displacements (velocity), (refs. 2-3) or with a whole field filtering technique, which yields isovelocity contours (ref. 3). The method, which has been selected and implemented by the Fluid Mechanics Research Laboratory at the Florida State University, is the Young's fringes method. The local displacement is determined using an focused laser beam to interrogate a small area of the multiple exposed photograph transparency. The diffraction produced by coherent illumination of the multiple images in the negative generates Young's fringes, in the Fourier plane of a lens, provided that the particle images correlate. This is shown schematically in Figure 2. These fringes have an orientation which is perpendicular to the direction of the local displacement and a spacing inversely proportional to the displacement. The use of Young's fringes eliminates the difficulties of finding the individual image pairs in the photograph. The basis of the Young's fringe method is described in reference 3.

### 3. DIRECTION SENSITIVITY AND DYNAMIC RANGE

The photographic recording method discussed above has the disadvantage that the photograph consists of a sequence of multiple particle images which have a  $180^\circ$  ambiguity in the direction of the velocity vector. In addition, it has been shown (reference 4) that the velocity dynamic range of the technique is limited to a maximum



value of about 10. In most flows of interest (e.g. boundary layers and separated flows), this dynamic range is not sufficient to capture the flow field in its entirety. These limitations are critical when measuring complex flows having flow reversals and stagnation areas.

A method to resolve both the ambiguity of the velocity vector as well as to improve the technique's velocity range is incorporated in this experiment. This method, commonly known as "velocity bias technique", consists of recording the flow field in a moving reference frame, thus superposing a known velocity bias to the actual flow velocity. This effect may be accomplished in several ways, in particular, using a moving camera during the photographic recording or by optical means using scanning or rotating mirrors. The method which is currently employed uses a scanning mirror to displace the image during the exposure with a predetermined velocity. A schematic of the scanning mirror arrangement is shown in figure 3. Consider two particle pairs  $A_0B_0$  and  $C_0D_0$  having equal displacements in opposite directions in the object plane. By introducing a mirror placed at  $45^\circ$  between the camera lens and the object plane, the corresponding displacements appear in the film plane as AB and CD with equal magnitudes. When the mirror is rotated by an angle of  $\Delta\theta$  between exposures, the displacements corresponding to  $A_0B_0$  and  $C_0D_0$  appear in the film plane as  $AB'$  and  $CD'$  with different magnitudes. The correct displacement or velocity with its direction can now be obtained upon removal of the velocity bias.

#### 4. VALIDATION OF THE TECHNIQUE

##### 4.1 Experimental configuration

The capabilities of the present technique are evaluated in a measurement of the transient flow over a NACA 0012 at high incidence, and the near-wake flow development behind a circular cylinder impulsively accelerated to constant velocity. Both flows were created by towing models in the reduced scale Fluid Mechanics Research Laboratory towing tank facility. The tank is 300 x 300 x 600mm. A detailed examination showed that the motion of the carriage is smooth and vibration free. In this facility, the towing carriage is driven by a variable D.C. motor, and the towing velocity can vary from 0 to 100mm/sec. For the photography a 35mm camera (NIKON F-3) is used. In order to photograph the flow at regular time intervals, the photographic camera is equipped with an electric winding device. The photographic time interval available with this camera can be continuously varied up to a maximum of 6 frames per second. Two options are available to fix the camera; one by attaching it to the towing carriage, which means an observation point fixed in relation to the model, and the other by attaching it to the frame of the water tank, which means an observation point fixed in relation to the fluid.

The NACA 0012 airfoil is 60mm in chord and at 30° incidence; the circular cylinder is 25.4mm in diameter. Both models were towed with a velocity of 23.5mm/sec. The fluid used in these experiments was water seeded with 4μm metallic coated particles (TSI model 10087). The corresponding Reynolds numbers were 1400 for the airfoil and 550 for the cylinder. These flows are excellent test cases because they include large scale vortical motions and extreme velocity gradients. These extreme gradients serve as a test to the technique's capabilities of providing information over a large velocity range.

For the illumination, a laser beam from a 5 watt Argon-Ion Laser (Spectra-Physics model 2000) is steered and focused to a diameter of .3mm using an inverse telescope lens arrangement. A cylindrical lens, with a focal length of -6.35mm, is used to diverge the focused beam in one dimension, creating a laser sheet. The laser sheet is 70mm wide and illuminates the mid-span section of the models. For the multiple exposure, the CW laser beam is modulated using a Bragg cell. In this experiment, the laser power density of the sheet was 0.27W/m<sup>2</sup>. In order to record the time development of the flow field, the camera is attached to the towing carriage. The aperture of the camera lens with a focal length of 50mm and a spacer of 12mm, is set at F# 5.6 and the magnification is 0.40. The film used in these experiments was a Polaroid Polagraph with a sensitivity of 400 ASA and a resolution of about 80 lines/mm. This resolution proved to be sufficient to accurately record the flow field. The advantages in the use of Polaroid film are (i) easy and fast processing of the film (ii) because the Polaroid Polagraph is a positive film it saves the need for contact printing of film negatives, prior to analysis, in order to increase the SNR of the data (ref. 1).

## 5. RESULTS

### 5.1 Flow past the NACA 0012 airfoil

Figure 4(a) is a multiple exposed photograph of the flow past an impulsively started airfoil captured at a stage of its development corresponding to non-dimensional time  $t^* = t \frac{U}{C} = 1.5$ , with  $t$  the time from start-up,  $U$  the free stream velocity and  $C$  the airfoil chord. This figure depicts the complexity of the flow field which exhibits large areas of flow reversal and stagnation regions. Analysis of this film transparency would provide the velocity vector information within the restriction mentioned above, i.e., with an 180° ambiguity in direction of the velocity vector and regions of drop-out where the flow velocity is less than the lower velocity range limit of the technique. Instead, the "velocity bias technique" is used and a "biased" image is recorded and analyzed (fig. 4(b)).

The velocity data is acquired in a square mesh by digital processing of the Young's fringes, produced by point-by-point scanning of the Polaroid transparency. The scanning step size and the dimension of the analyzing beam are 0.5mm, which corresponds

to a spatial resolution of about 1.25mm in the object plane or about  $\frac{1}{50}$  chord of the airfoil. The resulting velocity field is presented in figure 5(a). The actual velocity field in the reference frame of the airfoil is presented in figure 5(b). This data is recovered upon removal of the velocity bias, which is, for this particular experiment, equal to 2 times the free-stream velocity.

## 5.2 Near-wake flow behind a circular cylinder

Similarly the flow behind a circular cylinder was captured at several stages of its development corresponding to  $t^*$ , the non-dimensional time based on the cylinder diameter, between 0.6 and 5.2. Figures 6(a) to (f) are the measured velocity fields, and consist of a good representation of the expected flow pattern. In these figures, the length of each vector is proportional to the local velocity at that point. Because of the high spatial resolution of these data, vorticity can be derived by taking spatial derivatives. Letting each grid location be labeled with indices,  $i, j$ , the  $z$ -vorticity component at location  $(i, j)$  is

$$\omega_{i,j} = \frac{1}{2} \left[ \frac{v_{i+1,j} - v_{i-1,j}}{2\Delta x} - \frac{u_{i,j+1} - u_{i,j-1}}{2\Delta y} \right]$$

where  $\Delta x$  and  $\Delta y$  are the mesh intervals in the streamwise and cross-stream direction, respectively. For convenience, the vorticity data normalized with respect to the free stream velocity and cylinder diameter, is displayed by color coding of each velocity vector. The color code represents the vorticity level, the magnitude of which is given by the color bar on the top of each figure. The red and blue colors represent the peak positive and negative vorticity regions respectively.

## 6. CONCLUSIONS

A recently developed velocity measurement technique, known as Particle Image Displacement Velocimetry has been briefly described. Using this technique rather complex time varying flow fields can be captured and analyzed with great detail. The potential of the technique is illustrated using two flow fields as test cases: Flow past an airfoil and behind a circular cylinder.

The technique has been shown to provide both flow visualization and quantitative measurements, which include velocity and vorticity fields.

## REFERENCES

1. Lourenco, L.; and Krothapalli, A.: "The role of photographic parameters in laser speckle or particle image displacement velocimetry". Experiments in Fluids, vol. 5, 1987, pp. 29-32.
2. Yao, C.S.; and Adrian, R.J.: "Orthogonal compression and 1-D analysis technique for measurement of 2-D particle displacements in pulsed laser velocimetry". Applied Optics, vol. 23, 1984, pp. 1667-1689.
3. Lourenco, L.; and Meynatt, R.: "Laser speckle velocimetry in fluid dynamics applications". VKI Lecture series 1984-03, Digital Image Processing in Fluid Dynamics, Belgium, 1984.
4. Lourenco, L.; Krothapalli, A.; Buchlin, J.M.; and Riethmuller, M.L.: "Non-invasive experimental technique for the measurement of unsteady velocity fields". AIAA Journal, vol. 24, 1986, pp. 1715-1717.

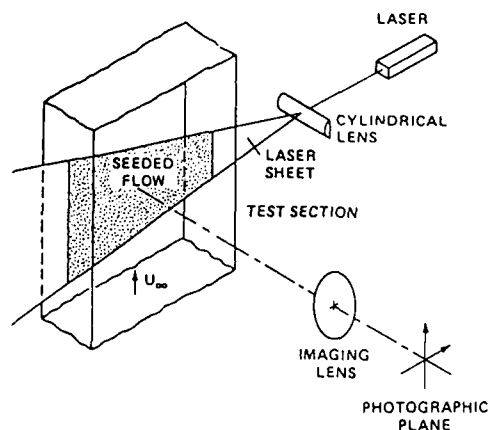
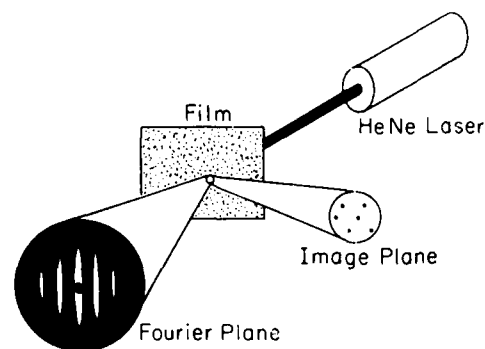


Figure 1. Schematic Arrangement for the Photographic Recording.

Figure 2. Schematic Arrangement for obtaining Young's Fringes



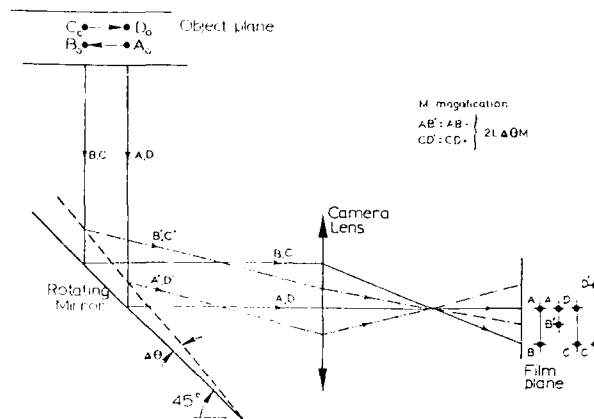


Figure 3. Scanning Mirror Arrangement for Velocity Bias.



Figure 4. Multiple Exposed Photograph a) Unbiased Image; b) Biased Image

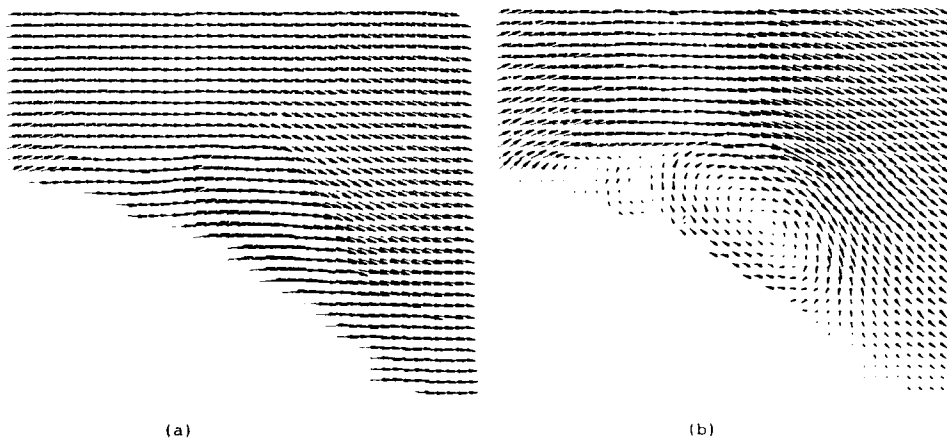


Figure 5. Instantaneous Velocity Field a) Before Removal of Velocity Bias; b) After Removal of the Velocity Bias.

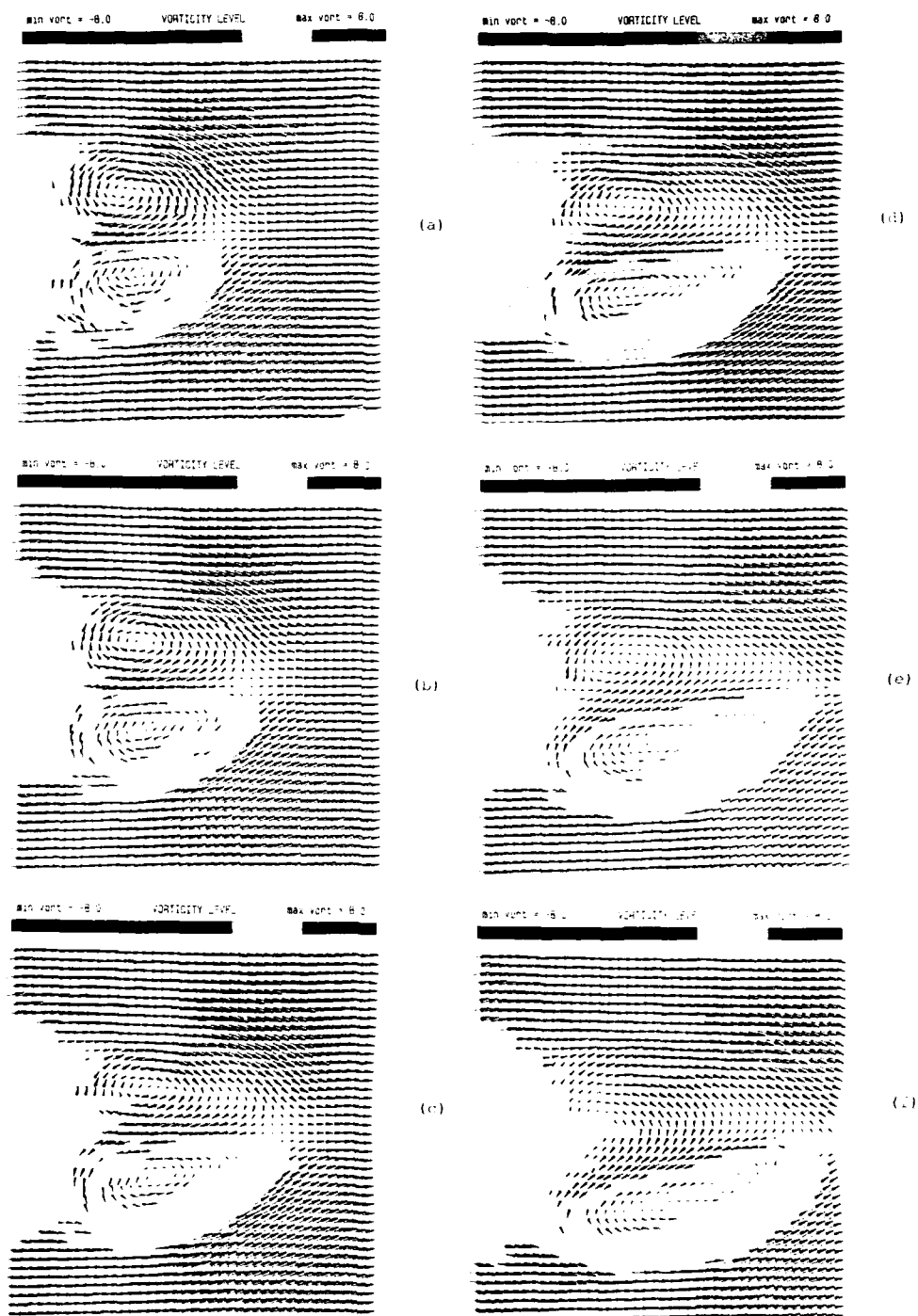


Figure 6. Velocity and Vorticity Field of the Wake Flow; a)  $t^* = 2.2$ ; b)  $t^* = 2.7$ ; c)  $t^* = 3.2$ ; d)  $t^* = 3.7$ ; e)  $t^* = 4.2$ ; f)  $t^* = 4.7$ .

# USE OF WATER TOWING TANKS FOR AERODYNAMICS AND HYDRODYNAMICS

by

Mohamed Gad-el-Hak  
Professor of Aerospace & Mechanical Engineering  
University of Notre Dame  
Notre Dame, IN 46556  
U.S.A.

## ABSTRACT

Wind tunnels and flumes have become standard laboratory tools for modeling a variety of aerodynamic and hydrodynamic flow problems. Less available, although by no means less useful, are facilities in which a model can be towed (or propelled) through air or water. This article emphasizes the use of the water towing tank as an experimental tool for aerodynamic and hydrodynamic studies. Its advantages and disadvantages over other flow rigs are discussed, and its usefulness is illustrated through many examples of research results obtained over the past few years in a typical towing tank facility.

## 1. INTRODUCTION

Fluid mechanics plays an important role in a variety of natural and technological phenomena. It is usually possible to formulate a mathematical model to describe a particular flow field. However, in most cases, the resulting partial differential equations are nonlinear, and an exact solution can only be derived if some of the terms in the equations can be neglected or approximated. Accordingly, fluid mechanics researchers rely heavily on experimental and numerical simulations. Wind tunnels and flumes are commonly used for controlled experimental studies to understand the physics of a particular flow field or to obtain data necessary for designing or improving a given product. Less common, but by no means less useful, are facilities in which an object can be towed (or propelled) through air or water. This article emphasizes the use of the water towing tank as an experimental tool for aerodynamic and hydrodynamic studies. Its advantages and disadvantages over other flow rigs are discussed, and its usefulness is illustrated through many examples of research results obtained over the past few years in a typical towing tank facility.

This paper is divided into six sections. In Section 2, a comparison is made between towing tanks and wind or water tunnels. The particular facility used to generate many of the results discussed in this article is described in Section 3. Available flow visualization and probe measurement techniques commonly used in water towing tanks are discussed in Section 4. Section 5 contains examples of the use of a typical towing tank facility, described in Section 3, to conduct basic research in the areas of stratified flows, boundary layers, compliant coatings, flow control, and steady and unsteady aerodynamics. Brief summary is given in Section 6.

## 2. WHY USE A TOWING TANK?

Whirling arms and railways have occasionally been used to propel an object through the air. For example, the United States Air Force operates an 11-km track for rocket testing. Water towing tanks are a little more commonly used for investigating aerodynamic and hydrodynamic flow problems. An object and the accompanying probes are towed (or propelled) through a large, stagnant body of water at a controlled speed. The probes can be towed independently from the object, if desired, and both speeds can be functions of time.

One advantage of using a towing tank rather than a wind or water tunnel is the fact that moving a model through a fluid requires much less power than driving a large volume of fluid past a stationary object. Another important advantage of a water tank is the ability to accomplish density stratification by heating or cooling the water or by the use of salt water. With care and using a proper filling system, essentially any desired, fairly arbitrary, stable density profile can easily be made in the towing tank. In contrast, extreme difficulties are encountered in designing and operating wind or water tunnels with the capability to be stratified sufficiently to produce substantial buoyancy forces that can compete with the inertial and viscous forces (Sirivat and Warhaft, 1983; Itsweire et al., 1986).

Other advantages of a water towing tank include the ability to use unique flow visualization techniques that are not possible in other test rigs, the ability to study accelerating or decelerating flows with relative ease, and the negligible background motion in the stagnant body of water. Some of these flow visualization techniques applicable in towing tanks are discussed in Section 4. The second point regarding unsteady towing can be appreciated by considering the difficulties of designing and operating a wind or a water tunnel with a time-dependent freestream velocity (Koromilas and Telionis, 1980; Reynolds et al., 1983). For a typical towing tank, on the other hand, one merely has to change the speed of an electric motor. Even more notably, a new water tank at the California Institute of Technology has a computer-controlled carriage that can move in two directions much the same as an ordinary X-Y plotter; thus, it is capable of achieving towing trajectories of arbitrary form and speed and simulating, for example, a manu-

evering aircraft. Such motions are obviously not possible in a wind tunnel or a flume. Note also that a body accelerating in a still fluid is not, in general, equivalent to an accelerating fluid past a stationary object. The last point regarding the negligible background motion is of extreme importance in studying stability or transition problems where the results are sensitive to the background turbulence. The difficulties of designing a water tunnel with low background noise are well known.

Among the drawbacks of using a towing tank is the inevitable carriage vibration and the limited running time associated with the finite length of the channel. Carriage vibration can be greatly reduced by the proper design of the towing and support systems. The towing tank described in Section 3 uses a carriage that rides on a continuously supplied film of oil to minimize vibration. To overcome the limited running time, sophisticated data acquisition systems and multichannel probes are usually part of a towing tank operation so that large amounts of data can be taken during a single run.

### 3. DESCRIPTION OF A TYPICAL FACILITY

The world's largest high-speed water towing tank facility is the David W. Taylor Model Basin located at the Naval Ship Research and Development Center in Bethesda, Maryland. Its 0.9-km track has to be adjusted to account for the Earth's curvature! Other, albeit smaller, water tanks include the ones operated by the Naval Research Laboratory, the Environmental Protection Agency, NASA-Langley, the University of Tel-Aviv, the National Maritime Institute, Massachusetts Institute of Technology, and Flow Research Company. This latter towing tank facility is briefly described in this section. More complete information regarding the design and construction of Flow Research's towing tank is available in the article by Pao et al. (1971).

#### 3.1 The Towing Tank

This water channel, shown in Figure 1, is 18-m long, 1.2-m wide and 0.9-m deep. It is supported by a steel main frame and constructed of two 9-m lattice truss units bolted together. The main frame is supported by four screw jacks and can be tilted and leveled. The jacks are in turn supported on specially designed rubber pads to minimize vibrations transmitted from external sources through the laboratory floor. The maximum deflection allowed in the center span between the jacks is less than 0.25 mm. This feature is essential for smooth operation of the oil-lubricated carriage, whose tracks are supported by the main frame.

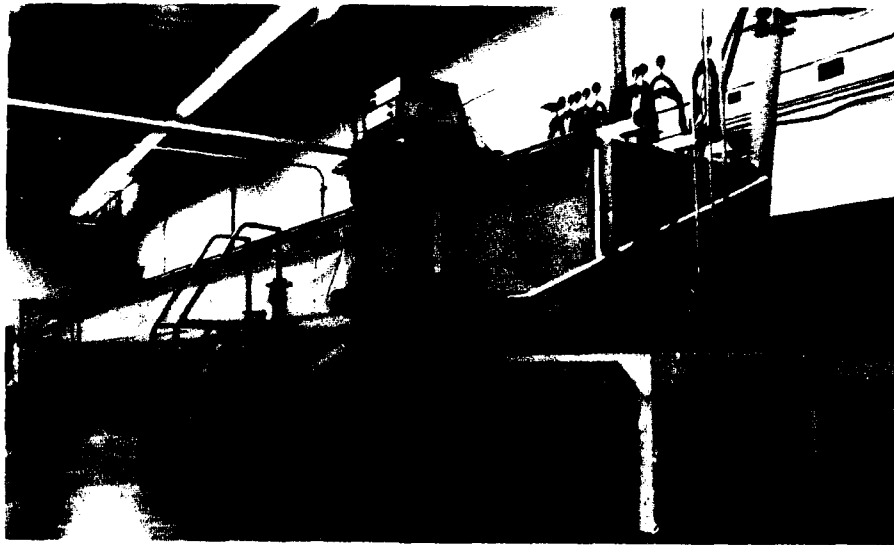


Figure 1. The Flow Research 18-m Towing Tank

Flow visualization can be made from the top, sides, bottom and end of the tank. The side and bottom walls are made of optical quality, 19-mm-thick plate glass, and the end walls are made of thicker, 38-mm-thick, Plexiglas. The towing tank has two 3-m-long test sections and eight 1.5-m-long sections. All the glass plates are cushioned against the steel frame with 6-mm-thick rubber strips and with patty-type Flexane to provide uniform load support along the edges of the plates.

#### 3.2 Filling System

As mentioned in Section 2, one of the primary reasons for building a water towing



channel is the ability to accomplish density stratification by heating or cooling the water or by the use of salt water. In contrast to a wind tunnel or a flume, a towing tank can easily be stratified to essentially any desired, fairly arbitrary, stable density profile.

For the present tank, water with a given salinity and temperature is used as the working fluid and is fed from the tank's bottom, layer by layer, with increasing specific gravity. The filling system consists of three 3785-liter fiberglass storage tanks, two 570-liter polyethylene constant-head tanks, two 0.75-hp pumps, a gas water heater, and two 18-m-long stainless-steel feed channels resting on the floor of the towing tank. The towing tank itself has a capacity of about 19,000 liters.

Two of the storage tanks are used to prepare a concentrated brine solution, and the third tank is filled with fresh water. The saline solution and the fresh water are then pumped separately to the two constant-head tanks. A mixing valve accurately regulates, by the adjustment of a loading spring, the flow rate from the two constant-head tanks to achieve a constant flow rate of water of a given salt concentration or a prescribed specific gravity. The displacement of the loading spring is set with a dial that has a resolution of 25 microns, and the mixing valve can either be operated manually or driven by a computer-controlled stepping motor. The mixture is then passed through a thermostat-regulated water heater for controlling its temperature before being fed to the bottom of the towing tank. The body of water in the tank is displaced upwards, and two overflow standpipes are used to discharge the excess fluid.

With the arrangement described above, a predetermined density stratification can readily be obtained by varying the thermostat setting and/or the (calibrated) dial setting of the mixing valve. The density gradient in the tank can be controlled by changing the water's temperature, salt concentration or both. This latter capability allows the study of double-diffusion problems, in which gradients of two properties exist with different molecular diffusivities. When temperature stratification is not needed, the water temperature is matched to that of the room, allowing accurate velocity measurements with hot-film probes operating at low overheat ratios (see Section 4.1).

### 3.3 Towing System

The towing system consists of five 3-mm-diameter stainless-steel cables, 11 driving pulleys of different diameters, a series of following pulleys, two 1.5-hp dc motors (Boston Gear) with Ratiotrol speed control, and two 5-hp ac induction motors (Mitsubishi) with a Transistor Inverter (Marathon Electronics) for accurate speed control. Each of the motor pairs is used to drive, through a reduction gear, two independent carriages, one for the model and the second for the accompanying probes. If desired, both the model and the probe's strut can be attached to the same carriage. The dc motors are used for low to moderate speeds (1 to 100 cm/s), while the more powerful 5-hp motors are used for speeds up to 3 m/s and acceleration/deceleration rates up to 6 m/s<sup>2</sup>. Both speed control systems are capable of regulating the carriage speed within an accuracy of 0.1 percent.

The towing cables form closed loops and are supported by pulleys mounted on two frames, one at each end of the tank. Proper tension is applied to each towing cable using a threaded rod and a phenolic pulley on a take-up channel. To isolate the towing tank from vibrations due to the motor, the racks to support the driving shaft and the motor rest on the floor and the tank is properly isolated from the floor as mentioned earlier.

### 3.4 Oil-Lubricated Carriage

Two oil-lubricated carriages are used to transport independently the model to be tested and the accompanying instruments and sensing probes. This feature allows wake measurements at varying distances from a body including the very far wake. The instrumentation carriage also provides a traversing mechanism that can position a probe strut laterally and vertically with an accuracy of 0.25 mm. A finer traverse with a resolution of 0.02 mm is also available for boundary layer measurements.

Two 18-m-long oil-lubricated tracks are mounted on top of the towing tank; one track is round and the other is flat. Each carriage has two round shoes and two flat shoes that ride on the corresponding track, supported by the pressure of oil that is continuously pumped from a reservoir through a supply line towed with the carriage. The oil is then collected into a gutter for recirculation and filtering. The surfaces of both tracks are carefully smoothed, and irregularities in the tracks are adjusted using fine screws on their support rods to less than 0.25 mm in height. This together with the oil-lubricated system ensures smooth, vibrationless operation.

The present oil-lubricated system has a carriage noise level far less than that of any other existing towing tank. The total noise level (root-mean square) as measured by a hot-film probe towed in the tank is less than 0.1 percent of the towing speed. This includes effects due to the electronic noise of the anemometer, residual motion and temperature fluctuations in the water, possible motor speed variations, vibration in the probe support induced by the flow around the strut, and finally carriage speed variations due to irregularities in the track. For towing tanks that use bearing- or wheel-supported carriages, the corresponding noise level is typically 1 percent of the towing speed.

### 3.5 Scaling Laws

Accurate simulation of field conditions in a laboratory study requires that the values of a number of dimensionless parameters attained in the field be matched in the laboratory. These dimensionless parameters must express the geometric, kinematic and dynamic similarities of the laboratory modeling with the field. It is generally not difficult to scale down (or up) all geometric objects and all velocities from the field case to the laboratory case, thus satisfying both geometric and kinematic similarities. Dynamic similarity means matching the ratios of a number of forces, such as buoyancy, inertia, viscosity, and surface tension. Typical dimensionless ratios of these forces are the Reynolds number, Mach number, Froude (or Richardson) number, Rossby number, etc. Some of these numbers can be matched in most towing tank facilities, while others are more difficult to scale proportionally from the field to the laboratory. For example, in simulating the wake of an underwater vehicle moving in the ocean, the Froude number can be matched in a typical low-speed towing tank although the field Reynolds number is too high to match. It is often argued, however, that, for unbounded turbulent flows, if the Reynolds number is high enough, then the large-scale features of the flow will be independent of the Reynolds number (Townsend, 1976). This conjecture must be supported by field or laboratory data for the particular problem under consideration. This point will be discussed further in the specific research examples given in Section 5.

## 4. MEASUREMENT TECHNIQUES

### 4.1 Probe Measurements

With few exceptions, the instrumentation used in a towing tank is identical to that used in a water tunnel. For mean and fluctuating velocities, measurements can be made with Pitot tubes, hot-film probes, laser Doppler velocimeters, vortex-shedding anemometers, etc. If stratification is involved, temperature and salinity fluctuations are also measured. To overcome the finite run time in a typical towing tank, however, multichannel probes are usually used.

When a hot-film anemometer is used, care must be taken to keep the water free of dirt, bubbles and other contamination. Low overheat ratios are used to prevent boiling and bubble formation. Accordingly, the hot-film gauge is sensitive to both velocity and temperature fluctuations. Extreme care is required, therefore, to control the water temperature. If the fluid in the tank is kept at constant room temperature, heat transfer to or from the ambient air is minimized. In cases where stratification is accomplished by heating or cooling the water, temperature fluctuations are unavoidable, and two independent measurements of velocity and temperature must be made to separate their variations.

If a laser Doppler velocimeter is towed with the model, special optics are required to compensate for the inevitable vibrations in the system. The velocimeter can, however, be fixed in the laboratory frame while the model is towed to obtain, for example, wake data at increasing distances from the body. The experiment can then be repeated several times and the velocity data ensemble-averaged to obtain meaningful statistics at each point behind the body.

Fast-response thermistors and conductivity gauges can be used to measure the instantaneous temperature and density, respectively. Common problems with these probes include insufficient spatial and temporal resolutions and drift with time. Care in selecting the probes and conducting the experiments alleviates much of the shortcomings of such measurements.

Internal waves are generated when a stably stratified medium is disturbed in any way. In a towing tank and in the absence of turbulent motion, the vertical displacements associated with these waves can be measured using either a conductivity probe or a laser displacement gauge (Liu and Lin, 1982). In the former technique, the known mean density profile in the tank is used to obtain the displacement from the local changes in density as measured by the conductivity probe. The laser displacement gauge measures the displacement of an optical interface, created by a horizontal layer of fluorescent dye and a vertical laser beam, using an electronically self-scanning array of photodiodes.

The tank length and the desired towing speed limit the running time per experiment. Accordingly, sophisticated data acquisition systems are usually a part of a towing tank operation. The idea is to collect large amounts of data with many probes during each run to reduce the total number of runs necessary. The limited run time should also be taken into account when higher-order moments are to be extracted from random signals such as turbulent velocity fluctuations. If the averaging time is insufficient for a statistical quantity to converge, ensemble-averaging of several runs should again be invoked.

### 4.2 Visualization Techniques

Water towing tanks are perhaps the best facility for conducting flow visualization studies. All the classical dye or particle tracer techniques can be used without recirculation problems and with the additional advantage of an extremely quiet background. In addition, the capability of stratification allows the use of flow visualization techniques that are based on index of refraction changes, such as shadowgraph or

schlieren methods. Moreover, some techniques, such as the dye-layer method, are unique to towing tank operations.

Many of the flow visualization techniques that can be used in towing tanks or water tunnels have been described in the books by Merzkirch (1974) and Goldstein (1983) and the article by Gad-el-Hak (1986a). Spherical or disk-shaped particles can be introduced into the flow to mark its motion. Both qualitative and quantitative data can be obtained by using hydrogen bubbles, neutrally buoyant oil or wax particles, or titanium-dioxide-coated mica particles. This latter technique allows a more dynamic visualization of the flow, since the disk-shaped particles are oriented in a systematic way by the three-dimensional rate-of-strain field in the fluid.

Both food-coloring and fluorescent dyes can be used with either floodlight or laser-sheet illumination. The combination of fluorescent dye and laser light sheet allows the viewing of the interior of the flow region, in contrast to the "skin" as viewed with conventional dye techniques. The dyes are introduced to the flow through slots and holes machined into a model. Dye can also be released uniformly from a towed model by covering its entire surface with a thin, porous cloth saturated with dry dye crystals (Gad-el-Hak and Ho, 1986a). A comparative analysis of the visualization techniques using floodlight/conventional dyes, laser/fluorescent dyes or disk-shaped particles has been presented by Gad-el-Hak et al. (1985).

The dye-layer technique (Gad-el-Hak, 1986b) utilizes layers of fluorescent dye placed into a slightly stratified tank prior to towing a model. The stable density gradient in the tank inhibits vertical mixing, and the layers of dye remain thin. Sheets of laser light are projected in the desired plane to excite the dye, thus marking both the rotational and the irrotational flow regions around a body.

## 5. TYPICAL RESEARCH RESULTS

### 5.1 Flow in Stratified Media

As mentioned earlier, towing tanks have an advantage over both wind and water tunnels in the ease of generating any desired, fairly arbitrary, stable density profile. Numerous studies have been conducted in towing tanks around the world to study different buoyancy effects in fluids and to simulate a variety of natural and man-made flow fields occurring in the ocean or the atmosphere (see, for example, the book by Turner, 1973, and the review articles by Yih, 1969, Long, 1972, Maxworthy and Browand, 1974, Lin and Pao, 1979, and Snyder, 1985).

Towing tanks can be used to model the behavior of stack plumes and their impact on air quality (Riley and Delisi, 1976). Snyder (1985) reports on several towing tank experiments to study the effects of stratification on plume behavior in complex terrain. He states that the Froude number is quite likely the most important single parameter to be matched when simulating strongly stable flow and diffusion in complex terrain. In the facility described in Section 3, Liu (1985) simulated plume dispersion in flat and rugged terrain under neutral and stable atmospheric conditions. Excellent agreement between simulated and full-scale plumes was demonstrated using dye visualization techniques. Liu also conducted detailed conductivity-probe measurements at discrete points to complement the overall flow patterns gleaned from the visualization pictures.

Lin and Pao (1979) reviewed research concerning wakes generated by moving grids and two- and three-dimensional bodies in stratified fluids. They reported on several experiments conducted in the 18-m towing tank (Section 3) to study the effects of stratification on vortex generation, the blocking phenomenon (upstream wake) and wake collapse. In a stratified medium, the wake of a three-dimensional body does not grow indefinitely. Rather, the vertical wake height reaches its maximum at about 0.3 times the Brunt-Väisälä period after passage of the body's stern, and then a substantial vertical wake collapse occurs. At a later time, the wake meanders and horizontal vortices are formed as shown in Figure 2. Lin and Pao (1979) provide a possible explanation for the mechanisms responsible for wake evolution in a stratified medium.

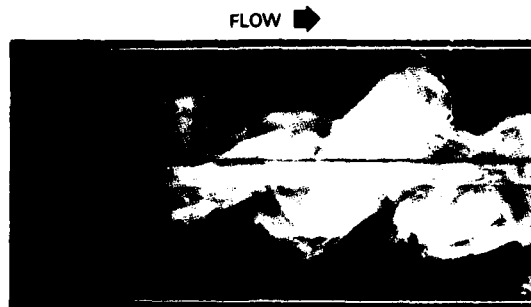


Figure 2. Horizontal Vortices in a Stratified Flow

## 5.2 Boundary Layer Research

The quiet background of a towing tank makes it an ideal test facility for studying laminar, transitional and turbulent boundary layers. Well-controlled experiments have been conducted in the present tank by towing a nominally zero-pressure-gradient flat plate. Gad-el-Hak et al. (1981) investigated the growth of turbulent regions in a laminar boundary layer. They argued convincingly that turbulent spots, initiated using a small buff from a hole on the plate, and turbulent wedges, which form behind a roughness element on the plate, grow in the lateral direction mostly by destabilizing the surrounding laminar flow rather than by the classical entrainment of irrotational fluid. Gad-el-Hak et al. (1981) also investigated the effects of stratification and drag-reducing polymers on the growth of turbulent spots. A top view of a typical turbulent spot, visualized using the laser/fluorescent dye technique, is shown in Figure 3. The dynamics within the spot appear to be controlled by many individual eddies, similar to those within a turbulent boundary layer. No evidence of one or two prominent vortical structures, as shown from the ensemble-averaged results obtained by Wignanski et al. (1976) and Cantwell et al. (1978), could be found in any single turbulent spot realization (Riley and Gad-el-Hak, 1985).

The stability of a decelerating laminar boundary layer was investigated experimentally and numerically by Gad-el-Hak et al. (1984a). A flat plate having a Blasius boundary layer was decelerated uniformly in the towing tank, and the resulting well-defined route to turbulence was documented using visualization and hot-film probe measurements. First, the boundary layer became unstable to two-dimensional waves, which, due to the inflectional character of the velocity profile associated with the decelerating plate, have substantially larger growth rates than their Tollmien-Schlichting counterparts. Second, the two-dimensional waves were themselves unstable and developed a regular spanwise modulation. This in turn led to the formation of hairpin vortices that lifted away from the wall, stretched and burst into turbulence. Figure 4, taken from Gad-el-Hak et al. (1984a), shows the typical sequence of transition events in a decelerating laminar boundary layer.

## 5.3 Compliant Coatings

A special class of boundary layers is that where the wall is not rigid but rather soft enough to respond to the pressure and viscous forces imposed by the fluid. The motion of such a compliant surface can in turn result in significant changes in the basic flow properties. Compliant wall research apparently originated from consideration of the low drag characteristics exhibited by dolphin skin and the desire to produce artificially a drag-reducing coating for man-made vehicles (Bushnell et al., 1977; Gad-el-Hak, 1986c; Metcalfe et al., 1988).

Several experiments have been conducted in the 18-m towing tank to investigate the interactions of elastic and viscoelastic compliant coatings with laminar, transitional and turbulent boundary layers (Gad-el-Hak et al., 1984b; Gad-el-Hak, 1986d; 1987). It was found that at sufficiently high speed, the compliant surface becomes unstable, and waves appear at the solid/fluid interface. The wave characteristics were measured from visual observations and also from the digital output of the laser displacement gauge (Liu and Lin, 1982). The waves forming on an elastic surface were found to be symmetric and to have a relatively high phase speed and small wavelength. In contrast, waves forming on a viscoelastic surface, static-divergence waves, were observed to be slow and highly nonlinear.

Either a turbulent boundary layer, a turbulent wedge or a turbulent spot can trigger the hydroelastic instabilities described above. No instabilities are observed, however, when the boundary layer is laminar, even at freestream speeds of over twice the corresponding onset velocity for the turbulent case. This is shown convincingly in the photograph in Figure 5. In that experiment, a turbulent wedge was formed in an otherwise laminar boundary layer by placing a single roughness element on the surface of the plate. Static-divergence waves are readily apparent in the viscoelastic surface under the turbulent wedge but not under the surrounding laminar region.

## 5.4 Flow Control

A sizable amount of energy is expended in overcoming the viscous drag due to the motion of a vehicle in a fluid medium. To reduce fuel consumption or to achieve higher speeds for a given power plant, skin friction drag must be reduced. This can be achieved by either delaying transition (laminar flow control) or controlling the turbulent boundary layer. Laminar flow control methods include the use of suction or surface heating (for vehicles moving in water). Among the methods that are currently considered for turbulent skin friction reduction are compliant coatings, large-eddy breakup devices, streamwise grooves, polymer injection, and suction/injection techniques.

In the present towing tank, several flow control experiments have been conducted to investigate a variety of drag-reducing methods. The use of compliant coatings was described above. Another experiment involved the artificial generation of bursting events in a turbulent boundary layer (Gad-el-Hak and Hussain, 1986). Bursts were generated using either a sudden suction pulse from two minute holes separated in the spanwise direction or by pitching a miniature delta wing that was flush-mounted to the wall. Either of these two actions generates a hairpin-like vortex and a low-speed streak that resemble naturally occurring structures. The resulting sequence of events that occurs at a given location can be uniquely controlled, thus allowing detailed

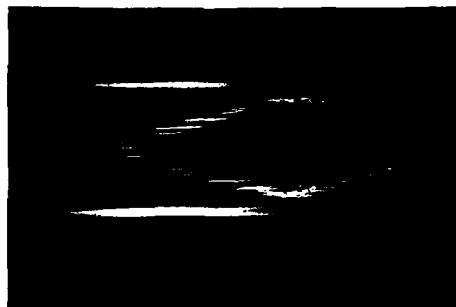


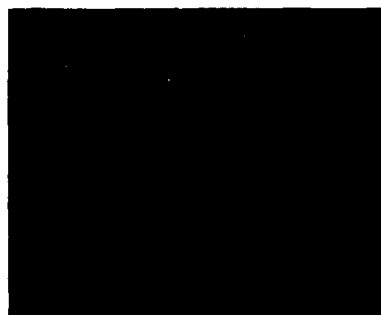
Figure 3. Turbulent Spot in a Laminar Boundary Layer (from Gad-el-Hak et al., 1981)

FLOW  
➡



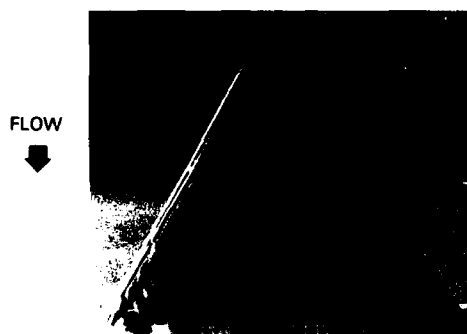
Figure 4. Transition Events in a Decelerating Laminar Flow (from Gad-el-Hak et al., 1984a)

FLOW  
➡

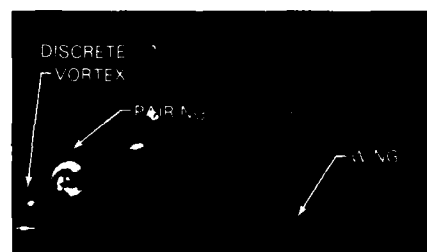


10 cm  
|-----|

Figure 5. Static Divergence Waves (from Gad-el-Hak et al., 1984b)



a. Top View



b. End View

Figure 6. Discrete Vortices Shed from the Leading Edge of a Delta Wing (from Gad-el-Hak and Blackwelder, 1986)

examination through the use of phase-locked measurements.

Another flow control technique currently under consideration combines the beneficial effects of a longitudinally ribbed surface and suction (Gad-el-Hak and Blackwelder, 1987a). The streamwise grooves act as a nucleation site causing the focusing of low-speed streaks over the peaks. Suction is then applied through longitudinal slots located at selected locations along these peaks, thus minimizing the pumping energy requirements.

Another flow control method currently under investigation is the use of spanwise, intermittent injection to generate large-scale, periodic structures in a turbulent shear flow (Gad-el-Hak and Blackwelder, 1987b). Such a device, while not necessarily reducing the viscous drag, is being considered for use on airborne laser platforms to reduce or eliminate optical distortion of the laser beam caused by turbulence in the aircraft's boundary layer.

### 5.5 Steady and Unsteady Aerodynamics

A variety of steady and unsteady aerodynamic studies have been conducted in the 18-m towing tank described in Section 3. The flow over a delta wing in steady flight has been investigated using flow visualization and fast-response velocity probe measurements (Gad-el-Hak and Blackwelder, 1985). It was found that the classical large vortices on delta wings originate as a series of smaller vortices shed from the leading edge of the airfoil. They rotate around each other and pair to form larger vortices while simultaneously moving downstream. Figure 6 shows top and end views of the discrete vortices. A method for controlling and enhancing these discrete vortices and the pairing process was described by Gad-el-Hak and Blackwelder (1986). The technique utilizes subharmonic perturbations from a leading edge slot.

The complex, time-dependent flow fields around three-dimensional lifting surfaces undergoing large-amplitude pitching harmonic oscillations have also been investigated in the present facility. The lifting surfaces considered were delta wings (Gad-el-Hak and Ho, 1985), slender bodies of revolution (Gad-el-Hak and Ho, 1986a), and swept wings, including those with zero sweep (Gad-el-Hak and Ho, 1986b). An example of the results, taken from Gad-el-Hak (1986b), is shown in Figure 7, depicting a small-aspect-ratio rectangular wing undergoing the pitching motion  $\alpha(t) = 15^\circ + 15^\circ \sin(2\pi ft)$  at three reduced frequencies,  $K = 0.2, 1.0$ , and  $3.0$ . The unsteady separation phenomena associated with these lifting surfaces were discussed by Gad-el-Hak (1986e).

Another example of unsteady aerodynamic problems is the complex flow around a model of a rotating-wing aircraft. A 1:40 scale model of an H-34 helicopter rotor was towed in the present water channel, and the advance ratio, collective pitch, and longitudinal and lateral cycling were adjusted independently over a normal range of field operating conditions. Under certain run parameters, a negative loading was present near the tip of the advancing blade, and a pair of counter-rotating vortices were shed from that tip. The interaction of these vortices with the succeeding blade, believed to be a major source of helicopter noise and vibration, was observed directly, for the first time, using the dye-layer technique (Section 4.2). It is obvious that it would be extremely difficult to conduct such an experiment in a water or wind tunnel using classical dye- or smoke-visualization methods. This is due to the complexity of the setup, where the blades are simultaneously rotating and undergoing cyclical pitching.

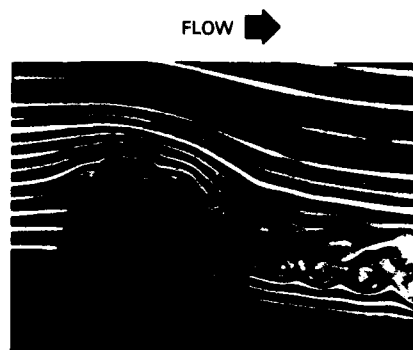
When modeling a high-reduced-frequency aerodynamic flow, existing studies on two- and three-dimensional, unsteady lifting surfaces have shown that the Reynolds number is not a primary control parameter (McCroskey, 1982; Gad-el-Hak and Ho, 1986a). While viscous effects are essential for producing the shear layer responsible for the onset of unsteady separation, viscosity does not play an important role on the subsequent dynamical processes within the already separated flow. The local unsteady separation, in turn, has a very strong effect on the global aerodynamic properties. Thus, unsteady effects dominate the flow and are mainly responsible for the variations of the aerodynamic forces. Results obtained in low-speed facilities are, therefore, useful in understanding the physics of unsteady flows occurring in the field at a much higher Reynolds number.

## 6. SUMMARY

Intercomparison of the advantages and disadvantages of wind tunnels, flumes, and towing tanks is discussed in this article. It is shown that each facility has its unique place in laboratory modeling. The goals and objectives of a particular study should determine the optimum flow rig to use.

The construction and operation of a particular water towing tank are detailed in this paper. Available measurement techniques are discussed, including flow visualizations and fast-response probes.

Many examples of fundamental aerodynamic and hydrodynamic studies are described. These include flows in stratified media, laminar, transitional and turbulent boundary layers, compliant coatings, flow control, and steady and unsteady aerodynamic flows. These examples illustrate the usefulness and versatility of towing tank facilities.



a. Reduced Frequency = 0.2



b. Reduced Frequency = 1.0



c. Reduced Frequency = 3.0

**Figure 7. Pitching Lifting Surface**  
(from Gad-el-Hak, 1986b)

## ACKNOWLEDGEMENTS

The writing of this article, together with the research of the author for the past five years, has been supported by the National Science Foundation Grant ISI-8560825, the Air Force Office of Scientific Research Contract F49620-82-C-0020, the Office of Naval Research Contract N00014-81-C-0453, and the National Aeronautics and Space Administration-Langley Research Center Contracts NAS1-18292 and NAS1-18213.

## REFERENCES

- Bushnell, D. M., Hefner, J. N., and Ash, R. L. (1977) "Effect of Compliant Wall Motion on Turbulent Boundary Layers," Phys. Fluids, Vol. 20, pp. S31-S48.
- Cantwell, B., Coles, B., and Dimotakis, P. (1978) "Structure and Entrainment in the Plane of Symmetry of a Turbulent Spot," J. Fluid Mech., Vol. 87, pp. 641-672.
- Gad-el-Hak, M. (1986a) "Review of Flow Visualization Techniques for Unsteady Flows," submitted to Exp. in Fluids.
- Gad-el-Hak, M. (1986b) "The Use of the Dye-Layer Technique for Unsteady Flow Visualization," J. Fluids Eng., Vol. 108, pp. 34-38.
- Gad-el-Hak, M. (1986c) "Boundary Layer Interactions with Compliant Coatings: An Overview," Appl. Mech. Reviews, Vol. 39, pp. 511-523.
- Gad-el-Hak, M. (1986d) "The Response of Elastic and Viscoelastic Surfaces to a Turbulent Boundary Layer," J. Appl. Mech., Vol. 53, pp. 206-212.
- Gad-el-Hak, M. (1986e) "Unsteady Separation on Lifting Surfaces," submitted to Appl. Mech. Reviews.
- Gad-el-Hak, M. (1987) "Compliant Coatings Research: A Guide to the Experimentalist," Fluids and Structures, Vol. 1, No. 2.
- Gad-el-Hak, M., and Blackwelder, R. F. (1985) "The Discrete Vortices from a Delta Wing," AIAA J., Vol. 23, pp. 961-962.
- Gad-el-Hak, M., and Blackwelder, R. F. (1986) "Control of the Discrete Vortices from a Delta Wing," submitted to AIAA J.
- Gad-el-Hak, M., and Blackwelder, R. F. (1987a) "Selective Suction for Controlling Bursting in Turbulent Boundary Layers," submitted to Phys. Fluids.
- Gad-el-Hak, M., and Blackwelder, R. F. (1987b) "Turbulence Control on Airborne Laser Platform," submitted to AIAA J.
- Gad-el-Hak, M., Blackwelder, R. F., and Riley, J. J. (1981) "On the Growth of Turbulent Regions in Laminar Boundary Layers," J. Fluid Mech., Vol. 110, pp. 73-95.
- Gad-el-Hak, M., Blackwelder, R. F., and Riley, J. J. (1984b) "On the Interaction of Compliant Coatings with Boundary Layer Flows," J. Fluid Mech., Vol. 140, pp. 257-280.
- Gad-el-Hak, M., Blackwelder, R. F., and Riley, J. J. (1985) "Visualization Techniques for Studying Transitional and Turbulent Flows," in Flow Visualization III, ed. W. J. Yang, Hemisphere, Washington, D.C., pp. 568-575.
- Gad-el-Hak, M., Davis, S. H., McMurray, J. T., and Orszag, S. A. (1984a) "On the Stability of the Decelerating Boundary Layer," J. Fluid Mech., Vol. 138, pp. 297-323.
- Gad-el-Hak, M., and Ho, C.-M. (1985) "The Pitching Delta Wing," AIAA J., Vol. 23, pp. 1660-1665.
- Gad-el-Hak, M., and Ho, C.-M. (1986a) "Unsteady Flow Around an Ogive-Cylinder," J. Aircraft, Vol. 23, No. 6.
- Gad-el-Hak, M., and Ho, C.-M. (1986b) "Unsteady Vortical Flow Around Three-Dimensional Lifting Surface," AIAA J., Vol. 24, pp. 713-721.
- Gad-el-Hak, M., and Hussain, A. K. M. F. (1986) "Coherent Structures in a Turbulent Boundary Layer. Part 1: Generation of 'Artificial' Bursts," Phys. Fluids, Vol. 29, No. 7.
- Goldstein, R. J. (1983) Fluid Mechanics Measurements, Hemisphere, Washington, D.C.
- Itsweire, E. C., Helland, K. N., and Van Atta, C. W. (1986) "The Evolution of Grid-Generated Turbulence in a Stably Stratified Fluid," J. Fluid Mech., Vol. 162, pp. 299-338.
- Koromilas, C. A., and Telionis, D. P. (1980) "Unsteady Laminar Separation: An Experimental Study," J. Fluid Mech., Vol. 97, pp. 347-384.



- Lin, J.-T., and Pao, Y.-H. (1979) "Wakes in Stratified Fluids," Ann. Rev. Fluid Mech., Vol. 11, pp. 317-338.
- Liu, H.-T. (1985) "Applications of a Tow Tank for Physical Modeling of Plume Dispersion: Flow Visualization," in Flow Visualization III, ed. W. J. Yang, Hemisphere, Washington, D.C., pp. 699-706.
- Liu, H.-T., and Lin, J.-T. (1982) "On the Spectra of High-Frequency Wind Waves," J. Fluid Mech., Vol. 123, pp. 165-185.
- Long, R. R. (1972) "Finite Amplitude Disturbances in the Flow of Inviscid Rotating and Stratified Fluids over Obstacles," Ann. Rev. Fluid Mech., Vol. 4, pp. 69-92.
- Maxworthy, T., and Browand, F. K. (1975) "Experiments in Rotating and Stratified Flows: Oceanographic Applications," Ann. Rev. Fluid Mech., Vol. 7, pp. 273-305.
- McCroskey, W. J. (1982) "Unsteady Airfoils," Ann. Rev. Fluid Mech., Vol. 14, pp. 285-311.
- Merzkirch, W. (1974) Flow Visualization, Academic Press, New York.
- Metcalfe, R. M., Riley, J. J., and Gad-el-Hak, M. (1988) "Compliant Coatings," Ann. Rev. Fluid Mech., Vol. 20.
- Pao, Y.-H., Lin, J.-T., Carlsen, R. L., and Smithmeyer, L. P. C. (1971) "The Design and Construction of a Stratified Towing Tank with an Oil-Lubricated Carriage," Flow Research Report No. 4, Kent, WA.
- Reynolds, W. C., Jayaraman, R., and Carr, L. W. (1983) "Experiments on Controlled, Unsteady, Separated Turbulent Boundary Layers," in Unsteady Separated Flows, eds. M. S. Francis & M. W. Luttges, University of Colorado, Boulder, pp. 158-164.
- Riley, J. J., and Delisi, D. P. (1976) "Survey of Laboratory Modeling of Plume Dynamics," Flow Research Report No. 75, Kent, WA.
- Riley, J. J., and Gad-el-Hak, M. (1985) "The Dynamics of Turbulent Spots," in Frontiers in Fluid Mechanics, eds. S. H. Davis & J. L. Lumley, Springer, Berlin, pp. 123-155.
- Sirivat, A., and Warhaft, Z. (1983) "The Effect of a Passive Cross-Stream Temperature Gradient on the Evolution of Temperature Variance and the Heat Flux in Grid Turbulence," J. Fluid Mech., Vol. 128, pp. 323-346.
- Snyder, W. H. (1985) "Fluid Modeling of Pollutant Transport and Diffusion in Stably Stratified Flows Over Complex Terrain," Ann. Rev. Fluid Mech., Vol. 17, pp. 239-266.
- Townsend, A. A. (1976) The Structure of Turbulent Shear Flow, Second Edition, Cambridge University Press.
- Turner, J. S. (1973) Buoyancy Effects in Fluids, Cambridge University Press.
- Wyganski, I., Sokolov, M., and Friedman, D. (1976) "On a Turbulent 'Spot' in a Laminar Boundary Layer," J. Fluid Mech., Vol. 78, pp. 785-819.
- Yih, C.-S. (1969) "Stratified Flows," Ann. Rev. Fluid Mech., Vol. 1, pp. 73-110.

A NEW LAMINAR WATER TUNNEL TO STUDY THE TRANSITION PROCESS  
IN A BLASIUS LAYER AND IN A SEPARATION BUBBLE AND  
A NEW TOOL FOR INDUSTRIAL AERODYNAMICS AND HYDRODYNAMIC RESEARCH

M. Strunz, J.F. Speth  
Institut für Aerodynamik und Gasdynamik  
Universität Stuttgart  
Pfaffenwaldring 21, 7000 Stuttgart 80  
Germany

#### SUMMARY

Two new watertunnels of the institute are presented. The first one is especially designed to study the stability of a laminar boundary layer. The second one is built to solve problems in industrial aero- and hydrodynamics. The construction of both tunnels is made of corrosion-resistant materials. They are built in glasfiber-reinforced-plastic-technology. Technical data and first applications are given.

#### 1. INTRODUCTION

Visualization plays an important, increasing role in understanding flow phenomena. This Lagrangian view makes the flow transparent for better knowledge in fluid research and gives a comprehensive information of particularities of fluid motion. The visualisation techniques in water are more effective than in air, because of its much lower diffusivity which is reciprocal to the density ( $\rho_{\text{water}} / \rho_{\text{air}} = 825$ ). An additional benefit studying flow phenomena in water at the same Reynoldsnumber and the same size of the model is the reduced flow velocity (15 times).

#### 2. CONSTRUCTION OF THE "Laminar Water Tunnel".

The tunnel is built like a laminar wind tunnel. The disturbances which are mostly proportional to the total pressure and which cannot be avoided in the closed circuit of a hydrodynamic tank are at a low energy level by reducing the flow velocity on the way back from the end of the measuring section to the entrance of the contraction cone.

Secondary flow induced by convection which leads to longitudinal vortices, is suppressed by a good thermal insulation. The segments of the circuit are manufactured in sandwich construction. PVC-foam with small voids has an adequate insulating property. In addition the vertical temperature gradient of the insulate laboratory room is very low ( $\approx 0.7$  degrees centigrade). This is possible by a masonry of stones, which can give there thermal capacity to the air of the laboratory. Both, the masonry and the 30 tons of water in the tank are in fact a "thermal flywheel" for long-term constancy.

Possible vibrations, which effects the flow, can be avoided by a suspension of the tank on air springs, which are activated by compressed air. The eigenfrequency of the whole tank is 1 cycle/second, additionally the fundamental frequency can be reduced by enlarging the active air content. One can imagine, that the whole facility is supported like a seismic mass. Vibrations in the building cannot reach the tank and therefore not the fluid.

A special designed axial-flow pump has a six-bladed-rotor (profile NASA GA(W)-1). Two side by side countercurrent axial pumps press the fluid through the circuit. The electro-drive is feedback speed controlled with a frequency transducer, so that long term constancy of the rate of revolutions is guaranteed. The temporary constant rotational speed is hold by a flywheel.

To reduce the turbulence level in the circuit we use screens to smooth the velocity distribution after the last turning vanes. At Reynolds-numbers of about 4 related to the thread of the screen there is no microturbulence behind the screens which needs a settling chamber for damping. Only viscosity is used to comparable the flow. In this special case the mesh size is a dominant parameter. The last screen must be a precision screen to reduce last nonuniformities. The wake behind such a synthetic precision screen made of tensed wires can be seen in the Figures 2. and 3. . The wake is no more visible 5mm downstream of the screen.

### 3. PROPERTIES OF THE "Laminar water tunnel".

The technical data are summarized in Table 1.

Measurements in the tunnel requires a long time of preparation. The temperature of the water has to be tuned to the temperature of the air in the laboratory and this is a delicate work. A very critical point is the free water surface. The psychrometric temperature-difference must be eliminated, otherwise streaks of cold water are introduced in the circuit.

Beside these temperature problems the boundary layer thickness in the corner of the measuring section must be reduced.

A quick test of the flow quality is the free surface. Tiny fluctuations of the pressure can be observed if one uses the free surface as a mirror. This technique only can be employed if the velocity is smaller than the velocity of the capillary-gravity waves.

As an application of the tunnel a separation bubble is examined. Figure 4 shows the instationary pulsation of a short bubble which leads to a transversal vortex by natural amplification. The rear part of a separation bubble, where turbulent reattachment occurs, is indicated in Figure 5. Some timelines assign an impression of the fluctuation in relationship to the wall distance. In a Blasius layer Tollmien-Schlichting waves are triggered by a vibrating ribbon. After the formation of lambda vortex-structures we can observe a new vortex behind the well known top vortex (Figure 6.). At the neck of the top vortex which lies at the border of the viscous layer a decay of the vortex can be observed.

### 4. CONSTRUCTION OF THE DEVICE "Large water tunnel".

The design of the recirculation tunnel is based on the criterions which holds for low turbulence wind tunnels. The plastic surface of the inner side of the tank is smooth and can easily be designed for low flow resistance. All sides of the test section are transparent. It has an adjustable floor and double side walls. This are usefull possibilities to adapt the test section to different flow problems. The test area (see Table 1.) is large enough to install a car on a reduced scale of 1:5 (Figure 11.1). With the equipped 23 kW electric drive a Re-number related to 1 m of  $2.5 \times 10^6$  is available. With a stronger motor a Re-number of  $4 \times 10^6$  will be reached.

The tank is built as one piece in GRP-technology. No leakage problem can occur. Therefore the pumps are top driven. A variation to higher Re-numbers is possible by heating the water.

### 5. APPLICATIONS WITH THE "Large water tunnel".

The tunnel is used for industrial aerodynamics and hydrodynamic research. Figure 8 points out a light intersection technique. Two staggett light sheets generated with one laser beam by using adjustable rotating mirrors, is a helpful tool for spatial flows. Vortices behind a rough cylinder at an effective Reynoldsnumber of  $1.3 \times 10^6$  are visualized by air bubbles. At this transcritical Re-number small longitudinal vortices between the large traverse vortex cores can be observed. This visualization technique has the advantage, that the light bubbles were concentrated in the core of the vortex, by the centrifugal force of the rotating water. Beside the techniques described in /1/, /2/ and /3/ to visualize the flow, we use dye the . For special problems (building aerodynamic) it is possible to increase the turbulent level from 0.18% up to 3% by screens which are posed at the beginning of the test section.

### 6. CONCLUSIONS

Two water tunnels built in GRP-sandwich technology have passed there examination. It is possible to built such tunnels without a steel frame. The corrosion resistant materials used for the construction is advantageous in respect to water purification. The first tunnel is an excellent tool for studying stability problems in the boundary layer. The second one suits well to visualize and measure spatial flows in hydrodynamics and aerodynamics.

## 7. REFERENCES

- /1/ Wortmann, F.X. Eine Methode zur Beobachtung und Messung von Wasserströmungen mit Tellur.  
Zeitschrift für angewandte Physik, Band 5, Heft 6, 1953, S.201-206.
- /2/ Geller, E.W. An elektrochemical method of visualizing the boundary layer.  
J. Aero. Sci. 22, New York 1955.
- /3/ Neuwert, G Strömungssichtbarmachung in Wasserkanälen mittels eines Verfahrens zur Erzeugung kleinster Luftbläschen.  
Z. Flugwiss. Weltraumforsch. 9 (1985), Heft 3, S. 187-189.

	<u>Laminar Water Tunnel</u>	<u>Large Water Tunnel</u>
overall length	: 15.5 m	11 m
test section (length width height)	: 10m x 1.2m x 0.2m (adjustable floor)	2.85m x 1.52m x 0.76m (tilt-angle and height- adjustable floor, double side walls)
velocity range	: 0.02 to 0.5 m/s	0.3 to 2.5 m/s
contraction ratio	: 7.7:1 (free surface) 12.8:1 (filled contraction cone)	7:1
drive system	: 2.3 kW (Speed controlled with flywheel, two side-by-side counter-current rotating axial-flow-pumps)	23 kW (Thyristor-controlled, two side-by-side co-current rotating axial-flow-pumps)
water volume	: 30 m <sup>3</sup>	70 m <sup>3</sup>
instrumentation	: hot film anemometrie, probe carriage (computer controlled), Tellur method (streaklines), H <sub>2</sub> bubble method (timelines), Laser-sheet-technique.  calibration device for hot film probes.	3 Component balance carrier frequency measuring bridge, pressure gauges.

Table 1. Technical data of the two hydrodynamic tanks.

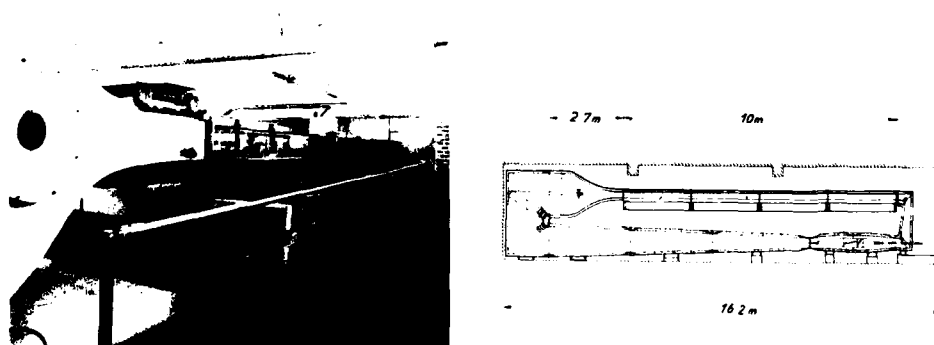


Figure 1. The "Laminar Water Tunnel" at the Institut für Aerodynamik und Gasdynamik

Velocity distribution behind a precision screen (screen-thread  $Re_d = 4$   
 bubble wire  $Re_d = 0.8$  )

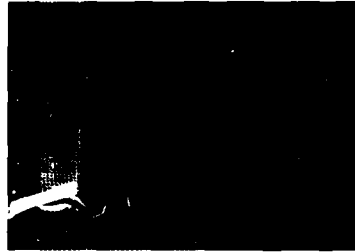


Figure 2. The bubblewire is 1mm downstream of the screen.



Figure 3. The bubblewire is 5mm downstream of the screen.



Figure 4. Separation of a wall streakline which marks as a streakline the recirculation region.



Figure 5. Timelines in the rear part of a separation bubble.



Figure 6. Timelines in the peak region of the lambda-vortex

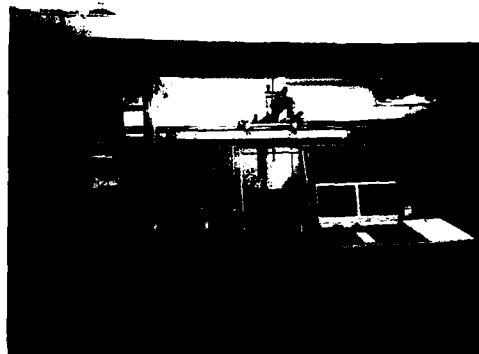


Figure 7. The "Large Water Tunnel" at the Institut für Aerodynamik und Gasdynamik.



Figure 8. Vortex behind a delta wing visualized by two light intersections generated with one laserbeam by adjustable mirrors on a polygon.

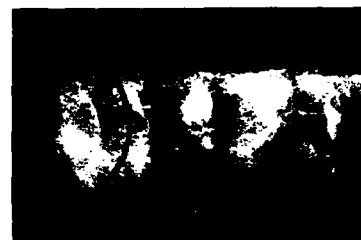


Figure 9. Longitudinal vortices between the traverse Karman-vortices at  $Re_d = 1.3 \times 10^5$



Figure 10. Testing stand of a wind turbine model on a trailer.



Figure 11. Flow in the front part of a car with open cooling duct.

# A COMPARATIVE STUDY OF VORTEX FLOWS IN WIND AND WATER TUNNELS

by

A. G. Davies,  
Aerodynamics Research Department, FPC 67  
Sowerby Research Centre,  
British Aerospace Naval Weapons Division,  
P.O. Box 5,  
Filton,  
Bristol. BS12 7QW  
ENGLAND

## SUMMARY

Characteristics of the flowfield around a generalised missile configuration using two flow visualisation techniques in a water tunnel are compared to corresponding wind tunnel data at subsonic and supersonic speeds. It is shown that the flowfields derived from the water tunnel can be representative of those found at subsonic speeds although isolated body vortex locations agree more with those measured at supersonic speeds and that separation angles on the body can be important. The addition of a cruciform set of fins is shown to modify the body vortex structure dramatically, the degree of modification varying with axial location of the fins. A speed effect is seen to exist in the water tunnel that can change some vortex flowfield characteristics from those of a subsonic flow to those observed at supersonic speeds. Finally crossflow velocities and circulations are compared between the water and wind tunnel.

## NOMENCLATURE

D Model Diameter (= 1 calibres)  
M Mach Number  
t/c Thickness to chord ratio  
S Path length  
V velocity  
x Axial distance from nose apex (calibres)  
x<sub>s</sub> Axial location of first separation (calibres)  
Y<sub>s</sub> Lateral distance of vortex centre from body centreline  
Z Vertical distance of vortex centre from body centreline  
Γ non dimensional circulation  
λ Fin roll angle, defined as λ = 0 when fins are horizontal and vertical  
θ Angle measured from windward stagnation line  
ρ Density

## 1. INTRODUCTION

Understanding the vortex patterns on the leeward side of a body of revolution has been, and still is, a major problem in aerodynamics. Above incidences of about 5° the boundary layer separates from the leeward side of the body along a separation line and hence introduces circulation into the flow. Up to about 25° to 35° incidence the circulation will concentrate itself around 2 symmetric vortices in the crossflow plane. Above this critical angle range the vortices become asymmetric. The interaction of these vortices with downstream surfaces such as controls can induce large variations in local angle of attack causing severe aerodynamic problems.

In an effort to improve aerodynamic prediction codes BAe has had a continuing interest in vortex dominated flowfields. As an aid to understanding the qualitative aspects of such flowfields a water tunnel has been found to be extremely useful in flow visualisation. The high density and low diffusivity of the working fluid enables dense flow tracers with high reflectivities, such as dyes or particles to be used successfully. BAe have amassed over the years data in the form of flow visualisation photographs concerned primarily with the characteristics of vortices shed from bodies of revolution and subsequent interactions with downstream surfaces. Studies have included the effects of curved flowfields on body vortices, the interaction of body vortices with intakes (Ref. 1) and of course, the effects of lifting panels on body vortex development (Ref. 2). Some of the more qualitative results of the studies have assisted in the development of aerodynamic prediction methods (Ref. 1). However concern has been expressed as to the validity of water tunnel techniques in representing flow at higher Reynolds Numbers. Reynolds Numbers are orders of magnitude lower in the water tunnel than in wind tunnels or free flight although at the high angles of incidence normally considered when investigating vortex effects and with the supersonic wing sections usually used in missile technology it is expected that separation on a wing is fixed at the sharp leading edge and hence the wing flow will be well represented. For the body, however, no such prominent feature fixes the separation position which, as is well known, can change significantly with Reynolds Number. Of primary interest therefore was a study of vortex locations derived from water tunnel data and compared to reliable wind tunnel data.

The derivation of vortex locations from wind tunnel data can be a difficult problem to solve. In many cases separation points are derived from surface pressure distributions, which can give rise to large uncertainties due to the interpretation required. Vortex locations are generally derived from flow visualisation in a wind tunnel, for instance vapour screen techniques which may require varying degrees of interpretation and tend not to be the primary objective of the tests with a consequent decrease in accuracy and scope. BAE were therefore fortunate in performing some work for the Royal Aircraft Establishment, Bedford, that included the analysis of flowfield data around a body of revolution collected for the specific purpose of investigating vortex locations and strengths.

## 2. WIND TUNNEL TESTS

To further the understanding of vortex dominated flowfields a comprehensive series of wind tunnel tests are being performed by RAE Bedford in the 8 ft x 8 ft wind tunnel on a generalised missile configuration.

The wind tunnel model used in the flowfield tests is shown in Figure 1. Overall length of the model was 13 calibres including the 1.5 calibre tangent ogive nose which was spherically blunted with a blunting radius of 0.05 calibres. An alternative 3 calibre sharp tangent ogive nose could be used, the overall body length remaining constant at 13 calibres. A cruciform set of delta fins set at  $0^\circ$  deflection relative to the body could be carried in either a forward or rear location as shown. The fins had an exposed span of 1 calibre with a leading edge sweep of  $45^\circ$  and were of a double wedge section with a 10% thickness/chord ratio.

The flow surveys had been performed using a set of five-hole yawmeters which had been previously calibrated at Mach Numbers from 0.4 to 2.0 and for angles of attack up to  $39^\circ$ . The yawmeters were carried on a purpose built traversing rig mounted co-axially with the sting mounted model (Figure 2). The traversing rig contained an axial drive to which various sting extensions could be added to place the yawmeters at any desired axial location along the body. Data were obtained throughout the chosen crossflow plane by using a combination of the radial drive built into the traversing rig and by rolling the entire traversing rig around the model.

At supersonic speeds of  $M = 1.8$  and  $1.45$  an array of 4 yawmeters were used covering the flow survey area shown in Figure 3 while at the subsonic speed of  $M = 0.7$  a single yawmeter was used to minimise interference effects and covered the flow survey area also shown in Figure 3. The radial extent of the flow surveys was determined by the capabilities of the traversing rig.

The flowfields at 4 axial stations were surveyed at 3 incidences of  $8^\circ$ ,  $14^\circ$  and  $20^\circ$ . Throughout the tests the Reynolds Number based on model diameter was kept constant at  $0.62 \times 10^6$ . The accuracy of the final results was estimated to be: yawmeter pitch and yaw angle to  $\pm 0.3^\circ$ ; local Mach Number to  $\pm 0.01$  and local total pressure to  $\pm 1.5\%$ . Positional accuracy in the crossflow plane was better than  $0.002 D$ , further details may be found in Ref. 3.

Data are normally presented as plots showing the velocity vectors in the crossflow plane at set axial stations. Vortex locations and wake characteristics are immediately apparent using this form of presentation. More quantitative information can be gained from plots showing the vorticity in the crossflow plane and the local total pressure ratio in the flowfield.

## 3. WATER TUNNEL TEST DETAILS

### 3.1 Water Tunnel Details

The BAE water tunnel at Warton is a recirculating type with a  $457 \times 457$  mm working section. It is driven by a 10 h.p. (7.5 kW) motor driving a simple impeller, with simple turning vanes located at the corners of the tunnel see Plate 1. A screen mounted ahead of the working sections goes some way to reducing the turbulence of the flow. With the screen removed flow speeds of up to 4 m/sec are possible although the fitting of the screen reduces the maximum permissible speed to 1 m/sec. The models are sting mounted on an arrangement that allows the model incidence to be varied while the tunnel is running. Roll angle, yaw angle and, of course, configuration changes require draining of the working section and removal of the access window. The incidence range is from  $-35^\circ$  to  $35^\circ$  and is limited by the model coming into close proximity to the tunnel walls. The centre of rotation in the pitch plane is approximately the centre of the viewing window.

Provisions are made for two flow visualisation techniques in the tunnel, namely dye line and hydrogen bubble techniques. Up to 5 separate dyes can be controlled individually by valves from a constant head of dye. The head of dye is such that the pressure of the dye is just above that of the water in the working section.

The hydrogen bubble technique facilities consist of a 110 V d.c. supply with 2 fused circuits. Various safety provisions ensure that no current is applied to the model when the tunnel is drained for configuration changes. The anode supply is connected to the



water tunnel metal shell while one of the cathode circuits is connected to the model which must be insulated from the tunnel.

### 3.2 Model Details

The water tunnel model was geometrically similar to the model tested in the wind tunnel although to a smaller scale. Overall length of the model was 13 calibres with a diameter of 28 mm. The forward 3 calibres was removable such that either a 3 calibre pointed tangent ogive nose or a 1.5 calibre blunted tangent ogive with a 1.5 calibre cylindrical section could be fitted, overall length remaining at 13 calibres.

The blunting radius of the 1.5 calibre nose was 0.05 calibre. The base of the model was changed in detail from the wind tunnel model to facilitate the smooth exit of the dye tubes from the nose of the model by extending and fairing the base into the sting support block as in Figure 4. A cruciform set of fins could be carried in either a forward or rear position. Fin geometry was a 45° delta of 1 calibre exposed semi span, with a thickness to chord ratio of 0.1. The fins were fixed at 0° deflection.

Dyes could be ejected from 17 holes positioned along the body; nine were positioned on the nose with 6 on one side and 3 positioned diametrically opposite holes No. 4, 5 and 6. Eight holes were positioned along the cylindrical section as shown in Figure 4. The model was constructed from stainless steel and was electrically insulated from the cast iron shell of the tunnel by a 'Tufnell' mounting block.

## 4. WATER TUNNEL TEST TECHNIQUES

Two flow visualisation techniques were attempted: dye line and hydrogen bubble techniques.

In the dye line technique water soluble dye is ejected from tubes set in the surface of the model. Up to five different coloured dyes can be independently controlled through separate valves. Consistency of the dyes had to be carefully adjusted such that the dyes were neutrally buoyant while remaining sufficiently dense as to be recorded on the photographic equipment. Care also had to be taken that the dye flow rate was not too high otherwise the dye would be ejected outside the boundary layer and not entrained into the vortices.

Still cameras were used to record the dyelines with one camera mounted level with the model recording the view through the side (access) window. The other camera was mounted vertically above the model looking directly down onto the model through the top window. The model was illuminated by 4 flashguns synchronised with the cameras. Due to the accumulative effect of the dye in the tunnel on the clarity of the water, the tunnel had to be drained and refilled frequently. Another operational drawback was the low speed needed, of the order of 10 cm/sec, to avoid dyeline breakup. Consequently the Reynolds Number was low.

The hydrogen bubble technique has been shown to be a very effective method of visualising the flow around bodies in water. Thomson in Australia (Ref. 4) has done much fundamental work on the technique. The technique developed at BAe Warton, Ref. 5, consists of the electrolytic generation of hydrogen bubbles from a cathode on the model. The bubbles produced by this method are very small, approximately 0.1 mm in diameter and are very responsive such that they can completely trace the flow over a body. Illuminating the flowfield produces internal reflection within the bubble and hence visualisation of the flowfield. The method has several advantages over other methods using dyes or reflecting particles. There is no contamination of the working fluid and the method is very convenient to use, i.e. on/off electrical switching. The cathode can be sized to produce bubbles over as much or as little of the model as necessary.

The hydrogen bubbles produced have a natural buoyancy which give them an upward force. This force is small for small bubbles so that when the dynamic fluid forces are much greater than the buoyancy forces, the latter become relatively negligible and the bubbles follow the pathlines accurately. It has been found that buoyancy effects become significant at speeds below 10 cm/sec.

An alternative cathode was manufactured that consisted of a horizontal wire suspended ahead of the model in the working section as in Figure 5. The wire was insulated from the tunnel walls and was kinked along its length. Bubbles collected at the bends in the wire such that a series of streams of bubbles were generated which crossed the model and were entrained into the body vortex.

Illumination of the flowfield was by a standard slide projector providing a sheet of light of approximately 2 cm thickness that could be positioned so as to illuminate the crossflow plane at any axial station on the model. A mirror angled at 45° to the model axis and mounted at the rear of the model enables the view looking up the model axis to be recorded by a still camera mounted outside of the tunnel working section. By choosing a shutter speed of about 1/15 sec and a flow speed of about 30 cm/sec the tracks of the bubbles in the crossflow plane when the model was at incidence were recorded as 'streaks', the length of which was proportional to the crossflow velocity.

As stated earlier the model was manufactured from stainless steel and was connected to the cathode of the D.C. supply. A waterproof paint was applied to those areas of the model that were not to produce bubbles. However it was found that after a short period of bubble generation the paint blistered causing asymmetries in the flowfield. Removal of the paint such that the entire surface of the model generated bubbles gave much improved results. It became apparent that the rate of bubble production was primarily dependent on the applied voltage but also on the potential distribution over the surface of the model and on the local velocity of the flow over the model. It was observed that more bubbles were generated over the nose section, where the surface curvature and hence potential gradient was greatest, than over the cylindrical section of the model. Furthermore it was observed that the rate of bubble production decreased in areas of low flow velocity, for example in the leeward separated region.

However it was found that bubble production was poor over unpainted fins. When the fins were painted with an insulating layer and approximately 1 mm around the leading edge was bared then bubble production increased dramatically, feeding directly into the leading edge vortex when the fins were at incidence.

## 5. DISCUSSION OF RESULTS

In the following sections the results from the water tunnel tests are compared to the corresponding wind tunnel tests. Not all of the data used in the analysis have been presented here; for instance wind tunnel vorticity and local total pressure ratio plots have been studied in some cases but could not be presented due to space considerations.

### 5.1 Dyeline Technique

Consider firstly the results obtained from the dyeline technique. The combination of the rotational velocity field set up in the leeward of the body by the vortex pair and the general axial flow results in a helical dyeline trace where the particles move around the vortex centre and downstream simultaneously. It should be noted that the pitch of the helix does not necessarily indicate the strength of the vortex but rather the position of the dye filament radially within the vortex. One immediate consequence of this is that the relative strength of a vortex becomes difficult to estimate. The patterns traced by the dye filaments were in the main steady, maintaining their vertical and lateral locations relative to the body centre line provided the oncoming flow was steady. Hence although the results shown in the photographs are the instantaneous positions as recorded by a still camera there was no evidence that the patterns were time dependent.

#### 5.1.1 Isolated Body

It is seen from the wind tunnel tests that at  $8^\circ$  incidence for the body alone configuration at  $M = 0.7$ , Figure 6, that there is very little vorticity in the flow although there were definite weak vortices. However the low rate of rotation in the vortices made identifying the centre of the vortices in the water tunnel by the use of dyelines very inaccurate. As the incidence increased to  $14^\circ$  there was sufficient vortex development to enable the vortex positions to be estimated and compared to the wind tunnel data. One implication of the inability of this technique to identify areas of low vorticity was the determination of the axial location of the first separation point,  $x_s$ , measured from the nose apex. This obviously has implications when comparing vortex positions with differing configurations on which  $x_s$  may be different. However the wind tunnel data gave no indication of  $x_s$  as data were collected at discrete axial locations, the furthest forward being 3.5 calibres aft of the nose. As both models were identical geometrically it was expected that there would be very little difference in  $x_s$  between water tunnel and wind tunnel and hence the vortex locations at discrete axial locations would be directly comparable.

Shown in Figure 7 are the results of vortex position derived from water tunnel data and wind tunnel data for the isolated body with blunt and sharp noses at  $14^\circ$  and  $20^\circ$  incidence. It is immediately seen that the water tunnel estimates of vortex location fall between the subsonic ( $M = 0.7$ ) and supersonic ( $M = 1.45$  and  $1.8$ ) wind tunnel results in both the Z and Y axes, although the results tend towards the supersonic estimates. It should be noted that in the y-direction there was a slight asymmetry in the vortex positions in those cases where dye was ejected from both sides of the flow. Investigation has shown that some apparent asymmetry was due to the camera mounted above the model being positioned slightly to one side of the tunnel centreline to avoid a structural support. Corrections have been applied for the misalignment.

#### 5.1.2 Body Plus Forward Fins

Consider now the addition to the blunt nose configuration of a cruciform set of fins in the forward position at  $0^\circ$  roll, Plates 2 and 3. It is immediately seen that the body vortex formation and development remains unaltered from the isolated body case until the fin wake is encountered. The fin wake is seen to have no clear coherent structure and to trail in a streamwise direction. When the fin wake encounters the body vortex it is seen clearly that the structure of the body vortex is destroyed and that the resulting wake continues in a broad streamwise direction. By comparing results at  $14^\circ$  and  $20^\circ$  incidence it is seen that the position of vortex destruction (burst) remains surprisingly constant as incidence increases. This is in partial agreement with the wind tunnel data. At subsonic speeds ( $M = 0.7$ ) the addition of forward mounted fins at  $0^\circ$  roll has the effect of drastically reducing the strong vortex structure seen in the body alone case (Figures

8 and 9). A weak recirculation region remains with a weak vortex structure. What was the body vortex feeding sheet region now appears as a relatively thick shear layer separating the essentially freestream outer flow from a body leeward flow that is approximately parallel to the body axis. It appears that the trailing wake of the fin is preventing the rolling up of the feeding region to form a body vortex system. Bearing in mind the earlier comments that the dyeline technique is poor at identifying areas of low vorticity then it is seen that the flowfield in the water tunnel approximates the wind tunnel flowfield. The shear layer will tend to spread the dye from the nose area over the flowfield showing that some fluid is flowing approximately parallel to the body axis whilst the canard wake trails in a streamwise direction. However the weak body vortex structure is not clearly seen at all.

When the fins are rolled through  $45^\circ$  the wind tunnel data show a slightly more distinct body vortex structure together with a canard vortex shed from the windward forward panel. However the dyeline results do not show any increased structure to the flowfield when compared to the  $0^\circ$  roll case, the flowfield remaining as a broad shear area.

At supersonic speeds ( $M = 1.8$ ) it is seen that addition of a forward set of fins results in the flowfield shown in Figure 10. The body vortex position has been modified from the isolated body case by a rotation to windward and moving closer to the body. There is some evidence of a canard vortex lying above the body vortex. From Ref. 3 it appears that the canard vortex trails in a streamwise direction and that this canard vortex originates from the windward panel. These results are in contrast to the subsonic results and the water tunnel results presented here and by Deane (Ref. 2) where the formation of a body vortex was almost entirely prevented aft of the fins.

Of interest in the water tunnel results is a small area of vorticity located at the base of the leeward panel when rotated to  $45^\circ$ . This small vortex is found at the junction of the fin leading edge to the body and extends up to 1 calibre downstream of the fin trailing edge before bursting, see Plate 4. No evidence of this phenomenon can be found in the wind tunnel data although to date data have been collected at the forward station for an incidence angle of  $14^\circ$  only.

#### 5.1.3 Body Plus Aft Fins

Considering the effect of aft mounted fins on body vortex position in the water tunnel it was observed at  $20^\circ$  incidence there was very little effect of the fin on the location of the body vortex for either  $0^\circ$  or  $45^\circ$  roll and up to  $12.2 D$  from the nose. However an effect is seen in Plate 5 where the fin wake, trailing in a streamwise direction encounters the body vortex. A distinct movement of the body vortex closer to the body is seen together with the initiation of what might be termed vortex breakdown by spiral instability (Ref. 6). However it must be remembered that in this area of the model the dye tubes exit from the base and hence can cause severe disruption to the flowfield.

The corresponding wind tunnel tests show similar results, Figures 11 and 12, although data are only available for  $14^\circ$  incidence. At subsonic speeds the body vortex is weakened to some extent as the feeding sheet is attenuated by the horizontal panels when at  $0^\circ$  roll, Figure 11. For  $45^\circ$  roll, Figure 12, the feeding sheet is again cut by the fin although remnants of it remain. At supersonic speeds the vorticity of the body vortex is greater and it is seen in Figure 11 that the effect of an horizontal fin attenuating the feeding sheet is less than in the  $M = 0.7$  case; also at  $45^\circ$  roll, Figure 12, the body vortex location remains similarly undisturbed even though the feeding sheet is cut by the fin. It is interesting to note that this configuration shows no evidence of the tightly coiled vortex region at the base of the leeward panel for  $45^\circ$  roll in either the water or wind tunnel.

#### 5.2 Hydrogen Bubble Technique

Looking now at the results from the hydrogen bubble technique it was immediately observed that areas of low vorticity, such as those found at  $8^\circ$  incidence could be seen adequately. Part of the reason for this may be the viewing angle, as low rotational velocities become more apparent when viewed in the axial direction rather than in the lateral direction. It should also be remembered that a higher flow speed is used of about 30 cm/sec leading to a higher Reynolds Number (of about 8500 compared to 3500 when using the dyeline technique).

It was also observed that in comparison with the dyeline technique many more of the flowfield details can be seen. For example with the complete body generating bubbles it was observed that the feeding sheet becomes visible, Plate 6, as does the separation lines on the surface although the latter have proved elusive to photograph in the current series of tests. The separation lines along the body become visible as bubbles generated just to the lee of the separation point are not swept away by the boundary layer. Thus a line of slow moving or stationary bubbles mark the separation lines.

#### 5.2.1 Isolated Body Results

Comparing the location of the body vortices with the wind tunnel data note that the water tunnel results were obtained for the sharp nose configuration with and without fins in the forward and rear position only due to time constraints. It is seen in Plate 6 that for the isolated body case a vortex structure very similar to that seen in the

crossflow vector diagram from the wind tunnel results, Figure 8, is directly visible in the water tunnel flow visualisation photographs. A feeding sheet is seen to connect the separation line to the body vortex such that the body vortex grows as it progresses parallel to the body axis. The location of the body vortices derived from the water tunnel by this technique are shown in Figure 7 compared to wind tunnel results and the dyeline technique. The results fall between the subsonic and supersonic wind tunnel results at  $14^\circ$  incidence but tend towards the supersonic results at  $20^\circ$  incidence (note that some uncertainty exists over the accuracy of the water tunnel result at  $x/D = 11.5$ ,  $\alpha = 20^\circ$  due to the flow being unsteady). The good agreement between the water tunnel data and the supersonic results for isolated body vortex locations is surprising. As part of an explanation it is perhaps worthwhile estimating the radial location in the crossflow plane of the separation line along the body. If, looking in the crossflow plane,  $\phi = 0^\circ$  is defined as the windward stagnation line then Ref. 7 shows that the separation point approaches the turbulent separation value of  $\phi = 110^\circ - 115^\circ$  for the subsonic case. However for the supersonic cases the separation points are closer to  $\phi = 90^\circ$  due to shock induced separation as the crossflow Mach Number becomes critical. From observation of the separation lines in the water tunnel using the hydrogen bubble technique it was noted that a line of bubbles remained essentially constant at about  $\phi = 90^\circ$  indicative of laminar separation at around  $\phi = 80^\circ$ . The separation line could be identified by the row of bubbles that collected in the stagnant region immediately downstream of the separation point. Hence, if it is assumed that the body vortex position is in some way related to the separation line position then it can be seen that, as the separation line position in the water tunnel is in better agreement with the supersonic than the subsonic value, then the body vortex locations in the water tunnel may well agree with the locations derived from the supersonic tests.

### 5.2.2 Body With Rear Fins

The addition of a rear set of fins at  $0^\circ$  roll produces flowfields as in Plate 7 for  $14^\circ$  incidence. Qualitatively comparing these results with the subsonic wind tunnel data of Figure 11 it is seen that there is good agreement. The size and location of the body vortex are well reproduced in the water tunnel as is the bright area at mid span on the horizontal panels. Bright areas are caused by a collection of bubbles moving at low crossflow velocities as is seen towards the centre of the body vortex. It is therefore reasonable to assume that the bright areas at part span on the horizontal panels are representative of the vortex structure observed just above the horizontal panel in the wind tunnel tests.

With the rear set fins rotated through  $45^\circ$  it is seen from the subsonic wind tunnel results of Figure 12 that there is a fin vortex structure again at part span together with a body vortex. The flow visualisation pictures, Plate 8 show a clear body vortex, slightly further away from the body than in the wind tunnel results for  $14^\circ$  incidence and  $M = 0.7$  although the water tunnel results are consistent with the isolated body locations from the water tunnel. The bright area coincides approximately with the position of the fin vortex in the wind tunnel data. It is seen in both sets of data that the usual feeding region has been severed by the presence of the fin and is replaced by a strong flow outboard along the fin. Comparison of the results for  $M = 1.8$  with the water tunnel results, show little agreement apart from body vortex location. Other flow details, such as fin vortex location do not seem to agree. Indeed there is very little evidence of a fin vortex in the supersonic data, the recirculation or vortex region seen in the subsonic data being replaced by a more general outboard flow.

### 5.2.3 Body With Forward Fins

With the addition of a forward set of fins at  $0^\circ$  roll, the fin wake prevents the roll up of the feeding sheet into a body vortex structure. Body vortices were observed in the water tunnel at stations ahead of the fin trailing edge position but aft of this position no body vortex structure was seen. Such a case is depicted in Plate 9 showing the crossflow plane at  $x = 8$  calibres from the nose tip for an incidence of  $20^\circ$ . It is seen that the leeside flow is essentially parallel to the body axis with a strong shear layer separating the leeside area from the freestream flow.

A similar but slightly more ordered flowfield is seen in the subsonic wind tunnel results, Figure 9, although data for  $14^\circ$  incidence only are available. The main difference between the wind tunnel results and the water tunnel results here is evidence of a weak body vortex detected in the wind tunnel. The water tunnel flow visualisation photograph show no real evidence of such a structure.

When the forward set of fins are rotated through  $45^\circ$  a similar flowfield to the above is observed. The fin wake again prevents the formation of a body vortex resulting in a leeside flow that is essentially parallel to the body axis and separated from the freestream by a shear layer.

For the case of the forward fins at  $45^\circ$  roll,  $20^\circ$  incidence and concentrating on a crossflow plane 5.5 calibres from the nose apex the flow speed through the water tunnel working section was increased from approximately 30 cm/sec to approximately 80 - 100 cm/sec. These flow speeds correspond to Reynolds Numbers of  $8.3 \times 10^3$  to  $2.7 \times 10^4$  respectively based on model diameter. It was observed that at the higher speed the structure of the flowfield changed dramatically. The region of low crossflow velocity and shear layer arrangement described earlier had been replaced by a 4-vortex structure. Plate 10 shows two body vortices together with areas that could best be described as canard vortices. These results show surprising qualitative agreement with the characteristics of the flowfield observed around a similar configuration in the wind

tunnel at  $M = 1.8$  where it was found that the body vortex structure aft of the forward fins continues parallel to the body axis although weakened from the isolated body case. In the subsonic case however, body vortex formation is completely prevented. For example, Figure 13 shows no evidence of a body vortex at subsonic speeds although there is a weak canard vortex structure (note though that data are only available for  $14^\circ$  incidence). Comparing the water tunnel data at the higher speed and at the aft flow survey station ( $x = 11.5 D$ ) with corresponding wind tunnel data at  $M = 1.8$ , albeit at  $14^\circ$  incidence, in Plate 11 it is seen that there is some qualitative agreement. Unfortunately the water tunnel photographs are of poor quality and it was observed that at this station the flowfield was of a more unsteady nature, possibly due to freestream turbulence.

Rather than compare flowfields on the basis of Reynolds Number which in the cases described above are orders of magnitude different it would seem to be reasonable to compare freestream momentum,  $\rho V$ . At a subsonic speed of  $M = 0.7$  and assuming sea level static conditions, the value of  $\rho V$  is of the order of  $300 \text{ kg m}^{-2} \text{ s}^{-1}$  which, when transferred to the water tunnel is equivalent to a speed of  $30 \text{ cm/sec}$ . Similarly if the water tunnel speed is increased to  $0.8 \text{ m/sec}$  the value of  $\rho V$  corresponds to that achieved at  $M = 1.92$  in free air (i.e. assuming  $\rho = 1.225 \text{ kg/m}^3$ ) which is close to  $M = 1.8$ .

From the preceding discussion of the change in the water tunnel flowfield characteristics at different speeds it appears that the flowfield characteristics of highly separated vortex dominated flows are more momentum sensitive than viscosity sensitive. Viscosity, however, will effect the separation line position.

### 5.3 Velocity and Circulation Estimates

As mentioned earlier velocity data may be extracted from views of the illuminated crossflow planes by measuring the length of the streaks created by the combination of bubble velocity and camera shutter speed on the photograph. In the majority of cases photographed it was found that the flowfield was saturated with these streaks with the result that it was almost impossible to distinguish individual streaks. However for the case of the body alone configuration with a sharp nose at  $20^\circ$  incidence there were sufficient individual streaks to enable representative velocities to be crudely estimated.

Figure 14 shows the velocities extracted from the photographs, non-dimensionalised with respect to the crossflow velocity and compared to the velocities for the same spatial locations measured in the wind tunnel at subsonic speed ( $M = 0.7$ ). As can be seen there are a few differences in the flowfield velocity distributions even though the vortex centres are at approximately the same locations. However it must be remembered that the method of estimating the magnitude of the velocities is not particularly precise although the estimation of direction is more accurate. It should also be noted that in the wind tunnel case local Mach Number ratios are measured and that there is a small variation in local speed of sound due to the total pressure loss in the vortex.

Considering now the estimation of circulation normal to the body axis around a closed path that includes the vortex centre. The circulation in this instance is defined as

$$\Gamma = \oint \left( \frac{V_L}{V_\infty} \right) \cdot ds$$

where  $\frac{V_L}{V_\infty}$  is the ratio of local to freestream crossflow velocity and circulation is defined as positive in an anticlockwise direction.

The circulation over the same crossflow area was estimated for both the subsonic and supersonic wind tunnel cases and for the water tunnel case and are shown below.

#### WATER TUNNEL TESTS

0.5205

#### WIND TUNNEL TESTS

##### SUBSONIC      SUPERSONIC

0.6244      0.8022

It is seen that the water tunnel estimates agree reasonably well with the subsonic estimates although they are some 17% low. In comparison it is seen that the supersonic case has a much higher circulation together with a velocity distribution, Figure 15, that is very different to the water tunnel and subsonic wind tunnel cases, the vortex being elongated in the crossflow direction.

## 6. CONCLUSIONS

A comparative study of vortex dominated flowfields around a generalised missile configuration in both a water tunnel and wind tunnel has been undertaken. Two flow visualisation techniques have been attempted in the water tunnel, a dyeline technique and a hydrogen bubble technique. Comparisons have included qualitative assessment of the flow fields as well as more quantitative information such as vortex positions, crossflow velocity vectors and crossflow plane circulation.

It has been found that flowfield characteristics derived from the water tunnel can be representative of those found at subsonic speeds in the wind tunnel data. Isolated vortex locations however have been found to agree more closely with those measured in the wind tunnel at supersonic speeds. Observations have suggested that this effect may be due to the separation angle around the cylindrical body being characteristic of laminar separation in the water tunnel compared to the turbulent flow separation angles found in the wind tunnel.

The addition of a cruciform set of fins has been found to modify the body vortex structure dramatically, the amount of fin/body vortex interaction varying with the axial location of the fins. These effects have been found to be in agreement with the results from the subsonic wind tunnel test series.

Using the hydrogen bubble technique it has been found that flow velocity in the water tunnel can have a dramatic effect on the flowfield pattern downstream of a set of canards. As the water tunnel speed increases the flowfield characteristics change from those of an essentially subsonic flowfield to those observed in a supersonic flowfield. It has tentatively been suggested that such effects imply that the dynamics of highly separated regions are governed by freestream momentum rather than the more usual Reynolds Number and it is suggested that some supersonic results may be modelled by judicious choice of water tunnel speed.

Finally a crossflow velocity distribution has been extracted from the water tunnel data and the circulation in the crossflow plane calculated. Reasonable agreement has been shown with subsonic wind tunnel results.

This paper has sought to validate the use of hydrodynamic facilities in investigating highly separated, vortex dominated flowfields. In doing so the water tunnel has been shown to be more versatile in investigating fundamental aerodynamic phenomena than originally envisaged.

## REFERENCES

1. Beaman, G.R., Results of a water tunnel flow visualisation study of the development of vortices on a missile with side mounted intakes. January 1986. JS10550
2. Deane, J.R., Visualisation of the vortex dominated flow around a missile-type wing-body combination using a water tunnel : preliminary report. December 1978. ST21299
3. Byram, T.R., Kitson, S., Petersen, A., Some results from a programme of research into the structure of vortex flowfields around missile shapes. AGARD CP-342
4. Thompson, D.H., Flow visualisation using the hydrogen bubble technique. 1978. ARL Aero note 338.
5. Hanney, P.D., Woodall, K.A., Development of the hydrogen bubble technique for flow visualisation in the Warton 0.46 m water tunnel. February 1978. AX 340
6. Payne, F.M., Ng, T.T., Nelson, R.C., Visualisation and flow surveys of the leading edge vortex structure on delta wing planforms. January 1986. AAI86-0330
7. Davies, A.G., Analysis of body alone data from RAE flow survey tests. July 1984. JS 10121

## ACKNOWLEDGEMENTS

The use of the water tunnel facilities and assistance of the staff of the low speed wind tunnel at BAe Warton is greatly acknowledged. The wind tunnel data presented here were analysed under Contract No. A288/349 for RAE, Bedford.

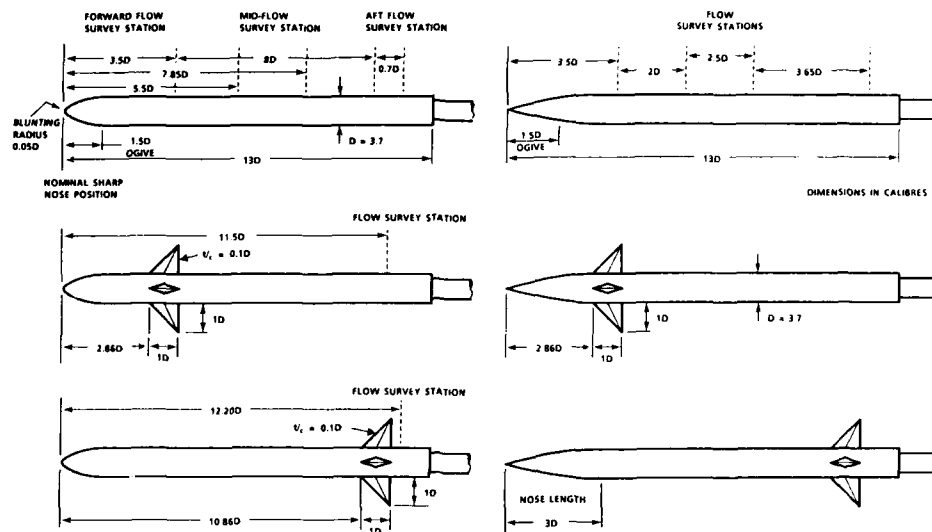


FIGURE 1: RAE MODEL CONFIGURATIONS

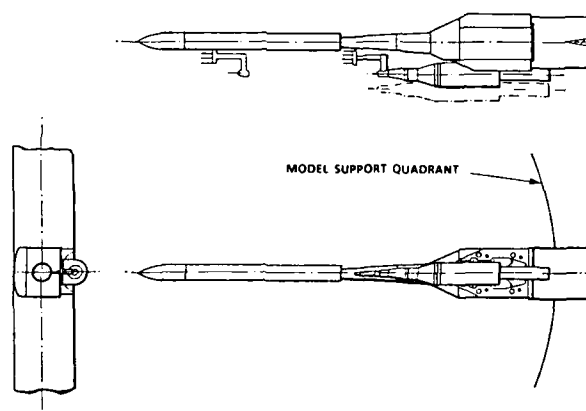


FIGURE 2: MODEL WITH FLOW SURVEY TRAVERSE RIG

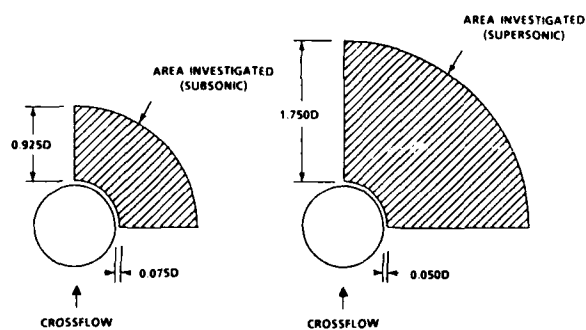


FIGURE 3: VIEW FROM THE REAR

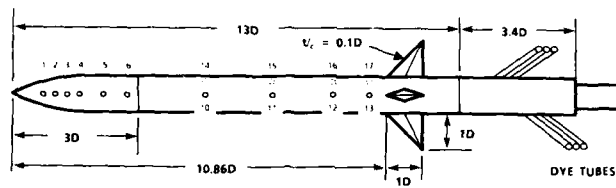
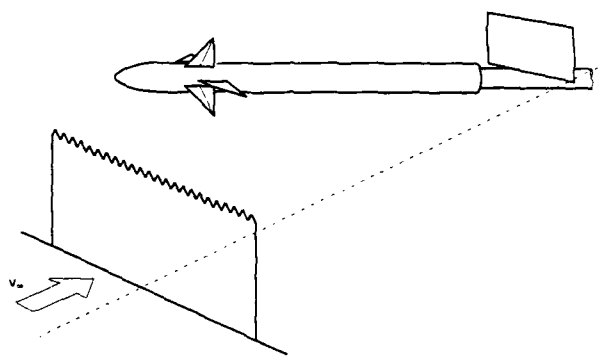
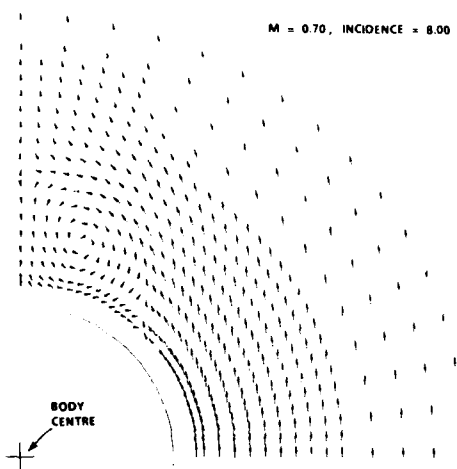


FIGURE 4: WATER TUNNEL MODEL

FIGURE 5: MODEL, MIRROR AND FREE BUBBLE  
GENERATOR ARRANGEMENTFIGURE 6: ISOLATED BODY;  $X/D = 11.50$



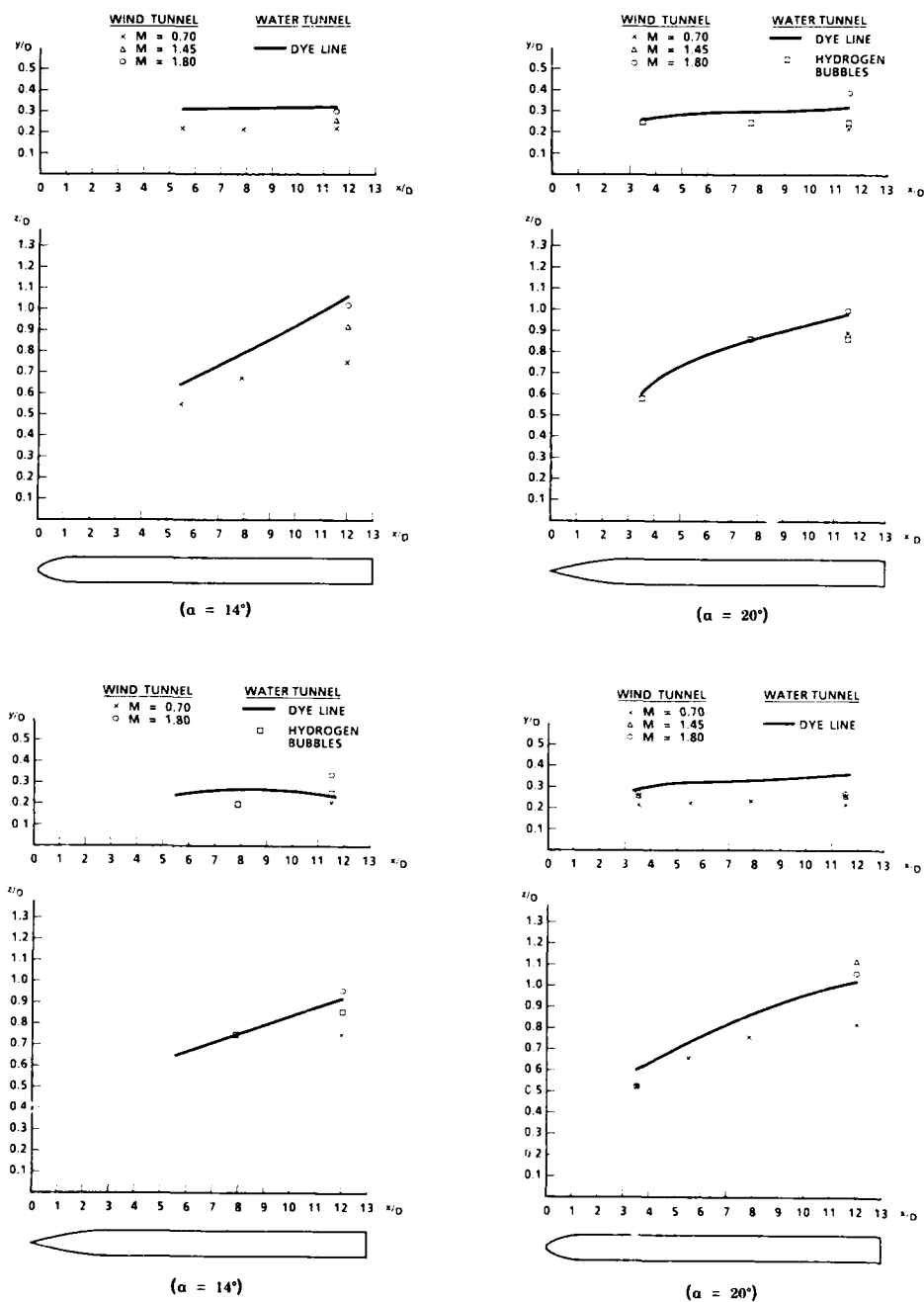


Figure 7: COMPARISON OF ISOLATED BODY VORTEX LOCATIONS

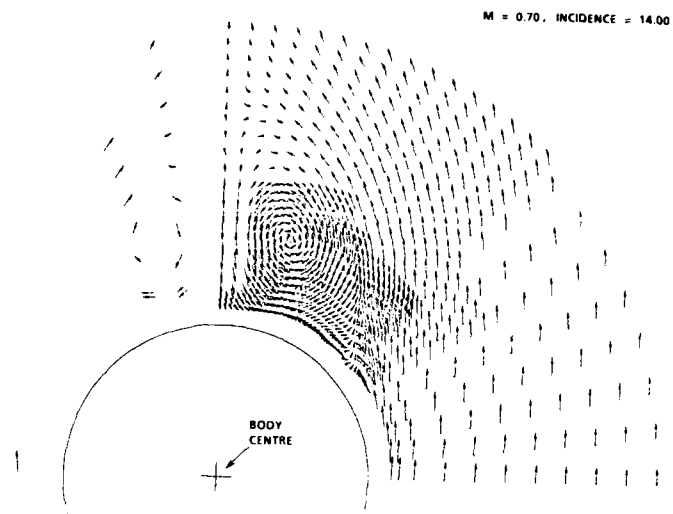


FIGURE 8: ISOLATED BODY:  $X/D = 11.50$

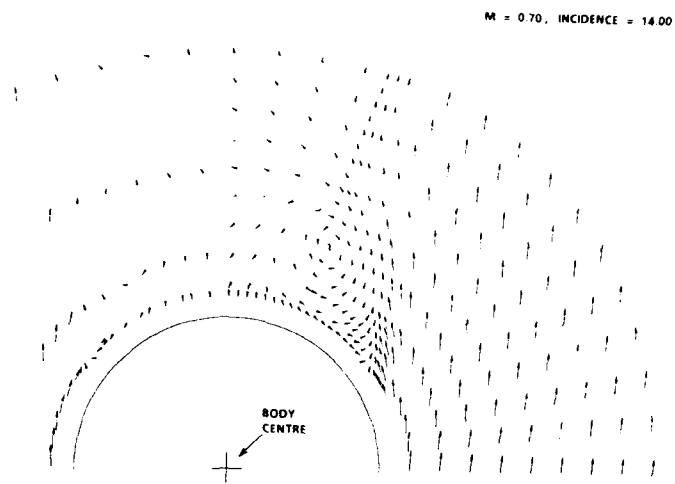
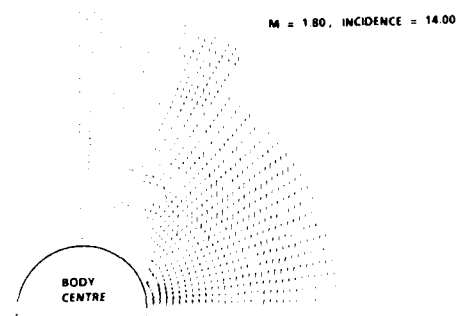
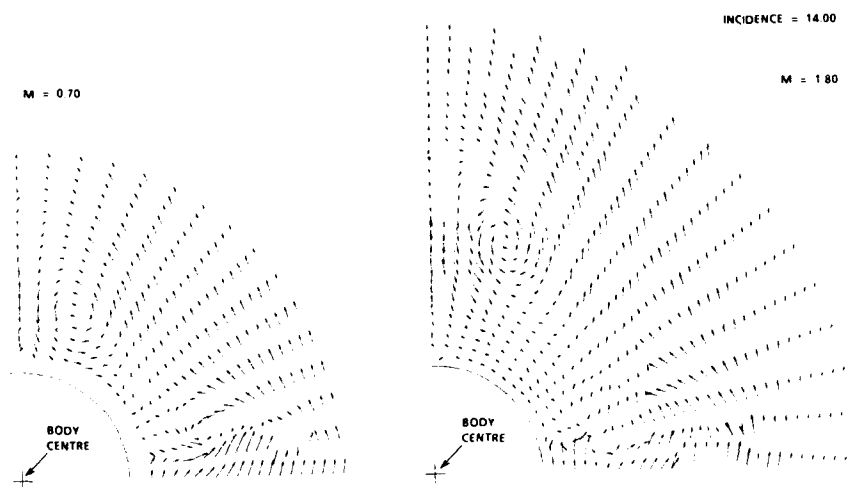
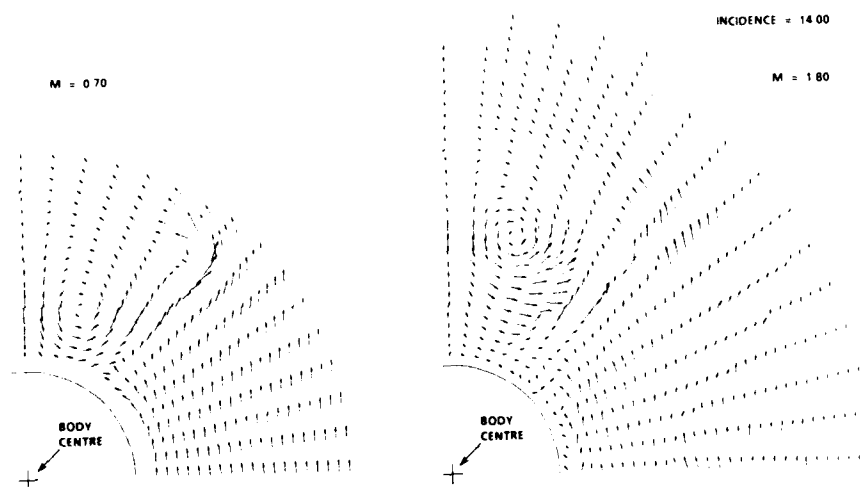


FIGURE 9: BODY PLUS FORWARD FINS,  $\lambda = 0^\circ$ ;  $X/D = 11.50$

FIGURE 10: BODY PLUS FORWARD FINS,  $\lambda = 0^\circ$ ;  $X/D = 11.50$ FIGURE 11: BODY PLUS REAR FINS,  $\lambda = 0^\circ$ ;  $X/D = 12.20$ FIGURE 12: BODY PLUS REAR FINS,  $\lambda = 45^\circ$ ;  $X/D = 12.20$

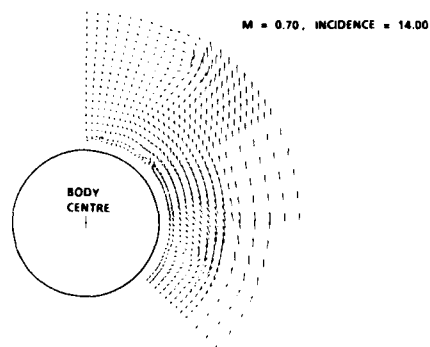


FIGURE 13: BODY PLUS FORWARD FINS,  $\lambda = 45^\circ$ ;  $X/D = 5.50$

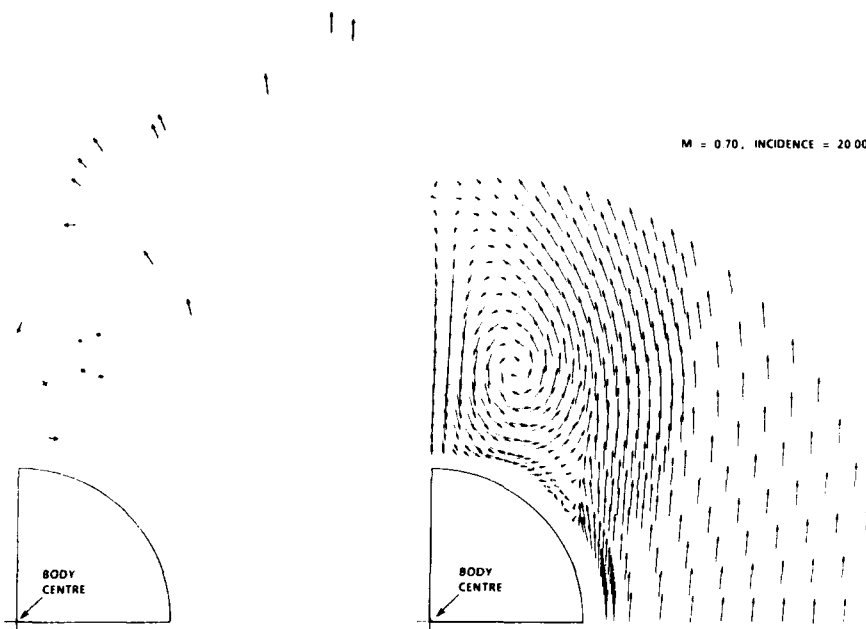


FIGURE 14: ISOLATED BODY;  $X/D = 11.50$

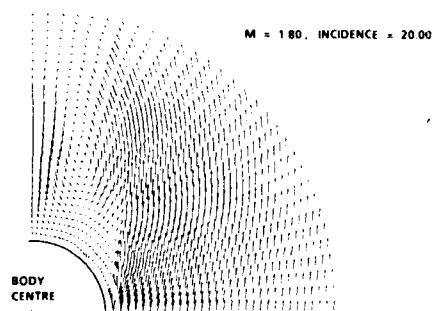
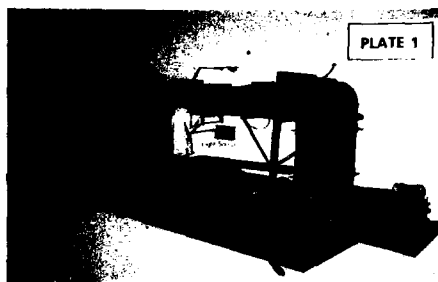
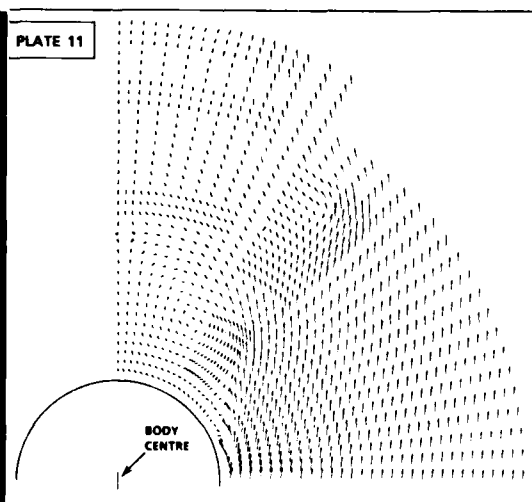
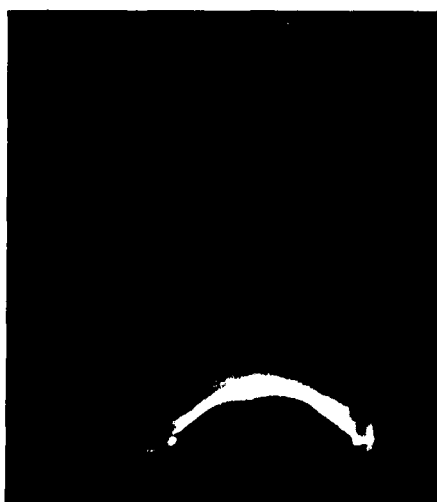
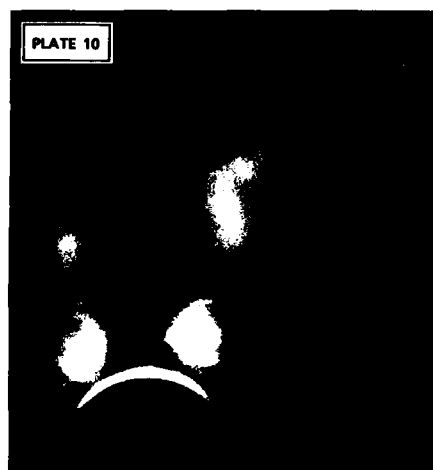
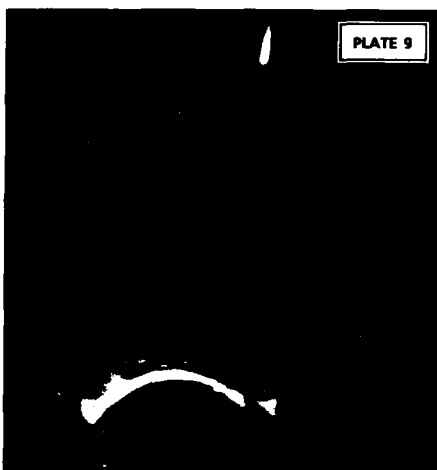
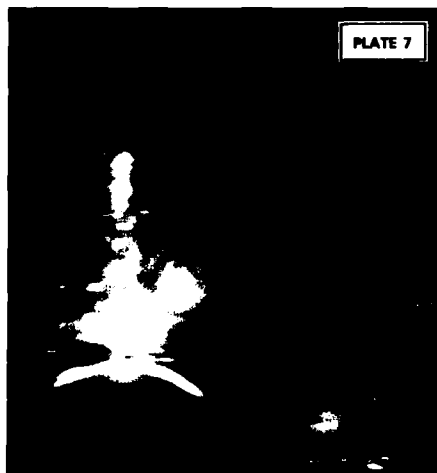


FIGURE 15: ISOLATED BODY;  $X/D = 11.50$





INVESTIGATION ON THE MOVEMENT OF VORTEX BURST POSITION WITH DYNAMICALLY  
CHANGING ANGLE OF ATTACK FOR A SCHEMATIC DELTAWING IN A WATERTUNNEL WITH  
CORRELATION TO SIMILAR STUDIES IN WINDTUNNEL.

Karl W. Wolffelt  
Senior Aerodynamics Engineer  
Windtunnel section  
Technology sector  
SAAB-SCANIA  
S-581 88 Linköping  
Sweden

Summary

The requirements for modern military aircraft to maintain good handling qualities at very high angles of attack is one of many reasons why an increased knowledge is necessary regarding the aerodynamic behaviour of vortex flows at non-stationary conditions. Linearized theory as it has been utilized in flight mechanics simulation using damping derivatives derived from for example forced oscillation technique, may no longer be valid at such conditions. With this background some investigations have been made by SAAB-SCANIA with the aim to study the hysteresis effects for non stationary vortex flows.

A schematic deltawing model which could also be equipped with a similar canardwing has been tested in a watertunnel. The model was supported in the watertunnel by a simple mechanism by which it could be forced to move in one of four different modes - pitching or plunging with either ramp or harmonic motion. The flow over the model was visualized with air bubbles and sequences were recorded on videotape. The sequences were analyzed and the movements of the leading edge vortex burst have been studied with the main interest focused on the hysteresis effects.

List of symbols

$X_{vb}$	lengthwise distance behind wing apex for leading edge vortex burst position
$\alpha(t)$	instantaneous angle of attack
$\alpha_s$	angle of attack at start of ramp or cycle
$\alpha_0$	angle of attack amplitude for oscillations
$\Delta\alpha$	angle of attack ramp length
$\dot{\alpha}$	angle of attack velocity
$t$	time
$\omega$	fly-wheel rotational velocity
$f$	absolute frequency
$K$	$\frac{\omega c}{U_\infty}$ reduced frequency
$c$	root chord
$U_\infty$	free stream velocity
$u = \frac{U_\infty t}{c}$	non-dimensional time

Introduction

Modern military aircraft are required to maintain good handling qualities and performance at very high angles of attack. Such aircraft have come to utilize the advantages under such conditions of highly swept wings, preferably in the shape of delta wings. On the delta wing the lift is created by separated but stable vortical flow structures rather than by the attached flow over the wing. The angle of attack at which the vortical flow breaks down can reach 30 deg or more. The physics of the stationary flow over a delta wing when vortices are existing has been studied extensively and reported by various researchers. The leading edge sweep angle, the cross sectional shape and the angle of attack determines the flowfield as reported by Örnberg (1). The angle of attack influence on the main leading edge vortex core positions has been reported by Elle (2) from studies in a water channel where air bubbles were used to visualize the flow. He found that for a flat plate delta wing the "spanwise" angle between the vortex cores, when normalized with the wing apex angle, does not change very much with the angle of attack but stays around 0.6. The vortex height over the wing surface lifts away with increasing angle of attack. Several researchers have investigated the pressure distribution over delta wings and found that the spanwise pressure peak always occurs under the main vortex although the presence of other secondary vortices may result in flatter pressure distributions than normally seen in the two-dimensional case. Unstationary flow over delta wings is however far less known. Lambourne et al (3) have studied the vortex behaviour following a sudden change of incidence. They found that the leading edge separation vortices went through a growth-decay change following a positive

or negative sudden change of the incidence. The vortices eventually reached the steady state spanwise and height location after a delay that at any chosen chordwise position was nearly equal to the time for the flow to travel at freestream velocity from the apex to the position studied. Gad el Hak et al (4,5) have studied a pitching delta wing and found a similar growth-decay cycle for the leading edge vortices. For both the sudden plunge and the pitching wing, those researchers found obvious hysteresis effects. I.e. at identical instantaneous attack angles, vortex locations and strength were different for upstroke and downstroke movements.

Predictions for aircraft maneuvers have as a common practise been made by the use of Taylor expansions including coefficients and derivatives which, based on linear theory, have been measured in various windtunnel tests. The damping derivatives are normally measured with forced oscillation technique. It is obvious that such a procedure must be doubtful when extended up to high angles of attack where nonstationary effects depending on the direction of the movement, are present.

For aircraft flying into gusts the only true simulation of course is a gust facility such as a gust track or a gust-tunnel. Neither a pitching nor a plunging motion in ramp or oscillatory mode can correctly simulate the gust in so far as to reproduce the sudden change of attack angle distributed over the chord as a function of time. It seems natural though to believe that a better knowledge of the nonstationary flow over a delta wing achieved for example by studying the vortex flows for the above mentioned four types of movement, would be helpful to improve the ground testing methods for aircraft maneuvering and flying into gusts, both experimentally and theoretically.

#### Experimental Approach

As mentioned above the leading edge vortices will change their core position when the angle of attack is varied. This movement however is not large and therefore experimentally difficult to assess with some accuracy. For a 60 deg delta wing with sharp leading edges the bursting of the vortices will be located over the wing for a wide range of attack angles. The movement of the burstpoint is easier to detect, much more sensitive to a change of incidence and has a major impact on pressure distribution and consequently on the lift and pitching moment of the wing. Experiments were performed in which investigations were made regarding the nonstationary flow over a schematic deltawing with and without a canardwing for four different types of movement:

1. Harmonic pitching  $u(t) = u_s + u_0 \sin \omega t$
2. Harmonic plunging  $u(t) = u_s + u_0 \cos \omega t$
3. Ramp pitching  $u(t) = u_s + \dot{u} t$
4. Ramp plunging  $u(t) = u_s + \dot{u} t$

In watertunneltests the vortex burst positions were monitored and measured as functions of the instantaneous attack angles. Visualization was made with air bubbles. Because of the possibility that the bursting mechanism would be influenced by the low Reynolds' number or/and by the air bubbles it was decided that some of the different types of movement should also be tested in a windtunnel where visualization would be achieved with smoke. As a check of the possible influence of the smoke also Schlieren pictures would be taken of the vortex cores. Windtunneltest also would enable measurement of loads and of damping derivatives with much less measurement problems than in a watertunnel.

#### Watertunneltest

A 60 deg delta wing with chamfered (sharp) leading edges was used for the test. The flat side of the wing was used as suction side. A 60 deg similar canard could be mounted ahead of the wing. Fig 1 is a sketch of the model.

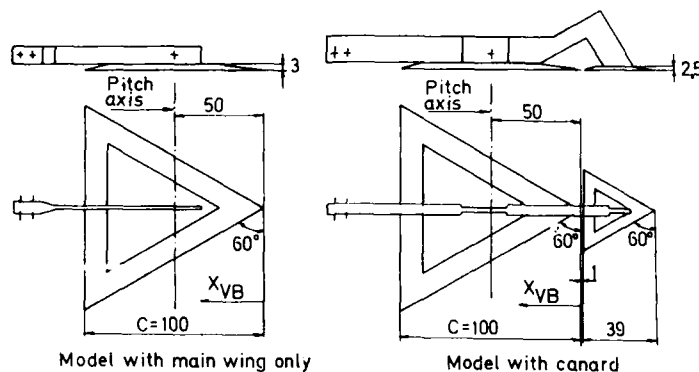


FIG 1. WATERTUNNEL MODELS-DIMENSIONS IN MILLIMETER



The Göttingen type watertunnel at Volvo Flygmotor, Trollhättan was used for the test. The test section tank has the width 0.45 m and the height 0.55 m; the flow nozzle has diameter 0.33 m. During the test the upper water surface in the test section was free (i.e. not enclosed by a wall). The water speed, originally planned to be 1 or 2 m/s was limited to 1 m/s by the light-sensitivity of the videocamera used for the documentation. Thus the Reynolds' number during the test based on root chord was  $1.0 \times 10^5$ . Fig 2 shows schematically the model installation in the watertunnel. The four different modes of motion were

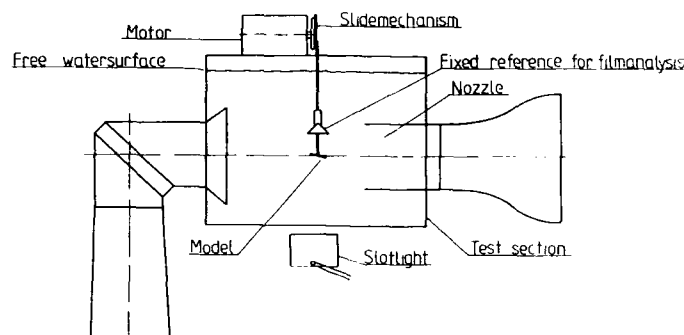


FIG. 2. WATERTUNNEL TEST ARRANGEMENT

achieved with a one- or two-bar - rig driven with either a slidemechanism or with a camshaft pulley. For the harmonic pitching motion a pin on a fly-wheel was driving a slide plate guided by two rails. Two bars, one fixed and one connected to the slide plate transferred the motion to the model. The pitch frequency was  $f = 0.58$  Hz, resulting in a reduced frequency  $K$  of 0.18. Fig 3 shows the mechanism in principle.

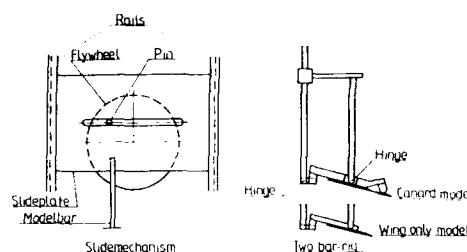


FIG. 3. HARMONIC PITCHING MECHANISM

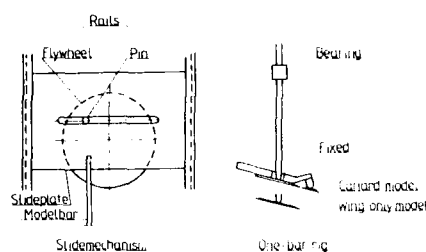


FIG. 4. HARMONIC PLUNGING MECHANISM

Harmonic plunging utilized a one-bar rig with the same slide mechanism. Frequencies were the same as for pitching motion. Fig 4 shows the mechanism. The ramp motion for pitch is designed to give a ramp with  $\dot{\alpha} = 0.6$  rad/s and a ramp length of  $\Delta\alpha = 10$  deg from a start angle of attack which can be set at choice between 0 deg and 30 deg. A camshaft pulley was made such as to enforce the ramp of  $\Delta\alpha = 10$  deg when the pulley rotated 0-45 deg. At 45-90 deg the attack angle is constant  $\alpha_s + 10$  deg. From 90-180 deg,  $\alpha(t)$  is decreased to  $\alpha_s$  and will then be steady while the pulley rotates from 180-360 deg., where the cycle will be repeated. With the chosen pitch velocity this means that the wing will be stationary at  $\alpha_s$  during 1.6 sec before the ramp starts and then be steady at  $\alpha_s + 10$  deg during .291 sec.

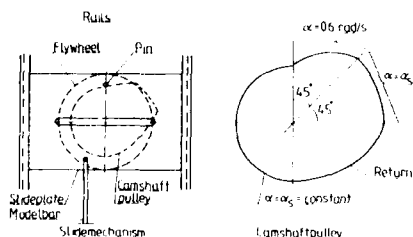


FIG. 5. RAMP PITCHING MECHANISM

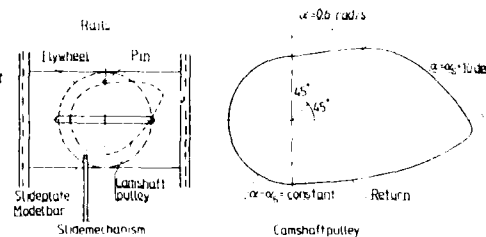


FIG. 6. RAMP PLUNGING MECHANISM

With freestream velocity 1 m/s this is equal to  $\mu=2.91$  using Lambourne's terminology, i.e. the free stream has traveled almost three times the chord and the flow over the whole wing should well have reached stationary conditions. Fig 5 shows this mechanism and the camshaft pulley. Ramp motion for plunging wing finally is also designed for  $\dot{\alpha}=0.6$  rad/sec and a ramp length of 10 deg.

MOTION	CONFIGURATION	PITCH VELOCITY RAD/S	FREQUENCY $f_z$	$\alpha_0$
HARMONIC PITCHING	WING ONLY	-	0.58	10, 15, 20
	WING AND CANARD	-	-	10, 15, 20, 25, 30
HARMONIC PLUNGING	WING ONLY	-	-	10, 15, 20
	WING AND CANARD	-	-	10, 15, 20, 25, 30
RAMP PITCHING	WING ONLY	0.6	-	10, 15, 20
	WING AND CANARD	-	-	10, 15, 20
RAMP PLUNGING	WING ONLY	-	-	10, 15, 20
	WING AND CANARD	-	-	10, 20

The plunging motion hence is non-linear for the time 0-0.291 sec and linear 0.251-0.582 sec. Steady conditions before and after the ramp are of same length as for the ramp pitching motion. The total plunge of the model is 0.077 m (3.02"). Fig 6 shows the mechanism and the camshaft/pulley.

The four types of motions described above were forced upon the model. A slot light (2 kW) was positioned parallel with the port side vortex, visualized with air bubbles. Sequences were recorded on videotape, which were then analyzed "frame by frame" and the burst position measured as a function of the instantaneous attack angle.

When a model with a canard was used, only the main wing vortex was analyzed. The canard vortex was too small to allow any measurements to be made. Vortex burst positions for the stationary case were also measured and are shown as a reference in figures 7-10.

The total test envelop is shown in table 1.

#### Experimental Results - Watertunnel test

In figures 7-10 the lengthwise burst position normalized by the rootchord  $X_{VB}/C$  is plotted as a function of  $\alpha(t)$  with  $X_{VB}=0$  being the wing apex. The accuracy of the assessed burst position is estimated to 2-3 % of the rootchord. When the burst is close to the apex or to the trailing edge of the wing the accuracy however is not so good because of influence, at the apex of the vortex on the other side of the wing and at the trailing edge of the flow from the wing pressure side. At the apex, also the absolute size of the wing is very small and air bubbles are relatively larger and may have a larger influence on the bursting mechanism.

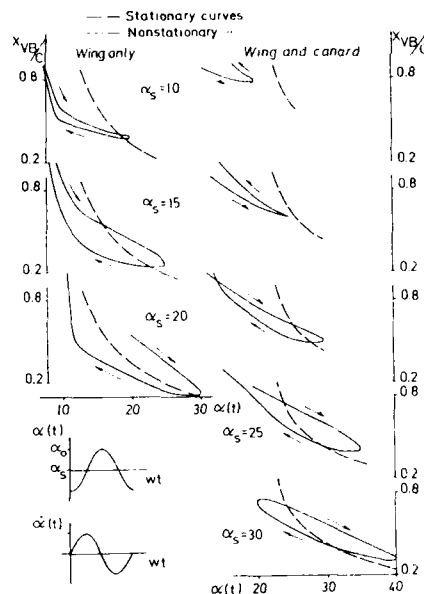


FIG. 7. VORTEX BURST POSITIONS FOR HARMONIC PITCHING MOTION

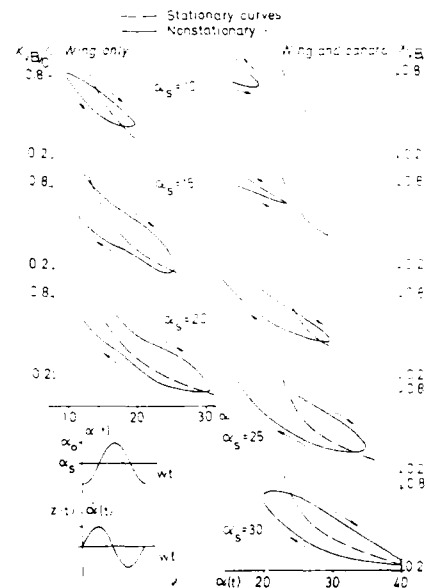


FIG. 8. VORTEX BURST POSITIONS FOR HARMONIC PLUNGING MOTION

Fig 7 shows the curves for harmonic pitching motion. For the case without a canard at  $\alpha_s=10$  deg the hysteresis effects are small but the displacement of the burst to one side for both up and downstroke motion compared to the stationary case is obvious. At the upper turningpoint  $\alpha(t)=20^\circ$  the curves coincide.

As  $\alpha_s$  increases the loop becomes wider and is at  $\alpha_s = 20$  deg almost symmetrical around the stationary curve. As  $\dot{\alpha}$  is zero in the turning points it could be expected that the burst position there is closer to the stationary condition than elsewhere.

For  $\alpha(t) = 10 + 10 \sin \omega t$  the motion will include attack angles where the stationary flow has no vortices. The displacement towards the apex of the burst at  $\alpha_s = 10^\circ$  for the nonstationary flow, therefore must be caused by vorticity emanating from the part of the wing ahead of the pitch axis where at downstroke motion the induced attack angle will reach high values.

Generally for the case without a canard the loops have a direction as could be expected for viscous damping. This however is not always the case for the model with a canard. At  $\alpha_s = 10$  and  $15$  deg the upstroke burst position is ahead of the downstroke. For  $\alpha_s = 10, 15$  and  $20$  deg the forward displacement of the burst compared with the stationary case is also obvious at the lower values of  $\alpha(t)$ . The reversed loop direction is supposed to depend on the interference from the canard, the flow of which besides its own hysteresis also influences the wing with a time-delay due to the distance ahead of the wing. The strengthening influence from the canard vortex onto the main wing vortex is delayed and the flow of the wing is more like the conditions without a canard in the nonstationary case.

Fig 8 shows the curves for harmonic plunging motion. It must be kept in mind that for the plunging motion the model is of course subject to different wall interference and to varying irregularities in the flow from the nozzle because of the movement, whereas for the stationary case such conditions are constant. The conditions are similar to the harmonic pitching motion but for the  $\alpha_s = 10$  case for wing only. For the plunging motion no similar forward displacement is seen, hence adding strength to the theory that the induced attack angle is the cause in the pitching motion.

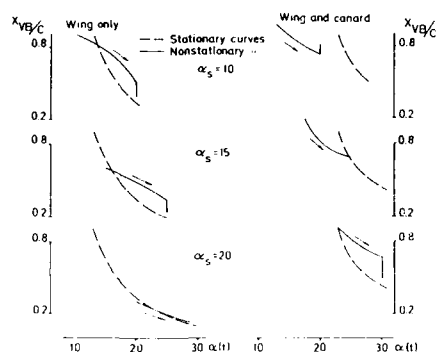


FIG 9. VORTEX BURST POSITIONS FOR RAMP PITCHING MOTION

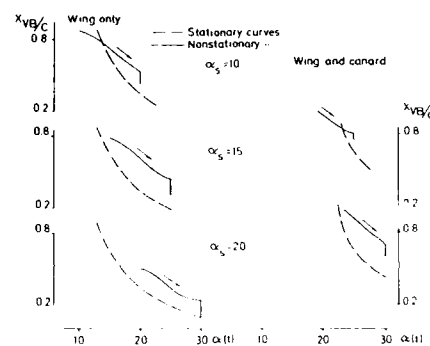


FIG 10. VORTEX BURST POSITIONS FOR RAMP PLUNGING MOTION

Ramp motion in pitch (fig 9) and in plunge (fig 10) also show similar-flow conditions. For all experiments without a canard there is a delay in the movement of the burst position which however at the end of the ramp continues to move and eventually comes close to the stationary position. It is again observed that for low  $\alpha_s$ -values with a canard the burst position is ahead of the stationary curve. At the end of the ramp the burst position also in those cases moves closer to the stationary position. During the ramp motion where  $\dot{\alpha}$  is always  $0.6$  rad/s, the distance from canard apex to wing apex ( $0.04$  m) corresponds, using freestream velocity ( $1.0$  m/s) to a delay in attack angle of only  $1.5$  deg. It must be concluded that the larger nonstationary effects with the canard configuration are due more to the hysteresis effects on the canard vortex itself before it influences the main wing vortex rather than to the delay for the canard flow to travel downstream to the main wing.

#### Windtunnel test

The windtunnel tests, which are not yet completely finished, are performed in the  $2 \times 2$  m low speed wind tunnel at the university of Stockholm (Division of the Aeronautical Research Institute of Sweden). The first part including harmonic pitching motion is finished, the second, ramp pitching has been delayed due to higher priority project work but is currently being installed in the wind tunnel. The model is geometrically identical with the watertunnel model but five times larger. It is mounted on a balance and hence has on the pressure side a tapping over the balance. The model is shown in fig 11.

The windspeed has been varied within the range  $20$  m/s- $65$  m/s. Reynolds' number therefore were  $0.7$ - $2.2 \times 10^6$  and the reduced frequencies  $0.003$ - $0.33$ . An existing mechanism designed for pitch damping derivatives test was used. - For the ramp mode this rig has been supplied with a stepmotor which electronically controlled, can move the model a ramp length of  $10$  deg at a pitch rate within the range  $0.1$  to  $5$  rad/s. The vortices were visualized with kerosene smoke and recorded with either a photographic or a videocamera. As a check of the

possible influence of the smoke on the burst mechanism it was also visualized with a shlieren system. It must be observed though, that unlike the watertunnel test where the burst movement was recorded and analyzed consecutively, in the windtunnel a triggered flash light was used. Triggering was arranged from a connector on the flywheel which could be changed to trigger at various attack angles. The curves showing the movement of the burst position hence are each achieved from many different occasions with intermediate stops of the oscillation.

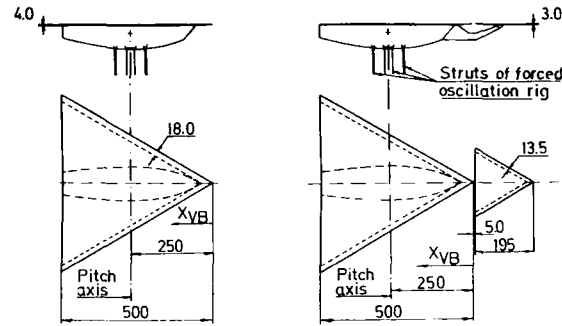


FIG 11. WINDTUNNEL MODELS

#### Experimental results in the windtunnel test. - Flow visualization

Referred here will be only those windtunnel results which are of interest in comparison with the watertunnel test.

Stationary vortex burst positions are shown in fig 12. A reasonably good agreement is found between the water- and windtunnel tests. A small difference exists between different visualization methods in the windtunnel. It must be kept in mind though that all the data are resulting from a personal opinion about where the burst is located. Different persons have analysed the photos and images are also somewhat different with the different methods of visualization. Nonstationary burst positions are shown in fig 13 for  $u(t)=20 \pm 8$  deg and reduced frequencies  $k=0.006-0.195$ . As expected, the frequency has a large influence on the hysteresis effects.

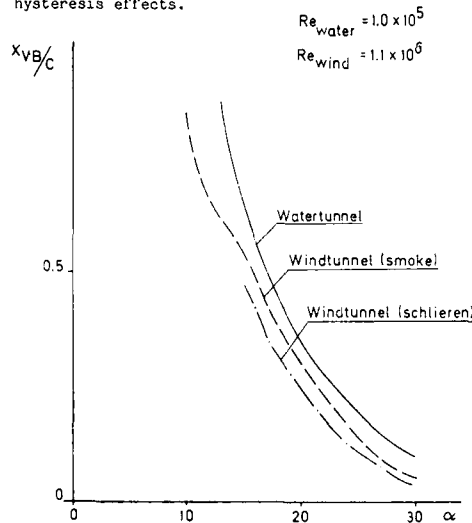


FIG 12. STATIONARY VORTEX BURST POSITION-COMPARISON WATERTUNNEL AND WINDTUNNEL

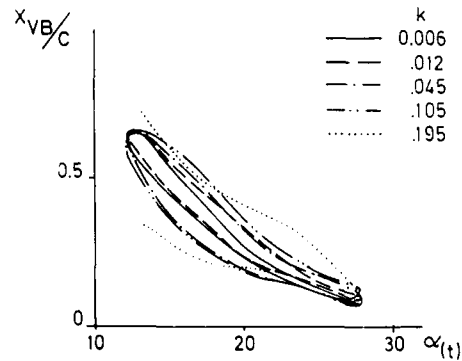


FIG 13. VORTEX BURST POSITIONS IN WINDTUNNEL

When compared with the watertunnel results (fig 14) a small shift forward for the burst position is seen for the windtunnel. The difference is of the same order as for the stationary case.

The difference between smoke and schlieren visualization is of the same order both stationary and nonstationary as can be seen from fig 12 and fig 15.

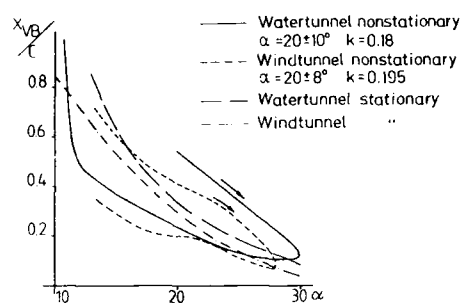


FIG 14. COMPARISON BETWEEN WATERTUNNEL AND WINDTUNNEL OF STATIONARY AND NONSTATIONARY VORTEX BURST POSITIONS

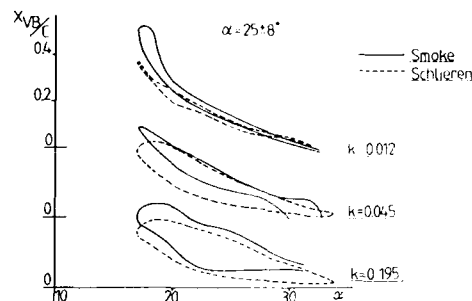


FIG 15. COMPARISON BETWEEN VISUALIZATION WITH SMOKE AND SCHLIEREN SYSTEM OF VORTEX BURST POSITION IN WINDTUNNEL

#### Experimental results in windtunnel test. - Force measurements

The loops in the vortex burst positions are also found in the measured loads. Fig 16 shows the case  $\alpha(t) = 25 \pm 8$  deg for  $k = 0.006-0.195$ .

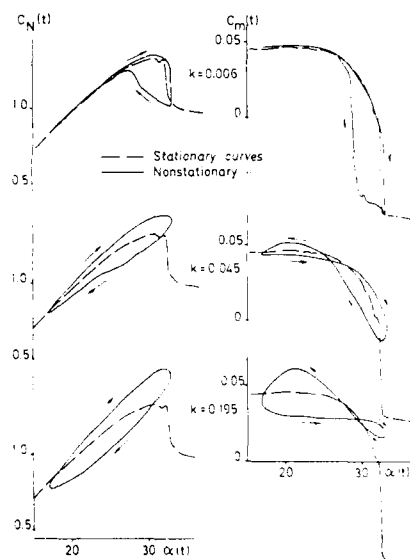


FIG 16. STATIONARY AND NONSTATIONARY  $C_L(t)$  AND  $C_m(t)$  LOADS FOR SOME DIFFERENT REDUCED FREQUENCIES IN WINDTUNNEL TEST

Nonstationary loads show similar hysteresis effects in the windtunnel test as have been found in the watertunnel test. Not even the mean values of the hysteresis loops are always in agreement with the stationary loads. Up-and downstroke loads are sometimes displaced to one side of the stationary loads. Forced oscillation test regarding damping derivatives must under such conditions be doubtful. Damping properties should be considered as discrete values depending on condition and direction of the movement.

#### Conclusions

Nonstationary flow over a flat sharp edged 60 deg delta wing at angles of attack where vortices are shed from the leading edges, is subject to large hysteresis effects as can be seen in the movements of the vortex burst positions. For the configuration without a canard wing the hysteresis is caused by a delay in the vortex burst movement. For the configuration with a canard, the vortex burst position is sometimes ahead of the stationary case, which can be explained by the delay of the strengthening effect from the canard vortices onto the wing vortices which is caused by similar hysteresis on the canard flow. As a consequence of this conclusion we are lead to assume that the dynamic stall for a pair of wings interacting with each other may not necessarily produce a higher maximum lift than the stationary case as often happens for a single wing. Water and windtunnel tests yield results principally identical and of very similar size. The variation of Reynolds' number does not seem to have significant influence. This has also been observed in the windtunnel test when different Reynolds' number have been used. Örnberg (Ref 1) and Elle (Ref 2) have observed similar low sensitivity to Reynolds' number for stationary conditions for the flat delta wing case. (The thicker profiled wing for which the vortices not always originate at the apex and which have leading edge bubble separation at the center wing, may well be different in this respect both stationary and nonstationary).

The visualization method with air bubbles in the watertunnel or with smoke in the windtunnel does not influence the vortex burst position significantly neither stationary nor nonstationary, which is in agreement with Elle (Ref 2).

References

<u>No</u>	<u>Author(s)</u>	<u>Title etc</u>
1	T Örnberg	A note on the flow around delta wings. Royal Institute of Technology Stockholm KTH Aero TN 38
2	B. J. Elle	An investigation at low speed of the flow near thin deltawings with sharp leading edges. Aeronaut. Res. Council England R & M No. 3176
3.	N. C. Lambourne D. W. Bryer J. F. M. Maybrey	The behaviour of the leading edge vortices over a delta wing following a sudden change of incidence. Aeronaut. Res. Council. England R & M No. 3645
4	M. Gad el Hak Chih-Ming Ho R. F. Blackwelder	A visual study of delta wing in steady and unsteady motion. Unsteady Separated Flows, edited by M. S. Francis and M. W. Luttges Univ. of Colorado, Colorado Springs Aug 1983 pp 45-51
5	M. Gad el Hak Chih-Ming Ho	The pitching delta wing. AIAA Journal Vol 23 No 11
6	K. W. McAlister L. W. Carr	Watertunnel visualizatiior of dynamic stall. American Society of Mechanical Engineers Vo. 101. Sept 1979

# FLOW VISUALIZATION STUDIES ON TURBULENT BOUNDARY LAYERS USING MULTIWIRE HYDROGEN BUBBLE GENERATION

by  
P. Hickland and K. Prishna Prasad  
Delft University of Technology  
P.O. Box 517  
2600 MB Delft  
The Netherlands

## SUMMARY

The present work provides some new results obtained with two visualization techniques that assist in describing essentially three dimensional phenomena: 1. With two wire pattern correlation we can describe the flow field in a large set of sections through a certain structure; 2. Multiple colour illumination allows recognition of movements in a direction normal to the plane of the photograph from changes in colour. Some quantitative work was made concerning the behaviour of low speed streaks as a function of  $y$  and the relation between streaks and some other structures. A new detection criterion for streaks is proposed. The distribution for the spanwise velocity of a streak was determined. It is shown that the detection criterion of Blackwelder and Kaplan essentially samples spanwise positions of streaks. A few results of multiple colour visualization are shown to indicate the relationship between the vertical transport associated with streaks.

## INTRODUCTION

The work of Kline, Browkey and others has caused an awareness of the fact that turbulence not only has a statistically defined structure, but also has a structure in time of coherent structures. Although a great amount of research effort has been put into making a description of these deterministic properties several problems remain unsolved. Many of these questions are associated with the problem that different experimental techniques emphasize different aspects of the flow. Sometimes they even seem to indicate conflicting results. For instance visualization of the flow field in a vertical plane shows bursts but does not show the movements of low speed streaks that are in general out of the plane of visualization while visualization of the flow field in a horizontal plane shows the movements of low speed streaks in general persisting during several burst periods. Conditional sampling measurements provide a rapidly changing picture and seem to indicate that after each burst a streak is replaced by high speed flow.

Since different definitions of coherent structure and low speed streak are used in current literature, we feel it necessary to state, what is meant by these words in this paper: A coherent structure is a connected region with a phase-correlated velocity-pressure field over its spatial extent. This flow pattern moves through the flow with a velocity in general different from the local fluid velocity like a wave. A low speed streak (further shortly named streak) is a region of flow with a relatively small streamwise velocity component, that is elongated in the streamwise direction and connected to the wall. The choice of a more quantitative criterion for the streamwise velocity in a streak is discussed later in this paper.

The present work is an extension of the hydrogen bubble flow visualization studies in plan view, presented earlier by the authors (1). Two distinguishing features of the present technique are the use of multiple wires and multi-colour photography. This paper assists in clarifying essentially three-dimensional phenomena with the aid of two dimensional photographs. A summary of some important observations in the earlier work is given below.

1. In the wall region we see a large number of long streaks, often longer than  $x^+ = 1000$ . They are meandering slowly through the illuminated areas, sometimes joining, sometimes separating, sometimes perturbed by other structures. Only a few of them with a visible beginning or end.
2. Many streaks extend upto  $y^+ = 50$ , for  $y^+ > 40$  the strength of the flow field drops along a streak.
3. Low speed streaks are very persistent and no photograph indicated that there was an abrupt break up of a streak. The visualization studies of Smith and Metcalfe (2) independently showed, that a streak persists over several burst periods.
4. Most vertical transport away from the wall in the region  $y^+ < 4$  was concentrated in a low speed streak. This result was affirmed by Fuen (3) for  $y^+ < 10$  using a multi-wire transparent film and synchronous laser visualization.

The present paper deals with four subjects:

1. Some quantitative data concerning the behaviour of streaks for increasing distance from the wall.
2. The data concerning the spanwise movement of streaks.

3. An explanation for the apparent contradiction between conditional sampling with the Blackwelder and Kaplan Detector, criterion and hydrogen bubble visualization concerning the persistence of streaks;
4. Some preliminary results with multiple colour illumination allowing recognition of movements in a direction normal to the plane of photography from changes in colour.

#### THE EXPERIMENTAL SET-UP AND THE VISUALIZATION METHODS

The experiments were carried out in an open-surface recirculating water channel. The working section is 9 m long and has a rectangular cross section of 1 x 1.80 m. A false floor with tripping wire, placed at 5 cm from the bottom served as a flat plate. The water depth above this plate was 35 to 41 cm. Most experiments were performed 1.71 m downstream of the leading edge of the plate with Reynolds number based on momentum thickness  $Re_\delta = 933$ . In the wall region most processes scale in wall units: for instance Brin and Metzler (1969) showed for  $Re_\delta = 1000$  that the statistics of the spanwise streak spacing solely scales in wall units and that the timeline patterns have a similar appearance. However, regarding the scaling of the burst frequency yet no consensus of opinion exists (4, 5, 6). Nevertheless probably most of the observations described in this paper are relevant for a much larger range of  $Re_\delta$ . The hydrogen bubbles were generated in the usual manner by applying electrical tension to one or more platinum wires (25  $\mu$ m in diameter). The wires were placed in the spanwise direction, the photographs and films are of plan view.

If a low speed streak is visualized merely by the timelines of a single wire it is not possible to decide whether this low speed flow region must be thought of as a finger protruding from the wall or as an elevated elongated ridge. This is an example of a more general problem: if the flow field is visualized with a single wire, we only obtain a one-dimensional structure. There is no dependence of extratimeline structure. A pattern obtained in a single wire is a two-dimensional structure. Furthermore since time dependent patterns can also be generated by an essentially time dependent process as well as by a persistent structure traversing the sheet of bubbles.

These problems are avoided by the simultaneous use of two wires parallel to each other separated some distance perpendicular to the plane of photography. In this work the wires are placed in the spanwise direction at the same streamwise coordinate and various distances from the wall  $y_1$  and  $y_2$ . In the type A three dimensional structure generating a certain pattern A at the wire at vertical coordinate  $y_1$ , we observe the patterns generated at the second wire at  $y_2$ . If the pattern A is of the type A, the patterns generated at the second wire are of the type A, B or C. If the pattern A is of the type B, the patterns generated at the second wire are of the type B, C or D. A third section of this type of structure can be obtained by placing the second wire at a new location  $y_3$ . We now compare the patterns generated at the wire  $y_1$  when at the wire at  $y_2$  a pattern A is observed. If we obtain from these data we obtain a picture showing a further refinement of a certain structure. An example of this refinement is presented later.

Two different methods were used to ensure that it was possible to discern the patterns generated simultaneously at the two wires.

1. The wire was placed vertically in the wall and fed by direct current. This wire is called a marker wire. The wire at distance  $y_2$  is essentially the same as a two-dimensional structure. We observe the patterns generated at the marker wire and the patterns generated at the wire at distance  $y_2$ . The patterns generated at the marker wire are of the type A, B or C. The patterns generated at the wire at distance  $y_2$  are of the type A, B or C. A third section of this type of structure can be obtained by placing the second wire at a new location  $y_3$ . We now compare the patterns generated at the wire  $y_1$  when at the wire at  $y_2$  a pattern A is observed. If we obtain from these data we obtain a picture showing a further refinement of a certain structure. An example of this refinement is presented later.
2. The flow field is illuminated by a laser sheet. The patterns generated at the marker wire are of the type A, B or C. The patterns generated at the wire at distance  $y_2$  are of the type A, B or C. A third section of this type of structure can be obtained by placing the second wire at a new location  $y_3$ . We now compare the patterns generated at the wire  $y_1$  when at the wire at  $y_2$  a pattern A is observed. If we obtain from these data we obtain a picture showing a further refinement of a certain structure. An example of this refinement is presented later.

#### THE DEBANDING OF THE PATTERNS GENERATED BY THE TWO WIRES

Figure 1 shows a typical pattern generated by a single wire. The pattern is of the type A. The patterns generated by the two wires are of the type A, B or C. The patterns generated at the marker wire are of the type A, B or C. The patterns generated at the wire at distance  $y_2$  are of the type A, B or C. A third section of this type of structure can be obtained by placing the second wire at a new location  $y_3$ . We now compare the patterns generated at the wire  $y_1$  when at the wire at  $y_2$  a pattern A is observed. If we obtain from these data we obtain a picture showing a further refinement of a certain structure. An example of this refinement is presented later.



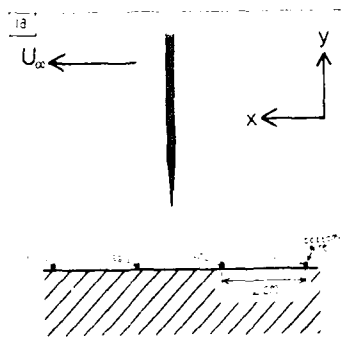


Fig. 1, a) configuration with pulsed wires and bottom wire, b) Pulsed wire at  $y^* = 15$  together with bottom wires.

An important result is that for  $y^* < 60$  only a few percent of the elongated low speed flow regions visualized by the pulsating wire was not nearly coinciding with one or more streak lines. Thus it is concluded that for  $y^* < 60$  an elongated low speed flow pattern nearly always is a section through a streak: a streak has the shape of a ridge and not of a lifting finger.

Some countings concerning the coincidence of the extrema in the streamwise velocity visualized with the pulsating wire with the lines generated by the bottom wires for different values of  $y^*$  of the pulsating wire are shown in table 1. The six types of patterns that were selected are represented in figure 2. (A): A single streakline (generated at the bottom wire almost coincides with a local minimum in the timelines; (B) and (C): Two and three streak lines almost coincide with a local minimum; (D): The timelines close to the wire near a streak line do not show a local minimum, but this local minimum occurs rather suddenly somewhat downstream, this pattern will be called a streak back; (E): The streak line does not coincide with any extremum; (F): The streak line almost coincides with a local maximum. In table 1 the distribution of streak lines over these six types of patterns is shown: These data illustrate, that if one counts streaks from a single pulsating wire, with increasing  $y^*$  position of the wire a decreasing amount of streaks per unit spanwise distance will be counted. Sometimes because a streak near the location of the wire does not



Figure 2. Two wire pattern correlation. six types of combinations of streaklines, generated at the bottom wires, and timelines generated at a pulsating wire.

$y^*$	15	30	45	60
A	48	29	28	23
B	2	10	9	11
C	0	3	2	2
D	14	7,5	9	4
E	23,5	31	36	42
F	11	6	4	3
A,B,C,D	65	48	47	30

all in %

Table 1. relative abundance of streaklines for six types of patterns.



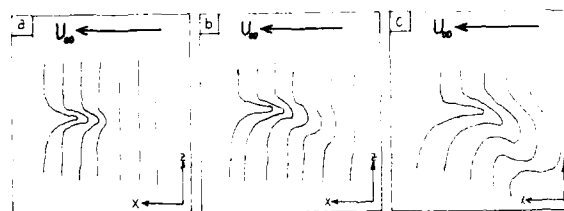


Figure 5 Development of a streakback as a function of time ( $y^+ = 15$ )

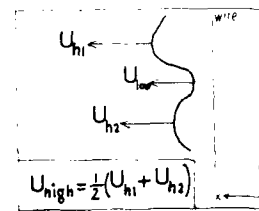


Figure 6 Quantitative detection criterion

A streak is counted to extend to a certain  $y^+$  if timelines generated at that coordinate show a local minimum of the streamwise velocity and a streak line generated by the bottom wire almost coincides with those local minima. Since two wire correlation for  $y^+ < 60$  showed that only a few percent of the local minima were not associated with a streak line it is not necessary any more to verify for  $y^+ < 60$  whether the second part of this criterion is satisfied. The first part of this criterion is qualitative and sensitive to the judgement of the observer. For this reason a more quantitative definition is required.

A detection criterion used by Smith and Metzler (2) is based on the relation between the streamwise velocities in a local minimum  $U_{low}$  and adjacent local maxima  $U_{high}$  (see figure 6).

$$U_{low}/U_{high} < \alpha \quad (1)$$

Smith showed that for  $\alpha = 0.7$  detection is rather insensitive to the choice of  $\alpha$ : both the use of  $\alpha = 0.58$  and  $\alpha = 0.85$  induced a change in the mean spanwise spacing  $\bar{y}^+$  of less than 5% relative to  $\alpha = 0.7$ . However, if we use perturbation theory we require a detection criterion that considers the strength of perturbations of the flow field  $\tilde{u}_1, \tilde{u}_h$ . In this respect criterion (1) is less favourable since it is not only dependent on  $\tilde{u}_1(y)$  and  $\tilde{u}_h(y)$  but also on  $\bar{u}(y)$ . A criterion solely considering  $\tilde{u}_1, \tilde{u}_h$  is:

$$\tilde{u}_h - \tilde{u}_1 = u_{high} - u_{low} < \beta u_{\infty} \quad (2)$$

Here  $\tilde{u}_1(y) = u_{low}(y) - \bar{u}(y)$

$\tilde{u}_h(y) = u_{high}(y) - \bar{u}(y)$  (3)

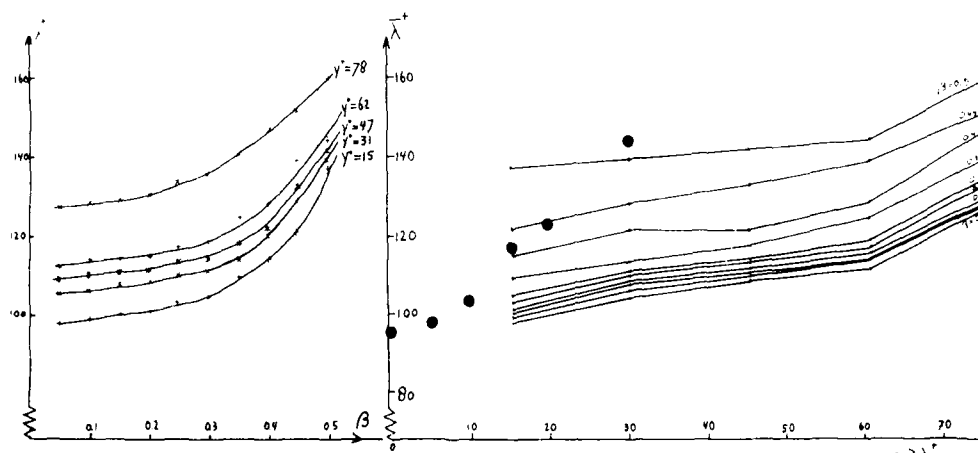


Figure 7 Average spanwise spacing of streaks as a function of height and detection level  
● Smith and Metzler (2)

Criterion (2) shows the height dependence of the perturbation. Criterion (1), however, for a streak becomes more stringent with increasing  $y$ . For a streak criterion (1) approximately indicates:

$$\frac{u_{\text{low}}}{u_{\text{high}}} < \frac{0,6 \bar{u}(y)}{1,1 \bar{u}(y)} \approx 0,7 \Rightarrow \bar{u}_h - \bar{u}_l = u_{\text{high}} - u_{\text{low}} < 0,3 \bar{u}(y) \quad (4)$$

Figure 7a shows the mean spanwise spacing of streaks  $\bar{\lambda}^+$  as a function of the detection level  $\beta$  for five values of  $y^+$ . We observe that for each value of  $y^+$  for  $\beta < 0,3$ ,  $\bar{\lambda}^+$  is rather insensitive to  $\beta$  while for  $\beta > 0,3$   $\bar{\lambda}^+$  is sensitive to  $\beta$ . Figure 7b shows the mean spanwise spacing  $\bar{\lambda}^+$  as a function of  $y^+$  for different values of  $\beta$ . In figure 7c the mean spanwise streak spacing as a function of  $y^+$  for the criterions (1) and (2) are compared. For criterion (1)  $\bar{\lambda}^+$  is increasing more with increasing  $y^+$ . This was to be expected because of Eq. (4).

#### SPANWISE MOVEMENTS OF STREAKS

We next present some quantitative information concerning the spanwise movements of a streak. The spanwise coordinate  $z^+$  of a streak at a fixed streamwise coordinate  $y$  near the wall is determined from the intersection of a streak line with a bottom wire. For several streaks the spanwise coordinate as a function of time was determined using a motion analyser for a film. A typical result is shown in figure 8. From these signals the spanwise velocity of the streak  $W_M$  at instant  $t$  can be determined when  $\Delta t$  is small enough by

$$W_M(t) = \frac{z(t + \Delta t) - z(t - \Delta t)}{2\Delta t} \quad (5)$$

If  $\Delta t$  is not sufficiently small we obtain a filtered version of the velocity signal. In table 2  $\bar{W}_M$  and  $\sigma(W_M)$  are shown for three values of  $\Delta t^+$ . Figure 9a shows histograms of  $W_M^+$  for three values of  $\Delta t^+$ . To obtain a clear picture only the histogram for  $\Delta t^+ = 1,6$  is normalised.

We next consider the timelines generated by a pulsed wire at  $y^+ = 15$ . If we draw a (streamwise) line connecting the local minima in timelines for different values belonging to a low speed streak, the spanwise movements of this line show the spanwise movements of the low speed streak. In this way we can study the spanwise movements of low speed streaks at  $y^+ = 15$  using the same method that was used for streaklines at  $y^+ = 0$ . A complication is caused by the rotating motion near the streak backs. We use the hypothesis that these rotations are a result of some additional mechanism and not ordinary meandering motions. For this reason these parts of streaks were left out of consideration. The histogram

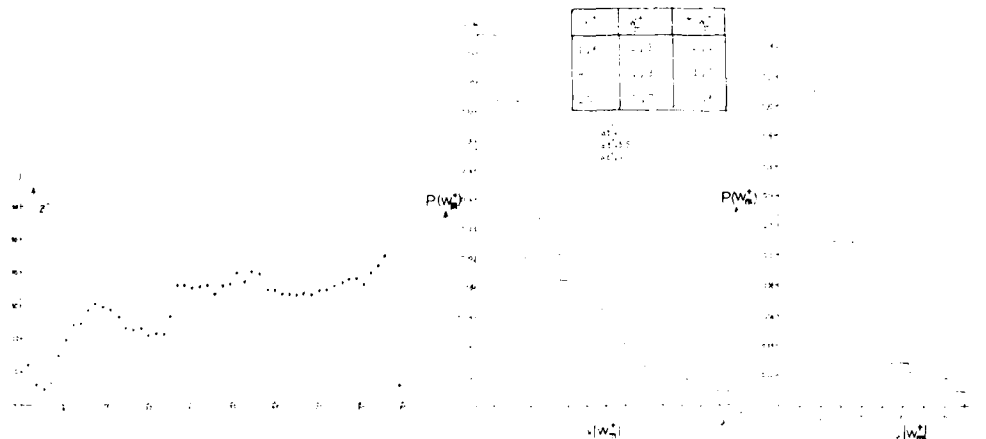


Fig. 9. Sample of the spanwise movements of a streak.

Fig. 9. Statistical results for the spanwise velocity of a streak for  $y^+ = 15$  and  $\Delta t^+ = 1.6$ .

obtained for  $W_m^+$  is represented in figure 9b. There is a reasonable resemblance between the histograms at  $y^+ = 0$  and  $y^+ = 15$ . However, if the spanwise movements of streak backs would be taken into consideration much longer spanwise movements would be observed.

#### THE INTERPRETATION OF THE CONDITIONAL AVERAGE OBTAINED WITH THE VITA CRITERION APPLIED TO THE U SIGNAL

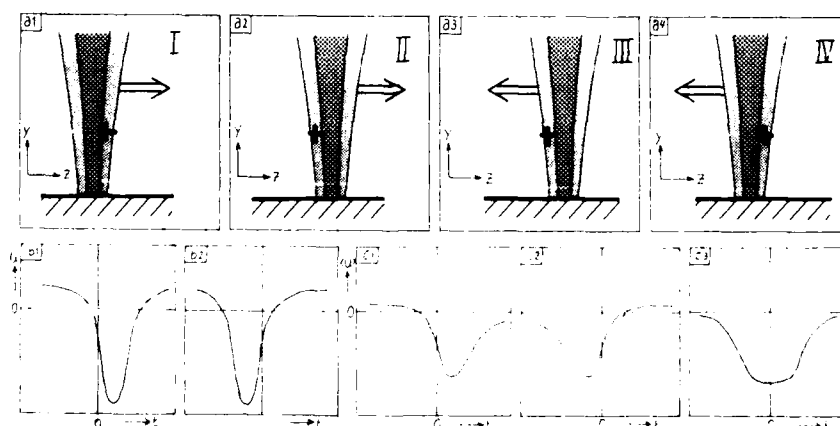
Conditional sampling with the VITA criterion is often used to study processes in the turbulent boundary layer. Properties of the conditional average by this method when applied to the streamwise velocity signal  $U$  can be found in (5), (6), (10), (11) & (12)\*. Some period before  $t = 0$  near the detector a low speed flow region is present. This region is very elongated in the streamwise direction  $l \sim \delta$  and rather small in the spanwise and vertical direction (11), (12). Shortly before  $t = 0$  the velocity profile shows an inflection point. Near  $t = 0$  the low speed flow is replaced by high speed flow rather suddenly. An explanation of this result was proposed by Blackwelder and Kaplan (11): before  $t = 0$  a streak is detected. This structure grows unstable (inflection point instability) and suddenly the streak is wiped out and replaced by high speed fluid. However, according to hydrogen bubble visualization streaks persist several burst periods (1), (2). So either the process sampled with the VITA-U is not visualized by the hydrogen bubble technique or these results must be interpreted differently.

A general discussion of errors for the hydrogen bubble technique was provided by Schraub et al (14). In this section we only consider whether some structures are not visualized by the hydrogen bubble technique. It was shown by the authors (1) that the hydrogen bubble technique tends to neglect structures, that have a small streamwise dimension or are short living. The low speed region obtained with conditional sampling neither is too short living nor has a small streamwise dimension so it will be visualized. The only elongated low speed flow patterns that are visualized in the wall region are streaks; thus the patterns sampled with the VITA-U method before  $t = 0$  must be streaks. The VITA-U criterion essentially samples sudden strong changes of streamwise velocity. Therefore it was postulated that the VITA-U criterion samples spanwise passages of streak (1) across the detector showing a sudden strong change of streamwise velocity (see figure 10a, b, c).

This hypothesis also explains the finding of Blackwelder and Haritonidis (5) that the burst frequency for VITA-U burst decreases if the hot wire length  $l^*$  is increasing for  $l^* > 20$  since the spanwise streak dimension is the order  $20 \sqrt{\nu u^*}$  and hence for  $l^* > 20$  the features of this structure are smeared out over a larger spanwise area.

This hypothesis was verified by Kunen (1984) using simultaneously a pulsating wire at  $y^+ = 29$  and laser doppler anemometry with measuring volume below the sheet of bubbles at  $y^+ = 15$ . The VITA-U criterion applied to the laser doppler signal sampled (37 detections) showed: (1) a meandering low speed streak: 60% of the detections; (2) streak backs: 30% of the detections; (3) a high speed region followed by a disorderly low speed streak: remaining 10%. These results affirm our hypothesis.

However, one aspect remains to be explained. According to our model passage of a streak across the detector will sample two planes of inflection at either spanwise end of a streak. Thus it can be expected that an ensemble of resulting detections will produce a symmetric conditional average profile.



10a) Ensemble average of streak. For types of events sampled by the VITA-U criterion (1) is detector; b) velocity signal for the events shown in a; c) composition of the total ensemble average

This is illustrated in figure 11. I and II represent detections of a streak moving past the detector from left to right. III and IV represent the reverse process. Figure 11 shows the velocity signal in the case of a symmetric flow field around the streak,  $b_1$  and  $b_2$  show the same velocity signal associated with the passage of the same streak, only the choice of  $t = 0$  (time of detection) is different. For velocity signal  $b_1$ , a declaration is detected; this can be both event I and event III. Similar velocity signal  $b_2$  is generated by event II or IV. We now add all events of type  $b_1$  that are detected. They will vary in intensity ( $U_{max}$ ) and duration so we obtain  $c_1$ ; for the contribution of the events  $b_1$  to the total ensemble average. Since all events  $b_2$  are one to one symmetric to an event  $b_1$  (passage of the same streak), the contribution of the events  $b_2$  to the total ensemble average  $c_2$  is symmetric to  $c_1$ ; hence the total ensemble average for symmetrical events is symmetric.

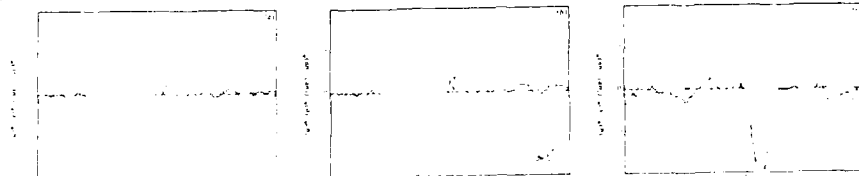


Fig. 11: Conditional averages of  $u$  and  $uv$  for events, detected in the signal with the VITA method: (a) all events; (b) events with positive slope; (c) events with negative slope. From Alfredsson and Johansson (13)

However, the total ensemble average obtained with the VITA-U criterion is not symmetrical (see figure 11), so we must expect the velocity signal associated with the spanwise passage of a streak also to be not symmetrical. This hypothesis was tested in three different ways for measurements made at  $y^+ = 15$ .

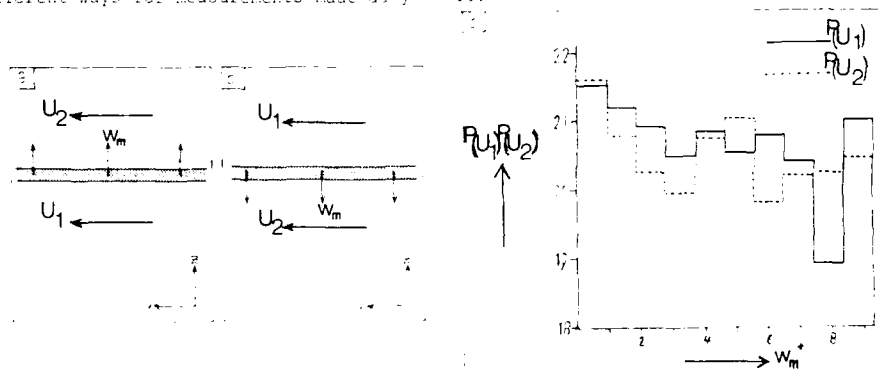


Fig. 12: (a, b) definition of  $U_1$ ,  $U_2$  depending on the direction of  $W_m$ ; (c) average values of  $U_1$  and  $U_2$  for 10 intervals of  $W_m$

A) We have compared the local maxima of the streamwise velocities on either side of a streak as it moves in the spanwise direction (figures 12a & b). Figure 12c shows the average values of  $U_1$ ,  $U_2$  for 10 intervals of  $W_m$ . Figure 12c showed the ensemble distribution for those intervals; we observed that for  $W_m^+ > 4.6$  the ensembles are small and hence the uncertainties high. On the average  $U_1 > U_2$ .

B, C) We compared the spanwise velocities  $W_{m1}$ ,  $W_{m2}$  adjacent to a high speed region for 9 ranges of the maximum streamwise velocity  $U_H$  in that region. Figure 13a shows the direction of movement of the streaks if  $W_{m1}$  and  $W_{m2}$  are positive. In figure 13b is compared the number of streaks moving towards the high speed region ( $W_{m1} > 0$  or  $W_{m2} < 0$ ) with those moving away from the high speed region ( $W_{m1} < 0$  or  $W_{m2} > 0$ ) for nine intervals of the flow velocity in that region. In figure 13c is compared the average spanwise velocity  $W_{m1}$ ,  $W_{m2}$  of the streaks adjacent to a high speed region for 9 ranges of the streamwise velocity. From figure 13b we can determine the relative amount of streaks per interval by adding the two distributions: For  $U_H^+ < 15$  and  $U_H^+ > 25$  the ensembles are small and thus the uncertainties high.

A schematic representation of these results is shown in figure 14a1, 14a2 and the corresponding velocity signals are shown in figure 14b1, 14b2. Events with a negative slope mainly concern streaks arriving at the detector at  $t = 0$  while events with a positive slope concern streaks at  $t = 0$  leaving the detector. As in figure 11 the signals 14b1 and 14b2 are identical; they show the passage of the same streak, only  $t = 0$  (time of detection) is different. Events  $b_1$  and  $b_2$  occur with the same frequency. However, in contrast to a symmetric velocity signal, for the asymmetric velocity signal the right slope is steeper than the left slope. When determining the total ensemble average we sample a large set of events with varying slopes. Thus in practice the right slope will be sampled more often than the left slope. The result is shown in figure 14c. The signals resemble the conditional average obtained with the VITA-U criterion (figure 11).

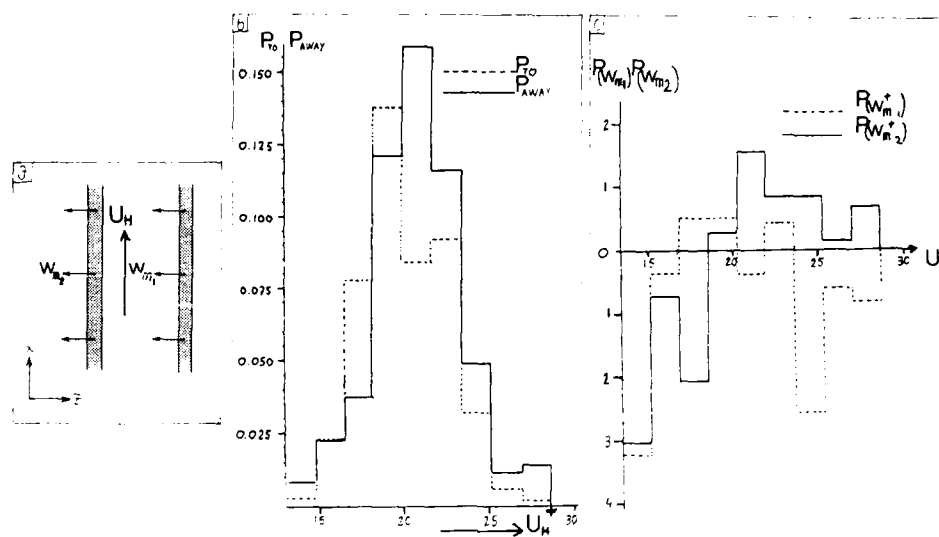


Fig. 13: a) definition of the directions of  $W_{m1}$  and  $W_{m2}$  relative to the high speed region between the two streaks, b) the number of streaks moving to, moving away c) average spanwise velocity

The ensemble for the VITA-U criterion for  $t \neq 0$  mainly consists of streaks distributed over a range of spanwise locations. This is illustrated in figure 15 for the events type II and IV. This results in a phenomenon called phase scrambling; for a general discussion see Yule (15). If we want to obtain a picture of the behaviour and movements at  $t \neq 0$  we must use a detection criterion selecting structures with only distinct velocity of structure. For this purpose a multipoint detection criterion would be necessary.

Similar argument probably can be used for a VITA type of criterion applied to a temperature signal near a slightly heated wall. The heat will be transported approximately

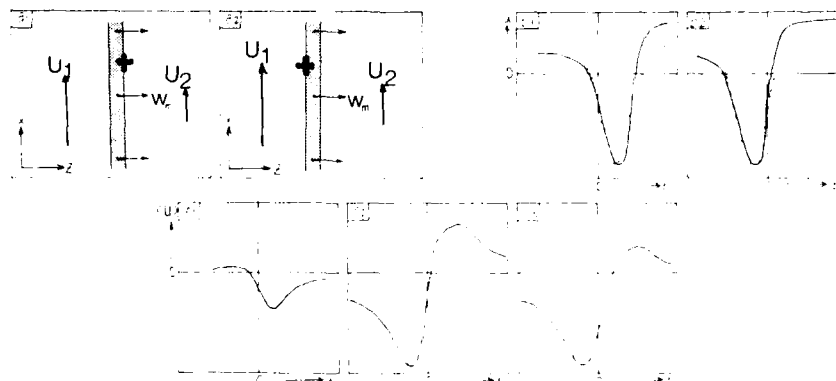


Fig. 14: Conditional average of spanwise streak passages,  $U_H$  is the signal

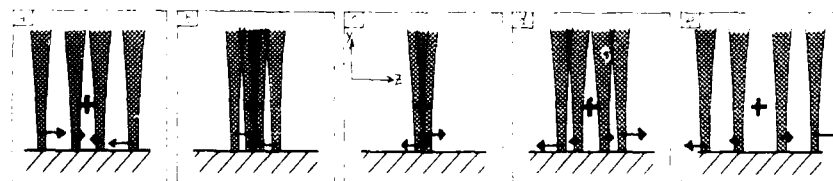


Fig. 15: Set of Events type II and IV at 5 adjacent time instants, a)  $t=0$ , b)  $t=t_1$ , c)  $t=t_2$ , d)  $t=t_3$ , e)  $t=t_4$

similar as hydrogen bubbles generated at the wall. Since all bubbles generated at the bottom wires are collected in streaks probably in case of a slightly heated wall streaks are the patterns of high temperature. Again mainly flanks of streaks will be sampled.

#### RECOGNITION OF VERTICAL TRANSPORT IN PLANE VIEW

To detect strong movements perpendicular to the plane of photograph a visualization technique was developed using two colour illumination. The technique permits simultaneous observation of streaks and ejections (or streaks and sweeps). Most important result was that in plane view for  $y^+ < 40$  an ejection nearly always is coincident with a streak line. To enhance the sensitivity of the technique instead of two colour illumination, multi colour illumination is used.

Figure 16 displays the main features of the experimental set-up. The illumination was achieved by a beam parallel in the vertical plane and divergent in the horizontal plane. A transparent sheet with horizontal lines in different colours is placed in this beam. The flow field now is illuminated by a light beam consisting of thin "layers" of different colours each with a diameter of 1 mm. The wire is placed at the interface blue-red. A bubble with a positive  $y$  velocity will traverse layers with colours red-yellow-green-blue etc. while a bubble with a negative  $y$  velocity will traverse layers with colours blue-green-yellow-red.

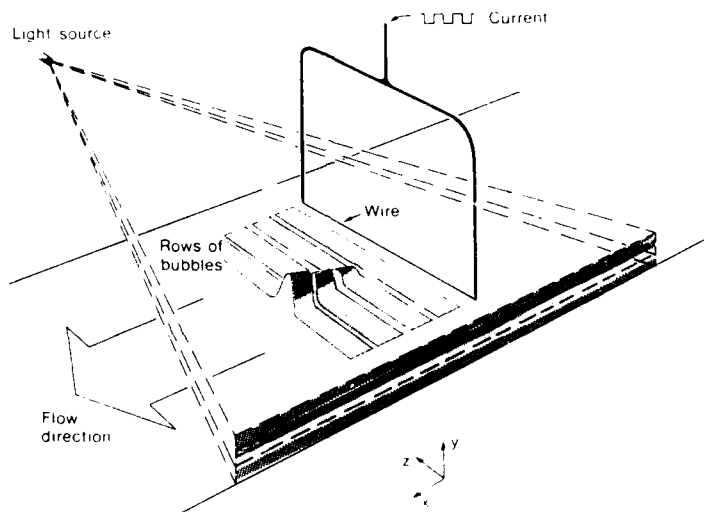


Fig. 16

Photographs 1 through 8 cover a period of 0.7 sec. at intervals of 0.1 sec. with a pulsating wire at  $y^+ = 20$ . We observe most vertical transport to be concentrated in the streak region. In between the streaks we observe a green pattern revealing wallward transport. This pattern somewhat resembles a pocket in stages I and II described by Falco. This type of photographs show the most direct evidence in support of our hypothesis that all vertical upward transport in the wall region is concentrated in the streaks. In addition it is also easy to observe the variation of the intensity of the vertical upward motion along a streak. The vertical downward motion is observed intermittently in the regions between the streaks.

#### REFERENCES

- (1) Blokland, R. and Krishna Prasad, K.: Some Visualization Studies on Turbulent Boundary Layers Using Multi Wire Hydrogen Bubble Generation. Proc. 8th Symposium on Turbulence 1983, Reed, X.B. Patterson, G.K. and Zakin J.L., eds., Dept. of Chem. Engng., University of Missouri-Rolla, 1984, p. 52.
- (2) Smith, C.R. and Metzler, S.P.: The characteristics of low-speed streaks in the near-wall region of a turbulent boundary layer, J. Fluid Mech., vol. 129, 1983, p. 27.



- (3) Kunen, J.M.G.: On the detection of coherent structures in turbulent flows. Doctoral Thesis, Delft University of Technology, 1984.
- (4) Bogard, D.G. and Tiederman W.G.: Investigation of flow visualization techniques for detecting turbulent bursts. Proc. 7th Symposium on Turbulence, 1981, Patterson, G.K. and Zakin, J.L., eds., Dept. of Chem. Engrg., University of Missouri-Rolla, 1983, p. 289.
- (5) Blackwelder, R.F. and Haritonidis, J.H.: Scaling of the bursting frequency in turbulent boundary layers. *J. Fluid Mech.*, vol. 142, 1983, p. 87.
- (6) Alfredsson, P.H. and Johansson, A.V.: Time scales in turbulent channel flow. *Phys. Fluids*, vol. 27, 1984, p. 1974.
- (7) Kline, S.J., Reynolds, W.C., Schraub, F.A. and Runstaller, P.W.: The structure of turbulent boundary layers. *J. Fluid Mech.*, vol. 12, 1972, p. 741.
- (8) Smith, D.K.: A synthesized model of the near-wall region in turbulent boundary layers. Proc. 8th Symposium on Turbulence, 1982, Foss, A.B., Haritonidis, J.H. and Zakin, J.L., eds., Dept. of Chem. Engrg., University of Missouri-Rolla, 1984, p. 101.
- (9) Falco, R.: The production of turbulence near a wall. AIAA 84-1111, 1984, 23rd Dynamics Conference, AIAA Paper 84-1111, 1984.
- (10) Blackwelder, R.F. and Kaplan, R.L.: On the wall structure of turbulent boundary layer. *J. Fluid Mech.*, vol. 7, 1970, p. 81.
- (11) Blackwelder, R.F. and Haritonidis, J.H.: On the wall structure of turbulent boundary layer. *J. Fluid Mech.*, vol. 142, 1983, p. 101.
- (12) Alfredsson, P.H. and Johansson, A.V.: On the structure of turbulent boundary layers. *J. Fluid Mech.*, vol. 142, 1983, p. 101.
- (13) Kline, S.J., Feltner, J.L., Smith, D.K., and Schraub, F.A.: On the structure of turbulent boundary layers. *J. Fluid Mech.*, vol. 142, 1983, p. 101.
- (14) Yule, A.J.: Phase scrambling effects and turbulence data analysis. *Advances in Turbulence*, vol. 1, 1979, p. 101.
- (15) Chen, J.P. and Blackwelder, R.F.: Large-scale motion in a turbulent boundary layer. A study using temperature contamination. *J. Fluid Mech.*, vol. 142, 1983, p. 101.
- (16) Subramanian, V.S., Karagapalan, V., Antonia, R.A. and Chambers, A.J.: Comparison of conditional sampling and averaging techniques in a turbulent boundary layer. *J. Fluid Mech.*, vol. 142, 1983, p. 101.
- (17) Antonia, R.A., Karagapalan, V., Subramanian, V.S. and Chambers, A.J.: Dependence of the structure of a turbulent boundary layer. *J. Fluid Mech.*, vol. 142, 1983, p. 101.

#### ACKNOWLEDGMENT

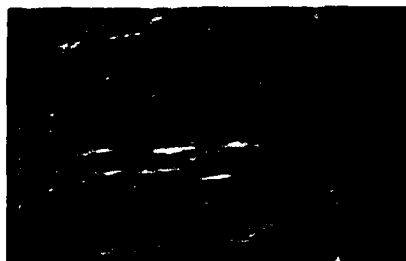
The authors wish to express their appreciation to Professor D.A. Brats, who helped to formulate this research. The multicolour hydrogen bubble technique is developed in collaboration with A.M. Fajen. The assistance of former student P. Siegmund in data handling and reduction is gratefully acknowledged. We also wish to thank Els van der Steen and Frits Fooran for typing this manuscript.



Photograph 1



Photograph 2



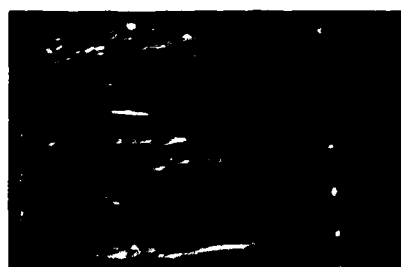
Photograph 3



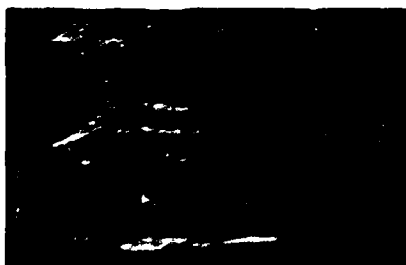
Photograph 4



Photograph 5



Photograph 6



Photograph 7



Photograph 8

## STRUCTURE OF UNSTEADY FLOWS AT LEADING- AND TRAILING-EDGES:

## FLOW VISUALIZATION AND ITS INTERPRETATION

by

D. Rockwell, R. Atta, L. Kramer, R. Lawson,  
D. Lusseyran, C. Magness, D. Sohn, T. Staubli  
Department of Mechanical Engineering and Mechanics  
354 Packard Laboratory, Building #19  
Lehigh University  
Bethlehem, Pennsylvania 18015

## SUMMARY

Unsteady two- and three-dimensional flow structure at leading- and trailing-edges of bodies can be characterized effectively using recently developed techniques for acquisition and interpretation of flow visualization. The techniques addressed herein include: flow image-surface pressure correlations; three-dimensional reconstruction of flow structure from flow images; and interactive interpretation of flow images with theoretical simulations. These techniques can be employed in conjunction with: visual correlation and ensemble-averaging, both within a given image and between images; recognition of patterns of flow structure from images; and estimates of velocity eigenfunctions from images.

## 1. INTRODUCTION

There are a wide variety of methods for visualizing and interpreting flow phenomena. The overviews of Emrich<sup>1</sup> and Merzkirch et al<sup>2</sup> assess a range of techniques including, for example: smoke and dye injection; laser-induced fluorescence; and density gradients induced in mixing of dissimilar fluids. These methods have provided valuable insight into a number of features of the flow structure.

Flow visualization using water as a working fluid has several advantages. Perhaps the foremost is the ease of marking and tracking fluid elements at relatively long time scales, i.e. low frequencies, in comparison with the corresponding scales in a gaseous medium. If instantaneous, as opposed to time-averaged, surface pressure, lift, etc. in conjunction with the visualized flow structure is desired, then the time and length scales offered by a water facility are highly advantageous. Although concurrent, quantitative measurement of unsteady velocity and pressure may be more delicate and laborious, judicious choice of the most physically meaningful locations for measurement of the flow field, identified with the aid of flow visualization, can reduce the amount of effort in this direction.

Interpretation of visualized steady flows is relatively straightforward; however this is not the case for unsteady flows, especially for perturbed shear flows. It is well known from linear stability theory that there exist drastic gradients of amplitude and phase of fluctuating velocity and pressure across an unsteady shear flow. As a consequence, the apparent, visualized flow structure may not be compatible with the actual, underlying vorticity field (Hama<sup>3</sup>; Lusseyran and Rockwell<sup>4</sup>). Clearly, considerable care must be exercised in interpreting unsteady phenomena. By proper choice of visualization technique, and employment of simple theoretical simulations, fallacies of interpretation can be precluded.

In the series of investigations described herein, we address techniques for implementing and interpreting a particular class of flow visualization methods: generation and tracking of lines of elements marked at specified times, i.e. timelines. Emphasis is on: correlating the instantaneous, visualized flow structure with instantaneous surface pressure; reconstruction of three-dimensional flow structure from dual views of the flow field; and interpretation of the flow visualization in conjunction with basic classes of theoretical simulation. In addition, possibilities are addressed for: visual correlation and ensemble-averaging of visualization images; pattern recognition of flow structure using images; and evaluation of images for determination of velocity eigenfunction and vorticity.

## 2. EXPERIMENTAL TECHNIQUES

All experiments were carried out in one of three water channel systems, custom designed for study of unsteady, separated flows. The cross-sectional areas of the test sections of these channels ranged from 1.5 ft<sup>2</sup> to 6 ft<sup>2</sup>. In all cases, the test sections were made entirely of plexiglas or glass to facilitate multi-dimensional views of the flow structure. Moreover, all components of the largest channel, including the test section contraction, inlet and outlet tanks, and all attendant piping are made of plexiglas or PVC in order to preclude difficulties arising from system corrosion.

Figure 1 shows an experimental arrangement that is generic to the variety of techniques employed in the fluid mechanics laboratory at Lehigh University. A platinum wire, or an arrangement of wires, generates hydrogen bubble timelines. The bubble lines or sheets are then tracked, recorded, and processed by employing: video cameras synchronized with the mainframe of the video system; a digitizing system; and an image processing system located in the computer-aided design (CAD) laboratory.

Using a custom-designed function generator, it is possible to generate hydrogen bubble timelines of desired frequency and width. Two stroboscopic (90 watt) lights, interfaced with the mainframe of the video system, illuminate these bubble timelines.

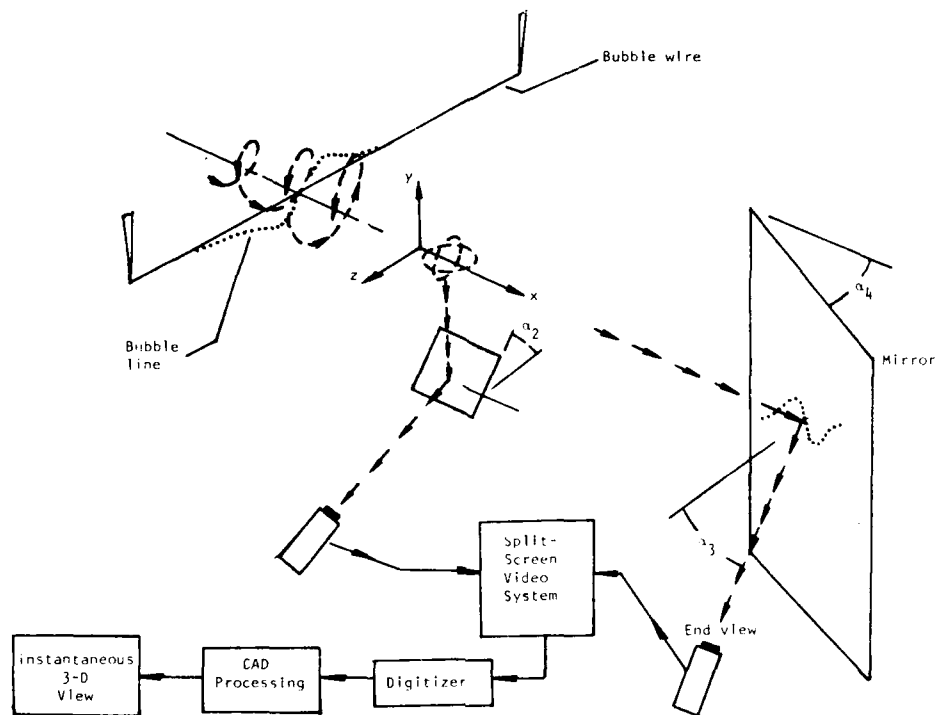


Figure 1: Schematic of technique for acquiring and processing flow visualization using two-camera, split-screen video system, digitizer, and computer-aided design system. Technique shown is generic to the variety of arrangements employed in the Lehigh University fluid mechanics laboratories.

Two simultaneous images, corresponding to two arbitrary views of the flow field, can be displayed on the split-screen video system. A variety of mirror arrangements provides views of the flow field from a number of perspectives. These mirrors are located either external to the transparent test section, or within the flow field at a location sufficiently far downstream of the region of interest.

Video images can be digitized using a Colorado video (model 270A) digitizer or a digitizing tablet. Images obtained from the digitizer are put on file in the CAD laboratory, allowing application of a range of image pre-processing and processing techniques.

Preprocessing of digitized images enhances the definition of the bubble timeline patterns. These processing operations include: a "band-pass" spatial filter; a thresholding operation; a thinning algorithm; a two-dimensional, low-pass filter; and other related techniques, which are described in detail by Gomas and Rockwell<sup>5</sup>. As a follow-on to this image pre-processing, it is possible to employ a curve-tracking technique which, in essence, transforms timelines having multiple gray levels to continuous well-defined timelines in binary form. Gomas<sup>6</sup> describes the curve-tracking algorithm, which is based on the concept of linear predictive coding.

### 3. QUANTITATIVE INTERPRETATION OF VISUALIZATION IMAGES

Figure 2 shows a typical timeline visualization photo, corresponding to antisymmetrical vortex shedding from a cylinder oscillating in the streamwise direction (Onqoren and Rockwell<sup>7</sup>). Also illustrated is a representation of the digitized timelines, providing a basis for quantitative interpretation of the flow structure. A timeline is, by definition, made up of all fluid elements originally marked at the same time at the upstream location of the bubble wire. Taking these timelines as representative, we address possibilities for: visual correlation and ensemble averaging of images; pattern recognition using visualization images; and image evaluation for velocity, eigenfunction, and vorticity.

AD-A199 357

AERODYNAMIC AND RELATED HYDRODYNAMIC STUDIES USING  
WATER FACILITIES (U) ADVISORY GROUP FOR AEROSPACE  
RESEARCH AND DEVELOPMENT NEUILLY-SUR-SEINE (FRANCE)  
JUN 87 ACARD-CP-413

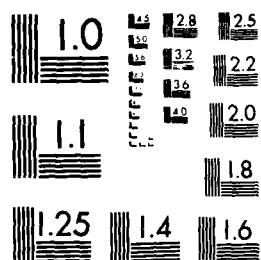
5/5

UNCLASSIFIED

P/G 2874

ML

END  
17788



MICROCOPY OF



Figure 2: Typical flow visualization photograph representing vortex shedding in antisymmetrical mode arising from streamwise perturbations of cylinder. Also shown is digitized representation of upper half of timeline pattern (Ongoren and Rockwell<sup>17</sup>; Kerstens and Rockwell<sup>8</sup>).

#### Visual correlation and ensemble-averaging of images

Although correlations of velocity and pressure at a point, or between two points, in a flow field have received considerable attention over the past few decades, relatively little effort has been devoted to defining a more globally-oriented correlation based on flow visualization. In doing so, it is necessary to define quantitatively the elemental portions of a visualization image. One possibility is to define the local tangent of each of the individual timelines as a function of position along the timeline. This local tangent is termed the tangent angle function  $\phi(x,y)$ . If we know the function  $\phi$  along all the timelines in an image, we have, in effect, defined the image on a physically meaningful basis.

The obvious approach to defining a correlation between two points A-1 and B-1 on two different timelines A and B is to consider the product of the respective tangent angle functions  $\phi_{A-1}\phi_{B-1}$ . However, as shown by Kerstens and Rockwell<sup>8</sup>, this definition is inadequate, as it cannot distinguish certain features of two curves oriented arbitrarily with respect to each other. Rather, it is useful to employ a correlation function based on the difference between tangent angle functions  $\phi_{A-1}-\phi_{B-1}$ . Employing such a definition, it is then possible to define a global, visual correlation between two timelines by integrating over the spatial extent of the normalized timelines. This approach can lead to various types of auto- and cross-correlations between defined regions of the flow field. Ideally, it would be desirable to carry out these correlations for segmented timelines, where a timeline is broken into discrete segments through use of a segmented bubble wire; then, by tracking these segments and carrying out the aforementioned visual correlation, a comparison can be made with the measured vorticity field.

The visual average of several successive images follows from the spatial averages of respective timelines in a number of successive images (Kerstens and Rockwell<sup>8</sup>). In selecting the images to be averaged, a physically meaningful criterion must be applied. If each of the selected images corresponds to a defined phase of an unsteady event within the flow, such as an extreme displacement of a body, then the averaging is of the ensemble-averaging type. In principle, a variety of sensors, including pressure and velocity transducers, can be employed as a phase reference for the ensemble averages; moreover, an interesting possibility involves use of a repetitive, coherent portion of the image itself in order to trigger the ensemble-averaging.

#### Pattern recognition using images

In the event that the flow is non-periodic, it is useful to determine how often certain large-scale features of the flow-structure occur. Consequently, it is necessary to formulate a technique for rapidly identifying these structures from flow images. If a library of basic types of flow patterns can be described, then comparison of visualized flow patterns with this library provides a basis for characterizing the frequency of appearance of elemental types of flow structure. This approach represents a type of pattern recognition.

A technique employed for identification of machine parts (Persoon and Fu<sup>9</sup>), handprint character recognition (Granlund<sup>10</sup>), and recognition of aircraft silhouettes (Wallace and Mitchell<sup>11</sup>) involves definition of a library of Fourier descriptors for basic types of patterns. The Fourier descriptor is simply the Fourier transform of the tangent angle function  $\phi$ , as previously defined. The advantage of the Fourier descriptor technique is that the curve description is essentially independent of orientation, position, and scale of the curve. Whereas the traditional use of the Fourier descriptor technique is for closed curves, flow images are typically made up of open curves in the form of streaklines, pathlines, or timelines. Gumas and Rockwell<sup>12</sup> describe implementation of the Fourier descriptor technique for open curves of the timeline type.

#### Image evaluation for velocity eigenfunction and vorticity

The displacement of a timeline over a given interval of time is related to the flow velocity.

Consequently, it is possible to relate the time of flight of timelines to the velocity distribution across the flow. In fact, Lu and Smith<sup>12</sup> have shown that the higher order statistics of a turbulent boundary layer can be determined using this concept; this approach can lead to insight beyond that attainable with traditional point measurements.

A primary advantage of the timeline technique is that it gives instantaneous information across the entire flow; it therefore leads to the instantaneous streamwise velocity component across the flow. Consequently, this method is well-suited to characterizing flows for which there are substantial gradients of velocity amplitude and phase in the cross-stream direction. That is, the local deflection of a timeline will be in accord with the local fluctuation amplitude and its relative phase. Lusseyran and Rockwell<sup>13</sup> have demonstrated that this technique can provide a reasonable estimate of the eigenfunction of the streamwise velocity component. Through application of the continuity equation, it leads to approximation of contours of constant vorticity in an unstable wake flow.

#### 4. FLOW IMAGE - SURFACE PRESSURE CORRELATION

In order to determine the underlying mechanisms that produce unsteady pressure fluctuations along a surface, it is desirable to correlate the instantaneous, visualized flow structure with the instantaneous surface pressure. One possibility is to record simultaneously the visualized flow and the time-dependent surface pressure from a large array of surface-mounted transducers. If the flow structure is highly organized then, in principle, it is possible to employ a single transducer switched to successive locations along the surface. By keeping track of pressure amplitude and phase, the instantaneous pressure field can be reconstructed.

In acquiring these pressure measurements, it is necessary to have an appropriate phase reference, which can take the form of a second pressure transducer signal, or a hot film or laser signal, appropriately located at the outer edge of the mean shear layer. Proper location of this reference is necessary to avoid phase gradients associated with the fluctuating field, as well as high frequency noise from the flow. In linking the unsteady surface pressure measurements to the visualized flow field, it is necessary to determine, at a given instant, the phase shift between the visualized flow structure and the instantaneous pressure. One possible technique for accomplishing this is to record simultaneously the flow structure and the oscilloscope trace of the reference signal on a split-screen video system. Obviously, there are other methods of indirectly determining this phase link.

Aside from the advantages of visualization, use of water as a working medium allows use of remote transducer locations, as opposed to the classical surface-mounting of transducers. The characteristic frequencies of the pressure fluctuations in water are typically very low - on the order of 1 Hz. At these low frequencies, the amplitude and phase distortion arising from locating the transducer away from the surface are insignificant, provided the connecting line between the surface tap and the transducer is properly designed.

A means of visually displaying the instantaneous flow structure and surface pressure has been developed in our CAD laboratory. First, the flow images are digitized and processed. Then each of these images is, in turn, displayed with the instantaneous surface pressure field. This field is obtained from cross-spectral analysis between the surface pressure at a given location and an appropriate phase reference. In the following, we discuss cases where the raw, instantaneous visualization images, without any processing or enhancement, are shown in conjunction with the instantaneous surface pressure.

Figure 3 shows the interaction of an incident vortex with an elliptical leading-edge. In this case, the vortex is generated in a mixing-layer flow arising from the inherent instability of the shear layer. As a consequence, the process of vortex-edge interaction is harmonic. Full details of this experiment, including the circulation and degree of concentration of vorticity of the incident vortex, are given by Sohn and Rockwell<sup>14</sup>. In the left column of Figure 3, the vertical hatched lines represent the amplitude envelope, and the closely-spaced hatched lines represent the instantaneous surface pressure fluctuations. Considering the visualization in the right column of photos in Figure 3, it is evident that the incident vortex undergoes substantial distortion as it encounters the leading-edge region. Concurrently, there is local flow separation from the leading portion of the edge, giving rise to a small-scale secondary vortex that becomes nested within the incident primary vortex. The third row of pressure-visualization shows that onset of flow separation induces a local negative pressure; the fourth and fifth rows show that this negative pressure region moves downstream as the formation of the secondary vortex evolves. It is clear, especially from the fourth row of Figure 3, that there are very large gradients of instantaneous pressure in the vicinity of the tip. In fact, maximum positive pressure occurs at the tip itself, and a short distance downstream of that location, there is a maximum of negative pressure.

Figure 4 shows the instantaneous loading and corresponding flow structure for the case of a fully turbulent boundary layer separating from an actively-controlled trailing-edge. In this case, the displacement perturbations of the trailing-edge are about two orders of magnitude smaller than its thickness. Nevertheless, the surface pressure fluctuations arising from the edge perturbations overshadow those of the background turbulent flow. Since the first harmonic component of these pressure fluctuations is very small, we can represent the fluctuating surface pressure as approximately sinusoidal, and employ the edge displacement as a phase reference in relating the instantaneous pressure to the flow structure. The top row of pressure-visualization shows the case of excitation at a frequency  $f_e$  just below the natural shedding frequency  $f_0$ , and the middle row at a frequency just above it. From the visualization, we note that the initially shed vortex switches from the bottom to the top corner of the trailing-edge as the excitation frequency increases. The bottom row of pressure-visualization represents the case of excitation at a frequency well above the natural shedding frequency. It is apparent that the initial vortex is still shed from the upper surface. In fact, only when the edge is excited at a frequency near that of the natural shedding is a switch in phasing of the initially-shed vortex possible.

In the corresponding pressure plots, the solid line and the cross-hatched regions represent respectively the amplitude envelope and the instantaneous value of the pressure amplitude at the forcing



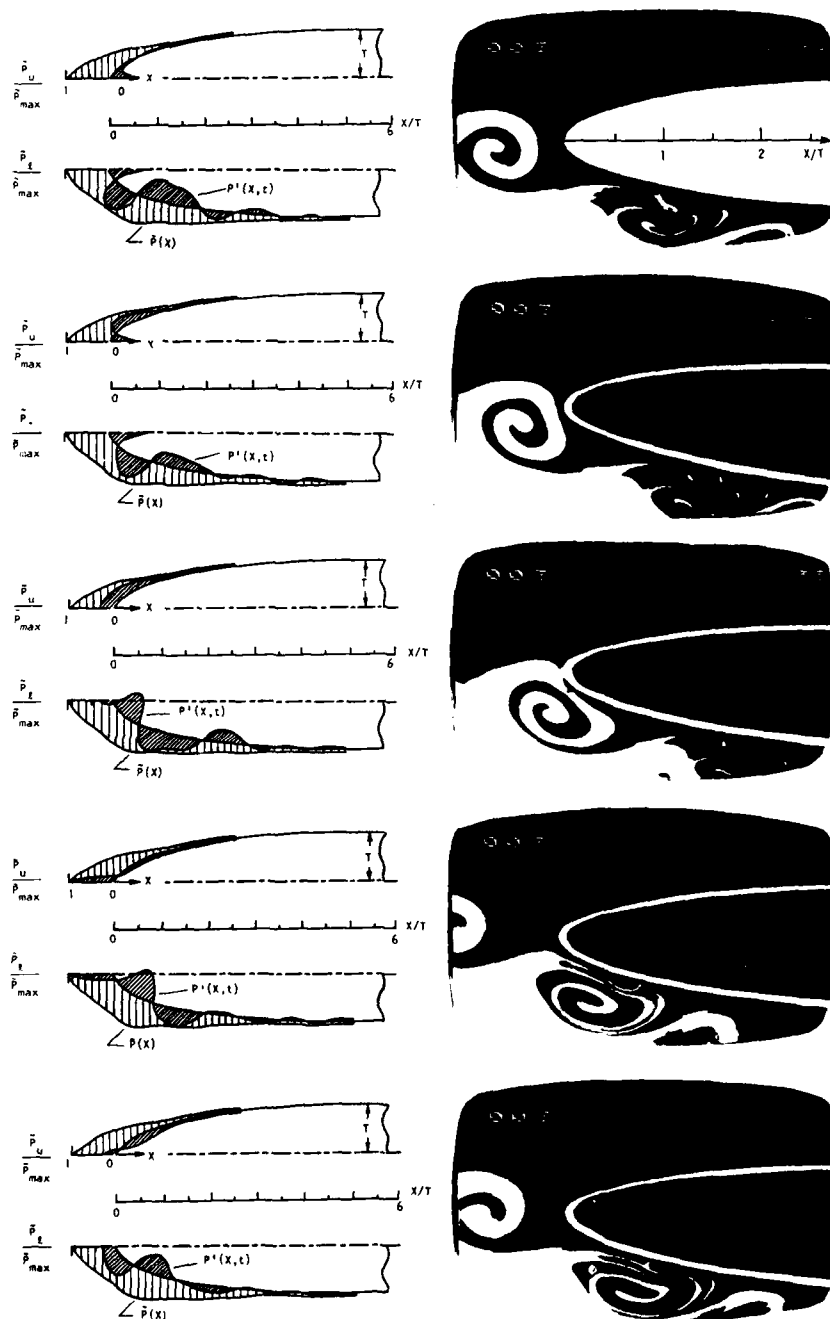


Figure 3: Interaction of vortex generated in mixing layer with elliptical leading-edge (Sohn and Rockwell<sup>14</sup>).

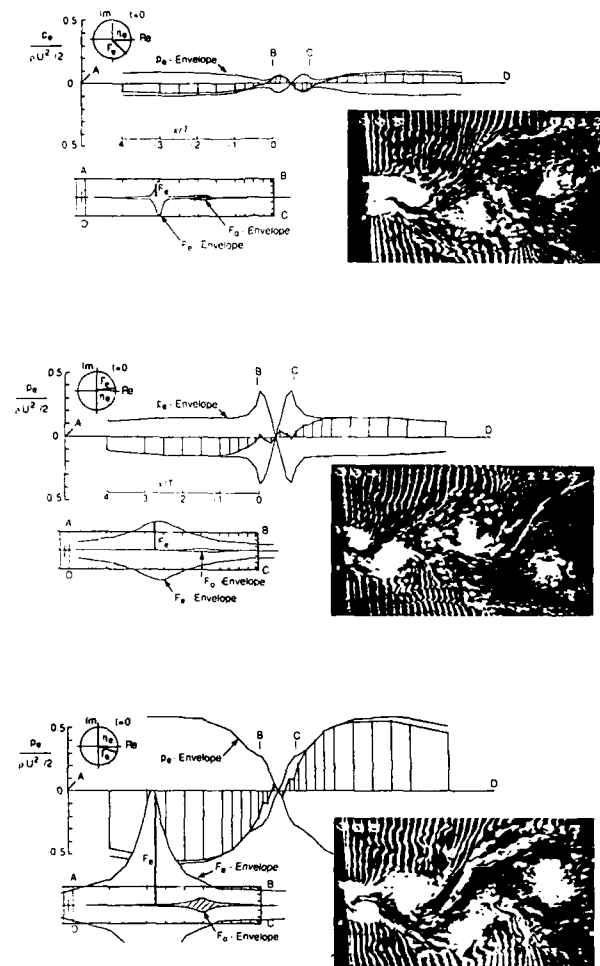


Figure 4: Flow structure and instantaneous surface pressure induced by oscillating trailing-edge. Approach boundary layer is fully turbulent and pressure field is that resulting from motion of edge. Frequency  $f_e$  of excitation relative to frequency  $f_0^s$  of shedding from stationary edge is:  $f_e/f_0^s = 0.87$  (top row); 1.07 (middle row); and 2.0 (bottom row) (Staubli and Rockwell<sup>15</sup>).

frequency. Moreover, within the schematic of the edge are shown the amplitude envelopes of the fluctuating force  $F_e$  at the excitation frequency  $f_e$  and the force  $F_0$  at the self-excited frequency component  $f_0^s$ . The vertical bar represents the instantaneous location of the force  $F_e$ . Finally, the phase clock in the upper left of each schematic shows that the force  $F_e$  lags the edge displacement  $\eta_e$  at the excitation frequency below the natural shedding frequency (top diagram), while it leads at a frequency above natural frequency (middle diagram) and again lags at high excitation frequency (bottom diagram). For the conditions of the top and middle diagrams, the amplitude of the fluctuating pressure rapidly increases as the corner (B) of the edge is approached; it goes to zero at the middle of the vertical base (BC). In the bottom diagram this is no longer the case, due to the high excitation frequency, the nonculatory ('added-mass') contribution to the surface pressure dominates that associated with shedding of vorticity, except in the base region BC.

These types of flow structure - pressure correlations have the potential for providing insight into the source of unsteady lift and drag acting on bodies; they are currently being interpreted in this context.

## 5. THREE-DIMENSIONAL RECONSTRUCTION FROM FLOW IMAGES

Determination of the instantaneous structure of time-dependent, three-dimensional flows poses a particular challenge. By use of a timeline marking technique, it is possible to reconstruct the three-dimensional evolution from two-dimensional images using computer-aided design methods. There are basically two types of approaches: a dual-view method, where the three-dimensional structure is determined from two arbitrary views of the flow field; and a single-view method, involving acquisition of phase-locked images from a single view of the flow field.

Smith and Paxson<sup>16</sup> have constructed a single three-dimensional surface by generating timelines from a single wire oriented in the spanwise direction, and using a two-camera system with two simultaneous views. Their study provides new insight into the character of a turbulent boundary layer. Ongoren and Rockwell<sup>17</sup> have generated a family of three-dimensional surfaces representing the wake from a three-dimensional body by employing phase-locked images of timelines from a single view. In this technique, the body was subjected to controlled oscillations. Its displacement served as a phase reference, thereby allowing definition of phase-locked images at successive spanwise planes. In the following, we demonstrate the dual-view method for obtaining three-dimensional surfaces representing separated flows from stationary and oscillating bodies.

Figure 5 shows time sequences of end and plan views of a tip vortex. In generating these images, a one mil, kinked platinum wire was employed. By pulsing the wire at a desired time, and over a defined interval, it is possible to reveal the principal features of the flow structure. In the end view of Figure 5, the pulse width is relatively long, being initiated just prior to the first photo and terminated prior to the last photo. The plan view of Figure 5 shows that the free-stream is moving in the downward direction. The vortex core has a significantly lower axial velocity than that of the free-stream. In these end and plan views, it is, in principle, possible to estimate the unsteady velocity field. In addition, as depicted at the bottom of Figure 5, three-dimensional surfaces can be constructed using the CAD system. The various views shown therein are from arbitrary perspectives. Real time, three-dimensional simulation of the structure of this tip vortex can be carried out either on the Unigraphics UG-2 terminal or the Evans and Sutherland PS-300 terminal in the Lehigh University CAD laboratory.

Another class of three-dimensional flows that can be characterized effectively by the dual view technique is that generated by an oscillating delta wing. To illustrate the complexity of the flow, we first consider a plan view of a delta wing oscillating in pitch about its trailing-edge (Figure 6). Since the tip of the delta wing undergoes large excursions during an oscillation cycle, only limited information can be obtained by examining timeline patterns from a fixed wire. A "flying wire" technique has been developed (Atta and Rockwell<sup>18</sup>); the platinum wire is aligned in the spanwise (z) direction, stretched between two supports located well away from the wing, and fixed to the mechanism that controls the wing motion. Consequently, the wire "flies" at the same angular velocity as the wing, and provides an indication of the degree to which the flow entering a plane parallel to the wing passes below, as opposed to above, the wing surface. For the photos of Figure 6, the wire is at the tip. Moreover, the reduced frequency  $K = 2\pi fC/U_\infty = 4.0$ , the mean angle of attack  $\alpha = 35^\circ$  and fluctuating angle of attack  $\Delta\alpha = 10^\circ$ . From quasi-steady considerations, one expects the pattern of vortex formation to be the same at a given value of angle of attack  $\alpha$ , irrespective of whether the tip of the wing is moving in the upward or downward direction. Comparison of photos C and E, taken at nearly the same value of  $\alpha$ , shows that the flow structure is markedly dissimilar. Evidently, there is strong hysteresis of the vortex rollup relative to the wing motion.

With bottom views of the sort shown in Figure 6, taken simultaneously with corresponding end views, it is possible to reconstruct the three-dimensional character of the flow on the CAD system. Figure 7 shows three-dimensional surfaces obtained using the flying wire technique for a similar experimental situation as that of Figure 7, i.e. a delta wing pitching about its trailing-edge. (Note that the hidden lines therein appear as solid lines). The top set of photos shows three basic views at relatively high reduced frequency. In this set, the bottom (plan) view shows that pronounced rollup of the sheet commences at about one-third chord and extends to about two-thirds chord. This rollup is particularly evident in the end view. Upstream of this region of rollup, there appear bulges of opposite curvature. In the bottom sets of plots, plan and end views are compared at the same instantaneous angle of attack. Within each set, from top to bottom, cases of static, moderate frequency, and high frequency are compared. Efforts are underway to relate basic patterns of three-dimensional distortion to the concepts of hysteresis and vortex breakdown.

## 6. FLOW STRUCTURE INTERPRETATION FROM IMAGES: INTERACTIVE VISUALIZATION AND SIMULATION

In any type of flow visualization technique, the visualized flow at any location represents the integrated history of the marked fluid elements. This history extends from the upstream location where the flow is marked to the downstream location where the flow structure is viewed. This concept can be used in conjunction with simple theoretical simulations of the flow structure in order to identify basic classes of vorticity concentration and circulation, as shown by Lusseyran and Rockwell<sup>14</sup>. In essence, they employ the velocity eigenfunctions from linear stability theory, in conjunction with the mean flow, to provide simulation of the vorticity field of an unstable wake. Since, in practice, we can often estimate a priori certain features of the mean flow, it should be possible to estimate the local circulation of the vorticity field when flow visualization is interpreted in conjunction with such a theoretical simulation.

Figure 8 shows simulation of the timeline patterns for a fixed- (upper diagram) and moving- (lower diagram) timeline marker (e.g., hydrogen bubble wire) for the case of a vorticity field having successively increasing values of dimensionless circulation  $\Gamma^* = 1, 2, 3$ , and 4. As illustrated in the middle schematic of Figure 8, the vorticity field, defined by the concentric contours is spatially periodic. Moreover, these contours of constant vorticity represent a neutral disturbance, i.e. the vorticity is neither amplifying or decaying. The amplitudes of the vorticity contours are related to the overall circulation; however, the shapes of the contours are relatively independent of the circulation.

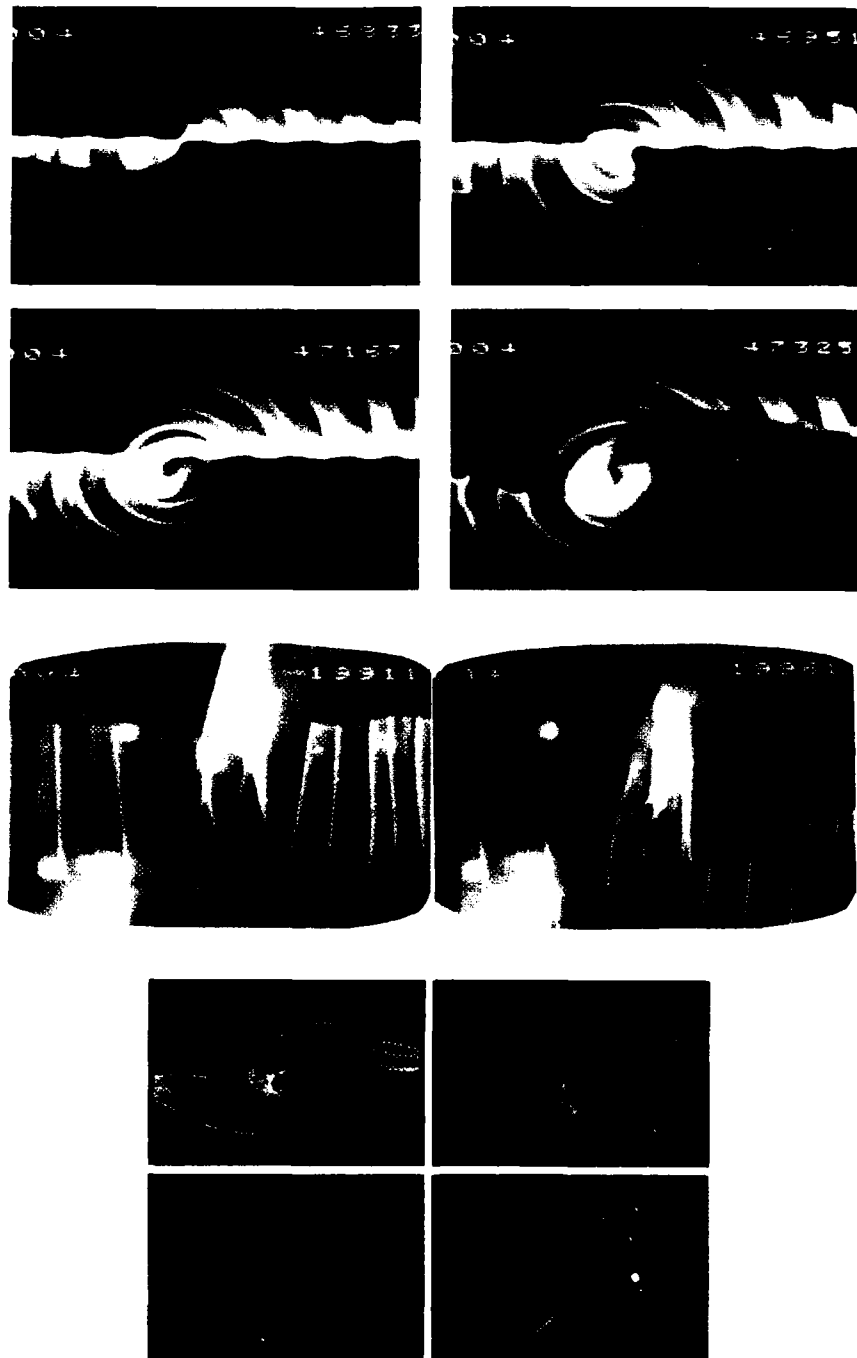


Figure 5: Visualization of tip vortex showing end and plan views of evolution in time, as well as three-dimensional representation of vortex development obtained from CAD simulation (Kramer and Rockwell<sup>19</sup>).

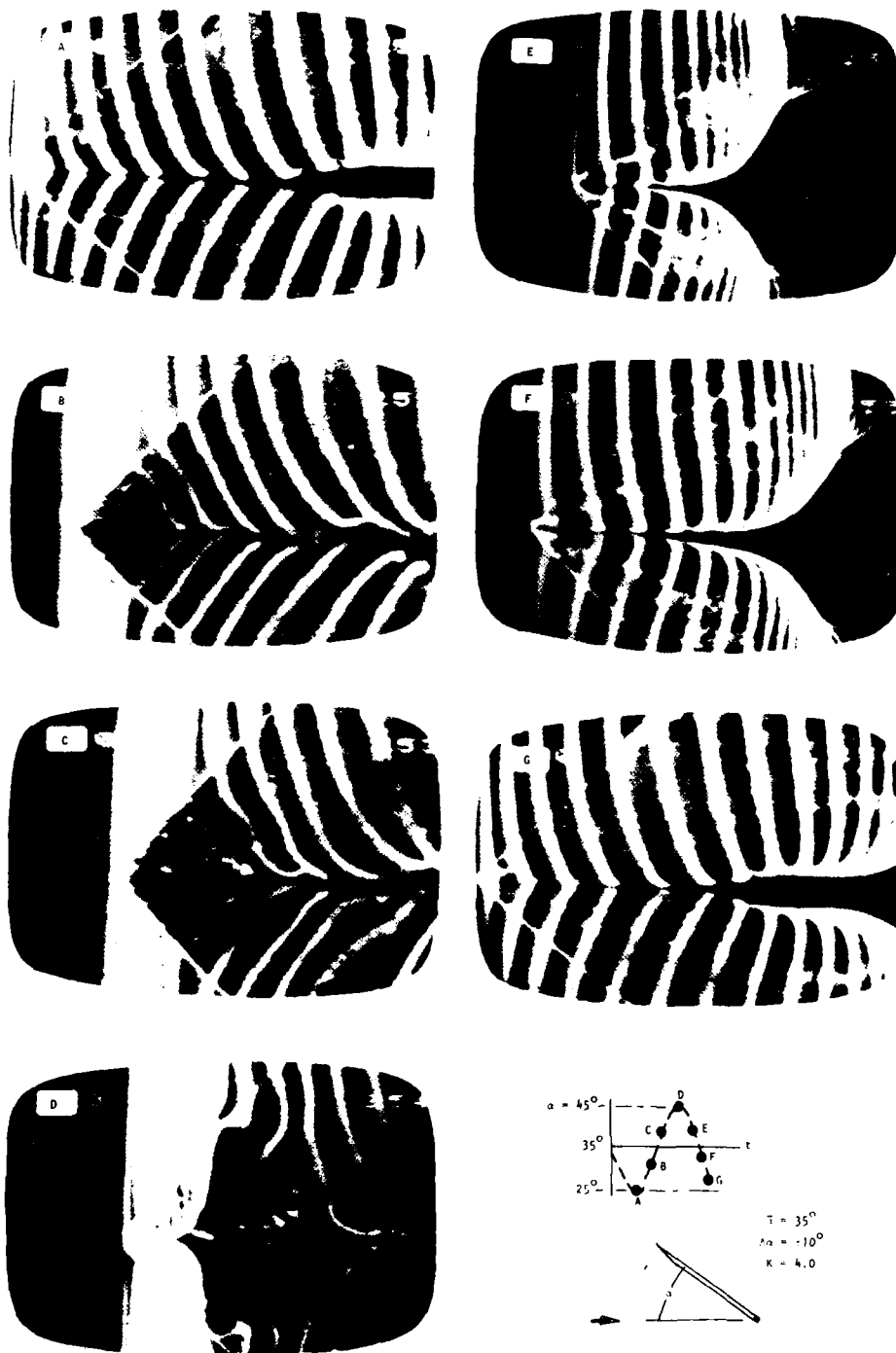


Figure 6: Flow structure at leading-edge of an oscillating delta wing obtained by "flying wire" technique. (Atta and Rockwell<sup>18</sup>).

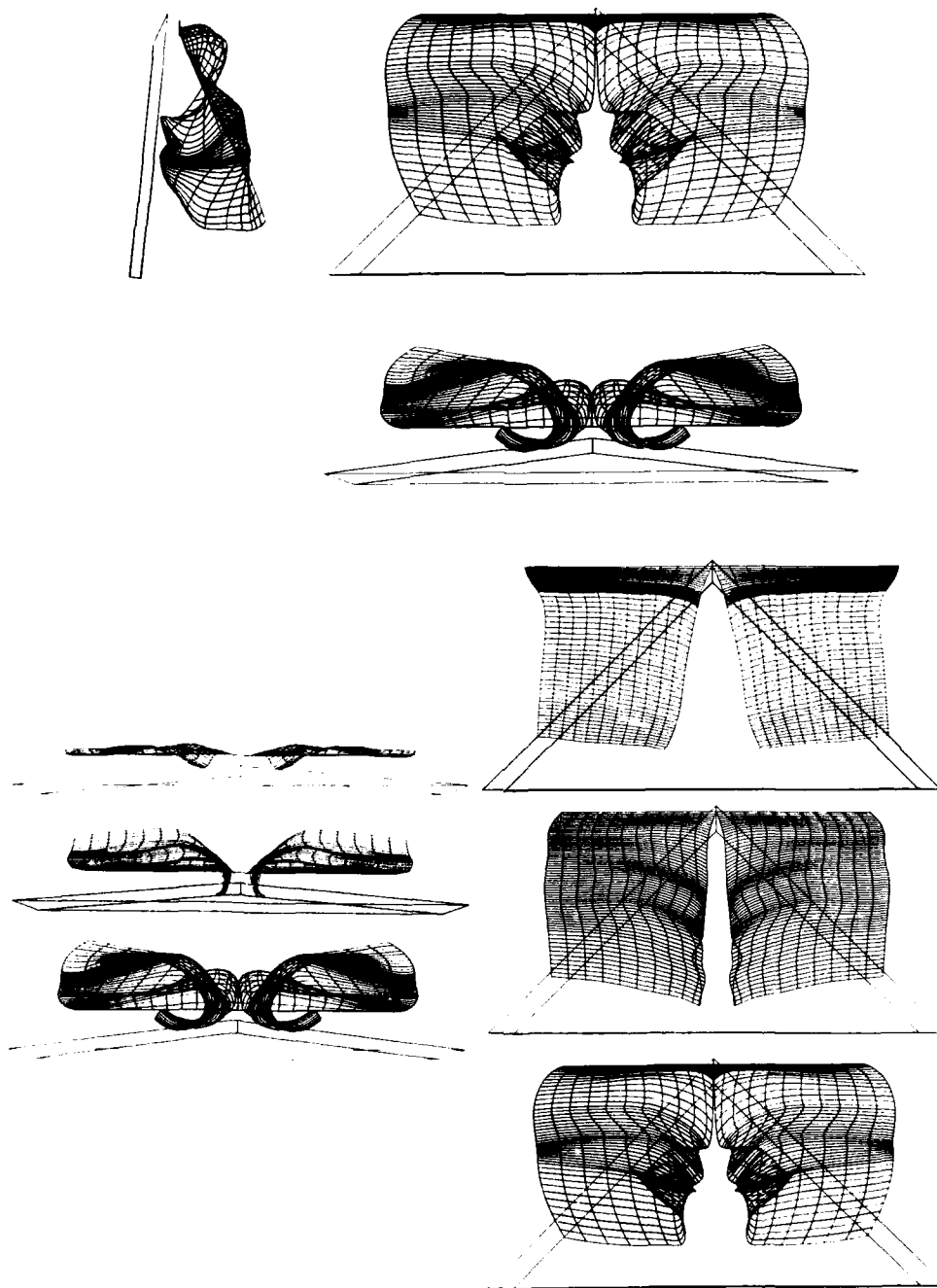


Figure 7: Various views of three-dimensional surface constructed from dual views of oscillating delta wing using CAD techniques. Original visualization data obtained from "flying wire" technique applied to wing pitching about its trailing-edge. Top set of views corresponds to relatively high reduced frequency. Bottom sets of views (from top to bottom) represents static, moderate, and high reduced frequencies. All views in this figure are at the same angle of attack (Magness, Lawson, and Rockwell<sup>20</sup>).

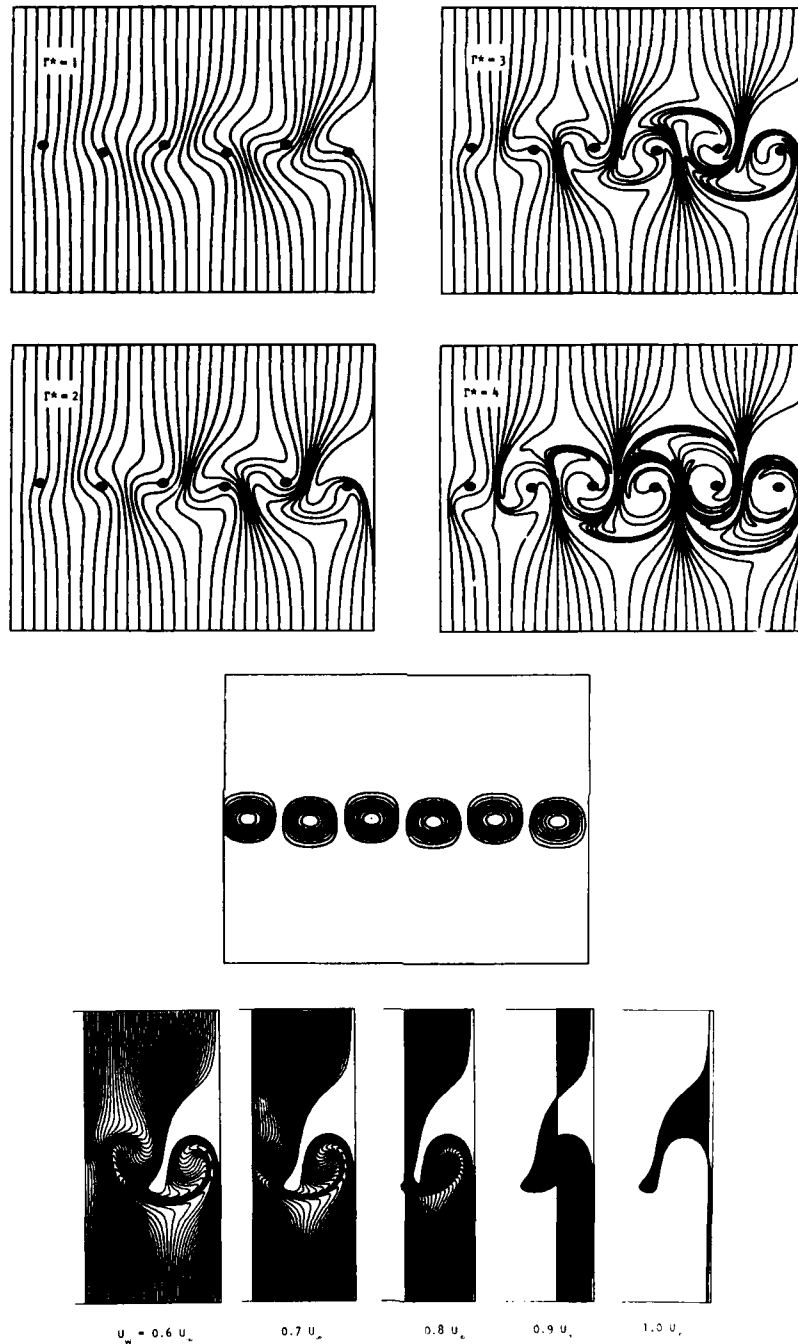


Figure 8: Simulation of flow visualization of a periodic wake using concepts of inviscid stability theory. Top series of diagrams represents timeline generation from a fixed wire located at lefthand side of each diagram; middle schematic shows the neutral, spatially-periodic vorticity field; and bottom diagram shows timeline generation from a wire moving at velocity  $U_w$  relative to the free-stream  $U_\infty$  (Lusseyran and Rockwell<sup>4</sup>).

In each of the four timeline plots, indicated in the upper part of Figure 8, the fixed timeline generator is located at the left side of each plot. Comparing these four timeline patterns, it is evident that the rate of "roll-up" of the timelines into a "vortex" appears to occur relatively slowly or rapidly depending upon the circulation  $\Gamma^*$ . The dots in these diagrams represent locations of vorticity extrema of the vorticity field illustrated in the middle diagram of Figure 8. The delay in deformation of the timeline pattern, from an initially vertical line, is related quantitatively to the circulation. By knowing the distance from the timeline generator required to turn an initially vertical timeline to an angle of, say  $45^\circ$ , a direct estimate of the circulation follows.

Further interpretation of the flow structure follows from use of a moving timeline generator as indicated in the bottom series of plots in Figure 8. The wire velocity  $U_w$  in the downstream section is a given fraction of the streamwise velocity  $U_\infty$ . In all diagrams, the vorticity field is the neutral one given in the middle plot of Figure 8; the corresponding circulation is  $\Gamma^* = 3$ . It is apparent that the apparent rate of roll-up of the timeline pattern changes with the value of  $U_w$ , even though the vorticity field has the same circulation in all cases. This concept can be used to our advantage to indirectly determine the circulation in conjunction with the aforementioned flow simulation. For each value of  $\Gamma^*$ , there is a unique, threshold value of  $U_w$  for which a timeline marker moves upstream of the wire. For the parameters here, it occurs at  $U_w = 0.8 U_\infty$ .

#### CONCLUDING REMARKS

From the foregoing, it is evident that there are a wide variety of possibilities for quantitatively interpreting flow visualization in conjunction with computer-aided image processing and simultaneous acquisition of pressure, lift, etc. Central to this approach, however, is a physically meaningful basis for defining the image. In fact, if portions of an image or portions of successive images are to be correlated with one another, then it is essential to have a means of identifying these domains. In a general sense, it is possible to generate an array of streaklines, pathlines, or timelines in order to accomplish this identification. However, one must be aware of the limitations inherent to flow visualization methods, namely that the visualized flow structure may not necessarily be an accurate representation of the underlying, unsteady vorticity field. Insofar as possible, it is desirable to implement techniques that employ a time of flight concept. That is, even though the velocity or vorticity may not be directly evident from the image, the marked fluid elements in the image should provide a basis for determining these central quantitative parameters.

#### ACKNOWLEDGEMENTS

The financial support of the Office of Naval Research, the Air Force Office of Scientific Research, the National Aeronautics and Space Administration, the National Science Foundation, and the Volkswagen Foundation is gratefully acknowledged.

#### LIST OF REFERENCES

1. Emrich, R. J., Methods of Experimental Physics: Fluid Dynamics, Vol. 18, Part A, Academic Press, New York, 1981.
2. Merzkirch, W., Chassery, J. M., Hesselink, L., Schon, J. P., Lourenco, L. and Monti, R., "Flow Visualization and Digital Image Processing" in von Karman Institute for Fluid Dynamics Lecture Series Monographs (1985-1986). Based on June 9-13, 1986, Lecture Series, Designated as 1986-09 Monograph.
3. Hama, F. R., "Streaklines in a Perturbed Shear Flow", Physics of Fluids, Vol. 5, No. 6, June 1962, pp. 644-650.
4. Lusseyran, D. and Rockwell, D., "On Interpretation of the Visualization in Unsteady Shear Layers", 1986, in preparation for publication.
5. Gumas, C. and Rockwell, D., "The Fourier Descriptor Technique: A Means of Pattern Description and Recognition in Fluid Mechanics", 1986, to be submitted for publication.
6. Gumas, C., "A General Pattern Recognition Technique for Open Curves", M.S. Thesis, Department of Computer Science and Electrical Engineering, Lehigh University, 1985.
7. Ongoren, A. and Rockwell, D., "Flow Structure from an Oscillating Cylinder. Part 1: Mechanisms of Phase Shift in the Near-Wake", 1986, submitted for publication.
8. Kerstens, P. and Rockwell, D., "Ensemble-Averaging on Correlation Techniques for Flow Visualization Images", 1986, to be submitted for publication.
9. Persoon, E. and Fu, K.-S., "Shape Discrimination Using Fourier Descriptors", IEEE Transactions on Systems, Man, and Cybernetics, Vol. SMC-7, No. 3, March 1977, pp. 170-179.
10. Granlund, G. H., "Fourier Processing for Hand Print Character Recognition", IEEE Transactions on Computers, Vol. C-21, February 1972, pp. 195-201.
11. Wallace, T. P. and Mitchell, O. R., "Analysis of Three-Dimensional Movement Using Fourier Descriptors", IEEE Transactions on Pattern Analysis and Machine Intelligence, Vol. PAME, No. 2 - No. 6, November, 1980, pp. 583-588.
12. Lu, L. J. and Smith, C. R., "Image Processing of Hydrogen Bubble Flow Visualization for Determination of Turbulence Statistics and Bursting Characteristics", Experiments in Fluids, Vol. 3, 1985, pp. 349-356.



13. Lusseyran, D. and Rockwell, D. "Estimation of Velocity Eigenfunction and Vorticity Distributions from the Timeline Visualization Technique", 1986, to be submitted to Experiments in Fluids.
14. Sohn, D. and Rockwell, D. "Vortex-Elliptical Edge Interactions", 1986, in preparation for publication.
15. Staubli, T. and Rockwell, D., "Pressure Fluctuations on an Oscillating Trailing-Edge", 1986, in preparation for publication.
16. Smith, C. R. and Paxson, R. D., "A Technique for Evaluation of Three-Dimensional Behavior in Turbulent Boundary Layers Using Computer Augmented Hydrogen Bubble-Wire Flow Visualization", Experiments in Fluids, Vol. 1, 1983, pp. 43-47.
17. Ongoren, A. and Rockwell, D., "Multiple Time-Surface Characterization of Time-Dependent, Three-Dimensional Flows", 1986, submitted for publication.
18. Atta, R. and Rockwell, D. 1986, in preparation for publication.
19. Kramer, L. and Rockwell, D. "Visualization of the Three-Dimensional, Time-Dependent Flow Structure of a Tip Vortex", Department of Mechanical Engineering and Mechanics, Lehigh University, 1986, unpublished.
20. Magness, C., Lawson, K., and Rockwell, D., 1986, in preparation for publication.

MEASUREMENTS OF THE TIME DEPENDENT VELOCITY FIELD  
SURROUNDING A MODEL PROPELLER IN UNIFORM WATER FLOW

by  
Jörg Blaurock, Dipl.-Ing.  
Gerd Lammers, Dipl.-Phys.  
Hamburg Ship Model Basin  
Bramfelder Strasse 164  
2000 Hamburg 60  
Federal Republic of Germany

SUMMARY

As a part of a research program, the flow field around an operating ship propeller was investigated in a water tunnel, using Laser-Doppler-velocimetry. The three-dimensional velocity field was measured in three planes at the suction side and four planes on the pressure side of the propeller at the design thrust coefficient of  $K_T = 0.185$ . In one of the planes in the propellers' slipstream, the measurements were repeated at thrust coefficients of  $K_T = 0.12$  and  $K_T = 0.25$ .

The velocity profiles measured in the propeller's slipstream are compared with the induced velocities derived from design calculations, and occurring deviations are discussed.

Furthermore, the instationary flow field allows to study the tip vortices at different distances behind the propeller. The measurements yield a quantitative description of the vortices, and the influence of propeller load at the blade tips on geometry and intensity of the tip vortices can be seen.

LIST OF SYMBOLS

$A_e/A_o$	blade area ratio of propeller
$C_{Th}$	thrust load coefficient $T/(\rho/2 \cdot v_o^2 \cdot \frac{D^2}{4})$
$D$	propeller diameter
$J$	advance coefficient $v_o/(n \cdot D)$
$K_Q$	torque coefficient $Q/(\rho \cdot n^2 \cdot D^5)$
$K_T$	thrust coefficient $T/(\rho \cdot n^2 \cdot D^5)$
$n$	frequency of revolution
$P$	propeller pitch
$Q$	torque
$R$	propeller radius $D/2$
$r$	local radius
$r_h$	hub radius
$T$	thrust
$v_o$	axial velocity of undisturbed flow
$w_a$	axial component of propeller induced velocity
$w_r$	radial component of propeller induced velocity
$w_t$	tangential component of propeller induced velocity
$x$ $y$ $z$	cartesian coordinates
$z$	
$z$	
$z$	number of propeller blades
$\eta_o$	efficiency of propeller $J \cdot K_T / (2 \cdot K_Q)$
$\rho$	density of water
$\theta$	angular position of propeller

INTRODUCTION

Design procedures for ship propellers are based on more or less complex theories. Design calculations result in a propeller which is supposed to satisfy certain requirements demanded before. Normally checking of propeller performance will be done by model tests as open water tests, propulsion and cavitation tests. If the experimental results differ from the expected characteristics, we will assume the design procedure or theory to be inadequate. Unfortunately, by the mentioned model tests not all details of the interaction between propeller and the surrounding flow can be verified.

Within the recent years, Laser-Doppler-Velocimetry (LDV) has become a well-known method for fluid mechanic research. By this technique it is possible to investigate the flow even in the immediate vicinity of an operating propeller. Mean value and time dependent variations of fluctuating velocity components can be measured. Hence, predicted velocity distributions can be compared with precise measurements, and this comparison may give rise to corrections of the design procedure or even the theory.

For uniform inflow to the propeller, the spatial distribution of flow velocities can be derived from time dependent measurements. This gives the opportunity for a detailed study of the tip vortice's shape and development, if the resolution of measurements is good enough.

#### EXPERIMENTAL EQUIPMENT

The measurements were done at HSVA's medium-sized cavitation tunnel, a circulating water tunnel with a maximum water velocity of 10 m/s. Standard equipment is provided for measurements of thrust, torque and speed of rotation of the investigated model propeller. For simulation of wake fields, a combination of wire screens and dummy models can be arranged in the measuring section. If omitted, the inflow to the propeller is uniform all over the square cross section of 0.57 m x 0.57 m except for boundary layers at the propeller shaft and the walls. At all the four sides of the measuring section there are two windows each. The LDV-system is operating through one of the upper windows. The system is a two-channel dual beam backscatter LDV. It allows simultaneous measurements of two orthogonal velocity components in the plane perpendicular to the front lenses optical axis. Channel separation is done by using two different colours from the spectrum of a 5 W argon-ion laser for the two components. A detailed description of the device is given in (1), (2). The front lens of the optical system has a focal length of 480 mm in air, and the laser beam pairs are focused down to a diameter of 70  $\mu$ m at the measuring point, which is shaped by the intersection of the beams. The measuring volume has a length of 1.1 mm at an intersection angle of 7.3°. The velocity is detected by measuring the frequency of scattered light oscillations from small scattering particles in the measuring volume. The oscillations are caused by an interference pattern ("fringe"-system) in the intersection point of coherent laser beams. The fringe spacing is 2.85  $\mu$ m for the blue interference pattern and 3.05  $\mu$ m for the green one. The blue channel is set up to measure the velocity component in the direction of the tunnel axis, the green channel for the horizontal cross-component.

Positioning of the measuring point in the y- and z-direction (Fig. 1) is done by step motors under computer control. Time for traversing is used for storing data on a floppy disc and calculating and displaying mean value and standard deviation of the two velocity components at the point measured before. For a propeller in uniform flow, the optical arrangement allows measurements of all three velocity components. The x-component is measured anyway, and the y-component is identical with the radial component for a horizontal profile and with the tangential component for a vertical profile, cutting the propeller's centre line. An encoder on the propeller shaft can be connected to the LDV-counter interface, and optionally the computer can combine the velocity information from each data transfer with the present position of the propeller blades. The encoder has a resolution of 3.6°. In this way, changes of velocity values - oscillating at the blade frequency - can be detected. In case of uniform inflow to the propeller, velocity measurements at a certain local radius r for many angular positions of the propeller are equivalent to measurements at the same radius for many angular positions of the measuring point at a fixed propeller position. Hence, velocity measurements with respect to the actual propeller position following a profile through the propellers' centre line give the velocity field all over the measuring plane at a certain moment.

#### INVESTIGATED PROPELLER

The investigated propeller was designed especially for a research program. The design was based on assumed operating conditions as they are usual for a commercial ship. However, uniform inflow to the propeller was assumed in spite of the fact that ship propellers normally operate in a highly inhomogeneous wake field. This assumption is in accordance with the task to investigate the propeller induced additional velocity components on the pressure side as well as on the suction side of the propeller. Allowing for an inhomogeneous inflow field would have enhanced the complexity of the problem, making it impossible to separate the influence of the propeller on the flow field from other effects. This fact was confirmed by a few tests with inhomogeneous inflow which were part of the research program but will not be presented in this paper.

The main operating conditions for the propeller were at an advance coefficient of  $J = 0.60$ , corresponding to a thrust coefficient of  $K_T = 0.185$ . Most of the tests were performed under these conditions. The investigated model propeller has the following main dimensions:

diameter	D = 260 mm
number of blades	Z = 4
pitch	P = 224 mm
blade area ratio	$A_e/A_0 = 0.50$

A more detailed description of the propeller geometry is given in fig. 2 and in table 1. The profiles are of NACA 16 type cambered by a NACA  $a = 0.8$  meanline. Maximum camber, profile thickness and length are listed in the above mentioned table.

#### DESIGN PROCEDURE

The design of a ship propeller is based on physical models describing a single propeller blade as a vortex line (lifting line theory) or as a vortex sheet (lifting surface theory). Generally these models cannot describe all details of the flow field around the propeller blade. After selection of the propeller's diameter and blade number, the propeller induced axial and tangential velocity components are calculated according to a presumed or given load distribution on the propeller blade, usually neglecting the radial velocity component.

Calculation of induced velocities is done by a procedure using induction factors described by H. Lerbs (3), based on a paper by H. Schubert (4). This procedure yields velocity and circulation distributions over the local radius  $r$ . The vortex distribution is then replaced by profiles causing the same distribution of circulation. Camber and pitch of the profiles are now determined by an iteration procedure based on lifting surface theory, replacing vortex lines by vortex sheet distributions (5). Iteration steps are repeated until a satisfactory result is obtained. In a last step, the calculated values are examined and perhaps slightly modified with respect to practical experience and manufacturing requirements.

Even the most sophisticated procedures presently cannot describe all phenomena with a sufficient accuracy. As an example, the region close to the blade tips, where a tip vortex of circulation dependent intensity is generated, is not taken into account adequately. Hence, geometrical outline has to be supported by experience. Furthermore, extremely inhomogeneous wake fields, occurring behind some single screw vessels, cause additional problems that common calculation methods fail to solve.

The reliability of calculation methods for the propeller induced velocity field can only be proved by experimental results. LDV - measurements of the total velocity in the flow field of a propeller can enable design engineers to select the calculation method or theory that is adequate to the problem.

#### EXPERIMENTAL RESULTS

As a basic model test for determination of the propeller's hydrodynamic properties, an open water test was done in HSVA's large towing tank. The results are thrust, torque and efficiency of the propeller as functions of the advance coefficient  $J$ , as they are shown in non-dimensional form in fig. 3. The correct operating conditions for the LDV - measurements can be derived from this diagram. Most of the LDV - measurements were done at the design condition of  $J = 0.60$ , corresponding to a thrust coefficient of  $K_T = 0.185$ . The open water test was carried out at a Reynolds number  $R_n = 6.7 \cdot 10^5$  for the profile at the radius  $r/R = 0.7$ .

As an initial test in the cavitation tunnel, the shape of the propeller's slipstream was determined. This was managed by positioning the LDV measuring volume at the tip vortex location, depressurizing the tunnel until the beginning of tip vortex cavitation. The high intensity of scattered light from the cavitating vortex allowed a positioning with an accuracy of  $\pm 0.5$  mm. The slipstream's diameter was measured at 20 distances from the propeller. The envelope of the slipstream is shown in fig. 4, where also the measuring planes for the following LDV - measurements are marked.

LDV - measurements of flow velocity were done at 7 different planes, 3 of them on the suction side and 4 on the pressure side of the propeller. In each of the planes, two profiles were measured: A vertical profile ( $x = x_0$ ,  $y = 0$ ) to obtain the axial and tangential component and a horizontal profile ( $x = x_0$ ,  $z = 0$ ) yielding the radial and once more the axial component. Using the mentioned shaft encoder, velocity values were separately stored for 100 different angular positions of the propeller. The distance between two neighbouring measuring radii had to be selected individually in accordance with the complexity of the flow field. On the suction side, a distance of about 10 mm gives an adequate resolution. On the pressure side, the distance was decreased down to 3 mm in the region of tip vortices. For each radius, 3000 single measurements for the three velocity components were done, yielding an average of 30 measurements for each angular position. This is sufficient for calculating mean value and standard deviation. Fig. 5 shows mean values of the velocity components in four planes on the pressure side of the propeller for a thrust coefficient  $K_T = 0.185$ . Since the axial velocity was measured twice, a check for reproducibility of the measurements could be done. The deviations proved to be negligible. Fig. 6 shows the mean velocity values for 3 measuring planes on the suction side at the same value of  $K_T = 0.185$ . For 3 different load conditions the mean velocities are shown in fig. 7.

All velocity values are given dimensionless, dividing them by the axial velocity of undisturbed flow, derived from the tunnel inflow velocity by a procedure according to R. Wood and R. Harris (6).

Mean values of velocity components for any measuring radius are obtained from 100 equidistant angular positions of the measuring volume relatively to the propeller. For

each angle  $\theta$  the velocity values are already mean values of about 30 single measurements. In fig. 8, for some selected measuring points close to the tip vortex the axial velocity components at 2 different operating conditions are plotted against the angular position  $\theta$ . The vertical limits of the plotted symbols are marks for positive and negative standard deviation from the mean value in the symbol centre. The time dependent velocity field is periodical with the blade frequency, except for small deviations that are due to limited resolution and perhaps manufacturing tolerances.

The following figures show the three-dimensional velocity field. Isotaches are drawn for the axial component, the cross components are plotted as a vector diagram in a plane parallel to the propeller plane. As the symmetry of the velocity field was proved before, only a little more than a quarter circle is plotted. In the vector diagrams there is one vector plotted for each measuring point. The corresponding isotaches are based on the same number of points. The measuring radii are marked on the z-axis. In any of the figures 9 through 17, the largest measuring radius is identical with the model propeller's radius.

At the propeller's pressure side, two subsequent measurements had to be combined for each measuring plane because of the large number of radii and limited computer capacity. Therefore, at one radius the measurements had to be repeated to obtain a correct connection for the plots. In the isotach diagrams the separating radius is marked, and a slight shift of isotaches crossing this line can be seen. In the vector diagrams there is also a good accordance of the two measurements at the same radius.

Figures 9 through 11 show the velocity field at the pressure side for the design thrust coefficient  $K_T = 0.185$  at three different measuring planes. Three measurements at the suction side at the same  $K_T$ -value are shown in fig. 12 through 14. The influence of different operating conditions on the velocity field 0.3 D behind the propeller can be seen in fig. 15 through 17. Figure 15 shows the velocity field at  $K_T = 0.119$ , fig. 16 for the design value  $K_T = 0.185$  and fig. 17 for  $K_T = 0.251$ . In fig. 17, negative values of axial velocities occur at the tip vortex, which is marked by using dotted lines for the isotaches.

#### DISCUSSION OF RESULTS

The presented velocity measurements can be used to verify the assumptions that are fundamental to the propeller design procedure as described previously. One result of design calculations is the induced velocity field that the operating propeller is supposed to generate in its fully developed slipstream. For the investigated propeller, calculated mean values of the axial and tangential velocity component are shown in fig. 5-2 and 5-3, compared with measured values at several planes in the slipstream.

The tangential component of the propeller induced velocity is theoretically predicted to be zero at any point on the suction side. This is confirmed by the measurements as shown in fig. 6-2, except for the region close to the propeller hub radius in the plane 0.1 D in front of the propeller. The small tangential component is caused by the boundary layer of the rotating propeller shaft and hub.

Immediately behind the propeller plane ( $x = -0.1$  D) the calculated tangential velocity is in good accordance with the measured values. At larger distances from the propeller plane, the accordance is restricted to a local radius of  $r/R > 0.4$ . The deviations at smaller radii are caused by the rotating boundary layer close to the hub. In the plane  $x = -1.0$  D behind the propeller at  $r/R = 0.08$  there is an extremely large tangential component (fig. 5-2), resulting from the hub vortex generated by the free vortex system being shed from each blade root as well as from the blade tips.

Significant axial components of the induced velocity can be seen at the propeller's suction side (fig. 6-3). The largest acceleration of flow occurs in the region of the propeller plane, between  $x = 0.1$  D and  $x = -0.1$  D. The axial velocities reach their maximum values at the plane  $x = -1.0$  D behind the propeller (fig. 5-3). These values again comply with the calculated velocities surprisingly well. Only close to the hub region reasonable deviations occur, similar to the tangential component. The velocity field generated by the propeller blades is superposed by the dead water flow behind the hub, which is not taken into account by design calculations.

Development of the radial induced velocity also starts already at the suction side. The largest value is reached close to the propeller plane, corresponding to the largest acceleration of the flow in axial direction. Behind the propeller, the radial component decreases as the contraction of the slipstream is going on, and goes to zero in the plane  $x = -1.0$  D where the slipstream is completely developed, and there is no further contraction (fig. 5).

Variations of the operating conditions will produce different values of induced velocities, while the character of mean velocity profiles remains similar to the design condition profiles (fig. 7). The slipstream's contraction is increased by a larger value of  $K_T$ .

Figures 9 through 17 allow a detailed view at the velocity field surrounding the propeller. All figures show the number of blades by symmetry. The spiral movement of flow in the slipstream can be seen by the different angular position of tip vortices in all figures regarding the pressure side. The contraction of the slipstream can be derived

from the radial position of the tip vortex centre, reaching its minimum radius almost at  $x = -0.5 D$  already.

The constant angular position of the maximum axial velocity at the suction side (fig. 12-2, 13-2, 14-2) shows the lack of rotational movement in front of the propeller. The measuring plane  $x = 0.1 D$  is situated close to the propeller's leading edge for a local radius of about  $r/R = 0.4$ . The minimum of axial velocity at the right hand of the vertical axis in fig. 14-2 is caused by the influence of the leading edge's stagnation point. This influence can as well be seen in fig. 14-1.

#### CONCLUSIONS

The described design procedure for ship propellers proved to be an adequate method for calculation of propeller induced velocities, as far as mean values are concerned. Time dependent velocity values were not compared with calculations, but the experimental data can be valuable for the design of all appendages and objects operating in a propeller's slipstream, such as rudders, contra-rotating propellers, vane wheels, etc.. For the description of flow phenomena, LDV - measurements can yield reliable data to verify calculation methods.

#### REFERENCES

- (1) Lammers, G., Laudan, J.:  
"LDV Flow Measurements"  
16th International Towing Tank Conference, Proc. Vol. 1, 1981
- (2) Lammers, G., Laudan, J.:  
"Ermittlung des effektiven Zustromfeldes der Propeller von Wasserfahrzeugen unter Verwendung eines Laser-Doppler-Anemometers"  
HSVA-Report No. 1521, 1981
- (3) Lerbs, H.:  
"Ergebnisse der angewandten Theorie des Schiffspropellers"  
Jahrbuch der Schiffbautechnischen Gesellschaft, 1955
- (4) Schubert, H.:  
"Die Berechnung der aerodynamischen Eigenschaften von Luftschrauben beliebiger Form bei schwacher Belastung"  
Jahrbuch 1940 der deutschen Luftfahrtforschung
- (5) Kerwin, I.E.:  
"Computer Techniques for Propeller Blade Section Design"  
ISP VOL 20, No. 227, July 1973
- (6) Wood, R.McK., and Harris, R.G.:  
"Some Notes on the Theory of an Airscrew Working in a Wind Channel"  
Br. A.R.C. R. and M. 662, 1920

#### ACKNOWLEDGEMENT

The mentioned research program has been sponsored by the German Ministry of Research and Technology.

#### APPENDAGES

Radius $r/R$	Profile Length mm	Leading Edge to Reference Line mm	Thickness mm	Camber mm	Pitch P/D
0.2	53.6	21.3	10.44	1.01	0.665
0.25	56.6	26.7	9.63	1.39	0.725
0.3	59.6	31.8	8.84	1.70	0.777
0.4	65.2	41.1	7.37	2.16	0.858
0.5	69.7	46.9	6.03	2.33	0.902
0.6	72.6	48.1	4.81	2.27	0.913
0.7	72.7	42.8	3.73	1.96	0.904
0.8	68.7	28.0	2.74	1.38	0.875
0.9	57.6	2.6	1.81	0.65	0.822
0.95	46.2	-14.8	1.37	0.32	0.787
1.0	8.3	-46.8	0.93	0.00	0.748

TABLE 1

PROPELLER GEOMETRY

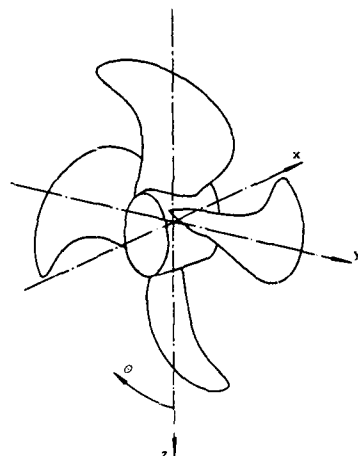


FIG. 1 COORDINATES AT THE PROPELLER

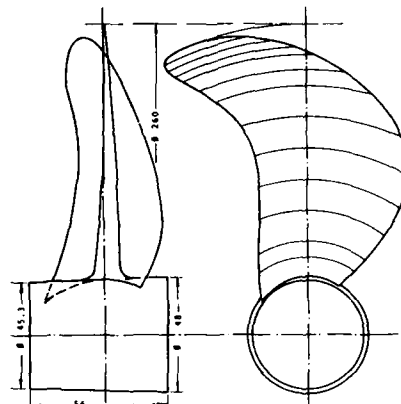


FIG. 2 OUTLINE OF THE PROPELLER

DIAMETER	D	= 260 mm
NUMBER OF BLADES	Z	= 4
MEAN PITCH RATIO	P/D	= 0.961
BLADE AREA RATIO	$A_e/A_0$	= 0.5
RIGHT HANDED		

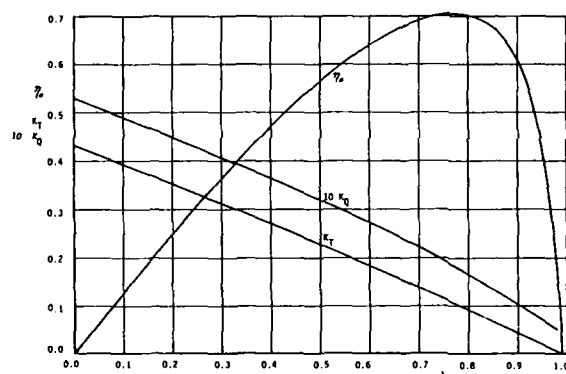


FIG. 3

PROPELLER OPEN WATER CURVES

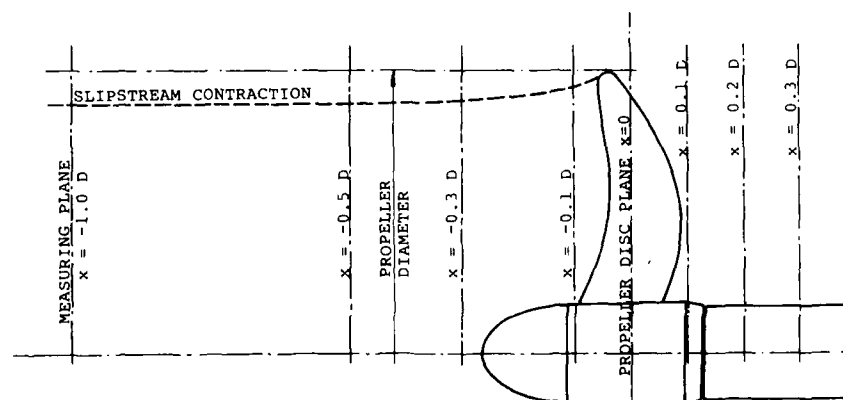


FIG. 4 SHAPE OF SLIPSTREAM

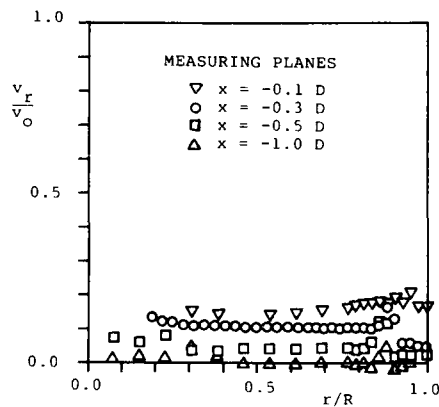


FIG. 5-1

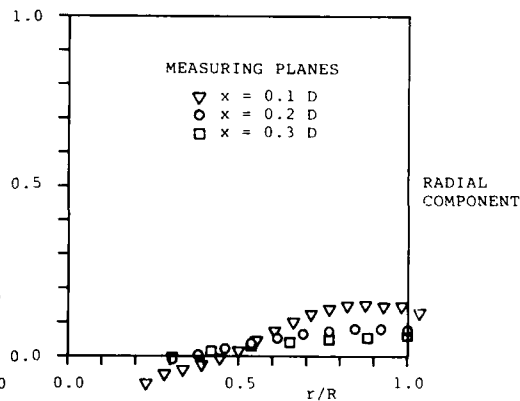


FIG. 6-1

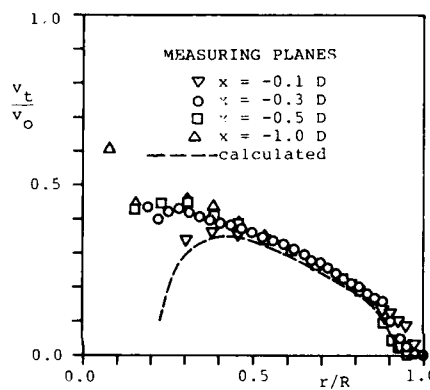


FIG. 5-2

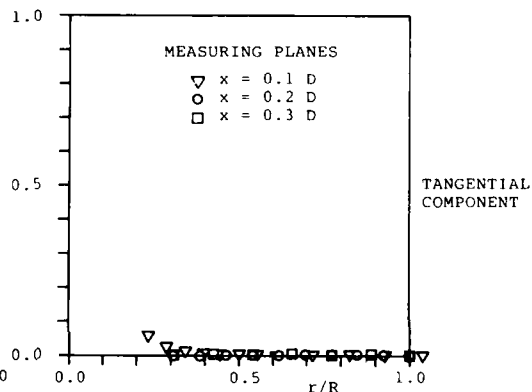


FIG. 6-2

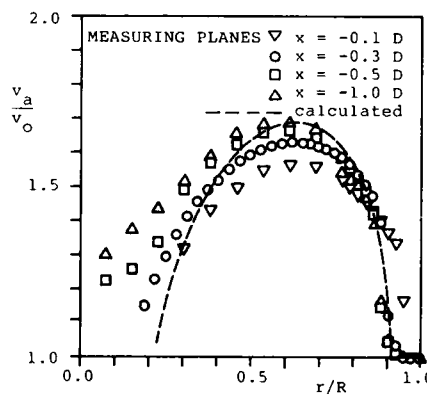


FIG. 5-3

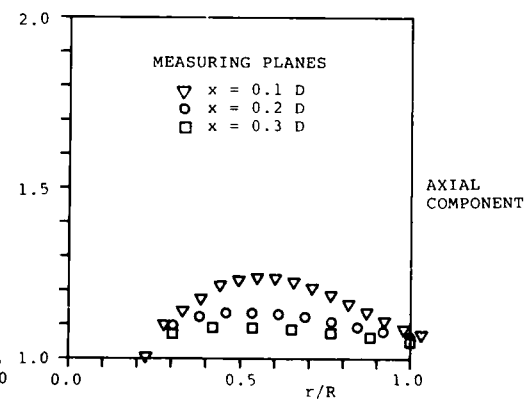


FIG. 6-3

MEAN VALUES OF FLOW VELOCITIES AT  $K_T = 0.185$

FIG. 5 BEHIND PROPELLER PLANE

FIG. 6 IN FRONT OF PROPELLER PLANE



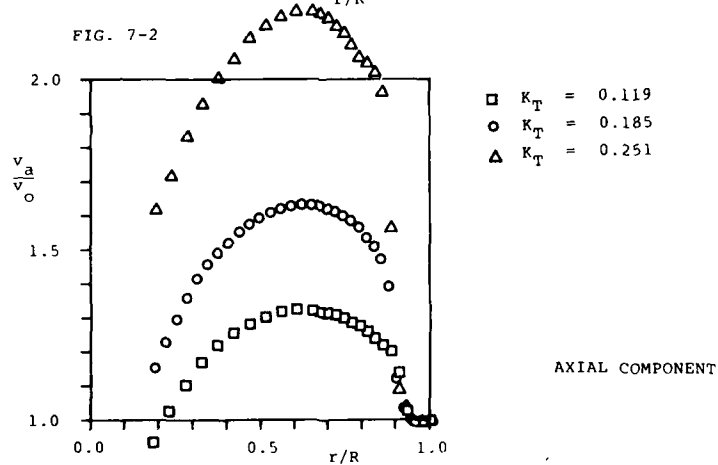
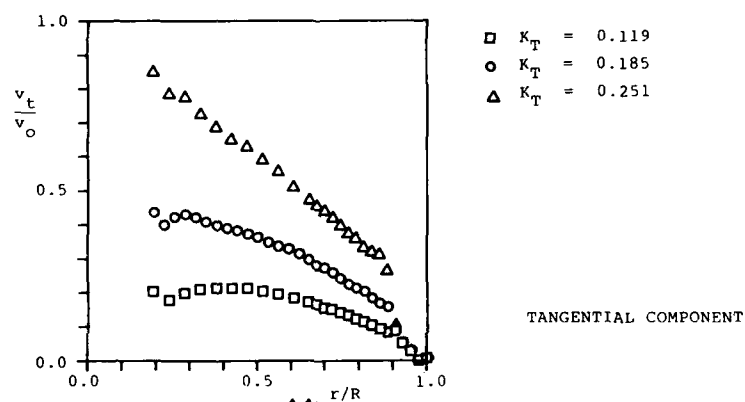
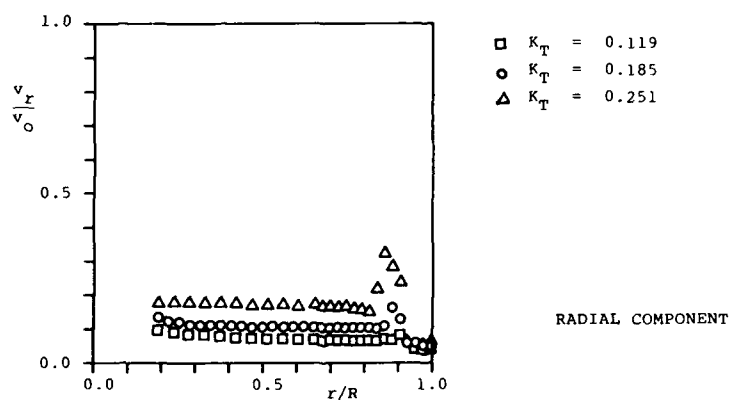


FIG. 7 MEAN VALUES OF FLOW VELOCITIES ON PRESSURE SIDE  $x = -0.3 D$  AT DIFFERENT  $K_T$ -VALUES

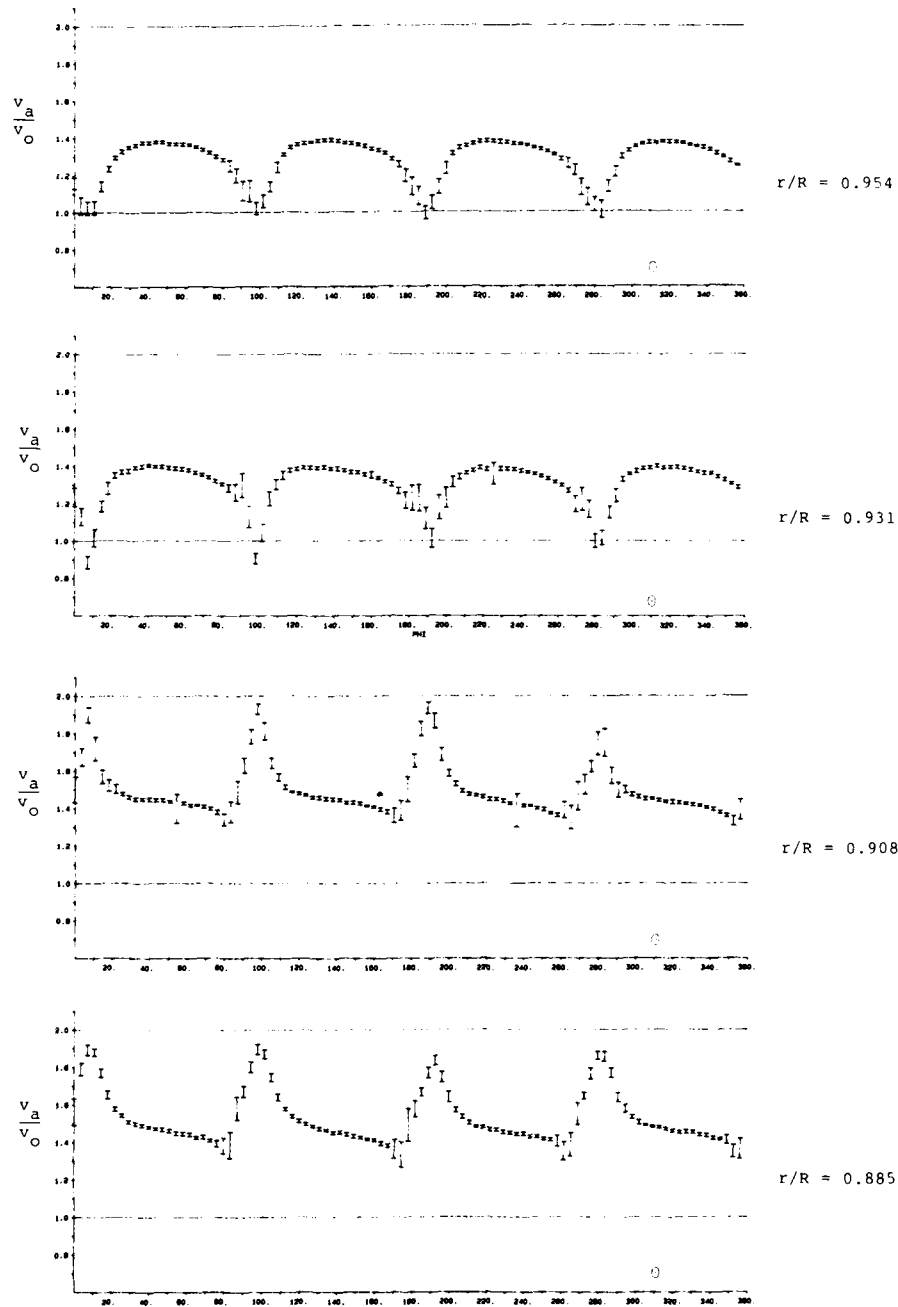


FIG. 8-1 AXIAL VELOCITY CLOSE TO THE TIP VORTEX

$$K_T = 0.119$$

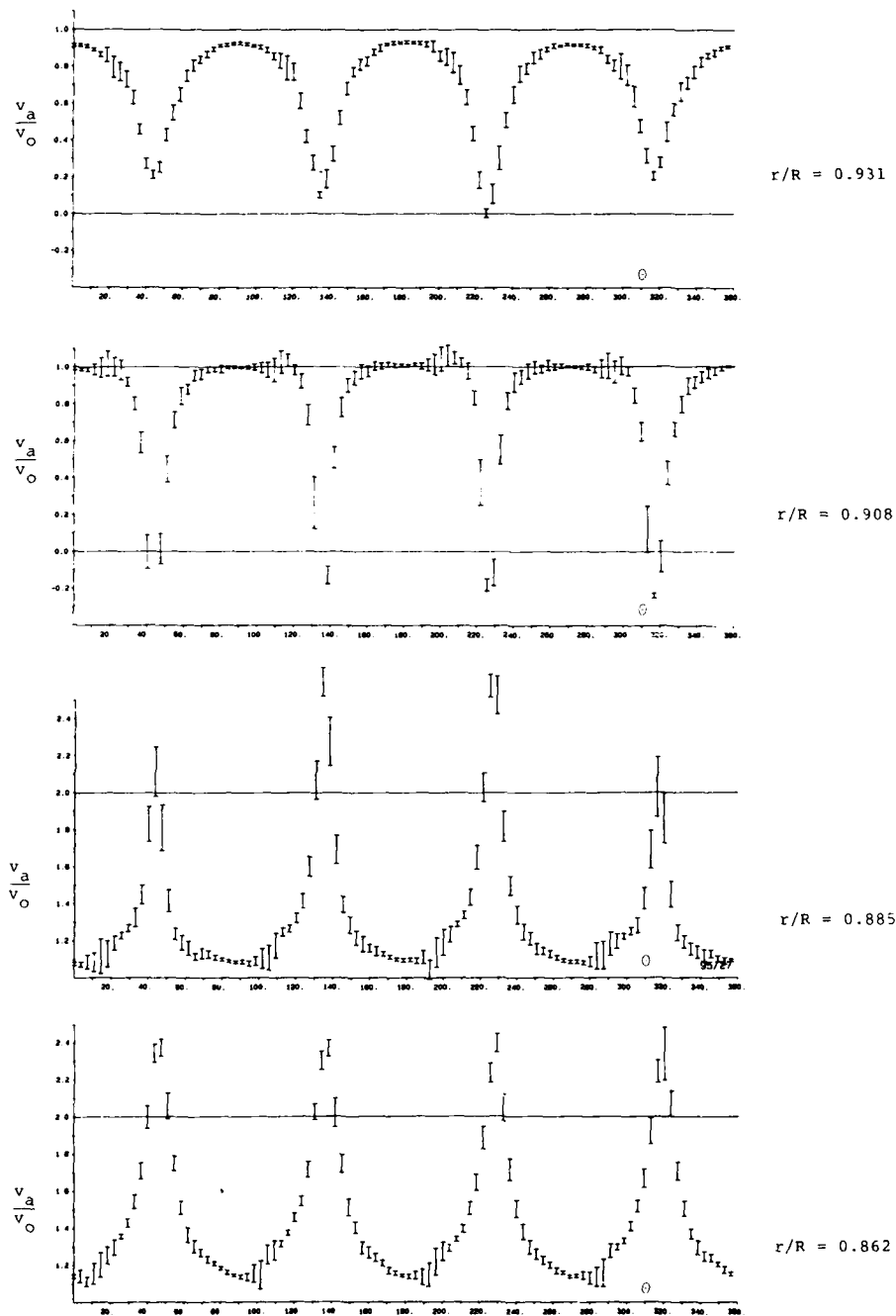


FIG. 8-2 AXIAL VELOCITY CLOSE TO THE TIP VORTEX  
 $K_T = 0.251$

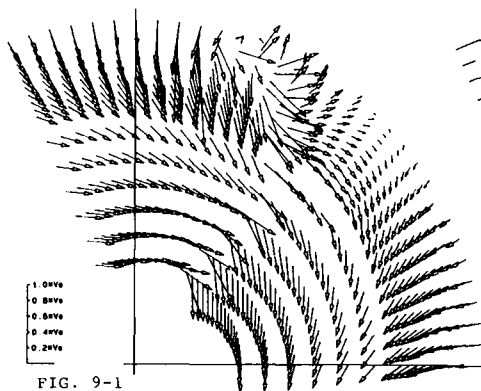


FIG. 9-1

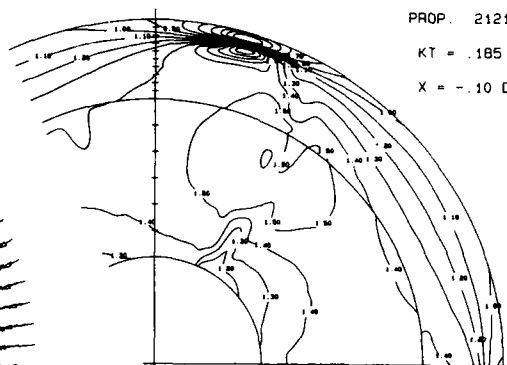


FIG. 9-2

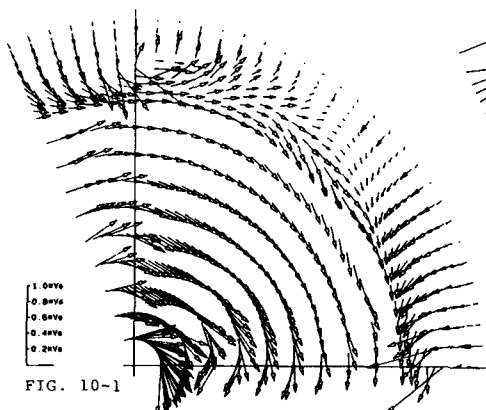


FIG. 10-1

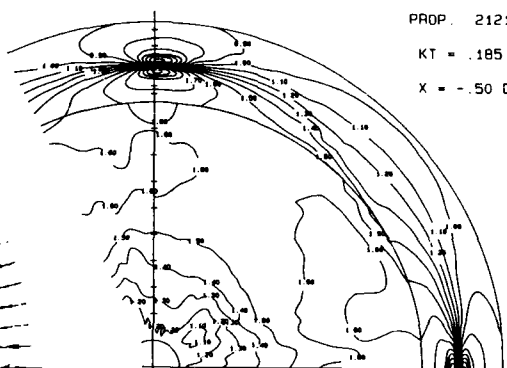


FIG. 10-2

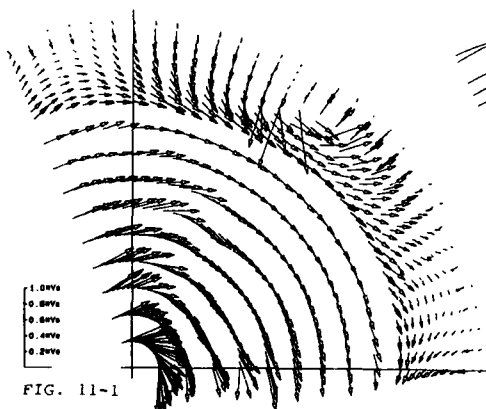


FIG. 11-1

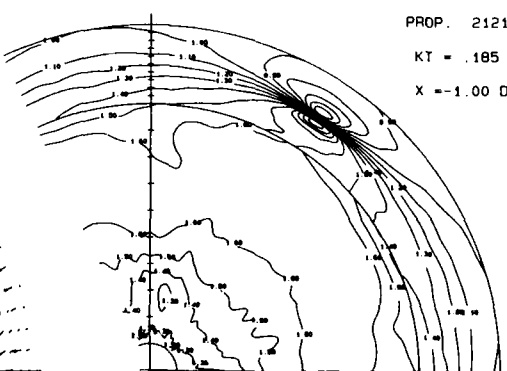
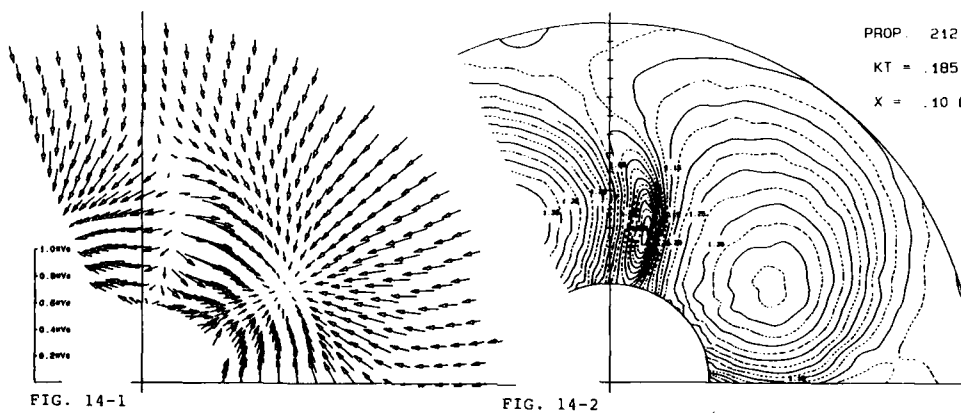
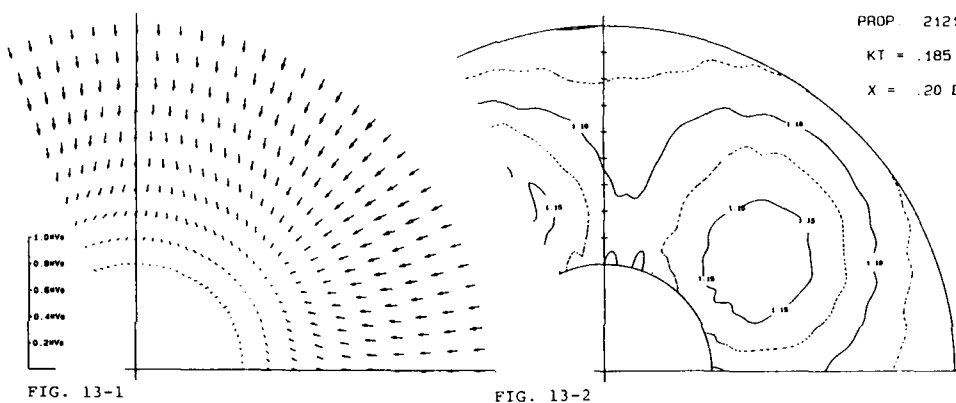
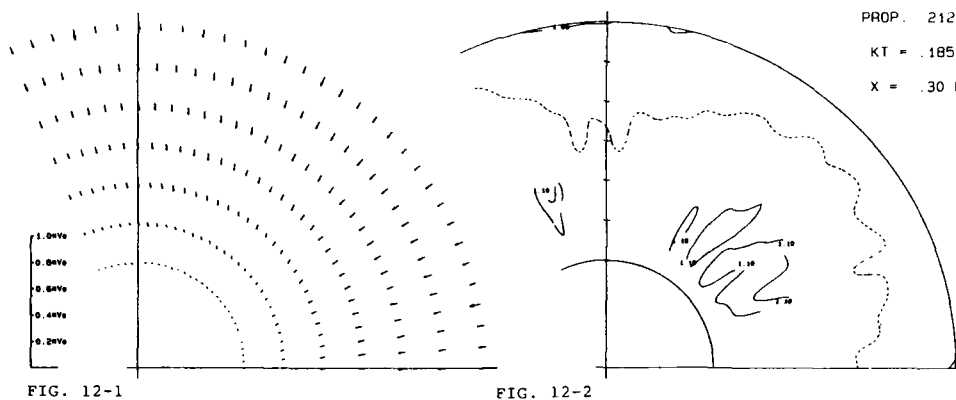


FIG. 11-2

VECTOR DIAGRAMS OF CROSS COMPONENTS

ISOTACHES OF AXIAL VELOCITIES

VELOCITY FIELD BEHIND PROPELLER



VECTOR DIAGRAMS OF CROSS COMPONENTS

ISOTACHES OF AXIAL VELOCITIES

VELOCITY FIELD IN FRONT OF PROPELLER

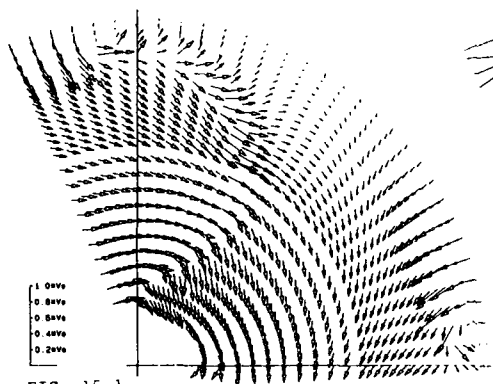


FIG. 15-1

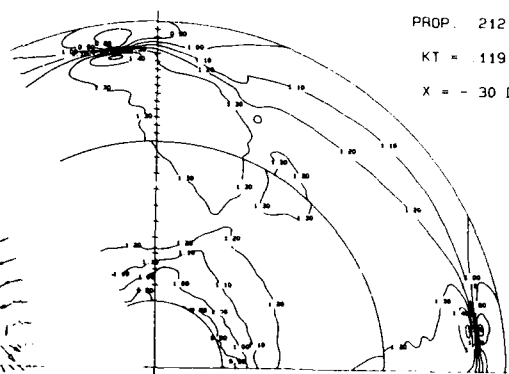


FIG. 15-2

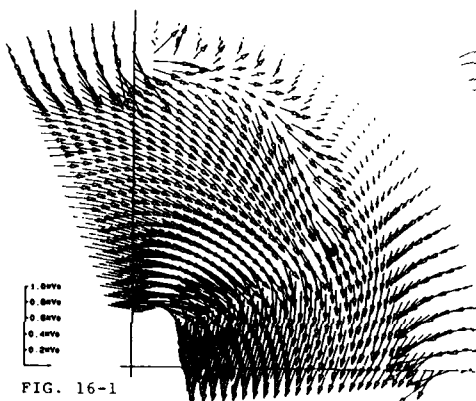


FIG. 16-1

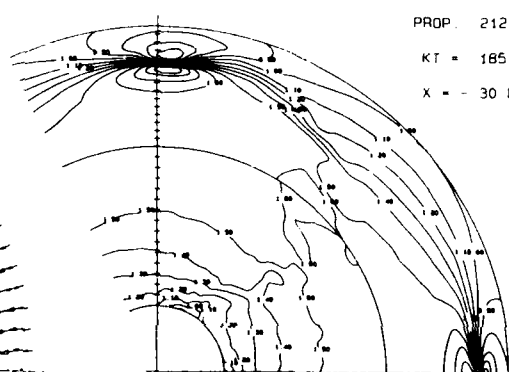


FIG. 16-2

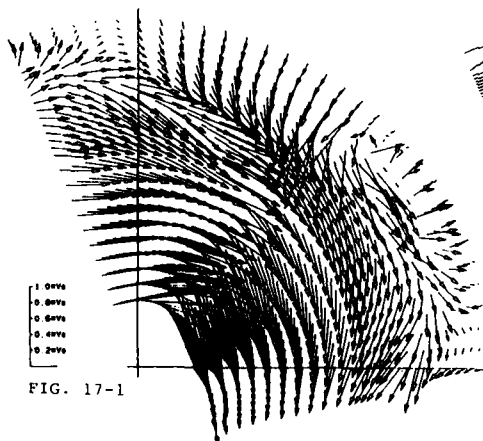


FIG. 17-1

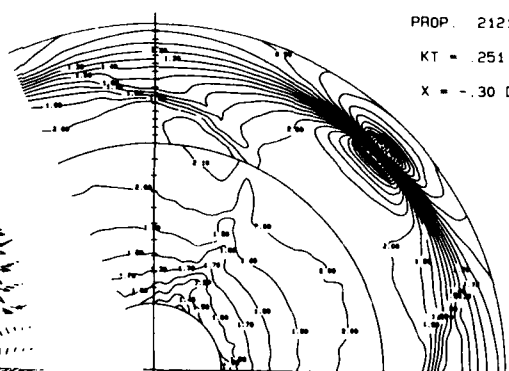


FIG. 17-2

ISOTACHES OF AXIAL VELOCITIES

VELOCITY FIELD BEHIND PROPELLER

## AERONAUTICS AND NAVAL HYDRODYNAMICS - CONNECTIONS

Marshall P. Tulin, Professor  
 Ocean Engineering Laboratory  
 University of California at Santa Barbara  
 Santa Barbara, California 93106

It is a pleasure to be here at this rare co-mingling of workers in aerodynamics and ship hydrodynamics. I know that Theodore von Karman the founder of AGARD wanted your organization to broaden their interests in the marine direction and this meeting, I'm sure, would please him very much. He would also have to be astounded at the advances which have been made in flow visualization since that day 75 years ago when aluminum powder made visible those unsteady vortices of his on the surface of that small open water channel at Gottingen.

I am an aeronautics person, trained at MIT and then employed in the 8' high speed tunnel at Langley, NACA; I turned to naval hydrodynamics in 1950. I am extremely grateful for my aeronautics experience, and particularly in the great and exciting laboratory which Langley then was. How better could a young engineer begin a career in fluid dynamics than to have close contact with John Stack (to whom we owe transonic developments then), Tony Ferri, Carl Kaplan, Adolf Busemann, Clint Brown, and many others; to participate in the pre-flight stability tests of the X-1 and D558; to test and analyze the performance of swept and low aspect ratio transonic propellers; and to be part of a small team which successfully converted the 8' tunnel to low supersonic operation ( $M=1.1; 1.2$ ). It was very exciting. It was also very noisy.

In the same way I am grateful for my experience at DTMB, with its wonderful staff and facilities, which significantly advanced the depth and breadth of my interest and knowledge in fluid dynamics and exposed me to an almost endless sequence of interesting and challenging problems in the naval hydrodynamics. Having come from the 8' HST those things which impressed me immediately at DTMB were the quiet in the cavernous dark tank and the beautiful patterns of ship waves and wakes.

Today, I take it as my pleasurable task here to provide you with some view of our large and diversified field of naval and marine hydrodynamics.

We have now in the marine field a variety of problems to face, starting with resistance and propulsion, including propeller design and operation in wakes. We have stability, control, and motion problems involving all the usual phenomena connected with forces on bodies, in addition to free surface effects. These include interactions between appendages such as submarine sails, control surfaces, and the hull itself, and often involve very viscous phenomena as vortex shedding, etc. There is great concern, too with the self-noise of ships produced by the boundary layer on the hull and sonar domes, by the propeller and wake, and especially due to cavitation, which occurs on propellers starting at speeds of surface ships around 12 knots or so; and of course the far field noise is of profound naval importance. Ocean structures introduce another range of problems: wave induced loads and motions, unsteady vortex shedding, etc. The air-sea interface is altogether a difficult, harsh environment. In addition, the submarine, which escapes this environment must often operate within a vertical range which is not very large in terms of its total length, imposing special stability and control requirements.

I cannot give you a glimpse of all these problem areas, and there are even more, so I thought that I would talk to you mainly about ship resistance for several good reasons. First, since the mission economics of both the ship and aircraft are to a large extent determined by resistance, it's very important for us to minimize this resistance to the extent that it is possible in the design and development phase. Second, resistance is the first subject which saw intensive work in fluid dynamics and has led to studies of varied basic complex phenomena; the resulting understanding comprises our common "gene pool". And, finally, ship resistance needs led to the very first establishment of modern facilities and techniques for the estimation of full scale performance by model testing. This was done by William Froude between 1859-69, to whom all of us owe a very great debt.

FLUID RESISTANCE IN SHIP HYDRODYNAMICS AND AERODYNAMICS

- COMMON IMPORTANCE FOR DESIGN AND OPTIMIZATION
- FIRST SUBJECT IN FLUID DYNAMICS  
INVOLVES MANY BASIC PHENOMENA: POTENTIAL FLOW; VISCOUS EFFECTS;  
TURBULENCE; GRAVITY AND SHOCK WAVES; WAKE AND CAVITY FLOWS; VORTEX WAKES;  
SPRAY AND BREAKING; NON-LINEAR PHENOMENA
- LED TO INITIATION OF MODERN EXPERIMENTAL METHODS:  
WILLIAM (AND ROBERT) FROUDE, 1867-79  
THE SHIP MODEL BASIN, OR TOWING TANK  
FATHER OF MODERN SHIP HYDRODYNAMICS

FIGURE 1.

I would like to indulge both in a brief history of fluid resistance, for reasons I hope will become apparent, and an update on some recent selected advances.

Let us begin in the pre-modern era. At the beginning, just prior to 1700, Isaac Newton began his studies of fluid resistance which he persisted in for forty years or more, presumably because of his interest in the motion of the celestial bodies and his desire to prove that space was empty.

PRE-MODERN HISTORY - FLUID RESISTANCE

NEWTON (b. 1642 - d. 1727)

- RECIPROCITY
- RESISTANCE = SUM: TENACITY + ATTRITION + INERTIAL
- INERTIAL ( $\rho, v^2$ , SHAPE)
- FLUID "SHOCK" THEORY:  $\rho v^2 \sin^2$  (INCIDENCE),  
ONLY FOREBODY PRODUCED DRAG
- THIS THEORY LARGELY PERSISTED UNTIL 1880 AND CAUSED DIFFICULTIES:  
FOR SHIPS - IGNORED THE STERN  
FOR AERONAUTICS -  $\sin^2$  DISCOURAGED LIGHT

FIGURE 2.

His accomplishments were many. First of all, Newton postulated reciprocity of relative motion, which is the basis of all wind tunnel testing. Then he came to the correct and bold conclusion that the resistance of a body to its motion depended on the density of the fluid, on the speed of the body, and upon the body's shape; furthermore he made the very brave and basically correct assumption that the resistance could be thought of as due to the sum of resistances due to different physical effects. The first of these he said was constant and due to "tenacity" which I think we could relate to solid friction; the second due to what he called "attrition" and proportional to velocity, where attrition would seem to be associated with viscosity; and the third varied as the square of the speed as Huygens had already measured and which Newton called inertial resistance, proportional to density, and related to the cross-sectional area of a body. Newton pressed further to postulate that the local inertial resistance on any forward portion of the body was proportional to the sine squared of the angle, say  $\alpha$ , between that



surface and the direction of motion, and was due to what he called the "shock" of the fluid. This idea was based on the model that the fluid was ignorant of the motion of the body until its impact and that the resulting local force was due to the deflection of the relative momentum of the fluid by the local body surface. We have the larger picture today, that this kind of effect doesn't come about until we reach hypersonic speeds when indeed the fluid ahead of the body is ignorant until the last moment of the existence of a body, and a simple rule like  $\sin^2 \alpha$  becomes more or less appropriate. In Newton's theory, the afterbody was not subject to fluid shock, and produced no resistance. The fluid shock theory was remarkably persistent from its introduction around 1700 until the late 1800's in the time of Froude. It caused two difficulties in engineering: in ship engineering, where it was very harmful to ignore the stern; and in aeronautics where the  $\sin^2 \alpha$  drastically underestimated lift for small  $\alpha$  and demoralized those who would sustain flight through dynamic lift. It was not until Rayleigh, 1876, that the  $\sin \alpha$  law was calculated theoretically, for a flat plate assuming full separation. This was an important achievement but it overestimated drag by far.

The interest and works of two great successors of Newton who worked in fluid dynamics seems to be in great part to have been motivated by their interest in the resistance in ships and in ship building. They were D'Alembert and Leonard Euler, both of whom worked through and until the latter part of the 18th century. Euler published several treatises on naval architecture, the first in 1749 and the second in 1773, the latter entitled "The Complete Theory of the Construction and of the Maneuvering of Vessels". He had this to say on the subject of ship resistance:

"From good models in miniature which represent vessels exactly as they are, very important experiments upon the resistance of vessels may be very usefully made, and which is so much the more necessary as the theory upon the subject is still so very defective."

You will recognize that this statement is precisely true today 200 years later although the defective theory, of which Euler spoke is not the same as the defective theory today, ours being much more sophisticated. This statement of Euler's in all probability reflects his struggle and frustration with the application of Newton's shock rule, which on the one hand Euler had trouble to fully reject but which at the same time he stated explicitly did not at all apply to the flow around the stern of the ship, the flow there being more complicated. D'Alembert seems clearly to have understood the importance of experiments and in fact he carried out together with Abbe Bossut and Condorcet experimental towing studies in a pond of the resistance of bodies which was supported by the French government in connection with the resistance of ships in canals. He wrote in connection with these tests that "the research on the resistance experienced by a solid body dividing a fluid is perhaps the most important problem of hydrodynamics both on account of its difficulty and of its applications to naval architecture, to the construction of dikes, of hydraulic Machines, etc." D'Alembert would not seem to have had much dedication to the  $\sin^2 \alpha$  theory of Newton. He explained with his colleagues very matter of factly in the conclusions of their towing research that the resistance of the fluid is sensibly proportional to the square of the velocity, increasing somewhat faster at higher speeds; proportional to the surface area of planes normal to the motion; that the rule for inclined plane resistance varies with  $\sin^2 \alpha$  only for angles between 50 and 90 degrees and must be abandoned for lesser angles; and, finally, that the influence of viscosity is extremely small, particularly if the velocity is somewhat high.

These Paris towing tests were by no means the first of their kind.

In the 200 odd years between Newton and Froude a large number of individual model tests were carried out by a wide variety of investigators invariably utilizing a towing cable driven by a falling weight as in the case of Samuel Fortrey in England in 1650, by the Society of Arts in England in 1761, by Benjamin Franklin in this country in a table top experiment in 1768, and later in the century by Mark Beaufoy in a very large dock, of 400 foot length in the period 1791-8. Beaufoy's tests included those on friction planks and were highly important in quantifying the significance of frictional effects for the first time. In the beginning of the 19th century during the period 1834 to 1840 John Scott Russell investigated the resistance of ships in canals using both horsepower and the falling weight system and in the process discovered what he termed "the great primary wave of translation" which we now celebrate as the granddaddy of the soliton.

PREF-MODERN TOWING TESTS

- CABLE - FALLING WEIGHT
- SAMUEL FORTREY, 1650 G.B.
- SOCIETY OF ARTS, 1761 G.B.
- BENJAMIN FRANKLIN, 1768 U.S.
- D'ALEMBERT, ABBE BOSSUT,  
MARQUIS CONDORCET, 1775 FR.
- MARK BEAUFOY, 1791-8 G.B.  
(400' DOCK)
- JOHN SCOTT RUSSELL, 1834-40 G.B.

FIGURE 3.

By the middle of the 19th century the sailing ship had begun to be replaced by iron ships with steam propulsion. And as time passed it became increasingly important for ship designers to have pre-knowledge of the resistance of the ship in order to size the propulsion plant. However, no real improvement in understanding of ship resistance had been brought about either amongst scientists or engineers. This, despite the promulgation of the Navier-Stokes laws in the period 1826 into the early 30's by various scientists and of the pipe resistance tests of Hagen and Poisseuille in about 1840.

Now I invite you to put yourself back in this really miserable state of affairs and to attend a meeting of the Royal Institute of Naval Architects in 1870, chaired by the same J. Scott Russell, a successful ship builder, and the inventor and very forceful proponent of an erroneous theory of ship resistance based on his earlier observations of shallow water waves. Russell, speaking from the chair, is confessing to designing and testing a ship's hull based on the solution of Newton's equation for solids of least resistance; these equations being derived from Newton's theory of fluid shock, the  $\sin^2 \alpha$  law. The subject of the meeting was ship resistance and, ironically, a major purpose was to discuss the proposal of William Froude, a retired engineer and already known for his successful analysis of ship rolling. The British admiralty faced with the great necessity to predict in advance the installed horsepower of its new iron ships had issued a "Request for Proposals" for the development of means for such prediction. Froude's proposal had been approved in the previous year and asked for the construction and development of a model basin for the scientific testing of ship models. The proposal was most vigorously, even testily opposed by Scott Russell at this meeting, as he claimed that his own experiments did not agree with full scale results. The quiet and earnest Froude replied from the audience: "I did not come here to make any long explanation to the meeting tonight. I see that the feeling of the meeting is very much against experiments with models, but I must say that my own experience leads me to judge quite differently. I think why experiments with models have hitherto been found to be a failure, and have misled those who have made them, as to the effect to be expected with regard to a full sized ship, is, that attention has not been paid to the relation which should subsist between the speed at which the model is moved, and the speed at which the ship is moved."

Thus was publicly announced the first of Froude's great contributions to our science of full-scale prediction and model testing. That is the very notion of similarity and of its application to the scaling of model tests based on the formulation of a non-dimensional parameter incorporating the governing dimensional quantities.

The second great contribution of William Froude to our science was to conceive, develop and construct literally with his own hands the first modern laboratory devoted to model testing. He brought model testing indoors, replaced the falling weight system with a towing carriage and rails, introduced the use of models built of hard paraffin wax, and devised suitable cutting Machines for them. His original model dynamometer and recorder were still in use in Britain until 1950.

## INITIATION - MODERN ERA

WM. FROUDE (1810-79)

- ROLLING (GT. EASTERN W. BRUNEL)
- SHIP RESISTANCE AND PROPULSION (1867-79)

## ACCOMPLISHMENTS:

- DYNAMIC THEORY OF ROLLING
- COHERENT, CORRECT VIEW OF RESISTANCE
- SIMILITUDE (SCALING) IN MODEL TESTS
- INDOOR LABORATORY, DYNAMOMETERS, ETC.
- FULL SCALE TESTS FOR CORRELATION
- SEPARATION OF RESISTANCE INTO COMPONENTS
- PLANK TESTS - LENGTH EFFECT
- UNDERSTOOD FRICTION LAYER
- WAVE RESISTANCE, GROUP VELOCITY
- BLADE ELEMENT THEORY ( $\sin \alpha$ ), WAKE EFFECTS

HE WAS THE FIRST SCIENTIST IN OUR FIELD TO REACH  
SYSTEMATIC AND DEEP CORRECT CONCLUSIONS REGARDING THE PHYSICAL  
NATURE OF A LARGE AREA IN OUR FIELD, FLUID RESISTANCE, ALMOST  
ENTIRELY THROUGH OBSERVATIONS AND MEASUREMENTS CARRIED OUT  
SYSTEMATICALLY.

FIGURE 4.

As a third contribution, he conceived and applied the important concept of full-scale testing in correlation with model tests. He first did this in the case of a small ship, now famous, called the Greyhound, for the purpose of validating the procedures and equipment which he had patiently developed for model tests.

In order to succeed in the successful prediction of ship resistance for model tests, it was not enough to recognize the law of similitude and to construct a towing tank with its diverse equipment; it was further necessary to understand the origin of ship resistance in its various components and the necessity to scale these components separately. Herein lay the fourth great contribution of Froude. He proposed following Newton to divide the resistance of a ship into its separate sources, these consisting of three items: surface friction, eddy resistance, and wave resistance. He understood perfectly the importance of streamlining and of "easy" shapes. His conception of the eddy resistance, as incidental to surface friction and resulting in a slight unbalancing of perfect fluid streamlines and pressure, exactly corresponds to our present view of what we call form resistance. He related the frictional resistance of a ship hull to that of a fine plank of the same length and area, empirically adjusted for effects of ship roughness. He also understood experimentally that the friction decreases with increasing length of surface. (Remember that Reynold's number of scaling had yet to be invented and was only related to skin friction by Rayleigh in 1900.)

Froude obtained a highly accurate flat-plate friction curve by towing fine planks of increasing length in his own model basin. Some 60 years later in 1934 these data, still in use in model basins throughout the world, were correlated with the Von Karman turbulent friction formula based on the notion of a self-similar outer law of the turbulent boundary layer. This was done by Karl Schoenherr of the experimental model basin in Washington, which had been constructed by Admiral David W. Taylor in about 1898.

Froude's importance in fluid mechanics is heightened when we realize that he was in all probability the first scientist in our field to reach systematic and deep correct conclusions regarding the physical nature of a large area in our field, in this case fluid resistance, almost entirely through observations and measurements carried out systematically. He was almost casual in these profound observations. For example, he described how the effects of friction on the ship were confined to what he called a "belt" of fluid near the ship hull, thus pre-dating Prandtl's description of the viscous boundary layer by over 25 years. Incidentally, Froude made a very important contribution to the subject of dispersive wave phenomena, a subject very important in physics, with his discovery of the phenomena of group velocity which occurred as a result of his observation of the waves produced upon turning on a wave maker which he had developed for his towing tank, also another first.

William Froude was much aided in all his efforts by his son Robert who continued them after his death in 1879, ten years after he began the work. At his death he was 69 years old. By the beginning of this century there were additional tanks located at Hasler in England (a naval laboratory), in Washington as I have mentioned, in Paris and in Berlin. Tanks were involved in not only resistance research but also propulsion and testing of the motions and turning properties of ships. At least in Paris a large rotating arm was installed for turning tests. Admiral David W. Taylor had apprenticed himself to the British laboratory at Hasler for the purpose of becoming acquainted with the model basin testing techniques. He was subsequently to build the first important wind tunnel in this country at the Experimental Model Basin in Washington and to be a founder and the first Chairman of the National Advisory Committee for Aeronautics in 1915 together with Jerome Hunsaker, a naval engineer, designer of the NC-4 seaplanes which early crossed the Atlantic, and the founder of the first Department of Aeronautical Engineering in this country which was located at MIT partially staffed with naval architects. It is not very well known that the NACA was first organized under the U.S. Navy. I have been told the story that only a minor administrative disagreement between NACA's first (and longtime) Secretary, Mr. John Victory, and the naval bureaucracy over travel claims, resulted in the separation of NACA into a separate agency.

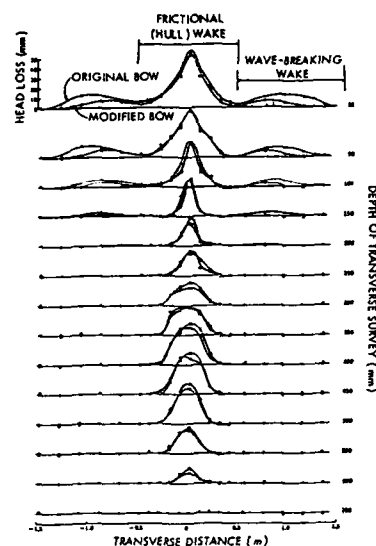
The first water tunnel of which I have any knowledge was innovated in 1895 by Sir Charles Parsons of England, the inventor and developer of the steam turbine for ship propulsion, in connection with the study of cavitation on ship's screws. Subsequently water tunnels of increasing size and sophistication were to be built in ship model basins and laboratories for the testing of ship propellers and for the study of their cavitation characteristics and effects. The wavemaker invented by Froude was commonly installed in ship towing tanks in planar form. In the last three or four decades wavemakers of increasing sophistication have been invented, and large basins have been installed at model basins for the study of not only ship motions in confused seas but also for the study of offshore problems of various kinds. There are probably 90 or 100 important model basins operating in the world today, and no greater compliment could be paid to William Froude than the fact that virtually all of these basins still utilize the basic techniques and procedures conceived of and developed by him for the measurement of ship resistance.

There have been additional experimental techniques introduced in the resistance field. For example, the transverse wake survey conducted at a short distance behind a ship allows the experimental determination of the total viscous resistance, both friction and form. Its real importance for the ship is to dissect the dynamometer resistance and assign more definitely its origin to various sources. This use of the wake survey is exemplified in a very highly successful application by Baba in Japan in 1969 who showed conclusively that the anomalous low speed residuary resistance of full ships like tankers was not due to wave making as previously believed but to wave breaking around the bow region of the ship.

Another important technique involves the use of a wave wire fixed in the tank which produces a longitudinal sampling of the waves along a track transverse to the ship as it passes the wire at some distance of beam and allows the spectrum of the ship's wave pattern to be calculated by analysis of the record and helps in making modifications to the ship hull in order to minimize the wave resistance of a ship.

And of course ship laboratory instrumentation has become increasingly sophisticated. Few serious towing carriages function today without one or two computers on board.

For more details concerning model basin techniques and procedures it will be necessary to read the very large literature on the subject: for example the Proceedings of the International Towing Tank Conference (ITTC) and its American counterpart the ATTC.



DISTRIBUTION OF TOTAL HEAD LOSS,  $F = 0.237$   
FROM: TANIGUCHI, TAMURA, BABA (1971)

FIGURE 5.

The connections between our fields which are so evident in history continue to this day through our interest in closely related phenomena and common problems and techniques for their solution. Any reasonably complete listing of these would be drawn from broad categories including: resistance prediction, drag reduction, loading predictions, stability and control analysis, motion dynamics, propeller and jet design and performance, flow noise and vibration, facilities and experimental techniques and instrumentation, computational theoretical methods, and general fluid phenomena. This is not the place for a comprehensive review of these connections. A brief selected listing is shown, Figure 6. I cannot discuss them all here, for lack of time. But they can be illustrated by giving, briefly, some particular examples from my own personal experience. These concern: the development of supercavitating flow theory and its application to the prediction of separated flows; the explanation and theoretical treatment of the transom resistance of fast ships; and the modeling of steady spilling breakers (breaking waves at sea). These all have some connection or analogy with aerodynamic phenomena, and that's why I've chosen them. They will also give you a taste of some of the challenges in naval hydrodynamics.

MODERN DEVELOPMENTS IN FLUID RESISTANCE (SHIPS).

CAVITY FLOWS → SEPARATION  
STERN WAKES → INDUCED DRAG  
WAVE BREAKING → COMPRESSION SHOCK  
DRAG REDUCTION (POLYMERS; SURFACE MODIFICATION)  
VISCOUS STERN FLOWS  
NON-LINEAR WAVE THEORIES  
VORTEX SHEDDING - UNSTEADY

FIGURE 6.

Cavitation causes a breakdown in performance and material erosion damage for even well designed marine propellers when operated on ships, hydrofoil craft, air cushion vehicles, etc. in excess of 40 or 50 knots. A solution to this engineering problem was found starting in about 1955 at the Taylor Model Basin in the development of the supercavitating propeller. The blade sections of this propeller operate with a fully wetted lower (pressure) surface, but with the upper surface fully immersed in a vapor cavity springing from the leading edge and collapsing at a sufficient distance to the rear of the foil. The actual motivation for this development arose from the need to propel newly developing hydrofoil craft and from the development of two dimensional supercavitating hydrofoil theory which for the first time revealed quantitatively how the camber of the lower surface could vastly improve the lift/drag ratio of lifting foils operating in the fully separated condition (a second order drag exists in this condition). The original low-drag hydrofoil theory (Tulin, 1954) made use of the methods of linear airfoil theory, developed originally by the Prandtl school, and therefore owes its origin to aerodynamic inspiration; what was involved, though, was to solve the unusual (integral equation) problem where the thickness and lifting parts of the solution are closely coupled. This successful development, coupled with a growing interest in foils and surface piercing struts operating in the supercavitating or ventilated condition (where the wake is comprised of air rather than water vapor), led to the intensive development of theories for bodies with full wakes, including the case of finite wakes, operation in tunnels, near free surfaces, etc.

Very useful non-linear models of finite wake flows were developed in this process, which can result in good predictions of the relationship between wake pressure and wake-cavity length and also allow for the effect of the final wake trailing behind the finite wake-cavity, see Figure 7. Recently this model has been used to treat the problem of the prediction of stabilized separated regions in aero-hydrodynamics, as the closed re-circulating separation region behind a flat plate broadside, or the leading edge bubble formed on a sufficiently sharp-nosed airfoil. The key to understanding these flows lies in the modeling of the outer flow as a free-streamline supercavitating flow utilizing an advanced cavity closure model (single-spiral) together with a modeling of the inner flow as a viscous shear region lying in the boundary between the potential flow outside and the essentially stagnant cavity inside. Each of these inner and outer flows allows a separate calculation of the drag on the body, and the matching between them is accomplished by matching the drags. The results for two interesting cases for which very good data are available for comparison are shown as Figure 8; Tulin and Hsu, "New Applications of Cavity Flow Theory," *Proceedings, 13th ONR Symposium on Naval Hydrodynamics*, Tokyo, 1980, National Academy Press, Washington, D.C., pp. 107-131. So here is an example of how theory developed originally for treating water flows can be successfully utilized in aerodynamics.

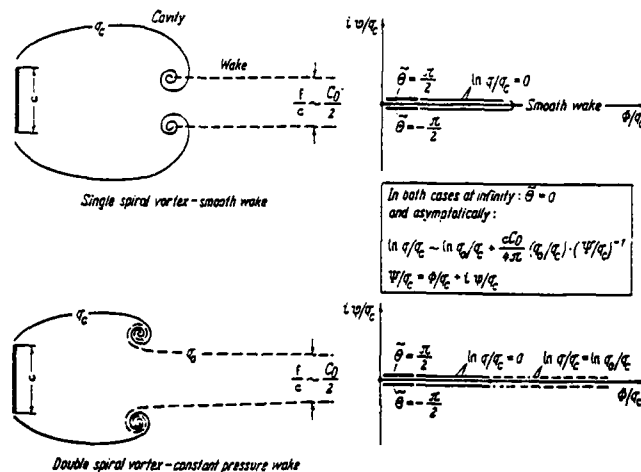


FIGURE 7 - SPIRAL VORTEX, TRAILING WAKE MODELS OF REAL CAVITY FLOWS FROM: TULIN

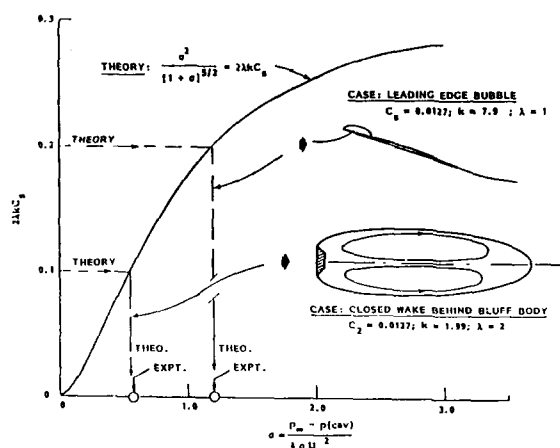
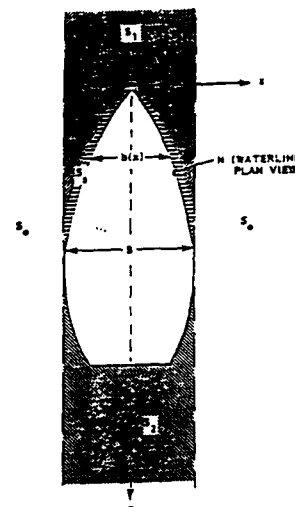
FIGURE 8 - COMPARISON OF THEORY AND EXPERIMENT FOR  $\alpha$ 

FIGURE 9 - FREE-SURFACE REGIONS, HIGH-SPEED SHIP

High speed ships have evolved with blunt sawed-off sterns, called transoms. Why is this? Towing tests on such ships show that at high Froude numbers, where the wave drag is small, the resistance of ships is significantly larger than frictional. What is this high speed drag? Recently, we, Tulin and Hsu, "Theory of High Speed Displacement Ships with Transom Sterns," Jour. Ship Research, Vol. 30, No. 3, Sept. 1986, have undertaken to analyze the flow about high speed ships in order to answer these questions and to provide theoretical means to optimize transom designs. The flow about a slender ship at high speeds is very similar to the flow about a thin wing (no thickness) since the condition of constant pressure on the free surface translates into a condition that the streamwise velocity perturbation be zero on the free water surface. The latter thus resembles the horizontal plane in which a cambered wing of no thickness lies. In our solution the ship is slender (it is not assumed to be flat or winglike) and the solution is thus harmonic in the cross flow planes (a relative of Munk's slender airship theory). In the front of the ship (region  $S_1$  of Figure 9) the flow adjusts to the ship's shape through a spray sheet (region  $S_2$ ). The fascinating revelation of the theory is that a vortex wake-like flow exists behind the ship (region  $S_2$ ) giving rise to a separate source of resistance, directly associated with the transom shape. This high speed transom resistance is exactly analogous to the induced drag of a wing. In the wing case, the wake and drag is determined by the spanwise distribution of lift, while for the ship it is determined by the shape of the waterline intersection of the hull aft of the maximum section and by the sternwise slope of the hull directly at the transom.

Waves break at sea in almost any significant wind; breaking is also always observed near ships, both at the bow and along and near the hull, which is in full scale usually surrounded by white water. What is the flow like in a spilling breaker? How can it be modeled quantitatively? Experimental studies of spilling breakers caused by a near surface but submerged two-dimensional hydrofoil have been carried out at Hydronautics, Inc.; see Duncan, "An Experimental Investigation of Breaking Waves Produced by a Towed Hydrofoil," Proc. R. Soc. London A, Vol. 377, pp. 331-348, 1981; and Duncan, "The Breaking and Non-Breaking Resistance of a Two-Dimensional Hydrofoil," J. Fluid Mech., Vol. 126, pp. 507-520, 1983. Duncan utilized light slit, flow visualization techniques which made visible both the breaker riding on the front of a wave (surf-rider) and the turbulent wake trailing behind it on the free surface, Figure 10. Recently in the Ocean Engineering Laboratory at UCSB, we have succeeded to model the breakers and to provide theory predicting its effect on the following waves (Duncan had observed experimentally that the larger the breaker, the weaker the following wave). In this theory, Tulin and Cointe, "A Theory of Spilling Breakers," Proceedings, 16th ONR Symposium on Naval Hydrodynamics, Berkeley, Ca., July 1986 National Academy Press (in press), Washington, D.C., the outer potential flow is an incoming wave on which a pressure is imposed equivalent to the weight of the breaker and its effective wake. This imposed pressure tends to cancel the incoming wave and results in its suppression. But, how is the distribution of pressure to be determined? This is done by utilizing an inner flow model in which an essentially stagnant eddy sits on the forward face of the wave in a surf-riding mode, held there by the

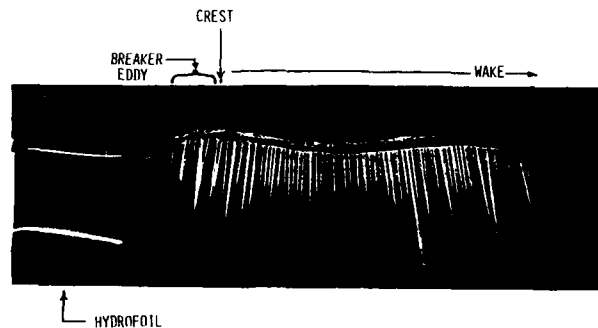


FIGURE 10 - BREAKING WAVE OVER A SUBMERGED HYDROFOIL  
(DUNCAN; LIGHT SLIT VISUALIZATION)

underlying friction acting in the shear zone between the eddy and underlying wave flow. The entire flow can be analyzed by utilizing a momentum flux balance across the breaker, taking into account the resistance of the eddy. To make an analogy with normal shock waves, the eddy acts as the viscous flow within the shock itself to deplete the energy of the incoming flow (wave), resulting in a less energetic rearward flow (wave), Figure 11.

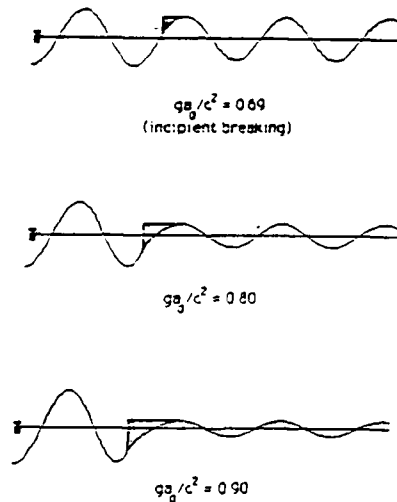


FIGURE 11 - COMPUTED WAVE PROFILES

I hope these brief remarks, both the history and the personal examples of research, have adequately expressed the great bond and bridge between our two fields. My own personal experience has been that life in research is much enhanced by breaking down artificial walls between fields and gaining the pleasure inherent in the appreciation and use of good scientific knowledge and results, wherever they are generated.



## EXPERIMENTS TO INVESTIGATE THE VORTICES SHED FROM A SUBMARINE-LIKE BODY OF REVOLUTION

by

A R J M Lloyd

(Admiralty Research Establishment, Haslar, Gosport, Hampshire, PO12 2UW, United Kingdom)

and

I M C Campbell

(Wolfson Unit for Marine Technology and Industrial Aerodynamics,  
University of Southampton, Southampton SO9 5NH, United Kingdom)

Presented at the 59th meeting of the AGARD FLUID DYNAMICS PANEL SYMPOSIUM

Monterey, California, USA, 20-23 October 1986

## SUMMARY

This paper describes experiments to determine the characteristics of the vortices shed from a submarine-like body of revolution at an angle of attack in a turn. The experiments used a new type of vorticity probe developed by Freestone at the City University in the United Kingdom. The probe allows the streamwise vorticity to be estimated from simple pressure measurements and rapid assessments of vortex position and strength can be made. The paper examines the expected performance of the probe using a simulation of an ideal viscous cored vortex and reports experience gained in the design and preliminary testing of the probe. Results of experiments to measure the vortex shed by a hydroplane at an angle of attack and a body of revolution in a turn are reported.

## NOTATION

1. Roman Letters	Units	
$a$	equivalent aspect ratio: $2s/c$	$R'$ non dimensional radius $R/R_0$
$C_L$	lift coefficient $L_h/3\rho U^2 sc$	$R'_0$ initial value of $R'$ metres
$c$	hydroplane chord metres	$r$ yaw rate radians
$D$	maximum diameter of body metres	$r'$ non dimensional yaw rate $r/U = 1/R_T$
$\frac{dC_L}{d\alpha}$	lift curve slope radians <sup>-1</sup>	$s$ hydroplane outreach metres
$i$	$\sqrt{-1}$	$s_1$ lateral location of vortex relative to hydroplane root metres
$k$	parameter in Eq 2)	$t$ time: age of vortex seconds
$K$	calibration factor for Conrad tube	$U$ free stream velocity m/s
$L$	length of body metres	$v$ velocity component parallel to y axis m/s
$L_h$	hydroplane lift Newtons	$w$ velocity component parallel to z axis m/s
$P_i$	pressure measured at $i$ th tube of Freestone probe $N/m^2$	$\bar{w}$ complex conjugate velocity in y-z plane: $v-iw$ m/s
$P_w$	pressure at windward tube of Conrad tube pair $N/m^2$	$x_c$ longitudinal distance from quarter chord axis (positive downstream) metres
$P_L$	pressure at leeward tube of Conrad tube pair $N/m^2$	$x_B$ distance from nose of body metres
$a$	tangential velocity induced by vortex m/s	$x_{B1}$ distance from nose of body to start of vortex metres
$q_\delta$	induced velocity at $R=\delta$ m/s	$x_{B2}$ distance from nose of body to vortex shedding point metres
$R$	radius from vortex centre metres	$y_B$ location of body vortex relative to body axis normal to plane of incident flow metres
$R_h$	radius at which vorticity is half maximum metres	$y_c$ lateral distance from hydroplane root metres
$R_T$	turn radius metres	$z_B$ location of body vortex relative to body axis in plane of incident flow metres
$R_B$	radial distance from body axis to vortex centre metres	
$R_0$	vortex core radius: radius at which induced velocity is maximum	
$R_{00}$	initial value of $R_0$ metres	

$z_c$	vertical distance from hydroplane axis	metres	$\delta$	"radius" of vorticity probe	metres
$Z$	complex coordinate $v+iz$	metres	$\delta'$	non dimensional probe radius: $\delta/R_0$	
$z$	<u>Greek Letters</u>		$\epsilon$	eddy viscosity	$m^2/s$
$\alpha$	body incidence	radians or degrees	$\zeta_x$	streamwise vorticity	$seconds^{-1}$
$\alpha_N$	local incidence at nose	"	$\zeta_{x0}$	maximum value of $\zeta_x$	$seconds^{-1}$
$\alpha_T$	local incidence at tail	"	$\zeta'_x$	non dimensional vorticity: $\zeta_x R_0^2/\Gamma$	
$\beta$	hydroplane incidence	"	$\zeta'_{x0}$	non dimensional value of $\zeta_{x0}$	
$\Gamma$	vortex strength or circulation	$m^2/s$	$\zeta_{xop}$	Freestone probe measurement of peak vorticity	$seconds^{-1}$
$\Gamma_v$	strength of viscous vortex	$m^2/s$	$\theta$	angular location of vortex centre ( $0^\circ$ =windward side $180^\circ$ =leeward side)	radians or degrees
$\Gamma_p$	strength of potential vortex	$m^2/s$	$\theta_0$	separation angle (Fig 4)	radians or degrees
$\gamma$	"pitch" angle of flow direction relative to Conrad tube axis	radians or degrees	$\Lambda$	arbitrary constant (see Eq 21)	
$\Delta v$	difference in velocity $v$ measured across Freestone probe	$m/s$	$\rho$	mass density of water	$1000 \text{ Kg/m}^3$ (fresh water) $1025 \text{ Kg/m}^3$ (sea water)
$\Delta w$	difference in velocity $w$ measured across Freestone probe	$m/s$	$\chi$	vortex core angle parameter	radians
			$\psi$	"yaw" angle of flow relative to Conrad tube axis	radians or degrees

### Introduction

Modern high speed submarines must operate in a relatively restricted layer of water only a few boat lengths in depth; if the boat goes too deep it will collapse and be lost; if it inadvertently comes to the surface its presence may be revealed to a watchful enemy. Adequate depth control is therefore of paramount importance. In addition the boat must have adequate manoeuvrability in the lateral as well as the vertical plane to cope with tactical situations.

So the submarine designer needs to be able to predict the submerged manoeuvring, stability and control characteristics of a projected submarine at an early stage in the design process. The techniques used at present are comparable to those employed for studies of aircraft stability and control characteristics. An empirical mathematical model is used to relate the hydrodynamic forces and moments imposed on the submarine by the water to the instantaneous values of the submarine's velocities, accelerations and control deflections.

The fluid forces and moments are given in terms of coefficients or "derivatives" expressing the sensitivity of each force and moment to each velocity, acceleration and control deflection. The coefficients are usually determined from experiments in which a scale model of the submarine is forced to follow some specified path by a rotating arm or a planar motion mechanism. The forces and moments necessary to sustain the motion are measured and plotted as functions of the imposed velocities, accelerations and control deflections. Curve fitting techniques are then used to estimate the required coefficients. Non linear and cross coupling terms are introduced where required to improve the empirical representation of the results.

The number of possible combinations of motions which could be tested is enormous and in practice various simplifications are made: for example, the effect of simultaneous roll and yaw rates has never, to the authors' knowledge, been investigated although this combination of motion undoubtedly occurs during many submarine manoeuvres. Many other hydrodynamic situations which are customarily ignored could be cited.

The manoeuvring predictions obtained by this method are, of course, never totally accurate and this has led to the parallel practice of testing complete free running models of submarines to measure their manoeuvring performance directly. Such tests avoid many of the problems of the coefficient based approach but they suffer from their own brand of difficulties. In particular, very complex self contained models with facilities for remote control are required and most manoeuvring basins are not deep enough to allow realistic simulation of depth change manoeuvres.

Both approaches are time consuming and expensive. Typically, the process of building a model, testing, analysing and interpreting the results will require several months of intensive effort and the use of a good deal of expensive equipment. By the time the results are available the design will, as often as not, have been changed for non hydrodynamic reasons so that the resulting manoeuvring predictions by either method will be invalid.

## 2. The SUBSIM Program

SUBSIM is an alternative approach which is currently being developed at the Admiralty Research Establishment at Haslar, Gosport, UK. In this model the continually changing hydrodynamic forces and moments acting on the boat during the course of a manoeuvre are calculated directly from a knowledge of the surrounding flow field. The flow model and the resulting forces and moments are updated at successive intervals of time as the manoeuvre simulation progresses.

The problem of simulating the separated flow field around an arbitrary shaped body is the subject of active research at the present time and progress is being achieved. However, the practical implementation of these new techniques requires large and fast computer installations and even then a single flow solution is likely to require several minutes of cpu time. Since it may be necessary to compute the flow field several thousand times during a typical simulated manoeuvre, it is clear that this is unlikely to offer a practical method for the submarine designer in the foreseeable future. Some other much faster and perhaps less rigorous method is required for SUBSIM.

An early version of the mathematical model used in SUBSIM was described in Reference 1. Since that time the program has been developed and refined but the basic concepts remain unchanged. Classical theoretical (lifting line) techniques are used to compute the forces generated by the submarine's appendages (hydroplanes, rudders and bridge fin). Each appendage generates a trailing vortex which is convected towards the stern of the submarine by the boat's forward motion (see Figure 1). In addition there is a pair of "body" vortices which are shed from the hull when the angle of attack exceeds a few degrees.

Velocities in planes normal to the submarine's axis are computed using classical potential flow equations assuming that the hull cross section is circular. This technique allows the computation of the transverse velocities and hence the local incidence and forces generated by each appendage. The flow in these transverse planes is dominated by the vortices (in particular by those shed from the body, which are often very much more powerful than

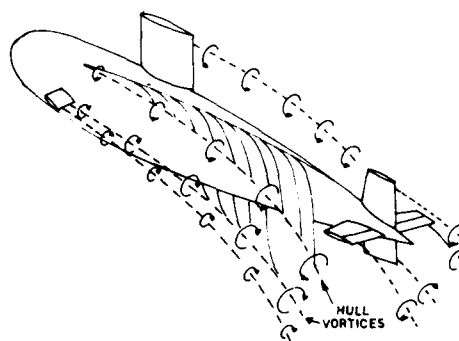


Figure 1  
Typical Pattern of Vortices  
on a Manoeuvring Submarine

the appendage vortices). It is therefore of paramount importance to represent these vortices correctly and this paper is concerned with model experiments to measure their strength and position on submarinelike bodies in turning manoeuvres.

## 3. Ideal Characteristics of Vortices

### 3.1 Equations for an Inviscid Vortex

Consider a vortex lying along the x axis as shown in Figure 2. The direction of the free stream velocity  $u$  is taken as parallel to the x axis and the vortex induces velocities  $v$  and  $w$  in transverse y-z planes. Figure 3 shows one of these transverse planes with the vortex located at the origin. A velocity

$$q = \sqrt{v^2 + w^2} \quad (1)$$

is induced at a radius

$$R = \sqrt{y^2 + z^2} \text{ metres} \quad (2)$$

from the origin.

Classical inviscid potential theory (see, for example, Reference 2) gives the induced velocity as

$$q = \Gamma / 2\pi R \text{ metres/second} \quad (3)$$

This leads to infinite induced velocity and shear at the origin (see Figure 3). In the context of the SUBSIM computer simulation this will yield very high induced incidence if a vortex is convected close to an appendage.

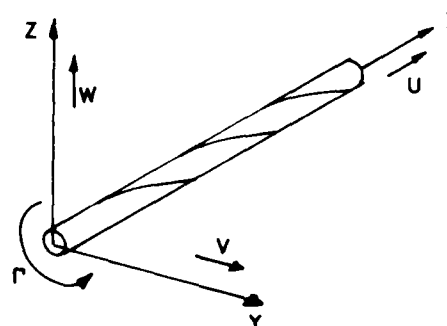


Figure 2  
Vortex Notation

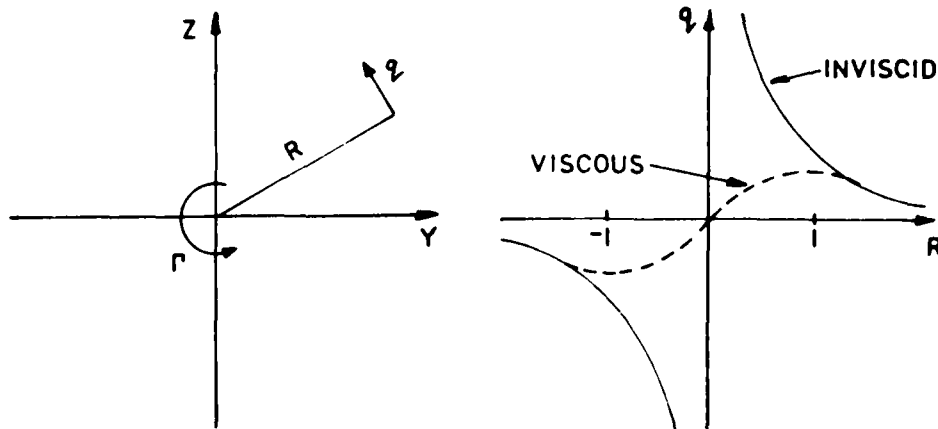


Figure 3  
Vortex Formulations

### 3.2 Equations for a Viscous Vortex

In practice viscous effects prevent these very large velocities occurring. The central part of the vortex is believed to rotate more or less as a solid core with the induced velocity close to the origin increasing linearly with the radial distance from the axis. This may be simulated by an empirical modification to Eq. (3).

$$q = \frac{\Gamma}{2\pi R} \left[ 1 - \exp \left[ -1.26 \cdot R'^2 \right] \right] \text{ metres/second} \quad (4)$$

where  $R' = R/R_*$  and  $R_*$  is the radius of the viscous core. The exponential term represents this effect by reducing the induced velocity to zero at the origin but allowing the velocity to approach its inviscid value at large distances from the origin. The factor 1.26 is introduced to ensure that the peak induced velocity occurs at the edge of the core, as shown in Figure 3.

Eq. (4) may be written in complex Cartesian terms as

$$\begin{aligned} \bar{w} &= v - iw = \frac{i\Gamma}{\pi Z} \left[ 1 - \exp \left[ -1.26 \frac{|Z|^2}{R_*^2} \right] \right] \\ &= \frac{-\Gamma}{2\pi(y^2 + z^2)} \left[ 1 - \exp \left[ -1.26 \frac{y^2 + z^2}{R_*^2} \right] \right] (z + iy) \text{ m/sec} \quad (5) \end{aligned}$$

Hence

$$v = \frac{-\Gamma z}{2\pi(y^2 + z^2)} \left[ 1 - \exp \left[ -1.26 \frac{y^2 + z^2}{R_*^2} \right] \right] \text{ m/sec} \quad (6)$$

$$w = \frac{\Gamma y}{2\pi(y^2 + z^2)} \left[ 1 - \exp \left[ -1.26 \frac{y^2 + z^2}{R_*^2} \right] \right] \text{ m/sec} \quad (7)$$

The vorticity at  $(v, z)$  is

$$\zeta'_x = \frac{\partial w}{\partial y} - \frac{\partial v}{\partial z} = \frac{1.26}{\pi R_*^2} \exp \left[ -1.26 \frac{y^2 + z^2}{R_*^2} \right] \text{ sec}^{-1} \quad (8)$$

or, in non dimensional terms

$$\zeta'_x = \frac{\zeta'_x R_*^2}{\Gamma} = \frac{1.26}{\pi} \exp \left[ -1.26 R'^2 \right] \quad (9)$$

The non dimensional vorticity is a maximum at the origin (0,0):

$$\zeta'_{x0} = 1.26/\pi = 0.401 \quad (10)$$

The non dimensional radius  $R'_h$  at which vorticity is half the peak vorticity is given by dividing Eq. (9) by Eq. (10):

$$\zeta'_x / \zeta'_{x0} = 0.5 = \exp \left[ -1.26 R'^2 \right]$$

which gives

$$R'_h = 0.742 \quad (11)$$

### 3.3 Equations for the Core Radius

It remains to determine the core radius  $R_*$ . Usually the vortex will have been created at some point upstream (say by a wing or a hydroplane) and the viscous core would be expected to age and grow as the fluid is convected away from the vortex birthplace. Reference 2 (and many other text books) give the induced velocity at radius  $R$  after time  $t$  as

$$q = \frac{\Gamma}{2\pi R} \left\{ 1 - \exp\left(-\frac{R^2}{4\epsilon t}\right) \right\} \text{ metres/second} \quad (12)$$

where  $\epsilon$  is the eddy viscosity. It follows that the core radius is

$$R_* = \sqrt{2.245\epsilon t} \text{ metres} \quad (13)$$

Rose and Dee suggested a modification to allow for an initial core radius  $R_{*0}$  in Reference 3:

$$R_* = \sqrt{R_{*0}^2 + 5.05\epsilon t} \text{ metres} \quad (14)$$

Grow investigated the trailing vortex system behind a series of model wings in a wind tunnel in Reference 4. The test wings all had a NACA 0012 section and included a set of rectangular planform wings with aspect ratios varying from 2.0 to 6.0. Reynolds number was  $0.35 \times 10^6$ . McCormick, Tangler and Sherrieb (Reference 5) found that Grow's measurements could be fitted by

$$R_{h0}/c = 0.02 + 0.35 C_L \quad (15)$$

or using Eq (11)

$$R_{*0}/c = 0.027 + 0.47 C_L \quad (16)$$

### 3.4 Lift and Circulation

The lift coefficient  $C_L$  may be estimated for low aspect ratio surfaces from Whicker and Fehlners formula for the lift curve slope (Reference 6):

$$\frac{dC_L}{d\alpha} = \frac{1.8\pi a}{1.8 + \sqrt{4 + a^2}} \text{ per radian} \quad (17)$$

The total circulation associated with a single hydroplane mounted on a plane wall is given by

$$\Gamma = L_h / \rho U s_1 \quad (18)$$

where  $s_1$  is the distance from the horseshoe vortex to the wall (see Reference 7). For elliptic loading Reference 7 gives

$$s_1 = \pi s / 4 \quad (19)$$

The total circulation is related to the vorticity by:

$$\Gamma = \int_{-\infty}^{\infty} \int_{-\infty}^{\infty} \zeta_x \, dy \, dz \text{ metres}^2/\text{second} \quad (20)$$

### 3.5 Body Vortices

Figure 4 shows the generally accepted understanding of the body vortices. When the body is at an appreciable angle of incidence (say 10 degrees) the boundary layer on part of the leeward surface separates. The location of the separation line may be quantified in terms of a "separation angle"  $\theta_0$ . Vorticity shed from the boundary layer is convected away and coalesces to form a somewhat diffuse pair of vortices whose cores are more or less parallel to the axis of the body. The strength of these vortices increases towards the tail of the body as more and more vorticity is added. In this respect the body vortices have a fundamentally different character from the appendage vortices which have essentially constant strength (apart from any variations due to changes in lift) and are much less diffuse. Eventually the vortices are shed from the immediate vicinity of the body and convected away downstream. After this point the strength

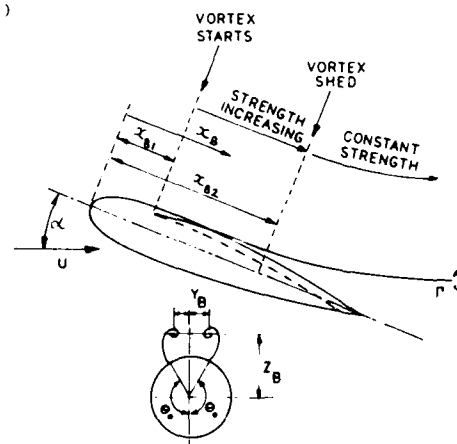


Figure 4  
Body Vortex Notation

remains constant because no more vorticity is added. If the body is sufficiently long and/or the incidence is sufficiently high, further vortices will begin to grow downstream of the shedding point and, in turn, be shed into the surrounding fluid. At very high angles of incidence an asymmetric pattern of vortices may develop giving rise to both steady and fluctuating side forces as well as the expected forces in the plane of the flow. Fortunately the angles of incidence experienced by submarines do not usually approach the levels at which these complicated phenomena begin to occur and they have been specifically excluded from SUBSIM.

### 3.6 Body Vortex Position

The aeronautical literature contains accounts of many experiments to measure the location of these vortices. Some examples are listed as References 8-11. In general, these experiments were intended to provide data for use in the design of missiles and were concerned with bodies with pointed noses and blunt tails and were often limited to supersonic speeds. Submarines invariably have rounded noses, pointed tails and operate firmly in the subsonic regime. The missile data were therefore not really appropriate although the techniques used and the general nature of the results obtained were, of course, of some interest.

Some simple flow visualisation experiments were therefore carried out to provide data on more appropriate body shapes. Three bodies of differing fineness ratios were tested in the Circulating Water Channel at ARP (Haslar). Details of the bodies are given in Tables 1 and 2 and they are illustrated in Figure 5. Each body had the same distribution of radius relative to the maximum radius and incorporated a lengthy parallel middle section.

The bodies were tested in rectilinear flow at angles of attack from 10 to 15 degrees at a flow velocity of 4.6 metres/second giving a Reynolds number (based on length) of  $5.8 \times 10^6$ . It was found that no special measures were necessary to make the vortices visible: their presence was plainly revealed by bubbles in the flow collecting in the cores as shown in Figure 6. Photographs of this nature were analysed to produce measured vortex trajectories. Examples for Models DMH and DMI (fineness ratios 10.5 and 12.5) are shown in Figure 7.

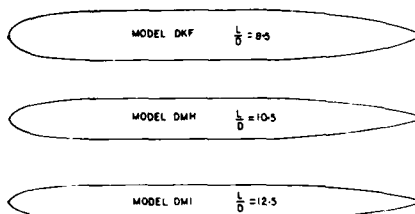


Figure 5  
Three Bodies of Revolution

### 3.7 Body Vortex Strength

The measurement of the strength of the vortices was not attempted because the required sophisticated instrumentation and data analysis facilities were not at that time available. Instead a formula proposed by Fidler (Reference 12) was used to estimate vortex strength. Fidler proposed that the total strength of each of these "viscous" vortices shed from the hull surface could be represented by

$$\frac{\Gamma_v}{(U)D} = \frac{A \sin \alpha}{2(\cot^2 \alpha + 1)^{1/2}} \int_{x_{R1}/D}^{x_{R2}/D} \frac{dx_B}{x_{R1}/D} \quad (21)$$

(see Figure 4 for an illustration of the notation).

A is an arbitrary constant defined as the ratio of the net vorticity flux away from the body to the vorticity flux in the cross flow boundary layer. Fidler suggested a value

$$A = 0.5 \quad (22)$$

$\alpha$  is the "vortex core angle parameter" which is given by Fidler as a function of the cross flow Mach Number. For zero Mach Number (applicable to submarines)

$$\alpha = 0.81$$

k is a parameter relating the cross flow velocity on the surface of the body to the free



Figure 6  
Vortices on a Body of Revolution

stream cross flow velocity and is given as a function of the separation angle  $\theta_0$  in Figure 8. Figure 9 gives Fidler's proposed relationship between  $\theta_0$  and the angle of incidence.

The integration between the limits  $x_{B1}/D$  and  $x_{B2}/D$  relates to the axial distance over which the vortex strength is growing before it is shed into the surrounding fluid. Clearly the vortex strength at some location upstream of the shedding point is given by integrating up to the appropriate value of  $x_B/D$ . In general, submarine fineness ratios are such that for moderate angles of incidence (say up to 10 degrees) the viscous vortices are not expected to be shed until they reach the tail of the body. Hence Fidler's formula may be used to estimate the viscous vortex strength at any location  $x_B$  by replacing the upper integration limit by  $x_B/D$ .

Fidler and Bateman point out in Reference 13 that there is, in addition, a pair of "potential" vortices arising from the normal force generated on the nose of the body. They give the potential vortex strength as

$$\Gamma_{PT}/UD = \pi \sin \alpha (2 \cos \alpha + \sin^2 \alpha) / 8 \quad (24)$$

For the purposes of the SUBSIM program it was assumed that the potential vortex strength grows at a constant rate from bow to stern until it reaches the value given by Eq. (24) at the tail of the body. In this case the potential vortex strength at a location  $x_B$  is given by

$$\Gamma_{PT}/UD = x_B \sin \alpha (2 \cos \alpha + \sin^2 \alpha) / 8L \quad (25)$$

Reference 14 gives the axial location at which the viscous vortices start to develop as

$$x_{B1}/D = 0.6 / \tan \alpha \quad (26)$$

for zero Mach Number

If the separation angle is assumed to be independent of  $x_B$  the parameter  $k$  is constant and the formulae derived above reduce to

$$\frac{\Gamma}{UD} = \left( \frac{x_B}{8L} \right) \sin \alpha (2 \cos \alpha + \sin^2 \alpha) \left( \frac{x_B}{D} \right)^k$$

$$\text{for } \frac{x_B}{D} < \frac{x_{B1}}{D} \quad (27)$$

or

$$\frac{\Gamma}{UD} = \left( \frac{x_B}{8L} \right) \sin \alpha (2 \cos \alpha + \sin^2 \alpha) \left( \frac{x_B}{D} \right) + \frac{k^2 \sin \alpha}{2(\cot^2 \alpha + k^2)^{1/2}} \left( \frac{x_B}{D} - \frac{0.6}{\tan \alpha} \right)$$

$$\text{for } \frac{x_B}{D} > \frac{x_{B1}}{D} \quad (28)$$

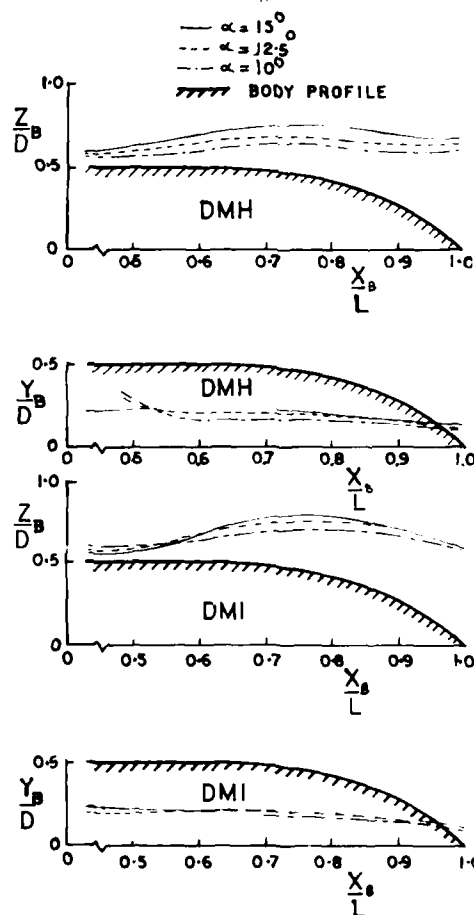


Figure 7  
Vortex Trajectories on Models DMH and DMI

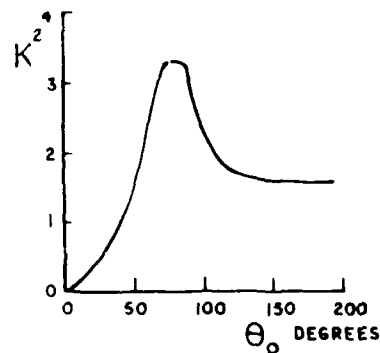


Figure 8  
Parameter k

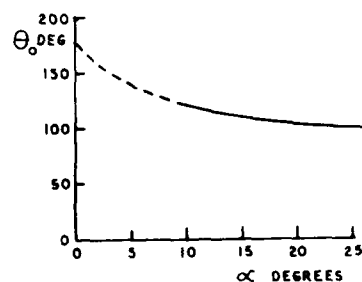


Figure 9  
Variation of Separation Angle  
with Angle of Incidence

Eq (28) is plotted for three different angles of incidence in Figure 10 and compared with the results of experiments published in References 8-11. Reasonable agreement is obtained by setting the arbitrary constant as

$$\Lambda = 0.9 \quad (29)$$

### 3.8 Use of Body Vortex in SURSIM

The body vortex trajectory data shown in Figure 7 were incorporated in the SURSIM program to provide estimates of the vortex location during simulated manoeuvres. Eq (28) was used to estimate the body vortex strength.

Neither of these techniques could be regarded as wholly satisfactory. The vortex strength data are largely based on experiments at supersonic speeds on bodies of inappropriate shape and both data sets were obtained in rectilinear flow with no curvature. A manoeuvring submarine's turning circle diameter may well be only a few times the boat length and the angle of incidence may vary appreciably from bow to stern. Clearly this curvature should be taken into account in these estimates and this paper describes experiments to measure the characteristics of vortices shed from a submarine like body in both rectilinear and curved flows.

## 4. Vortex Measurements

### 4.1 Orthodox Methods of Measuring Vortices

The simplest method of measuring vortices involves the use of a small vane wheel free to rotate about an axis aligned with the vortex core. Optical counting methods are used to measure the rate of rotation of the wheel which spins when it is close to the centre of the vortex. This will give an accurate measurement of the location of the vortex core but it may be less than adequate for determining the vortex strength.

More complex methods of measuring vortices involve several hundred measurements of local flow velocities and directions in order to build up a vector map of the flow field around the vortex. These may be obtained from systematic traverses using hot wire yaw meters or five hole pitot probes. Such techniques require well organised data processing facilities to handle the enormous amounts of data produced. Laser doppler methods are now becoming available and these, too, might be capable of producing the required information with the penalty of high capital and development costs.

Consideration was given to developing systems of this nature but they were rejected in favour of a much simpler and more convenient technique proposed by Freestone in Reference 15.

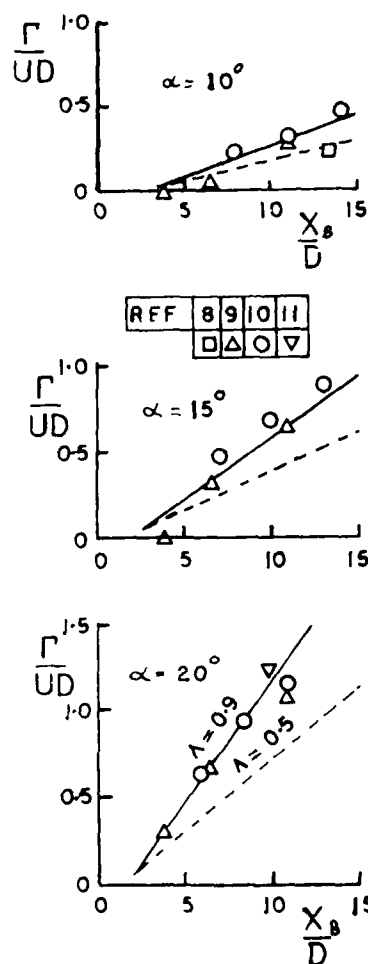


Figure 10  
Body Vortex Strength



#### 4.2 The Freestone Vorticity Probe

Freestone's vorticity probe is a development of the Conrad tube yaw meter illustrated in Figure 11. This consists of a pair of total head tubes whose faces are chamfered at an angle of order 45 degrees. The pressure difference measured across the two tubes is found to be sensitive to changes in the flow direction in the plane of the tubes (ie the angle  $\psi$  in Figure 11) but not to changes in the flow direction in the plane normal to the tubes (the angle  $\gamma$  in Figure 11). Freestone assumed that the response of the tubes could be written as

$$P_W - P_L = K \rho U^2 \tan \psi \quad \text{N/m}^2 \quad (30)$$

Freestone found that the calibration factor  $K$  lay in the range 2.47 - 2.72 for tubes chamfered at 45 degrees. Presumably the variations are caused by small errors in manufacturing tolerance.

Figure 12 shows the essential features of Freestone's vorticity probe. Four Conrad tube yaw meters are arranged around a central longitudinal axis. Suitable combination of the pressures measured by the tubes yields a pressure difference which is proportional to the streamwise vorticity.

Freestone showed that the streamwise vorticity is given, to first order, by

$$\zeta_x = \partial w / \partial y - \partial v / \partial z \quad (31a)$$

$$= \Delta w / 2\delta - \Delta v / 2\delta \quad (31b)$$

$$= \frac{\Delta P}{\frac{1}{2} \rho U^2} \frac{U}{2K\delta} \quad \text{seconds}^{-1} \quad (31c)$$

where  $\delta$  is the probe "radius" as defined in Figure 12.  $\Delta P$  is the difference of the "sum of the odd numbered pressures" and the "sum of the even numbered pressures":

$$\Delta P = \sum_{i \text{ odd}} P_i - \sum_{i \text{ even}} P_i \quad (32)$$

It is convenient to connect all the odd numbered tubes to a common plenum chamber and all the even numbered tubes to a second plenum chamber. Freestone showed that, subject to certain easily satisfied conditions, the pressure difference between the two plena is

$$\Delta P \approx \Delta P / 4$$

and Eq (31c) becomes

$$\zeta_x = \frac{\Delta P}{\frac{1}{2} \rho U^2} \frac{2U}{K\delta} \quad (33)$$

It is convenient to incorporate a pitot static tube on the axis of the probe so that the dynamic pressure and the velocity can be measured at the same time as the vorticity.

#### 4.3 Predicted Performance of the Freestone Probe

If the Freestone probe is positioned at the centre of the vortex its output will be determined by Eq (31b) with

$$\Delta w = -\Delta v = q_\delta \quad (34)$$

where  $q_\delta$  is the induced velocity at a radial distance  $\delta$  metres. The Freestone probe should therefore give an estimated non dimensional peak vorticity

$$\zeta_{xop} = 1/\pi\delta'^2 (1 - \exp(-1.26\delta'^2)) \quad (35)$$

where

$$\delta' = \delta/R_v \quad (36)$$

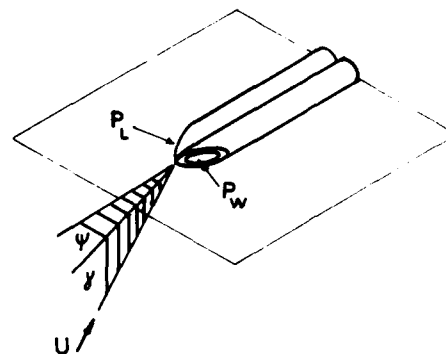


Figure 11  
The Conrad Tube Yaw Meter

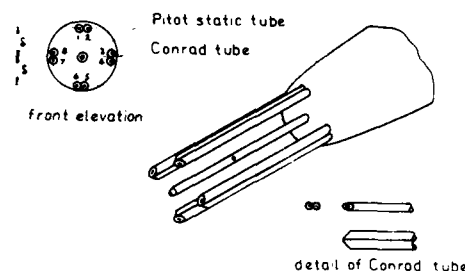


Figure 12  
The Freestone Vorticity Probe

Eq (35) may be rearranged to give

$$R_*/\delta = 1/\sqrt{-0.794 \log_e(-1 \pi \zeta_{xop} \delta^2/r)} \quad (37)$$

and this relationship is plotted in Figure 13. It allows the core radius to be estimated from measurements of the peak vorticity.

The true non dimensional peak vorticity is given by Eq (10). Relating this to Eq (35) we obtain the ratio of the measured and true peak vorticities in an ideal viscous vortex:

$$\frac{\zeta_{xop}}{\zeta_{xo}} = \frac{1 - \exp(-1.26 \delta')}{1.26 \delta'^2} \quad (38)$$

This relationship is plotted in Figure 14 and suggests that the probe radius should be kept as small as possible to minimise errors in the estimation of peak vorticity. For example, a probe radius equal to the core radius would be expected to underestimate the peak vorticity by over 40%. However, in practice very small probes may be undesirable because the measured pressure difference is proportional to the probe radius (as can be seen from Eq (33)). Extremely sensitive pressure transducers may therefore be required for such probes.

The effects of the finite size of the Freestone probe were further studied using a computer simulation based on Eq (31b). The program was used to calculate the vorticity levels expected from traversing the probe through an ideal viscous vortex as defined by Eq (4). Typical results are shown in Figure 15. A probe with an infinitesimal radius gives, of course, an exact reproduction of the vorticity. As the probe radius is increased (relative to the vortex core radius) the measured peak vorticity is reduced as already shown by Eq (38). However, the vorticity measurements obtained well away from the core are then too high and for very large probes it may be impossible to detect the centre of the vortex. It was also noted that the simulation predicted that the probe would produce a small negative output at the edge of the vortex.

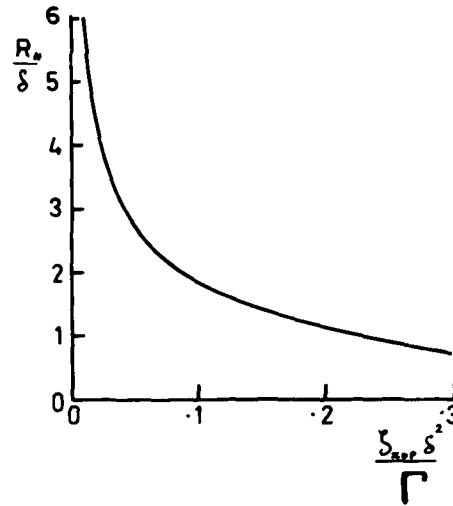


Figure 13  
Vortex Core Radius Estimation Diagram

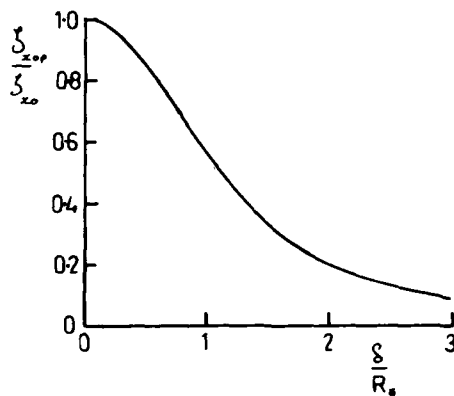


Figure 14  
Effect of Probe Radius on Measured Peak Vorticity

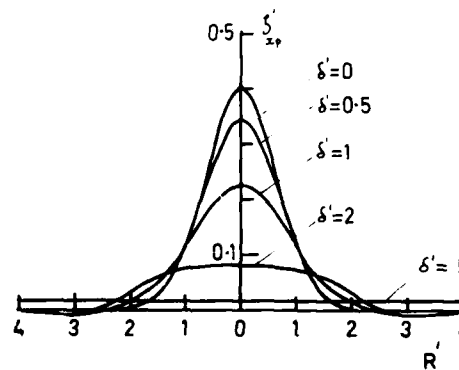


Figure 15  
Simulated Vorticity Probe Traverse through  
an Ideal Viscous Vortex

The program was also used to estimate the effects of probe size on the validity of integrating the measured vorticity to obtain the total circulation using Eq (20). Probe radius was found to have surprisingly little effect on the result in spite of the failure of the larger probes to detect the peak vorticity. Evidently the high measured vorticity levels well away from the core are sufficient to compensate for this loss more or less exactly.

#### 4.4 Design and Testing of a Freestone Probe

In order to gain some practical experience a prototype Freestone probe, designated probe A, was manufactured to the design shown in Figure 16. Probe radius was 5 mm. The individual tubes were not connected together so that the performance of each Conrad tube yaw meter could be determined by yawing the probe in uniform flow. Figure 17 shows a typical set of results obtained in the Circulating Water Channel at ARE (Haslar). These confirm the relationship suggested by Freestone in Eq (30).



Figure 16  
Prototype Vorticity Probes

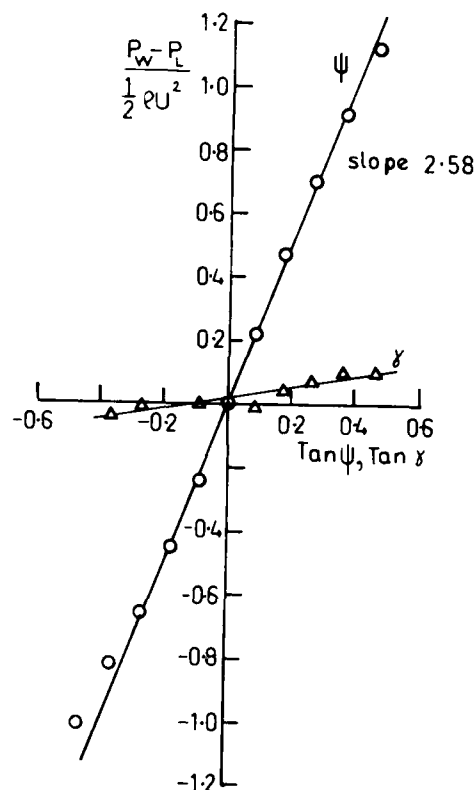


Figure 17  
Conrad Yawmeter Calibration

The separate tubes in this probe required eight long small bore plastic tubes to transmit the "vorticity" pressures to external manifolds which were, in turn, connected to the transducer located outside the channel. In addition, a further pair of tubes was required for the pitot static tube pressures. Since the probe was used in water it was necessary to fill these tubes completely with water to ensure that all air bubbles had been purged from each tube. Moreover, the great lengths of tubes made the response of the probe very sluggish.

An improved 5 mm probe, designated probe B, was therefore manufactured. In this probe the individual tubes of each yaw meter pair were connected to a plenum chamber within the central body of the probe. Only two tubes were then required to transmit the required "vorticity" pressure difference to the external pressure transducer. These tubes were of somewhat larger diameter than those used for the prototype probe and the response time of the instrument was much improved.

It was impossible to calibrate the individual tubes in this probe and a nominal calibration factor

$$K = 2.5$$

(39)

was assumed for all subsequent measurements.

Subsequent experience with this probe showed that it gave spurious vorticity readings when yawed or pitched in a uniform flow. This was attributed to small differences in the alignment of the yaw meter tubes on the opposite sides of the probe and the quality of the finish of their chamfered ends. It is also possible that the wake of the central pitot static tube may have interfered with the leeward yaw meter tubes. It was also found in the ship tank experiments (Section 6) that the pressure differences measured with this probe were rather small.

A third probe, designated probe C, was therefore manufactured to the same general design but with radius 10 mm. This is illustrated in position on the model body of revolution in Figure 18. It was expected that the larger size would allow better accuracy of manufacture and give greater pressure differences for the same vorticity levels (see Eq (33)).

5. Experiments to Determine the Behaviour of the Vortex Shed by a Hydroplane at an Angle of Incidence

The 5 mm probe B was tested in the Circulating Water Channel at ARE Haslar. A simple hydroplane, shown in Figure 19, was used to generate a suitable vortex. These experiments provided useful experience with the new techniques required and also yielded valuable information on the behaviour of the vortex shed by a hydroplane.

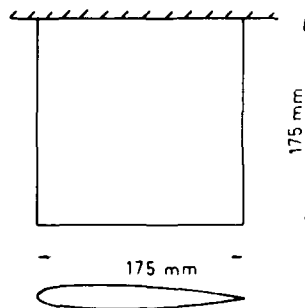


Figure 19  
Hydroplane

Pressures were measured using suitable differential pressure gauges and the signals were processed on line using a RRC Model B microcomputer. This was programmed to calculate the vorticity from Eq (33) and the local velocity from the pitot static tube measurements. The program allowed the vorticity results from each traverse to be displayed graphically on the terminal screen and this facility was an invaluable aid during the experiments.

Preliminary flow visualisation experiments were used to reveal the location of the vortex. This was accomplished by injecting air bubbles through a small diameter tube upstream of the hydroplane: the bubbles collected in the vortex core making it plainly visible. It was found that although the vortex appeared to be quite steady immediately behind the hydroplane it became progressively more unsteady towards the downstream end of the working section. This appeared to be due to a relatively high level of large scale turbulence in the channel.

The experiments were conducted with water speeds in the range 3.0 - 5.0 metres/second giving a Reynolds number range (based on hydroplane chord) from  $0.44 \times 10^6$  to  $0.75 \times 10^6$ . Angles of incidence of 10.5 and 20.5 degrees (leading edge up) were used and vorticity traverses were completed at various locations downstream of the hydroplane stock axis. The results of one such traverse through the estimated centre of the vortex are shown in Figure 21 and Figure 22 shows a contour plot of vorticity obtained at this downstream location. This shows an approximately circular vortex with a well defined peak vorticity of about  $580 \text{ sec}^{-1}$ .

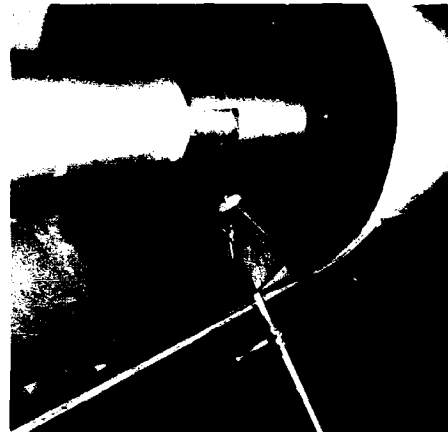


Figure 18

10 mm Vorticity Probe on Model

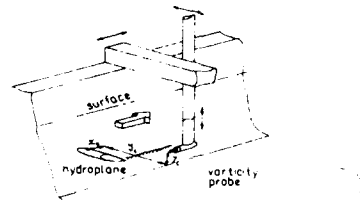


Figure 20  
CWC Rig

Figure 20 shows the experiment rig used. The hydroplane was mounted on the channel wall close to the upstream end of the working section. The vorticity probe was mounted on a simple x-y-z traverse mechanism so that it could be positioned at any selected location in the channel.

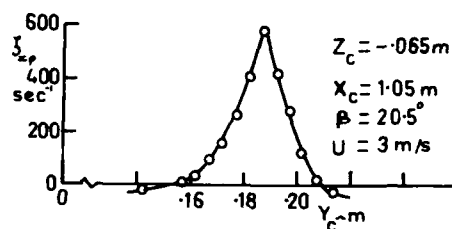


Figure 21  
Transverse Distribution of Vorticity  
behind Hydroplane

The positive vorticity contours were integrated to obtain the estimated total circulation in the vortex (see Eq (20)).  $\Gamma = 0.22 \text{ metres}^2/\text{second}$ . This was about 77% of the circulation expected from the estimated lift of the hydroplane (Eqs (17)-(19)).  $\Gamma = 0.29 \text{ metres}^2/\text{second}$ .

This result was considered to be quite encouraging in view of the simple method used to estimate the hydroplane lift and the uncertainties associated with possible ambient vorticity in the flow.

The peak vorticity was measured at a number of locations and water speeds and the results are shown as a function of the vortex age ( $t = x_c/U$ ) in Figure 23. These show that the measured peak vorticity decays as the vortex is convected downstream. Eq (37) has been used with these results to estimate the vortex core radius and the results are compared with predictions using Eqs (14) and (16) in Figure 24.

Eq (16) gives a very good estimate of the initial core radius as the vortex is shed from the trailing edge of the hydroplane. However, the subsequent growth of the core is not well predicted by Eq (14) with any value of the eddy viscosity. It is believed that this is caused by the large scale turbulent eddies revealed by the flow visualisation experiments described above. These caused the vortex to meander as it passed down the channel resulting in an underestimation of the peak vorticity, giving overestimates of the core radius. The estimated initial core radius will not have been affected very much by this phenomenon because the vortex was much steadier immediately behind the hydroplane.

#### 6. Experiments to determine the behaviour of the vortices shed from a body of revolution in rectilinear flow

##### 6.1 Introduction

Although, as already discussed, the investigation was concerned with the flow around a body of revolution in a curved path, a preliminary set of experiments was conducted in rectilinear flow in No 2 Ship Tank at ARE (Haslar). A 5m model, designated DOR, was used in the experiments.

This model had a fineness ratio of 8.5 and was geometrically similar to Model DRF described earlier. The model was tubulated using standard pins placed near the nose and was generally tested at a speed of 2 m/s yielding a Reynolds Number of  $1.0 \times 10^6$  based on diameter.

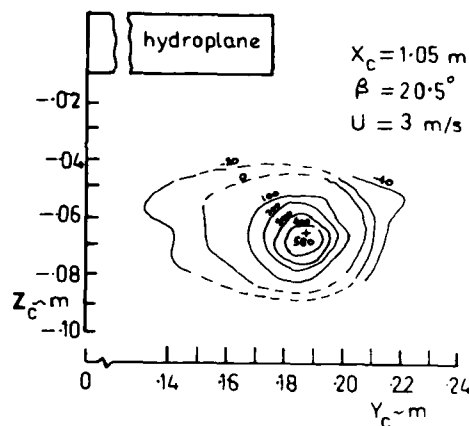


Figure 22  
Vorticity Contours Behind Hydroplane

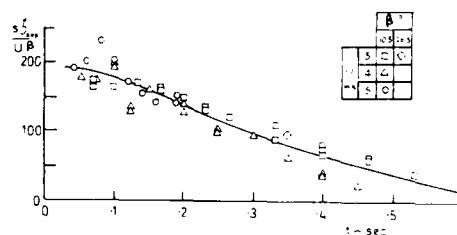


Figure 23  
Decay of peak vorticity

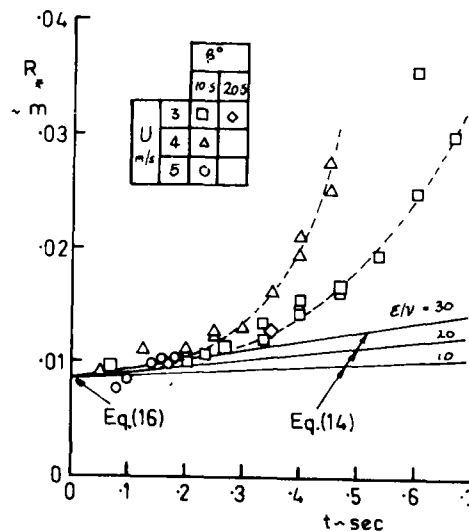


Figure 24  
Estimated Growth of Vortex Core Radius

These experiments provided valuable experience in the design and manufacture of the required equipment and in the development of suitable experimental techniques. Many improvements to the model, the Freestone probe and its traversing mechanism were made prior to embarking on the experiments in curved flow described in Section 7.

The rectilinear flow results could have been obtained more readily from wind tunnel tests. These would have allowed indefinite running during which the probe could have been traversed through the vortices continually. In contrast, the restricted usable length of the Ship Tank (about 100 metres) limited the number of measurements which could be obtained in one run. However, the towing tank provided more relevant experience for the subsequent Rotating Arm tests and, in spite of reservations about the accuracy and applicability of the results, revealed many interesting features of the shed vortices.

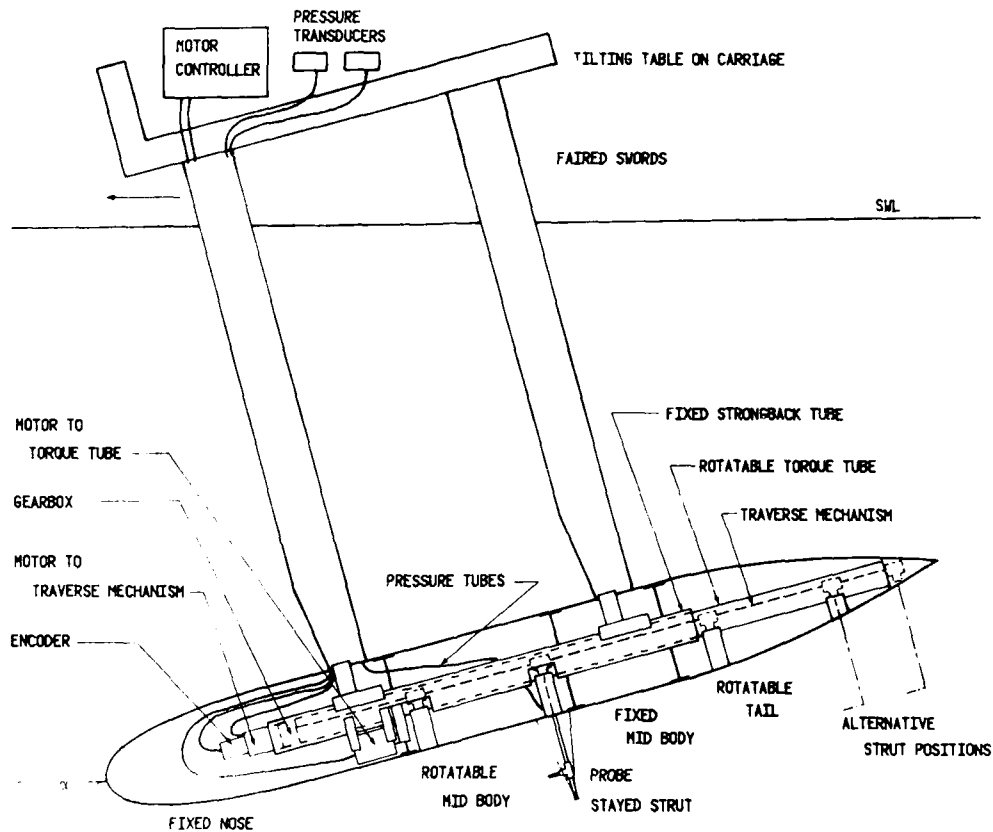


Figure 25  
Schematic Arrangement of Model for Towing Tank Experiments

## 6.2 Experimental Rig

The system designed to traverse the Freestone probe through the vortex was fitted to the model rather than remotely mounted from the towing carriage. This provided a sturdy arrangement which ensured accurate positioning of the probe relative to the body and which was suitable for use both in the towing tank and on the Rotating Arm. However, with such an arrangement there were necessarily interruptions in the smooth surface of the body and the probe remained aligned with the body axes rather than with the undisturbed flow.

A general arrangement of the experimental rig is shown in Figure 25 from which it can be seen that the Freestone probe was traversed radially from the body along a stayed circular strut. This strut was mounted in alternative positions along the axis of the body. Since the body had circular sections it was possible to arrange the strut to rotate with segments of the GRP skin rather than through slots in the skin. The skin was divided into four segments: a fixed nose; a rotatable parallel mid body; a fixed after body; and a rotatable tail. Sliding seals were fitted at the three circumferential joints between the segments but imperfections in the roundness and

concentricity of the segments prevented these seals from lying flush with the skin at all points around the circumference.

The Freestone probe was traversed along the strut by a lead screw rotated by a stepper motor and its position was monitored from a shaft encoder. The strut and skin segments were also rotated by a stepper motor mounted inside the model but their angular position was monitored using marks around the fixed and rotating segment.

The differential pressure and the pitot static pressure produced by the Freestone probe were transmitted via water filled plastic tubes to transducers mounted on the carriage. Careful consideration was given to the design of the strut. Obviously it was desirable to keep the strut as small as possible to minimise its intrusion in the flow; but it was also necessary to have a strut stiff enough to minimise the bending caused by the drag force and the oscillations caused by its own vortex shedding. In addition the strut had to accommodate the pressure tubes from the Freestone probe which were led inside and on into the model. The 19 mm diameter stainless steel circular tube selected did not oscillate noticeably but proved to be rather small to contain both the lead screw and the pressure tubes. The use of a streamlined strut section was rejected because of the effect on the general flow of the lift that would be generated from the incidence of the strut to the flow.

The pressures were measured from two low range wet/wet differential transducers. These commercially available French built Elec Torr FA64 transducers were relatively large at approximately 100 mm diameter but had the advantage of being rugged so could tolerate the high over-pressure produced when air was bled from the 1.5 mm diameter pressure tubes. The pitot pressure was measured using a transducer with 100 mb range. However, the pressure from the Freestone probe was considerably less so a transducer with only a 10 mb range was used. Because this system contained a relatively large volume of water and was flexible, it was found necessary to leave a settling time of several seconds between pressure measurements although the frequency response was considerably faster than this.

The measurement system was based around an Apple II europolis microcomputer which was used to: command the stepper motor controller, read the encoder, acquire the signals from the pressure transducer, and operate on the data. By using such a system it was possible to obtain data from up to four probe positions during one run down the tank. Each pressure measurement was the arithmetic average of several seconds of acquired data and inspection of these data showed them to contain a number of pressure fluctuations which changed in character depending upon the proximity of the measurement to the vortex core.

### 6.3 Vorticity Measurements

Measurements were made at sections located 50%, 85% and 92.5% of the body length aft from its nose and at various incidences between 5 and 20 degrees in pitch.

Since the output from the Freestone probe, when suitably processed, gave a direct measure of the vorticity it was possible to search for the peak of the vortex during the tests without having to map the entire flow. The results from a set of traverses at the tail of the body are shown in Figure 26 and the position of the peak vorticity can be clearly identified. However, because the levels of vorticity measured were small, the inaccuracies in the Freestone probe, previously discussed in section 4.4, caused some uncertainty regarding the extent of the vortex and the position of the measured peak. It became clear from measurements made away from the wake of the body, at up to twice the body radius from its centre, that the output from the Freestone probe in zero vorticity varied with the incident flow speed and direction. Corrections were made for the flow speed based on the pitot pressure obtained at each position but the effect of incident flow direction could only be assessed near the outer edge of the vortex. These probe errors were subsequently investigated in wind tunnel tests on the probe and its design was developed and performance thus considerably improved prior to the tests in curved flow.

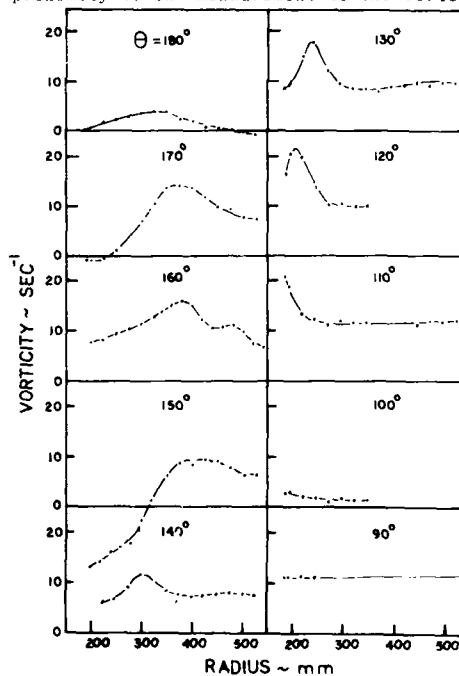


Figure 26  
Vorticity Traverses in Rectilinear Flow.  
 $x_B/L = 0.925$ ;  $\alpha = 15$  degrees

Information on the vortex trajectory obtained from earlier flow visualisation

experiments, conducted in the Circulating Water Channel, was used to help in the search for the vortex centre and a comparison of the results is given in Figure 27. It should be noted that the incidence to the flow of 15 degrees was rather high and subsequent investigations have given additional information about the vortex positions.

Tests at 10 and 20 degrees of incidence showed the vortex position to move slightly away from the body with incidence and for the peak vorticity to increase as expected. However, no vortex could be detected in this region at 5 degrees incidence, albeit from only limited measurements near the tail of the body.

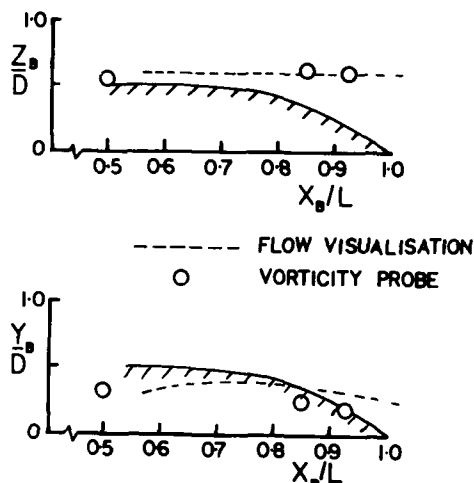


Figure 27  
Comparison of Estimated Vortex Centres  
from Towing Tank and Circulating Water  
Channel Experiments.  $\alpha = 15$  degrees

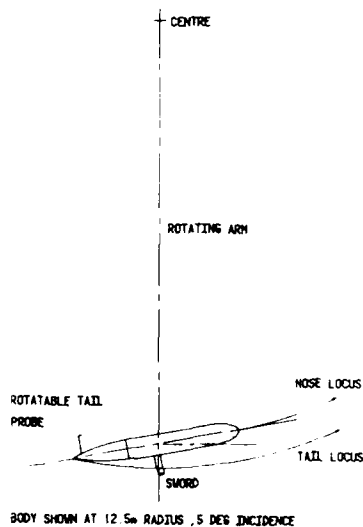


Figure 29  
Schematic Arrangement of Model for  
Rotating Arm Experiments

A new Freestone probe (probe C) was built with a radius of 10 mm in order to double the

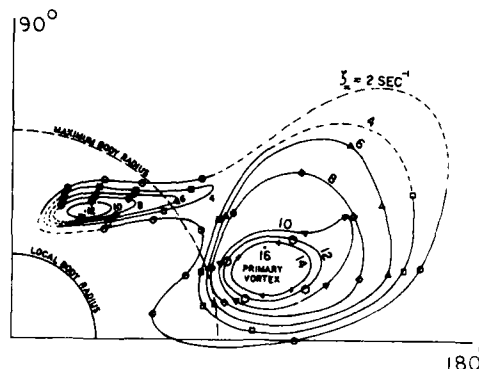


Figure 28  
Vorticity Contours in Rectilinear Flow,  
 $x_B/L = 0.925$ ;  $\alpha = 15$  degrees

A simple procedure for correcting the vorticity measurements for the effects of flow direction at the probe was developed and this enabled the plot of vorticity contours shown in Figure 28 to be produced from the traverses shown in Figure 26. It became apparent that there was a significant region of vorticity rather closer to the body and further around towards the windward side than had been anticipated. This appeared to be a second smaller vortex. Unfortunately no measurements were made in this region at 5 degrees incidence at which it was possible that only one vortex existed. The measurements in curved flow, to be discussed later, have indicated only one vortex to be present with its centre near that of the second vortex found in rectilinear flow.

#### 7. Experiments to determine vortices shed by a body of revolution in curved flow

##### 7.1 Experimental rig

The model DOR, previously tested in the towing tank, was suitably modified and attached to the Rotating Arm at ARE (Haslar) via a sword positioned on the outboard side of the model as shown in Figure 29. Measurements were made on the inboard side of the turn with the drift angle  $\alpha$  set with the nose pointed into the turn.

The outer skin of the model was refaired and arranged so only the tail section rotated. The out of roundness of the tail and body at this joint were measured to be 2 mm. However, the concentricity was adjusted such that when the tail rotated through the measurement range the local discontinuity between the skins was less than 3 mm.



output and halve the effect of any manufacturing inaccuracies. The new probe also incorporated a larger pitot tube from which it was possible to make static measurements. The whole probe and strut assembly was tested in a wind tunnel at various incident flow angles and a calibration was determined for the pitot static tube.

A larger strut was built, to accommodate measurements out to a radius of  $1.5 \times$  body diameter, and the strut diameter was increased to 32 mm.

The traversing mechanism was improved and the pressure tubes from the probe left free to stream behind the strut before entering the model. These changes allowed the probe to be traversed faster, which was of some importance because the run time was restricted to one turn of the Rotating Arm to avoid contaminating the results by re-entering the wake from the previous turn. Depending on the test radius, it proved possible to take measurements at three or four positions at a radial spacing of 25 mm. This was the optimum for the vortex size given the run time and the times required to traverse the probe, allow the pressures to settle and acquire data for a reasonable period.

## 7.2 Vorticity Measurements

A comprehensive set of measurements was taken at each of the conditions summarised in Table 3. The probe was traversed from close to the body through to the outer edge of the vortex at angular intervals of  $\theta = 10$  degrees and within a quadrant on the leeward side of the tail from  $\theta = 90^\circ$  to  $\theta = 180^\circ$ . A typical set of vorticity measurements is shown in Figure 30.

The inboard measurement positions were limited to the probe radius plus a margin dictated by the operation of the traverse gear, so estimates of the vorticity very close to the body were made by extrapolation and cross fairing of all the measurements. The vorticity measured away from the wake of the body, at  $1.5D$  from its centre, varied with incidence and strut angle by up to 4 rad/s from the nominal zero. This variation was considerably less than found in the tank tests and its characteristics were more regular. It therefore proved possible to make suitable corrections to each vorticity traverse. Figure 30 shows the estimated effective zero vorticity level for each traverse.

The dynamic pressure and hence local flow speed were also measured during each traverse. These tended towards the free stream values away from the body but within the region of high vorticity and close to the body the measured values reduced considerably from those in the free stream.

Contours of constant vorticity were derived from the traverse plots. The example shown in Figure 31 was plotted from the data shown in Figure 30. Contours close to the body, which were estimated using extrapolated data, are shown dotted in Figure 31. A contour of negative vorticity relative to the main area of vorticity is also shown in Figure 31. In some regions this may just have been an output from the probe caused by its size as discussed in Section 4.3. However, some regions of negative vorticity were more extensive than could be caused by this effect alone.

## 8. Discussion of Results

### 8.1 Rectilinear Flow

In the general description of the flow around a body of revolution in Section 3.5 the possibility of a secondary vortex being generated downstream of the primary vortex

was mentioned. The vorticity contour plot for  $\alpha = 15$  degrees shown in Figure 28 clearly reveals the presence of this secondary vortex system. It is much less diffuse

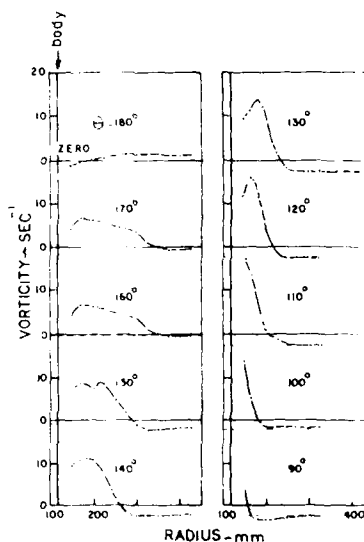


Figure 30  
Vorticity Traverses in Curved Flow  
 $r' = 0.2$ ;  $\alpha = 5$  degrees;  $x_R/L = 0.925$

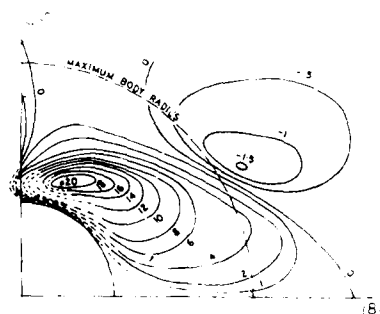


Figure 31  
Vorticity Contours in Curved Flow  
 $r' = 0.2$ ;  $\alpha = 5$  degrees;  $x_R/L = 0.925$

than the primary vortex and the peak vorticity is not so high. The primary vortex is located further toward the windward side of the body and this reinforces the belief that it is the result of flow separation near the tail.

### 8.2 Curved Flow

In curved flow the angle of incidence varies along the length of the body. If the nominal angle of incidence (at midships) is small the local angle of incidence at the nose and tail of the body are given approximately by

$$\alpha_N = \alpha - \tan^{-1} \frac{r'}{2} \quad \text{radians} \quad (40a)$$

$$\alpha_T = \alpha + \tan^{-1} \frac{r'}{2} \quad (40b)$$

The local angles of incidence for the conditions tested on the Rotating Arm are given in Table 3.

Figure 32 illustrates this variation of flow direction. For large angles of incidence and small turn rates the flow is always from the outboard side of the body and any shed vortices would be expected to reside on the body's inboard side. For small angles of incidence and high turn rates the angle of incidence at the nose becomes negative and the local flow direction at the nose is then from the inboard side of the body. In these circumstances we might expect to find flow separation and shed vorticity of opposite sign on the outboard side of the body. In due course this negative vorticity would be expected to be convected around the body to the inboard side. It would then appear either as a reduction in the level of vorticity or as a separately identifiable pocket of negative vorticity.

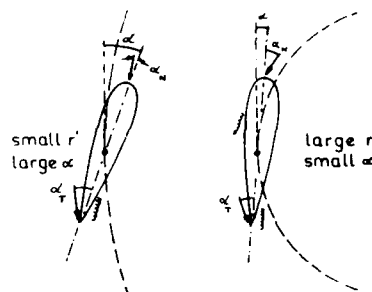


Figure 32  
Local Angles of Incidence at the  
Nose and Tail of the Body

Separate pockets of negative vorticity were sometimes identified. One such pocket can be seen in Figure 31. In most cases these negative areas of vorticity were not particularly well correlated with the negative angles of attack at the nose of the body. They may have been caused by the local discontinuity at the rotating joint in the skin of the model or by errors caused by the finite size of the probe (see Section 4.3).

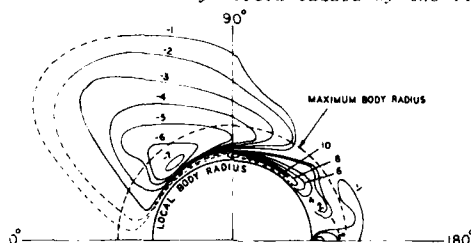


Figure 33  
Vorticity Contours in Curved Flow  
 $r' = 0.3$ ;  $\alpha = 2.5$  deg;  $x_R/L = 0.85$

### 8.3 Circulation

Each vorticity contour plot was integrated using a planimeter to obtain the "volume" under the contours. This is equivalent to the total circulation (see Eq 20). The integration was confined to the positive vorticity contours of the "tail" vortices.

The resulting total circulation is plotted in non dimensional form in Figure 34. As expected, the circulation increases monotonically with incidence, but appears to reach a maximum value at  $r' = 0.35$ . This may perhaps be attributed to the influence of the negative vorticity emanating from the nose of the body at high turn rates, as described above.

The traverses at  $x_R/L = 0.85$  were, however, extended around towards the outboard side of the model for the condition  $r' = 0.3$ ,  $\alpha = 2.5$  degrees and the results are shown in Figure 33. This model test condition experienced quite large negative angles of incidence at the nose (see Table 3) and the vorticity contour plot does indeed show a substantial vortex of opposite sign on the outboard side of the body.

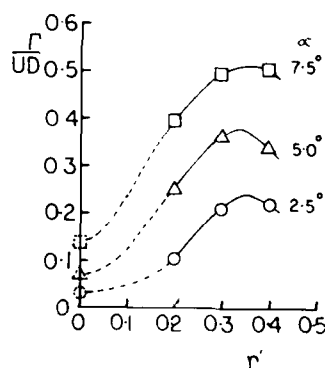


Figure 34  
Total Circulation in Curved Flow  
 $x_R/L = 0.925$

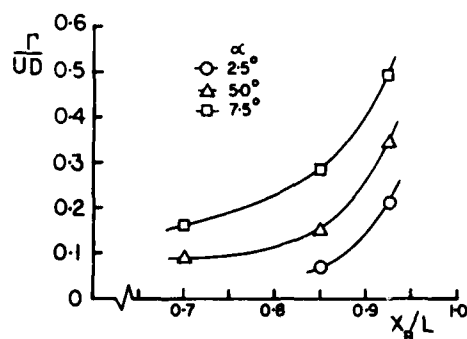


Figure 35  
Growth of Circulation in Curved Flow  
 $r' = 0.3$

Figure 35 shows the growth of circulation with distance from the nose of the body for  $r' = 0.3$ . As expected, the circulation rises rapidly towards the tail of the body.

#### 8.4 Body Vortex Location

Figure 36 shows the radial and polar location of the estimated centres of the body "tail" vortices. In many cases the exact vortex centre (the position of maximum vorticity) could not be precisely determined because the probe could not be positioned close enough to the surface of the body.

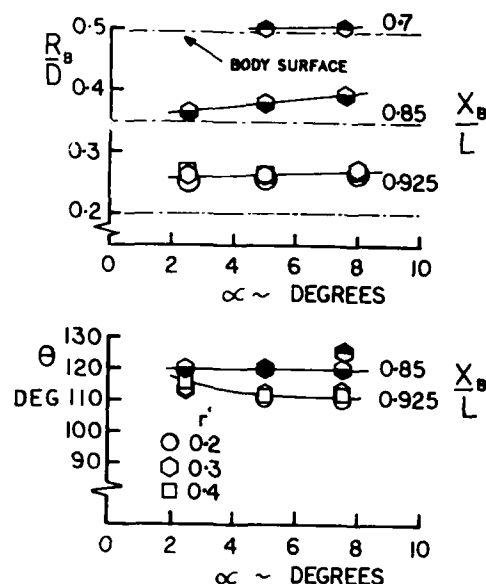


Figure 36  
Estimated Location of Vortex Centres  
in Curved Flow

The results should therefore be treated with caution. Nevertheless, they show, as expected, that the vortex hugs the surface of the body and migrates around it towards the outboard side as the tail is approached. The vortex tends to depart from the body surface as the incidence is increased but has little effect on the vortex location.

#### 8.5 Body Vortex Core Radius

Eq 37 was used with the calculated total circulation to estimate equivalent core radii for each of the vorticity contour plots obtained. Results are given in Figures 37 and 38. Given the difficulty of estimating the peak levels of vorticity for each case and the somewhat unwarranted assumption that the vortex is circular (implicit in Eq 37) the results must be treated with some circumspection. Nevertheless, they show that the core radius is of the order of one tenth of the body diameter and seems to increase with the angle of incidence and decrease with turn rate.

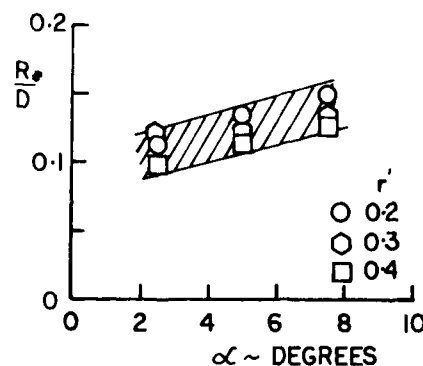


Figure 37  
Body Vortex Core Radius: Effect of  
Incidence and Turn Rate  $X_B/L = 0.925$

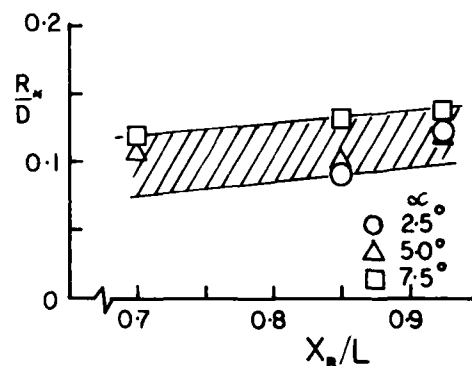


Figure 38  
Growth of Body Vortex Core Radius  
with Distance from the Nose  $r' = 0.3$

### 9. Conclusions

This paper has described experiments to investigate the vortex system associated with a body of revolution at an angle of attack in a curved flow. To the authors' knowledge this is the first time such experiments have been attempted and these experiments also represent the first serious use of the Freestone vorticity probe.

The Freestone vorticity probe proved to be simple and robust in use although a very sensitive pressure transducer was required in the present application. Some difficulties were encountered with spurious vorticity readings obtained when the probe was pitched or yawed in a uniform flow. The probes were also found to be potentially sensitive to changes in the dynamic pressure. In the 5 mm probe B these errors were of significant proportions and were traced to inadequate quality control of the alignment of the Conrad tube pairs and the finish and accuracy of their chamfered faces. Clearly the yaw meter faces must be as nearly as possible identical so that equal and opposite pressures are produced in uniform flow. Manufacturing problems were eased by adopting a larger probe C with a radius of 10 mm and this proved much more satisfactory. The larger probe had the added advantage of yielding larger pressure differences due to vorticity but it may have led to underestimates of the peak vorticity.

One problem with the Freestone probe lies in the difficulty of calibration if the individual yaw meter tubes are permanently connected to the plenum chambers. This arrangement precludes separate calibrations and the only way a satisfactory calibration can then be achieved is by measuring the response to a known level of vorticity. Clearly this is impractical but it has been suggested that a given level of vorticity might be simulated by spinning the probe in a uniform flow. This would, of course, introduce problems of extracting the pressure response from the spinning probe but these should not be insurmountable.

The probe was used to examine the vortex systems generated by a model hydroplane and a body of revolution in rectilinear and curved flows. Integration of the vorticity contours behind the hydroplane yielded a total circulation comparable to that expected from an estimation of the lift and supported the belief that the probe gave a generally satisfactory measurement of vorticity. The results were used to estimate the growth of the vortex core. This proved less satisfactory because the high turbulence level experienced in the Circulating Water Channel made the vortex appear to grow at an unrealistic rate. Immediately behind the hydroplane, however, the estimated core radius was in very close agreement with independent wind tunnel measurements on wings of similar geometries.

In rectilinear flow the body vortex core locations agreed reasonably well with those obtained earlier in flow visualisation experiments on a model of smaller scale. The probe revealed the unexpected presence of a secondary vortex at an angle of attack of 15 degrees.

The main effort was devoted to examining the vortex system in curved flow and an extensive series of experiments was completed. These showed that the flow curvature generally increases the vortex strengths but does not shift the vortex locations very much. In certain circumstances a secondary system of vortices of opposite sense is apparently generated on the outboard side of the body and these may be responsible for limiting the total circulation in tight turns near the tail of the body.

The results obtained in this investigation will be incorporated in the SUBSIM computer program for predicting deeply submerged submarine manoeuvres.

## REFERENCES

1. LLOYD ARJM: Progress towards a Rational Method of Predicting Submarine Manoeuvres, RINA Symposium on Naval Submarines, London 1983.
2. DUNCAN WJ, THOMAS AS, YOUNG AD: Mechanics of Fluids, Second Edition, Edward Arnold 1970.
3. ROSE R, DEE FW: Aircraft Vortex Wakes and their Effect on Aircraft, CP795, Aeronautical Research Council 1970.
4. GROW TL: The Effect of Wing Geometry and Lower Surface Boundary Layer on the Rolled Up Vortex, MS Thesis, Pennsylvania State University 1967.
5. McCORMICK RW, TANGLER JL, SHERRIFFER HE: Structure of Trailing Vortices, Journal of Aircraft, Vol 5 No 3 May-June 1968.
6. WHICKER LP, SEHLINGER LP: Free Stream Characteristics of a Family of Low Aspect Ratio All Movable Control Surfaces for Application to Ship Design, DTMB Report 933, December 1955.
7. GLAUERT H, The Elements of Aerofoil and Airscrew Theory, Cambridge University Press, Second Edition 1959.
8. SPENCE A, TREBRIE WJG, Low Speed Tunnel Tests on the Flow Structure Behind a Body of Revolution of Fineness Ratio 16 2/3:1, RAF TN Aero 2406 October 1955.
9. MELLO JF, Investigation of Normal Force Distributions and Wake Vortex Characteristics of Bodies of Revolution at Supersonic Speeds, Journal of Aerospace Sciences, Vol 26 No 3 1959.
10. ORERKAMPF WL, BARTEL TJ, Symmetric Body Vortex Wake Characteristics in Supersonic Flow, AIAA Paper No 78-1337, 1978.
11. TINLING TF, ALLIEN CO, An Investigation of the Normal Force and Wake Characteristics of an Ogive Cylinder Body at Subsonic Speeds, NASA TN d-1297, April 1962.
12. FIDLER JF, Approximate Method for Estimating Wake Vortex Strength, AIAA Journal p633, May 1974.
13. FIDLER, JF, BATEMAN MC, Asymmetric Vortex Effects on Missile Configurations, Journal of Spacecraft, Vol 12 No 11, 1975.
14. THOMSON KD, The Estimation of Viscous Normal Force, Pitching Moment, Side Force and Yawing Moment on Bodies of Revolution at Incidence up to 90 Degrees, WRF Report 782 (Australia) October 1972.
15. FREESTONE MH, Approximate Measurement of Streamwise Vorticity in Aeronautical Flows by a Simple Pressure Probe, I Mech E Symposium on Developments in Measurement and Instrumentation Engineering, Hatfield Polytechnic, September 1985.

TABLE 1

## Dimensions of Bodies of Revolution

Model Code	Length metres	Maximum Diameter metres	Fineness Ratio	Volume metres <sup>3</sup>
DKF	1.524	0.179	8.5	0.0302
DMH	1.524	0.145	10.5	0.0198
DMJ	1.524	0.122	12.5	0.0139

TABLE 2

## Ordinates of Bodies of Revolution

$x'/L$	$R/R_{max}$
0.000	0.000
0.05	0.699
0.10	0.905
0.15	0.988
0.20	1.000
0.25	1.000
0.30	1.000
0.35	1.000
0.40	1.000
0.45	1.000
0.50	1.000
0.55	1.000
0.60	1.000
0.65	1.000
0.70	0.983
0.75	0.932
0.80	0.840
0.85	0.701
0.90	0.513
0.95	0.286
1.00	0.000

TABLE 3

## Test Conditions for Rotating Arm Experiments

Test Radius m	12.5			16.7			25.0		
Turn parameter r'	0.4			0.3			0.2		
Incidence angles deg									
at sword	2.5	5.0	7.5	2.5	5.0	7.5	2.5	5.0	7.5
nose	-8.8	-6.3	-3.8	-6.0	-3.5	-1.0	-3.2	-0.7	1.8
tail	13.8	16.3	18.8	11.0	13.5	16.0	8.2	10.7	13.2

## Conditions tested

Measurement section  
 $x/L$  from nose

92.5	x	x	x	x	x	x	x	x	x
85				x	x	x			
70					x	x			

A REVIEW OF THE NATO SPECIAL GROUP OF EXPERTS ON  
NAVAL HYDROMECHANICS AND RELATED PROBLEMS

John Charlesworth  
Head/Submarine Hydrodynamics and  
Experiment Services Division  
Admiralty Research Establishment  
Haslar, Gosport  
Hants PO12 2AG  
England

L. John Leggat  
Head/Hydrodynamics Section  
Defence Research Establishment Atlantic  
P.O. Box 1012  
Dartmouth, Nova Scotia  
Canada  
B2Y 3Z7

#### SUMMARY

The Special Group of Experts on Naval Hydromechanics and Related Problems [(SGE(HYDRO))] was formed following an exploratory meeting on 3 and 4 November 1982. Its formation was spurred to a large degree by the need within NATO for a forum to promote multinational co-operation in the general area of naval hydromechanics testing and research for problems not adequately covered by other NATO international exchange groups and the International Towing Tank Conference.

The Group's mandate allows it to address current aspects of interest to naval hydromechanics including test and research facilities, testing techniques and instrumentation, prediction methods, model to full scale correlations, full scale trials, model tests, mathematical modelling and simulation and implications of instrumentation development in other fields of activity.

Four Research Study Groups (RSG) have been formed. The RSG's on Full Scale Wave Measurements and on Sea Loads, Slamming and Green Seas Impact and Wake Measurements finished this phase in December 1985. The RSG on Cavitation Noise Scaling completed its initial planning phase in June 1986.

The paper outlines the scope and objectives of the SGE(HYDRO) with special emphasis on the activity of the RSGs. In particular, the hydromechanic problems being addressed by the RSGs and the approach the RSGs have adopted to conduct the research are described. Plans for future co-operative research are also outlined.

#### 1. INTRODUCTION

##### 1.1 Origins

In April 1982, on the initiative of the Netherlands, the Defence Research Group sponsored a seminar held in the Hague on Advanced Hydrodynamic Testing Facilities. This proved to be a stimulating three-day meeting, with 27 papers contributed by Canada, France, Germany, Italy, the Netherlands, Norway, the United Kingdom and the United States of America on topics ranging from "Open Water Testing for Seakeeping Research" through "Cavitation Test Facilities" "Acoustic Measurements", "Dynamic Tests for Manoeuvring" to "Tests in Wind Tunnels for Hydrodynamic Research"<sup>1</sup>.

The seminar culminated in a round table discussion which concluded that NATO needed a forum to ensure, particularly in times of financial shortages, that the best use was made of existing facilities and to co-ordinate the creation of new facilities. Furthermore there was a need for a forum to exchange classified information, and this was only possible within NATO; other bodies such as the International Towing Tank Conference had too broad a membership for such activities.

##### 1.2 Formation

Following exploratory meetings in NATO HQ in Brussels towards the end of 1982, the formation of the Special Group of Experts on Naval Hydromechanics and Related Problems [(SGE(HYDRO))] was authorized by the Defence Research Group (DRG) with the participation of Canada, Denmark, France, the Netherlands, Norway and the United Kingdom. The Group first met in June 1983, by which time the membership had grown to include Germany, Spain and the United States of America. There has since been the occasional involvement of Greece and Italy. Denmark has now left the Group. The first Chairman of the Group was Dr. Jan Dirkzwager of the Netherlands in recognition of the Netherlands' initiating events that led to the formation of the Group.

##### 1.3 Scope

The Special Group of Experts is concerned with a variety of aspects of naval hydromechanics testing and research which include:

- Test and Research Facilities,
- Testing Techniques and Instrumentation,
- Prediction Methods and Model to Full-Scale Correlation,
- Full-Scale Trials,
- Model Tests,
- Theoretical Aspects including Mathematical Modelling and Simulation, and
- Implications of Instrumentation Development in Other Fields of Activity.

The emphasis of the Group is based on naval issues such as the reduction of drag and noise of submarines; the behaviour of surface naval vessels in high sea states; the dynamic behavior of towed systems, bodies and arrays; and the performance of underwater weapons and advanced naval vehicles. Furthermore, the Group is not limited to hydrodynamics in the narrow sense, but includes the inter-relation between the medium and moving bodies and the resulting elastic effects, stresses and vibration covered by the term "hydromechanics".

#### 1.4 Objectives

With the background and scope already outlined, the SGE(HYDRO) has adopted the general objective to improve the overall effectiveness of the combined capabilities of the alliance in the area of naval hydromechanics through information exchange and multi-national co-operation. It is expected that this will be achieved by the following activities:

The exchange of information with a view to identifying areas of common interest suitable for multi-national co-operation.

Improvements of the conditions of mutual utilization of the existing facilities (test procedures; standards for testing techniques, equipment and data presentation; procedures for costing and charging for tests; and protection of classified or propriety information and equipment).

Making proposals for the improvement of existing facilities to make them more responsive to NATO needs.

Arranging for the temporary allocation of staff for such purposes as supplementing local staff for a period of time or educating staff in relation to techniques not available in their parent establishment.

Improvement of the mutual development and utilization of theoretical methods including mathematical modelling and simulation.

Exchanging information on national developments and projects concerning test and research activities or research projects, with a view to avoiding duplication of costly facilities or improving the design of plant facilities, and more generally improving the use of resources available to NATO.

Making proposals for such undertakings as performing tests, co-ordinating research programmes, and commonly funding facilities or research projects. Implementing these proposals either under SGE(HYDRO) auspices or otherwise.

#### 1.5 Mode of Operation

The Group has not differed from the other DRG Groups in using the medium of Research Study Groups as the best way to study special problems. It is the main purpose of this paper to discuss the groups formed so far, and the problems they are addressing. However, before considering their research tasks some mention should be made of hydrodynamic facilities. Through its member nations, the SGE(HYDRO) and its RSG's have a very wide range of hydrodynamic facilities from which to choose when addressing a particular task. It will be apparent from the following sections that the prediction techniques employed for hydrodynamic performance are often dictated by the facility chosen. It is not possible to survey all the facilities available, but the most common are towing tanks, cavitation tunnels, circulating water channels and seakeeping/manoeuvring basins. Less common and more specialist facilities include rotating arms, a depressurized towing tank, ice tanks and a reverberant water tank. These model test facilities are matched at full scale by ranges both for tracking and noise measurement, and again there is a wide diversity of capabilities. These facilities have been compiled into a catalogue which will become a NATO document<sup>1</sup>. The catalogue also makes reference to aerodynamic facilities that are known to be used for hydrodynamic work. The type of work undertaken has been primarily in the area of noise measurement and the survey of air flow over decks and around superstructures.

### 2. RESEARCH TASKS

#### 2.1 Topics of Current Interest

In the early stages of the SGE(HYDRO) a list of topics of current interest was developed by the participating nations. Table 1 lists the topics, and provides an indication of both the level of interest and ability to contribute, by nation, for each topic. Interest is ranked in descending order from the highest score of "A" to the lowest of "C", and similarly for ability to contribute, where the highest score is denoted by "1" and the lowest by "3".

Exploratory groups were then established to determine whether co-operation would be possible in two general topics: seakeeping and propulsion. A pilot nation was appointed for each topic. The United States took on the task for seakeeping and the Netherlands for propulsion. The pilot nations canvassed the membership, and on the basis of the returns determined the most promising areas for co-operative research. In the seakeeping topic, the two areas were Full Scale Wave Measurements (RSG 1) and Sealoads, Slamming and Green Seas Impact (RSG 2). The propulsion areas of common interest were Cavitation Noise Scaling (RSG 3) and Wake Measurements (RSG 4). These four RSG's were initiated in December 1984, and their initial planning phase was completed a year later. The Groups are presently pursuing their mandates. The duration of the RSG's is either 3 or 4 years. A description of the research of each RSG follows in later Sections.

#### 2.2 Relation to Other Bodies

Because of the large size of the naval architecture community, the SGE(HYDRO) must keep abreast of developments in other bodies with related interest.

Perhaps of most importance is the NATO NNAG IEG/6 on ship design and its sub-groups. All of the research being undertaken in the SGE(HYDRO) must be of direct relevance to the needs of the naval ship designer. Liaison with this body is maintained through national representatives and contact between the chairmen.



There are a number of other groups whose activities are complementary to those of the SGE(HYDRO). These include Project Group 27 (NATO Frigate Replacement), the Long Term Study on Naval Warfare MO/2005 (Implications of New Technologies for Maritime Operations), the International Towing Tank Conference, the Netherlands Ship Model Basin Co-operative Research, and the International Ship Structures Congress. Reports on the activities of these Groups are normally given at the meetings of the SGE(HYDRO) by members who either sit on the council or committees of these bodies, or by those who have attended their meetings and conferences.

The wish of the SGE(HYDRO) is to avoid duplicating work that may be underway in other fora. Thus the scope and progress of each RSG needs to be carefully reviewed to ensure that it does not address concerns that are already being pursued by working groups of other organizations. The SGE(HYDRO) is the only body whose interests are purely naval. Therefore while disciplines and technology developments may overlap with other organizations, the application of the technology in most cases is to naval problems and naval marine vehicles.

### 3. RSG 1 - FULL SCALE WAVE MEASUREMENTS

#### 3.1 Background

The wave characteristics of the world's oceans are of interest to nearly every facet of marine activity. From the naval architectural point-of-view, it is necessary to quantify the seaway during ship dynamics and structural loading trials. From these data, ship performance specifications and numerical prediction methods can be verified. In addition, accurate wave measurements are required to validate operational wave forecasting models, parametric idealized wave spectral models and wave climatologies.

Wave measurements are routinely carried out with confidence using point spectral buoys. When buoy outputs are analyzed using standard spectral analysis routines, the result is a satisfactory means of determining wave height and period relationships, and hence for defining sea state using conventional definitions. Wave spectra, in this case measured with a ship-borne wave recorder during seakeeping trials,<sup>3</sup> are shown in Figure 1.

Of course, a point spectral buoy can only define a wave elevation time series, suggesting a simple definition of the sea surface, as in Figure 2<sup>3</sup>. In reality, the sea surface is much more complex, with variation in wave direction as well as height and frequency. Figure 3 shows a directional spectrum measured during a seakeeping trial over 20 years ago.

Directional spectra like Figure 3 are amenable to idealization, as shown in Figures 4 and 5<sup>4</sup> where spectral energy is assumed to vary as  $\cos^2 \mu$  ( $\mu$  is the angle away from the predominant wave direction). Other variations have been proposed, but this simple generalization often has been used as the standard for ship design and for performance prediction applications.

Unfortunately, real sea states are generally the product of moving weather systems, and can best be described by multimodal spectra. Figure 6 gives an example taken from Reference 5, where an advancing low pressure system in the Norwegian Sea has superimposed a wind-generated sea on an old swell. The swell has a higher spectral peak than the wind generated sea. Clearly, a cosine-squared spreading function applied to a point spectrum could not describe this sea state.

Finally, Figure 7 compares directional spectral measured at the same site with two different buoy types<sup>6</sup>. While Figure 6 emphasizes the need for directional measurements, as opposed to estimates, Figure 7 suggests that we still have technical difficulty in doing so.

#### 3.2 Objectives

With the above in mind, RSG 1 determined that the research objectives for the Group would be follows: to establish reliable directional wave measurements and analyses and to expand the capability for providing reliable, routine measurements during full scale trials and operations.

To meet the objectives, a cooperative multinational trial is being planned for March 1987 off the coast of Newfoundland. This area was selected because of its good probability of high sea states and coincidence with the track of the now cancelled SIR-B' Space Shuttle Mission, which would have provided synthetic aperture radar (SAR) measurements of wave directionality. The object of the trial is to evaluate available directional wave buoys and SAR (which will now be provided only by aircraft). Directional wavebuoys will be deployed from the Canadian research ship CFAV QUEST and the Netherlands research ship R.N.L.S. TYDEMAN. Additionally, operational wave forecasts will be produced by the United States Fleet Numerical Oceanography Center (FNOCC), Monterey. The Center will provide directional wave spectral forecasts from the Global Spectral Ocean Wave Model (GSOWM).

#### 3.2 Experimental Arrangements

There are six nations participating in the trial: Canada, France, the Netherlands, Norway, Spain and the United States. Each country will participate in the trial by contributing scientists and instrumentation to teams aboard CFAV QUEST and R.N.L.S. TYDEMAN. Canada plans to deploy Endeco Wavetrack and Datawell Wavec buoys; the Netherlands, Datawell Wavec and Delft disposable buoys; Norway, a Wavescan buoy; Spain, a Datawell Waverider buoy; and the United States, Endeco Wavetrack, MBA Controls Ltd. Wavcrest, and Delft disposable buoys. France and Spain may deploy buoys currently under development. France and Germany will also fit infrared and ultrasonic relative motion probes to R.N.L.S. TYDEMAN to derive encounter point spectra.

Figure 8 shows the probable experimental stations for the RSG1 trial. R.N.L.S. TYDEMAN will work at a northern GSOWM grid point and CFAV QUEST at a southern one. At each of these stations a moored buoy, or

buoys, will be laid so that anchored and drifting buoys of the same type can be compared. During the trials, two days will be spent at an intermediate grid point where both comparative buoy and comparative seakeeping trials will be conducted.

Some of the SAR overflights will be conducted by the Canadian Centre for Remote Sensing (CCRS) Convair 580, which is supporting another experiment scheduled in conjunction with SIR-B'. The Labrador Marginal Ice Zone Experiment (LIMEX) is performing both local oceanographic and SAR measurements in the Newfoundland spring ice-pack marginal zone. The CCRS SAR overflights will supplement proposed flights by a NASA SAR and radar-altimeter equipped P-3 aircraft.

#### 4. RSG 2 - SLAMMING, SEALOADS AND GREEN SEAS IMPACT

##### 4.1 Background

The waters of the North Atlantic and North Pacific oceans provide some of the most severe wave conditions of the oceans of the world. As these areas are of considerable strategic importance to the navies of NATO nations, there is considerable interest in the degree to which the wave environment hinders the operability of naval vessels, and in the aspects of ship response which are primarily responsible for reduced seakeeping performance. Studies carried out by NATO MAC IEG/6 SG/5 have shown that slamming and green seas impact play a major role in limiting the speed of naval vessels of the frigate and destroyer size. Typically in seas approaching sea state 5 (6m significant wave-height), the most modern ships of this size are limited to speeds of about 20 kt. Older ships fare considerably worse. The IEG/6 SG/5 study which surveyed captains of NATO frigates and destroyers revealed that the prime cause of speed reduction was slamming and with green seas impact a secondary cause.

##### 4.2 Objectives

The importance of slamming and green seas loads on naval ship operations placed this topic high on the list of research projects that could be undertaken cooperatively. It was agreed that the aim of the research would be to investigate the mechanisms responsible for slamming and green seas impact with a view to identifying means of improving ship performance in high sea states.

RSG-2, comprised of Canada, Germany, the Netherlands, Norway, Spain, the United Kingdom and the United States, has recently completed its Initial Planning Phase. A plan for the study was formulated and tasks assigned to the participating countries. The research is heavily slanted toward experimental work. Both full scale trials and related model tests will provide a data base for bow flare slamming and green seas loading with which results from theoretical methods will be compared. The Canadian research ship CFAV QUEST will be the primary trials ship, with R.N.L.S TYDEMAN supplying additional data. The data from the full scale trial will be used for evaluating numerical modelling methods and results from physical model tests. Numerical modelling is presently underway in a number of the participating nations.

##### 4.3 Full Scale Trials

The focal point of the full scale experiment is the trial with CFAV QUEST. She is a 2200 tonne acoustics research vessel operated by the Defence Research Establishment Atlantic (Figure 9). The ship will be instrumented to allow measurement of ship motions, main girder strains, flare slamming pressures and green seas deck loadings. Measurements will take place in March 1987 in conjunction with the trial of RSG 1.

CFAV QUEST is not an ideal platform for the RSG 2 trial, but represents a platform of opportunity as a result of the RSG 1 work plan. Unfortunately, none of the participants could commit a frigate or destroyer for trials. This is particularly relevant as QUEST's large freeboard makes significant green seas loading events unlikely.

QUEST has recently completed a routine refit during which 10 pressure transducer recessed mountings were installed in way of the starboard bow flare as shown in Figure 10. The transducers are of a special design and are based on those used for measuring ice loads on oil rigs.

Canada will also provide instrumentation to measure and record the six components of ship motions and the main girder strains. Germany has offered to support the green seas load measurements. Both Norway and the United Kingdom will contribute to the analysis of the results.

##### 4.4 Model Tests

Model tests in sea conditions corresponding to the full scale trials will be carried out by Norway at the Norwegian Marine Technology Research Institute (Marintek), in Trondheim. It will be necessary to manufacture a new model of both QUEST and TYDEMAN, as existing models are not of a suitable scale. Canada or Spain will provide a new model for the tests. The model tests will address primarily the measurement of bow flare slamming pressures, as the measurement of main girder bending moments is a time consuming and expensive process on model scale, and model green seas loading tests are fraught with difficulties.

Drop tests of two-dimensional sections will also be conducted. These will provide insight into the development of the girthwise slamming pressure distribution and the influence of scale effects.

##### 4.5 Correlation Studies

To complete the study, comparisons will be made between theoretical, numerically derived results and those measured on model and full scale ships, for bow flare slamming pressures, main girder strains and deck wetness. The RSG 1 measurements will provide reliable and complete sea state description to the computer programs, many of which rely primarily on strip theory for prediction of ship motions and

relative bow velocity estimates used to predict slamming pressures. Strip theory, which is based on two-dimensional potential flow theory, is generally suitable for predicting the motions of slender ships such as frigates and destroyers but has been found less reliable for the prediction of wave induced loads. Fully three-dimensional methods (eg. finite difference methods) could be used to achieve improved predictive accuracy. The final report will assess the merits of the various predictive methods and will recommend additional research as into sea loads mechanism and predictive techniques.

## 5. RSG 3 - CAVITATION NOISE SCALING

### 5.1 Background

In addition to the interest in seakeeping which resulted in the two RSGs already discussed, the SGE(HYDRO) has had a particular interest in propulsion from the very outset. However, the interest is not primarily in speed, power, efficiency, endurance, etc, but is concentrated on the noise making propensities of propulsors and in this context, cavitation noise is of prime importance. This topic is critical to naval operations particularly in the area of underwater warfare, and this has been underlined by the conclusions of a number of long term scientific studies.

### 5.2 Objectives

The basic objective of the Group is the development of reliable cavitation noise scaling techniques. The SGE(HYDRO) envisaged that progress towards this goal could be achieved by studying the following topics.

Assessment of current scaling methods used by cavitation test facilities.

Selection and calibration of facilities most appropriate to the prediction of full-scale cavitation noise. This would include assessing background noise, reflection properties, etc.

Multi-facility comparisons with respect to measurement techniques.

Development of measurement systems.

Correlation between model tests and full-scale measurements to improve prediction reliability.

Noise measurement from a series of identically shaped model items (propeller forms or other shapes) to enable a judgement of scaling effects on cavitation noise prediction.

The Group has recently completed the preparation of its programme of collaborative activities to be undertaken during its working phase.

### 5.3 Assessment of Current Methods

This study was initiated with a survey of the state of the art on model cavitation noise measurements and acoustic scaling methods. The results revealed that a wide range of facilities are being used to conduct acoustic experiments, and a wide range of expertise is available within the countries that have provided the information. The most popular facility is the cavitation tunnel. This is to be expected since cavitation tunnels are readily available at most hydrodynamics testing establishments and the installation of a hydrophone is a simple task (Figures 11 and 12). However, they provide a constrained and possibly noisy environment, with the associated problems of detecting the signal against the background noise and converting the measurements to free field conditions. Alternatively, facilities such as the acoustic barge and planing craft largely eliminate these problems but there is much less control available over the test parameters. The depressurized towing tank provides an environment between these two types of facilities. For a wide range of frequencies, the direct sound field in the tank predominates the reverberant field. It is also possible to exercise better control over the major test parameters.

Most of the acoustic measurements appear to be made using omni-directional hydrophones, the lower limits on the frequency generally being due to the background noise level and the upper limits due to the characteristics of the instrumentation. The acoustic calibration techniques quoted for all the cavitation tunnels are similar and are based on comparisons between measurements using a known sound source at the propeller position in the tunnel and those using the same source and receiver in the free field.

The detailed test procedure varies between the facilities; however, it consists fundamentally of the measurement of the noise level with the propeller operating under given conditions (Figure 13), together with a similar measurement with the propeller replaced by a dummy hub (Figure 14). The results are generally presented as 1/3 octave band levels. The repeatability of the measurements is quoted as within 3 or 4 dB. Visual observation of the cavitation is a routine procedure during acoustic testing.

Specific information on the scaling methods employed to derive full-scale noise levels from model data were given by only two countries; namely, the Netherlands and the USA. This is partly a reflection of the fact that several countries have not yet reached the stage of attempting to predict full-scale performance. Clearly, collaborative development in this area will become more beneficial when additional countries have reached this stage in their studies.

### 5.4 The Way Ahead

The evaluation of all the data gathered during the planning phase of the Research Study Group has resulted in the proposed activities being categorized as follows:

Derivation of theoretical scaling laws,

Measurement Technology, and

Correlation between model and full-scale data.

Two areas of work where the diverse abilities of the members could be employed are considered to be the effect of free gas on high frequency cavitation noise and its inclusion in the scaling process, and the measurement and scaling of low frequency cavitation noise. A series of specific tasks relating the proposed activities in these areas of work has been determined. These tasks have been assigned to member countries. The scope of the tasks is outlined below.

For the derivation of theoretical scaling laws, an investigation is proposed into the use of hull pressure measurements to predict low frequency cavitation noise and a study into the physics of low frequency sound emission from propeller cavitation.

Under measurement technology, both the high and low frequency ranges can be considered in relation to the acoustics of the hydrodynamic facilities, the hydromechanic simulation of the problem and the special sensors and signal processing required particularly at low frequencies. Hydrodynamic simulation will include the physical modelling of the problem, turbulence stimulation, and nuclei seeding. The potential for development in all these areas is being explored for both fully-developed and incipient cavitation.

For correlation between model and full scale data, the assessment of current scaling methods will continue, accompanied by an exchange of the supporting model and full scale data in a standard format. There will also be an evaluation of the variability of full scale data and the reproducibility of model data.

#### 6. RSG 4 - WAKE MEASUREMENTS

##### 6.1 Background

This RSG, concerned with a propulsion topic, again places emphasis on advancing experimental techniques for defining the fluid flow conditions in which a propulsor operates. In the future, the results will allow better informed judgements to be made in balancing the often conflicting requirements for high propulsive efficiency and low propeller cavitation extents, noise and vibration. Again these attributes are of prime concern to naval forces. Lower noise and vibration levels will improve operational effectiveness by reducing the risk of detection and the interference with home forces sonar.

##### 6.2 Objectives

The main objective of the work is to establish a reliable and accurate wake prediction procedure for use in the design of propellers for surface naval ships. It was envisaged that this objective would be achieved by the following activities:

Reviewing existing full-scale and corresponding wake data.

Establishing the scaling methods currently used by each participant.

Evaluating on the basis of the above the suitability of existing scaling methods.

If existing methods were found to be inadequate, recommending further work that would be necessary to establish reliable and accurate alternative procedures.

It was foreseen that many of the recent measurements referred to above will have involved the use of Laser Doppler Velocimetry. It is therefore implicit in these activities that experience would be exchanged on the use of LDV in various types of hydrodynamic facilities and ship trial.

##### 6.3 Exchange of Existing Wake Measurement Data

No wake prediction procedure can be validated without reliable model and full-scale data. This, of course, is further complicated by the variety of ship types and the experimental facilities used to test them. So, as a first step, it was agreed to exchange such data as were available, particularly those relevant to naval vessels. Data have been made available by four countries, namely the United States, United Kingdom, Canada, and Germany. The data received cover the following topics:

From the USA - wake measurements on a surface ship, the R/V ATHENA, at model scale in a towing tank and in a wind tunnel at full-scale.

From the United Kingdom - wake measurements on a frigate, HMS PENELOPE, at model and full-scale. Figure 15, taken from Reference 7, indicates the type of data collected from this sort of work.

From Canada - model tests and full-scale trials data for the research vessel, CFAV QUEST.

From Germany - wake data for single screw merchant ships.

In addition to the above, the United States made available wake data from wind tunnels for bodies of revolution in infinite flow, along with some full-scale submarine data. Also, Spain was able to provide some model wake data for a frigate and two corvettes.

#### 6.4 Wake Measurement Techniques

Much of the current interest in wake measurement techniques is linked to the use of lasers, and there are many international fora which are active in reporting the use of LDV systems in a wide variety of applications. However, it is clear that the countries currently operating LDV systems (Germany, Netherlands, France, the United Kingdom and the United States) in their hydrodynamic facilities are using them in a development sense rather than as a routine experimental technique. Thus, interest was expressed in exchanging experiences on these developments. However, it was considered that this would be most effectively achieved by bi-lateral exchanges.

#### 6.5 Wake Scaling Methods

Statements on current wake scaling methods have been received from four of the countries participating in the group. Most countries consider that for twin screw ships, wake scaling for the mean wake is unnecessary. For single screw ships scaling is necessary, and the ITTC method is used. However, this approach meets with varying success. Despite the general consensus on the situation regarding single screw and twin screw ships, there were some interesting views expressed. For example, the Netherlands use a semi-empirical method and are of the opinion that this method needs to be improved. Similarly, Italy considers that there is considerably more to be discovered about scale effects on wakes and was interested in investigating this subject collaboratively. Recent work in the UK (Reference 8) has also concluded that existing theoretical and experimental work requires further extension in order to address fully the problem of predicting the influence of wake on cavitation, for developing improved, noise reduced hull, propulsor combinations.

### 7. CONCLUDING REMARKS

It is apparent from the foregoing that there is a great diversity of capabilities and facilities available to the defence hydrodynamic and naval architectural community within the NATO Alliance. The SGE(HYDRO) is only three years old and there is much to be done if the groups objectives are to be achieved. A start has been made particularly in the areas of information exchange, testing techniques and instrumentation, full scale trials, prediction methods and model to full scale correlation. However, the SGE will now need to pursue vigorously those topics which are unique to a forum devoted to the naval operational requirement. It will also need to forecast the future needs of the defence hydrodynamics community and in this it will be greatly aided by the deliberations of the Panel on Long-Term Scientific Studies.

#### 7.1 Extension of Research Tasks

It is clear from Table 1 that difficult choices had to be made in selecting the topics for study by the existing RSG's. There is no doubt that the work already in hand, particularly full-scale wave measurements, could lead to studies of stabilization and the damaged and ultimate stability of ships. Similarly the investigations of sealoads can be followed by work on the optimization of hull fairing. In the propulsion field, wake measurement has obvious application to afterbody design methods and could also be extended to consider other forms of marine vehicles, eg Small Waterplane Area Twin Hulled (SWATH) vessel, submarine etc. Likewise, cavitation noise scaling is directly relevant to propeller design methods. All these subjects have received priorities when considered by the SGE(HYDRO) and its exploratory groups.

The research tasks can also be extended by putting more emphasis on the consideration of specific marine vehicles rather than on aspects of hydrodynamic performance discussed above. In this context some interest has been shown in the SWATH vessel concept, the surface effect ship and towed systems. The model testing and prediction of performance of these vehicles offer challenges which have still to be accepted.

#### 7.2 Development of Experimental Techniques

It is a fundamental aspect of the work of SGE(HYDRO) to be concerned with testing techniques and instrumentation, and with the implications of instrumentation developments in other fields of activity. The time is perhaps opportune to carry out a review of topics of common interest in these fields of activity as they relate to hydrodynamics. Some topics which could be pursued have already been mentioned; eg pressure transducers for full scale and model work, noise measurement, laser Doppler velocimetry particularly with the full-scale application in mind. However, there are other topics such as tracking systems, acoustic and optical methods for model and full-scale manoeuvrability and control work, wave generation equipment for seakeeping basins and so on.

#### 7.3 Use of Aerodynamic Facilities for Hydrodynamic Studies

Mention has already been made of the use of aerodynamic facilities for noise measurements and for the study of air flow over decks and superstructures. There will undoubtedly be a continuing and growing need for wind tunnel tests particularly with regard to aviation facilities in ships. However, there are several other applications which deserve more extensive utilization. In the field of underwater vehicles, much work in the areas of flow visualization, propulsion and stability and control can be carried out in a wind tunnel. Work can also be carried out at high Reynolds numbers, which would otherwise be impossible and this is applicable for research on both underwater vehicles and surface ships. Some of the techniques used for underwater vehicles in flow visualization and boundary layer measurements can also be used for surface ships measurements by the employment of a double-hull model.

It can be seen, therefore, that there is considerable scope for the use of wind tunnels in hydrodynamic and naval architectural tasks and perhaps it will be the duty of SGE(HYDRO) to sponsor a symposium similar to this one, in the not too distant future, entitled "Hydrodynamic and Related Aerodynamic Studies Using Air Facilities".

1. Twenty-Second Defence Research Group Seminar on Advanced Hydrodynamic Testing Facilities. the Hague - Netherlands, April 1982.
2. NATO/DRG/SGE(HYDRO) Catalogue of Test Facilities, June 1984.
3. Canham, H.J.S., Cartwright, D.E., Goodrich, G.J., and Hogben, N.: "Seakeeping Trials on the O.W.S. Weather Reporter". Trans. RINA, Vol. 104, 1962.
4. Comstock, J.P. (Ed): Principles of Naval Architecture. The Society of Naval Architects and Marine Engineers, New York, 1967.
5. Lygre, A. and Krogetad, H.E.: "Maximum Entrophy Estimation of the Directional Distribution in Ocean Wave Spectra" Seminar on Measurements of 3-Dimensional Seas, Marintek, Trondheim, 3 June 1986.
6. Juszko, B.A.: "Directional Wave Spectrum Intercomparison Study. Volume III, Intercomparison of Results." Environmental Studies Revolving Fund Ref. 090-17-08, June 1985.
7. Canham, H.J.S.: "Resistance, Propulsion and Wake Tests with HMS PENELOPE", Transactions of the RINA, Vol 117, 1975.
8. Ball, W.E.: "The Influence of Ship Wake on Propeller Cavitation". ASME International Symposium on Cavitation Inception, New Orleans, December 1984.

TOPICS	CANADA	DENMARK	FRANCE	GERMANY	THE NETHERLANDS	NORWAY	SPAIN	UNITED KINGDOM	UNITED STATES
<u>SHIP DYNAMICS</u>									
1. Seakeeping	A1	A1	A1	A1	A1	A1	A3	B1	A1
2. Hull series tests for FDS - very slender ships, etc.	A1	C3	B2	B1	A1	C3	A1	B2	A1
3. Hull loading in seaway	A2	B2	A3	B1	A1	A1	A3	C3	B2
4. Rudder roll stabilization active control systems etc	A2	B1	A1	C3	A1	B3	B2	C2	B2
5. Transverse stability in high sea states	B3	A2	B3	A1	A1	A1	A2	B1	C3
6. Manoeuvring	C3	B1	B2	A1	A1	B3	B1	B1	B2
7. Submarine and underwater body dynamics	A3	A3	A1	A2	A1	C3	A3	A1	A2
<u>ADVANCED NAVAL VEHICLES</u>									
8. SMATH	A1	C3	B2	A3	A1	C3	B2	B2	A1
9. Surface effect ships	C2	C3	A1	A3	C2	C3	B1	C2	C2
<u>HYDRODYNAMICS</u>									
10. Section design (of hydrofoils)	A1	C3	C2	A2	B1	B1	B2	C3	A3
11. Propulsors - model/full-scale correlation	A1	A1	A1	A1	A1	A1	A1	A1	A1
12. Afterbody design - propeller - hull interaction	B2	A1	A1	A1	A1	A1	A1	B1	A1
13. Noise reduction measures (hull and propeller)	A2	B1	A2	A1	C3	B3	B2	A1	A2
14. Flow studies (visualization, etc)	B2	C2	B2	B1	B2	A3	B2	A2	B2
15. Propeller - hull interaction for submarines - vibration	A3	A3	A1	B1	A1	C3	B3	A1	A2
<u>TOWED ARRAYS</u>									
16. Towed array system dynamics	B1	C3	A2	A2	A3	A3	C3	A1	B2
17. Self noise of towed arrays	B2	C3	B2	A3	A3	C3	C3	C3	B3
<u>OTHER SUBJECTS</u>									
18. Ship strength and vibration - interaction	A2	C3	C3	B2	A1	C3	B3	C3	C3
			High	-	Low				
	Interests		A		C				
	Ability to Contribute		1		3				

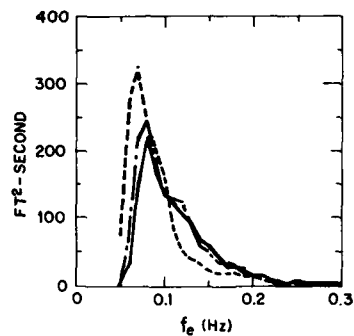


FIGURE 1: POINT SPECTRA MEASURED BY SHIP-BORNE WAVE RECORDER<sup>3</sup>

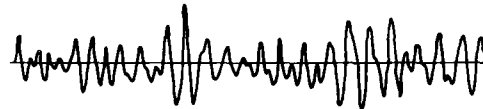


FIGURE 2: TYPICAL IRREGULAR SEA TIME SERIES<sup>2</sup>

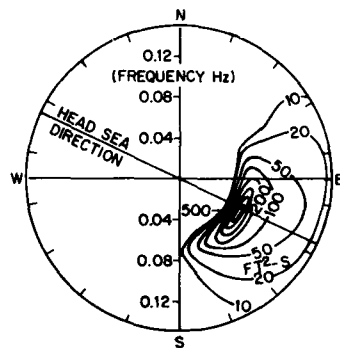


FIGURE 3: DIRECTIONAL SPECTRUM MEASURED BY WAVE-BUOY<sup>3</sup>

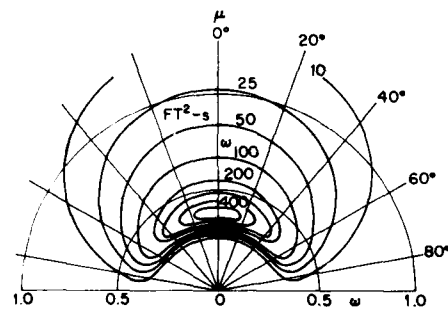


FIGURE 4: IDEALIZED DIRECTIONAL WAVE SPECTRUM<sup>4</sup>

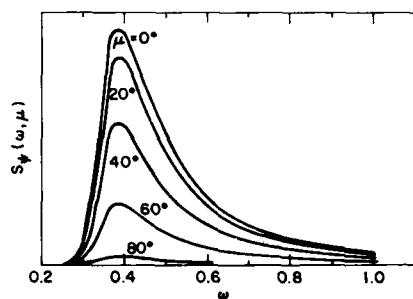


FIGURE 5: ANGULAR COMPONENTS OF IDEALIZED DIRECTIONAL WAVE SPECTRUM<sup>4</sup>

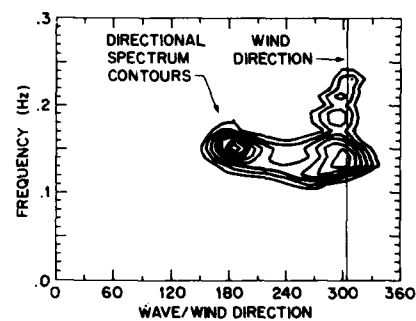


FIGURE 6: MULTI-MODAL DIRECTIONAL SPECTRUM MEASURED USING A WAVE AND METEOROLOGICAL BUOY<sup>5</sup>

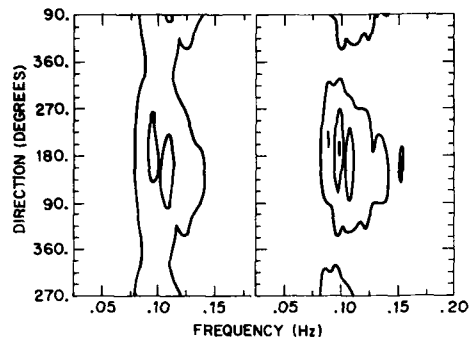


FIGURE 7: COMPARISON OF DIRECTIONAL SPECTRAL MEASURED BY TWO BUOYS AT THE SAME SITE\*

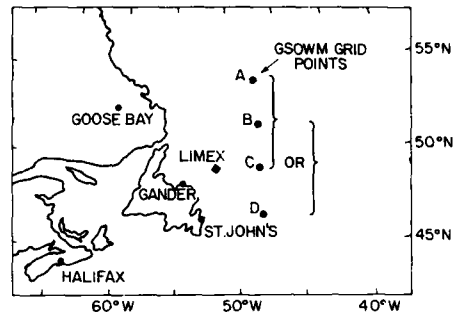


FIGURE 8: PROBABLE RSGI EXPERIMENTAL STATIONS AT THREE GSOWM GRID POINTS

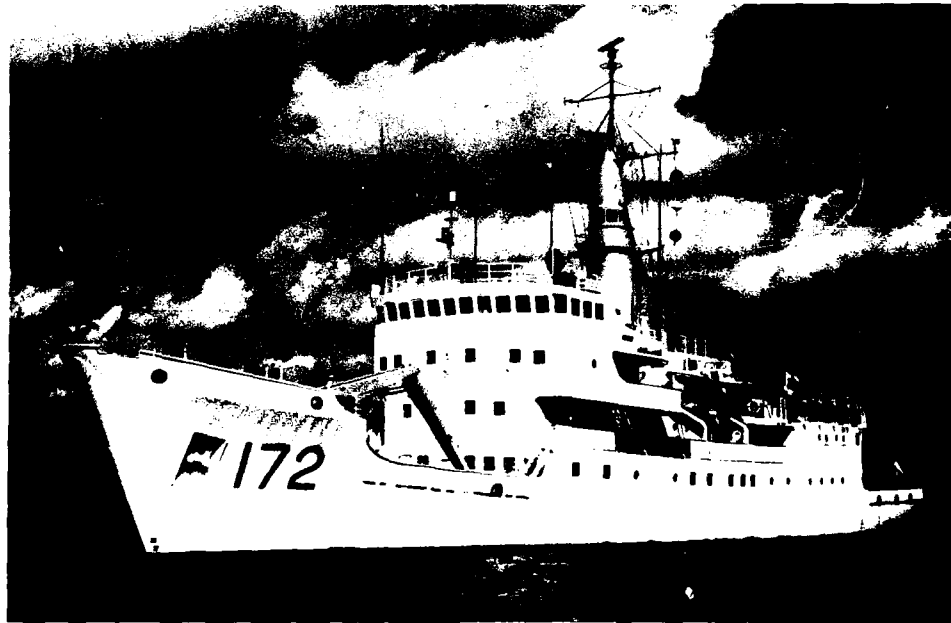


FIGURE 9: THE RESEARCH SHIP CFAV QUEST



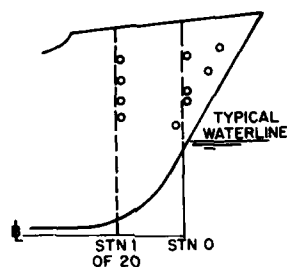


FIGURE 10: LOCATION OF PRESSURE TRANSDUCERS ON CFV QUEST BOW FLARE

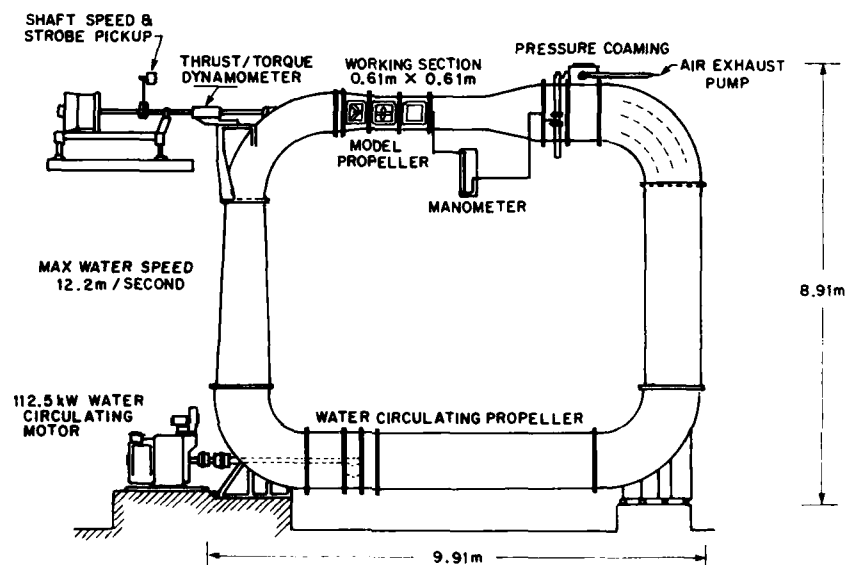


FIGURE 11: TYPICAL CAVITATION TUNNEL

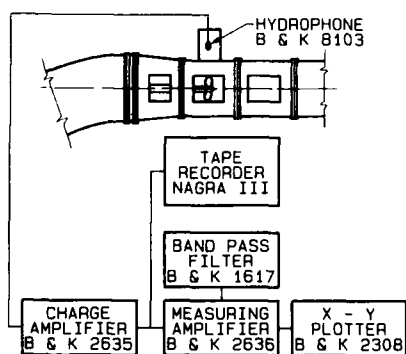


FIGURE 12: INSTRUMENTATION SCHEME

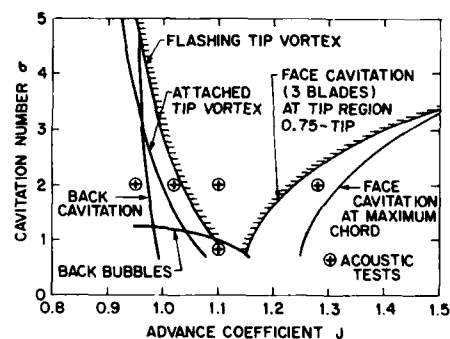
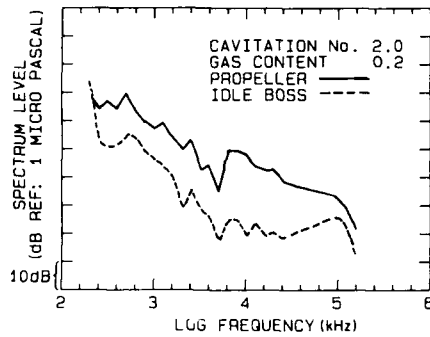
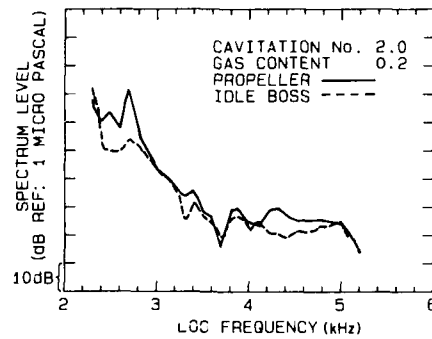


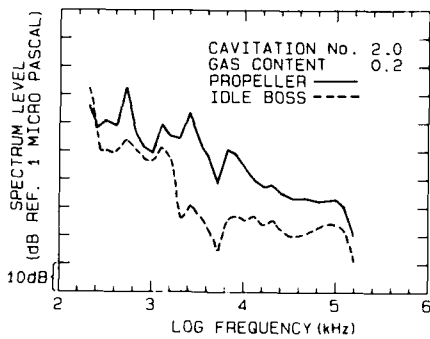
FIGURE 13: CAVITATION INCEPTION DIAGRAM SHOWING TYPICAL POINTS FOR ACOUSTIC TESTS



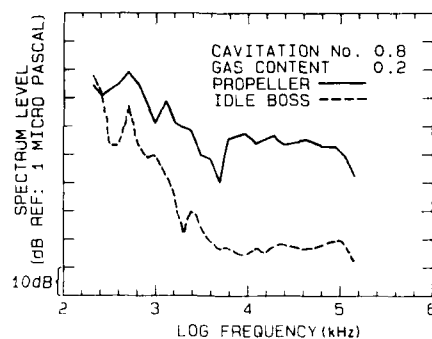
a. ADVANCE COEFFICIENT 1.01



b. ADVANCE COEFFICIENT 1.10



c. ADVANCE COEFFICIENT 1.20



d. ADVANCE COEFFICIENT 1.10

FIGURE 14: NOISE LEVELS MEASURED IN A CAVITATION  
TUNNEL RELATIVE GAS CONTENT 0.2 - 0.3,  
HYDROPHONE ABOVE PROPELLER

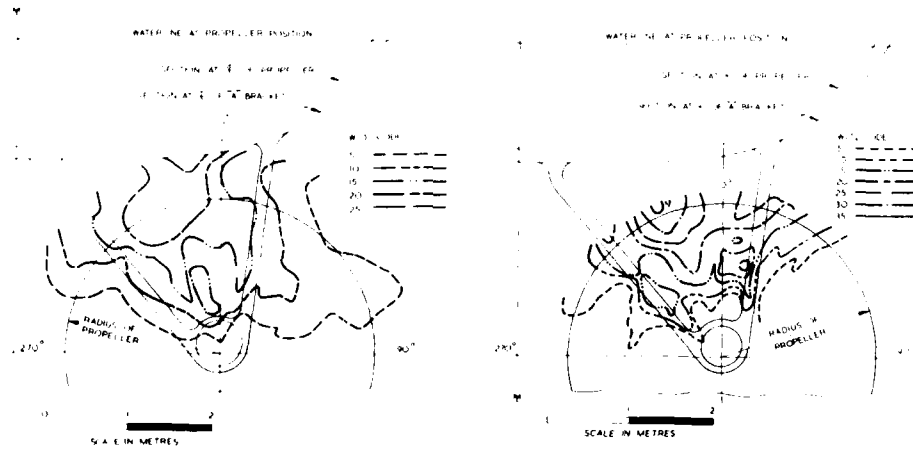


FIGURE 15: FULL SCALE AND MODEL SHIP WAKE

AGARD SYMPOSIUM  
AERODYNAMIC AND RELATED HYDRODYNAMIC STUDIES USING WATER FACILITIES

ROUND TABLE DISCUSSION

A.M.O. Smith

Thank you Dr. Slooff and Ladies and Gentlemen. It is both a pleasure and a responsibility to be here to outsmart you all and make significant comments, but I'll try. Dr. Slooff said that I had an aeronautics background and I want to mention once more that that probably influences my thinking to a certain extent. Also, I think that I should say that I am probably a biased critic here because I believe at least for an airplane type of project that there not only should be regular wind tunnel models, some low speed, high speed types, some aeroelastic models but also some kind of a flow visualization model to look at and see what you see and see if some wake is going someplace that you didn't quite expect it to and it leads to buffeting or something like that. If I was a chief engineer of some company starting a new airplane project, that is a model that I would insist on. Also a little bit of further background, I think I first got exposed to some of these odd problems back around 1950 or 1952 when I was involved in the problem of a tumbling body which has separations and everything else connected with it.

There was one French translated report in that area and that is all that I could find, and no aerodynamics textbook had anything on the subject. My most help was J.P. den Hartog's book Mechanical Vibration. It has some stuff about wire vibrations and that kind of thing. I talked to Dr. A.L. Kline at Cal Tech about this wild flow business to see if he could give me any help and he couldn't, but he characterized it as a term that maybe you should remember here when you think of some of the leading edge extension and strake types of flows and so on. He called it "funny aerodynamics". That was his term. One more thing, I thought back about other flow visualization meetings and in fact, I searched in the Cal Tech library a bit. While there are other meetings on turbulent flows and stuff like that, more specialized, I didn't really see any other meeting of this sort and I only recall, one which I attended in 1960, an ASME meeting on flow visualization. It was general flow visualization, not just water type of stuff. When you look back at that time and compare with now, we have sure made a lot of progress. We have got a number of different instruments and techniques. We have gotten lasers since then and LDV type of devices and of course computers. We had electronic computers then, but they were certainly a lot slower than those we have now. Also the fast Fourier transform has come in. I am not sure has been used in here, but I am certain with all the data handling and stuff that this is going to find a lot of use, too. Concerning techniques, as I sit here and remember the old days, you only had smoke and free surface type of testing like Prandtl did and things like that. Incidentally, I introduced the hydrogen bubble flow visualization at the ASME meeting, that is why I was there.

I really have a series of notes here, I don't have this very well organized. I couldn't get down to cases until last night after listening to most of the meetings. I have a note here that flow visualization is especially useful when you are not sure that you know the problem. That is one of the big reasons for doing it; you don't know where the flow is going and maybe you see a kink in some coefficient curve and you wonder why it is there. Well, what you do is you can do a lot of different kind of measurements or something or other, or you can get some flow visualization and you would probably see that there is some unwanted vortex going by someplace and it intersected something at that time. In fact I likened the problem of using regular force and hotwire and other kind of measurements to that of a blind man with a cane; he is trying to find out the shape of something or other. Similarly, you are going to do a lot of testing and you finally may come out with a good idea of the flow, but it is sure not like just looking at it. This meeting I would like to say was more general than most AGARD meetings because of the nature of the subject. It is a technique, it is not a specialized thing, let's say like turbulent boundary layers or some kind of turbulence or different kind of things like that. In fact I would say that the equivalent of this meeting is what's done and learned in windtunnels. If you wanted the analogue of this meeting, it is the same kind of symposium with wind tunnels. If you had such a meeting it would be pretty large and pretty diverse. It is also quite good to get all the flow visualization efforts together. That is probably why the meeting was organized so that everybody that is concerned with work like this are all in one place and see the different ideas and can trade information and all that kind of thing.

Furthermore it seems to me that the efforts have gained quite a bit more acceptance recently. Flow visualization, as I generally call it, but I am thinking of water type of testing too. Anyway flow visualization has not been a very important adjunct to regular type of testing and it seems to me in seeing all the facilities that have come up here and been mentioned, it is gaining further acceptance but it has a long ways to go. Another comment is that the use of water or liquids offers extreme versatility; that is the reason that we are here. I say liquids, I don't know the origins of this meeting, but in some ways I like to think of liquids other than water at times. Maybe you want to test something for some reason or other, something that is at real low Reynolds number, then you can get a highly viscous fluid and use it. Most of our work is looking at stuff as a whole, like an airplane where you wished you had higher Reynolds numbers. But sometimes I wished for low Reynolds number a long time ago. There was a flow in a suction slot for laminar flow control where the Reynolds number was about 100 or so, of course, this meeting also helps people who are developing methods because it brings all the ideas and techniques together. Also being all together like this it shows what can be done at the present time. Although I am not at all sure about this, I had the general impression that the techniques and tunnel part was a little bit better than the research result part. The reason I say that is mostly it seemed to me research results are the type of things more in the process of finding and the investigations haven't been completed. While that is true also for most of the tunnel and techniques, at least for the techniques type of stuff, I still have the impression that they are further along, for what it is worth. Also, I want to say that there is quite good progress in going quantitative.

RTD-2

I guess we could go quantitative in two-dimensional flows a long time ago. After all, even with the old aluminum powder tow tank technique one could look at the length of an aluminum particle and get some idea from a timed photo of the velocities and all that, but getting into three dimensions is something else, and it looks like we are getting there. There were quite a few papers here on that aspect, and I thought they all looked promising. Anyway I am impressed by all those methods. Another comment I have as well is that while general results in these different investigations can often be found, a lot of times the results are so complicated, e.g. let's say some of the strake flows, (that type of stuff has nothing to do with the flows down in the bottom of a boundary layer or anything like that) that you are not going to get very much general information, you are just going to find out the results for this general configuration of whatever sort it is and you'll use them in that case. I think over the years that you are liable to look at things in great detail and not come up with any kind of general answers. Of course, we have seen some of the general answers so the general answers accompany it like where to put the blowing on the strake where it is most effective, but there are still many problems. Well, we are getting to the point where we can look in such tremendous detail that every new thing is different.

In that connection with all this tremendous amount of data that I see there, I see a problem with the data handling and presentation. That's been faced some, but certainly it is one of the problems; as we get better and better in bringing out faster and faster measurements and stuff, we are just going to get swamped by all the data. People have to work on that problem. I have a little note here that reminded me of an old saying I have heard that a politician is one who knows less and less about more and more until he knows nothing about everything and a scientist knows more and more until he knows everything about nothing. I see some of that type of situation here which made me think of it as we get swamped with all the data. I just hope that all this detail will lead to fundamental improvements, really fundamental improvements. Just seeing more details isn't going to do us much good unless we can make further sense out of them.

I happened to talk with Prof. Young yesterday and he made an interesting comment. After all the earlier talks, really all the way through, tracing all those crazy vortices over wings and stuff, he commented that this meeting could be called one on vortical flows. It is in a way. Nearly any really complicated flow is a vortical flow; I guess it wouldn't be complicated if it didn't have any vorticity in it at all, it would just be potential flow.

Another note I have here is about not enumerating the advantages of using water. I thought of doing that in the beginning, but that has been too well covered. The whole week has been on that and there are some nice lists on the advantages.

There is another thing that I noticed; the argument comes up about Reynolds numbers, the low Reynolds numbers in much of this type of testing. One thing that is a bit of a saving feature is that when you can see the flow you have a better idea of whether Reynolds number is important. You can see generally whether a transition is there or some separation is occurring or something like that. I found in my old testing that maybe we would have some laminar separations on a body and we would put a trip on it, and when it was turbulent we would find that the turbulent separation point was about the same as a full scale. So you can just see a lot of things that counteract the low Reynolds number. It is a secondary advantage, I guess you would call it, of a water type of testing. Because you can see so much more, you make a lot more intelligent judgements. Also, the water facilities are generally cheap compared with wind tunnels. I don't know whether this will stay that way. If they become more popular, people may be willing to invest more money, then they will make bigger tunnels, and they will eventually get more expensive. Anyway, the cheap ones are certainly useful. Also I have a note here that I will not comment on the papers themselves. I would need to let them soak in more, and I am also not active in that area and not that self confident to make any real comments. I will still mention that several papers on quantitative evaluation which I have mentioned before in connection with three-dimensional type of stuff struck me as specially interesting.

A word of caution also; when I look at the pictures or slides, a lot of the slides, while you can see the flow on some kind of model, maybe its nothing more than a Karman vortex street behind a cylinder. But we are all fascinated by that kind of thing. We have to be careful, just seeing some pretty picture here is not necessarily an advance, after all, we have seen these pretty pictures. We saw them on Prandtl's film and several other places, and so when you do some kind of a simple flow, it's all right to show it, but you should be working towards some kind of an advance in the theory. I would look at a paper and a number of these pictures and maybe my first impression was that here was one more Karman vortex street or something or other, but gradually, I would see what someone was trying to do, and it would look like, in every case the objective was worthy, but it is something to think about in the future paper selections. Pretty pictures are not necessarily enough.

I had something I called oversights here. The first one was liquids. I just tend to think when it is a fluid, it isn't necessarily just water, it is water most of the time, but maybe it is glycerine or something else. It might be something to think about in any future one.

I also had a note about hot water. I wondered if it was going to be raised and it was. That's fine and the stratification also, and Prof. Hornung, I believe it was, mentioned about seeing vorticity or shear stress. He wondered if it could be colored or something or other. Way back about World War II days, there is a NACA report about using ethylene glycol and methyl ether acetate and then shining polarized light through it. Then you get direct measurements of shear stress. With all of our LDV devices and stuff like that, I don't know whether that is useful, but anyway there are different possibilities. Things like that were for the low Reynolds number tests. In fact, I was trying to sell something with that kind of a device which would essentially magnify the flow by about a hundred fold, a hundredth of an inch gap would turn into a one inch gap.

Cavitation has been talked about a good deal this morning, but there has been very little about the use of the old cavitation bubble, or air bubble, type of technique to get fairing shapes. I still think it is a good method, the Germans used it in some of their World War II fighter developments. I forgot, I used to know if it was for the ME 264 or 110. One of the things they did was to let some air in on the top side of the wing in a water tunnel and the air kind of spread out over it, and since they knew the pressures inside, they knew the velocities and they found that this bulge on the top side of the wing gave them 30 gallons more fuel capacity and reduced the drag at the same time. While that is not something that is in the transonic range, it is still a good first approximation a lot of times to getting some better fairing.

Incidentally, when I was down talking to Prof. Roshko about the meeting, T. Kiceniuk came in and reminded me of a technique that he had been involved in in running the water tunnel. We were trying to find the nacelle shape for the A3D. We just had a hollow tube for the air (water in this case) that went through the engine and then blew air on the outside so we formed a proper cavitation bubble. This was all under the wing on a complete model. In order to observe a shape, photo-gramatry is a way, but we were in more of a hurry. One fellow came up with the idea of putting little spines kind of like a porcupine about a sixteenth of an inch chord about two thousands of an inch thick. A whole series of little spines were soldered all around the tube, more than a hundred, just clear around. Then he copper flash-plated them. The spines were long enough to stick outside the bubble but not really disturb it. Then you turn on the electricity for a second or two and the part sticking into the water would plate off, and there you had the contours. It worked fine but we didn't pursue it further. That's about all I have to say. I'll close by saying again that for many problems, flow visualization with water is either needed or necessary, but if it is needed, it is the best way. So this symposium helps answer that need and I thought it was very good and there should be another symposium on this general subject in a few years, another one is in order some time in the future.

#### J.W. Slooff

Thank you very much Dr. Smith. I think that this has set the scene very well for the general discussion that we are supposed to have now. Maybe in order to put some structure in this discussion, we should try to follow roughly the order of the sessions that we have had these two days. We could start with comments or questions; whatever you have. As far as facilities are concerned, their possibilities and limitations and so forth, it is very difficult to separate the kind of techniques one uses in the facilities, so I think that we should address those at the same time and then have the second part of the discussion giving our attention toward the results.

Who would like to say something on facilities and techniques? By the way, please make sure that you say your name and affiliation clearly because this is being recorded. You will have a written version of what you said sent back to you which you can correct later, but if you don't announce your name and affiliation we won't be able to send it to you.

#### M.S. Cahn, Van Every and Associates

There has been quite a bit of discussion about the low Reynolds number that exists in most flow visualization water tunnels. I would like to make some comments on that.

- (1) Low Reynolds number is generally conservative if you're trying to prevent some damaging flow separation. If you are successful at the low Reynolds number, you are not too concerned about it at the higher Reynolds numbers.
- (2) For good flow visualization, the Reynolds number has to be small. When you are in a wind tunnel or a water tunnel or any other fluid, if you try a higher Reynolds number for purposes of seeing high Reynolds number or getting forces or something, you can't do the flow visualization, at least not as easily. You can't do it with food coloring in water, which is the cheapest way to do it that I know of.
- (3) It is better to have seen the flow at the wrong Reynolds number than not to have seen it at all. You shouldn't be afraid to look, but you ought to know some fluid mechanics, and then you won't be misled.

In the early '70's at Northrop we started using water tunnels for fast easy inexpensive testing. Now they are becoming more and more elaborate and I think that something has been lost. John Del Frates, who is here, did a lot of water tunnel flow visualization work and very good work, at NASA, Dryden. He has been quoted in an article as saying how valuable it was to see the flow field, and I like his expression when he said that, "there are no numbers here". In other words, the purpose of the water tunnel is to get an overall view of the flow field as A.M.O. Smith just said.

But looking at the water tunnels that have been built since we built a small simple one at Northrop it seems that something was lost. What has been lost? The Hamm's beer commercial says, "It's the water". Well in this case it is not the water. It was the availability of the facility and its ease of being used that made the water tunnel a very valuable research tool at Northrop and I'm sure at other places. If we wanted to know about a configuration or some problem in a new design, we could take a pair of tin snips and go to the water tunnel and cut out something and have a technician stick it in the water and look at it and in half an hour you saw what you were looking for; we often saw something we didn't expect, and we got a great insight into the problem. We had a smoke tunnel; whether we used it or the water tunnel depended on what we wanted to see or how much time we wanted to take; the smoke tunnel was often a little easier, you could stick your hands in it when it was running.

I think that in all companies or anyplace where people are interested in fluid flow, there should be what we called at one time a "crabgrass" laboratory. We now use the term "diagnostic" laboratory to mean a lab where fast, easy inexpensive research can be conducted. One of our configurations was in the design stage for nine years and much money was being spent on pressure tests and force tests to get data to four decimal place accuracy. We built a small 6 inch water tunnel and got our hands on a little display model and put it in the tunnel and put some food coloring in with a probe and saw immediately some fantastic things that we didn't know existed. As soon as we saw them, we said, "Oh, of course". You knew they were there after you saw them. But for 9 years we did not pay any attention to this particular region, so the point I am trying to make is that it is not the water that can make a water tunnel useful. It is the availability of the facility to the engineer. I think that there should be a "crabgrass" lab in any place where people are interested in fluid mechanics or fluid flow. And it should be available to the working engineer, this is an important point, just like the company library, and it could be even cheaper to operate than the company library. That is the important point that I think has been lost.

What other items should be in a "crabgrass" laboratory? There should be a computer with software that allows you to see two-dimensional flow fields. Maybe you can do three-dimensional, but I have an Apple II computer at home and I look at two-dimensional flow fields. Everyone says that two-dimensions are not important, because everything is three dimensional, but I learned in a book co-authored by Prof. Roshko that you had better get to know one dimension before you can understand two and you had better know two before you go to three. Most people never get past two; they explain everything in terms of two-dimensions.

I'm kind of upset with the way computers have been used in recent years. They have been used to crunch enormous masses of data and to do complex financial things. I learned some years ago when I was working with Dr. Tulin at Langley and Busemann, Katsoff and people like that, that using the elegance of two-dimensional flow theory, complex flow theory, you can always put together something that helps explain the phenomenon. Now that we have these modern computers that you can afford yourself, you can have one at home, in your bedroom or bathroom or wherever you want to use it, you can look at these two-dimensional flow fields and get a great insight into many fluid flow problem. I have been animating them, making several pictures, storing them in the computer and then recalling them rapidly and seeing animated forms of typical two-dimensional flow fields. I think that with a little better equipment, not even coming close to the Cray that we saw the other day, much more of this could be done and it could be compared with water tunnel flow.

One more important point about how to use quantitative data. All the quantitative measurements I have seen at this symposium of detailed structure of flow I think can be useful to get further insight into fluid flow at high Reynolds numbers. You can show that above a very low Reynolds number the inviscid flow is present. The inviscid flow is always there, even in separated flows, even when great separation occurs. The inviscid flow is there with vorticity super-imposed on it.

When flow is impulsively started you get the inviscid flow. With computer power handling the data and the measurement techniques we have seen here, we should be able to separate the inviscid flow from the flow that follows and then operate on the viscous flow and have it decay less severely and put it back in to get a great insight into flow at higher Reynolds numbers. That is the way some of these experimental techniques could be used, and I would like to encourage that.

Finally, I would like to say that I think that this has been a very interesting meeting. It has been one of the best I have seen since the days of the IAS. I would like to thank Prof. Roshko who I understand conceived this idea. I have enjoyed it very much. Thank you.

J.W. Slooff, NLR

Thank you very much Mr. Cahn for your very colorful contribution. Being a sort of number cruncher myself, I was particularly intrigued by your remark that a picture by itself can be very interesting and you don't always need numbers. I fully agree. I think that we all can appreciate a beautiful woman without numbers.

F. K. Owen, Comp'lere Inc.

I would like to take a few seconds to point out a couple of instruments or techniques that were not really mentioned in much detail at this meeting. The first one is the LV that to some extent was criticized for being a point measurement device. However, with very simple changes to the receiving optics, one can incorporate either a rotating or scanning mirror which could be synchronized with flow features so that measurements can be made which essentially freeze the flow. The point here is that since, in water, we have low velocities and ease of seeding, one can essentially obtain continuous wave LV signals, so that, by scanning the flow field in a rapid manner, one can get scan to scan variations and can look at the flow field turbulence structure in both space and time.

The other point I would like to make is that we also have techniques using fluorescent dyes to selectively seed the flow fields and trace the heredity of turbulent structures. For example, in the paper we gave on Monday morning when we were looking at the control of vortex flows, a better understanding of the mechanisms involved could be obtained by selectively seeding parts of the flow field and looking at the history and the development. In water, we can measure the velocity concentration cross correlation and from that one can determine mixing rates, and, conditionally sample at given concentration levels, so that we can look at what's happening to certain flow features as they progress downstream. Both techniques are referenced in my paper.

K.R. Saripalli, McDonnell Douglas

This is a comment on what Dr. Cahn said in three areas. Number one is the Reynolds number. He mentioned that flow visualization at high Reynolds numbers is difficult and we can't see much. I cannot agree with that in the sense that we did flow visualization at high Reynolds numbers, about a quarter of a million, using a high speed video camera and digital image processing techniques. We were able to get a lot more information than what you can see at low Reynolds numbers. So this kind of technique, that is being developed currently in the market, definitely will enhance the range of the Reynolds numbers that one can work with water using flow visualization and that is an added advantage that we will be having as water proponents.

The second thing is about the name that you give to the facility. For example, I was the first to propose a water facility to McDonnell Douglas which is primarily an aerospace company building fighter jets, and I had my own share of almost unsurmountable problems in getting approval and in coming up with an operating water facility. Anyway I overcame all of that, and we have a good working facility; but after having seen the results, the reaction of the management is 180 degrees opposite. Part of the reason for that I think has to do with the name you give to the facility. When you say that the water facilities are quick and dirty, I don't think that it is right. Because when you have a good Reynolds number simulation and good flow visualization techniques, it is no longer quick and dirty. It is a full and perfect replacement for a wind tunnel, in some cases at least. So, I think that the name you give to the facilities is also important. You should give it some fancy name just like wind tunnels.

The other comment I want to make is on the low Reynolds numbers. Dr. Cahn mentioned that the quick and dirty "crabgrass" laboratory could be given to operating engineers; but at the same time, they should be aware of the limitations or pitfalls that one can get into when you are working in low Reynolds numbers and extrapolating the results you get to the high Reynolds numbers. Unless you are aware of the complete range of the behavior of the particular flow at different Reynolds numbers, the extrapolations you make can really be very false depending on who makes it.

W.B. Morgan, David Taylor Naval Ship R&D Center

I just want to point out that the International Towing Tank Conference (ITTC) publishes a catalogue of facilities but unfortunately the ITTC does not have a permanent staff so one has to know whom to contact to obtain a copy. There are many towing tank people at this conference so if you want to contact one of us, we will try to obtain a copy of the catalogue for you. It seems that everybody here is making their own water tunnel; whereas in the marine industry most new water tunnels are purchased from Kemp and Remmers in Hamburg, Germany. So if you want to obtain a standard water tunnel, they can be purchased from off the shelf designs.

The second comment I will make is to expand on what Marshall Tulin said about the new cavitation tunnel that we are trying to build. As of this morning, it still appears to be in the budget. As Marshall said, the test section is 10 by 10 foot square with a length of 40 feet. I started out by calling it a 3 meter by 3 meter test section because I thought that sounded smaller, and we would be more apt to keep it in the budget. The tunnel is about 273 feet long, or slightly less in length than a football field, and the height is about 65 feet. This is not the size of the building, but the overall size of the water tunnel. This should give you some idea of the size of these large water tunnels. The tunnel is for testing model ships and submarines where we need to obtain a high enough Reynolds number to duplicate full scale flow phenomenon into the propulsor and over the appendages. I do appreciate the comments made on small facilities and of course we have a number of them and use them continuously, but when you are predicting cavitation or boundary layer flows into the propulsor or over stern appendages, these small facilities just don't do you any good at all. We need to obtain a section Reynolds number of the order of 5 million at the 0.7 radius of the propeller to obtain a good prediction of cavitation inception. The work done by Gault at Ames indicated that there is a possibility of laminar separation on some aerofoils near the leading edge at Reynolds numbers lower than 5 million. We have confirmed the need to obtain these relatively high Reynolds numbers for a good prediction of cavitation inception. As far as flow visualization is concerned, cavitation is a good flow visualizer so we do not have flow visualization problems during cavitation testing at these high Reynolds numbers.

J.W. Slooff, NLR

Before we hand the mike to Mr. Goodman again, I think it is fair to ask Dr. Lloyd to react on your first series of questions and comments on his paper if he wishes.

A.R.J.M. Lloyd, ARE(H)

Just to come back to the comments of Dr. Goodman. I'm not sure that I can remember everything that you said but one thing that was mentioned was why didn't we use 5 hole pitots. We could well have used them but the Freestone probe seemed to give very much the information that we wanted very much more quickly and very much more simply. A 5 hole pitot just gives velocity and direction and then you have to do lots of complicated traversing and data manipulation in order to obtain the vorticity measurements you really want. The other question which was raised was the one about lifting line theory. The paper is not really about the simulation, this is only briefly mentioned. It is true that simulation does use lifting line theory but this is corrected to take account of low aspect ratio. There was another question about static holes, and I think that I will ask my colleague Ian Campbell to reply to that one.

RTD-6

I.M.C. Campbell, University of Southampton

I think that with any instrument there are compromises that have to be made. We wouldn't like to put an instrument into the flow at all if we could avoid it, but with the restricted time that was available to do the test, the size of the test and the difficulty of operating off a rotating arm, we opted to use the Freestone probe because of the advantages it offered. As the paper indicates, the errors in the probe were examined as carefully as we could do and there is obviously still more work to be done. In particular, the effect of the nose on the static pressures into the static intake, of the pitot probe was calibrated during the wind tunnel tests on the probe. Finally I suspect that a lot of these inherent errors are of second order compared with the overall accuracies that we were looking for.

J.W. Slooff, NLR

Mr. Goodman, would you like to say something?

A. Goodman

Pitot-static tubes have been available for many, many years and are quite easily obtainable in this country, they are very inexpensive and can be acquired in small sizes of 4.5 to 5 mm in diameter. You can assemble them into a rake. I refer you to Reference 19 in my paper which gives the detailed description of the NACA work on the development of such probes as well as the description of the rake that was used in the study. I also ask you to contact Jerry Feldman when you visit him at NSRDC and examine the data in the other report I mentioned on the SON 688 which also used a similar pitot-static yawhead rake for quantifying the flow, for both the appended and unappended body. I also refer you to the NACA papers which deal with the design of such probes and the effects of the holder on the static pressure tube and the design criteria that they suggest which avoids problems of Reynolds number and other problems that you might encounter. As far as lifting line theory, that is an old story. In this day and age with lifting surface theories available, it seems for the sophisticated type of model that you are trying to achieve and for calculating the fin body interference effects the lifting line theory is not going to provide the correct answer. Bill Morgan preempted me on the ITTC. There is a very nice compilation which he mentioned which lists the major water tunnels, towing tanks, sea-keeping tanks, located throughout the world.

For example, Japan has 60 towing tanks, for those of you might be interested. The compilation presents all the physical characteristics and the capabilities. Without putting the burden on Prof. Bruce Johnson at the U.S. Naval Academy, he's on the committee that is responsible for maintaining the volume up to date, you might be able to contact him and if there are extra copies around, he might be able to send you one. With regard to Reynolds number, I think that we are all aware of the effects of Reynolds number on  $C_L(\max)$ . For example, on a lifting wing there is a very strong effect, the difference between a Reynolds number of 100,000 and several million is very well demonstrated in the literature. So I caution people when they are looking at high angles of attack or wings near stall to perform tests at high Reynolds number.

J.W. Slooff, NLR

Thank you Mr. Goodman for the valuable information on the ITTC, and also Mr. Morgan.

It seems the clock is almost at 1 and we will have to start bringing this to an end. Is there anybody still left that feels he would like to comment?

A.M.O. Smith

I don't have anything really more to say here, but I have listened to the arguments about low Reynolds number and everything, and I just want to remind you that this is an extremely diverse audience - all kinds of problems, anything from trying to find out some kind of wild convolutions in the bottom of a 1/16 inch thick boundary layer to some kind of flow over a 15 foot submarine, and I really don't see any kind of resolution of this kind of thing.

There are just going to be all kinds of tests and you better just remember that there are going to be some facilities for small investigations and some for large and there are going to be all kinds. Low Reynolds number has its place and high Reynolds number has its place. Just put it all together. I don't see any kind of a clean answer.

J.W. Slooff, NLR

I was almost going to say that this was a very appropriate final remark for this meeting, but there is one more comment.

K.R. Sarippali

I concur with what A.M.O. Smith said that just because you don't have the ability to simulate the right Reynolds number, you should not be discouraged. A perfect example is the helicopter test we presented. We did not simulate the Reynolds number appropriately, but the effects that we wanted to see were somewhat Reynolds number independent. So, that is why we were able to it in the water and also translate directly into the flight configuration with fantastic results. So, just because you are unable to simulate, you should not be discouraged.

The other thing that I wanted to mention was in response to what A.M.O. Smith said in the beginning that there is no flow visualization conference that deals just with flow visualization. But, for people who are interested in flow visualization, this is the perfect place to see all the latest developments in flow visualization.



J.W. Slooff, NLR

This has to be it, I am afraid. Thank you for all your contributions to the general discussion. I will now ask Prof. Roshko to close the meeting.

A. Roshko, Cal Tech

I would like to thank everybody that participated and I would like to turn the actual closing of the meeting to Peter Sacher, the Chairman of the Fluid Dynamics Panel.

P. Sacher, MBB

Ladies and Gentlemen, let me try to bring this Symposium to an end. We have been listening to more than 30 papers and we all have seen exciting examples for flow visualization, for new techniques, to help the engineers understand and to analyze the complex fluid flow situations. In the opening sessions it was said that the goal of this meeting was three-fold; to exchange experiences, to present results obtained by different applications, and to discuss the future prospects of this technology. I think according to many discussions at the end and during the meeting from the floor, and due to the excellent presentation of papers, I think this goal has been reached to a large extent. So first of all now I would like to thank all of our speakers for their delivery of excellent papers and the audience for participating actively in many discussions. I hope that you will agree to congratulate and thank very much our program committee for arranging this successful meeting and we acknowledge the tremendous effort made by the two co-chairmen of the program committee, by Prof. Anatol Roshko from Cal Tech and Prof. Joop Slooff from the NLR in Amsterdam.

In addition we have to thank all our members from the program committee and our session chairmen, Dr. Orlik Ruckemann, Dr. Bignell, Prof. Reshotko, Prof. Hornung, Dr. Bucciantini, for leading us through the various papers and the discussions. I would also like to address once more our appreciation to the National Delegates of the U.S. for having invited us. Especially I thank Dr. Flax for his opening remarks and Admiral Austin for his opening address and his warm welcome at the reception. We thank very much in addition the U.S. Naval Graduate School for providing this excellent technical facility for our meeting. I appreciate very much the sponsorship of Fluidyne Engineering Corporation from Minneapolis - they have provided the folders for all the participants.

An outstanding performance, I think we all agree, has been achieved by our local coordinator, Dr. Keith Richey from Wright Patterson for organizing the various activities throughout the whole week.

To conclude I have to address our acknowledgment to our technical staff which has supported this meeting. First of all I would like to thank our new Executive, Michael Fischer and his secretary Anne Marie Rivault for providing again excellent service on the administrative side. Then we have to thank specially Mrs. Cindy Maffei, Naval Post Graduate School from Monterey, Mrs. Karen Smith representing Major John Meeuwissen as the US National Coordinator for AGARD, Mr. Al Coleman and Mr. Kelvin Arrington technicians from the State Department, Washington, Mr. Harry Thomas, our projectionist here in the room and we have to thank our interpreters for doing an excellent work, Miss Madelaine Fishkin, Mrs. Monique Harway, Miss Lillian Paxson and Mr. John Woronoff. And last not least, Mr. Neal Grover and Mr. Jim Johnson, our U.S. hosts for doing all the work for the ladies program and arranging the tours. Thank you all very much for your excellent support.

Now let me conclude with a short review on FDP's future activities. Our program for 1987; we have two Symposia. The first on Aerodynamics of Hypersonic Lifting Vehicles in Bristol, UK in April next year and the second one in the fall on Aerodynamic Data Accuracy, Quality Requirements and Capabilities in Wind Tunnel Testing, in Italy. Then we have two special courses in Belgium at the von Karman Institute. One is on Modern Theoretical and Experimental Approaches to Turbulent Flow Structure and Modelling and the second on Missile Aerodynamics. We have currently three working groups running; on Boundary Layer Control and Simulation in Wind Tunnel, on 3-D Viscous Flow Boundary Layer Limits and on Rotary Balances. I would like to invite you here to participate also in our future activities and to join our future program. Thank you for attending this meeting.

REPORT DOCUMENTATION PAGE									
1. Recipient's Reference	2. Originator's Reference	3. Further Reference	4. Security Classification of Document						
	AGARD-CP-413	ISBN 92-835-0419-4	UNCLASSIFIED						
5. Originator	Advisory Group for Aerospace Research and Development North Atlantic Treaty Organization 7 rue Ancelle, 92200 Neuilly sur Seine, France								
6. Title	AERODYNAMIC AND RELATED HYDRODYNAMIC STUDIES USING WATER FACILITIES								
7. Presented at	the Symposium of the Fluid Dynamics Panel in Monterey, California, United States, 20-23 October 1986.								
8. Author(s)/Editor(s)	Various		9. Date June 1987						
10. Author's/Editor's Address	Various		11. Pages 476						
12. Distribution Statement	This document is distributed in accordance with AGARD policies and regulations, which are outlined on the Outside Back Covers of all AGARD publications.								
13. Keywords/Descriptors	<table border="0"> <tr> <td>Aerodynamics</td> <td>Fluid flow</td> </tr> <tr> <td>Hydrodynamics</td> <td>Test facilities</td> </tr> <tr> <td>Hydraulic test tunnels</td> <td>Meetings</td> </tr> </table>			Aerodynamics	Fluid flow	Hydrodynamics	Test facilities	Hydraulic test tunnels	Meetings
Aerodynamics	Fluid flow								
Hydrodynamics	Test facilities								
Hydraulic test tunnels	Meetings								
14. Abstract	<p>The papers contained herein review related problems, experiences and advancements in aeronautical and maritime fluid dynamics through the use of water facilities. In recent years there has been an increasing use of water facilities for aerodynamic investigations. These include water tunnels, towing channels and stationary tanks. Examples include basic research problems as well as flow fields around fighter aircraft, inlet flows, recirculation flow patterns associated with VTOL, ramjet simulation, etc. and, in general, three dimensional flows with vortices or separated regimes as prominent features.</p> <p>This Symposium was organized to provide an appropriate forum for the exchange of information within the aeronautical and maritime fluid dynamics community.</p>								

AGARD Conference Proceedings No.413 Advisory Group for Aerospace Research and Development, NATO AERODYNAMIC AND RELATED HYDRODYNAMIC STUDIES USING WATER FACILITIES Published June 1987 476 pages  The papers contained herein review related problems, experiences and advancements in aeronautical and maritime fluid dynamics through the use of water facilities. In recent years there has been an increasing use of water facilities for aerodynamic investigations. These include water tunnels, towing channels and stationary tanks. Examples include basic research problems as well as flow fields around fighter aircraft, inlet flows, recirculation P.T.O	AGARD-CP-413  Aerodynamics Hydrodynamics Hydraulic test tunnels Fluid flow Test facilities Meetings	AGARD-CP-413  Aerodynamics Hydrodynamics Hydraulic test tunnels Fluid flow Test facilities Meetings	AGARD Conference Proceedings No.413 Advisory Group for Aerospace Research and Development, NATO AERODYNAMIC AND RELATED HYDRODYNAMIC STUDIES USING WATER FACILITIES Published June 1987 476 pages  The papers contained herein review related problems, experiences and advancements in aeronautical and maritime fluid dynamics through the use of water facilities. In recent years there has been an increasing use of water facilities for aerodynamic investigations. These include water tunnels, towing channels and stationary tanks. Examples include basic research problems as well as flow fields around fighter aircraft, inlet flows, recirculation P.T.O	AGARD-CP-413  Aerodynamics Hydrodynamics Hydraulic test tunnels Fluid flow Test facilities Meetings
AGARD Conference Proceedings No.413 Advisory Group for Aerospace Research and Development, NATO AERODYNAMIC AND RELATED HYDRODYNAMIC STUDIES USING WATER FACILITIES Published June 1987 476 pages  The papers contained herein review related problems, experiences and advancements in aeronautical and maritime fluid dynamics through the use of water facilities. In recent years there has been an increasing use of water facilities for aerodynamic investigations. These include water tunnels, towing channels and stationary tanks. Examples include basic research problems as well as flow fields around fighter aircraft, inlet flows, recirculation P.T.O	AGARD-CP-413  Aerodynamics Hydrodynamics Hydraulic test tunnels Fluid flow Test facilities Meetings	AGARD-CP-413  Aerodynamics Hydrodynamics Hydraulic test tunnels Fluid flow Test facilities Meetings	AGARD Conference Proceedings No.413 Advisory Group for Aerospace Research and Development, NATO AERODYNAMIC AND RELATED HYDRODYNAMIC STUDIES USING WATER FACILITIES Published June 1987 476 pages  The papers contained herein review related problems, experiences and advancements in aeronautical and maritime fluid dynamics through the use of water facilities. In recent years there has been an increasing use of water facilities for aerodynamic investigations. These include water tunnels, towing channels and stationary tanks. Examples include basic research problems as well as flow fields around fighter aircraft, inlet flows, recirculation P.T.O	AGARD-CP-413  Aerodynamics Hydrodynamics Hydraulic test tunnels Fluid flow Test facilities Meetings

<p>flow patterns associated with VTOL, ramjet simulation, etc. and, in general, three dimensional flows with vortices or separated regimes as prominent features.</p> <p>This Symposium was organized to provide an appropriate forum for the exchange of information within the aeronautical and maritime fluid dynamics community.</p> <p>Papers presented and discussions held at the Symposium of the Fluid Dynamics Panel in Monterey, California, United States, 20—23 October 1986.</p> <p>ISBN 92-835-0419-4</p>	<p>flow patterns associated with VTOL, ramjet simulation, etc. and, in general, three dimensional flows with vortices or separated regimes as prominent features.</p> <p>This Symposium was organized to provide an appropriate forum for the exchange of information within the aeronautical and maritime fluid dynamics community.</p> <p>Papers presented and discussions held at the Symposium of the Fluid Dynamics Panel in Monterey, California, United States, 20—23 October 1986.</p> <p>ISBN 92-835-0419-4</p>
<p>flow patterns associated with VTOL, ramjet simulation, etc. and, in general, three dimensional flows with vortices or separated regimes as prominent features.</p> <p>This Symposium was organized to provide an appropriate forum for the exchange of information within the aeronautical and maritime fluid dynamics community.</p> <p>Papers presented and discussions held at the Symposium of the Fluid Dynamics Panel in Monterey, California, United States, 20—23 October 1986.</p> <p>ISBN 92-835-0419-4</p>	<p>flow patterns associated with VTOL, ramjet simulation, etc. and, in general, three dimensional flows with vortices or separated regimes as prominent features.</p> <p>This Symposium was organized to provide an appropriate forum for the exchange of information within the aeronautical and maritime fluid dynamics community.</p> <p>Papers presented and discussions held at the Symposium of the Fluid Dynamics Panel in Monterey, California, United States, 20—23 October 1986.</p> <p>ISBN 92-835-0419-4</p>

AGARD

NATO OTAN

7 rue Ancelle · 92200 NEUILLY-SUR-SEINE  
FRANCE

Telephone (1)47.38.57.00 · Telex 610 176

**DISTRIBUTION OF UNCLASSIFIED  
AGARD PUBLICATIONS**

AGARD does NOT hold stocks of AGARD publications at the above address for general distribution. Initial distribution of AGARD publications is made to AGARD Member Nations through the following National Distribution Centres. Further copies are sometimes available from these Centres, but if not may be purchased in Microfiche or Photocopy form from the Purchase Agencies listed below.

NATIONAL DISTRIBUTION CENTRES

**BELGIUM**

Coordonnateur AGARD — VSL  
Etat-Major de la Force Aérienne  
Quartier Reine Elisabeth  
Rue d'Evere, 1140 Bruxelles

**CANADA**

Defence Scientific Information Services  
Dept of National Defence  
Ottawa, Ontario K1A 0K2

**DENMARK**

Danish Defence Research Board  
Ved Idraetsparken 4  
2100 Copenhagen Ø

**FRANCE**

O.N.E.R.A. (Direction)  
29 Avenue de la Division Leclerc  
92320 Châtillon

**GERMANY**

Fachinformationszentrum Energie,  
Physik, Mathematik GmbH  
Kernforschungszentrum  
D-7514 Eggenstein-Leopoldshafen

**GREECE**

Hellenic Air Force General Staff  
Research and Development Directorate  
Holargos, Athens

**ICELAND**

Director of Aviation  
c/o Flugrad  
Reykjavik

**ITALY**

Aeronautica Militare  
Ufficio del Delegato Nazionale all'AGARD  
3 Piazzale Adenauer  
00144 Roma/EUR

**LUXEMBOURG**

See Belgium

**NETHERLANDS**

Netherlands Delegation to AGARD  
National Aerospace Laboratory, NLR  
P.O. Box 126  
2600 AC Delft

**NORWAY**

Norwegian Defence Research Establishment  
Attn: Biblioteket  
P.O. Box 25  
N-2007 Kjeller

**PORTUGAL**

Portuguese National Coordinator to AGARD  
Gabinete de Estudos e Programas  
CLAFa  
Base de Alfragide  
Alfragide  
2700 Amadora

**TURKEY**

Milli Savunma Bakanlığı  
ARGE Daire Başkanlığı  
Ankara

**UNITED KINGDOM**

Defence Research Information Centre  
Kentigern House  
65 Brown Street  
Glasgow G2 8EX

**UNITED STATES**

National Aeronautics and Space Administration (NASA)  
Langley Research Center  
M/S 180  
Hampton, Virginia 23665

THE UNITED STATES NATIONAL DISTRIBUTION CENTRE (NASA) DOES NOT HOLD STOCKS OF AGARD PUBLICATIONS. AND APPLICATIONS FOR COPIES SHOULD BE MADE DIRECT TO THE NATIONAL TECHNICAL INFORMATION SERVICE (NTIS) AT THE ADDRESS BELOW.

PURCHASE AGENCIES

National Technical  
Information Service (NTIS)  
5285 Port Royal Road  
Springfield  
Virginia 22161, USA

ESA/Information Retrieval Service  
European Space Agency  
10, rue Mario Nikis  
75015 Paris, France

The British Library  
Document Supply Division  
Boston Spa, Wetherby  
West Yorkshire LS23 7BQ  
England

Requests for microfiche or photocopies of AGARD documents should include the AGARD serial number, title, author or editor, and publication date. Requests to NTIS should include the NASA accession report number. Full bibliographical references and abstracts of AGARD publications are given in the following journals:

Scientific and Technical Aerospace Reports (STAR)  
published by NASA Scientific and Technical  
Information Branch  
NASA Headquarters (NIT-40)  
Washington D.C. 20546, USA

Government Reports Announcements (GRA)  
published by the National Technical  
Information Service, Springfield  
Virginia 22161, USA



Printed by Specialised Printing Services Limited  
40 Chigwell Lane, Loughton, Essex IG10 3TZ

ISBN 92-835-0419-4

END

DATE  
FILMED

11 - 88